Universidade de Aveiro
2024

Priscilla Oliveira Brosler

Superfícies de Diamante Eletroativas para a Remoção Eficaz de Poluentes Orgânicos Persistentes da Água

Electroactive Diamond Surfaces for Effective Removal of Persistent Organic Pollutants from Water

Universidade de Aveiro
2024

Priscilla Oliveira Brosler

Superfícies de Diamante Eletroativas para a Remoção Eficaz de Poluentes Orgânicos Persistentes da Água

Electroactive Diamond Surfaces for Effective Removal of Persistent Organic Pollutants from Water

Tese apresentada à Universidade de Aveiro para cumprimento dos requisitos necessários à obtenção do grau de Doutor em Nanociências e Nanotecnologia, realizado sob a orientação científica do Doutor Filipe José Alves de Oliveira, Investigador Principal do Departamento de Engenharia de Materiais e Cerâmica da Universidade de Aveiro, e sob a co-orientação do Professor Doutor João André da Costa Tedim, Professor Associado do Departamento de Engenharia de Materiais e Cerâmica da Universidade de Aveiro.

PT | Este trabalho foi desenvolvido no âmbito do projeto CICECO-Instituto de Materiais de Aveiro, UIDB/50011/2020 & UIDP/50011/2020, financiado por fundos nacionais através da da Fundação para a Ciência e Tecnologia/MCTES. Este estudo foi financiado pelo PRR - Plano de Recuperação e Resiliência e pelos fundos NextGenerationEU na Universidade de Aveiro, no âmbito da Agendas Mobilizadoras para a Inovação Empresarial "DRIVOLUTION - Transição para a fábrica do futuro" (Projeto n.º 23 com a candidatura C644913740-00000022). A autora deste trabalho recebeu apoio financeiro da Universidade de Aveiro na forma de uma Bolsa de Ciência e Gestão de Tecnologia BGCT/DEMAC/8407/2018 para a realização deste estudo.

EN | This work was developed within the scope of the project CICECO-Aveiro Institute of Materials, UIDB/50011/2020 & UIDP/50011/2020, financed by national funds through the Portuguese Foundation for Science and Technology/MCTES. This study was funded by the PRR – Plano de Recuperação e Resiliência and by the NextGenerationEU funds at Universidade de Aveiro, through the scope of the Agenda for Business Innovation “DRIVOLUTION - Transição para a fábrica do futuro” (Project no.23 with the application C644913740-00000022). The author of this work received financial support from the University of Aveiro in the form of a Science and Technology Management Scholarship BGCT/DEMAC/8407/2018 for the completion of this study.

Dedico este trabalho à minha irmã e ao meu pai, este cuja dedicação à ciência moldou diretamente minha jornada. Ambos não estão mais fisicamente conosco, porém o amor e apoio de cada um continuam a me guiar todos os dias, são minha fonte eterna de inspiração e saudade. Dedico igualmente este trabalho à minha mãe e ao meu irmão, pelo apoio incondicional, amor e paciência que demonstraram ao longo do tempo, suportando minha longa distância, mesmo durante os momentos mais difíceis.

o júri

Presidente

Doutora Maria Adelaide de Pinho Almeida
Professora Catedrática da Universidade de Aveiro

Vogais

Doutora Sandra Maria Fernandes Carvalho
Professora Catedrática da Universidade de Coimbra

Doutora Ana Maria Carreira Lopes
Professora Associada da Universidade da Beira Interior

Doutor João André da Costa Tedim
Professor Associado da Universidade de Aveiro

Doutor Diogo Miguel Franco dos Santos
Professor Auxiliar Convidado da Universidade de Lisboa

Doutora Paula Celeste da Silva Ferreira
Investigadora Coordenadora da Universidade de Aveiro

Agradecimentos

É com imensa gratidão que começo esta expressão de agradecimento, ciente de que só cheguei até aqui graças ao apoio e colaboração de muitas pessoas extraordinárias.

Meus pais, meu irmão e todo nosso círculo familiar, merecem minha gratidão por sempre me incentivarem a buscar conhecimento desde cedo. Sem o suporte e a motivação que recebi deles, nada disso teria sido possível.

Às pessoas que me guiaram e moldaram meu percurso acadêmico, meus orientadores, Doutor Filipe José Alves de Oliveira e Professor Doutor João André da Costa Tedim, minha profunda gratidão. Suas palavras de encorajamento, apoio incondicional, compreensão e humanidade nos momentos desafiadores, tanto no âmbito académico quanto pessoal, foram essenciais para o sucesso deste trabalho. Foi uma grande honra e privilégio ser orientada por vocês.

Desejo expressar minha sincera gratidão aos professores Doutor Francisco Cristóvão Lourenço de Melo e Professor Doutor Rui Ramos Ferreira e Silva. Foi com o apoio inabalável e a motivação que recebi deles que tomei a decisão de embarcar nesta jornada académica em Portugal, sem a qual este doutoramento jamais teria se concretizado.

Aos colegas investigadores que compartilharam esta jornada comigo, quero expressar minha apreciação. Sua presença e prontidão para superar desafios tornaram esta fase da vida mais leve e agradável, além de terem forjado laços de amizade que valorizo profundamente: Doutora Marina Mennucci, Doutora Violeta Girão, Doutora Isabel Sousa, Doutor Miguel Neto, Doutora Cristina Neves, Doutor Dhananjay Sharma e tantos outros que contribuíram para este trabalho.

Meus colegas de laboratório, vocês foram uma parte essencial deste processo, sempre dispostos a ajudar e trazendo bom humor ao nosso dia a dia. Marco Medeiros, Inês Oliveira, Mónica Faria, Doutora Aneeta Jaggernauth, Sérgio Pratas, Alice Marciel, Doutor Jorge Santos, Doutor Eduardo Silva, Doutor Ricardo Silva e todos aqueles que passaram por nosso laboratório, vocês são verdadeiros parceiros.

Ao grupo SECOP, minha gratidão por sua colaboração inestimável.

A todos os colegas e membros da equipe de técnicos, funcionários e professores do Departamento de Engenharia de Materiais e Cerâmica da Universidade de Aveiro, meu sincero agradecimento pelo suporte constante.

Agradeço também ao CICECO pelo apoio e contribuições fundamentais para o desenvolvimento deste trabalho.

Ao António José Silva Fernandes, o Tozé, do Departamento de Física da Universidade de Aveiro, minha gratidão pelas inúmeras vezes em que auxiliou na caracterização por Espectroscopia Raman, uma técnica que foi essencial para este trabalho.

À Doutora Helena Nadais e Diana Patoilo do Departamento de Ambiente e Ordenamento da Universidade de Aveiro, agradeço o apoio na caracterização das amostras de água contaminada.

Aos professores do Departamento de Engenharia de Materiais da Faculdade de Engenharia de Guaratinguetá, da UNESP, a todos os professores do Programa Doutoral em Nanociências e Nanotecnologia da Universidade de Aveiro, e aos colegas da Divisão de Materiais do Instituto de Aeronáutica e Espaço, do DCTA, minha gratidão pelas bases que me proporcionaram para este trabalho.

Aos amigos que fiz em Aveiro e em Portugal, que tornaram esta jornada mais alegre e significativa, tornaram este lugar um lar longe de casa, meu profundo agradecimento.

Aos queridos amigos de longa data, Ana Laura Areco, Ana Paula Meireles e Felipe Solferini, que, mesmo à distância, estiveram sempre presentes e me apoiaram, meu eterno reconhecimento.

Agradeço também à querida Bernardette Espírito Santo Brandão Fonsi, cuja orientação foi fundamental para minha resiliência e superação em momentos desafiadores. Sua ajuda foi um apoio inestimável ao longo desta jornada.

A meu companheiro, Pedro Rocha, meu mais sincero agradecimento pelo apoio incondicional.

Por fim, desejo expressar minha profunda gratidão à Universidade de Aveiro pelo apoio financeiro concedido por meio da Bolsa de Ciência e Gestão de Tecnologia. Este suporte foi fundamental para a realização deste doutoramento.

A todos que contribuíram, direta ou indiretamente, para este trabalho, saibam que sua participação foi fundamental.

A todos vocês, minha mais sincera gratidão. Este trabalho é também uma expressão da colaboração e do apoio que recebi ao longo desta jornada. Obrigado por fazerem parte desta realização.

palavras-chave

diamante dopado com boro, tratamento de água, poluentes orgânicos persistentes, oxidação eletroquímica, elétrodo funcional, deposição química em fase vapor, nitreto de silício, compósito cerâmico

Resumo

O tratamento eficiente da água contaminada por poluentes orgânicos persistentes (POPs) é uma questão de grande relevância ambiental e de saúde pública. Esses poluentes, conhecidos pela sua persistência e efeitos prejudiciais, exigem soluções inovadoras. Nesta tese, explorou-se a aplicação de elétrodos de diamante dopado com boro (BDD) em processos de oxidação eletroquímica avançada (EAOPs) como uma abordagem promissora para a remoção de POPs da água.

O trabalho teve início com uma revisão crítica da literatura, foi sendo atualizada ao longo do tempo, destacando os métodos EAOPs disponíveis e a sua superioridade quando utilizados em conjunto com elétrodos BDD, bem como a comparação com outros materiais de elétrodo. Também foi realizada uma análise comparativa entre elétrodos BDD de fabricação em laboratório e comerciais, destacando as diferenças e vantagens de cada abordagem. Além disso, conduziu-se uma avaliação abrangente de todos os parâmetros que influenciam as propriedades finais e desempenho dos filmes BDD, bem como métodos para avaliar o desempenho final dos elétrodos. Essa análise crítica estabeleceu a base para o desenvolvimento subsequente da tese.

Posteriormente, a pesquisa concentrou-se no desenvolvimento de um substrato inovador, composto por cerâmicos de Si_3N_4-TiN, que proporcionam durabilidade e robustez aos elétrodos BDD e são eletricamente condutores. Essa escolha de substrato visou garantir alto desempenho na remoção de poluentes e viabilidade de aplicação em larga escala. Além disso, explorou-se a otimização das condições de deposição dos filmes BDD por meio da aplicação do método Taguchi. Este estudo teve como objetivo aprimorar a qualidade dos filmes BDD e compreender os efeitos dos diferentes parâmetros de deposição nas propriedades finais dos filmes.

Após a otimização dos filmes BDD, procedeu-se à demonstração da eficácia dos elétrodos BDD/Si_3N_4-TiN na remoção de poluentes, tendo sido apresentada uma prova de conceito, focada na degradação do fenol, um dos POPs mais comuns na água. Essa fase experimental validou a abordagem inovadora.

Adicionalmente, investigou-se a modificação química das superfícies dos elétrodos BDD/Si_3N_4-TiN por meio de tratamentos de plasma, com o objetivo de melhorar o desempenho eletroquímico no tratamento de água contaminada.

Por fim, exploraram-se estratégias para melhorar a eficiência dos processos de oxidação eletroquímica com elétrodos BDD, apresentando um método inovador que consiste num processo cíclico de eletrooxidação com obstrução/reativação rápida, reduzindo significativamente o tempo e o consumo energético associados a processos de oxidação eletroquímica, um dos aspetos mais desafiantes na implementação destes métodos à escala industrial.

Em suma, este estudo destaca a importância de abordar os POPs e sua presença generalizada na água, sublinhando a necessidade de métodos de tratamento eficazes que cumpram os requisitos ambientais cada vez mais exigentes. Os EAOPs, particularmente em conjunto com os elétrodos BDD, emergem como uma solução promissora e eficiente para enfrentar esse desafio ambiental crucial, oferecendo benefícios como a degradação completa de poluentes sem a geração de produtos tóxicos, economia de energia e viabilidade de aplicação em larga escala.

keywords

boron-doped diamond, water treatment, persistent organic pollutants, electrochemical oxidation, functional electrode, chemical vapor deposition, silicon nitride, ceramic composite

abstract

The efficient treatment of water contaminated with persistent organic pollutants (POPs) is a matter of significant environmental and public health concern. These pollutants, known for their persistence and harmful effects, demand innovative solutions. In this thesis, the application of boron-doped diamond electrodes (BDD) in advanced electrochemical oxidation processes (EAOPs) was explored as a promising approach for removing POPs from water.

The research began with a critical literature review, highlighting the available EAOPs methods and their superiority when used in conjunction with BDD electrodes compared to other electrode materials. A comparative analysis between laboratory made and commercial BDD electrodes was also conducted, emphasizing the differences and advantages of each approach. Additionally, a comprehensive evaluation of all parameters influencing the final properties and performance of BDD films was carried out, along with methods to assess the overall electrode performance. This critical analysis laid the foundation for the subsequent development of the thesis.

Subsequently, the research focused on the development of an innovative substrate composed of Si_3N_4-TiN ceramics, providing durability and robustness to BDD electrodes. This substrate choice aimed to ensure high-performance pollutant removal and scalability.

Furthermore, the optimization of BDD film deposition conditions was explored through the application of the Taguchi method. This study aimed to enhance the quality of BDD films and understand the effects of deposition parameters on the final film properties.

To demonstrate the effectiveness of BDD/Si_3N_4-TiN electrodes in pollutant removal, a proof of concept was presented, focusing on the degradation of phenol, one of the most common POPs in water. This experimental phase validated the innovative approach.

Additionally, the modification of BDD/Si_3N_4-TiN electrode surfaces through plasma treatments was investigated to improve their electrochemical performance in treating contaminated water.

Finally, strategies to improve the efficiency of electrochemical oxidation processes with BDD electrodes were explored, presenting an innovative method involving a cyclic fouling and rapid reactivation process, significantly reducing the time and energy consumption associated with electrochemical oxidation processes.

This study underscores the importance of addressing POPs and their widespread presence in water, emphasizing the need for effective treatment methods that meet increasingly stringent environmental requirements. EAOPs, particularly in conjunction with BDD electrodes, emerge as a promising and efficient solution to tackle this crucial environmental challenge, offering benefits such as complete pollutant degradation without the generation of toxic byproducts, energy savings, and scalability.

Contents

List of Abbreviations, Acronyms and Symbols

ACE	Average current efficiency
AFM	Atomic force microscopy
AO	Anodic oxidation
AO-H_2O_2	Anodic oxidation with electrogenerated H_2O_2
AOPs	Advanced oxidation processes
BDD	Boron-doped diamond
CB	Carbon black
$C_{diamond}$	Purity of chemically vapor deposited diamond
C_{dl}	Double-layer capacitance
COD	Chemical oxygen demand
CPE	Constant phase element
CTE	Coefficient of thermal expansion
CV	Cyclic voltammetry
CVD	Chemical vapor deposition
DC	Direct current
DLC	Diamond-like carbon
DoE	Design of experiments
DSAs	Dimensionally stable anodes
E	Elastic modulus (in Chapter II, Section 1)
EAOPs	Electrochemical advanced oxidation processes
EC	Energy consumption
EDM	Electrical discharge machining
EDS	Energy dispersive spectroscopy
EDX	Energy dispersive X-ray analysis
EELS	Electron energy-loss spectroscopy
EF	Electro-Fenton
E_{FB}	Flat-band potential
EIS	Electrochemical impedance spectroscopy
EO	electrochemical oxidation
EPW	Electrochemical potential window
FOM	Figure-of-merit (in Chapter II, Section 2)
FWHM	Full width at half maximum
G	Shear modulus (in Chapter II, Section 1)

GDE	Gas diffusion electrodes
GDOES	Glow discharge optical emission spectroscopy
H	Hardness (in Chapter II, Section 1)
HER	Hydrogen evolution reaction
HFCVD	Hot-filament chemical vapor deposition
HPLC	High-performance liquid chromatography
HTHP	High pressure-high temperature
ICE	Instantaneous current efficiency
I_{diam} or $I_{diamond}$	Integral intensity of the diamond band
I_G	Integral intensity of the G band
i_p	Peak current
ISO	International Organization for Standardization
J_{appl}	Applied current density
$J_{cut\text{-}off}$	Arbitrary current density cut-off
J_{limit}	Limiting current density
k_0	Standard rate constant
k_{app}	Apparent rate constant
K_{IC}	Fracture toughness
LSV	Linear sweep voltammetry
MCD	Microcrystalline diamond
MCE	Mineralization current efficiency
MOx	Metallic oxides
MPCVD	Microwave plasma chemical vapor deposition
N_A	Dopant density
NCD	Nanocrystalline diamond
NDC	Non-diamond carbon
NDP	Neutron depth profile
OEP	Oxygen evolution potential
OER	Oxygen evolution reaction
OPT	Optimized sample
PAHs	Polycyclic aromatic hydrocarbons
PCBs	Polychlorinated biphenyls
PEF	Photoelectro-Fenton
POPs	Persistent organic pollutants
PTFE	Polytetrafluoroethylene

Q'	Average charge required for pollutant degradation
Q^t	Average charge
R_2	Electron transfer resistance (in Chapter II, Section 2)
R_{ct}	Electron transfer resistance
RF	Radio frequency
RFCVD	Radio frequency plasma chemical vapor deposition
RVC	Reticulated vitreous carbon
SCE	Saturated calomel electrode
SDG	Sustainable development goals
SEF	Sonoelectro-Fenton
SEM	Scanning electron microscopy
SHE	Standard hydrogen electrode
SIMS	Secondary ion mass spectrometry
SLR	Systematic literature review
SNTN	Silicon nitride-titanium nitride
SPEF	Solar photoelectro-Fenton
$t_{1/2}$	Half-life
TOC	Total organic carbon
TPA	Trans-polyacetylene
UNCD	Ultra-nanocrystalline diamond
UV	Ultraviolet
V/A	Volume-to-area ratio
XPS	X-ray photoelectron spectroscopy
XRD	X-ray diffraction
ZCPE	Constant phase element impedance
[B]	Boron concentration
$\Delta\vartheta$	Diamond peak shift
β	Raman quality fraction (in Chapter I, Section 2)
η_c	Combustion efficiency
θ	Contact Angle
σ	Disk technique bending strength (in Chapter II, Section 1)
σ_r	Residual stress
Ψ	Kinetic parameter

Preface

Thesis Motivation and Structure

The aim of this introduction is to provide the reader with a clear understanding of the motivation behind this thesis, its main objectives, and a brief overview of its structure.

Introduction

Persistent organic pollutants (POPs) are a group of harmful chemicals that pose significant risks to both human health and the environment on a global scale (1). These substances are characterized by their remarkable ability to persist in the environment for extended periods, often accumulating and spreading through the food chain, affecting various species along the way (2). The sources of these POPs are diverse and encompass various industries and practices (3).

One of the primary sources of POPs is petroleum refinery wastewaters, known for their high chemical oxygen demand (COD) and a complex mixture of hazardous compounds, including aromatic organic compounds such as polyaromatic hydrocarbons and phenols, as well as various inorganic substances like magnesium, calcium, sulfur, chlorine, and sulfate ions (4-6). Additionally, wastewaters from medical and hazardous waste incineration, as regulated by the Stockholm Convention on Persistent Organic Pollutants, contribute to the presence of POPs in our environment (1, 7). Pulp and paper manufacturing, pesticide use (such as DDT, chlordane, aldrin, dieldrin, heptachlor, endrin, mirex, and toxaphene), industrial chemicals like polychlorinated biphenyls (PCBs) and hexachlorobenzene, and unintentional byproducts of industrial processes, notably dioxins, polycyclic aromatic hydrocarbons (PAHs), and furans, are all significant sources of these pollutants (8, 9).

POPs are widespread, existing in our food, soil, air, and water, with both wildlife and humans carrying levels of POPs in their bodies that often approach or exceed harmful thresholds (2, 3). These compounds pose severe threats to the environment and the health of animals and humans (2). In humans, exposure to POPs has been associated with a range of health issues, including reproductive and developmental problems, behavioral and neurological disorders, endocrine disruption, cardiovascular diseases, various types of cancer, diabetes, birth defects, as well as compromised immune and reproductive systems, leading to adverse health effects (2). For instance, phenols, which are highly soluble in water, can undergo chlorination or methylation, forming even more harmful chlorophenols and cresols, which may exhibit carcinogenic, teratogenic, or mutagenic properties (5, 10).

Removing contaminants from wastewater poses both economic and environmental challenges crucial for achieving sustainable development. Wastewaters exhibit complex compositions, demanding proper treatment to meet the standard limits set by environmental agencies before their discharge into aquatic ecosystems (11). With growing societal and political concerns about the environment, environmental regulations are becoming increasingly stringent. There is a concerted effort to reduce the impact of water pollution and ensure safe wastewater disposal.

Traditional treatment methods for industrial wastewater involve two stages. The first stage employs physicochemical and mechanical processes responsible for oil-water separation and coagulation, reducing suspended matter like oil and grease (12). The second stage focuses on advanced treatment, aiming to lower contaminant levels to specific acceptable discharge limits (5). Among the various advanced treatment techniques, biological treatment and bioremediation are the most commonly applied methods at an industrial scale (13).

However, biological systems face limitations due to the variability of wastewater compositions, which can include non-biodegradable components (14). These techniques also present issues such as residual sludge production, pollutant phase transfer, toxic gas generation, large land requirements, and the inability to destroy refractory compounds (15). Hence, there is an urgent need to develop an economical and efficient method that can remove pollutants from wastewaters, especially persistent organic pollutants (POPs), without the drawbacks associated with biological treatment systems.

Numerous techniques have been proposed as potential solutions, including enhanced photo-degradation (16), chemical coagulation (17, 18), membrane bioreactors (19), ceramic membrane filtration (20), electron-beam (21), ozonation (22), and electrochemical advanced oxidation processes (EAOPs), such as anodic oxidation, electro-Fenton, photoelectro-Fenton, solar photoelectro-Fenton, and sonoelectrochemistry (23, 24). Among these, EAOPs stand out as the most promising and innovative alternative technologies (15, 25, 26). These electrochemical methods gained significant attention due to their ability to chemically oxidize a wide range of organic substances, resulting in complete mineralization to CO_2 and H_2O (5, 27). Moreover, electrochemical treatments are cost-effective, facilitate rapid degradation of organic pollutants without generating new toxic species, require minimal or no chemical reagents, and offer several advantages, including environmental compatibility, selectivity, versatility, energy efficiency, safety, and suitability for automation (27, 28).

Within the realm of EAOPs, the choice of electrode materials is critical for achieving efficient wastewater treatment. Materials such as lead dioxide (PbO_2), tin dioxide (SnO_2), sub-stoichiometric TiO_2, and boron-doped diamond (BDD) have demonstrated high potential (23). Notably, BDD stands out as the most promising material, boasting a high overpotential for water decomposition, the broadest known electrochemical window, exceptional efficiency in hydroxyl radical production (29, 30), and robust electrochemical stability and corrosion resistance, even in harsh chemical environments with minimal adsorption (31). Consequently, BDD electrodes have found applications in treating various substances,

including organic pollutants (32), dyes (33), pharmaceuticals (34), synthetic wastewater (35), industrial wastewater (36-38), swimming pool water (28), landfills leachates (39, 40), among others.

While BDD films have been effectively deposited over extensive areas, including those as large as 0.5 m² (41), and both laboratory and pilot tests on wastewater have shown promising outcomes (38, 39, 42, 43), the considerable challenge for their large-scale use still revolves around the absence of appropriate substrates. Though BDD electrodes have been deposited on substrate materials such as Si, Ti, Nb, Ta, and W (44-46), these substrates have limitations such as low conductivity, low mechanical strength, or high cost, making them unsuitable for large-scale use. Ideally, the substrate material should exhibit low resistivity, high mechanical strength, inert electrochemical activity, favorable relationship between cost and durability, and compatibility with diamond growth (47, 48).

To address these challenges and develop BDD electrodes suitable for large-scale wastewater treatment, this thesis proposes a novel substrate material: electroconductive Si_3N_4-TiN ceramics. Si_3N_4 is a refractory ceramic material known for its compatibility with CVD diamond growth, exceptional resistance to wear and corrosion, and resistance to harsh chemicals (49, 50). It also exhibits crucial mechanical properties, including high hardness, excellent fracture toughness, and a high elasticity modulus (50). When TiN particles are incorporated into a Si_3N_4 matrix, the ceramic's electrical resistivity decreases, rendering Si_3N_4-TiN electroconductive (51). The degree of conductivity depends on the quantity of TiN particles added. These attributes collectively position BDD/Si_3N_4-TiN as a promising electrode for large-scale wastewater treatment through EAOPs.

Addressing water contamination caused by persistent organic pollutants presents a multifaceted challenge requiring innovative solutions. The development of efficient treatment methods, such as EAOPs employing BDD/Si_3N_4-TiN electrodes, holds significant promise in addressing this widespread environmental issue.

Objectives

The main goal of this thesis is to develop BDD surfaces with high electrochemical activity that may be scaled for use as industrial-scale electrodes in treating persistent organic pollutants found in wastewater, through electrochemical advanced oxidation processes. Simultaneously, an innovative approach is proposed for producing these electrodes, by depositing BDD films over electroconductive Si_3N_4-TiN ceramic substrates. The specific objectives associated are outlined as follows:

- Investigate the impact of deposition parameters on the final properties of BDD surfaces produced using the Hot Filament Chemical Vapor Deposition (HFCVD) technique.
- Develop electrically conductive Si_3N_4-TiN ceramic substrates with excellent electrical conductivity and robust mechanical properties.
- Examine how Si_3N_4-TiN substrates influence HFCVD BDD growth and resulting properties.
- Validate BDD coatings for the oxidation process of highly toxic pollutants present in wastewater.
- Establish a correlation between the electrochemical performance of a given electrode and specific BDD film characteristics, such as the sp^3/sp^2 ratio, crystallite size, grain morphology, surface roughness, and surface chemistry.
- Utilize the combined strengths of BDD and Si_3N_4-TiN substrates to apply BDD/Si_3N_4-TiN electrodes in chemically aggressive environments.
- Develop electrodes with longer lifespans compared to traditional ones, taking advantage of the chemical inertness of diamond surfaces.
- Develop strategies to minimize energy consumption and enhance the efficiency of EAOPs with BDD electrodes.

Thesis Structure

This thesis consists of five chapters, organized in a way to provide readers with a comprehensive understanding of key concepts in the fields covered in this work. The fundamentals and state of the art, as well as new experimental results are presented in the form of four papers published in peer-reviewed journals, two papers currently in the revisions stage for publication in peer-reviewed journals, and one manuscript ready for submission at the time of writing.

Chapter I offers an extensive overview of EAOPs and BDD electrodes for water treatment and is based entirely on two published papers. It reviews the literature on EAOPs employing BDD electrodes. Additionally, it compares in-house-made and commercially available BDD electrodes. In Section I.1, published in the journal *Environments* (52), we delve into EAOPs with BDD electrodes, emphasizing the superior performance of BDD electrodes compared to alternative materials. We also discuss techniques for enhancing anodic oxidation using BDD technology, including persulfate radicals, ozone, photoelectrocatalysis, and Fenton-based reactions. Section I.2, published in the journal *Frontiers In Materials* (53), presents a systematic review of both in-house-made and commercially available BDD electrodes. It analyzes the growth, trends, and factors influencing BDD electrode performance, accompanied by case studies on phenol-containing solutions and landfill leachate treatment.

The work in Chapter II, based in two papers, introduces a novel substrate material for BDD electrodes and optimizes BDD film deposition conditions. The goal is to ensure the durability and robustness of the BDD/substrate assembly while maintaining efficient pollutant removal. This chapter is divided into two sections. Section II.1 contains the work discussed in a paper published in *Ceramics International* (54), detailing the development of electroconductive ceramic substrates based on Si_3N_4-TiN powder composites. Section II.2 is a paper published in *Diamond and Related Materials* (55), which optimizes the conditions for BDD film deposition using the Taguchi method in an HFCVD reactor.

The discussion presented in Chapter III describes the performance of BDD electrodes deposited on electroconductive Si_3N_4-TiN substrates for the application targeted in this thesis (proof of concept). In Section III.1, a paper submitted to *Next Sustainability* discusses the characterization and testing of BDD/Si_3N_4-TiN electrodes for oxidizing phenol, a highly prevalent persistent organic pollutant in contaminated water. Additionally, Section III.2 provides a manuscript, pending publication, exploring the use of radiofrequency plasma treatments to functionalize BDD/Si_3N_4-TiN surfaces and enhance their electrochemical performance.

In Chapter IV we describe a strategy to improve the efficiency of electrochemical oxidation processes with BDD electrodes, focusing on reducing time and energy consumption. This approach is presented in a paper submitted to *Separation and Purification Technology*, involving a cyclic fouling and rapid reactivation process applied to a BDD/Si_3N_4-TiN electrode using a square wave pattern. The aim is to accelerate the conversion of phenol into more readily biodegradable compounds, addressing the pressing need for effective and eco-friendly water treatment methods, especially for water contaminated by persistent organic pollutants.

Chapter V summarizes the key findings of the thesis, delving into their significance, impact, and potential for future research. It also outlines how the thesis outcomes were shared with the scientific community.

References

1. US Environmental Protection Agency. Persistent Organic Pollutants: A Global Issue, A Global Response; [reviewed 2023 September 26; cited date 2023 September 26]. Available from: https://www.epa.gov/international-cooperation/persistent-organic-pollutants-global-issue-global-response.

2. Guo W, Pan B, Sakkiah S, Yavas G, Ge W, Zou W, *et al.* Persistent Organic Pollutants in Food: Contamination Sources, Health Effects and Detection Methods. Int J Environ Res Public Health. 2019;16(22).

3. Ashraf MA. Persistent organic pollutants (POPs): a global issue, a global challenge. Environ Sci Pollut R. 2017;24(5):4223-7.

4. Yan L, Wang YF, Li J, Ma HZ, Liu HJ, Li T, *et al.* Comparative study of different electrochemical methods for petroleum refinery wastewater treatment. Desalination. 2014;341:87-93.

5. Al-Khalid T, El-Naas MH. Organic Contaminants in Refinery Wastewater: Characterization and Novel Approaches for Biotreatment. Recent Insights in Petroleum Science and Engineering2018.

6. El-Naas MH, Alhaija MA, Al-Zuhair S. Evaluation of a three-step process for the treatment of petroleum refinery wastewater. J Environ Chem Eng. 2014;2(1):56-62.

7. Kour G, Goria K, Pathak A, Kothari R, Pathania D, Dhar S, *et al.* Role of Incineration in the Production of Persistent Organic Pollutants: Is It Safe? In: Kumar NS, Vertika editor. Persistent Organic Pollutants in the Environment. Boca Raton: CRC Press; 2021.

8. Tripathi S, Yadav S, Purchase D, Singh K, Al-Shwaiman HA, Chandra R. Characterization of persistent organic pollutants and culturable and non-culturable bacterial communities in pulp and paper sludge after secondary treatment. Chemosphere. 2022;295:133892.

9. Anh NT, Can LD, Nhan NT, Schmalz B, Luu TL. Influences of key factors on river water quality in urban and rural areas: A review. Case Studies in Chemical and Environmental Engineering. 2023;8.

10. Praveen P, Loh KC. Simultaneous extraction and biodegradation of phenol in a hollow fiber supported liquid membrane bioreactor. J Membr Sci. 2013;430:242-51.

11. Santos ID, Afonso JC, Dutra AJB. Behavior of a Ti/RuO2 anode in concentrated chloride medium for phenol and their chlorinated intermediates electrooxidation. Sep Purif Technol. 2010;76(2):151-7.

12. El-Naas MH, Al-Zuhair S, Al-Lobaney A, Makhlouf S. Assessment of electrocoagulation for the treatment of petroleum refinery wastewater. J Environ Manage. 2009;91(1):180-5.

13. Diya'uddeen BH, Daud WMAW, Aziz ARA. Treatment technologies for petroleum refinery effluents: A review. Process Saf Environ Prot. 2011;89(2):95-105.

14. Shokrollahzadeh S, Azizmohseni F, Golmohammad F, Shokouhi H, Khademhaghighat F. Biodegradation potential and bacterial diversity of a petrochemical wastewater treatment plant in Iran. Bioresource Technol. 2008;99(14):6127-33.

15. Gargouri B, Gargouri OD, Gargouri B, Trabelsi SK, Abdelhedi R, Bouaziz M. Application of electrochemical technology for removing petroleum hydrocarbons from produced water using lead dioxide and boron-doped diamond electrodes. Chemosphere. 2014;117:309-15.

16. Stepnowski P, Siedlecka EM, Behrend P, Jastorff B. Enhanced photo-degradation of contaminants in petroleum refinery wastewater. Water Res. 2002;36(9):2167-72.

17. Al-Shamrani AA, James A, Xiao H. Destabilisation of oil-water emulsions and separation by dissolved air flotation. Water Res. 2002;36(6):1503-12.

18. Altas L, Buyukgungor H. Sulfide removal in petroleum refinery wastewater by chemical precipitation. J Hazard Mater. 2008;153(1-2):462-9.

19. Rahman MM, Al-Malack MH. Performance of a crossflow membrane bioreactor (CF–MBR) when treating refinery wastewater. Desalination. 2006;191(1-3):16-26.

20. Zhong J, Sun XJ, Wang CL. Treatment of oily wastewater produced from refinery processes using flocculation and ceramic membrane filtration. Sep Purif Technol. 2003;32(1-3):93-8.

21. Emami-Meibodi M, Parsaeian MR, Amraei R, Banaei M, Anvari F, Tahami SMR, *et al.* An experimental investigation of wastewater treatment using electron beam irradiation. Radiat Phys Chem. 2016;125:82-7.

22. Suarasan I, Mudura M, Chira R, Andrei G, Munceleanu I, Morar R. A novel type ozonizer for wastewater treatment. J Electrostat. 2005;63(6-10):831-6.

23. Moreira FC, Boaventura RAR, Brillas E, Vilar VJP. Electrochemical advanced oxidation processes: A review on their application to synthetic and real wastewaters. Appl Catal B Environ. 2017;202:217-61.

24. Sires I, Brillas E, Oturan MA, Rodrigo MA, Panizza M. Electrochemical advanced oxidation processes: today and tomorrow. A review. Environ Sci Pollut Res Int. 2014;21(14):8336-67.

25. Martínez-Huitle CA, Brillas E. Decontamination of wastewaters containing synthetic organic dyes by electrochemical methods: A general review. Appl Catal B Environ. 2009;87(3-4):105-45.
26. Panizza M, Cerisola G. Direct and mediated anodic oxidation of organic pollutants. Chem Rev. 2009;109(12):6541-69.
27. Oturan MA, Aaron J-J. Advanced Oxidation Processes in Water/Wastewater Treatment: Principles and Applications. A Review. Crit Rev Env Sci Tec. 2014;44(23):2577-641.
28. Matthée T, Fryda M, Schäfer L, Tröster I. Electrochemical advanced oxidation process using DiaChem®electrodes. Water Sci Technol. 2004;49(4):207-12.
29. Angus JC, Martin HB, Landau U, Evstefeeva YE, Miller B, Vinokur N. Conducting diamond electrodes: Applications in electrochemistry. New Diamond Front Carbon Technol. 1999;9(3):175-87.
30. Zhou B, Yu Z, Wei Q, Long H, Xie Y, Wang Y. Electrochemical oxidation of biological pretreated and membrane separated landfill leachate concentrates on boron doped diamond anode. Appl Surf Sci. 2016;377:406-15.
31. Electrochemistry for the Environment. 1 ed. Comninellis C, Chen G, editors: Springer-Verlag New York; 2010.
32. Scialdone O, Randazzo S, Galia A, Silvestri G. Electrochemical oxidation of organics in water: role of operative parameters in the absence and in the presence of NaCl. Water Res. 2009;43(8):2260-72.
33. Saez C, Panizza M, Rodrigo MA, Cerisola G. Electrochemical incineration of dyes using a boron-doped diamond anode. J Chem Technol Biotechnol. 2007;82(6):575-81.
34. Zhao X, Qu J, Liu H, Qiang Z, Liu R, Hu C. Photoelectrochemical degradation of anti-inflammatory pharmaceuticals at Bi2MoO6–boron-doped diamond hybrid electrode under visible light irradiation. Appl Catal B Environ. 2009;91(1-2):539-45.
35. Mascia M, Vacca A, Polcaro AM, Palmas S, Ruiz JR, Da Pozzo A. Electrochemical treatment of phenolic waters in presence of chloride with boron-doped diamond (BDD) anodes: experimental study and mathematical model. J Hazard Mater. 2010;174(1-3):314-22.
36. Yavuz Y, Koparal AS, Öğütveren ÜB. Treatment of petroleum refinery wastewater by electrochemical methods. Desalination. 2010;258(1-3):201-5.
37. Urtiaga A, Gómez P, Arruti A, Ortiz I. Electrochemical removal of tetrahydrofuran from industrial wastewaters: anode selection and process scale-up. J Chem Technol Biotechnol. 2014;89(8):1243-50.

38. dos Santos EV, Sena SF, da Silva DR, Ferro S, De Battisti A, Martinez-Huitle CA. Scale-up of electrochemical oxidation system for treatment of produced water generated by Brazilian petrochemical industry. Environ Sci Pollut Res Int. 2014;21(14):8466-75.
39. Anglada A, Urtiaga AM, Ortiz I. Laboratory and pilot plant scale study on the electrochemical oxidation of landfill leachate. J Hazard Mater. 2010;181(1-3):729-35.
40. Dominguez-Ramos A, Aldaco R, Irabien A. Electrochemical Oxidation of Lignosulfonate: Total Organic Carbon Oxidation Kinetics. Ind Eng Chem Res. 2008;47(24):9848-53.
41. Haenni W, Rychen P, Fryda M, Comninellis C. Chapter 5 Industrial applications of diamond electrodes. In: Nebel CE, Ristein J, editors. Thin-Film Diamond II. Semiconductors and Semimetals. 77: Elsevier; 2004. p. 149-96.
42. Alvarez Pugliese CE, Martínez Hernández L, Imbachi Ordoñez S, Marriaga Cabrales N, Machuca Martínez F. Pilot scale anodic oxidation of pretreated vinasse using boron doped diamond electrodes. CT&F - Ciencia, Tecnología y Futuro. 2016;6(4):67-77.
43. Anglada A, Urtiaga A, Ortiz I. Pilot scale performance of the electro-oxidation of landfill leachate at boron-doped diamond anodes. Environ Sci Technol. 2009;43(6):2035-40.
44. Chaplin BP, Wyle I, Zeng H, Carlisle JA, Farrell J. Characterization of the performance and failure mechanisms of boron-doped ultrananocrystalline diamond electrodes. J Appl Electrochem. 2011;41(11):1329-40.
45. Shaw J, Jones AN, Monk PMS, Rego CA. Electrochemical behaviour of graphite- and molybdenum electrodes modified with thin-film diamond. Diamond Relat Mater. 2002;11(9):1690-6.
46. Fryda M, Herrmann D, Schafer L, Klages CP, Perret A, Haenni W, *et al.* Properties of diamond electrodes for wastewater treatment. New Diamond Front Carbon Technol. 1999;9(3):229-40.
47. Chen G. Electrochemical technologies in wastewater treatment. Sep Purif Technol. 2004;38(1):11-41.
48. He Y, Lin H, Guo Z, Zhang W, Li H, Huang W. Recent developments and advances in boron-doped diamond electrodes for electrochemical oxidation of organic pollutants. Sep Purif Technol. 2019;212:802-21.
49. Almeida FA, Amaral M, Oliveira FJ, Fernandes AJS, Silva RF. Nano to micrometric HFCVD diamond adhesion strength to Si3N4. Vacuum. 2007;81(11-12):1443-7.

50. Petzow G, Herrmann M. Silicon Nitride Ceramics. In: Jansen M, editor. High Performance Non-Oxide Ceramics II. Structure and Bonding. Berlin, Heidelberg: Springer Berlin Heidelberg; 2002. p. 47-167.
51. Bellosi A, Guicciardi S, Tampieri A. Development and characterization of electroconductive Si3N4-TiN composites. J Eur Ceram Soc. 1992;9(2):83-93.
52. Brosler P, Girão AV, Silva RF, Tedim J, Oliveira FJ. Electrochemical Advanced Oxidation Processes Using Diamond Technology: A Critical Review. Environments. 2023;10(2).
53. Brosler P, Girão AV, Silva RF, Tedim J, Oliveira FJ. In-house vs. commercial boron-doped diamond electrodes for electrochemical degradation of water pollutants: A critical review. Front Mater. 2023;10.
54. Brosler P, Silva RF, Tedim J, Oliveira FJ. Electroconductive silicon nitride-titanium nitride ceramic substrates for CVD diamond electrode deposition. Ceram Int. 2023.
55. Brosler P, Neto, MA, Silva RF, Tedim J, Oliveira FJ. Customized boron-doped diamond electrodes for efficient water treatment via HF-CVD parameter optimization. Diam Relat Mater. 2024

Chapter I

Fundamentals and State of the Art

This chapter offers an overview of the various subjects pertinent to this thesis. This encompasses fundamental concepts, as well as a review of research directions explored within the existing literature.

Section I.1 presents a critical review article published in the journal *Environments* (1), which delves into Electrochemical Advanced Oxidation Processes (EAOPs) utilizing BDD electrodes. The study investigates how anodic oxidation with BDD technology can synergize with other oxidation methods. Importantly, this work underscores the superior performance of BDD electrodes in EAOPs compared to alternative electrode materials. The discussion in this research covers diverse techniques aimed at enhancing the anodic oxidation performance of BDD technology, such as persulfate radicals, ozone, photoelectrocatalysis, and Fenton-based reactions.

Section I.2 presents a critical review article published in the journal *Frontiers In Materials* (2) that conducts a systematic literature review to compare in-house-made and commercially available BDD electrodes. The review examines the dissemination, growth, and trends in using BDD electrodes for degrading water pollutants. It also provides a thorough analysis of factors influencing BDD electrode performance, including substrate material selection and pre-treatment, chemical vapor deposition method, deposition parameters, film properties, characterization methods, and operational conditions. This work discusses various performance indicators from the literature and includes two case studies: one on the degradation of phenol-containing solutions and another on landfill leachate treatment, utilizing either commercial or in-house-made BDD electrodes.

---

1. Brosler P, Girão AV, Silva RF, Tedim J, Oliveira FJ. Electrochemical Advanced Oxidation Processes Using Diamond Technology: A Critical Review. Environments. 2023;10(2).

2. Brosler P, Girão AV, Silva RF, Tedim J, Oliveira FJ. In-house vs. commercial boron-doped diamond electrodes for electrochemical degradation of water pollutants: A critical review. Front Mater. 2023;10.

I.1. Electrochemical Advanced Oxidation Processes Using Diamond Technology: A Critical Review

Priscilla Brosler[1], Ana Violeta Girão[1], Rui F. Silva[1], João Tedim[1], Filipe J. Oliveira[1]

[1] CICECO Aveiro Institute of Materials, Department of Materials and Ceramic Engineering, University of Aveiro, 3810-193, Aveiro, Portugal

The present work was published on: Environments

Published on: 19 January 2023

doi: 10.3390/environments10020015

Abstract

Re-evaluation of conventional wastewater treatment processes is of paramount importance to improve the overall quality of our aquatic environment. Electrochemical Advanced Oxidation Processes (EAOPs) are the most promising alternative methods with application in wastewater treatment facilities since in situ electrogenerated oxidant agents degrade and mineralize a wide range of water pollutants. Boron-doped diamond (BDD) technology has proven its excellency in the anodic oxidation (AO) of different pollutants. In this work, we describe the use of a systematic literature review (SLR) methodology and a bibliometric analysis tool for the assessment of a representative sample of work (hundreds of publications) concerning the synergism between AO using BDD technology and other oxidation methods. One section of the discussion relates to different techniques used to enhance the AO performance of BDD technology, namely persulfate radicals or ozone and photoelectrocatalysis, whereas the second one considers Fenton-based reactions. A standard synergism effect occurs between AO using BDD technology and the add-ons or the Fenton-based methods, resulting in the enhancement of the degradation and mineralization efficiencies. The future of EAOPs using BDD technology must include renewable energy sources to self-sustain the overall process, and further research on the subject is mandatory to enable the effective acceptance and application of such processes in wastewater remediation facilities.

I.1.1. Introduction

The water crisis has triggered the urgent need to develop economical and efficient methods to remove contaminants without the common drawbacks associated with the widely applied conventional bioremediation techniques (1), such as residual sludge production, phase transfer of pollutants, generation of toxic gases, and demand for large territorial areas (2). Although these methods remove many of the dissolved organic carbons, they are insufficient due to the presence of persistent organic pollutants (POPs) in wastewaters, threatening the environment and human health (3,4). Significant attempts are being developed to reduce the impact caused by water pollution and to ensure safe wastewater disposal onto the environment. Numerous alternative methods have been proposed as more efficient and sustainable water treatment methods. They include enhanced photocatalytic degradation (5), chemical coagulation (6), electrocoagulation (7), membrane bioreactor (8), membrane filtration (9), electron beam (10), wet air oxidation (11), electroreduction (12), adsorption (13), electroadsorption (14), electrochemical hydrodechlorination (15), electrokinetic separation (16), ozonation (17), and the so-called Electrochemical Advanced Oxidation Processes, EAOPs (Figure I.1.1) (18).

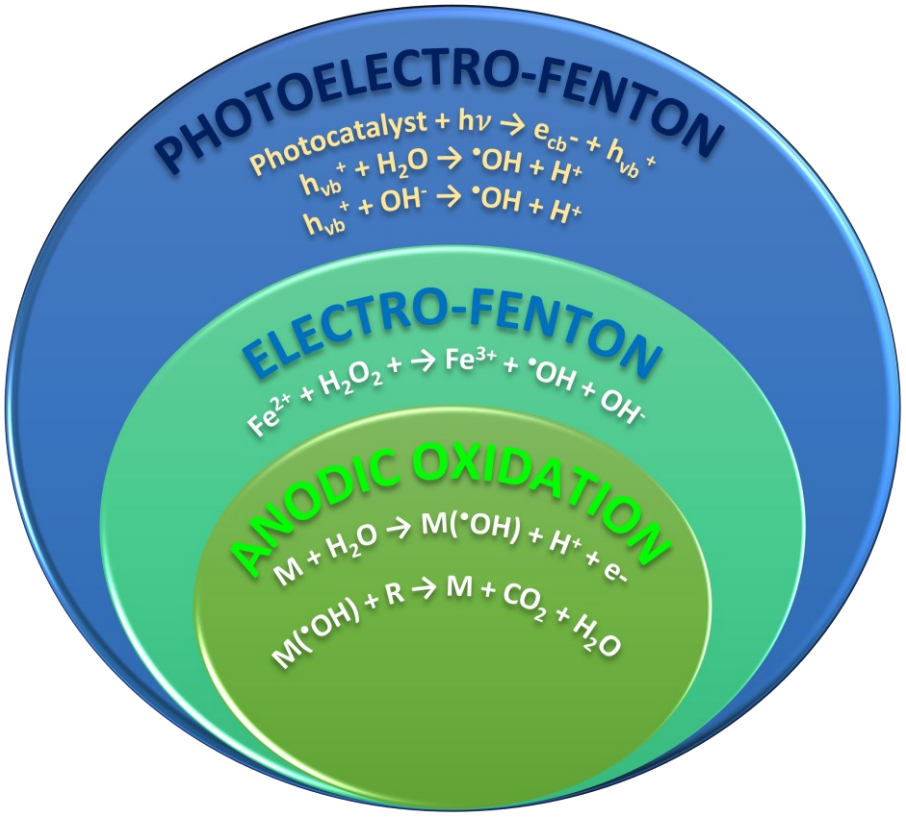

Figure I.1.1. Diagram illustrating the main chemical reactions in EAOPs.

The advances in electrochemical technology led to the development of EAOPs (19,20) and are considered the most promising and innovative alternative water treatment technologies (2,21,22). The basis of EAOPs is the electrochemical generation of highly reactive oxidizing species, such as hydroxyl radicals, capable of mineralizing the target pollutants (23,24). These techniques aim to mineralize contaminants to CO_2 and water, or, at least, convert them into harmless, easily degradable products whilst avoiding the formation of new toxic species (20). Since electrochemical methods are based on the transfer of electrons, EAOPs require no or low amounts of additional chemical reagents or catalysts during the process (19). Thus, EAOPs are particularly interesting because they are environmentally compatible, versatile, and a highly effective means to eliminate a large variety of pollutants from wastewater (19,25).

The materials used as anodes in EAOPs are crucial for achieving efficient water treatment, since they are responsible for the generation of the oxidant species (26). These electrodes must have a high oxygen evolution overpotential (OEP), such as lead dioxide (PbO_2), tin dioxide (SnO_2), sub-stoichiometric TiO_2, boron-doped diamond (BDD), and some composites such as Sb-SnO_2, Co-PbO_2, TiO_2-nanotubes with PbO_2, Ti/Sb-SnO_2, and La-Y-PbO_2 (24,27). It has also been established that the higher the OEP, the higher the oxidation output of the anode (28). PbO_2, SnO_2, and sub-stoichiometric TiO_2 present high OEP and are generally cheap and simple to manufacture, though with poor electrochemical stability (29). Graphite and glassy carbon electrodes also have relatively high OEPs but are highly vulnerable to surface oxidation and fouling (30). Among the many materials tested as potential anodes, BDD has proven its excellent ability in the electrochemical oxidation of pollutants showing the highest overpotential for water decomposition, the widest known electrochemical potential window, and excellent efficiency in producing hydroxyl radicals (31,32). Furthermore, BDD has a high electrochemical stability and resistance to corrosion, even in chemically aggressive media, presenting inert surfaces with very low adsorption, and works under the whole pH range (33–35).

Diamond’s natural low conductivity and large bandgap have limited its use in electrochemical applications (36). However, with the development of Chemical Vapor Deposition (CVD) methods, the use of diamond in such applications became possible. CVD growth of diamond requires the generation of carbon radicals and a high concentration of dissociated hydrogen (37). This is achieved by activating a gas mixture of a carbon-containing source gas, such as methane, mixed with molecular hydrogen. The dissociation of molecular hydrogen to react with the carbon-containing gas source and produce reactive

carbon-containing radicals, the growth precursors, is typically done using various methods such as hot-filament CVD, RF-plasma CVD, microwave plasma CVD, DC plasma, DC arc-jet, or even by using an oxy-acetylene flame (38). The CVD growth parameters such as deposition time, substrate temperature, pressure, bias voltage, substrate nature, and gas composition control the final properties of the diamond film (39). Introducing boron atoms into the CVD reactor's environment has unlocked the possibility of combining high electrical conductivity with the unique diamond properties (40). Due to its relatively small charge carrier activation energy (0.37 eV) and small atomic radius, boron can effectively occupy the same position as displaced carbon atoms (41). Thus, a high enough boron concentration can be incorporated in the diamond lattice to achieve metal-like conductivity (37). For this reason, although other impurity atoms have been applied in diamond doping, such as nitrogen (42) and phosphorus (43), BDD will be the focus of this critical review since it is more well-suited for electrochemical studies such as electrochemical oxidation, electroanalysis, electrosynthesis, and energy conversion (41,44).

The individual application of BDD technology as an EAOP for wastewater treatment is widely published, proving to be one with the highest degradation efficiency, including the elimination of several sources of water contamination, such as refractory organics (45), dyes (46), pharmaceuticals (47), pesticides (48), byproducts of industrial processes (49), domestic sewage (50), and landfill leachate (51), amongst many others. Consequently, the reported literature concerning BDD technology is quite extensive, but, to the best of our knowledge, a critical review gathering information on overcoming the few drawbacks of BDD technology by combining it with other EAOPs would be very useful. Conventional wastewater facilities employ a combination of different treatment techniques and perhaps the "apparent" high cost of BDD technology is the main reason why it has not seriously been considered or adopted. It is also intended, with this review, to clearly demonstrate to the industrial business that the effective and sustainable application of BDD technology will shortly add up value to all of its benefits.

Thus, a systematic literature review (SLR) and bibliometric analysis are conducted in this critical review to select publications and extract information on the trends and future directions of EAOPs using BDD electrodes for wastewater treatment. The anodic oxidation (AO) EAOP, also referred to as electrochemical oxidation (EO), is the most straightforward and applied EAOP using BDD technology. This is basically carried out by applying an electric current directly to a pair of electrodes (anode and cathode) immersed in the aqueous solution to be treated, and then promoting the direct oxidation of pollutants through the generation of reactive oxygen species (mainly hydroxyl radicals) generated during water

splitting (22). The main drawback of this technology is the fact that these short-lifetime oxidant species are limited to the surface reaction layer of the BDD anode (22). It is our main goal to identify and discuss EAOPs that employ diamond technology but go beyond the apparently simple AO process. We will discuss the advantages, disadvantages, and limitations of the methods identified through the SLR, as well as the role and performance of diamond electrodes. We will also identify the synergism between EAOPs and BDD technology as a possible solution to the main disadvantage of AO based on BDD electrodes.

I.1.2. Electrochemical Advanced Oxidation Processes Using Diamond Technology: A Bibliometric Analysis

The number and diversity of scientific publications in the last few decades have exponentially increased, which leads to the constant need for consistent and updated review articles (52). Systematic Literature Review (SLR) is a method of scientific research used when the objects of analysis are significant literature sources, enabling the authors to identify, select, and critically evaluate the research results to answer a clearly formulated question (53). SLR is a highly standardized and structured approach that follows a well-defined protocol in which the criteria are clearly stated before the analysis is performed, leading to a comprehensive, unbiased, transparent, and accountable study (54).

In this critical review, we applied the SLR method to identify what is known, what is unknown, the limitations, the trends, and the future directions of existing research on Electrochemical Advanced Oxidation Processes (EAOPs) using BDD technology. A previous rough analysis to determine the most applied EAOP methods using diamond electrodes was performed, followed by advanced Boolean search queries in the Scopus database for each identified method (anodic oxidation- AO or EO, anodic oxidation with electrogenerated H_2O_2, electro-Fenton- EF, photoelectro-Fenton- PEF, and solar photoelectro-Fenton- SPEF), adopting the main keywords commonly used for each of the processes. Table I.1.1 provides details on the advanced search queries by EAOP type.

Table I.1.1. Details of the advanced Boolean search queries performed in the Scopus database regarding the most applied EAOP type using diamond technology.

EAOP	Boolean Advanced Search Query	Scopus Results (Sept/22)
Anodic oxidation/electrochemical oxidation (AO/EO)	(TITLE-ABS-KEY (bdd OR "doped diamond") AND TITLE-ABS-KEY ("anodic oxidation" OR "electrochemical oxidation")) AND (LIMIT-TO (LANGUAGE, "English"))	1410
Anodic oxidation with electrogenerated H_2O_2 (AO-H_2O_2)	(TITLE-ABS-KEY (bdd OR "doped diamond") AND TITLE-ABS-KEY ("anodic oxidation" OR "electrochemical oxidation") AND TITLE-ABS-KEY ("electrogeneration of H2O2" OR "electrogenerated H2O2" OR "AO-H2O2" OR "EO-H2O2" OR "AO/H2O2" OR "EO/H2O2")) AND (LIMIT-TO (LANGUAGE, "English"))	67
All Fenton-based processes	(TITLE-ABS-KEY (bdd OR "doped diamond") AND TITLE-ABS-KEY (*fenton)) AND (LIMIT-TO (LANGUAGE, "English"))	364
Electro-Fenton (EF)	(TITLE-ABS-KEY (bdd OR "doped diamond") AND TITLE-ABS-KEY (fenton) AND NOT TITLE-ABS-KEY ("photo-Fenton" OR "photoelectro-Fenton" OR "PEF" OR "Solar photoelectro-Fenton" OR "SPEF" OR "photoassisted" OR "photo-assisted" OR "photo enhanced" OR "photo-enhanced" OR "sunlight" OR "solar")) AND (LIMIT-TO (LANGUAGE, "English"))	209
Photoelectro-Fenton (PEF)	(TITLE-ABS-KEY (bdd OR "doped diamond") AND TITLE-ABS-KEY (fenton) AND TITLE-ABS-KEY ("photo-Fenton" OR "photoelectro-Fenton" OR "PEF" OR "photoassisted" OR "photo-assisted" OR "photo enhanced" OR "photo-enhanced")) AND (LIMIT-TO (LANGUAGE, "English"))	153
Solar photoelectro-Fenton (SPEF)	(TITLE-ABS-KEY (bdd OR "doped diamond") AND TITLE-ABS-KEY (fenton) AND TITLE-ABS-KEY ("Solar photoelectro-Fenton" OR "SPEF" OR "sunlight" OR "solar")) AND (LIMIT-TO (LANGUAGE, "English"))	55

The bibliometric searches were carried out through search strings connecting the topics by the title, abstract, and keyword fields of articles published until September 2022. The full period of research results and all types of documents were considered, but searches were limited to articles published in the English language. The combination of all search queries performed in the first sampling results in a total of 1590 publications (Figure I.1.2).

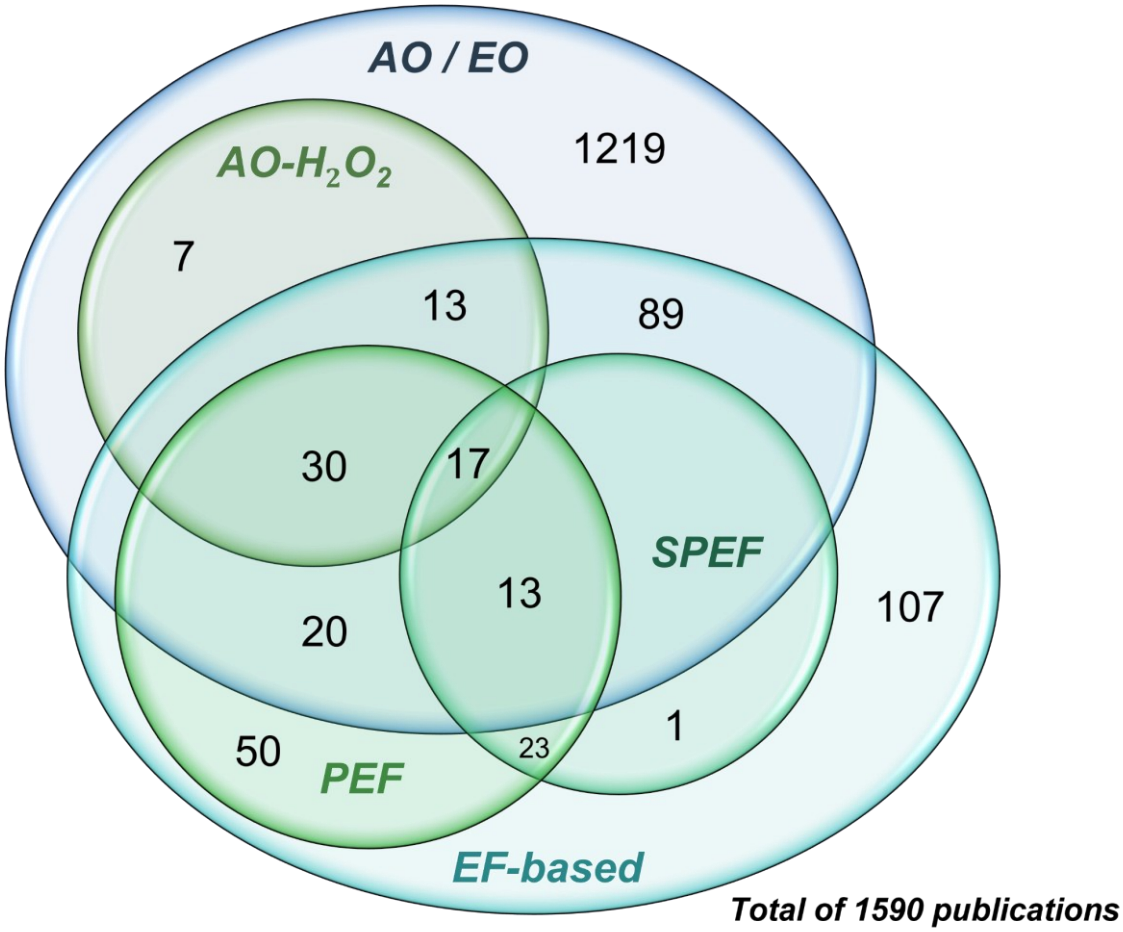

Figure I.1.2. Venn diagram representing EAOP combinations from the first SLR test sample.

The focus of this work was restricted to articles that do not consider the anodic oxidation (AO) process using BDD technology as the common keyword. Therefore, our study was based on the number of publications excluded by the AO cluster (light-blue line in Figure I.1.2), i.e., contemplating 181 out of the total 1590 found publications. Therefore, the selection of articles for the SLR following a first line of thought would be based on these 181 publications. As one of the principles behind SLR methods is to make the selection of documents easily reproducible by anyone, and the method used in this first search requires running many search queries and combining them to arrive at the final selection, we decided to test a second approach to simplify the selection method with only one advanced search string, detailed in Table I.1.2.

Table I.1.2. Details of the Boolean advanced search query: theme, strings, search query, and results, based on the Scopus database.

Theme	Boolean Advanced Search	Scopus Results
Electrochemical Advanced Oxidation Processes using diamond technology	(TITLE-ABS-KEY (diamond AND eaop*) OR TITLE-ABS-KEY (diamond AND aop*)) AND (LIMIT-TO (LANGUAGE, "English"))	164 (Sept/2022)

After performing a previous criteria sampling, the keywords "diamond", "EAOP*", and "AOP*" (abbreviation for Advanced Oxidation Process) were selected for composing this simpler search query. As previously, the search string also connected the topics by the title, abstract, and keyword fields of articles published until September 2022, including the full period of research and all types of documents published in the English language. A total of 164 publications met the set criteria.

By combining the two selection criteria (Table I.1.3), we identified that 154 publications are common to both selections, which represent 94% of the simpler search string results.

Table I.1.3. Details of the Boolean advanced search query combining both tested sample selection methods.

Boolean Advanced Search	Scopus Results
(((TITLE-ABS-KEY (bdd OR "doped diamond") AND TITLE-ABS-KEY ("anodic oxidation" OR "electrochemical oxidation"))) AND NOT (((TITLE-ABS-KEY (bdd OR "doped diamond") AND TITLE-ABS-KEY ("anodic oxidation" OR "electrochemical oxidation") AND NOT TITLE-ABS-KEY ("electrogeneration of H2O2" OR "electrogenerated H2O2" OR "AO-H2O2" OR "EO-H2O2" OR "AO/H2O2" OR "EO/H2O2" OR "Fenton" OR "electro-Fenton" OR "Fered-Fenton" OR "EF" OR "photoelectro-Fenton" OR "PEF" OR "Solar photoelectro-Fenton" OR "SPEF" OR "photoassisted" OR "photo-assisted" OR "photo enhanced" OR "photo-enhanced"))) AND NOT (((TITLE-ABS-KEY (bdd OR "doped diamond") AND TITLE-ABS-KEY ("anodic oxidation" OR "electrochemical oxidation") AND TITLE-ABS-KEY ("electrogeneration of H2O2" OR "electrogenerated H2O2" OR "AO-H2O2" OR "EO-H2O2" OR "AO/H2O2" OR "EO/H2O2"))) OR ((TITLE-ABS-KEY (bdd OR "doped diamond") AND TITLE-ABS-KEY (fenton) AND NOT TITLE-ABS-KEY ("photo-Fenton" OR "photoelectro-Fenton" OR "PEF" OR "Solar photoelectro-Fenton" OR "SPEF" OR "photoassisted" OR "photo-assisted" OR "photo enhanced" OR "photo-enhanced"))) OR ((TITLE-ABS-KEY (bdd OR "doped diamond") AND TITLE-ABS-KEY (fenton) AND TITLE-ABS-KEY ("photo-Fenton" OR "photoelectro-Fenton" OR "PEF" OR "photoassisted" OR "photo-assisted" OR "photo enhanced" OR "photo-enhanced"))) OR ((TITLE-ABS-KEY (bdd OR "doped diamond") AND TITLE-ABS-KEY (fenton) AND TITLE-ABS-KEY ("Solar photoelectro-Fenton" OR "SPEF" OR "sunlight" OR "solar")))))) AND NOT ((TITLE-ABS-KEY (diamond AND eaop*)) OR (TITLE-ABS-KEY (diamond AND aop*))) AND (LIMIT-TO (LANGUAGE, "English"))	154 (Sept/22)

Therefore, the second approach was adopted to select the articles for this review since it is unbiased and can be easily replicated, whilst the first method requires a combination of several queries limited to the methods previously identified (biased). Furthermore, including

EAOP and AOP in the search string makes the selection more representative, including other EAOPs that are not so frequently applied with diamond technology and were not evaluated in the first selection, such as ozonation, photocatalysis, and peroxone process, among others. These alternative EAOPs explain the extra 10 results identified in the second selection in relation to the total 154 documents common to both approaches. From this point onwards, the entire discussion of the bibliometric analysis is based on the 164 articles identified in the second sample (Table I.1.2). These also form the basis of discussion for the specific topics for each type of EAOP discussed in subsequent sections. When necessary, publications relevant to each type of EAOP that have not been selected by the SLR are added to deepen the discussion on each section.

Over the last twenty years, the topic of EAOPs using diamond technology has gained increased interest, especially after the year 2009, reaching a peak in the number of publications ten years later. Figure I.1.3 presents the temporal analysis of the obtained SLR results.

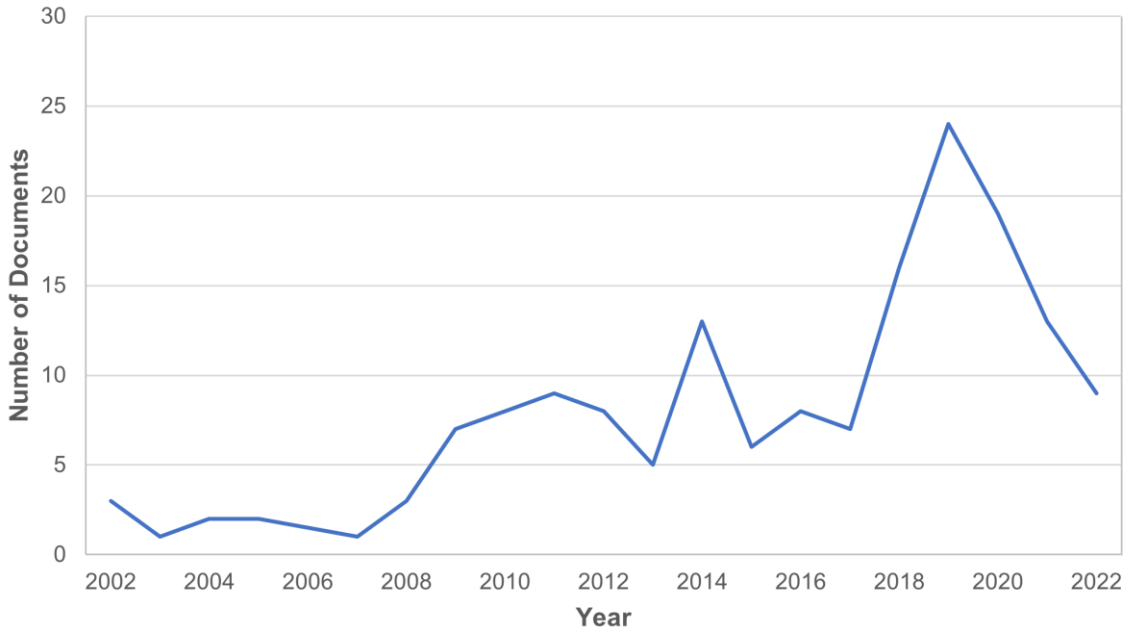

Figure I.1.3. Number of publications per year on EAOPs using diamond technology for water treatment, based on the Scopus database.

Although the number of published articles has decreased over the last two years, it remains scientifically relevant, with 10 publications in the year 2022. The subject areas of Environmental Science, Chemistry, and Chemical Engineering appear as the areas of

interest most related to the theme. It is also important to highlight the areas of Engineering and Materials Engineering which are directly related to the manufacture and optimization of diamond electrodes used in EAOPs. Figure I.1.4 shows the map distribution of the related subject areas.

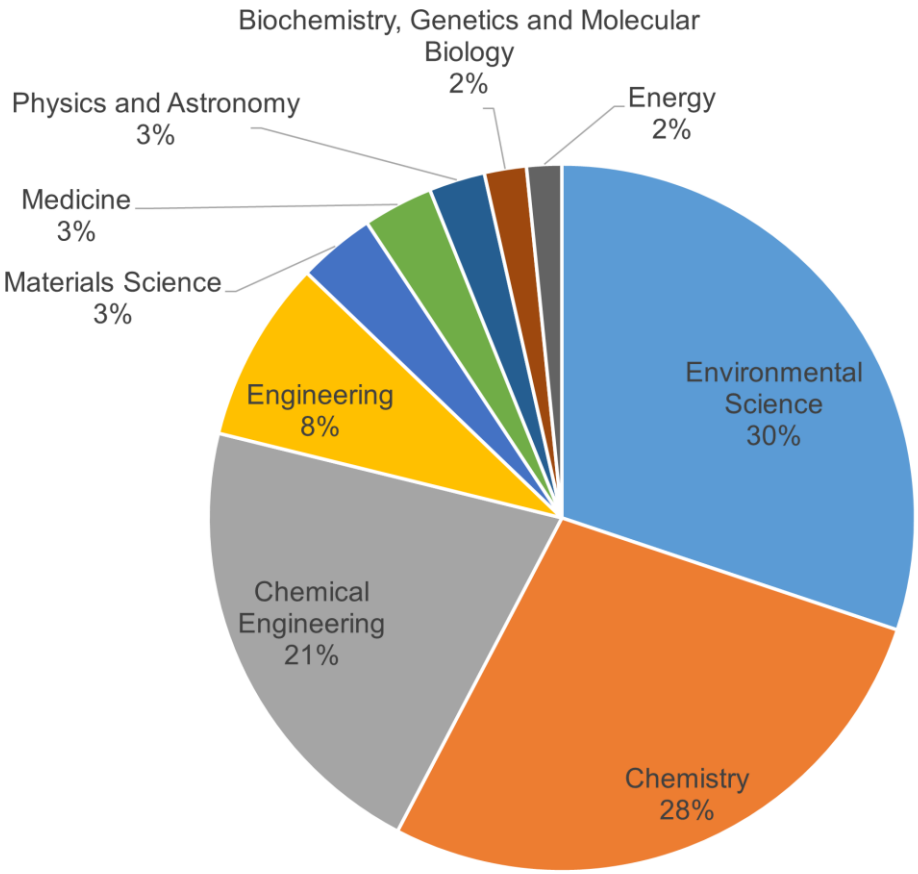

Figure I.1.4. Distribution of the scientific publications according to subject area, based on the SLR article selection performed in the Scopus database. Considered period: 2002–2022.

In these 20 years of research on the subject, most communications were presented in the form of original papers, representing 88% of the SLR results. Six reviews published on the topic were identified, concentrated in the years 2014, 2019, and 2020. In addition, four book chapters were published, and the subject was presented at, at least, nine conferences. Figure I.1.5 shows the distribution of the document type found in the SLR results.

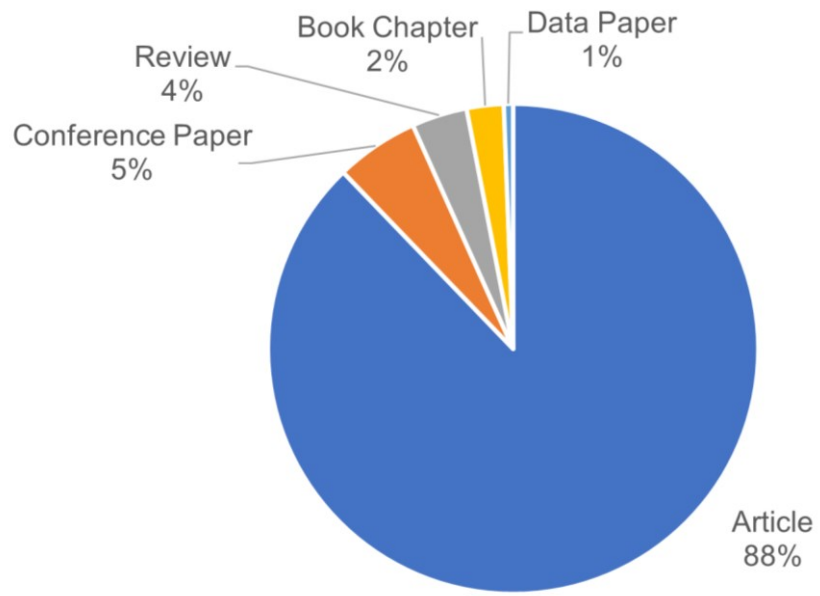

Figure I.1.5. Distribution of publications according to document type, based on the SLR article selection performed in the Scopus database. Considered period: 2002–2022.

In terms of dissemination, articles can be found in more than 60 different journals. Nevertheless, half of those publications are found in only nine of these journals, with more than 30% of the articles published either in Chemosphere, Water Research, Journal Of Electroanalytical Chemistry, or the Chemical Engineering Journal. Figure I.1.6 shows all the journals with at least three publications on the topic.

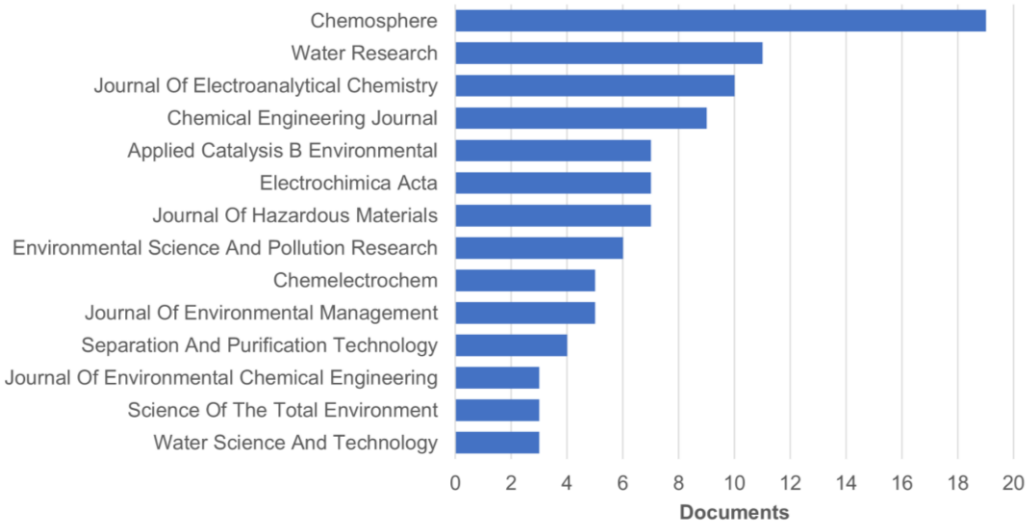

Figure I.1.6. Number of publications per journal with more than three publications on EAOPs using diamond technology for water treatment, based on the SLR article selection performed in the Scopus database. Considered period: 2002–2022.

These results point to widespread research on diamond technology applied in EAOPs for water treatment across the world, with articles published by universities and research centers from all continents. Figure I.1.7.a shows the distribution of articles by country.

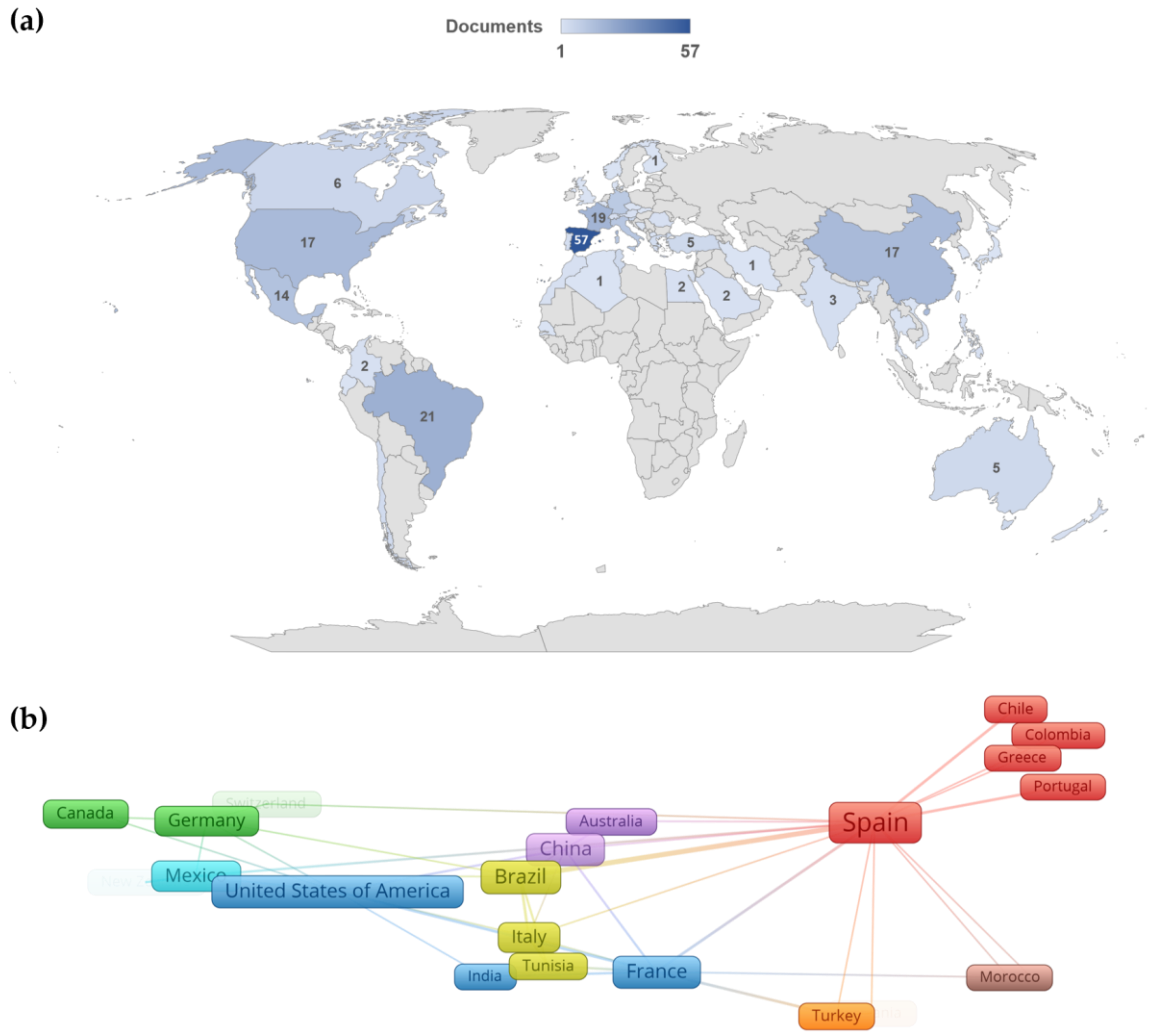

Figure I.1.7. (a) Number of publications per country on EAOPs using diamond technology for water treatment; (b) countries' co-authorship network (minimum of two occurrences) representation on the application of EAOPs using diamond technology for water treatment, based on the VOSviewer bibliometric mapping software (55). All results were based on the SLR article selection performed in the Scopus database. Considered period: 2002–2022.

The country that stands out in the number of papers on the subject is Spain, having a large share of 35% of publications, followed by Brazil (13%), France (12%), China (10%), and the United States (10%). Together, these five countries account for 80% of the articles on the

selected theme. Bibliometric mapping using the VOSviewer tool (55) enables the evaluation of co-authorship of the documents in relation to the countries of publication, as shown in Figure I.1.7.b. The countries that collaborated the most were Spain and Brazil, and we can also highlight France, the United States of America, and Italy for their high link strengths, in other words, their elevated number of collaborations with other countries.

As expected, due to the high number of articles from Spain, when we evaluate publications by universities and research centers, the Spanish institutions also stand out in number. Notably, the Universitat de Barcelona (Spain) is accountable for 35% of all publications on the topic, in addition to participating in 100% of Spanish publications. Figure I.1.8 presents the distribution of published articles according to universities and research centers that have at least four publications on the subject.

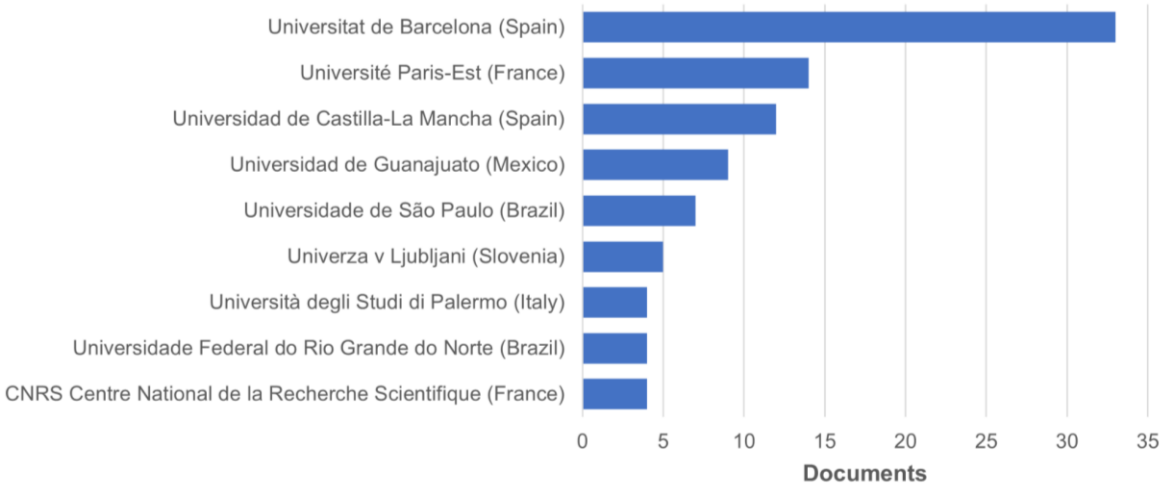

Figure I.1.8. Number of publications per university and research center with more than four publications on EAOPs using diamond technology for water treatment, based on the SLR article selection performed in the Scopus database. Considered period: 2002–2022.

Other outstanding institutions are also worth mentioning in the contribution to the theme, such as Université Paris-Est (France), Universidad de Castilla-La Mancha (Spain), Universidad de Guanajuato (Mexico), and Universidade de São Paulo (Brazil).

A keyword network graph (Figure I.1.9) was built to identify the trends in the use of diamond technology in water treatment through EAOPs, and to verify the relationship among the major topics. In order to build this map, a dictionary of keywords was created, and a pre-treatment of the data was carried out so that there were no repetitions of keywords with the same meaning (e.g.: boron-doped diamond, boron doped diamond, doped diamond, and BDD) but written in a slightly different manner.

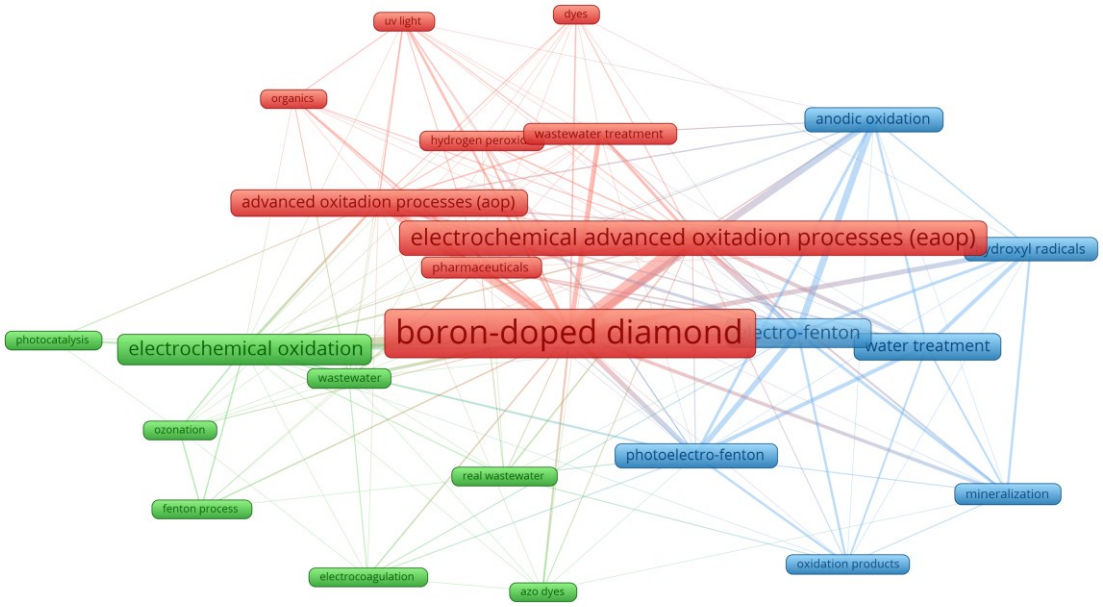

Figure I.1.9. Keywords co-occurrence network (minimum of five occurrences) representation of the trends on the application of EAOPs using diamond technology for water treatment, based on the Scopus database and VOSviewer as the bibliometric mapping software (55,56).

There are three major clusters visible in the keywords network graph. As expected, the largest one (red color) represents mostly the use of BDD electrodes in EAOPs for water treatment. This cluster also shows add-ons (complementary techniques) used in different EAOPs, such as UV light or the generation of hydrogen peroxide. Furthermore, the red cluster also presents the most applied pollutants in degradation studies, such as organics, dyes, and pharmaceuticals. The blue cluster mainly represents the most applied EAOP methods: anodic oxidation (AO), electro-Fenton (EF), and photoelectron-Fenton (PEF), as well as the hydroxyl radicals. Their electrogeneration at the diamond surface is the basic requirement for effectively treating water through anodic oxidation since they are the main actors in the mineralization of the pollutants. Finally, the green cluster shows other wastewater treatment methods (photocatalysis, ozonation, Fenton process, and electrocoagulation) that were compared to EAOPs using diamond technology or combined with BDD electrodes to improve efficiency. The keywords: wastewater, real wastewater, and azo dyes also appear, indicating that the group of articles represented by this cluster mostly

applied the above-mentioned methods to treat real wastewater and water contaminated with azo dyes.

After careful analysis of the methods applied in water treatment mentioned in each of the SLR-selected articles, we built a network map (Figure I.1.10.a), along with a chart containing data on the distribution and frequency of the methods (Figure I.1.10.b).

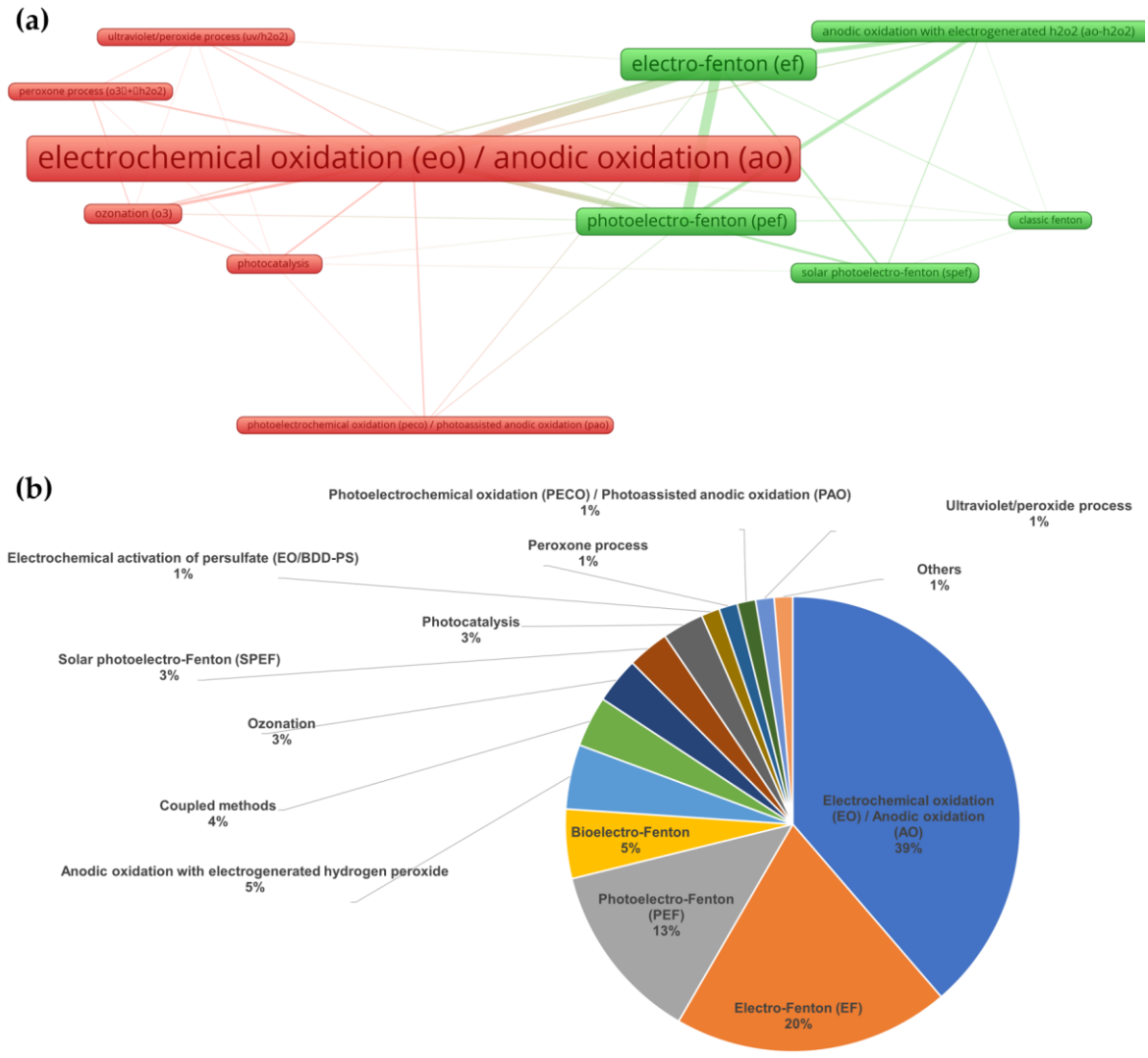

Figure I.1.10. (a) EAOPs co-occurrence network (minimum of two occurrences) representation on the application of diamond electrodes for water treatment, based on the VOSviewer bibliometric mapping software (55,56); (b) Distribution data on EAOPs applied in the publications selected by the SLR, based on the Scopus database.

The most widely applied method was anodic oxidation (AO), also frequently referred to as electrochemical oxidation, mentioned in 39% of the articles. Secondly, it was electro-Fenton (EF) (20%), which is based on the electrochemical production of H_2O_2 with the addition of

Fe^{2+} in the bulk solution to produce additional hydroxyl radicals as a by-product of the Fenton reaction (57). The third most applied method was photoelectro-Fenton (PEF) (13%), which is based on the combination of EF with UV light irradiation to enhance the degradation efficiency (58). In addition, other identified relevant methods were bioelectro-Fenton, anodic oxidation with electrogenerated H_2O_2, ozonation, solar photoelectro-Fenton, photocatalysis, electrochemical activation of persulfate, peroxone process, photoassisted anodic oxidation, and ultraviolet/peroxide process. The methods network graph allowed us to identify which techniques co-occur in the articles, highlighting those that were frequently compared with each other, namely AO, EF, and PEF. A high number of articles comparing these processes with electrogenerated H_2O_2 was also observed, agreeing with the previous indications given by the Venn diagram in Figure I.1.1.

SLR analysis equally revealed the importance of the keywords adopted by each author. Despite applying a systematic method like SLR, we noticed that many articles had not been identified due to the use of non-uniformized keywords or different descriptions for the same EAOP throughout the literature, complicating the identification and proper selection of searched articles. Adopting such practice would only benefit the scientific community and the authors themselves. It would most probably enable the authors to reach out to a higher number of researchers and, consequently, obtain more citations only by adopting standard terms in their titles, abstracts, and keywords. It is certainly important for an author carrying out an SLR to previously identify the maximum possible number of keywords related to the researched topic. However, when there is a large variation between terms representing the same subject, it is likely that some of them will be unknown and/or unidentified. Furthermore, by applying the SLR method using simpler and more comprehensive keywords (such as just “diamond”, “EAOP”, and “AOP”), we were able to analyze a small but representative sample of hundreds of publications concerning diamond technology applied to EAOPs and extract important insights and relevant information on the theme.

The next sections of this manuscript are organized following the main indications given by the SLR analysis.

I.1.3. Doped Diamond Technology Add-Ons

This section focuses on the main explored combination of other techniques (add-ons) to the AO process applying BDD technology: indirect electrolysis to generate additional strong oxidant agents (persulfates, perphosphates, perchlorates or hypochlorite, ozone) and photocatalysis, which enhances the anodic oxidation by the addition of photocatalysts to the AO process.

I.1.3.1. Indirect Electrolysis

As previously stated, EAOPs are essentially methods based on the electrooxidation reaction between strong and specific oxidative species and organic water pollutants. Ideally, such chemical reactions should be nonselective and lead to the complete mineralization of the pollutants (R) into carbon dioxide, water, and innocuous inorganic compounds. The efficiency of these eco-friendly processes relies on the on-site generation of the reactive species and their oxidative strength, which, in turn, highly depends on the aqueous media's chemical nature. The hydroxyl radical (•OH) is probably the most reported oxidizing agent, since it rapidly interacts with the organic pollutants in a radical oxidation chain reaction (22). BDD anodes electrogenerate a considerable amount of these radicals (Eq. I.1.1 and Eq. I.1.2), but their short lifetime is restricted to the surrounding area of the electrode surface (22).

$$BDD + H_2O \rightarrow BDD(^{\bullet}OH) + H^+ + e^- \qquad \textbf{Eq. I.1.1}$$

$$BDD(^{\bullet}OH) + R \rightarrow BDD + CO_2 + H_2O \qquad \textbf{Eq. I.1.2}$$

Another approach to oxidize water pollutants is *in situ* generation of additional oxidizing agents through indirect electrolysis. On the other hand, BDD electrodes have also been used in the electrochemical synthesis of strong oxidants such as persulfates, perphosphates, perchlorates, or hypochlorite (59). Anodic oxidation of sulfate, carbonate, or phosphate ions present in the solution produces these mediators according to Eq. I.1.3–I.1.5 (22).

$$2SO_4^{2-} \rightarrow S_2O_8^{2-} + 2e^- \qquad \textbf{Eq. I.1.3}$$

$$2CO_3^{2-} \rightarrow C_2O_6^{2-} + 2e^- \qquad \textbf{Eq. I.1.4}$$

$$2PO_4^{3-} \rightarrow P_2O_8^{4-} + 2e^- \qquad \textbf{Eq. I.1.5}$$

Thus, conductive diamond anodes simultaneously produce hydroxyl radicals as well as other strong oxidizing agents from supporting electrolytes present in wastewaters or added to those with low conductance. Reportedly, these mediated oxidation processes demonstrate higher overall oxidation efficiency when compared to that of conventional BDD electrooxidation (22,59–72). The success of EAOPs in basic or neutral media has only been

recently evaluated, and it appears to be slightly limited. The limitations can be overcome if persulfate radicals are generated at BDD anodes by the electro-activation of sulfate. When competing with water oxidation, these mediators contribute to the inhibition of oxygen evolution and deter mass-transfer limitations. Moreover, EAOP's drawbacks are compensated, and their efficiency and cost reduction are enhanced (73–75).

Ozone is a clean and strong oxidant thoroughly used in pathogenic and bacterial disinfection and in the oxidation of inorganic or organic compounds. It was one of the first oxidants used in the disinfection of public swimming pools and municipal water treatment plants due to its high oxidation standard potential (E° = 2.1 V) (76). According to Eq. I.1.6 and Eq. I.1.7, the production efficiency of electrogenerated ozone at the anode is limited by the thermodynamically favored oxygen evolution, which takes place at a lower potential (22).

$$3H_2O \rightarrow O_3 + 6e^- + 6H^+ \ (E^o = 1.51V \text{ vs. SHE}) \qquad \textbf{Eq. I.1.6}$$

$$2H_2O \rightarrow O_2 + 4e^- + 4H^+ \ (E^o = 1.23V \text{ vs. SHE}) \qquad \textbf{Eq. I.1.7}$$

In water disinfection and remediation, ozone production has been focused on reaching higher electrochemical ozone production efficiency (77). This is primarily attained when performing electrolysis at low temperatures, low interfacial pH (higher degradation efficiency in basic medium compared to the acidic one (78,79)), and using electrodes with high oxygen evolution overpotential such as metallic oxides (MOx, M = Pb, Ti, Ir, Sn, Sb, Ru, Pd, Rh) (79–81). Electrogenerated ozone using BDD anodes was first reported (to the best of our knowledge) by Katsuki *et al.*, concluding that the percentage of current efficiency was low and dependent on the current density and operating temperature (82). Since then, several efforts have been made to maximize the current efficiency as well as the amount of ozone produced. Michaud *et al.* studied the electrolysis in aqueous $HClO_4$ and H_2SO_4 solutions using BDD electrodes and found that small amounts of O_3 and H_2O_2 are formed in both electrolytes (83). Based on these results, they proposed a simple mechanism for the electrogeneration of hydroxyl radicals, hydrogen peroxide, and ozone, and it is globally adopted. Park demonstrated that ozone was stably generated at BDD anodes for long periods of time (84,85), and Arihara *et al.* innovated the design of such electrodes and used a freestanding perforated doped diamond electrode which achieved a current efficiency of about 29% at the applied current of 1 A (86). The design of the electrodes and/or of the electrochemical cell was further explored by Kraft *et al.* using a sandwich with a diamond

anode, Nafion® polymer electrolyte, and diamond cathode, concluding that ozone production is favored by increasing flow rate and current, but it decreases with increasing conductivity of the electrolysed waters (87). Sekido and Kitaori developed a small-sized generator driven by a dry-cell (later improved) for use in the average household, obtaining an ozone concentration of over 4 mg/L, which is sufficient for water disinfection (88,89). A few years later, Honda *et al.* followed the trend and used a free-electrolyte system including a couple of BDD electrodes as the anode and cathode in combination with Nafion® N117/H^+ as the separating membrane, reaching around 40% of current efficiency (90). At this point, and side-by-side with nickel-antimony-doped tin dioxide, doped diamond is a promising technology for electrogenerated ozone with a current efficiency of over 30% under mild experimental conditions (81). Choi *et al.* studied the influence of inert supporting electrolytes on a solid polymer electrolyte/BDD system and provided a better mechanistic understanding of such an effect (91), and Park *et al.* tried to find a correlation between the physical and chemical properties of BDD anodes and the ozone concentration found in the water (92). Kanfra *et al.* explored the viability of replacing harmful pesticides with short-lived oxidants, such as ozone produced by low operating voltages diamond-based generators, with possible application in agricultural outdoor operation (93). The geometry and electrochemically active surface area of the BDD electrodes for ozone generation was further investigated by Liu *et al.* using a microporous BDD electrode etched by oxygen plasma (94). The latter showed 3.76-times improved ozone generation capacity (under the same unit energy consumption) when compared to the bare BDD. Wood *et al.* reported the synthesis of nitrogen-doped diamond microparticles under high pressure and high temperature (HPHT), which were then compacted to a freestanding solid electrode and then laser micromachined to give a perforated electrode (95). These anodes yielded 2.23 ± 0.07 mg/L of ozone per ampere of current, at consistent levels for a continuous 20 h period. Recently, Li *et al.* explored a solid polymer electrolyte electrolyzer and found that ozone production is favored by the medium current density (125 mA/cm^2) and higher water flow rate (63 L/h) (96). An ozone concentration of 4.86 mg/L was achieved at the highest current efficiency of 51.29% and the lowest specific power consumption of 37.95 Wh/g.

Photo-assisted electrooxidation using BDD anodes has also been explored as an alternative process for wastewater treatment. Predominantly, the UV/*in situ* electrochemical oxidation of contaminants is more effective if compared to direct UV irradiation (photolysis) or electrochemical oxidation by BDD technology (97–106). This is mainly due to the production of homogeneous $^{\bullet}OH$ radicals from *in situ* generated oxidants such as H_2O_2, O_3, and $S_2O_8^{2-}$ which results in a unique synergistic degradation mechanism with enhanced

oxidation and mineralization conditions (98,98–101). Moreover, electricity is the only required input sustaining the combined UV/AO, which can easily be replaced by the use of solar energy alone (107).

I.1.3.2. Photoelectrocatalysis

Conventional chemical advanced oxidation processes (AOPs) usually involve oxidizing species such as hydrogen peroxide (H_2O_2) and a catalyst such as the ferrous ion (Fe^{2+}), known as Fenton or Fenton-like processes, further addressed in Section 4. Photocatalysis is another traditional AOP that requires light irradiation/photons to photolyze the oxidant agent with resulting $^{\bullet}OH$ radicals. Generally, the photocatalyst is a semiconductor and must be excited with higher energy (irradiation with a specific wavelength) than that of its bandgap. The excited electrons are then promoted into the conduction band (e_{cb}^-), leaving positive vacancies or holes (h_{vb}^+) that oxidize water or hydroxide ions, and $^{\bullet}OH$ radicals are then generated, as illustrated in Eq. I.1.8–I.1.10 (108).

$$\text{Photocatalyst} + h\nu \rightarrow e_{cb}^- + h_{vb}^+ \qquad \textbf{Eq. I.1.8}$$

$$h_{vb}^+ + H_2O \rightarrow {}^{\bullet}OH + H^+ \qquad \textbf{Eq. I.1.9}$$

$$h_{vb}^+ + OH^- \rightarrow {}^{\bullet}OH \qquad \textbf{Eq. I.1.10}$$

Thus, photocatalysis has been widely adopted as an AOP. Among several semiconductors tested in photocatalysis, titanium dioxide (TiO_2) is the most frequently used. It is a UV-based photocatalyst (crystalline anatase bandgap of 3.2 eV) but is also energy-consuming (108). Therefore, numerous visible light active photocatalysts have also been described as well as modified TiO_2 catalysts (109,110). Considering the process application, the photocatalysts can be directly added to the medium enabling a large contact surface between the photons and the catalyst and assuring that the quantum yield is high enough for oxidation of the pollutants. Nevertheless, the suspended catalyst needs to be recovered in a further separation stage. The alternative is to immobilize it onto a carefully chosen substrate and guarantee strong adhesion between the photocatalyst and the support and stability during photocatalysis (109,111,112).

EAOPs became the efficient alternative that provides *in situ* and constant generation of oxidizing agents during electrolysis solely using clean electrons. Furthermore, immobilization of the photocatalysts onto different supports led to different configurations for photocatalytic reactors, and the possible synergy resulting from the combination of

photocatalysis and electrochemical anodic oxidation shortly started to be explored, including BDD technology (113). The main findings for photoelectrocatalytic studies are summarized in Table I.1.4.

Table I.1.4. Examples of reported studies on photoelectrocatalysis using BDD technology.

Support	Catalyst	Pollutant	EAOP	* TOC %	* COD %	** ED %	Ref.
Thin film	TiO_2	Red X-3B	TiO_2+UV BDD+UV TiO_2@BDD+UV	29.8 67.6 74.2			(114)
Thin film	$ZnWO_4$	Red X-3B	$ZnWO_4$+UV BDD+UV $ZnWO_4$@BDD+UV	-	-	-	(115)
Thin film	Ce-TiO_2	Red X-3B	Ce-TiO_2+UV BDD Ce-TiO_2@BDD+UV			0.067 (h^{-1}) 0.137 (h^{-1}) 0.445 (h^{-1})	(116)
Thin film	ZnO	Yellow 15	ZnO@BDD+UV B-ZnO@BDD+UV			35 73	(117)
Film	ZnO	Methyl orange	ZnO@BDD+UV			~85	(118)
Thin film	TiO_2/Sb-doped SnO_2	Bisphenol A	BDD TiO_2/Sb-doped SnO_2@BDD+UV			58.9 67.3	(119)
Film	TiO_2	-	TiO_2@BDD+UV	-	-	-	(120)
Thin film	TiO_2	Methyl orange	TiO_2+simulated solar light BDD TiO_2@BDD+simulated solar light			45 56 100 (4 h)	(121)
Thin film	TiO_2	Methylene blue	BDD TiO_2@BDD+UV			~20 ~55	(122)
Thin film	TiO_2	Glyphosate	BDD TiO_2@BDD+UV	67 85.3	81 95.2		(123)
Nanoparticles	TiO_2	Herbicides	TiO_2+simulated solar light BDD TiO_2@BDD+simulated solar light			90 (18.05 h) 90 (1.98 h) 90 (1.15 h)	(124)
Thin film	TiO_2	Diclofenac	BDD TiO_2@BDD+UV	76.1 80.1	83.6 84.7	85.6 98.5	(125)
Thin film	$BiVO_4$	Tetracycline hydrochloride	$BiVO_4$@BDD+ simulated solar light			45.1(10 min)	(126)

** Mineralization parameters: TOC—Total Organic Carbon; COD—Chemical Oxygen Demand. ** ED—Efficiency in pollutant degradation into broken-down products.*

Most of the reported works are successful efforts using BDD as the physical support for the combined photocatalysts (mainly TiO_2), which avoids an additional removal step of the catalysts after the process, and enables their recycling and reuse (115–120,125). Moreover, these studies also demonstrate that photoelectrocatalysis improves the degradation and mineralization of the pollutants when compared to conventional BDD anodic oxidation (114,122,124). Thus, interesting synergistic effects in the composite photoanode with a 3D framework structure are observed, although, in both oxidation processes, the adopted experimental conditions largely define the degradation and mineralization kinetics of the contaminants. The n/p-type heterojunction established between most of the photocatalysts and BDD has also been further explored, and it is concluded that the nanoparticles properties and the interface structure are highly critical to optimize the accelerated production rate of $^{\bullet}OH$ radicals (121,126). Lastly, some works also include the determination of energy efficiencies which are equally significant parameters to be taken into account when evaluating EAOPs (125).

In this section, a brief overview of additional strong oxidants simultaneously formed during the electrooxidation of water pollutants was carried out, particularly persulfate radicals and ozone. The electrogeneration of persulfate radicals is a sustainable synergetic effect but is strongly pH dependent which presents a real limitation. On the other hand, anodically activated persulfate radicals through naturally occurring electrolysis processes (resistive heating or combination with UV photolysis as a post-treatment step) further improve the electrocatalytic performance of BDD anodes (69). Diamond-based clean technology also clearly proved to be one of a few able to efficiently electrogenerate ozone water for disinfection, sterilization, and treatment purposes. The stability of BDD anodes allied with their performance in terms of high-yielding hydroxyl and ozone concentration, with no harmful NO_X formation, greatly benefits EAOPs used in water remediation.

Photoelectrocatalysis offers another add-on to BDD anodic oxidation. In this case, the amount of hydroxyl radicals produced at the diamond anode surface (water electrolysis) is enhanced by additional hydroxyl radicals generated by irradiation of a photocatalyst which, in turn, oxidizes water or hydroxide ions. This process shows good potential, but further development of the design and fabrication of the photoanodes is still required to improve the efficiency of wastewater treatment using BDD technology, and additional costs must also be assessed.

I.1.4. EAOPs Synergism with Doped Diamond Technology

In this section, Fenton-based EAOPs applying BDD technology are discussed in detail. The first subsection is related to the literature found on electro-Fenton (EF), and the second one to photo-enhanced electro-Fenton processes.

I.1.4.1. Electro-Fenton

The era of Fenton chemistry began in 1894 when Henry J. Fenton first discovered that Fe(II) salts could activate H_2O_2 to oxidize tartaric acid (127). Peroxides (often H_2O_2) and iron ions undergo reactions known as Fenton reactions (Eq. I.1.11), which result in active oxygen species (primarily hydroxyl radicals) that oxidize organic or inorganic compounds (20).

$$Fe^{2+} + H_2O_2 \rightarrow Fe^{3+} + {}^{\bullet}OH + OH^- \qquad \textbf{Eq. I.1.11}$$

The electro-Fenton (EF) process is an indirect electrochemical process as opposed to anodic oxidation (AO), which is a direct electrooxidation method. It involves the electrogeneration of H_2O_2 at the cathode with the addition of an iron catalyst (Fe^{2+}, Fe^{3+}, or iron oxides) to the solution (128), mostly used among the Fenton-based advanced oxidation processes. Electrogeneration of H_2O_2 is performed by either directly infusing oxygen into Gas Diffusion Electrodes (GDEs) or dissolving O_2 or air into the solution to then be reduced at suitable cathode materials (Eq. I.1.12) (129).

$$O_2 + 2H^+ + 2e^- \rightarrow H_2O_2 \qquad \textbf{Eq. I.1.12}$$

Examples of cathodes usually applied in EF are carbon-polytetrafluoroethylene (carbon-PTFE) (130), graphite (131), carbon felt (132), reticulated vitreous carbon (133), carbon nanotubes (134), activated carbon fiber (135), and carbon sponge (136). The process is known as anodic oxidation with electrogenerated H_2O_2 (AO-H_2O_2) if no catalyst is added to the solution (137).

Further development and effective application of Fenton-based reactions have been delayed by flaws such as excessive chemical use, resulting in Fe-rich sludge, generation of refractory Fe(III)-carboxylate complexes, and low efficiency as a result of parasitic reactions (137,138). However, its combination with electrochemistry allowed the research community to get around most of the above-mentioned drawbacks. In EF processes, the commonly

used large amounts of iron salts (Fe^{3+}) are reduced at the cathode (E^o = 0.77 V vs SHE**)** and then converted back to Fe^{2+} (Eq. I.1.13) (129).

$$Fe^{3+} + e^- \rightarrow Fe^{2+} \qquad \textbf{Eq. I.1.13}$$

The cost of the chemical reagents, the sludge generation, and the dangers related to the transport and storage of peroxides are all avoided by the continuous production of H_2O_2 and electro-regeneration of Fe^{2+} at the optimal operational pH value (3.0) (139). In EF water treatment, organic compounds are oxidized by hydroxyl radicals produced through water oxidation at the reaction layer of the anodes and in the bulk solution by the additional hydroxyl radicals resulting from the Fenton reaction between H_2O_2 and Fe^{2+} (Eq. I.1.11) (128). Other reactive oxygen-based species, such as H_2O_2 and the hydroperoxyl radical ($^{\bullet}HO_2$), also contribute to the oxidation of organics in EF-based processes in undivided electrochemical cells (57). The oxidation of H_2O_2 to O_2 at the anode surface produces $^{\bullet}HO_2$ radicals as intermediate products (Eq. I.1.14) (140).

$$H_2O_2 \rightarrow {}^{\bullet}HO_2 + H^+ + e^- \qquad \textbf{Eq. I.1.14}$$

Some researchers also suggest that high-valent oxo-iron complexes may participate in Fenton-based oxidation processes, usually referred to as the non-classical Fenton pathway (141). There is some consensus among researchers that classical and non-classical mechanisms coexist and predominate in different ways depending on the operating conditions (142).

The first mention (to the best of our knowledge) of an EF process dates back to 1986 when Sudoh *et al.* applied the method to mineralize phenol in aqueous solutions (139). Different anode materials (PbO_2, doped SnO_2, IrO_2, RuO_2, and Pt) were tested throughout the earlier publications on EF organics mineralization (128,139,143–145). Nearly two decades later, BDD began to be applied as the anode in EF methods based on the demonstrated indication that BDD technology is the most suitable anode material for EF water treatment (146). According to a study by Flox *et al.*, a PbO_2 anode, compared with BDD, was able to completely eliminate *m*-cresol from aqueous solutions in a shorter amount of time (147). However, the mineralization process of *m*-cresol with PbO_2 was significantly less effective under comparable conditions. The BDD anode achieved a quasi-complete mineralization rate of 98%, with an energy consumption of 139 kWh/m^3, while the PbO_2 attained a much

lower mineralization rate (68%) and required higher energy consumption (165 kWh/m^3) to achieve the total disappearance of aromatic intermediates. Ganiyu *et al.* studied the EF mineralization of the analgesic antipyretic 4-aminophenazone with BDD and sub-stoichiometric TiO_2 anodes (148). After 8 h of treatment with a 30 mA/cm^2 applied current density, the EF/BDD process achieved a Total Organic Carbon (TOC) removal of 96%, while the EF/sub-stoichiometric TiO_2 only removed 51% of TOC. Bocos *et al.* studied a sequential combination of electrocoagulation (EC) with EF as a post-treatment process to treat solutions spiked with bronopol, a common antiseptic and preservative used in cosmetics and hygiene products to prevent bacterial growth (130). Four types of anode material were compared in the EF treatment of electrocoagulated solutions: Pt, BDD, IrO_2-based and RuO_2-based dimensionally stable anodes (DSAs). The Pt, IrO_2-based and RuO_2-based anodes were not able to significantly remove TOC from the electrocoagulated solution containing very refractory organic compounds. In contrast, the BDD electrode could eliminate TOC up to 85% from the same solution after 420 min of global treatment (60 min of electrocoagulation and 360 min of EF/BDD). Klidi *et al.* compared a commercial BDD electrode with a DSA anode (Ti/IrO_2-Ta_2O_5) for the treatment of real paper-mill wastewater samples, and the superior performance of BDD over DSA electrodes was again demonstrated (149). After 5 h of continuous EF treatment, BDD could remove 85% of TOC from the samples, with a 22% current efficiency (CE), while the DSA anode only removed 40% of TOC, with a 12% CE. In another study, Olvera-Vargas *et al.* applied the EF process to remediate artificial solutions containing five drugs and one industrial chemical detected in a real pharmaceutical company effluent (135). Again, BDD achieved better results in terms of TOC removal and CE, promoting almost complete mineralization (97.30 %) after 6 h of EF under optimized conditions (compared to a DSA electrode (Ti/IrO_2−RuO_2)). Despite the optimum solution pH value for EF being considered as 3.0 (139), Olvera-Vargas *et al.* were able to notably achieve good results treating solutions with near-neutral pH (6.0) (135). There is also extensive literature comparing BDD with Pt anodes in EF processes. The TOC removal ability and current efficiency of BDD have proved to be superior in the EF degradation of diverse pollutants such as the antibiotic sulfamethoxazole (150), the herbicide mesotrione (151), the dye azure B (152), the herbicide atrazine (153), the pharmaceutical paracetamol (154), and the biocide chloroxylenol (155). The set of previously mentioned publications confirms that the oxidative action of hydroxyl radicals is substantially more efficient when BDD is used as the anode in EF processes instead of traditional electrodes. In addition to higher efficiency, the durability and inertness of BDD technology are strong advantages over other materials. Although BDD anodes are

expensive to produce, this disadvantage is easily overcome due to their long operating life. According to Muddemann *et al.*, it is possible to tune the BDD electrode for a service life of up to 18 years (156). Furthermore, BDD is less prone to fouling compared to other electrode materials (41). Even when fouling occurs, simple polarization inversion can easily clean their surfaces (41). In addition, they do not release harmful agents, as in the case of the unstable PbO_2 anode, which tends to release significant amounts of lead into the solution turning it even more harmful than in its pretreatment state (128).

The mineralization efficiency of EF processes highly depends on the H_2O_2 electrogeneration and the Fe^{2+} regeneration rate. Therefore, it is crucial to select the most appropriate cathode material to work with BDD anodes to achieve the highest possible process efficiency. Pérez *et al.* tested three types of cathodes coupled with BDD anodes to improve efficiency and reduce EF's energy consumption and costs (157). They employed cathodes of stainless-steel, reticulated vitreous carbon (RVC) electrode covered with a carbon black (CB), and polytetrafluoroethylene (PTFE) mixture to act as the active phase for the generation of H_2O_2, referred to as the CB/PTFE-RVC cathode, and an aluminum foam modified with CB and PTFE, referred to as the CB/PTFE-Al. The tests were performed in Na_2SO_4 solutions containing the herbicide clopyralid as the model biorefractory organic pollutant in a microfluidic-flow cell coupled with a jet aerator to reduce ohmic resistance and improve mass transfer. Both BDD+CB/PTFE-RVC and BDD+CB/PTFE-Al combinations could completely remove clopyralid in less than 2 h of EF treatment, showing far superior results compared to the BDD-stainless steel couple (56%). The CB/PTFE-Al and BDD electrode pair had the most impressive results, promoting a 64% reduction in cell voltage compared to CB/PTFE-RVC for the same current density. Through this electrode combination and reactor configuration, degradation of clopyralid was fast, efficient, and completed in less than 1 h, with total energy consumption as low as 20 kWh/kg (157). Klidi *et al.* combined BDD anodes with carbon felt, modified carbon felt, and GDE cathodes for paper-mill wastewater treatment (149). The oxidation efficiency after 5 h presented the following order as a function of the cathode material: GDE (40% TOC removal) > modified carbon felt (29% TOC removal) > carbon felt (16% TOC removal). Özcan *et al.* verified whether the efficiency of the EF process in the removal of propham was improved if using Pt or carbon sponge cathodes paired with BDD electrodes (136). The TOC removal efficiency after 6 h was similar for the Pt and carbon sponge cathodes. However, the BDD/carbon sponge configuration was the most energy-effective system, presenting a 21.6% lower energy consumption (4.72 kWh/m^3) compared to that of Pt (6.02 kWh/m^3). BDD technology has also been applied as cathodes (158–162). Cruz-González *et al.* studied the ability to

electrochemically produce H_2O_2 through O_2 reduction on a BDD cathode in EF. After 40 min of electrooxidation at 23 mA/cm^2, 88 mg/L of H_2O_2 were accumulated at the BDD cathode (158). Espinoza-Montero *et al.* reported 250.1 mg/L H_2O_2 electrogeneration after 540 min of electrolysis at 1.5 mA/cm^2 in acidic media using a BDD cathode (159). The addition of phenol required a higher current density of the system (2.5 mA/cm^2) to obtain 153.0 mg/L of H_2O_2 and achieve total mineralization within the same 540 min. Garcia *et al.* observed that, with increased current densities (from 7.8 to 31 mA/cm^2), H_2O_2 generation at the BDD cathode is inhibited by the larger acceleration of reduction of O_2 to OH^- and protons to H_2 (160). According to Oturan, BDD cathodes in EF processes do not offer advantages once equivalent or superior outcomes could be obtained by employing other cathodes that are more reasonably priced (carbon felt, gas diffusion cathode, or carbon sponge) (138). Nevertheless, studies on the use of BDD as a cathode are still scarce. In addition, due to the limited number of publications combining BDD anodes with different cathode materials and BDD itself, it is not possible to clearly state which configuration is the most suitable for EF processes. BDD technology, paired with different cathodes under the same experimental conditions, requires further investigation to achieve the highest EF efficiencies possible.

Regarding degradation efficiency, the advantages of adopting the EF/BDD process for wastewater treatment over AO/BDD are not consensual in the found literature. Oturan *et al.* compared both EAOPs for the atrazine herbicide mineralization in Na_2SO_4 solutions (153). Electrolysis at a current intensity of 1000 mA for 8 h led to 93% TOC removal for AO/BDD and 97% for EF/BDD. The superiority of EF was associated with a higher amount of hydroxyl radicals present in the bulk solution than that generated by BDD, promoting additional organics oxidation. Pinheiro *et al.* also obtained better mineralization rates for EF/BDD (90.2% TOC) compared to AO/BDD (62.4% TOC) for paracetamol degradation, and the energy consumption was substantially lower for the EF/BDD process (2080 kWh/kg$_{TOC}$) than that of AO/BDD (5141 kWh/kg$_{TOC}$) (154). For bronopol (130) and 4-Aminophenazone (148) degradation, EF/BDD again presented higher TOC removal rates than AO with electrogenerated H_2O_2 (AO-H_2O_2). However, both achieved mineralization rates higher than 90%, and their differences were fairly similar. Thus, these are a few studies pointing out that EF/BDD has higher relative oxidation power than AO/BDD. In contrast, Murati *et al.* compared mesotrione herbicide mineralization rates applying BDD technology to both AO and EF processes, and both EAOPs resulted in similar TOC removal rates such as 87% and 85% for AO/BDD and EF/BDD, respectively (151). The performance of AO/BDD was also found to be higher than that of EF/BDD for the biocide chloroxylenol in a study by

Skoumal *et al.*, with TOC removal of 94.6% for AO/BDD and 82.5% for EF/BDD (155). Results from the degradation of some water pollutants applying EF based on BDD technology are summarized in Table I.1.5.

Table I.1.5. Examples of studies that applied BDD anodes to treat pollutants by electro-Fenton processes.

Pollutant	EAOP	Anode	Cathode	Fe^{2+} conc. (mM)	pH	Initial conc. (mM)	Initial TOC (mg/L)	% TOC Removal	Time (min)	Ref.
bronopol	AO-H_2O_2	BDD	carbon-PTFE	-	3	2.78	100	95%	480	(130)
	AO-H_2O_2	BDD	carbon-PTFE	-	-	2.78	100	simulated water: 90%	480	
	EF	BDD	carbon-PTFE	0.5	3	2.78	100	>99%	480	
	EF	BDD	carbon-PTFE	0.5	-	2.78	100	simulated water: >99%	480	
sulfamethoxazole	EF	BDD	carbon-felt	0.2	3	1.3	150	88%	600	(150)
	EF	Pt	carbon-felt	0.2	3	1.3	150	84%	600	
4-Aminophenazone	AO-H_2O_2	BDD	carbon-felt	-	3	0.192	30	98%	480	(148)
	AO-H_2O_2	Pt	carbon-felt	-	3	0.192	30	82 %	480	
	EF	BDD	carbon-felt	0.2	3	0.192	30	99%	480	
	EF	Pt	carbon-felt	0.2	3	0.192	30	94%	480	
paper mill wastewater	EF	BDD	modified carbon felt	0.5	3	-	115	85%	300	(149)
	EF	DSA	modified carbon felt	0.5	3	-	115	40%	300	
mesotrione	AO	BDD	carbon-felt	-	3	0.1	17	95%	480	(151)
	EF	BDD	carbon-felt	0.1	3	0.1	17	94%	480	
	EF	Pt	carbon-felt	0.1	3	0.1	17	91%	480	
azure B	AO-H_2O_2	BDD	carbon-felt	-	3	0.1	18	96%	480	(152)
	EF	BDD	carbon-felt	0.1	3	0.1	18	95%	480	(135)

	EF	Pt	carbon-felt	0.1	3	0.1	18	85%	480	
pharmaceuticals mixture	EF	BDD	carbon-fiber brush	3.33 * mg/L	6	-	40	97.3%	360	(135)
	EF	$Ti/IrO_2–RuO_2$	carbon-fiber brush	3.33 * mg/L	6	-	40	~91%	360	
atrazine	AO	BDD	carbon felt	-	6.7	0.1	10	93%	480	(153)
	EF	BDD	carbon felt	0.1	3	0.1	10	97%	480	
	EF	Pt	carbon felt	0.1	3	0.1	10	81%	480	
propham	EF	BDD	carbon sponge	0.2	3	0.5	62.3	78%	120	(136)
	EF	BDD	Pt	0.2	3	0.50	62.3	68%	120	
	EF	Pt	carbon sponge	0.2	3	0.50	62.3	61%	120	

** TOC—Total Organic Carbon.*

This section shows that BDD is the most promising anode material for EF applications. It was also noted that there is no definition of which type of cathode is best suited to be used in conjunction with BDD anodes in EF processes. To reach such a conclusion, comparing different cathode materials will be necessary, considering the costs, durability, H_2O_2 generation rates, and energy consumption for each electrode pair. EF/BDD presented, in general, higher mineralization rates compared to AO/BDD due to the more significant presence of hydroxyl radicals, especially in the bulk of the solution, promoting indirect oxidation in addition to direct anodic oxidation at the BDD's surface. However, AO/BDD presented mineralization rates similar to or even superior to EF/BDD for certain types of pollutants. Thus, to conclude which process is the most suitable for real large-scale application, it is also necessary to consider the nature of the pollutants and the additional costs and maintenance that EF can generate due to the use of catalysts, pH correction to the optimal values during the process, post-treatment (pH neutralization), or even when GDEs are used, adding gas costs.

I.1.4.2. Photo-Enhanced Electro-Fenton Processes

A few years after the first studies in EF (139), Sun and Pignatello suggested irradiating solutions with UV light to improve the oxidizing power of Fenton-based systems (163). A faster generation of hydroxyl radicals was observed due to the photo-reduction of $Fe(OH)^{2+}$

species at wavelength values higher than 300 nm (Eq. I.1.15) (141,164). Additionally, Fe(III)-carboxylate complexes undergo photo-decarboxylation by the incident photons (Eq. I.1.16), promoting Fe^{2+} regeneration, which improves the mineralization efficiency (164,165).

$$Fe(OH)^{2+} + hu \rightarrow Fe^{2+} + {}^{\bullet}OH \qquad \textbf{Eq. I.1.15}$$

$$Fe(COOR)^{2+} + hu \rightarrow Fe^{2+} + CO_2 + {}^{\bullet}R \qquad \textbf{Eq. I.1.16}$$

These findings led to the development of the so-called photoelectro-Fenton (PEF) process. These combine EF with either UVA (λ = 315–400 nm), UVB (λ = 285–315 nm), or UVC (λ < 285 nm) radiation emitted from artificial sources (155).

Mineralization of paracetamol (154) and chloroxylenol (166) was compared employing AO/BDD, EF/BDD, and PEF/BDD, with PEF/BDD performing better and achieving nearly complete mineralization (>97%) after 6 h of electrolysis. Alcaide *et al.* observed extremely low TOC removal rates (<3%) for bentazon herbicide after 240 min when using AO-H_2O_2 with BDD anodes (167). On the other hand, by applying PEF/BDD, around 77% was removed from the solution. Fernandes *et al.* also achieved superior performances while applying PEF instead of AO and photo-assisted AO for imidacloprid oxidation using BDD technology (168). Although UV irradiation of the AO/BDD system enhanced TOC removal rates from 42% to 49%, PEF was more efficient, eliminating 66% of TOC. In contrast, Tirado *et al.* could remediate real cheese whey wastewaters more efficiently with AO photo-assisted using a UVA lamp, demonstrating that PEF does not necessarily have a better performance than photo-assisted AO (169). In a recent study, Bravo-Yumi *et al.* compared AO with EF and PEF for the degradation of synthetic solutions containing tannery dyes Violet RL and Green A and using BDD anode/stainless steel cathode (170). Experiments were carried out under three current densities: 25, 35, and 50 mA/cm^2. For the lowest current density, AO/BDD could remove approximately 64%, 44%, and 63% of color from the solutions containing Green A (80 mg/L), Violet RL (80 mg/L), and a mixture of both dyes (35 mg/L), respectively, after 60 min of electrolysis. After the same time of electrolysis, EF/BDD treatment exhibited approximately 86%, 82%, and 91% of color removal for the solutions contaminated with Green A, Violet RL, and a mixture of both dyes, respectively. The PEF/BDD yielded similar results but slightly superior removal rates: 86% for Green A, 88% for Violet RL, and 93% for the mixture of both dyes. Despite removal efficiencies pointing to PEF/BDD as the best solution compared to AO/BDD and EF/BDD, the

conclusion of the aforementioned study points to another finding. Bravo-Yumi *et al.* also performed a statistical analysis to determine optimum conditions under the lowest operational costs, higher kinetics, and higher degradation efficiency. Thus, the authors considered factors such as current density, EAOP type, initial dye concentration, and dye type. In contrast with the previously mentioned results, the statistical analysis pointed out that AO/BDD has a better performance. This clearly demonstrates that unequivocal conclusions may be drawn from very different results in relation to which EAOPs performs better in real wastewater remediation. Looking closely at the actual panorama, determining the most cost-effective EAOP strongly depends on several outcomes and independent variables but certainly on the main goal to be achieved. One such variable is, for example, the degradation medium itself. Studies comparing EF-based processes applied to synthetic solutions and real water samples (real wastewater (171,172) and reuse, tap and mineral water (173)), showed that degradation of pollutants is more efficient in real samples.

The recent method of solar photo-electro-Fenton (SPEF) was proposed by Casado *et al.* to tackle the problem of the high cost of electrical energy associated with artificial UV lamps employed in PEF processes (165). The SPEF technique involves EF oxidation whilst exposing the solution to sunlight and making use of an inexpensive and renewable energy source with wavelengths higher than 300 nm (57). Solar light provides superior UV radiation intensity as well as extra absorption at wavelengths greater than 400 nm. For example, it is believed that SPEF's mineralization rates are higher for the photolysis of Fe(III)-carboxylate complexes when compared to those by EF or PEF processes (58,155). As demonstrated in the previous subsection regarding EF processes, BDD technology also features prominently in PEF and SPEF. Pinheiro *et al.* studied the mineralization of paracetamol by PEF with BDD and Pt anodes (154). PEF/BDD reached a higher performance in terms of energy consumption (1947 kWh/kg_{TOC}), mineralization efficiency (8.1% MCE), and TOC removal (98.4%) after 6 h of electrolysis at constant applied potential (−2.7 V). Under the same conditions, PEF/Pt achieved values of 2076 kWh/kg_{TOC}, 5.2% MCE, and 86.2% for energy consumption, mineralization efficiency, and TOC removal, respectively. Skoumal *et al.* also observed faster TOC removal rates and higher mineralization efficiencies for PEF/BDD compared with PEF/Pt in the oxidation of the biocide chloroxylenol (166). While the PEF/BDD process eliminated around 97% of TOC from the solution after 5 h of treatment, the PEF/Pt process required 6 h to eliminate approximately 93% of TOC. In another study by Skoumal *et al.*, ibuprofen mineralization by EF, PEF, and SPEF was also enhanced when BDD technology was employed instead of Pt. This is easily explained by the fact that hydroxyl radicals generated at BDD show higher oxidizing ability than those produced over

Pt (155). Thiam *et al.* tested four different anode materials to compare their performances in the degradation of the herbicide chloramben using PEF (BDD, PbO_2, IrO_2-based, and RuO_2-based anodes) (137). The obtained current efficiency was around 4–5% for all the tested anodes, but the highest mineralization power was that of the BDD anode, particularly in the early stages of the PEF process. These results are similar to those from other authors who established the following oxidation power sequence for PEF and SPEF systems: BDD > PbO_2~IrO_2-based > RuO_2-based (172,174).

SPEF consistently stands out in terms of mineralization performance and energy consumption when compared to other EAOPs. Salmerón *et al.* compared AO and SPEF in the degradation of pyrimethanil and methomyl pesticides at a pilot plant scale fitted with filter-press-type electrochemical cells equipped with BDD technology (175). Treating 75 L samples containing 71 mg/L of dissolved organic carbon by SPEF during 120 min eliminated 76% and 70% of pyrimethanil and methomyl, respectively. AO only removed 19% and 33% of pyrimethanil and methomyl, respectively, under the same conditions. Steter *et al.* treated aqueous mixtures of methyl, ethyl, and propylparaben in real urban wastewater with low conductivity by AO-H_2O_2, EF, and SPEF (172). AO-H_2O_2 and EF reached similar TOC removal rates within the 35–36% range, whereas SPEF eliminated 51% of TOC. Salazar *et al.* observed higher mineralization rates for the SPEF treatment of simulated wastewater containing the industrial textile dye Disperse Blue 3 compared with solar photoassisted AO-H_2O_2 and EF (176). Furthermore, the SPEF process consumed less energy (around 64 kWh/kg_{TOC}) to achieve similar TOC removal rates (90–96%). The superior performance of SPEF in relation to EF was also demonstrated by Flox *et al.* in the oxidation of *o*-cresol (128 mg/L) in 0.05 M Na_2SO_4 solutions containing 0.25 mM Fe^{2+} (147). After 180 min of treatment under 50 mA/cm^2, EF removed around 53% of TOC, whereas SPEF achieved almost complete mineralization (around 95%). Many authors have compared SPEF with PEF using BDD technology in water remediation containing pollutants such as erythrosine B dye (177), pesticide triclopyr (178), bronopol (179), landfill leachate (180,181), Evans blue diazo dye (182), ibuprofen pharmaceutical (155), and herbicide mecoprop (183). Although most of these studies were carried out under very different operating conditions (aqueous medium, pollutant concentration, Fe^{2+} concentration, applied current density, irradiation intensity, and cell configuration), SPEF was always pointed out as the best in terms of mineralization if compared to PEF. Skoumal *et al.* demonstrated that irradiating solutions with either UV or sunlight promotes a significant improvement in the kinetic rate, making the process more efficient due to the faster hydroxyl radical production and Fe^{2+} regeneration due to the enhanced photodecomposition of Fe(III)-complexes with

acidic intermediates (155). Under solar irradiation, this phenomenon becomes even more accelerated compared to artificial UV sources (155), explaining the SPEF superiority over PEF and other EAOPs. Nevertheless, the temperature influence over time should also be assessed in SPEF processes.

Experiments conducted without the application of electrical current indicate that the effect of direct photolysis in degradation is negligible (177), demonstrating the excellent synergism between direct oxidation at the BDD surface and photo-enhanced Fenton reactions to achieve faster and more efficient wastewater treatment. However, the degradation mechanisms become slower with time, and in extended electrolysis, oxidation is mainly driven by the hydroxyl radicals formed at the reaction layer of the BDD anode (155,177). In addition, energy consumption is again an important factor in the EAOP selection. In the study by Clematis *et al.*, PEF and SPEF consumed 515.6 kWh/m³ and 20.9 kWh/m³, respectively, to achieve similar degradation performances. In other words, PEF is not entirely suitable for real applications due to its high energy consumption. However, SPEF is limited by weather conditions and the availability of sunlight in many countries throughout the year. Using inexpensive sunlight as a photon source certainly reduces the energy demand, but supplying sufficient power to the electrode set increases the overall cost. Nevertheless, this can easily be overcome by coupling photovoltaic panels or other renewable energy sources to directly power the electrochemical reactor. Thus, the electrical demand for operating the process might be lowered if one turns the process to an entirely self-sufficient system. Furthermore, recent discussions point out that mineralization efficiencies and cost-effectiveness can be further improved by optimizing the design of the electrochemical reactors (184,185).

A few cost studies of different advanced oxidation processes (AOPs) are found in the literature and, for example, three AOPs—AO using BDD electrodes, ozonation, and Fenton oxidation were evaluated by Cañizares *et al.* (186). For all wastes, only AO was able to mineralize the contaminants completely. This study also showed that the degradation efficiency fluctuated with the pollutant concentration due to mass transfer control. It was observed that the nature of the contaminants affected the results obtained in the oxidation by ozonation (at pH 12) or by Fenton oxidation and that large amounts of refractory chemicals were typically accumulated during these treatments. Economic analysis revealed that Fenton oxidation has lower operating costs than AO or ozonation, despite the fact that AO may successfully compete with the Fenton process in the treatment of a variety of pollutants. Regardless of the nature of the pollutant, the investment cost for the ozonation process appeared to be higher than that of either AO or Fenton oxidation. In a more recent

study, Mousset *et al.* evaluated the operational cost efficiency of six distinct types of AOPs, including ozonation, Fenton oxidation, H_2O_2 photolysis, photo-Fenton, electro-Fenton, and photoelectro-Fenton (187). Unfortunately, AO and SPEF were not considered in this study. The most economical AOP overall was electro-Fenton (108–125 €/m^3), considering the use of chemicals, power, and sludge management in the operational cost calculations.
Table I.1.6 summarizes some of the results obtained in studies applying BDD technology in photo-enhanced EF processes for the degradation of water pollutants.

Table I.1.6. Examples of pollutants treated with BDD anodes in photo-enhanced electro-Fenton processes.

Pollutant	EAOP	Fe^{2+} conc. (mM)	pH	Initial conc. (mg/L)	Initial TOC (mg/L)	%TOC Removal	EC (kWh/kg_{TOC})	Time (min)	Ref.
bentazon	AO-H_2O_2	-	3	20	-	<3%	-	240	(167)
	PEF	0.5	3	20	-	77.0%	* 10.1 kWh/m³	240	
4-Aminoantipyrine	PEF	* 47.75 mg/L	3	62.5	40.6	pure water: 64.6%	-	170	(171)
	PEF	* 47.75 mg/L	3	62.5	51.1	municipal secondary wastewater: 65.8%	-	170	
Disperse Blue 3 dye	EF	0.5	3	* 200 mM	~427	90%	~69	360	(176)
	Solar AO-H_2O_2	-	3	* 200 mM	~328	93%	~87	360	
	SPEF	0.5	3	* 200 mM	~427	96%	~64	360	
paracetamol	AO	-	2.9–3.0	157	100	62.4%	5141	360	(154)
	EF	1	2.9–3.0	157	100	90.2%	2080	360	
	PEF	1	2.9–3.0	157	100	98.4%	1967	360	
chloroxylenol	AO	-	3	100	61.5	94.6%	-	360	(166)
	EF	1	3	100	61.5	82.5%	-	360	
	PEF	1	3	100	61.5	97%	-	300	
imidacloprid	AO	-	3	50	-	42%	-	360	(168)
	PEF	1	3	50	-	66%	-	360	
	AO+UV	-	3	50	-	49%	-	360	
	Photochemical oxidation	-	3	50	-	−4% (increased)	-	360	

	SPEF	1	3	50	-	89%	-	360	
chloramben	PEF	0.5	3.4	* 1.19 mM	100	96.3%	-	300	(137)
o-cresol	EF	0.25	3	128	100	~53%	-	180	(147)
	SPEF	0.25	3	128	100	~95%	-	180	
	SPEF	1	3	128	100	>98%	155	180	
m-cresol	SPEF	0.25	3	128	100	~96%	-	180	
	SPEF	1	3	128	100	>98%	155	180	
p-cresol	SPEF	0.25	3	128	100	~94%	-	180	
	SPEF	1	3	128	100	>98%	155	180	
mixtures of methyl, ethyl, and propyl paraben	AO-H_2O_2	-	3	* 0.3 mM each	-	35%	-	240	(172)
	EF	0.2	3	* 0.3 mM each	-	36%	-	240	
	SPEF	0.2	3	* 0.3 mM each	-	real wastewater: 66%	84	240	
	SPEF	0.2	3	* 0.3 mM each	-	51%	-	240	
cheese whey wastewater	AO	-	3	-	21.6	34.7%	-	420	(169)
	AO+UV	-	3	-	21.6	48.8%	-	420	
	PEF	-	3	-	21.6	41.8%	-	420	
	UVA light alone	-	3	-	21.6	32.2%	-	420	
17α-Ethinylestradiol (EE2)	PEF	0.5	3	20	-	deionized water: 74.5%	-	180	(173)
	PEF	0.5	3	20	-	reuse water: 88.4%	8598	180	
	PEF	0.5	3	20	-	tap water: 88.3%	8952	180	
	PEF	0.5	3	20	-	mineral water: 93.6%	7764	180	
erythrosine B dye	EF	0.1	3	100	115	~90%	* 21 kWh/m³	120	(177)
	PEF	0.1	3	100	115	>99%	* 515.6 kWh/m³	120	
	SPEF	0.1	3	100	115	>99%	* 20.9 kWh/m³	120	

triclopyr	AO-H_2O_2	-	7	* 12 mM	17.2	38%	* 2.34 kWh/g_{TOC}	300	(178)
	EF	0.06 mM Fe(III)–EDDS (1:1)	7	* 12 mM	17.2	47%	* 1.81 kWh/g_{TOC}	300	
	PEF	0.06 mM Fe(III)–EDDS (1:1)	7	* 12 mM	17.2	65%	* 19.2 kWh/g_{TOC}	300	
	SPEF	0.06 mM Fe(III)–EDDS (1:1)	7	* 12 mM	17.2	62%	* 1.33 kWh/g_{TOC}	300	
bronopol	AO-H_2O_2	-	3	* 0.28 mM	10	58%	-	360	(179)
	PEF	0.50	3	* 0.28 mM	10	~91%	-	360	
	SPEF	0.50	3	* 0.28 mM	10	94%	* 4 kWh/g_{TOC}	360	
landfill leachate	EF	* $[TDI]_0$ = 60 mg//L	2.8	-	* 337–430 mg/L DOC	~43% DOC	-	300	(180) (181)
	PEF	* $[TDI]_0$ = 60 mg//L	2.8	-	* 337–430 mg/L DOC	~72% DOC	-	300	
	SPEF	* $[TDI]_0$ = 60 mg//L	2.8	-	* 337–430 mg/L DOC	~78% DOC	* 137 kWh/kg_{DOC}	300	
Evans Blue diazo dye	EF	0.5	3	* 0.245 mM	* 100 mg/L DOC	~85% DOC	-	360	(182)
	PEF	0.5	3	* 0.245 mM	* 100 mg/L DOC	>98% DOC	-	360	
	SPEF	0.5	3	* 0.245 mM	* 100 mg/L DOC	>96% DOC	-	150	
ibuprofen	EF	0.5	3	41	* 31 mg/L DOC	81% DOC	-	360	(155)
	PEF	0.5	3	41	* 31 mg/L DOC	94% DOC	-	360	
	SPEF	0.5	3	41	* 31 mg/L DOC	92% DOC	-	240	
mecoprop	AO	-	3	100	56	49%	-	540	(183)

EF	0.5	3	100	56	69%	-	540
PEF	0.5	3	100	56	>96%	-	540
SPEF	0.5	3	100	56	>96%	-	540

** TOC—Total Organic Carbon; MCE—Mineralization Current Efficiency; EC—Energy consumption; $[TDI]_0$—Initial Total Dissolved Iron concentration; DOC—Dissolved Organic Carbon; EDDS—ethylenediamine-N,N'-disuccinic.*

In this subsection, it was demonstrated that diamond technology still stands out in photo-enhanced EF processes, as equally found in the previous subsection concerning EF processes. It was also observed that a combination of a radiation source, either artificial (UV lamps) or natural (sunlight), improves the efficiency of the Fenton-based process and the overall mineralization efficiency. The reported works equally point out the benefits of solar irradiation when compared to artificial UV sources, particularly in terms of energy consumption, mineralization rates, and general costs. Combining SPEF with renewable power supplies may be a more cost-effective solution. Nevertheless, SPEF is limited by weather conditions and geolocation. Furthermore, PEF and SPEF are enhanced EF processes with extra costs to be added due to particular requirements such as the use of catalysts, pH correction during and after the process, and gas sources when gas diffusion cathodes are used. Unfortunately, the cost of the latter is often not considered in the overall calculations presented in the literature. Therefore, for real wastewater treatment applications, all costs and life-cycles involved in each EAOP process must be evaluated in order to determine which one is the most cost-effective without compromising long-term quality and efficiency.

I.1.5. Final Considerations and Future Prospects

Anodic electrooxidation (AO) carried out using boron-doped diamond (BDD) technology is an electrochemical advanced oxidation process (EAOP) by itself, and these thin films are excellent electrode materials for the previously stated well-known reasons. It is a green process that only requires an electrical current input. BDDs are indeed expensive, but their long operating life clearly redeems any required initial investment. Similar to any other EAOP, there are also a few weaknesses in AO that require further consideration if one intends to apply BDD technology in wastewater treatment effectively. Consequently, it is not surprising that many researchers have started to explore possible synergism between different EAOPs. In this work, the aim was to evaluate the literature concerning BDD technology as the common denominator applied in enhanced AO strategies, including different EAOPs.

SLR analysis demonstrated the importance of using adequate keywords in any scientific report since it incessantly introduces a degree of discrepancy to this systematic methodology. Authors will certainly benefit if standard terms are employed, and this action alone will certainly have clear repercussions on the future number of citations as well as on the effortless finding of publications when using search mechanisms such as Scopus, Web of Science, Google Scholar, PubMed, amongst others. The application of SLR allowed to review a representative sample of work among hundreds of publications concerning doped diamond technology applied in EAOPs. We strongly believe that SLR methodology will always be an updated, useful tool and, most probably, a mandatory one in the future.

In this review, it was possible to generally conclude that add-ons such as persulfate radicals (amongst others) clearly show a synergistic effect, improving the overall AO process using BDD technology. These *in situ* electrogenerated radicals compensate for the weaker electrooxidation in the bulk of the wastewater since the production of hydroxyl radicals by the BDD anodes is restricted to the surrounding area of the electrode. Adding extra chemicals to generate persulfate or other radicals is not by all means sustainable, and it may even point to an additional treatment step in the whole process. Electrogenerated ozone add-on enhances the amount of hydroxyl radicals present in the wastewater and overcomes the pH constriction effect on the production of persulfate radicals. Ozone is a powerful oxidant, and it mass-balances the localized production of hydroxyl radicals at the BDD electrodes. On the other hand, associated costs are yet unaccounted for in order to properly assess the success of this add-on. Photoelectrocatalysis shows good potential as an add-on, but, unfortunately, the design and fabrication of the photoanodes is time-

consuming and most possibly not a cost-effective add-on with effective large-scale application in wastewater treatment.

Considering the Fenton-based processes using BDD technology, it is generally accepted that the electro-Fenton (EF) method shows higher mineralization rates if compared to simple AO. Among them, mineralization efficiency typically occurs in the following order: solar photo-electro-Fenton (SPEF) > photo-electro-Fenton (PEF) > electro-Fenton (EF). An obvious drawback of Fenton-based processes is that they always involve a required amount of iron compounds to be added to the wastewater, and consequently, a post-treatment step to remove the residual iron is necessary. These steps certainly have associated costs but may be reduced or overcome if the iron source is deposited onto the BDD electrode, as previously observed for the photoanodes in the photoelectrocatalysis add-on. Nevertheless, one needs to ensure that fouling does not occur, and that the extension of the Fenton reaction is not restricted to the surrounding areas of the composite anode. Regarding the cathode material, literature shows that a consensus has not yet been reached for EF-based methods. In addition, pH correction of wastewaters with chemicals is nearly mandatory, generating additional expenses and complications when implemented in large-scale facilities. For extended treatment periods of time, the oxidation mechanisms promoted by EF-based methods slowly decrease with time and mineralization becomes dominated by direct AO. Ultimately, PEF is an effective process but requires the use of artificial UV lamps, and again, it means additional expenses and an increase in energy consumption. The use of solar radiation easily overcomes this problem, but it is limited to weather conditions and the intensity of sunlight depending on geolocation and the season of the year.

EAOPs are definitely the future for sustainable wastewater treatment. Nevertheless, EAOPs are also of great complexity with many accountable variables and extended difficult implementation and/or substitution of the conventional treatment methods. A recent study evaluated the operational cost efficiency of six distinct types of AOPs, including ozonation, Fenton, H_2O_2 photolysis, photo-Fenton, electro-Fenton, and photoelectro-Fenton (unfortunately, AO and SPEF were not considered). The detailed study included the use of chemicals, power, and sludge management. It was found that electro-Fenton was the most economical AOP, with a cost of around 108–125 €/m^3. One should note that the future of all EAOPs includes upgrading the power supplies to renewable energy sources enabling self-sufficiency, low maintenance requirements, and consequent applicability.

One of the aspects that we consider relevant, from a performance point of view, is the generality of EAOPs processes as solutions for multiple pollutants and types of wastewater. If the mineralization process is incomplete, complex samples with different organic

compounds may generate possible byproducts with some toxicity level. Currently, it is not possible to generalize EAOPs processes without optimizing them for each type of water. Most publications do not provide enough detailed studies concerning the chemistry of treated water, which is a critical requirement for future practical applications of EAOPs.

EAOPs largely achieve excellent degradation and mineralization efficiencies when combined with doped diamond technology. On the other hand, these efficiencies are restricted by the common limits of AO using BDD anodes. Overall, further research is still needed to enhance its technology readiness level and allow effective acceptance and application in wastewater remediation.

I.1.6. References

1. Diya'uddeen, B.H.; Daud, W.M.A.W.; Aziz, A.R.A. Treatment Technologies for Petroleum Refinery Effluents: A Review. Process Saf. Environ. Prot. 2011, 89, 95–105.

2. Gargouri, B.; Gargouri, O.D.; Gargouri, B.; Trabelsi, S.K.; Abdelhedi, R.; Bouaziz, M. Application of Electrochemical Technology for Removing Petroleum Hydrocarbons from Produced Water Using Lead Dioxide and Boron-Doped Diamond Electrodes. Chemosphere 2014, 117, 309–315.

3. Shokrollahzadeh, S.; Azizmohseni, F.; Golmohammad, F.; Shokouhi, H.; Khademhaghighat, F. Biodegradation Potential and Bacterial Diversity of a Petrochemical Wastewater Treatment Plant in Iran. Bioresour. Technol. 2008, 99, 6127–6133.

4. U.S. Environmental Protection Agency Persistent Organic Pollutants: A Global Issue, A Global Response; [reviewed 2022 October 6; cited date 2022 October 6]. Available from: https://www.epa.gov/international-cooperation/persistent-organic-pollutants-global-issue-global-response.

5. Arfanis, M.K.; Adamou, P.; Moustakas, N.G.; Triantis, T.M.; Kontos, A.G.; Falaras, P. Photocatalytic Degradation of Salicylic Acid and Caffeine Emerging Contaminants Using Titania Nanotubes. Chem. Eng. J. 2017, 310, 525–536. https://doi.org/10.1016/j.cej.2016.06.098.

6. Verma, A.K.; Dash, R.R.; Bhunia, P. A Review on Chemical Coagulation/Flocculation Technologies for Removal of Colour from Textile Wastewaters. J. Environ. Manag. 2012, 93, 154–168. https://doi.org/10.1016/j.jenvman.2011.09.012.

7. Mollah, M.Y.A.; Morkovsky, P.; Gomes, J.A.G.; Kesmez, M.; Parga, J.; Cocke, D.L. Fundamentals, Present and Future Perspectives of Electrocoagulation. J. Hazard. Mater. 2004, 114, 199–210. https://doi.org/10.1016/j.jhazmat.2004.08.009.

8. Meng, F.; Chae, S.-R.; Drews, A.; Kraume, M.; Shin, H.-S.; Yang, F. Recent Advances in Membrane Bioreactors (MBRs): Membrane Fouling and Membrane Material. Water Res. 2009, 43, 1489–1512. https://doi.org/10.1016/j.watres.2008.12.044.

9. Dickhout, J.M.; Moreno, J.; Biesheuvel, P.M.; Boels, L.; Lammertink, R.G.H.; de Vos, W.M. Produced Water Treatment by Membranes: A Review from a Colloidal Perspective. J. Colloid Interface Sci. 2017, 487, 523–534. https://doi.org/10.1016/j.jcis.2016.10.013.

10. Truc, L.V.T.; Can, L.D.; Luu, T.L. Electron Beam as an Effective Wastewater Treatment Technology in Lab-Scale Application. J. Hazard. Toxic Radioact. Waste 2021, 25, 03120003. https://doi.org/10.1061/(ASCE)HZ.2153-5515.0000584.

11. Kim, K.-H.; Ihm, S.-K. Heterogeneous Catalytic Wet Air Oxidation of Refractory Organic Pollutants in Industrial Wastewaters: A Review. J. Hazard. Mater. 2011, 186, 16–34. https://doi.org/10.1016/j.jhazmat.2010.11.011.

12. Koparal, A.S.; Öğütveren, Ü.B. Removal of Nitrate from Water by Electroreduction and Electrocoagulation. J. Hazard. Mater. 2002, 89, 83–94. https://doi.org/10.1016/S0304-3894(01)00301-6.

13. Chen, Z.; Zheng, R.; Wei, W.; Wei, W.; Zou, W.; Li, J.; Ni, B.-J.; Chen, H. Recycling Spent Water Treatment Adsorbents for Efficient Electrocatalytic Water Oxidation Reaction. Resour. Conserv. Recycl. 2022, 178, 106037. https://doi.org/10.1016/j.resconrec.2021.106037.

14. Chen, Z.; Wei, W.; Liu, X.; Ni, B.-J. Emerging Electrochemical Techniques for Identifying and Removing Micro/Nanoplastics in Urban Waters. Water Res. 2022, 221, 118846. https://doi.org/10.1016/j.watres.2022.118846.

15. Liu, R.; Zhao, H.; Zhao, X.; He, Z.; Lai, Y.; Shan, W.; Bekana, D.; Li, G.; Liu, J. Defect Sites in Ultrathin Pd Nanowires Facilitate the Highly Efficient Electrochemical Hydrodechlorination of Pollutants by H^*_{ads}. Environ. Sci. Technol. 2018, 52, 9992–10002. https://doi.org/10.1021/acs.est.8b02740.

16. Thompson, J.R.; Crooks, R.M. Electrokinetic Separation Techniques for Studying Nano- and Microplastics. Chem. Sci. 2022, 13, 12616–12624. https://doi.org/10.1039/D2SC04019K.

17. Ternes, T.A.; Stüber, J.; Herrmann, N.; McDowell, D.; Ried, A.; Kampmann, M.; Teiser, B. Ozonation: A Tool for Removal of Pharmaceuticals, Contrast Media and Musk Fragrances from Wastewater? Water Res. 2003, 37, 1976–1982. https://doi.org/10.1016/S0043-1354(02)00570-5.

18. Ganiyu, S.O.; Martínez-Huitle, C.A.; Oturan, M.A. Electrochemical Advanced Oxidation Processes for Wastewater Treatment: Advances in Formation and Detection of Reactive Species and Mechanisms. Curr. Opin. Electrochem. 2021, 27, 100678. https://doi.org/10.1016/j.coelec.2020.100678.

19. Oturan, M.A.; Aaron, J.-J. Advanced Oxidation Processes in Water/Wastewater Treatment: Principles and Applications. A Review. Crit. Rev. Environ. Sci. Technol. 2014, 44, 2577–2641.

20. Sires, I.; Brillas, E.; Oturan, M.A.; Rodrigo, M.A.; Panizza, M. Electrochemical Advanced Oxidation Processes: Today and Tomorrow. A Review. Environ Sci Pollut Res Int 2014, 21, 8336–8367.

21. Martínez-Huitle, C.A.; Brillas, E. Decontamination of Wastewaters Containing Synthetic Organic Dyes by Electrochemical Methods: A General Review. Appl. Catal. B Environ. 2009, 87, 105–145.
22. Panizza, M.; Cerisola, G. Direct and Mediated Anodic Oxidation of Organic Pollutants. Chem. Rev. 2009, 109, 6541–6569.
23. Glaze, W.H.; Kang, J.W.; Chapin, D.H. The Chemistry of Water-Treatment Processes Involving Ozone, Hydrogen-Peroxide and Ultraviolet-Radiation. Ozone-Sci. Eng. 1987, 9, 335–352.
24. Moreira, F.C.; Boaventura, R.A.R.; Brillas, E.; Vilar, V.J.P. Electrochemical Advanced Oxidation Processes: A Review on Their Application to Synthetic and Real Wastewaters. Appl. Catal. B Environ. 2017, 202, 217–261.
25. Matthée, T.; Fryda, M.; Schäfer, L.; Tröster, I. Electrochemical Advanced Oxidation Process Using DiaChem®electrodes. Water Sci. Technol. 2004, 49, 207–212.
26. Martínez-Huitle, C.A.; Ferro, S.; De Battisti, A. Electrochemical Incineration of Oxalic Acid: Role of Electrode Material. Electrochim. Acta 2004, 49, 4027–4034. https://doi.org/10.1016/j.electacta.2004.01.083.
27. Martínez-Huitle, C.A.; Panizza, M. Electrochemical Oxidation of Organic Pollutants for Wastewater Treatment. Curr. Opin. Electrochem. 2018, 11, 62–71. https://doi.org/10.1016/j.coelec.2018.07.010.
28. Comninellis, C.; Kapalka, A.; Malato, S.; Parsons, S.A.; Poulios, I.; Mantzavinos, D. Advanced Oxidation Processes for Water Treatment: Advances and Trends for R&D. J. Chem. Technol. Biotechnol. 2008, 83, 769–776. https://doi.org/10.1002/jctb.1873.
29. Nidheesh, P.V.; Divyapriya, G.; Oturan, N.; Trellu, C.; Oturan, M.A. Environmental Applications of Boron-Doped Diamond Electrodes: 1. Applications in Water and Wastewater Treatment. ChemElectroChem 2019, 6, 2124–2142. https://doi.org/10.1002/celc.201801876.
30. Luong, J.H.; Male, K.B.; Glennon, J.D. Boron-Doped Diamond Electrode: Synthesis, Characterization, Functionalization and Analytical Applications. Analyst 2009, 134, 1965–1979.
31. Angus, J.C.; Martin, H.B.; Landau, U.; Evstefeeva, Y.E.; Miller, B.; Vinokur, N. Conducting Diamond Electrodes: Applications in Electrochemistry. New Diam. Front. Carbon Technol. 1999, 9, 175–187.
32. Zhou, B.; Yu, Z.; Wei, Q.; Long, H.; Xie, Y.; Wang, Y. Electrochemical Oxidation of Biological Pretreated and Membrane Separated Landfill Leachate Concentrates on Boron Doped Diamond Anode. Appl. Surf. Sci. 2016, 377, 406–415.

33. Swain, G.M. The Use of CVD Diamond Thin Films in Electrochemical Systems. Adv. Mater. 1994, 6, 388–392.

34. Ramesham, R.; Rose, M.F. Electrochemical Characterization of Doped and Undoped CVD Diamond Deposited by Microwave Plasma. Diam. Relat. Mater. 1997, 6, 17–26.

35. Swain, G.M. The Susceptibility to Surface Corrosion in Acidic Fluoride Media: A Comparison of Diamond, HOPG, and Glassy Carbon Electrodes. J. Electrochem. Soc. 2019, 141, 3382–3393.

36. Balmer, R.S.; Brandon, J.R.; Clewes, S.L.; Dhillon, H.K.; Dodson, J.M.; Friel, I.; Inglis, P.N.; Madgwick, T.D.; Markham, M.L.; Mollart, T.P.; *et al.* Chemical Vapour Deposition Synthetic Diamond: Materials, Technology and Applications. J. Phys. Condens. Matter 2009, 21, 364221. https://doi.org/10.1088/0953-8984/21/36/364221.

37. Yang, N.; Yu, S.; Macpherson, J.V.; Einaga, Y.; Zhao, H.; Zhao, G.; Swain, G.M.; Jiang, X. Conductive Diamond: Synthesis, Properties, and Electrochemical Applications. Chem. Soc. Rev. 2019, 48, 157–204. https://doi.org/10.1039/C7CS00757D.

38. Srikanth, V.V.S.S.; Jiang, X. Synthesis of Diamond Films. In Synthetic Diamond Films; Brillas, E., Martínez-Huitle, C.A., Eds.; John Wiley & Sons, Inc.: Hoboken, NJ, USA, 2011; pp. 21–55, ISBN 978-1-118-06236-4.

39. Das, D.; Singh, R.N. A Review of Nucleation, Growth and Low Temperature Synthesis of Diamond Thin Films. Int. Mater. Rev. 2007, 52, 29–64. https://doi.org/10.1179/174328007X160245.

40. Poferl, D.J.; Gardner, N.C.; Angus, J.C. Growth of Boron-doped Diamond Seed Crystals by Vapor Deposition. J. Appl. Phys. 1973, 44, 1428–1434. https://doi.org/10.1063/1.1662389.

41. Macpherson, J.V. A Practical Guide to Using Boron Doped Diamond in Electrochemical Research. Phys. Chem. Chem. Phys. 2015, 17, 2935–2949. https://doi.org/10.1039/C4CP04022H.

42. Kajihara, S.A.; Antonelli, A.; Bernholc, J.; Car, R. Nitrogen and Potential n -Type Dopants in Diamond. Phys. Rev. Lett. 1991, 66, 2010–2013. https://doi.org/10.1103/PhysRevLett.66.2010.

43. Haenen, K.; Nesládek, M.; De Schepper, L.; Kravets, R.; Vaněček, M.; Koizumi, S. The Phosphorous Level Fine Structure in Homoepitaxial and Polycrystalline N-Type CVD Diamond. Diam. Relat. Mater. 2004, 13, 2041–2045. https://doi.org/10.1016/j.diamond.2004.06.016.

44. He, Y.; Lin, H.; Guo, Z.; Zhang, W.; Li, H.; Huang, W. Recent Developments and Advances in Boron-Doped Diamond Electrodes for Electrochemical Oxidation of Organic Pollutants. Sep. Purif. Technol. 2019, 212, 802–821. https://doi.org/10.1016/j.seppur.2018.11.056.

45. Iniesta, J.; Michaud, P.A.; Panizza, M.; Cerisola, G.; Aldaz, A.; Comninellis, Ch. Electrochemical Oxidation of Phenol at Boron-Doped Diamond Electrode. Electrochim. Acta 2001, 46, 3573–3578. https://doi.org/10.1016/S0013-4686(01)00630-2.

46. Flox, C.; Ammar, S.; Arias, C.; Brillas, E.; Vargas-Zavala, A.V.; Abdelhedi, R. Electro-Fenton and Photoelectro-Fenton Degradation of Indigo Carmine in Acidic Aqueous Medium. Appl. Catal. B Environ. 2006, 67, 93–104. https://doi.org/10.1016/j.apcatb.2006.04.020.

47. Sopaj, F.; Rodrigo, M.A.; Oturan, N.; Podvorica, F.I.; Pinson, J.; Oturan, M.A. Influence of the Anode Materials on the Electrochemical Oxidation Efficiency. Application to Oxidative Degradation of the Pharmaceutical Amoxicillin. Chem. Eng. J. 2015, 262, 286–294. https://doi.org/10.1016/j.cej.2014.09.100.

48. Samet, Y.; Agengui, L.; Abdelhédi, R. Electrochemical Degradation of Chlorpyrifos Pesticide in Aqueous Solutions by Anodic Oxidation at Boron-Doped Diamond Electrodes. Chem. Eng. J. 2010, 161, 167–172. https://doi.org/10.1016/j.cej.2010.04.060.

49. Gomez-Ruiz, B.; Gómez-Lavín, S.; Diban, N.; Boiteux, V.; Colin, A.; Dauchy, X.; Urtiaga, A. Efficient Electrochemical Degradation of Poly- and Perfluoroalkyl Substances (PFASs) from the Effluents of an Industrial Wastewater Treatment Plant. Chem. Eng. J. 2017, 322, 196–204. https://doi.org/10.1016/j.cej.2017.04.040.

50. Garcia-Segura, S.; Keller, J.; Brillas, E.; Radjenovic, J. Removal of Organic Contaminants from Secondary Effluent by Anodic Oxidation with a Boron-Doped Diamond Anode as Tertiary Treatment. J. Hazard. Mater. 2015, 283, 551–557. https://doi.org/10.1016/j.jhazmat.2014.10.003.

51. Anglada, A.; Urtiaga, A.; Ortiz, I. Pilot Scale Performance of the Electro-Oxidation of Landfill Leachate at Boron-Doped Diamond Anodes. Environ. Sci. Technol. 2009, 43, 2035–2040. https://doi.org/10.1021/es802748c.

52. Daldrup-Link, H.E. Writing a Review Article—Are You Making These Mistakes? Nanotheranostics 2018, 2, 197–200. https://doi.org/10.7150/ntno.24793.

53. Heather MacKenzie; Ann Dewey; Amy Drahota; Sally Kilburn; Paul R Kalra; Carole Fogg; Donah Zachariah Systematic Reviews: What They Are, Why They Are Important, and How to Get Involved. J. Clin. Prev. Cardiol. 2012, 1, 193–202.

54. Brennan, M.L.; Arlt, S.P.; Belshaw, Z.; Buckley, L.; Corah, L.; Doit, H.; Fajt, V.R.; Grindlay, D.J.C.; Moberly, H.K.; Morrow, L.D.; *et al.* Critically Appraised Topics (CATs) in Veterinary Medicine: Applying Evidence in Clinical Practice. Front. Vet. Sci. 2020, 7, 314. https://doi.org/10.3389/fvets.2020.00314.

55. VOSviewer—Visualizing Scientific Landscapes; [reviewed 2022 October 25; cited date 2022 October 25]. Available from: https://www.vosviewer.com.

56. van Eck, N.J.; Waltman, L. Software Survey: VOSviewer, a Computer Program for Bibliometric Mapping. Scientometrics 2010, 84, 523–538. https://doi.org/10.1007/s11192-009-0146-3.

57. Brillas, E. Electro-Fenton, UVA Photoelectro-Fenton and Solar Photoelectro-Fenton Treatments of Organics in Waters Using a Boron-Doped Diamond Anode: A Review. J. Mex. Chem. Soc. 2014, 58, 239–255.

58. Brillas, E. A review on the degradation of organic pollutants in waters by UV photoelectro-Fenton and solar photoelectro-Fenton. J. Braz. Chem. Soc. 2014, 25, 393–417. https://doi.org/10.5935/0103-5053.20130257.

59. Bennedsen, L.R.; Muff, J.; Søgaard, E.G. Influence of Chloride and Carbonates on the Reactivity of Activated Persulfate. Chemosphere 2012, 86, 1092–1097. https://doi.org/10.1016/j.chemosphere.2011.12.011.

60. Araújo, D.M.; de; Sáez, C.; Martínez-Huitle, C.A.; Cañizares, P.; Rodrigo, M.A. Influence of Mediated Processes on the Removal of Rhodamine with Conductive-Diamond Electrochemical Oxidation. Appl. Catal. B Environ. 2015, 166–167, 454–459. https://doi.org/10.1016/j.apcatb.2014.11.038.

61. Farhat, A.; Keller, J.; Tait, S.; Radjenovic, J. Removal of Persistent Organic Contaminants by Electrochemically Activated Sulfate. Environ. Sci. Technol. 2015, 49, 14326–14333. https://doi.org/10.1021/acs.est.5b02705.

62. Radjenovic, J.; Petrovic, M. Sulfate-Mediated Electrooxidation of X-Ray Contrast Media on Boron-Doped Diamond Anode. Water Res. 2016, 94, 128–135. https://doi.org/10.1016/j.watres.2016.02.045.

63. Bu, L.; Zhou, S.; Shi, Z.; Deng, L.; Gao, N. Removal of 2-MIB and Geosmin by Electrogenerated Persulfate: Performance, Mechanism and Pathways. Chemosphere 2017, 168, 1309–1316. https://doi.org/10.1016/j.chemosphere.2016.11.134.

64. Groenen Serrano, K. Chapter 6—Indirect Electrochemical Oxidation Using Hydroxyl Radical, Active Chlorine, and Peroxodisulfate. In Electrochemical Water and Wastewater Treatment; Martínez-Huitle, C.A., Rodrigo, M.A., Scialdone, O., Eds.; Butterworth-Heinemann: Oxford, UK, 2018; pp. 133–164 ISBN 978-0-12-813160-2.

65. Chen, L.; Lei, C.; Li, Z.; Yang, B.; Zhang, X.; Lei, L. Electrochemical Activation of Sulfate by BDD Anode in Basic Medium for Efficient Removal of Organic Pollutants. Chemosphere 2018, 210, 516–523. https://doi.org/10.1016/j.chemosphere.2018.07.043.

66. Cai, J.; Niu, T.; Shi, P.; Zhao, G. Boron-Doped Diamond for Hydroxyl Radical and Sulfate Radical Anion Electrogeneration, Transformation, and Voltage-Free Sustainable Oxidation. Small 2019, 15, 1900153. https://doi.org/10.1002/smll.201900153.

67. da Silva, S.W.; Navarro, E.M.O.; Rodrigues, M.A.S.; Bernardes, A.M.; Pérez-Herranz, V. Using P-Si/BDD Anode for the Electrochemical Oxidation of Norfloxacin. J. Electroanal. Chem. 2019, 832, 112–120. https://doi.org/10.1016/j.jelechem.2018.10.049.

68. da Silva, S.W.; do Prado, J.M.; Heberle, A.N.A.; Schneider, D.E.; Rodrigues, M.A.S.; Bernardes, A.M. Electrochemical Advanced Oxidation of Atenolol at Nb/BDD Thin Film Anode. J. Electroanal. Chem. 2019, 844, 27–33. https://doi.org/10.1016/j.jelechem.2019.05.011.

69. Shin, Y.-U.; Yoo, H.-Y.; Ahn, Y.-Y.; Kim, M.S.; Lee, K.; Yu, S.; Lee, C.; Cho, K.; Kim, H.; Lee, J. Electrochemical Oxidation of Organics in Sulfate Solutions on Boron-Doped Diamond Electrode: Multiple Pathways for Sulfate Radical Generation. Appl. Catal. B Environ. 2019, 254, 156–165. https://doi.org/10.1016/j.apcatb.2019.04.060.

70. Cai, J.; Zhou, M.; Pan, Y.; Du, X.; Lu, X. Extremely Efficient Electrochemical Degradation of Organic Pollutants with Co-Generation of Hydroxyl and Sulfate Radicals on Blue-TiO2 Nanotubes Anode. Appl. Catal. B Environ. 2019, 257, 117902. https://doi.org/10.1016/j.apcatb.2019.117902.

71. Li, W.; Liu, G.; Miao, D.; Li, Z.; Chen, Y.; Gao, X.; Liu, T.; Wei, Q.; Ma, L.; Zhou, K.; *et al.* Electrochemical Oxidation of Reactive Blue 19 on Boron-Doped Diamond Anode with Different Supporting Electrolyte. J. Environ. Chem. Eng. 2020, 8, 103997. https://doi.org/10.1016/j.jece.2020.103997.

72. Yang, W.; Liu, G.; Chen, Y.; Miao, D.; Wei, Q.; Li, H.; Ma, L.; Zhou, K.; Liu, L.; Yu, Z. Persulfate Enhanced Electrochemical Oxidation of Highly Toxic Cyanide-Containing Organic Wastewater Using Boron-Doped Diamond Anode. Chemosphere 2020, 252, 126499. https://doi.org/10.1016/j.chemosphere.2020.126499.

73. Nashat, M.; Mossad, M.; El-Etriby, H.K.; Gar Alalm, M. Optimization of Electrochemical Activation of Persulfate by BDD Electrodes for Rapid Removal of Sulfamethazine. Chemosphere 2022, 286, 131579. https://doi.org/10.1016/j.chemosphere.2021.131579.

74. Feijoo, S.; Kamali, M.; Pham, Q.-K.; Assoumani, A.; Lestremau, F.; Cabooter, D.; Dewil, R. Electrochemical Advanced Oxidation of Carbamazepine: Mechanism and Optimal

Operating Conditions. Chem. Eng. J. 2022, 446, 137114. https://doi.org/10.1016/j.cej.2022.137114.

75. Lu, Z.; Liu, L.; Gao, W.; Zhai, Z.; Song, H.; Chen, B.; Zheng, Z.; Yang, B.; Geng, C.; Liang, J.; *et al.* Manufacturing 3D Nano-Porous Architecture for Boron-Doped Diamond Film to Efficient Abatement of Organic Pollutant: Synergistic Effect of Hydroxyl Radical and Sulfate Radical. Sep. Purif. Technol. 2022, 302, 122080. https://doi.org/10.1016/j.seppur.2022.122080.

76. Meas, Y.; Godinez, L.A.; Bustos, E. Ozone Generation Using Boron-Doped Diamond Electrodes. In Synthetic Diamond Films; John Wiley & Sons, Ltd.: Hoboken, NJ, USA, 2011; pp. 311–331, ISBN 978-1-118-06236-4.

77. Medel, A.; Lugo, F.; Meas, Y. Application of Electrochemical Processes for Treating Effluents from Hydrocarbon Industries. In Electrochemical Water and Wastewater Treatment; Butterworth-Heinemann: Oxford, UK, 2018; pp. 365–392.

78. Gągol, M.; Przyjazny, A.; Boczkaj, G. Effective Method of Treatment of Industrial Effluents under Basic PH Conditions Using Acoustic Cavitation—A Comprehensive Comparison with Hydrodynamic Cavitation Processes. Chem. Eng. Process. Process Intensif. 2018, 128, 103–113. https://doi.org/10.1016/j.cep.2018.04.010.

79. Boczkaj, G.; Fernandes, A. Wastewater Treatment by Means of Advanced Oxidation Processes at Basic PH Conditions: A Review. Chem. Eng. J. 2017, 320, 608–633. https://doi.org/10.1016/j.cej.2017.03.084.

80. Okada, F.; Naya, K.; Okada, F.; Naya, K. Electrolysis for Ozone Water Production; IntechOpen: Rijeka, Croatia, 2012; ISBN 978-953-51-0793-4.

81. Wang, Y.-H.; Chen, Q.-Y. Anodic Materials for Electrocatalytic Ozone Generation. Int. J. Electrochem. 2013, 2013, e128248. https://doi.org/10.1155/2013/128248.

82. Katsuki, N.; Takahashi, E.; Toyoda, M.; Kurosu, T.; Iida, M.; Wakita, S.; Nishiki, Y.; Shimamune, T. Water Electrolysis Using Diamond Thin-Film Electrodes. J. Electrochem. Soc. 1998, 145, 2358. https://doi.org/10.1149/1.1838643.

83. Michaud, P.-A.; Panizza, M.; Ouattara, L.; Diaco, T.; Foti, G.; Comninellis, Ch. Electrochemical Oxidation of Water on Synthetic Boron-Doped Diamond Thin Film Anodes. J. Appl. Electrochem. 2003, 33, 151–154. https://doi.org/10.1023/A:1024084924058.

84. Park, S.-G. Stable Ozone Generation by Using Boron-Doped Diamond Electrodes. Russ. J. Electrochem. 2003, 39, 321–322. https://doi.org/10.1023/A:1022892230969.

85. Park, S.G.; Kim, G.S.; Park, J.E.; Einaga, Y.; Fujishima, A. Use of Boron-Doped Diamond Electrode in Ozone Generation. J. New Mater. Electrochem. Syst. 2005, 8, 65–68.

86. Arihara, K.; Terashima, C.; Fujishima, A. Application of Freestanding Perforated Diamond Electrodes for Efficient Ozone-Water Production. Electrochem. Solid-State Lett. 2006, 9, D17. https://doi.org/10.1149/1.2206009.

87. Kraft, A.; Stadelmann, M.; Wünsche, M.; Blaschke, M. Electrochemical Ozone Production Using Diamond Anodes and a Solid Polymer Electrolyte. Electrochem. Commun. 2006, 5, 883–886. https://doi.org/10.1016/j.elecom.2006.02.013.

88. Sekido, K.; Kitaori, N. Development of a Small-Sized Generator of Ozonated Water Using an Electro-Conductive Diamond Electrode. Biocontrol. Sci. 2008, 13, 119–123. https://doi.org/10.4265/bio.13.119.

89. Kitaori, N.; Yoshioka, M.; Sekido, K.; Ohnishi, N.; Maeda, N.; Matsuishi, S. Development of a Small-Sized Electrolyzed Water Generator for Sterilization. Electrochemistry 2013, 81, 627–633. https://doi.org/10.5796/electrochemistry.81.627.

90. Honda, Y.; Ivandini, T.A.; Watanabe, T.; Murata, K.; Einaga, Y. An Electrolyte-Free System for Ozone Generation Using Heavily Boron-Doped Diamond Electrodes. Diam. Relat. Mater. 2013, 40, 7–11. https://doi.org/10.1016/j.diamond.2013.09.001.

91. Choi, J.; Kim, C.; Kim, J.; Kim, S.; Tak, Y.; Lee, C.; Yoon, J. Electrochemical Ozone Production in Inert Supporting Electrolytes on a Boron-Doped Diamond Electrode with a Solid Polymer Electrolyte Electrolyzer. Desalination Water Treat. 2016, 57, 10152–10158. https://doi.org/10.1080/19443994.2015.1043490.

92. Park, Y.M.; Bae, M.K.; Kim, J.W.; Kim, T.G. Electrochemical Oxidation of High-Concentration Ozone Generation in Flowing Water Through Boron Doped Diamond Electrodes. Nanosci. Nanotechnol. Lett. 2019, 11, 1257–1262. https://doi.org/10.1166/nnl.2019.3001.

93. Kanfra, X.; Elhady, A.; Thiem, H.; Pleger, S.; Höfer, M.; Heuer, H. Ozonated Water Electrolytically Generated by Diamond-Coated Electrodes Controlled Phytonematodes in Replanted Soil. J. Plant Dis. Prot. 2021, 128, 1657–1665. https://doi.org/10.1007/s41348-021-00524-0.

94. Liu, F.; Deng, Z.; Miao, D.; Chen, W.; Wang, Y.; Zhou, K.; Ma, L.; Wei, Q. A Highly Stable Microporous Boron-Doped Diamond Electrode Etched by Oxygen Plasma for Enhanced Electrochemical Ozone Generation. J. Environ. Chem. Eng. 2021, 9, 106369. https://doi.org/10.1016/j.jece.2021.106369.

95. Wood, G.; Rodriguez, I.T.; Tully, J.; Chaudhuri, S.; Macpherson, J. Electrochemical Ozone Generation Using Compacted High Pressure High Temperature Boron Doped Diamond Microparticle Electrodes. J. Electrochem. Soc. 2021, 168, 126514. https://doi.org/10.26434/chemrxiv-2021-00rj4.

96. Li, H.Y.; Deng, C.; Zhao, L.; Gong, C.H.; Zhu, M.F.; Chen, J.W. Ozone Water Production Using a SPE Electrolyzer Equipped with Boron Doped Diamond Electrodes. Water Supply 2022, 22, 3993–4005. https://doi.org/10.2166/ws.2022.029.

97. Vahid, B.; Khataee, A. Photoassisted Electrochemical Recirculation System with Boron-Doped Diamond Anode and Carbon Nanotubes Containing Cathode for Degradation of a Model Azo Dye. Electrochim. Acta 2013, 88, 614–620. https://doi.org/10.1016/j.electacta.2012.10.069.

98. Hurwitz, G.; Pornwongthong, P.; Mahendra, S.; Hoek, E.M.V. Degradation of Phenol by Synergistic Chlorine-Enhanced Photo-Assisted Electrochemical Oxidation. Chem. Eng. J. 2014, 240, 235–243. https://doi.org/10.1016/j.cej.2013.11.087.

99. Hurwitz, G.; Hoek, E.M.V.; Liu, K.; Fan, L.; Roddick, F.A. Photo-Assisted Electrochemical Treatment of Municipal Wastewater Reverse Osmosis Concentrate. Chem. Eng. J. 2014, 249, 180–188. https://doi.org/10.1016/j.cej.2014.03.084.

100. Souza, F.L.; Saéz, C.; Lanza, M.R.V.; Cañizares, P.; Rodrigo, M.A. Removal of Pesticide 2,4-D by Conductive-Diamond Photoelectrochemical Oxidation. Appl. Catal. B Environ. 2016, 180, 733–739. https://doi.org/10.1016/j.apcatb.2015.07.038.

101. Souza, F.; Quijorna, S.; Lanza, M.R.V.; Sáez, C.; Cañizares, P.; Rodrigo, M.A. Applicability of Electrochemical Oxidation Using Diamond Anodes to the Treatment of a Sulfonylurea Herbicide. Catal. Today 2017, 280, 192–198. https://doi.org/10.1016/j.cattod.2016.04.030.

102. Santos, E.V.; dos; Sáez, C.; Cañizares, P.; Rodrigo, M.A.; Martínez-Huitle, C.A. Coupling Photo and Sono Technologies with BDD Anodic Oxidation for Treating Soil-Washing Effluent Polluted with Atrazine. J. Electrochem. Soc. 2018, 165, E262. https://doi.org/10.1149/2.1281805jes.

103. Cotillas, S.; Clematis, D.; Cañizares, P.; Carpanese, M.P.; Rodrigo, M.A.; Panizza, M. Degradation of Dye Procion Red MX-5B by Electrolytic and Electro-Irradiated Technologies Using Diamond Electrodes. Chemosphere 2018, 199, 445–452. https://doi.org/10.1016/j.chemosphere.2018.02.001.

104. Mena, I.F.; Cotillas, S.; Díaz, E.; Sáez, C.; Mohedano, Á.F.; Rodrigo, M.A. Sono- and Photoelectrocatalytic Processes for the Removal of Ionic Liquids Based on the 1-Butyl-3-Methylimidazolium Cation. J. Hazard. Mater. 2019, 372, 77–84. https://doi.org/10.1016/j.jhazmat.2017.12.015.

105. Fernández-Marchante, C.M.; Souza, F.L.; Millán, M.; Lobato, J.; Rodrigo, M.A. Does Intensification with UV Light and US Improve the Sustainability of Electrolytic Waste

Treatment Processes? J. Environ. Manag. 2021, 279, 111597. https://doi.org/10.1016/j.jenvman.2020.111597.

106. Zheng, Z.; Yuan, J.; Jiang, X.; Han, G.; Tao, Y.; Wu, X. Combining Ultraviolet Photolysis with In-Situ Electrochemical Oxidation for Degrading Sulfonamides in Wastewater. Catalysts 2022, 12, 711. https://doi.org/10.3390/catal12070711.

107. Ochiai, T.; Nakata, K.; Murakami, T.; Fujishima, A.; Yao, Y.; Tryk, D.A.; Kubota, Y. Development of Solar-Driven Electrochemical and Photocatalytic Water Treatment System Using a Boron-Doped Diamond Electrode and TiO2 Photocatalyst. Water Res. 2010, 44, 904–910. https://doi.org/10.1016/j.watres.2009.09.060.

108. Schneider, J.; Matsuoka, M.; Takeuchi, M.; Zhang, J.; Horiuchi, Y.; Anpo, M.; Bahnemann, D.W. Understanding TiO2 Photocatalysis: Mechanisms and Materials. Chem. Rev. 2014, 114, 9919–9986. https://doi.org/10.1021/cr5001892.

109. Ren, G.; Han, H.; Wang, Y.; Liu, S.; Zhao, J.; Meng, X.; Li, Z. Recent Advances of Photocatalytic Application in Water Treatment: A Review. Nanomaterials 2021, 11, 1804. https://doi.org/10.3390/nano11071804.

110. Saeed, M.; Muneer, M.; Haq, A.; Akram, N. Photocatalysis: An Effective Tool for Photodegradation of Dyes—A Review. Environ. Sci. Pollut. Res. 2022, 29, 293–311. https://doi.org/10.1007/s11356-021-16389-7.

111. Dong, S.; Feng, J.; Fan, M.; Pi, Y.; Hu, L.; Han, X.; Liu, M.; Sun, J.; Sun, J. Recent Developments in Heterogeneous Photocatalytic Water Treatment Using Visible Light-Responsive Photocatalysts: A Review. RSC Adv. 2015, 5, 14610–14630. https://doi.org/10.1039/C4RA13734E.

112. Wang, H.; Li, X.; Zhao, X.; Li, C.; Song, X.; Zhang, P.; Huo, P.; Li, X. A Review on Heterogeneous Photocatalysis for Environmental Remediation: From Semiconductors to Modification Strategies. Chin. J. Catal. 2022, 43, 178–214. https://doi.org/10.1016/S1872-2067(21)63910-4.

113. Mousset, E.; Dionysiou, D.D. Photoelectrochemical Reactors for Treatment of Water and Wastewater: A Review. Environ. Chem. Lett. 2020, 18, 1301–1318. https://doi.org/10.1007/s10311-020-01014-9.

114. Zhang, C.; Gu, L.; Lin, Y.; Wang, Y.; Fu, D.; Gu, Z. Degradation of X-3B Dye by Immobilized TiO2 Photocatalysis Coupling Anodic Oxidation on BDD Electrode. J. Photochem. Photobiol. A Chem. 2009, 207, 66–72. https://doi.org/10.1016/j.jphotochem.2009.01.014.

115. Zhao, X.; Liu, H.; Qu, J. Photoelectrocatalytic Degradation of Organic Contaminant at Hybrid BDD-ZnWO4 Electrode. Catal. Commun. 2010, 12, 76–79. https://doi.org/10.1016/j.catcom.2010.08.013.

116. Wang, P.; Cao, M.; Ao, Y.; Wang, C.; Hou, J.; Qian, J. Investigation on Ce-Doped TiO_2-Coated BDD Composite Electrode with High Photoelectrocatalytic Activity under Visible Light Irradiation. Electrochem. Commun. 2011, 13, 1423–1426. https://doi.org/10.1016/j.elecom.2011.09.009.

117. Yu, Q.; Li, J.; Li, H.; Wang, Q.; Cheng, S.; Li, L. Fabrication, Structure, and Photocatalytic Activities of Boron-Doped ZnO Nanorods Hydrothermally Grown on CVD Diamond Film. Chem. Phys. Lett. 2012, 539–540, 74–78. https://doi.org/10.1016/j.cplett.2012.04.051.

118. Gao, S.; Jiao, S.; Lei, B.; Li, H.; Wang, J.; Yu, Q.; Wang, D.; Guo, F.; Zhao, L. Efficient Photocatalyst Based on ZnO Nanorod Arrays/p-Type Boron-Doped-Diamond Heterojunction. J. Mater. Sci. Mater. Electron. 2015, 26, 1018–1022. https://doi.org/10.1007/s10854-014-2498-6.

119. Fan, J.; Shi, H.; Xiao, H.; Zhao, G. Double-Layer 3D Macro–Mesoporous Metal Oxide Modified Boron-Doped Diamond with Enhanced Photoelectrochemical Performance. ACS Appl. Mater. Interfaces 2016, 8, 28306–28315. https://doi.org/10.1021/acsami.6b01929.

120. Han, Y.; Zhang, L.; Wang, Y.; Zhang, H.; Zhang, S. Photoelectrocatalytic Activity of an Ordered and Vertically Aligned TiO2 Nanorod Array/BDD Heterojunction Electrode. Sci. Bull. 2017, 62, 619–625. https://doi.org/10.1016/j.scib.2017.03.009.

121. Jian, Z.; Yang, N.; Vogel, M.; Zhou, Z.; Zhao, G.; Kienitz, P.; Schulte, A.; Schönherr, H.; Jiao, T.; Zhang, W.; *et al.* Tunable Photo-Electrochemistry of Patterned TiO2/BDD Heterojunctions. Small Methods 2020, 4, 2000257. https://doi.org/10.1002/smtd.202000257.

122. Suzuki, N.; Okazaki, A.; Kuriyama, H.; Serizawa, I.; Hirami, Y.; Hara, A.; Hirano, Y.; Nakabayashi, Y.; Roy, N.; Terashima, C.; *et al.* Synergetic Effect in Water Treatment with Mesoporous TiO2/BDD Hybrid Electrode. RSC Adv. 2020, 10, 1793–1798. https://doi.org/10.1039/C9RA10318J.

123. Alulema-Pullupaxi, P.; Fernández, L.; Debut, A.; Santacruz, C.P.; Villacis, W.; Fierro, C.; Espinoza-Montero, P.J. Photoelectrocatalytic Degradation of Glyphosate on Titanium Dioxide Synthesized by Sol-Gel/Spin-Coating on Boron Doped Diamond (TiO_2/BDD) as a Photoanode. Chemosphere 2021, 278, 130488. https://doi.org/10.1016/j.chemosphere.2021.130488.

124. Zheng, Z.; Zhang, K.; Toe, C.Y.; Amal, R.; Zhang, X.; McCarthy, D.T.; Deletic, A. Stormwater Herbicides Removal with a Solar-Driven Advanced Oxidation Process: A Feasibility Investigation. Water Res. 2021, 190, 116783. https://doi.org/10.1016/j.watres.2020.116783.

125. Sigcha-Pallo, C.; Peralta-Hernández, J.M.; Alulema-Pullupaxi, P.; Carrera, P.; Fernández, L.; Pozo, P.; Espinoza-Montero, P.J. Photoelectrocatalytic Degradation of Diclofenac with a Boron-Doped Diamond Electrode Modified with Titanium Dioxide as a Photoanode. Environ. Res. 2022, 212, 113362. https://doi.org/10.1016/j.envres.2022.113362.

126. Huang, J.; Meng, A.; Zhang, Z.; Ma, G.; Long, Y.; Li, X.; Han, P.; He, B. Porous BiVO4/Boron-Doped Diamond Heterojunction Photoanode with Enhanced Photoelectrochemical Activity. Molecules 2022, 27, 5218. https://doi.org/10.3390/molecules27165218.

127. Fenton, H.J.H. LXXIII.—Oxidation of Tartaric Acid in Presence of Iron. J. Chem. Soc. Trans. 1894, 65, 899–910. https://doi.org/10.1039/CT8946500899.

128. Brillas, E.; Mur, E.; Casado, J. Iron(II) Catalysis of the Mineralization of Aniline Using a Carbon-PTFE O 2—Fed Cathode. J. Electrochem. Soc. 1996, 143, L49–L53. https://doi.org/10.1149/1.1836528.

129. Brillas, E.; Sirés, I.; Oturan, M.A. Electro-Fenton Process and Related Electrochemical Technologies Based on Fenton's Reaction Chemistry. Chem. Rev. 2009, 109, 6570–6631. https://doi.org/10.1021/cr900136g.

130. Bocos, E.; Brillas, E.; Sanromán, M.Á.; Sirés, I. Electrocoagulation: Simply a Phase Separation Technology? The Case of Bronopol Compared to Its Treatment by EAOPs. Environ. Sci. Technol. 2016, 50, 7679–7686. https://doi.org/10.1021/acs.est.6b02057.

131. Nidheesh, P.V.; Gandhimathi, R.; Sanjini, N.S. NaHCO3 Enhanced Rhodamine B Removal from Aqueous Solution by Graphite–Graphite Electro Fenton System. Sep. Purif. Technol. 2014, 132, 568–576. https://doi.org/10.1016/j.seppur.2014.06.009.

132. Orata, E.D.; De Leon, P.D.P.; Doma, B.T. Degradation of Metformin in Water Using Electro-Fenton Process. In Proceedings of the IOP Conference Series: Earth and Environmental Science, Macao, China, 16–19 July 2019; Weng, C.-H., Ed.; Institute of Physics Publishing: New York, NY, USA, 2019; Volume 344.

133. Ramírez-Pereda, B.; Álvarez-Gallegos, A.; Rangel-Peraza, J.G.; Bustos-Terrones, Y.A. Kinetics of Acid Orange 7 Oxidation by Using Carbon Fiber and Reticulated Vitreous Carbon in an Electro-Fenton Process. J. Environ. Manag. 2018, 213, 279–287. https://doi.org/10.1016/j.jenvman.2018.01.022.

134. Su, P.; Zhou, M.; Ren, G.; Lu, X.; Du, X.; Song, G. A Carbon Nanotube-Confined Iron Modified Cathode with Prominent Stability and Activity for Heterogeneous Electro-Fenton Reactions. J. Mater. Chem. A 2019, 7, 24408–24419. https://doi.org/10.1039/C9TA07491K.

135. Olvera-Vargas, H.; Wee, V.Y.H.; Garcia-Rodriguez, O.; Lefebvre, O. Near-Neutral Electro-Fenton Treatment of Pharmaceutical Pollutants: Effect of Using a Triphosphate Ligand and BDD Electrode. ChemElectroChem 2019, 6, 937–946. https://doi.org/10.1002/celc.201801732.

136. Özcan, A.; Şahin, Y.; Koparal, A.S.; Oturan, M.A. A Comparative Study on the Efficiency of Electro-Fenton Process in the Removal of Propham from Water. Appl. Catal. B Environ. 2009, 89, 620–626. https://doi.org/10.1016/j.apcatb.2009.01.022.

137. Thiam, A.; Sirés, I.; Salazar, R.; Brillas, E. On the Performance of Electrocatalytic Anodes for Photoelectro-Fenton Treatment of Synthetic Solutions and Real Water Spiked with the Herbicide Chloramben. J. Environ. Manag. 2018, 224, 340–349. https://doi.org/10.1016/j.jenvman.2018.07.065.

138. Oturan, M.A. Outstanding Performances of the BDD Film Anode in Electro-Fenton Process: Applications and Comparative Performance. Curr. Opin. Solid State Mater. Sci. 2021, 25, 100925. https://doi.org/10.1016/j.cossms.2021.100925.

139. Sudoh, M.; Kodera, T.; Sakai, K.; Zhang, J.Q.; Koide, K. Oxidative Degradation of Aqueous Phenol Effluent with Electrogenerated Fenton's Reagent. J. Chem. Eng. Jpn.1986, 19, 513–518. https://doi.org/10.1252/jcej.19.513.

140. Brillas, E. Solar-Assisted Electro-Fenton Systems for Wastewater Treatment. In Electro-Fenton Process; Zhou, M., Oturan, M.A., Sirés, I., Eds.; Springer Singapore: Singapore, 2017; Volume 61, pp. 313–342, ISBN 978-981-10-6405-0.

141. Pignatello, J.J.; Liu, D.; Huston, P. Evidence for an Additional Oxidant in the Photoassisted Fenton Reaction. Environ. Sci. Technol. 1999, 33, 1832–1839. https://doi.org/10.1021/es980969b.

142. Pignatello, J.J.; Oliveros, E.; MacKay, A. Advanced Oxidation Processes for Organic Contaminant Destruction Based on the Fenton Reaction and Related Chemistry. Crit. Rev. Environ. Sci. Technol. 2006, 36, 1–84. https://doi.org/10.1080/10643380500326564.

143. Brillas, E.; Mur, E.; Sauleda, R.; Sànchez, L.; Peral, J.; Domènech, X.; Casado, J. Aniline Mineralization by AOP's: Anodic Oxidation, Photocatalysis, Electro-Fenton and Photoelectro-Fenton Processes. Appl. Catal. B Environ. 1998, 16, 31–42. https://doi.org/10.1016/S0926-3373(97)00059-3.

144. Masomboon, N.; Lu, M.-C.; Ratanatamskul, C. Effect of Hydrogen Peroxide on the Degradation of 2,6-Dimethylaniline by Fenton Processes. Fresenius Environ. Bull. 2008, 17, 1073–1081.

145. Wang, A.; Qu, J.; Liu, H.; Ru, J. Mineralization of an Azo Dye Acid Red 14 by Photoelectro-Fenton Process Using an Activated Carbon Fiber Cathode. Appl. Catal. B Environ. 2008, 84, 393–399. https://doi.org/10.1016/j.apcatb.2008.04.016.

146. Brillas, E.; Boye, B.; Sirés, I.; Garrido, J.A.; Rodríguez, R.M.; Arias, C.; Cabot, P.-L.; Comninellis, C. Electrochemical Destruction of Chlorophenoxy Herbicides by Anodic Oxidation and Electro-Fenton Using a Boron-Doped Diamond Electrode. Electrochim. Acta 2004, 49, 4487–4496. https://doi.org/10.1016/j.electacta.2004.05.006.

147. Flox, C.; Arias, C.; Brillas, E.; Savall, A.; Groenen-Serrano, K. Electrochemical Incineration of Cresols: A Comparative Study between PbO_2 and Boron-Doped Diamond Anodes. Chemosphere 2009, 74, 1340–1347. https://doi.org/10.1016/j.chemosphere.2008.11.050.

148. Ganiyu, S.O.; Oturan, N.; Trellu, C.; Raffy, S.; Cretin, M.; Causserand, C.; Oturan, M.A. Abatement of Analgesic Antipyretic 4-Aminophenazone Using Conductive Boron-Doped Diamond and Sub-Stoichiometric Titanium Oxide Anodes: Kinetics, Mineralization and Toxicity Assessment. ChemElectroChem 2019, 6, 1808–1817. https://doi.org/10.1002/celc.201801741.

149. Klidi, N.; Proietto, F.; Vicari, F.; Galia, A.; Ammar, S.; Gadri, A.; Scialdone, O. Electrochemical Treatment of Paper Mill Wastewater by Electro-Fenton Process. J. Electroanal. Chem. 2019, 841, 166–171. https://doi.org/10.1016/j.jelechem.2019.04.022.

150. Dirany, A.; Sirés, I.; Oturan, N.; Oturan, M.A. Electrochemical Abatement of the Antibiotic Sulfamethoxazole from Water. Chemosphere 2010, 81, 594–602. https://doi.org/10.1016/j.chemosphere.2010.08.032.

151. Murati, M.; Oturan, N.; Zdravkovski, Z.; Stanoeva, J.P.; Aaron, S.E.; Aaron, J.-J.; Oturan, M.A. Application of the Electro-Fenton Process to Mesotrione Aqueous Solutions: Kinetics, Degradation Pathways, Mineralization, and Evolution of Toxicity. Maced. J. Chem. Chem. Eng. 2014, 33, 121–137. https://doi.org/10.20450/mjcce.2014.407.

152. Olvera-Vargas, H.; Oturan, N.; Aravindakumar, C.T.; Paul, M.M.S.; Sharma, V.K.; Oturan, M.A. Electro-Oxidation of the Dye Azure B: Kinetics, Mechanism, and by-Products. Environ. Sci. Pollut. Res. 2014, 21, 8379–8386. https://doi.org/10.1007/s11356-014-2772-4.

153. Oturan, N.; Brillas, E.; Oturan, M.A. Unprecedented Total Mineralization of Atrazine and Cyanuric Acid by Anodic Oxidation and Electro-Fenton with a Boron-Doped Diamond

Anode. Environ. Chem. Lett. 2012, 10, 165–170. https://doi.org/10.1007/s10311-011-0337-z.

154. Pinheiro, V.S.; Paz, E.C.; Aveiro, L.R.; Parreira, L.S.; Souza, F.M.; Camargo, P.H.C.; Santos, M.C. Mineralization of Paracetamol Using a Gas Diffusion Electrode Modified with Ceria High Aspect Ratio Nanostructures. Electrochim. Acta 2019, 295, 39–49. https://doi.org/10.1016/j.electacta.2018.10.097.

155. Skoumal, M.; Rodríguez, R.M.; Cabot, P.L.; Centellas, F.; Garrido, J.A.; Arias, C.; Brillas, E. Electro-Fenton, UVA Photoelectro-Fenton and Solar Photoelectro-Fenton Degradation of the Drug Ibuprofen in Acid Aqueous Medium Using Platinum and Boron-Doped Diamond Anodes. Electrochim. Acta 2009, 54, 2077–2085. https://doi.org/10.1016/j.electacta.2008.07.014.

156. Muddemann, T.; Neuber, R.; Haupt, D.; Graßl, T.; Issa, M.; Bienen, F.; Enstrup, M.; Möller, J.; Matthée, T.; Sievers, M.; *et al.* Improving the Treatment Efficiency and Lowering the Operating Costs of Electrochemical Advanced Oxidation Processes. Processes 2021, 9, 1482. https://doi.org/10.3390/pr9091482.

157. Pérez, J.F.; Llanos, J.; Sáez, C.; López, C.; Cañizares, P.; Rodrigo, M.A. On the Design of a Jet-Aerated Microfluidic Flow-through Reactor for Wastewater Treatment by Electro-Fenton. Sep. Purif. Technol. 2019, 208, 123–129. https://doi.org/10.1016/j.seppur.2018.04.021.

158. Cruz-González, K.; Torres-López, O.; García-León, A.; Guzmán-Mar, J.L.; Reyes, L.H.; Hernández-Ramírez, A.; Peralta-Hernández, J.M. Determination of Optimum Operating Parameters for Acid Yellow 36 Decolorization by Electro-Fenton Process Using BDD Cathode. Chem. Eng. J. 2010, 160, 199–206. https://doi.org/10.1016/j.cej.2010.03.043.

159. Espinoza-Montero, P.J.; Vasquez-Medrano, R.; Ibanez, J.G.; Frontana-Uribe, B.A. Efficient Anodic Degradation of Phenol Paired to Improved Cathodic Production of H_2O_2 at BDD Electrodes. J. Electrochem. Soc. 2013, 160, G3171–G3177. https://doi.org/10.1149/2.027307jes.

160. García, O.; Isarain-Chávez, E.; Garcia-Segura, S.; Brillas, E.; Peralta-Hernández, J.M. Degradation of 2,4-Dichlorophenoxyacetic Acid by Electro-Oxidation and Electro-Fenton/BDD Processes Using a Pre-Pilot Plant. Electrocatalysis 2013, 4, 224–234. https://doi.org/10.1007/s12678-013-0135-4.

161. Villaseñor-Basulto, D.; Picos-Benítez, A.; Bravo-Yumi, N.; Perez-Segura, T.; Bandala, E.R.; Peralta-Hernández, J.M. Electro-Fenton Mineralization of Diazo Dye Black

NT2 Using a Pre-Pilot Flow Plant. J. Electroanal. Chem. 2021, 895, 115492. https://doi.org/10.1016/j.jelechem.2021.115492.

162. Garza-Campos, B.R.; Guzmán-Mar, J.L.; Reyes, L.H.; Brillas, E.; Hernández-Ramírez, A.; Ruiz-Ruiz, E.J. Coupling of Solar Photoelectro-Fenton with a BDD Anode and Solar Heterogeneous Photocatalysis for the Mineralization of the Herbicide Atrazine. Chemosphere 2014, 97, 26–33. https://doi.org/10.1016/j.chemosphere.2013.10.044.

163. Sun, Y.; Pignatello, J.J. Photochemical Reactions Involved in the Total Mineralization of 2,4-D by Iron(3+)/Hydrogen Peroxide/UV. Environ. Sci. Technol. 1993, 27, 304–310. https://doi.org/10.1021/es00039a010.

164. Andreozzi, R. Advanced Oxidation Processes (AOP) for Water Purification and Recovery. Catal. Today 1999, 53, 51–59. https://doi.org/10.1016/S0920-5861(99)00102-9.

165. Casado, J.; Fornaguera, J.; Galán, M.I. Mineralization of Aromatics in Water by Sunlight-Assisted Electro-Fenton Technology in a Pilot Reactor. Environ. Sci. Technol. 2005, 39, 1843–1847. https://doi.org/10.1021/es0498787.

166. Skoumal, M.; Arias, C.; Cabot, P.L.; Centellas, F.; Garrido, J.A.; Rodríguez, R.M.; Brillas, E. Mineralization of the Biocide Chloroxylenol by Electrochemical Advanced Oxidation Processes. Chemosphere 2008, 71, 1718–1729. https://doi.org/10.1016/j.chemosphere.2007.12.029.

167. Alcaide, F.; Álvarez, G.; Guelfi, D.R.V.; Brillas, E.; Sirés, I. A Stable CoSP/MWCNTs Air-Diffusion Cathode for the Photoelectro-Fenton Degradation of Organic Pollutants at Pre-Pilot Scale. Chem. Eng. J. 2020, 379, 122417. https://doi.org/10.1016/j.cej.2019.122417.

168. Fernandes, C.H.M.; Silva, B.F.; Aquino, J.M. On the Performance of Distinct Electrochemical and Solar-Based Advanced Oxidation Processes to Mineralize the Insecticide Imidacloprid. Chemosphere 2021, 275, 130010. https://doi.org/10.1016/j.chemosphere.2021.130010.

169. Tirado, L.; Gökkuş, Ö.; Brillas, E.; Sirés, I. Treatment of Cheese Whey Wastewater by Combined Electrochemical Processes. J. Appl. Electrochem. 2018, 48, 1307–1319. https://doi.org/10.1007/s10800-018-1218-y.

170. Bravo-Yumi, N.; Villaseñor-Basulto, D.L.; Pérez-Segura, T.; Pacheco-Álvarez, M.A.; Picos-Benitez, A.; Rodriguez-Narvaez, O.M.; Peralta-Hernández, J.M. Comparison and Statistical Analysis for Post-Tanning Synthetic Wastewater Degradation Using Different Electrochemical Processes. Chem. Eng. Process. Process Intensif. 2021, 159, 108244. https://doi.org/10.1016/j.cep.2020.108244.

171. da Silva, L.M.; Gozzi, F.; Cavalcante, R.P.; de Oliveira, S.C.; Brillas, E.; Sirés, I.; Machulek, A. Assessment of 4-Aminoantipyrine Degradation and Mineralization by

Photoelectro-Fenton with a Boron-Doped Diamond Anode: Optimization, Treatment in Municipal Secondary Effluent, and Toxicity. ChemElectroChem 2019, 6, 865–875. https://doi.org/10.1002/celc.201801651.

172. Steter, J.R.; Brillas, E.; Sirés, I. Solar Photoelectro-Fenton Treatment of a Mixture of Parabens Spiked into Secondary Treated Wastewater Effluent at Low Input Current. Appl. Catal. B Environ. 2018, 224, 410–418. https://doi.org/10.1016/j.apcatb.2017.10.060.

173. Machado, M.L.O.; Paz, E.C.; Pinheiro, V.S.; de Souza, R.A.S.; Neto, A.M.P.; Gaubeur, I.; dos Santos, M.C. Use of WO2.72 Nanoparticles/Vulcan® XC72 GDE Electrocatalyst Combined with the Photoelectro-Fenton Process for the Degradation of 17α-Ethinylestradiol (EE2). Electrocatalysis 2022, 13, 457–468. https://doi.org/10.1007/s12678-022-00724-8.

174. Coria, G.; Sirés, I.; Brillas, E.; Nava, J.L. Influence of the Anode Material on the Degradation of Naproxen by Fenton-Based Electrochemical Processes. Chem. Eng. J. 2016, 304, 817–825. https://doi.org/10.1016/j.cej.2016.07.012.

175. Salmerón, I.; Plakas, K.V.; Sirés, I.; Oller, I.; Maldonado, M.I.; Karabelas, A.J.; Malato, S. Optimization of Electrocatalytic H2O2 Production at Pilot Plant Scale for Solar-Assisted Water Treatment. Appl. Catal. B Environ. 2019, 242, 327–336. https://doi.org/10.1016/j.apcatb.2018.09.045.

176. Salazar, R.; Brillas, E.; Sirés, I. Finding the Best Fe^{2+}/Cu^{2+} Combination for the Solar Photoelectro-Fenton Treatment of Simulated Wastewater Containing the Industrial Textile Dye Disperse Blue 3. Appl. Catal. B Environ. 2012, 115–116, 107–116. https://doi.org/10.1016/j.apcatb.2011.12.026.

177. Clematis, D.; Panizza, M. Electro-Fenton, Solar Photoelectro-Fenton and UVA Photoelectro-Fenton: Degradation of Erythrosine B Dye Solution. Chemosphere 2021, 270, 129480. https://doi.org/10.1016/j.chemosphere.2020.129480.

178. Da Costa Soares, I.C.; Oriol, R.; Ye, Z.; Martínez-Huitle, C.A.; Cabot, P.L.; Brillas, E.; Sirés, I. Photoelectro-Fenton Treatment of Pesticide Triclopyr at Neutral PH Using Fe(III)–EDDS under UVA Light or Sunlight. Environ. Sci. Pollut. Res. 2021, 28, 23833–23848. https://doi.org/10.1007/s11356-020-11421-8.

179. Ye, Z.; Guelfi, D.R.V.; Álvarez, G.; Alcaide, F.; Brillas, E.; Sirés, I. Enhanced Electrocatalytic Production of H_2O_2 at Co-Based Air-Diffusion Cathodes for the Photoelectro-Fenton Treatment of Bronopol. Appl. Catal. B Environ. 2019, 247, 191–199. https://doi.org/10.1016/j.apcatb.2019.01.029.

180. Moreira, F.C.; Soler, J.; Fonseca, A.; Saraiva, I.; Boaventura, R.A.R.; Brillas, E.; Vilar, V.J.P. Electrochemical Advanced Oxidation Processes for Sanitary Landfill Leachate

Remediation: Evaluation of Operational Variables. Appl. Catal. B Environ. 2016, 182, 161–171. https://doi.org/10.1016/j.apcatb.2015.09.014.

181. Moreira, F.C.; Soler, J.; Fonseca, A.; Saraiva, I.; Boaventura, R.A.R.; Brillas, E.; Vilar, V.J.P. Incorporation of Electrochemical Advanced Oxidation Processes in a Multistage Treatment System for Sanitary Landfill Leachate. Water Res. 2015, 81, 375–387. https://doi.org/10.1016/j.watres.2015.05.036.

182. Antonin, V.S.; Garcia-Segura, S.; Santos, M.C.; Brillas, E. Degradation of Evans Blue Diazo Dye by Electrochemical Processes Based on Fenton's Reaction Chemistry. J. Electroanal. Chem. 2015, 747, 1–11. https://doi.org/10.1016/j.jelechem.2015.03.032.

183. Flox, C.; Garrido, J.A.; Rodríguez, R.M.; Cabot, P.-L.; Centellas, F.; Arias, C.; Brillas, E. Mineralization of Herbicide Mecoprop by Photoelectro-Fenton with UVA and Solar Light. Catal. Today 2007, 129, 29–36. https://doi.org/10.1016/j.cattod.2007.06.049.

184. Cornejo, O.M.; Murrieta, M.F.; Castañeda, L.F.; Nava, J.L. Characterization of the Reaction Environment in Flow Reactors Fitted with BDD Electrodes for Use in Electrochemical Advanced Oxidation Processes: A Critical Review. Electrochim. Acta 2020, 331, 135373. https://doi.org/10.1016/j.electacta.2019.135373.

185. Cornejo, O.M.; Murrieta, M.F.; Castañeda, L.F.; Nava, J.L. Electrochemical Reactors Equipped with BDD Electrodes: Geometrical Aspects and Applications in Water Treatment. Curr. Opin. Solid State Mater. Sci. 2021, 25, 100935. https://doi.org/10.1016/j.cossms.2021.100935.

186. Cañizares, P.; Paz, R.; Sáez, C.; Rodrigo, M.A. Costs of the Electrochemical Oxidation of Wastewaters: A Comparison with Ozonation and Fenton Oxidation Processes. J. Environ. Manag. 2009, 90, 410–420. https://doi.org/10.1016/j.jenvman.2007.10.010.

187. Mousset, E.; Loh, W.H.; Lim, W.S.; Jarry, L.; Wang, Z.; Lefebvre, O. Cost Comparison of Advanced Oxidation Processes for Wastewater Treatment Using Accumulated Oxygen-Equivalent Criteria. Water Res. 2021, 200, 117234.

I.2. In-house vs. Commercial Boron-Doped Diamond Electrodes for Electrochemical Degradation of Water Pollutants: A Critical Review

Priscilla Brosler[1], Ana Violeta Girão[1], Rui F. Silva[1], João Tedim[1], Filipe J. Oliveira[1]

[1] CICECO Aveiro Institute of Materials, Department of Materials and Ceramic Engineering, University of Aveiro, 3810-193, Aveiro, Portugal

The present work was published on: Frontiers In Materials

Published on: 23 March 2023

doi: 10.3389/fmats.2023.1020649

Abstract

Boron-doped diamond (BDD) electrodes are eco-friendly and widely used in efficient water remediation through electrochemical advanced oxidation processes (EAOPs). These anodes can completely mineralize a wide range of pollutants, only requiring electrical energy. Over the last two decades, numerous commercially available BDD electrodes have emerged, but little is known about their electrooxidation performance, particularly if compared to laboratory-produced anodes by different research groups. In this critical review, a comparison between in-house-made and commercially available BDD electrodes based on a systematic literature review (SLR) is carried out. SLR was quite useful in locating and selecting the scientific publications relevant to the topic, enabling information gathering on dissemination, growth, and trends in the application of BDD electrodes in the degradation of water pollutants. More specifically, data concerning the origin of the employed BDD electrodes, and their physicochemical properties were extracted from a thorough selection of articles. Moreover, a detailed analysis of the main parameters affecting the BDD electrodes' performance is provided and includes selection and pre-treatment of the substrate material, chemical vapor deposition (CVD) method, deposition parameters, characterization methods, and operational conditions. This discussion was carried out fully based on the numerous performance indicators found in the literature. Those clearly revealed that there are only a few analogous points across works, demonstrating the challenge of establishing an accurate comparison methodology. In this context, we propose

a figure-of-merit equation which aims at normalizing BDD degradation results for a specific contaminant, even if working under different experimental conditions. Two case studies based on the degradation of solutions spiked with phenol and landfill leachate treatment with commercial or in-house-made BDD electrodes are also presented. Although it was not possible to conclude which electrode would be the best choice, in this paper we propose a set of guidelines detailing a consistent experimental procedure for comparison purposes in the future.

I.2.1. Introduction

Over the last two decades, boron-doped diamond (BDD) has gained increased attention and has been extensively studied for electrochemical applications due to its distinct physical and chemical properties from conventional electrode materials. These include a wide electric potential window in aqueous and non-aqueous solutions (1, 2), good stability and corrosion resistance (3, 4), inert surface with low adsorption (5), low double-layer capacitance and background current (6), high current density electrolysis (1–10 $A.cm^{-2}$) (7), and high overpotential for both hydrogen and oxygen evolution (2).

The electric potential window of BDD electrodes is much wider than that of any other material (8), with the hydrogen evolution reaction (HER) starting at about −1.2 V/SHE (Standard hydrogen electrode) and the oxygen evolution reaction (OER) at approximately +2.3 V/SHE (1, 2). This broad potential window arises from the BDD's high overvoltage for water splitting (8). The HER and OER are inner-sphere reactions that generally consist of multi-step electron transfer reactions that depend on reaction intermediates' adsorption (9). The carbon sp^3-hybridized orbitals in diamond show weak adsorption ability towards these intermediates and, consequently, the catalytic effect for HER and OER in BDD electrodes is weak (8). The diamond sp^3-hybridized orbitals form strong covalent bonds and are responsible for the BDD's good stability and corrosion resistance. Studies have shown that BDD electrodes are stable in strong acid media, even for long-term cycling of potential ranging from hydrogen to oxygen evolution reaction overpotentials (3, 4). Electrodes based on conventional materials such as glassy carbon or graphite usually have higher surface adsorption ability, forming a polymeric adhesive film on their surface, leading to electrode fouling (7). The sp^2-hybridised orbitals present in the surface of these electrodes increase the adsorption strength (10), while the sp^3-hybridised orbitals present in the diamond structure shows weak adsorption capacity (8). Electrode fouling is easily avoided in BDD electrodes if working above the potential region of water splitting (11). BDD electrodes can also be self-cleaned through the polarization of such polymeric films (12). The surface of BDD electrodes resists deactivation processes, showing stable voltametric responses towards $Fe(CN)_6^{4-/3-}$ even after two weeks of continuous potential cycling (5). BDD electrodes are also particularly interesting for electroanalysis and sensing applications since they present low background current and consequent low double-layer capacitance, resulting in lower detection limits for trace analysis when compared to other sensors (13). The above-mentioned excellent electrochemical behavior of BDD electrodes can vary drastically depending on their physicochemical properties.

More important is the role BDD anodes are currently playing in water remediation through OER and the generated oxygen-based radicals that can completely eliminate a wide range of pollutants, including non-biodegradable compounds (14). Recent reviews on the electrochemical degradation of contaminants with BDD electrodes can be found in the literature (9, 15-30). These include studies performed using BDD anodes prepared by chemical vapor deposition (CVD), commercially available and in-house-made, and applied in spiked water and real wastewater treatment systems.

In this critical review, we will evaluate if it is possible to compare the performance of commercial BDD electrodes with those produced in-house towards electrooxidation of water pollutants. We will also discuss how the CVD deposition conditions, the physicochemical properties of the anodes, and the electrooxidation process influence the interpretation of the degradation efficiency results. This assessment will be carefully carried out using bibliometric analysis. Afterwards, an attempt will be made to reach a consensus on possible guidelines and/or degradation performance indicators for future comparison of BDD electrodes from different origins.

I.2.2. Electrochemical degradation of contaminants with BDD electrodes: a bibliometric analysis

Bibliometrics is a research method that uses quantitative and statistical analysis to describe patterns in publications. Bibliometric studies are frequently used to investigate structural interrelationships and to increase the understanding of a specific subject state of the art (31). In order to properly carry out these studies, it is essential to know Lotka's inverse square laws regarding the calculation of authors' productivity, Bradford's law for the dispersion of authors in different journals, and Zipf's law concerning the frequency of words in each document (32, 33). Systematic literature review (SLR) was chosen as the method of searching for publications since it is widely used and because it is a structured way of locating and selecting the relevant publications, increasing the reproducibility and reliability of the method (31).

In this work, bibliometric analysis was used (i) to identify the growth and trends in the application of BDD in the degradation of contaminants; (ii) to identify the dissemination of information with quantification of publications by journals, universities, and research centers, and by country; and (iii) to verify the keywords relationship between themes through their co-occurrence in a network graph. The tools used to visualize the results and create the graphics were Microsoft Excel and VOSViewer (34).

The bibliometric search of the topic “electrochemical degradation of contaminants with BDD electrodes” was carried out by a Boolean advanced search query in the Scopus database through a search string connecting the topics by the title field of publications in April 2022. The details of this search query can be found in the Supplementary Table I.2.1. A total of 875 articles meeting the established criteria were obtained. The search was restricted to scientific articles as the document type and only to the English language. This result went through a process of elimination of duplicates and irrelevant results (not related to the subject), reaching a final number of 868 publications for further bibliometric analysis. The list of strings used in the search query was defined based on a previous broader search in which the fundamental terms used to describe the electrochemical degradation of contaminants were identified (Supplementary Table I.2.2). Figure I.2.1 illustrates the number of publications per year on BDD as an electrode for electrooxidation of contaminants.

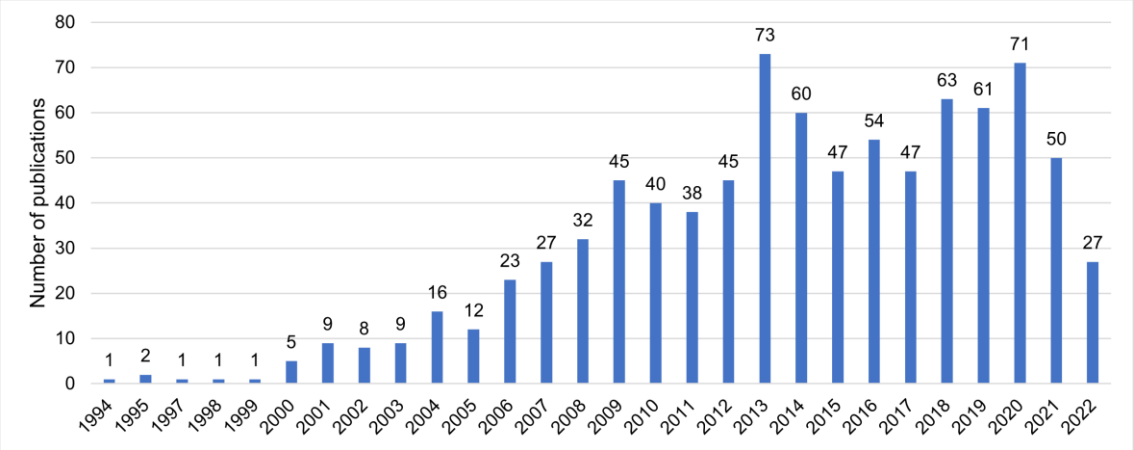

Figure I.2.1. Number of publications per year on BDD as an electrode for electrooxidation of contaminants, based on the Scopus database.

The first publication identified in the SLR was published in 1994 (35), although the first one ever reported on the electrochemical behavior of CVD diamond dates back to 1987 (36). However, the latter does not address pollutant degradation studies. In the early 1990s, studies of BDD used as electrodes began to emerge all over the world: Japan (37), the USA (5, 6) or China (38, 39). The number of publications increased rapidly in the 2000s, reaching a peak of 73 publications in one single year (2013). Nearly the same number of publications was achieved again in 2020. By the time these data were gathered, early 2022 already accounted for 27 publications, clearly indicating that the topic has excellent scientific

relevance and is still extensively explored. The dissemination of information was identified through the analysis of publications by journals, as shown in Figure I.2.2.

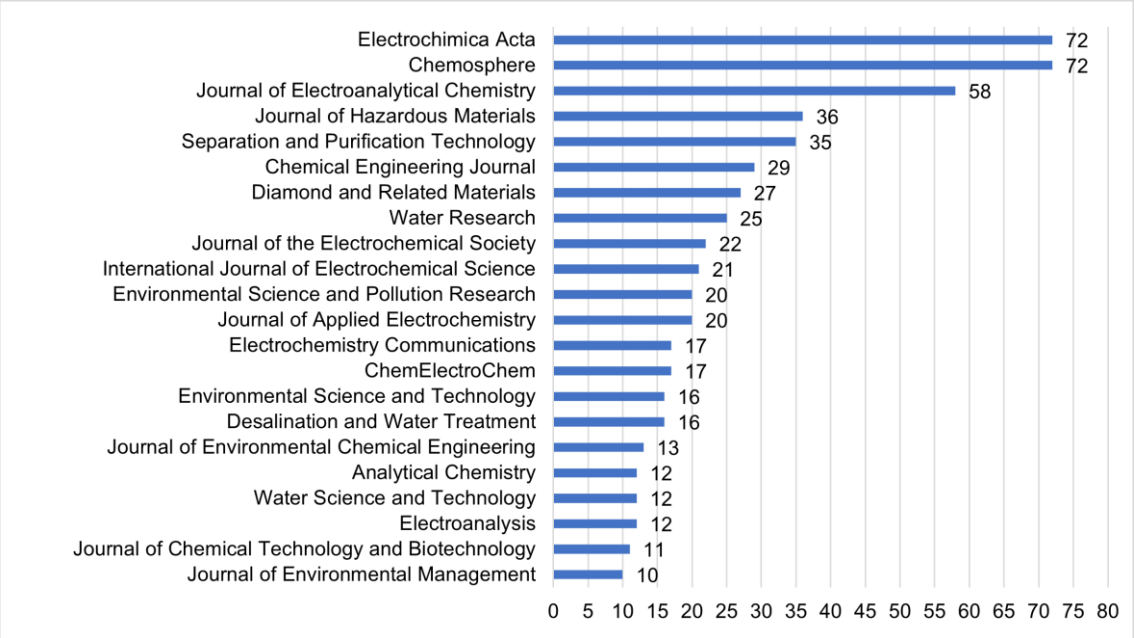

Figure I.2.2. Number of publications per journal with more than 10 publications on BDD as an electrode for electrooxidation of contaminants, based on the Scopus database.

Articles on the topic were published in more than 160 different journals. *Chemosphere*, *Electrochimica Acta,* and *Journal of Electroanalytical Chemistry* published around 23% of all the articles on BDD as an electrode for electrooxidation of contaminants. Therefore, researchers on this subject should consult information primarily in these three journals. Figure I.2.3 presents the bibliometric study finding the dissemination of information by universities and research centers with more than 20 publications on the topic, as well as the number of publications per country.

The institution contributing the most to disseminating this topic is the Universitat de Barcelona (Spain). Switzerland ranks 11th, but one should note that the École Polytechnique Fédérale de Lausanne has the fourth-highest number of publications on the subject. China, Spain, Brazil, France, Italy, Mexico, and Japan represent more than 50% of publications. The most significant contributors are China with 157 publications, Spain with 127, and Brazil with 113. To identify the trends in the application of BDD anodes in the degradation of contaminants and verify the relationship within the main themes, a keyword network graph (Figure I.2.4) was constructed.

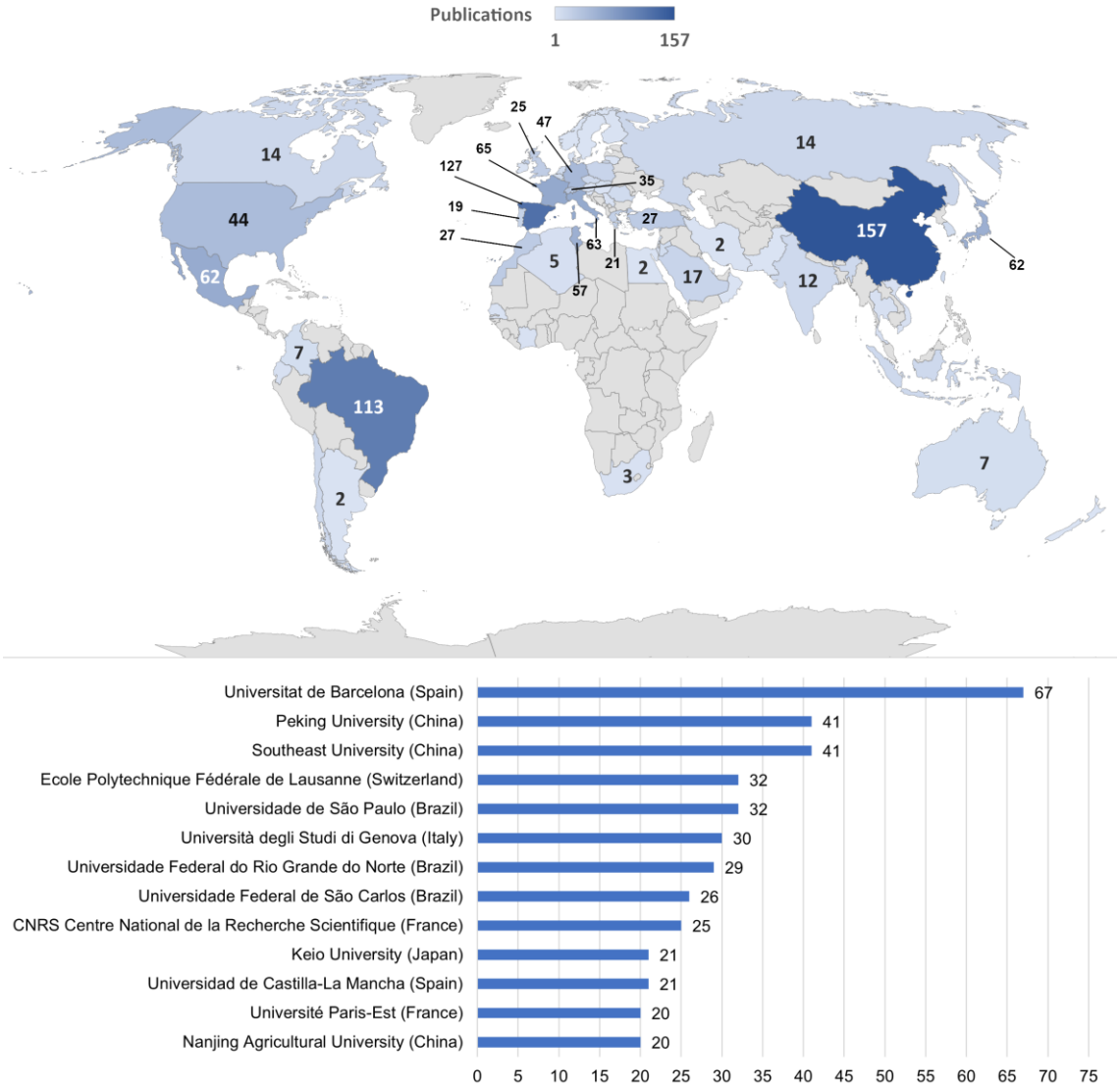

Figure I.2.3. Number of publications per country on BDD as an electrode for electrooxidation of contaminants (upper); and universities and research centers with more than 20 publications on BDD as an electrode for electrooxidation of contaminants (below). All results were based on the Scopus database.

The network graph shows six main clusters where the red highlights response surface methodology studies that encompass cyclic voltammetry measurements to evaluate the electrochemical properties of BDD anodes and the electrooxidation of pollutants. The larger the frame of a given keyword, the more frequent it is across the literature. In the red cluster, pesticides appear as the primarily studied pollutant. The purple cluster represents the analysis of energy consumption by the electrooxidation processes using BDD anodes, and the cyan cluster is mainly related to wastewater disinfection. BDD electrochemistry, electrochemical oxidation of phenol and dyes, and the toxicity of the resulting byproducts are featured in the green cluster. The blue one involves water treatment containing

pharmaceuticals (primarily studied contaminants) by different EAOPs (anodic oxidation, electro-Fenton, and photoelectron-Fenton). This cluster includes intermediate oxidation products such as carboxylic acids (oxalic, acetic, or formic), often used as models to investigate the reaction mechanisms and electrocatalytic properties of the anode materials (40). The yellow group gathers information on the production of hydroxyl radicals and carboxylic acid intermediates during the final mineralization process. Overall, the keyword network graph in Figure I.2.4 reveals that BDD anodes for water remediation have been primarily used in the electrooxidation of pharmaceuticals, pesticides, carboxylic acids, phenolic compounds, dyes, and for water disinfection of bacteria and viruses.

SLR verified that the degradation of water pollutants through BDD electrodes is a subject particularly targeted in the last two decades, highly relevant (mentioned in more than 160 journals) and studied on all continents. The keywords co-occurrence network map allowed the identification of the most studied types of water pollutants and applied EAOPs, as well as other relevant issues to the degradation process: the generation of byproducts and their toxicity and associated energy consumption/costs.

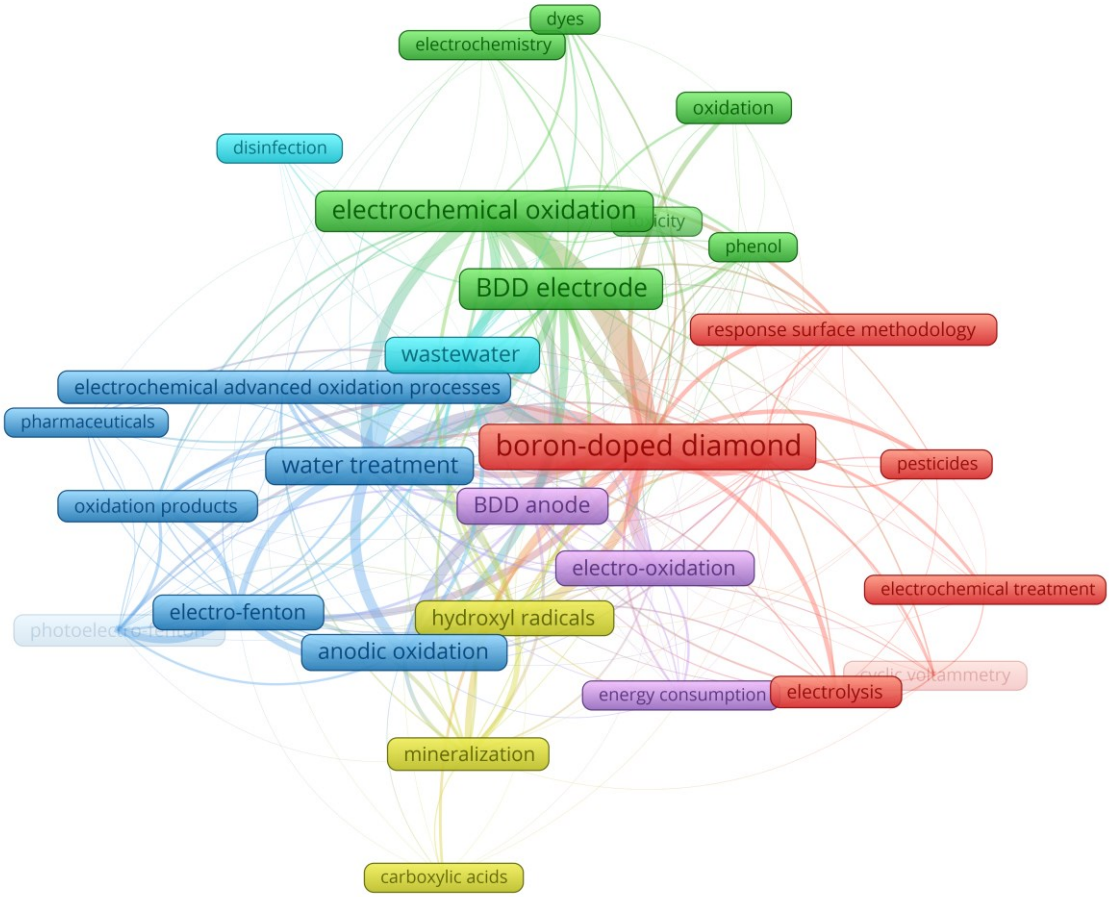

Figure I.2.4. Keywords co-occurrence network (minimum of 10 occurrences) representation of the trends on the application of BDD anodes in the degradation of contaminants and corresponding relationship within the main themes, sorted in six clusters represented in different colors, based on the Scopus database and VOSviewer as the bibliometric network graph software.

I.2.3. Utilization of laboratory produced and commercial BDD electrodes

From 1994 to 2001, electrooxidation of pollutants using BDD anodes was exclusively performed with lab-made electrodes (Figure I.2.5). Commercial BDD electrodes started to gain ground and were first reported in 2002. The number of studies considering the application of commercial BDD anodes increased, and since 2006 they are around 4 times greater (average) than those using in-house-made electrodes. However, only 20% of the 868 identified publications were related to laboratory-made BDD anodes, and 63% applied commercially available electrodes. The remaining unspecified 17% of the reported studies

can probably be associated with commercial BDD electrodes, which would sum up to 80% of the publications implementing such electrodes. Such a high percentage of the use of commercial electrodes may indicate the technology's maturity is being achieved.

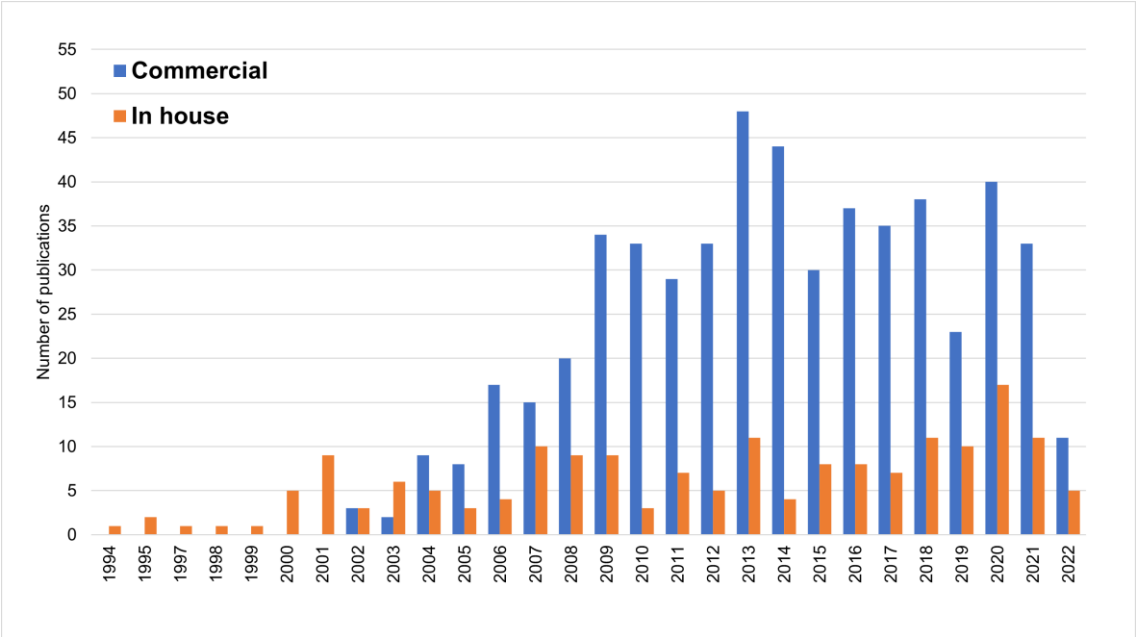

Figure I.2.5. Number of publications per year on commercial and in-house BDD anodes in the degradation of contaminants, based on the bibliometric analysis search.

Figure I.2.6 shows the distribution of the companies whose BDD electrodes were used in the analyzed publications. A list of commercial BDD suppliers, including companies that did not appear in the articles from the SLR, is available in the Supplementary Table I.2.3. Commercial electrodes from Adamant Technologies (Switzerland) and NeoCoat (Switzerland), which are spin-off companies of CSEM (Switzerland), together with those manufactured by CSEM itself, sum up to 58% of presence in the articles from the SLR, followed by 26.8% from Condias GmbH (Germany), and 4.1% from Mekatem™ (Germany).

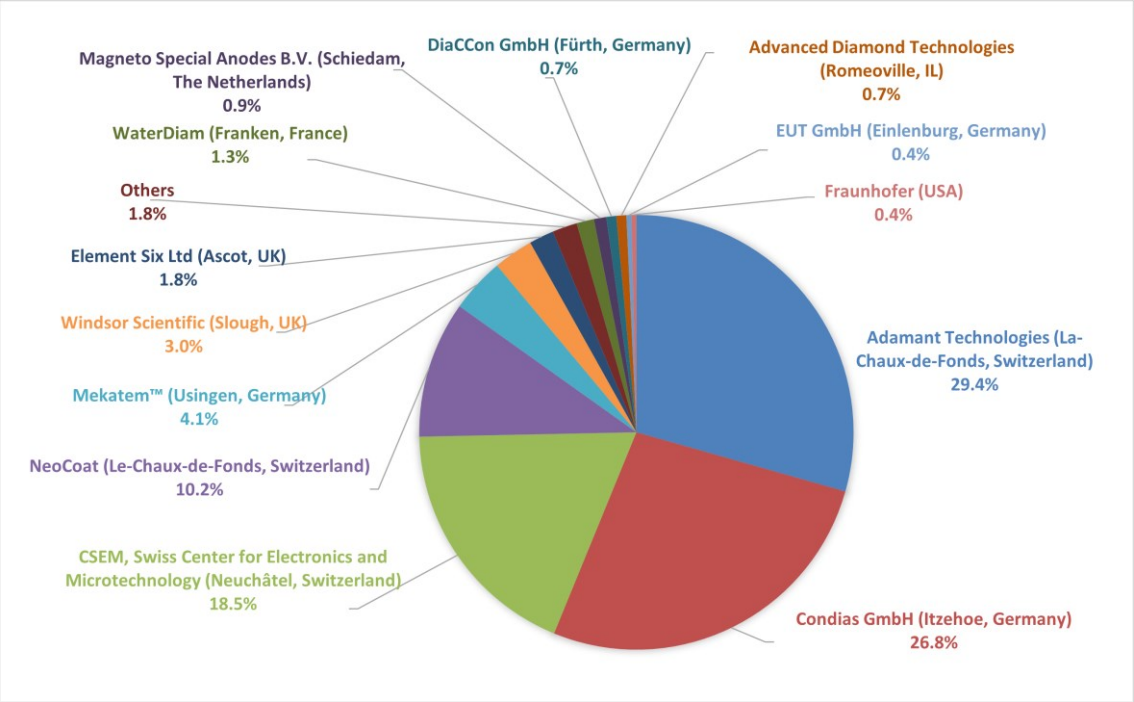

Figure I.2.6. Commercial BDD manufacturer preference based on the bibliometric analysis search.

Commercially manufactured BDD electrodes may offer greater reproducibility since companies are committed to delivering high quality and reproducible materials to their clients but are also costly and with a fixed set of morphological and electrochemical characteristics, such as sp^3/sp^2 ratio, boron doping level, film morphology and thickness, electrochemical potential window, capacitance, among others. Nevertheless, they enable numerous research groups without in-house CVD equipment to explore the use of such BDD electrodes in their studies, further expanding their application range and effectively contributing to knowledge expansion of these thin films.

The main advantage of producing in-house BDD electrodes is growing customizable films by exploring and controlling their properties, such as the sp^3/sp^2 ratio, thickness, boron doping level, growth rate, and grain size. These properties strongly define the working potential window of the electrode, its conductivity and selectivity. Hence, in theory, precise BDD films can be created and adapted to each type of target pollutant. In addition, in-house BDD deposition allows the exploration of different deposition conditions and/or substrate materials. The full potential of BDD electrodes can only be attained by appropriate and specific electrode design for each application and/or target contaminant (21).

Nonetheless, in-house BDD film deposition may also imply lower reproducibility, depending on the CVD reactors used and their operability. Additionally, the overall area of the BDD films is limited by the volume and operation design of the CVD chamber reactor (41),

typically smaller than the commercial ones. The in-house production of BDD electrodes is expensive for universities and research centers, when including the cost of the CVD equipment and the process associated costs such as electricity consumption, water cooling system, and reactive gases (42). Furthermore, a well-prepared infrastructure is mandatory to meet all the necessary safety requirements, including electrical hazards and the use of dangerous reactive gases. These, and the lack of know-how, contribute to limiting the spread of such equipment in laboratories working mostly on water purification processes.

I.2.4. BDD electrodes from different sources

It is a challenge to compare the performance of different in-house BDD electrodes regarding the electrooxidation of water pollutants. First, the design and working conditions of the adopted CVD technique can vary widely: the deposition method (hot-filament -HFCVD, or microwave plasma -MPCVD); the experimental deposition parameters (CH_4/H_2 ratio, pressure, substrate temperature, boron doping source, [B]/[C] ratio); and the substrate material and its prior preparation (43, 44). Altogether, these parameters will influence the final physicochemical properties of the BDD electrode, such as sp^3/sp^2 ratio, effective boron doping level, grain size, film thickness, electrical conductivity, electrochemical potential window, oxygen evolution potential (OEP), electron transfer rate, surface roughness, and surface termination (44-47).

Second, the application of the BDD anodes in the electrooxidation of contaminants includes several other accountable factors such as the degradation conditions used in the experiments (current density, type of EAOP, pH and type of electrolyte, active electrode area, volume of solution, type and concentration of the pollutant, electrochemical cell design, or fluid dynamics), and the water system itself (spiked water or real wastewater) (48-51).

The number of publications concerning BDD anodes in electrochemistry has drastically increased due to the emergence of commercial BDD manufacturers. It broadened the application of BDD electrodes resulting in high-quality publications but further entangled possible comparisons between electrodes' performance. Most reports on tested commercial BDD electrodes lack information on their physicochemical properties and preparation process. The manufacturing process of such complex thin films dictates their performance (52), and it may vary significantly from one company to another. In this section, we discuss how these factors control the final physicochemical properties of BDD coatings, hence their implementation in degrading pollutants present in water systems.

I.2.4.1. Substrate material and preparation

In the preparation of BDD electrodes, the primary function of the substrate for electrochemical applications is to allow the flow of electric current through the electrode, providing physical support to the thin film and conferring enough mechanical stability to the electrode (53). The first thing to keep in mind is that the substrate nature might influence the BDD final properties. Thus, its selection must meet criteria such as stability under extreme conditions (high current density, intense erosive and/or abrasive wear, and strong acids or bases media) (54).

Ideally, the substrate material must withstand the CVD deposition conditions, present high affinity towards diamond thin film growth, high mechanical strength, good electrical conductivity, and electrochemical inertness or the ability to easily form a protective passivation layer on its surface (9, 53). A carbide buffer layer may be formed during CVD deposition, restricting further substrate carburization and promoting easy diamond nucleation and crystal growth (55). Furthermore, a substrate material with low carbon solubility and diffusion coefficient yields higher diamond nucleation rates (54). Temperature gradients interfere with the surface reactions and diamond growth kinetics (56). Therefore, the diffusion coefficient of the carbon atoms, the substrate thermal conductivity, and its coefficient of thermal expansion (CTE) influence the adhesion strength of the diamond thin film, grain size, growth rate, and residual stress, dictating its service life (54).

Several materials have been proved suitable substrates for BDD deposition, including Si, Nb, Ta, W, Mo, Ti, Zr, and graphite (57-59); dielectric ceramics (60); high pressure-high temperature (HPHT) diamond (61); carbon fibers (62); SiO_2 fibers (63); carbon nanotubes (64); TiO_2 nanotubes (65); or metal foams (66). Polished silicon wafers are by far the most applied substrate material, being identified in more than 36% of the published articles (Supplementary Figure I.2.1), especially p-doped Si commercial wafers. Their characteristic low electrochemical activity and ability to form stable and compact oxide films help prevent film delamination (67). However, Si substrates still have many limitations for large-scale applications since they are not suitable in aggressive water treatment environments, mainly due to their relatively low conductivity and brittleness (68). Contrary to Si substrates' short durability, Nb/BDD electrodes have shown a lifetime of more than 850 h during electrolysis (0.5 M H_2SO_4) at very high current densities such as 10 A/cm² (59). The SLR indicates that currently, the second most used substrate material is Nb, followed by Ti and Ta, which are metals capable of forming stable and protective passivation layers. It is important to emphasize that Nb became the preferred choice of substrate material over the years (Supplementary Figure I.2.2) and, since 2013, started to surpass the use of Si substrates.

Roughly, the approximate substrate stability for diamond film deposition obeys the following order: Ta > Si > Nb > W > Ti (57). The CTE of the substrate material is the main factor influencing its compatibility with the BDD film deposition and ideally, it should be as close as possible to that of diamond (0.7-2.0 × 10^{-6} K^{-1}) (7, 43, 69). A CTE mismatch can cause delamination of the BDD film with possible consequent corrosion of the substrate due to electrolyte permeation through the thin film (57). Nevertheless, the high cost of Nb, Ta, and W substrates makes them unattainable for widespread use in large-scale applications (26). Ti has been considered a desirable substrate among those mentioned above due to its lower cost, high conductivity, corrosion resistance, and excellent mechanical properties (70). Yet, Ti/BDD electrodes have shown short service life due to the formation of a TiC intermediate layer generated by the diffusion of carbon species onto the metal during the deposition, resulting in a rough and porous structure that promotes early deterioration of the BDD film adhesion and stability (9, 59, 71). The most likely reasons of electrode failure are assumed to be the TiC layer corrosion at the substrate/film interface, the quality and adhesion of the BDD film, the residual stress produced in the CVD process, and the degradation of the diamond film (72). According to Lu *et al.*, the delamination process occurs in two main stages. The first stage of electrode failure is caused mainly by pore-type defects in the BDD films that allow the electrolyte to penetrate the BDD film and corrode the TiC intermediate layer, which is unstable and quickly decomposes causing the BDD film to delaminate from the substrate. The second stage is caused primarily by corrosion holes created in the Ti substrate. Several attempts have been made to improve the service life of Ti/BDD electrodes, such as developing multilayered structures or increasing the boron concentration in the CVD deposition to inhibit the TiC layer growth, with different levels of success (73-76).

Following the choice of the appropriate substrate material, its pre-treatment for CVD deposition may also affect the final characteristics of the BDD film. The surface properties of the substrate influence the diamond film roughness, adhesion strength, and electroactivity (77). Diamond growth over non-diamond materials usually requires pre-treatment of their surface by a seeding stage (78). This is necessary to obtain proper diamond nucleation density with a complete and packed growth of the thin film, without any substrate area exposed to the solution, which could compromise the working electrode. An effective seeding process depends on the size of the diamond abrasive particles, processing time, and the adopted method (e.g., manually scratching, ultrasonic bath). There are a few studies reporting on the effect of substrate preparation on the nucleation and growth of BDD films (57, 79) showing that ultrasonic seeding is more effective than seeding

through manual scratching. In addition, a rougher Nb substrate prepared by sandblasting with alumina particles (75~106 μm) resulted in the most effective electrode lifetime compared to that with the untreated substrate or the sandblasted one with smaller alumina particles (80).

Considering the direct influence of the substrate material on the electrochemical properties of BDD, when Nb/BDD (planar) and Ti/BDD (Ti mesh) electrodes were compared for phenol degradation, Nb/BDD showed the best performance (81). However, the electrodes had different geometries (consequently, different specific areas), boron doping levels, and different film thicknesses, limiting comparisons between the different metallic substrates. Si/BDD and Nb/BDD electrodes have been compared in different studies for the electrooxidation of acid violet 7 dye (67) and norfloxacin (79). In both cases, the Si/BDD electrode showed higher removal rates with lower associated energy consumption. BDD films deposited over Nb, Si, Ti, and TiN_x/Ti by HFCVD were compared in terms of their performance, particularly chemical oxygen demand (COD) removal and *Escherichia coli* sterilization from livestock wastewaters (76). The TiN_x/Ti/BDD electrode with a TiN_x intermediate layer showed better performance and higher service life than Nb/BDD, Si/BDD, and Ti/BDD. It is quite difficult to evaluate the effect of the substrate material on the BDD electrodes' performance since the published experimental conditions and parameters are not described in detail. Finally, a recent study (54) is perhaps the most systematic and complete comparison to determine the substrate effect, providing enough detailed information on the BDD deposition and substrate preparation conditions and characterization. The influence of the substrate material (Si, Ta, Nb, and Ti substrates) was examined in terms of electrochemical properties, microstructure, degradation of the antibiotic tetracycline, and service life of the identically deposited BDD films. Their results showed that the physicochemical properties of the substrate have a significant impact on the growth and microstructure of the BDD film, and the growth rate followed: Si > Ta > Nb $\gg$ Ti. In addition, the surface finish of both substrate and BDD film also influenced the performance of the BDD electrode. The Ti/BDD electrode showed the best performance in terms of OEP, background current, electron transfer kinetics, and energy consumption, but far shorter service life than Si/BDD, Ta/BDD, and Nb/BDD. In terms of tetracycline removal and current efficiency, the performance of the electrodes followed: Si/BDD > Ti/BDD > Nb/BDD > Ta/BDD. Yang *et al.* indicated that the type of substrate does not significantly affect the boron doping level and diamond quality of BDD electrodes. However, they suggest that the degradation performance of BDD electrodes is affected by the intermediate carbide interlayers formed in the interface between the substrate and the BDD film during

CVD deposition. These interlayers are closely related to the substrate material and affect film thickness, grain size, and electron transfer resistance, thus the surface state of BDD films and, consequently, their organics electrooxidation capability.

Laboratory and pilot tests on wastewaters have been successful in showing the feasibility of BDD electrodes (82-94), but the absence of a universally appropriate and accepted substrate with a defined size and established durability are a tremendous challenge for large scale application of such anodes. Furthermore, practical long-term application of BDD electrodes (highly stable under anodic polarization) in the degradation of pollutants is still subjected to failure at high applied current densities (e.g., 1 $A.cm^{-2}$), mainly due to poor film adhesion with consequent film delamination (95).

The above literature analysis demonstrates that evaluation of the substrate effect on the BDD electrode final performance is not straightforward. It depends on numerous factors leading to very different conclusions. Hence, a further detailed and systematic research is required, and it should also include the complete analysis of the microstructure and physicochemical properties of BDD films like grain size, surface roughness, growth rate, conductivity, sp^3/sp^2 ratio, residual stress, adhesion strength, electron transfer rate, OEP, electrochemical potential window, background current, and boron doping level, deposited under the same CVD deposition conditions over several different substrate materials. Then, possible guidelines may be provided for adequate selection of substrate material for the deposition of BDD thin films for specific water treatment applications.

I.2.4.2. The chemical vapor deposition process

CVD diamond thin films are usually carried out by activating a mixture of a carbon-containing gas (usually methane in low concentration) with molecular hydrogen. During its course, carbon radicals are generated and react with dissociated hydrogen in high concentration to give the diamond growth precursors (96). Chemical vapor deposition techniques include hot-filament (HFCVD), RF-plasma (RFCVD), microwave plasma (MPCVD), and related DC plasma, DC arc-jet, or oxy-acetylene flame (97). Regarding BDD film deposition, SLR detailed analysis indicates that 71.2% of the articles employed hot-filament (HFCVD) and 28.8% microwave plasma (MPCVD), as illustrated in Figure I.2.7.

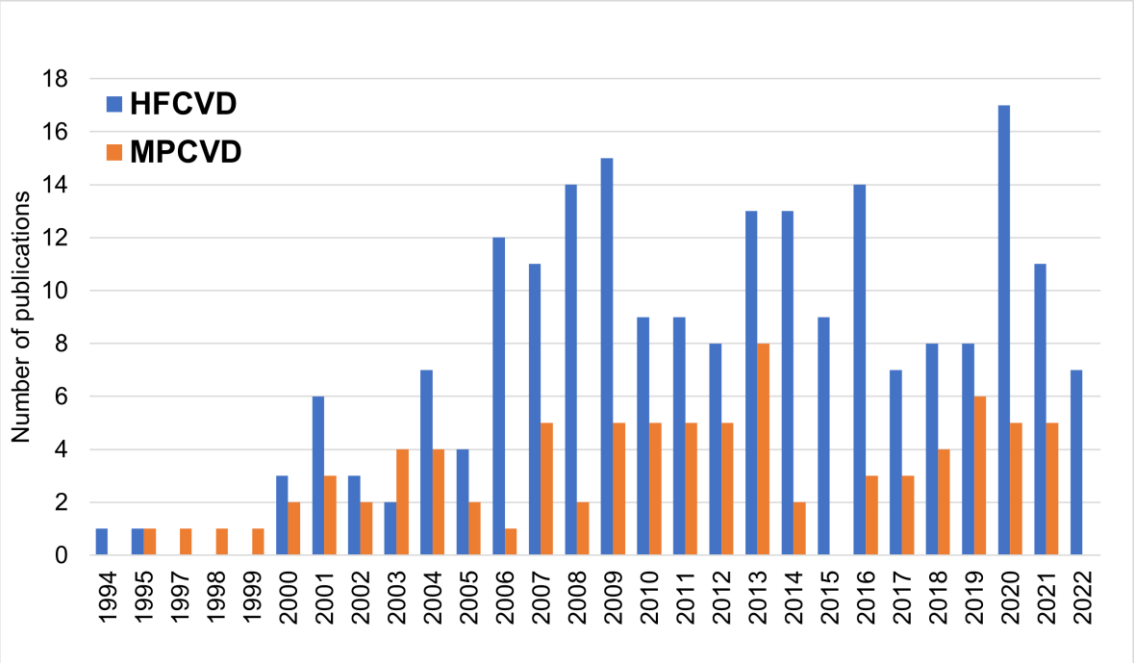

Figure I.2.7. Number of publications per year on commercial and in-house BDD anodes, employing HF or MPCVD deposition methods, based on the bibliometric analysis search.

In HFCVD deposition, an appropriate filament temperature will guarantee molecular hydrogen dissociation, usually obtained at temperatures above 2000ºC. The melting point and purity of the metallic filaments (*e.g.,* W, Ta, and Re) are always considered to avoid or minimize their degradation, which causes film contamination (98). Suitable diamond growth kinetics is also dependent on the distance between each of the filaments and that between them and the substrate's surface. In MPCVD, the microwave power and frequency are the important parameters that require careful control and optimization. Microwave frequency can vary from 300 MHz to 300 GHz, with most depositions performed in commercial reactors (e.g., Seki-ASTeX reactors) typically at 2.45 GHz (99). MPCVD depositions using higher microwave powers exhibit increased feed gas temperature and dissociation efficiency, resulting in larger grain sizes and improved growth rates (100).

Manufacturers of commercial diamond films tend to adopt the HFCVD method due to the possibility of growing films over large surface areas, similarly to some authors who implemented such method to deposit BDD films over areas as large as 0.5 m² (101). In contrast, MPCVD enables higher growth rates, higher phase purity, and better reproducibility since HFCVD temperatures are limited to the filaments' melting point, restricting the concentration of dissociated hydrogen atoms (102). The latter is the main reason for using MPCVD in free-standing diamond deposition (99). In addition, the degradation of the filaments used in HFCVD can promote metal contamination of the films

(99), interfering with the quality of the final films and, for example, hindering the film adhesion to the substrate or inducing graphitization points (98, 103, 104). On the other hand, the plasma area is limited by the wavelength of the microwave radiation in the MPCVD method (102), greatly restricting industrial-scale production of BDD electrodes for pollutant degradation. The preference for HFCVD is also explained by the simplicity of its apparatus and lower cost compared to MPCVD (43).

As demonstrated in the previous section, a comparison between the distinct deposition parameters used in the production of commercial and in-house electrodes constitutes a challenge. Each CVD reactor has specific dimensions and characteristics, as well as optimized deposition parameters (52). For example, two different reactors using the same deposition conditions will not necessarily yield similar BDD films with the very same characteristics due to geometric constraints within the reactor that directly affect the deposition kinetics (105). Table I.2.1 and Table I.2.2 summarize some of the HFCVD and MPCVD deposition parameters respectively, found in the articles within the SLR.

Table I.2.1. HFCVD deposition conditions present in the literature based on the bibliometric analysis search.

University, research center, or commercial manufacturer	Substrate	CH_4/H_2 (%)	Boron source	Filament temperature (°C)	Substrate Temperature (°C)	Pressure (mbar)	[B]/[C] (ppm)	Ref.
Adamant Technologies (Switzerland)	p-Si; Ti	1.0%	Trimethylborane	2440-2560	830	-	100-8000	(106)
Condias GmbH (Germany)	Nb	0.5%-2.5 %	Diborane	2200-2600	700-925	10-50	500-8000	(107)
CSEM, Swiss Center for Electronics and Microtechnology (Switzerland)	p-Si	1.0%	Trimethylborane	2440-2560	830	-	800-8000	(108)
Central South University, China	Si; Ta; Nb; Ti	1%-4%	Diborane	2200-2400	650-850	30	2000-20000	(109) (110)
	Si	3.0%	Diborane	-	850	20	-	(111)
École Polytechnique Fédérale de Lausanne (EPFL), Switzerland	p-Si	1.0%	Trimethylborane	2440-2560	830	-	2500-10000	(112)
	-	1.0%	Trimethylborane	-	760-870	10-100	600	(113)
Instituto Nacional de Pesquisas Espaciais (INPE), Brazil	Ti	0.5%-5.0%	B_2O_3	-	650	53-67	100-30000	(114)
Jilin University, China	Ti	1.0%	Trimethylborate	2000	-	70	8000	(115)
Slovak University of Technology in Bratislava, Slovak Republic	n-Si	1.0%	Trimethylborane	-	650 ± 20	30	10000	(116)
	Si	2.0%	Trimethylborane	2100	650	30	10000	(117)
Tianjin University of Technology, China	Ta	2.0%	Trimethylborate	-	950	50	-	(118)
	Ta	0.7%	B_2O_3	-	800-1000	~67	-	(119)
	Ta	0.7%	B_2O_3	2000	800	25	-	(120)
Zhejiang University, China	Ta	2.0%	Diborane	2500	800	50	-	(121)

**TMD: trimethylborane*

Table I.2.2. MPCVD deposition conditions present in the literature based on the bibliometric analysis search.

University, research center, or commercial manufacturer	Substrate	CH_4/H_2 (%)	Boron source	Substrate Temperature (°C)	Pressure (mbar)	Power (kW)	[B]/[C] (ppm)	Ref.
Keio University, Japan	p-Si	-	Trimethylborate	-	-	5	2000-10000	(122)
	Si	-	Trimethylborane	-	~113	5	-	(123)
Michigan State University, USA	p-Si	0.5%-1%	B_2O_3	850	~47	1.0-1.3	100-1000	(124)
Peking University, China	Ti	1%-2%	Diborane	800	~53	1.2	1000-5000	(125)
University of Technology, Poland	p-Si	1.0%	Diborane	1000	~67	1.3	1000-10000	(126)
University of Tokyo, Japan	n-Si	0.5%	B_2O_3	800-900	~153	1.5	8000	(113)
	p-Si	3.0%	Diborane	880	40	-	6000	(113)
	n-Si; p-Si	3% ± 1%	B_2O_3	800-900	~153	5	10000	(127) (128)
Utsunomiya University, Japan	p-Si	-	B_2O_3	540	~93	1.4	10000	(129)

**TMD: trimethylborane*

CVD polycrystalline diamond deposition is generally performed using a CH_4/H_2 gas mixture, with microcrystalline (MCD) and nanocrystalline diamond (NCD) being typically grown under hydrogen-rich gas mixtures. The introduction of argon into the gas mixture increases the diamond re-nucleation rate, preventing enlargement of the crystallites, and ultra-nanocrystalline diamond (UNCD) is usually grown under argon-rich CVD environments (43). According to the van der Drift regime (43, 130), MCD and NCD grain size and thickness are determined by the deposition time, while UNCD presents a nodular morphology with negligible crystal faceting, disobeying the standard regime (96, 130). Some researchers also add small amounts (<2%) of O_2 to the gas mixture to limit impurity incorporation and non-epitaxial defect formation (131). The gas mixture influences the grain size, diamond quality, and the surface finish of the diamond film (132). The temperature of the substrate plays a significant role in the film growth kinetics. MPCVD diamond growth was evaluated over HPHT diamond substrates in a broad range of substrate temperatures (750–1150 °C) and CH_4/H_2 gas mixture ratios (1–13%) (56). Results showed that an appropriate substrate temperature could significantly improve growth rate, and higher CH_4/H_2 ratios favor enhanced growth rates. Increasing CH_4 content leads to enhanced non-diamond carbon incorporation. Competitive etching by atomic hydrogen showed a strong effect at low CH_4/H_2 ratios (1%), and a transition from growth to etching was observed at substrate temperatures higher than 1000ºC and low CH_4 concentrations (1-4%).

Application of a direct bias current between the filaments and the substrate is not mandatory, but doing so can enhance nucleation density during the deposition and improve diamond quality (133). The gas pressure may change the mean free path of particles (primarily hydrocarbons radicals) and, in consequence, their activity due to the absorption of energy from electrons provided by the filaments (134). In addition, pressure has been shown to affect film quality, boron-doping concentration, and diamond crystallographic plane growth direction (134). During the CVD diamond deposition process, the crystal morphology and orientation are directly related to the growth parameter, which specifies the ratio of the growth rates on different grain orientations (namely, between the (100) and (111) crystallographic planes for CVD diamond) (72). The growth parameter is mainly determined by different deposition parameters such as pressure, gas composition, and the temperature of the substrate (135-138).

The choice of boron doping source and its concentration in the gas mixture significantly affect the BDD's molecular structure, electronic properties, composition, impurities, and direction of crystallographic diamond facets (21). The most used sources of boron in CVD diamond growth are gases such as trimethylborane ($B(CH_3)_3$), trimethylborate ($B(OCH_3)_3$),

or diborane (B_2H_6). Solid-state sources such as boron oxide (B_2O_3) diluted in ethanol or methanol have also been successfully used (8, 132). Controlling the [B]/[C] ratio in the feed gas inside the reactor is established by determining appropriate mixing ratios based on Raoult's law (139). Different boron sources may require different CVD growth conditions since boron incorporation depends on its source type. Gaseous boron precursors enable more precise control of the boron doping level over a wide concentration range (140).

In addition to the commonly reported parameters, other factors related to the CVD reactor design and operation also affect the final characteristics of the BDD electrode. For example, the temperature measurement instruments and their position (thermocouple, pyrometer), the gas inlet point(s) in the reactor chamber, the direction of the gases' extraction, the chamber volume, or residence time of the gas mixture (depends on the chamber volume and gas flow/pressure). Slow cooling rates favor film adhesion due to lower residual stress caused by the CTE mismatch between the substrate material and the diamond film (141). The cooling atmosphere will also affect diamond surface chemical termination (142).

Both in-house and commercially made BDD electrodes show strong heterogeneities in their final characteristics due to the diverse deposition conditions and methods applied. The development of new technology or modified CVD reactors delivering homogeneous power into the diamond growth surface, together with selective BDD surface modifications, would be possible solutions to help minimize the currently found heterogeneities of BDD films (21).

I.2.5. Characterization of boron-doped diamond coatings

The microstructure, growth rate, sp^3/sp^2 ratio, boron doping level, and surface termination are key factors that determine the electrochemical properties of BDD. These characteristics significantly control their conductivity, OEP, electrochemical potential window, molecular adsorption, and electron transfer kinetics. Thus, a detailed characterization of a BDD film is also an important point when comparing BDD electrodes from different sources.

In this section, the properties that most influence the electrochemical performance of the BDD electrodes will be discussed to better understand the efficiency of pollutants removal. The difficulty in comparing the diamond quality and boron doping levels in BDD thin films when determined by different characterization methods will also be addressed. One should bear in mind that the following considerations refer to BDD electrodes with planar geometry since distinct diamond-based architectures (e.g., BDD particles, nanostructured BDD, diamond-nanocarbon structures) may exhibit different behaviors (21, 143).

I.2.5.1. Presence of non-diamond carbon

Raman spectroscopy is the most accepted and used technique for diamond quality assessment. It enables the detection of non-diamond carbon (NDC), allowing the determination of the carbon sp^3 (diamond-like)/sp^2(graphite-like) ratio, which is the commonly adopted diamond quality indicator. The presence of NDC in the BDD films significantly influences their electrocatalytic properties, particularly the voltametric background current, potential window, molecular adsorption, and electron transfer kinetics (102). High NDC content affects the electrocatalytic inertia of the electrode (102) and modifies its adsorption characteristics, decreasing the potential window (10) and increasing fouling susceptibility (144). Relevant presence of sp^2 carbon in the BDD films may induce voltametric responses like glassy carbon and graphite (9). The substantial presence of NDC in the grain boundaries of the diamond film causes lower electrode stability when under anodic polarization and, ultimately, the disintegration of the electrode (145). The NDC content is also related to higher background current and double-layer capacitance (146). For water treatment applications, a lower level of sp^2 carbon favors the ability for the mineralization of organics, and electrochemical combustion over conversion, thus avoiding the generation of hazardous byproducts (10).

Different laser wavelengths ranging from 257 to 1064 nm have been used in Raman spectroscopy to evaluate the quality of the diamond thin films (147). The determination of the sp^3/sp^2 ratio strongly depends on the excitation wavelength, and it increases with the increasing energy of the used laser (147, 148). Typically, the peaks used for sp^3/sp^2 calculations are the first-order diamond band (sp^3) at 1332 cm^{-1}; the G-band between 1500-1600 cm^{-1} (related to the C=C sp^2 bond stretching mode); and the D-band usually located at 1345 cm-1 (represents most sp^2 structures) (149, 150). In the case of nanocrystalline diamond films, the first-order diamond peak is only detected under UV excitation (147).

The comparison of different sp^3/sp^2 ratios is only accurate if the same excitation energy is used to acquire the spectra and if determined by the same method and mathematical expression. Several authors have used the ratio between the integral intensity of the diamond band ($I_{diamond}$) and the integral intensity of the G-band (I_G) (151). Others divide $I_{diamond}$ by the total integrated intensity of the Raman spectrum (I_{total}) (45, 152). The full width at half maximum (FWHM) of the first-order peak for diamond has also often been used to estimate its crystalline quality and dopant concentration since lower FWHM values indicate lesser structural defects and/or grain boundaries, hence higher diamond quality (147, 153-155). Different expressions for the calculation of the diamond quality are found in the literature, depending on the applied excitation wavelength. For example, if the 514 nm

excitation line is used, authors usually determine the diamond quality by Eq. I.2.1 (156), Eq. I.2.2 (157), or Eq. I.2.3 (158).

$$sp^3/sp^2\ ratio\ = \frac{I_{diamond}}{250\ \times \sum I_{non-diamond}} \quad \textbf{Eq. I.2.1}$$

$$sp^3/sp^2\ ratio\ = 100\ \times \frac{I_G}{75\ \times I_{diamond} + I_G} \quad \textbf{Eq. I.2.2}$$

$$\beta\ = \frac{I_{diamond}}{I_{diamond} + I_{total}} \quad \textbf{Eq. I.2.3}$$

In Eq. I.2.1, Inon-diamond is the integral intensity of non-diamond bands of the Raman spectrum, and 250 is the factor related to the Raman scattering efficiencies between the sp^3 band and other forms of non-diamond carbon. In Eq. I.2.3, β is the figure-of-merit or the Raman quality fraction (158). If the 488 nm excitation wavelength is used to acquire the Raman spectra, then the purity of the CVD diamond can be expressed by Cdiamond, as seen in equation Eq. I.2.4, where 50 is a correction factor for the substantial resonant Raman scattering effect of sp^2 bonded carbons (154, 159).

$$C_{diamond}\ = 100\ \times \frac{I_{diamond}}{I_{diamond} + {I_G}/{50}} \quad \textbf{Eq. I.2.4}$$

It is important to emphasize that all the above equations for diamond quality assessment should be used with caution since several other factors influence the sp^3/sp^2 ratio. For instance, the polarization changes if micro or macro-Raman measurements are employed or if measurements are carried out over grains with different orientations (especially in micro-Raman) (147).

I.2.5.2. Surface morphology and roughness

Scanning electron microscopy (SEM), atomic force microscopy (AFM), and 3D optical profilometry easily provide surface morphology and roughness analysis information. In polycrystalline BDD, the crystal defects are usually linked to NDC, mainly located in the grain boundaries. Therefore, higher surface roughness arises from large grain sizes and low grain boundary density, indicating a reduced amount of NDC present at the BDD surface

(160, 161). Except in the case of UNCD films, CVD diamond films usually grow according to the van der Drift regime, in which the average grain size increases with the increasing film thickness (130). Therefore, grain size, roughness, and film thickness are closely related to the BDD surface's electrochemical properties, which, in their turn, are highly influenced by variation in the amount of NDC. Consequently, the overpotential for oxygen evolution is lower for thinner films (and finer grains), and the capacitance of BDD electrodes is also related to surface roughness (162).

I.2.5.3. Boron doping level

The conversion of insulator diamond to metal-like conductivity is required for effective practical electrochemical applications and attained at certain doping levels (96). The evolution of resistivity in diamond as a function of boron concentration ([B]) in BDD thin films has been studied (163). For [B] bellow 10^{19} cm^{-3}, the conduction in diamond is dominated by free electrons within the valence band. Up to 3 x 10^{20} cm^{-3}, the conduction is of the hopping type, diamond behaves as a semiconductor, and the resistivity decreases strongly with the increase of boron content. Diamond reaches metal-like conductivity when [B] is above 3 x 10^{20} cm^{-3}.

Nevertheless, effective doping is not linear since boron does not homogeneously incorporate diamond, being simultaneously substitutional and interstitially distributed within the crystalline framework. Thus, effective boron doping does not linearly increase with the boost of boron concentration in the CVD feed gas (46). Boron preferentially incorporates the (111) diamond facets compared to (100) facets (78, 164). Electric conductivity in (111) planes is estimated to be approximately 10^4 times higher than that in (100) planes (78), with consequent faster electron transfer kinetics in (111) planes (21). Furthermore, boron atoms are not electrically active when incorporated within the grain boundaries (165), which means that the measured doping level is usually higher than the effective carrier concentration (holes) (96). Several techniques have been used for quantitative and/or semiquantitative determination of the boron doping level in BDD films. It includes secondary ion mass spectrometry (SIMS), X-ray photoelectron spectroscopy (XPS), electron energy-loss spectroscopy (EELS), and neutron depth profile (NDP). However, these methods are time-consuming, expensive, and difficult to apply, especially when a full depth analysis of boron distribution within the diamond lattice is desired (46). Recently, pulsed RF glow discharge optical emission spectroscopy (GDOES) has been used to semi-quantify boron doping levels, and it was demonstrated that the technique provides high-speed depth profiles (46). In the case of heavily doped BDD films, many authors use a non-destructive and contactless

measurement using Raman spectroscopy data to estimate the boron doping concentration. The following equation (Eq. I.2.5) was proposed, and it is valid for boron doping concentration within the 2 x 10^{20} ~10^{22} cm^{-3} range (166):

$$[B]\ cm^{-3} = 8.44 \times 10^{30} \exp(-0.048\omega) \quad \textbf{Eq. I.2.5}$$

where ω is the wavenumber (cm^{-1}) of the Lorentzian component of the Raman peak at about 500 cm^{-1}. Care must be taken when using this method since the intensity of the Raman peaks varies with the wavelength of the used laser (147).

Understanding the electrical conductivity of BDD electrodes is complex and is not solely determined by the efficient amount of boron incorporation. Heterogeneities such as NDC content, lattice hydrogen, and dangling bonds also affect such property (52). Enhanced BDD electrochemical performance is commonly linked to high boron doping levels, which provide higher carrier concentration and electrical conductivity (52), thus electrochemical reactions are faster for heavier doped BDD electrodes (162). The doping level influence on the chemical surface of diamond electrodes was studied, and results indicate that highly doped diamond films show more reversible performances in the electrochemical response to the $\mathrm{Fe(CN)}_6^{4-/3-}$ redox couple (167). Conversely, in the same study, other results indicate that increased doping level is associated with smaller grain size, with consequent increase of the grain boundary density that leads to a higher amount of NDC and surface oxidation states. The doping level effect of boron on the width of the electrochemical potential window of the electrodes revealed that low boron doping levels led to a broader potential range and slower response to the overpotential of both HER and OER (168). This behavior is related to the minor concentration of boron-rich sites on the surface, blocking both hydrogen and oxygen adsorption steps required for HER and OER, respectively. Increasing boron content led to smaller electrochemical windows, as well as higher electron transfer rate constants and active electrochemical areas (169). Boron concentration also affects the adhesion strength of the film (74), diamond nucleation density, grain size, and overall diamond quality (170). Most published works on the electrochemical degradation of pollutants using BDD anodes do not provide information on effective boron content determination. In some cases, a rough estimative is expressed based on the [B]/[C] ratio in the feed gas during the CVD process. This estimate is inaccurate since boron incorporation in the diamond lattice is not linearly related to the feeding concentration, as previously demonstrated. An optimum balance between doping level and diamond quality must be reached to produce BDD electrodes with the desired and top electrochemical performance. Proper and accurate

determination of the effective boron doping level is required to fine-tune the electrochemical properties of BDD films, although for practical applications the electrical conductivity can be used as a proxy for doping efficiency.

I.2.5.4. Surface termination

The surface termination of BDD electrodes can drastically influence their electrochemical kinetics (171, 172). Hydrogen is the foremost gas used in the CVD growth of diamond films, and their surface presents a hydrogen-terminated surface if cooled down to room temperature under such flow. These surfaces are hydrophobic and show typical water contact angles around 90° (132). However, H-terminated diamond surfaces slowly oxidize with time when in contact with air, becoming more hydrophilic (142, 173). Several studies demonstrate that O-terminated BDD surfaces present a wider potential window, lower background current, and higher surface resistivity when compared to H-terminated surfaces (172, 174-176). Anodic polarization (177) and oxygen plasma treatment are common means to obtain O-terminated BDD surfaces (8). Oxidation of the BDD surface can also be achieved by adding small amounts of O_2 or using an oxygen-containing boron source during the CVD deposition (132). The oxygen atoms incorporate the doped films by bonding with carbon atoms, mainly as C–O–C and C=O terminating groups (132). Evidence shows that increased boron doping levels lead to higher oxygen amounts with a consequent decrease in the water contact angle, showing a more hydrophilic character (167). O-terminated diamond surfaces show water contact angles ranging from 0.6° to 65° (102). The difference between H and O-terminated diamond surfaces is mainly associated with their electronic structures and surface bandgap (opposite bond polarities) (176). The former ($-\mathrm{C}^{\delta-} - \mathrm{H}^{\delta+}$) increases the energy levels of the valence (E_{VB}) and conduction bands (E_{CB}), as well as the negative electron affinity. The latter ($\mathrm{C}^{\delta+} - \mathrm{O}^{\delta-}$) lowers the energy levels and shows higher positive electron affinity (102).

The functional groups terminating the surface of BDD electrodes strongly influence the electron transfer kinetics of inner-sphere redox couples (178). The H-terminated BDD functional groups are usually ═CH_2 and ≡C–H groups that, when oxidized under anodic polarization, show hydroxyl (≡C–OH), carbonyl (═C═O), carboxylic (–COOH), carbon radical (≡C$^{\bullet}$), and hydroxyl radical (≡C–O$^{\bullet}$) functional groups (95). These functional groups may vary according to the chosen anodic polarization procedure and the different grain orientations on the polycrystalline diamond surface (179). Diamond surfaces with (111) orientation tend to be dominated by hydroxyl groups since only one chemical bond to a single carbon atom is available at the first surface layer. The latter then inhibits the formation

of carbonyl and ether groups at the surface of the electrode (180). Diamond surfaces with (100) texture present two available chemical bonds for a single carbon atom, promoting carbonyl and ether group formation (180). For example, the $Fe(CN)_6^{4-/3-}$ redox system exhibits slow electron transfer for O-terminated surfaces but fast electron transfer for H-terminated surfaces (172). In addition, H-terminated surfaces show narrower solvent potential windows than those O-terminated (181).

Electrochemical pre-treatments and polishing have been carried out to enhance the BDD electroanalytical performance, increase the electrochemically active surface area, lower detection limits, and broader linearity ranges (182).

I.2.5.5. Electrochemical characterization

In a summarized way, the four main points to be taken into account in the electrochemical characterization of BDD electrodes are (102): good electrical contact to avoid ohmic drop effects, the cell apparatus, quantification of the capacitance and solvent potential window of the electrode, and assessment of the electron transfer kinetics with outer-sphere redox mediators.

Assessment of the solvent potential window is essential because it specifies the potential range over which the anode works prior to the electrolysis of the solvent (102). The electrochemical potential window will be the first quality indicator to be considered for the evaluation of the electrode performance, particularly if important information on the electrode is known (sp^3/sp^2 ratio, conductivity, surface termination, and morphology). The window range is pH-dependent and may vary depending on the electrolyte concentration, the electrode geometry, potential/current value, scan rate, and temperature. Electrolyte solutions commonly reported include KNO_3 (183), H_2SO_4 (184), $HClO_4$ (11), Na_2SO_4 (185), NaBr, NaCl (186), within a wide range of concentrations.

As already stated in the present review, the lack of information for comparison purposes includes the experiment temperature, whose increase leads to narrower electrochemical potential windows (187). Another one is the adopted methodology regarding the determination of the solvent window (from the voltammogram), which is commonly carried out by applying a method based on defining the window at an arbitrary current density cut-off ($J_{cut\text{-}off}$) value or a linear fit method (188). The arbitrary method is highly influenced by the mass transport of the electrolyte (187), and the setting of $J_{cut\text{-}off}$ values has been diversely defined in the literature, limiting possible comparison of the obtained results (189). On the other hand, the linear fit method is less affected by the experimental conditions for

each measurement system, becoming the recommended one for accurately comparing solvent potential windows (187).

The OEP of an electrode material and the enthalpy of adsorption of the hydroxyl radicals on its surface are the main factors that determine its oxidation power (190). This parameter is simple to obtain, it is also a good indicator of electrode quality, and it should be carefully evaluated. OEP determines if the anode presents an active or a nonactive behavior (190). Usually, BDD is considered a nonactive anode due to its high OEP, which indicates a more significant restriction of the oxygen evolution from water electrolysis and the production of hydroxyl radicals at the surface of the electrode (191). Comparison of OEP values is only valid if obtained for the same solution concentration and electrolyte.

Determination of the double-layer capacitance (C_{dl}) is also a helpful indicator of electrode quality (102). C_{dl} can be calculated from cyclic voltammetry applying Eq. I.2.6 or through electrochemical impedance spectroscopy (EIS) measurements.

$$C_{dl} = \frac{i_{av}}{A\nu} \qquad \textbf{Eq. I.2.6}$$

where i_{av} is the average current from the forward and reverse sweep, A is the electroactive area, and ν is the scan rate. Nevertheless, the application of this equation becomes challenging due to the topographic nature of the BDD surface (especially in MCD), which restricts the accurate determination of the electroactive area (102).

The electron transfer kinetics may be evaluated from cyclic voltammogram measurements for inner-sphere and outer-sphere redox couples. The most studied redox couples are the inner-sphere $Fe(CN)_6^{-3/-4}$ and the outer-sphere $Ru(NH_3)_6^{3+/2+}$ redox couples. The latter is valuable for qualitative estimation of the boron doping level. BDD films with a dominant electrical transport mechanism (i.e., metal-like conductivity) show a reversible or quasi-reversible faradaic peak current response under conditions where the electron transfer rate is much faster than the diffusional rate (102). However, the oxidation and reduction reaction rate of $Ru(NH_3)_6^{2+/3+}$ is little affected by surface defects, film microstructure, adsorbed sp^2 carbon, or surface terminations like oxygen-containing groups (192, 193). On the contrary, the $Fe(CN)_6^{3-/4-}$ redox couple electron transfer rate is significantly affected by the surface chemistry of the BDD coating and the presence of defects such as NDC impurities (192).

I.2.5.6. Electrode service life

Ultimately, comparing the service time of different BDD electrodes is equally important to balance performance and lifetime service with optimal cost-benefit in large-scale water treatment applications. Accelerated life tests are a practical way of evaluating the BDD's electrochemical stability over time (194). Accelerated service life tests have been performed on BDD films deposited over various substrate materials (*e.g.,* Nb, Si, Ti, Ta) through electrolysis at high current densities ranging from 0.5 to 10 A/cm² in concentrated electrolyte solutions of H_2SO_4 or HNO_3. Table I.2.3 shows the accelerated life tests and their experimental conditions found in the literature.

Table I.2.3. Accelerated life test results and experimental conditions found for several studied BDD electrodes.

Electrolyte	Substrate material	Current density (A/cm²)	Accelerated life test result (h)	Ref.
0.5 M H_2SO_4	Nb	10	850	(59)
1 M H_2SO_4	Nb	1.32	88-130	(80)
		1	484	(195)
	Si	1	262	(196)
	Ti	1	127	(197, 198)
3 M H_2SO_4	Nb	1	> 1600	(54)
	Si	1	> 1600	(54)
	Ta	1	> 1600	(54)
	Ti	1	1530	(54)
		1	264	(199)
		1	95	(200)
		0.5	89	(201)
6 M HNO_3	Nb	0.5	1620-1810	(202)

I.2.6. Design of pollutant degradation experiments

The mineralization efficiency is influenced by the applied current density, EAOP, pollutant concentration, properties of the degraded pollutant, pH of the solution, supporting electrolyte, temperature, the volume of solution, fluid dynamics, dissolved oxygen, electrode

configuration, active electrode area, cell design, and agents added in the solution, e.g., chloride, sulfate, phosphate, carbonate, and oxygen (49, 50, 102, 187, 203-206). Comparing the degradation performance of BDD electrodes is again a repetitive challenge.

I.2.6.1. Electrochemical advanced oxidation process

In EAOPs, the primary processes are classified as anodic oxidation (AO) via intermediates of oxygen evolution and electro-Fenton-based processes. Anodic oxidation via intermediates (hydroxyl radicals formed from water oxidation at the anode surface) resulting from oxygen evolution may directly destroy organic pollutants (207). Electrogeneration of H_2O_2, denominated AO with electrogenerated H_2O_2 (AO-H_2O_2), is another anodic oxidation method (208). The efficiency of both methods depends on the type of material used as anode, that must present high OEP (209). Anodic oxidation can also be accomplished by adding anions to the bulk solution, such as chloride, sulfate, phosphate, and carbonate, that generate oxidants like active chlorine, persulfate, perphosphate, and percarbonate species, respectively (206). The electro-Fenton (EF) process arises from the electrochemical production of H_2O_2 with the addition of Fe^{2+} in the bulk solution producing additional hydroxyl radicals as a by-product of the Fenton's reaction (210). Photoelectro-Fenton (PEF) and solar photoelectro-Fenton (SPEF) are a combination of the EF method with the irradiation of UV light and natural sunlight, respectively, that enhance degradation efficiency (211). The sonoelectro-Fenton (SEF) process is performed under EF conditions and simultaneous application of ultrasound radiation (212). Electrochemical degradation experiments combining UV or ultrasound irradiation demonstrated improved outcomes if compared to direct anodic oxidation (213-215). Ultrasound radiation improves the transfer of pollutants to the BDD surface though it requires higher energy consumption; and UV irradiation increases hydroxyl radical generation (213), preventing the formation of undesirable and hazardous byproducts (e.g., chlorate and perchlorates) during the electrochemical degradation process (216). The key EAOPs are AO, AO-H_2O_2, EF, PEF, and SPEF (48). Other EAOPs such as peroxi-coagulation (217) and Fered-Fenton (218) are also proposed for remediation of various pollutants in wastewater.

The main disadvantages of EAOPs are high energy consumption and mandatory solution high conductivity which is directly correlated to lower energy conditions (219). Although some effluents from several industries and urban wastewater may have low conductivities, adding a supporting electrolyte enables water treatment by direct application of electrochemical processes (51). Still, this extra leads to increased operational costs and/or toxic byproducts generation (219). Alternatives include reduction of ohmic resistances and

increasing the mass transport of the pollutants towards the surface of the electrode through a solid polymer electrolyte (SPE) (220), or capillary microfluidic cells (51), respectively. A review on the electrochemical oxidation of organic pollutants in low conductive solutions can be found elsewhere (219).

I.2.6.2. Cell design

Various configurations and apparatus have been used in pollutant degradation with BDD electrodes, including simple electrochemical cells under static conditions and commercial multi-cell flow reactors. Thus, the influence of the electrode configuration and cell design on the intrinsic fluid dynamics (e.g., volumetric flow, Reynolds number, and mass transport) is an important factor (49, 50).

Cells are usually equipped with two types of electrode configurations: monopolar and bipolar designs (49). In the first one, the anode is BDD, and the cathode is another material, usually a stainless-steel plate. In bipolar design, BDD is used as both anode and cathode. Both configurations under the same operating conditions were tested, and the bipolar electrodes provided higher efficiency in water disinfection (49). Moreover, reactors designed for cells with bipolar configuration allow switching the polarity of electrodes to electrochemically clean their surface and prevent electrode deactivation (221). Nevertheless, one should bear in mind that monopolar electrodes consume less energy (49).

The type and geometry of the cell and the BDD electrodes are essential aspects since they will determine the flow dispersion and consequent mass transport within the container. The latter will directly influence the potential and current distribution of the working electrode, affecting the current efficiency and overall energy consumption associated with the degradation process (24, 222).

I.2.6.3. Operating conditions

According to the literature, the adopted operating conditions to perform electrochemical oxidation of contaminants in wastewater are diverse. However, the removal of organic carbon from treated solutions is mainly influenced by the applied current density, mass transfer effects, and the properties of degraded pollutants (50).

Many degradation experiments are performed with the addition of a supporting electrolyte, particularly in high concentrations (higher solution conductivity) where electrooxidation proficiency is enhanced (51). The effect of different supporting electrolytes in phenol

degradation using BDD electrodes has been assessed (223). In the absence of chloride ions, the oxidation kinetics constants follows the order: $Na_2SO_4 \approx Na_2CO_3 > H_2SO_4 > H_3PO_4$. In chloride-mediated process, the reaction kinetics considerably increases with a new order: $H_2SO_4 > Na_2SO_4 > Na_2CO_3$. Therefore, the supporting electrolyte plays a crucial role in generating different oxidative species like peroxocarbonate, peroxosulfate, or hypochlorite (205). The choice of electrolyte will affect the pH value, and acidic media is correlated to the improvement of pollutant degradation efficiency, benefiting the production of hydroxyl radicals at the anode surface (224-227). However, in terms of pH effect, there are diverse and even contradictory results which are dependent on the pollutant chemistry (50, 203, 228). Ideally, the electrochemical behavior of BDD electrodes should be evaluated in different pH and electrolyte solutions before the degradation experiments (204).

Mineralization rates are linearly related to the current density (j_{appl}) with two different operating regimes depending on it: current and mass transport-controlled oxidations (203). In these regimes, the limiting current density (j_{limit}) for electrooxidation of the organic pollutant is estimated according to the following equation:

$$j_{limit} = n\, k_m\, F\, [Pollutant] = 4\, k_m\, F\, COD \qquad \textbf{Eq. I.2.7}$$

where j_{limit} is the limiting current density, [Pollutant] is the organic pollutant concentration, k_m is the mass-transfer coefficient, n is the number of electrons exchanged in the oxidation of a molecule of the pollutant, F is the Faraday constant, and COD is the chemical oxygen demand. Current-controlled oxidation takes place when $j_{appl} < j_{limit}$, and the contaminant concentration decreases linearly over time with a current efficiency of 100% (229). On the other hand, mass transport-controlled oxidation occurs when $j_{appl.} > j_{limit}$, and secondary reactions like oxygen evolution occur. In this case, the contaminant degradation follows an exponential trend, and the current efficiency is below 100% (229).

The geometric area of the BDD anode should be controlled since its conductivity is not entirely uniform along with the film due to its surface heterogeneities. Restricted areas prevent poor current density distribution and, consequently, lower degradation efficiency and possible formation of undesired byproducts (49). The relationship between the electrode area and the applied current density is meaningful: the same degradation performance with a reduced electrode area is achieved by increasing the current density. Its maximum is defined by the quality, defect density, and adhesion strength of the BDD film

to the substrate. Still, lower current densities may avoid the production of non-desired or hazardous byproducts (chlorate, perchlorate, or organo-chlorinates) (230).
The total volume of solution affects the residence time and, consequently, the degradation efficiency (231). In addition, high pollutant concentration leads to lower mineralization rates but higher temperature promotes faster mineralization rates due to further mass transfer towards the anode surface (203).

I.2.6.4. Performance indicators for pollutant degradation

The measurement of COD in the solution containing the contaminant under study is the most applied approach to assess the degradation performance of BDD electrodes. Some authors also evaluate the total organic carbon (TOC) of the solution, or both COD and TOC, and others prefer to express degradation results as a function of the contaminant concentration. The latter is usually determined by UV-vis spectroscopy and/or high-performance liquid chromatography (HPLC).
The COD method is used to quantify the performance of the electrodes. It determines the average current efficiency (ACE) and instantaneous current efficiency (ICE) of the BDD electrode, expressed in Eq. I.2.8 and Eq. I.2.9, respectively (232):

$$ACE = \frac{F\,V\,(COD_0 - COD_t)}{8\,I\,\Delta t} \qquad \textbf{Eq. I.2.8}$$

$$ICE = \frac{F\,V\,(COD_t - COD_{t+\Delta t})}{8\,I\,\Delta t} \qquad \textbf{Eq. I.2.9}$$

where F is the Faraday constant (96485 C mol^{-1}); t is the time (s); V is the volume of the electrolyte (dm^3); COD_0 is the initial COD concentration (g_{O2} dm^{-3}); COD_t and $COD_{t+\Delta t}$ are the COD concentration at times t and t+Δt (s), respectively; I is the applied current (A); and 8 is the dimensional factor for unit consistency (meaning 32 g of O_2 / 4 mol e^- mol^{-1} of O_2).
Likewise, current efficiency results have also been measured as a function of TOC. For example, the mineralization current efficiency (MCE) is calculated considering TOC removal (Eq. I.2.10) (233). In addition, the combustion efficiency (Eq. I.2.11) can be determined by calculating the ratio between the TOC and the COD decrease rates (234):

$$MCE = \frac{n\,F\,V\,\Delta TOC}{4.32\times 10^{7} m\,I\,t} \qquad \textbf{Eq. I.2.10}$$

$$\eta_c = \frac{32}{12}\left(\frac{n}{4m}\right)\frac{dTOC}{dCOD} \qquad \textbf{Eq. I.2.11}$$

where n is the number of electrons required for the complete combustion of the organic pollutant, m is the number of carbon atoms in the molecule of the organic pollutant, F is the Faraday constant, V is the volume of the electrolyte (L), I is the applied current (A), t is the time (h), ΔTOC is the total organic carbon reduction (mg/L), dTOC is the TOC decrease rate, and dCOD is the COD decrease rate.

If the concentration of the pollutant is evaluated over its electrooxidation time, the results are usually demonstrated in plots of removal percentage, or contaminant concentration, against the charge amount Q^t (Eq. I.2.12).

$$Q^t\ (Ah/L) = \frac{\mathrm{jAt}}{V} \qquad \textbf{Eq. I.2.12}$$

However, Q^t does not consider the total removed concentration of the pollutant from the solution. Therefore, we propose a different approach to determine the degradation performance, which enables comparison between the reported results. It starts by calculating the average Q' (Ah/kg) required for the pollutant degradation, expressed through Eq. 2.13.

$$Q'(Ah/kg_{pollutant}) = Q^t \times \frac{1}{\Delta C_{pollutant}} = \frac{\mathrm{jAt}}{V\,\Delta C_{pollutant}} \qquad \textbf{Eq. I.2.13}$$

We propose Q', a new figure-of-merit to be used when COD and TOC are undetermined and the cell potential value is unavailable, i.e., when the calculation of energy consumption is not possible. Q' is a base parameter to enable comparison between different performances of the BDD electrodes from different sources (in-house and commercially manufactured). Energy consumption values have been reported in several ways as a function of the removed concentration of the studied analyte (Eq. I.2.14), COD (Eq. I.2.15), and TOC (Eq. I.2.16). Additionally, some authors have expressed energy consumption

values only as a function of the volume of the treated solution (Eq. I.2.17). However, the latter expression of consumption does not consider the pollutant concentration and may induce misinterpretation of the electrode performance.

$$Energy\ consumption\ \left(\frac{kWh}{kg_{pollutant}}\right) = Q^t \times \frac{E}{\Delta C_{pollutant}} = \frac{E\mathrm{jAt}}{V\ \Delta C_{pollutant}} \quad \textbf{Eq. I.2.14}$$

$$Energy\ consumption\ \left(\frac{kWh}{kg_{COD}}\right) = Q^t \times \frac{E}{\Delta COD} = \frac{E\mathrm{jAt}}{V\ \Delta COD} \quad \textbf{Eq. I.2.15}$$

$$Energy\ consumption\ \left(\frac{kWh}{kg_{TOC}}\right) = Q^t \times \frac{E}{\Delta TOC} = \frac{E\mathrm{jAt}}{V\ \Delta TOC} \quad \textbf{Eq. I.2.16}$$

$$Energy\ consumption\ (kWh/m^3) = Q^t \times E = \frac{E\mathrm{jAt}}{V} \quad \textbf{Eq. I.2.17}$$

where Q^t is the charge (Ah/dm³) at time t (h), j is the applied current density (A dm^{-2}), t is the electrolysis time (h), A is the BDD electrode geometric area (dm²), V is the volume (dm³) of the solution, E is the average electrode potential (V), $\Delta C_{pollutant}$ is the total concentration of pollutant removed from the solution (kg/dm³), ΔCOD is the total amount of COD removed (kg/dm³), and ΔTOC is the total amount of TOC removed (kg/dm³).

The previous equations allow normalization of the BDD degradation results for a specific contaminant (Eq. I.2.14) or complex matrixes (Eq. I.2.15 and Eq. I.2.16) based on diverse experimental conditions like applied current density, electrode potential, geometric electrode area, degradation time, the volume of solution, and initial pollutant concentration. Although one may use such figures-of-merit, understanding the different results is only achieved through proper and complete characterization of the BDD films, as discussed in the previous sections. In addition, a comparison of the results is only possible within each specific calculation method. For example, the COD method (ICE, ACE, energy consumption in kWh/kg_{COD}), TOC (MCE, η_c, energy consumption in kWh/kg_{TOC}), and pollutant concentration (Q', and energy consumption in $kWh/kg_{pollutant}$). A summary of the figures of merit discussed in this section is provided in Table I.2.4.

Table I.2.4. Summary of figures of merit used as performance indicators for pollutant degradation.

Figure-of-merit (FOM)	Pros	Cons
$ACE = \frac{F\,V\,(COD_0 - COD_t)}{8\,I\,\Delta t}$ $EC_{COD} = \frac{E\mathrm{jAt}}{V\,\Delta COD}$	Most used FOMs, allowing comparison with most published results COD measurements are less expensive than TOC	Does not give information on the oxidation of a specific pollutant The COD analysis uses hazardous reagents (dichromate), can be time-consuming, have a relatively high detection limit, and may suffer interference from inorganics (e.g. chlorides). In addition, dichromate does not oxidize some organic species, which can imply false low COD values
$ICE = \frac{F\,V\,(COD_t - COD_{t+\Delta t})}{8\,I\,\Delta t}$	Provide instantaneous current efficiency data	
$MCE = \frac{n\,F\,V\,\Delta TOC}{4.32 \times 10^7 m\,I\,t}$ $EC_{TOC} = \frac{E\mathrm{jAt}}{V\,\Delta TOC}$	TOC analyses are usually faster than COD and often result in accuracy over an extensive range of concentrations from 1 ppb to 50,000 ppm	TOC measurements require relatively expensive equipment (in comparison with other analytical techniques)
$\eta_c = \frac{32}{12}\left(\frac{n}{4m}\right)\frac{dTOC}{dCOD}$		Requires both COD and TOC measurements
$Q' = \frac{\mathrm{jAt}}{V\,\Delta C_{pollutant}}$	Ideal for comparing results when the cell potential value is unavailable Does not require COD and/or TOC analysis	Requires pollutant quantification techniques (e.g., UV-vis spectroscopy, HPLC)
$EC_{Pollutant} = \frac{E\mathrm{jAt}}{V\,\Delta C_{pollutant}}$	Does not require COD and/or TOC analysis	
$Q^t = \frac{\mathrm{jAt}}{V}$ $EC_{Volume} = \frac{E\mathrm{jAt}}{V}$	Does not require quantification methods (e.g., pollutant concentration, COD or TOC)	Does not consider the pollutant concentration or any other water quality parameter, which may lead to misinterpretation

**EC: energy consumption*

I.2.7. Case studies and comparisons according to the literature

There are only a few studies comparing in-house electrodes with commercial ones (47, 177). For example, eleven different BDD electrodes deposited over Nb substrates by HFCVD were produced by varying the $B(OCH_3)_3/CH_4$ gas mixture (0.125%–0.75%), CH_4/H_2 ratio (0.5%–1.0%), and gas pressure (5–15 torr) (47). They were then compared to commercial BDDs manufactured by Neocoat and Diachem in terms of electrochemical degradation of guaifenesin (pharmaceutical) and TOC removal. Four in-house prepared

BDD electrodes showed more significant OEP values reaching a value of 2.45 V against 2.36 V (vs. Ag/AgCl) (commercial). The in-house electrodes ($B(OCH_3)_3/CH_4$ ratio of 0.75%, CH_4/H_2 ratio of 1%, 5 torr pressure) exhibited the second-best performance in terms of electrochemical degradation of the contaminant as well as TOC removal. The best-performance in-house produced electrode showed a pseudo-first-order reaction rate constant for guaifenesin degradation of 0.33 min^{-1}, compared to 0.35 min^{-1} (Neocoat) and 0.27 min^{-1} (Diachem). After 120 min of electrolysis, the TOC removal efficiency was 100% for the in-house electrode, 100% for Neocoat and 97% for Diachem. Thus, in-house produced BDD anodes may exhibit similar or even superior performance than commercial ones. However, for such statement it is necessary to ensure that the electrodes performance data are reliable and statistically relevant.

According to SLR, phenol and landfill leachate appeared as the analytes with the highest occurrence among articles that use BDD electrodes for electrochemical degradation of water pollutants. In this section, we will discuss most of the published results (to the best of our knowledge) and the diversity of operating conditions when degrading spiked solutions with phenol (Supplementary Table I.2.4) or treating landfill leachate (Supplementary Table I.2.5). One should note that the information included in the previous tables only relates to results obtained using planar BDD electrodes under the simplest operating conditions for each published article. Moreover, when results were absent along the text and tables of the analyzed articles, data was extracted from plotted graphs using the WebPlotDigitizer tool (235).

The operating conditions used for the electrochemical treatment of phenol and landfill leachate are diverse. In the case of phenol (Supplementary Table I.2.4), ACE values range from 12.3% to 87%, and energy consumption from 26.6 to 475 kWh/kg_{COD}. The average ACE for in-house electrodes is 32.4%, against 44% for commercial electrodes. Energy consumption data is insufficient to establish further comparisons since it is presented in different units (e.g., kWh/kg_{COD}, kWh/kg_{TOC}, $kWh/kg_{phenol,}$ and kWh/m^3). Overall data analysis indicate that commercial electrodes appear to consume less energy and present better current efficiency for phenol degradation. Nevertheless, it is impossible to unambiguously confirm this trend due to the different operating conditions and configuration variability of the electrodes and reactors.

Considering landfill leachate treatment (Supplementary Table I.2.5), ACE values range from 14.4% to 193%, and energy consumption from 5.7 to 285 kWh/kg_{COD}. Disregarding experimental conditions, in-house electrodes present higher ACE values but higher energy consumption when compared to commercial ones. Again, one should note that the

operating conditions are significantly divergent, and that landfill leachates are complex and variable mixtures that may interfere with synergistic or antagonistic effects.

This review largely reflects the significant variability within the results and the influence of several parameters on the performance of the BDD electrodes (summarized in Figure I.2.8). Considering the few possible comparisons withdrawn in this work, it is not possible to conclude which electrode would be the best choice. Such decision highly depends on proper and effective comparisons under the same degradation conditions and electrochemical cell configuration for a wide range of model pollutants and real wastewater systems. Only then it will be possible to properly evaluate and compare in-house electrodes with commercial ones.

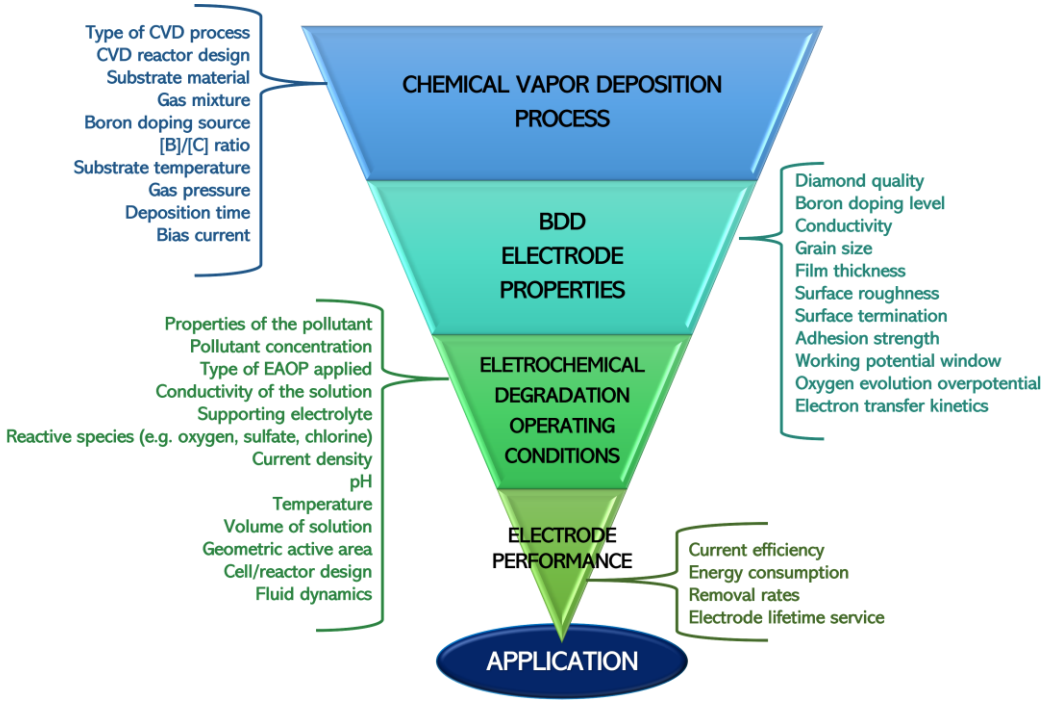

Figure I.2.8. Main factors influencing the performance of BDD electrodes in the electrochemical degradation of pollutants.

I.2.8. Critical perspectives and future outlook

In this critical review, a detailed discussion of the most relevant parameters that influence the performance of BDD electrodes in the electrooxidation of water pollutants was carried out. The SLR and bibliometric network graphs were valuable tools to identify the most studied water pollutants, applied EAOPs, and relevant issues such as energy consumption, byproducts and toxicity of the treated waters. Based on the gathered information, an attempt was made to compare the electrooxidation performance between in-house and commercially available BDD electrodes. Both types of electrodes show strong heterogeneities in their final physicochemical characteristics due to the diversity of deposition conditions and applied methods. The comparison attempt is further complicated by the variety of methods, parameters, or electrochemical cells used in the pollutant degradation experiments. Due to the lack of essential information for such comparison, it is not possible to state which one would be the best.

Over the years, many different figures-of-merit based on COD, TOC, or the concentration of the pollutant studied, have been proposed to determine the performance of BDD electrodes. Here, we propose a figure-of-merit equation which normalizes BDD degradation results for a specific contaminant, even if working under different experimental conditions like applied current density or initial pollutant concentration. This is however a remedial solution to allow comparing data obtained under very different conditions.

Data analysis for phenol degradation and landfill leachate treatment generally suggest that commercial BDD electrodes appear to consume less energy and present better current efficiency than in-house prepared anodes. These indications are subjective to a certain point since there is significant variability in the reported operating conditions, which precludes unequivocal conclusions to be made. Nevertheless, there is a strong indication that if in-house electrodes are further optimized, they could reach or surpass the performance of those commercially available. This analysis also points ways for these companies to improve the efficiency of their products.

Our suggestion is to create a uniform reporting/testing procedure: authors could provide further details on the produced BDD electrodes (film thickness, grain size, diamond quality through Raman spectroscopy, resistivity, and working potential window) in three model electrolytes (e.g., 0.1 M KNO_3, 0.1 M H_2SO_4, and 0.1 M $HClO_4$). Based on the case study of phenol, we further suggest that all laboratories could perform three water electrooxidation tests, each one with a different model pollutant (*e.g.,* phenol, reactive blue 19 dye, diclofenac pharmaceutical), through direct anodic oxidation in an undivided single-compartment electrolytic cell, under constant stirring, using a BDD anode and a stainless-

steel cathode (same geometric area). Moreover, a pollutant concentration of 1 mM, applied current density of 30 mA/cm², electrolyte solution of Na_2SO_4 for fixing solution conductivity and pH, and a fixed volume of solution to electrode area ratio of 25 (cm³/cm²) should be adopted. The degradation results should be compared as a function of pollutant and COD removal percentage, ACE, energy consumption (in $kWh/kg_{pollutant}$ and kWh/kg_{COD}), and degradation time. The proposed procedure is summarized in a flowchart (Figure I.2.9).

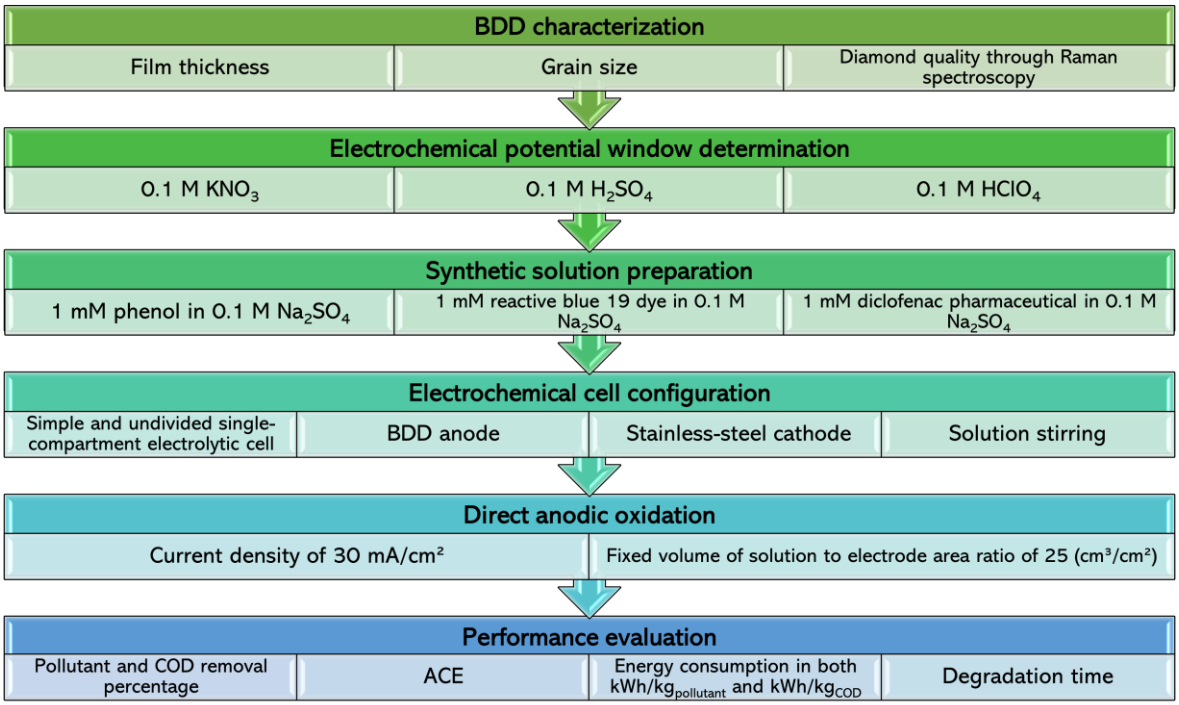

Figure I.2.9. Experimental procedure proposed for evaluating BDD electrodes.

Ideally, a standard or normalized procedure should be elaborated, bringing the scientific community and manufacturers together to discuss and reach a consensus on the best practices to evaluate and compare the electrooxidation performance of a BDD electrode, independently of their origin. The creation of such consensual standard would enable faster developments and a straightforward transition of in-house BDD electrodes to commercial production with consequent effective large-scale application in water treatment plants.

I.2.9. References

1. Swain GM, Anderson AB, Angus JC. Applications of Diamond Thin Films in Electrochemistry. Mrs Bull. 2013;23(9):56-60.
2. Martin HB, Argoitia A, Landau U, Anderson AB, Angus JC. Hydrogen and Oxygen Evolution on Boron-Doped Diamond Electrodes. J Electrochem Soc. 2019;143(6):L133-L6.
3. Swain GM. The Susceptibility to Surface Corrosion in Acidic Fluoride Media: A Comparison of Diamond, HOPG, and Glassy Carbon Electrodes. J Electrochem Soc. 2019;141(12):3382-93.
4. Ramesham R, Rose MF. Electrochemical characterization of doped and undoped CVD diamond deposited by microwave plasma. Diamond Relat Mater. 1997;6(1):17-26.
5. Swain GM. The use of CVD diamond thin films in electrochemical systems. Adv Mater. 1994;6(5):388-92.
6. Swain GM, Ramesham R. The electrochemical activity of boron-doped polycrystalline diamond thin film electrodes. Anal Chem. 2002;65(4):345-51.
7. Luong JH, Male KB, Glennon JD. Boron-doped diamond electrode: synthesis, characterization, functionalization and analytical applications. Analyst. 2009;134(10):1965-79.
8. Brillas E, Martínez-Huitle CA. Synthetic Diamond Films: Preparation, Electrochemistry, Characterization, and Applications: Wiley; 2011.
9. He Y, Lin H, Guo Z, Zhang W, Li H, Huang W. Recent developments and advances in boron-doped diamond electrodes for electrochemical oxidation of organic pollutants. Sep Purif Technol. 2019;212:802-21.
10. Medeiros de Araújo D, Cañizares P, Martínez-Huitle CA, Rodrigo MA. Electrochemical conversion/combustion of a model organic pollutant on BDD anode: Role of sp 3 /sp 2 ratio. Electrochem Commun. 2014;47:37-40.
11. Iniesta J. Electrochemical oxidation of phenol at boron-doped diamond electrode. Electrochim Acta. 2001;46(23):3573-8.
12. Ryl J, Burczyk L, Bogdanowicz R, Sobaszek M, Darowicki K. Study on surface termination of boron-doped diamond electrodes under anodic polarization in H2SO4 by means of dynamic impedance technique. Carbon. 2016;96:1093-105.
13. Stanković DM, Kalcher K. Amperometric quantification of the pesticide ziram at boron doped diamond electrodes using flow injection analysis. Sensor Actuat B-Chem. 2016;233:144-7.
14. Cornejo OM, Murrieta MF, Castañeda LF, Nava JL. Electrochemical reactors equipped with BDD electrodes: Geometrical aspects and applications in water treatment. Curr Opin Solid State Mater Sci. 2021;25(4).
15. He Y, Zhao D, Lin H, Huang H, Li H, Guo Z. Design of diamond anodes in electrochemical degradation of organic pollutants. Curr Opin Electrochem. 2022;32.

16. Wang Z, Liu S, Zhao G. In situ electrochemical spectroscopy for boron-doped diamond electrode reactions: recent progress and perspectives. Curr Opin Electrochem. 2022;32.
17. Oliveira TMBF, Ribeiro FWP, Morais S, de Lima-Neto P, Correia AN. Removal and sensing of emerging pollutants released from (micro)plastic degradation: Strategies based on boron-doped diamond electrodes. Curr Opin Electrochem. 2022;31.
18. Mousset E. Interest of micro-reactors for the implementation of advanced electrocatalytic oxidation with boron-doped diamond anode for wastewater treatment. Curr Opin Electrochem. 2022;32.
19. De Luna Y, Bensalah N. Review on the electrochemical oxidation of endocrine-disrupting chemicals using BDD anodes. Curr Opin Electrochem. 2022;32.
20. Crispim AC, da Silva Mendonça de Paiva S, de Araújo DM, Souza FL, Dos Santos EV. Ultrasound and UV technologies for wastewater treatment using boron-doped diamond anodes. Curr Opin Electrochem. 2022;33.
21. Bogdanowicz R, Ryl J. Structural and electrochemical heterogeneities of boron-doped diamond surfaces. Curr Opin Electrochem. 2022;31.
22. Karim AV, Nidheesh PV, Oturan MA. Boron-doped diamond electrodes for the mineralization of organic pollutants in the real wastewater. Curr Opin Electrochem. 2021;30.
23. Clematis D, Panizza M. Application of boron-doped diamond electrodes for electrochemical oxidation of real wastewaters. Curr Opin Electrochem. 2021;30(100844).
24. Cornejo OM, Murrieta MF, Castañeda LF, Nava JL. Characterization of the reaction environment in flow reactors fitted with BDD electrodes for use in electrochemical advanced oxidation processes: A critical review. Electrochim Acta. 2020;331:135373.
25. Trellu C, Chakraborty S, Nidheesh PV, Oturan MA. Environmental Applications of Boron-Doped Diamond Electrodes: 2. Soil Remediation and Sensing Applications. ChemElectroChem. 2019;6(8):2143-56.
26. Nidheesh PV, Divyapriya G, Oturan N, Trellu C, Oturan MA. Environmental Applications of Boron-Doped Diamond Electrodes: 1. Applications in Water and Wastewater Treatment. ChemElectroChem. 2019;6(8):2124-42.
27. McBeath ST, Wilkinson DP, Graham NJD. Application of boron-doped diamond electrodes for the anodic oxidation of pesticide micropollutants in a water treatment process: a critical review. Environ Sci-Wat Res. 2019;5(12):2090-107.
28. Ganiyu SO, Martínez-Huitle CA. Nature, Mechanisms and Reactivity of Electrogenerated Reactive Species at Thin-Film Boron-Doped Diamond (BDD) Electrodes During Electrochemical Wastewater Treatment. ChemElectroChem. 2019;6(9):2379-92.
29. Freitas JM, Oliveira TDC, Munoz RAA, Richter EM. Boron Doped Diamond Electrodes in Flow-Based Systems. Front Chem. 2019;7(APR):190.

30. Cobb SJ, Ayres ZJ, Macpherson JV. Boron Doped Diamond: A Designer Electrode Material for the Twenty-First Century. Annual Review of Analytical Chemistry: Annual Reviews Inc.; 2018. p. 463-84.
31. Donthu N, Kumar S, Mukherjee D, Pandey N, Lim WM. How to conduct a bibliometric analysis: An overview and guidelines. Journal of Business Research. 2021;133:285-96.
32. Araújo CAÁd. Bibliometria: evolução histórica e questões atuais. Em Questão. 2006;12(1):11-32.
33. Guedes VLS, Borschiver SI, 6., pp. 1-18, , 2005. Bibliometria: uma ferramenta estatística para a gestão da informação e do conhecimento em sistemas de informação, de comunicação e de avaliação científica e tecnológica. Encontro Nacional de Ciência da Informação; Salvador, Brazil2005. p. 1-18.
34. van Eck NJ, Waltman L. Software survey: VOSviewer, a computer program for bibliometric mapping. Scientometrics. 2010;84(2):523-38.
35. Mitra P, Chattopadhyay KK, Chaudhuri S, Pal AK. Electrical properties of boron-doped diamond films prepared by dc plasma decomposition of CO2 + H2. Mater Lett. 1994;21(1):95-9.
36. Pelskov YV, Sakharova AY, Krotova MD, Bouilov LL, Spitsyn BV. Photoelectrochemical properties of semiconductor diamond. Journal of Electroanalytical Chemistry and Interfacial Electrochemistry. 1987;228(1-2):19-27.
37. Patel K, Hashimoto K, Fujishima A. Application of Boron-Doped CVD-Diamond Film to Photoelectrode. Denki Kagaku oyobi Kogyo Butsuri Kagaku. 1992;60(7):659-61.
38. Zhu P, Zhu J, Yang S, Zhang X, Zhang G. Electrochemical characterization of boron-doped polycrystalline diamond thin-film electrodes. Fresen J Anal Chem. 1995;353(2):171-3.
39. Zhu JZ, Yang SZ, Zhu PL, Zhang XK, Zhang GX, Xu CF, *et al.* Electrochemical behaviors of boron-doped diamond film electrodes grown selectively. Chin Chem Lett. 1995;6(8):707-10.
40. de Queiroz JLA, da Silva ARL, de Moura DC, da Silva DR, Martínez-Huitle CA. Electrochemical study of carboxylic acids with Nb-supported boron doped diamond anode. Part 1: Potentiodynamic measurements and bulk oxidations. J Electroanal Chem. 2017;794:204-11.
41. Mehedi HA, Achard J, Rats D, Brinza O, Tallaire A, Mille V, *et al.* Low temperature and large area deposition of nanocrystalline diamond films with distributed antenna array microwave-plasma reactor. Diamond Relat Mater. 2014;47:58-65.
42. Railkar TA, Kang WP, Windischmann H, Malshe AP, Naseem HA, Davidson JL, *et al.* A Critical Review of Chemical Vapor-Deposited (CVD) Diamond for Electronic Applications. Critical Reviews in Solid State and Materials Sciences. 2000;25(3):163-277.
43. Gracio JJ, Fan QH, Madaleno JC. Diamond growth by chemical vapour deposition. J Phys D: Appl Phys. 2010;43(37).

44. May PW, Ludlow WJ, Hannaway M, Smith JA, Rosser KN, Heard PJ. Boron Doping of Microcrystalline and Nanocrystalline Diamond Films: Where is the Boron Going? MRS Proceedings. 2011;1039.

45. Salgueiredo E, Amaral M, Neto MA, Fernandes AJS, Oliveira FJ, Silva RF. HFCVD diamond deposition parameters optimized by a Taguchi Matrix. Vacuum. 2011;85(6):701-4.

46. Sharma DK, Girao AV, Chapon P, Neto MA, Oliveira FJ, Silva RF. Advances in RF Glow Discharge Optical Emission Spectrometry Characterization of Intrinsic and Boron-Doped Diamond Coatings. ACS Appl Mater Interfaces. 2022;14(5):7405-16.

47. Huang K-L, Chao P-J, Kuo Y-M, Chi K-Y, Cheng HM, Wu R-Z, *et al.* Response surface methodology-based fabrication of boron-doped diamond electrodes for electrochemical degradation of guaifenesin in aqueous solutions. J Taiwan Inst Chem Eng. 2021;123:124-33.

48. Sires I, Brillas E, Oturan MA, Rodrigo MA, Panizza M. Electrochemical advanced oxidation processes: today and tomorrow. A review. Environ Sci Pollut Res Int. 2014;21(14):8336-67.

49. Cano A, Barrera C, Cotillas S, Llanos J, Cañizares P, Rodrigo MA. Use of DiaCell modules for the electro-disinfection of secondary-treated wastewater with diamond anodes. Chem Eng J. 2016;306:433-40.

50. Xu SG. Modeling and Experimental Study of Electrochemical Oxidation of Organics on Boron-Doped Diamond Anode. CNL Nucl Rev. 2016:1-15.

51. Ma P, Ma H, Sabatino S, Galia A, Scialdone O. Electrochemical treatment of real wastewater. Part 1: Effluents with low conductivity. Chem Eng J. 2018;336:133-40.

52. Einaga Y, Foord JS, Swain GM. Diamond electrodes: Diversity and maturity. Mrs Bull. 2014;39(6):525-32.

53. Chen G. Electrochemical technologies in wastewater treatment. Sep Purif Technol. 2004;38(1):11-41.

54. Yang W, Tan J, Chen Y, Li Z, Liu F, Long H, *et al.* Relationship between substrate type and BDD electrode structure, performance and antibiotic tetracycline mineralization. J Alloys Compd. 2022;890.

55. Xiang-Liu J, Fang-Qing Z, Jiang-Qi L, Bin Y, Guang-Hua C, editors. Systematic studies on transition layers of carbides between CVD diamond films and substrates of strong carbide-forming elements. ProcSPIE; 1991.

56. Bushuev EV, Yurov VY, Bolshakov AP, Ralchenko VG, Khomich AA, Antonova IA, *et al.* Express in situ measurement of epitaxial CVD diamond film growth kinetics. Diamond Relat Mater. 2017;72:61-70.

57. Chaplin BP, Wyle I, Zeng H, Carlisle JA, Farrell J. Characterization of the performance and failure mechanisms of boron-doped ultrananocrystalline diamond electrodes. J Appl Electrochem. 2011;41(11):1329-40.

58. Shaw J, Jones AN, Monk PMS, Rego CA. Electrochemical behaviour of graphite- and molybdenum electrodes modified with thin-film diamond. Diamond Relat Mater. 2002;11(9):1690-6.
59. Fryda M, Herrmann D, Schafer L, Klages CP, Perret A, Haenni W, *et al.* Properties of diamond electrodes for wastewater treatment. New Diamond Front Carbon Technol. 1999;9(3):229-40.
60. Neto MA, Silva EL, Ghumman CA, Teodoro OM, Fernandes AJS, Oliveira FJ, *et al.* Composition profiles and adhesion evaluation of conductive diamond coatings on dielectric ceramics. Thin Solid Films. 2012;520(16):5260-6.
61. Denisenko A, Pietzka C, Romanyuk A, El-Hajj H, Kohn E. The electronic surface barrier of boron-doped diamond by anodic oxidation. J Appl Phys. 2008;103(1).
62. Jian Z, Heide M, Yang N, Engelhard C, Jiang X. Diamond fibers for efficient electrocatalytic degradation of environmental pollutants. Carbon. 2021;175:36-42.
63. Zhang J, Yu X, Zhang Z-Q, Zhao Z-Y. Preparation of boron-doped diamond foam film for supercapacitor applications. Appl Surf Sci. 2020;506.
64. Zanin H, May PW, Fermin DJ, Plana D, Vieira SM, Milne WI, *et al.* Porous boron-doped diamond/carbon nanotube electrodes. ACS Appl Mater Interfaces. 2014;6(2):990-5.
65. Vernasqui LG, Sardinha AF, Oishi SS, Ferreira NG. Nanoscale control of high-quality boron-doped ultrananodiamond on dioxide titanium nanotubes as a porous composite. J Mater Res Technol. 2021;12:597-612.
66. Zhang J, Yu X, Zhao Z-y, Zhang Z, Li J. Influence of pore size of Ti substrate on structural and capacitive properties of Ti/boron doped diamond electrode. J Alloys Compd. 2019;777:84-93.
67. Brito CN, Ferreira MB, de O. Marcionilio SML, de Moura Santos ECM, Léon JJL, Ganiyu SO, *et al.* Electrochemical Oxidation of Acid Violet 7 Dye by Using Si/BDD and Nb/BDD Electrodes. J Electrochem Soc. 2018;165(5):E250-E5.
68. Yu X, Zhou M, Hu Y, Groenen Serrano K, Yu F. Recent updates on electrochemical degradation of bio-refractory organic pollutants using BDD anode: a mini review. Environ Sci Pollut R. 2014;21(14):8417-31.
69. Moelle C, Klose S, Szücs F, Fecht HJ, Johnston C, Chalker PR, *et al.* Measurement and calculation of the thermal expansion coefficient of diamond. Diamond Relat Mater. 1997;6(5-7):839-42.
70. Braga NA, Cairo CAA, Matsushima JT, Baldan MR, Ferreira NG. Diamond/porous titanium three-dimensional hybrid electrodes. J Solid State Electrochem. 2009;14(2):313-21.
71. Lim PY, Lin FY, Shih HC, Ralchenko VG, Varnin VP, Pleskov YV, *et al.* Improved stability of titanium based boron-doped chemical vapor deposited diamond thin-film electrode by modifying titanium substrate surface. Thin Solid Films. 2008;516(18):6125-32.

72. Lu XR, Ding MH, Zhang L, Yang ZL, Lu Y, Tang WZ. Optimizing the Microstructure and Corrosion Resistance of BDD Coating to Improve the Service Life of Ti/BDD Coated Electrode. Mater. 2019;12(19).

73. Guo L, Chen G. Long-Term Stable Ti/BDD Electrode Fabricated with HFCVD Method Using Two-Stage Substrate Temperature. J Electrochem Soc. 2007;154(12):D657-D61.

74. Gerger I, Haubner R. The behaviour of Ti-substrates during deposition of boron doped diamond. Int J Refract Met Hard Mater. 2008;26(5):438-43.

75. Sun J, Lu H, Lin H, Huang W, Li H, Lu J, *et al.* Boron doped diamond electrodes based on porous Ti substrates. Mater Lett. 2012;83:112-4.

76. Kwon J-I, You M-n, SeohanKim, Keun SP. Performance of BDD Electrodes Prepared on Various Substrates for Wastewater Treatment. Journal of The Korean Institute of Surface Engineering. 2019;52(2):53-7.

77. Guimaraes GAA, Lacerda JN, Xing Y, Ponzio EA, Pacheco WF, Semaan FS, *et al.* Development and application of electrochemical sensor of boron-doped diamond (BDD) modified by drop casting with tin hexacyanoferrate. J Solid State Electrochem. 2020;24(8):1769-79.

78. Spitsyn BV, Bouilov LL, Derjaguin BV. Vapor growth of diamond on diamond and other surfaces. J Cryst Growth. 1981;52(Apr):219-26.

79. da Silva SW, Navarro EMO, Rodrigues MAS, Bernardes AM, Perez-Herranz V. The role of the anode material and water matrix in the electrochemical oxidation of norfloxacin. Chemosphere. 2018;210:615-23.

80. Choi Y-S, Lee Y-K, Kim J-Y, Kim K-M, Lee Y-K. Influence of Manufacturing Conditions for the Life Time of the Boron-Doped Diamond Electrode in Wastewater Treatment. Korean J Mater Res. 2017;27(3):137-43.

81. Hangarter CM, O'Grady WE, Stoner BR, Natishan PM. Electrochemical Oxidation of Phenol Using Boron-Doped Diamond Electrodes. ECS Transactions. 2015;64(46):1-9.

82. Salmeron I, Oller I, Plakas KV, Malato S. Carbon-based cathodes degradation during electro-Fenton treatment at pilot scale: Changes in H2O2 electrogeneration. Chemosphere. 2021;275:129962.

83. Monteil H, Pechaud Y, Oturan N, Trellu C, Oturan MA. Pilot scale continuous reactor for water treatment by electrochemical advanced oxidation processes: Development of a new hydrodynamic/reactive combined model. Chem Eng J. 2021;404.

84. Maldonado VY, Becker MF, Nickelsen MG, Witt SE. Laboratory and Semi-Pilot Scale Study on the Electrochemical Treatment of Perfluoroalkyl Acids from Ion Exchange Still Bottoms. Water-Sui. 2021;13(20).

85. Tawabini BS, Plakas KV, Fraim M, Safi E, Oyehan T, Karabelas AJ. Assessing the efficiency of a pilot-scale GDE/BDD electrochemical system in removing phenol from high salinity waters. Chemosphere. 2020;239:124714.

86. Roccamante M, Salmerón I, Ruiz A, Oller I, Malato S. New approaches to solar Advanced Oxidation Processes for elimination of priority substances based on electrooxidation and ozonation at pilot plant scale. Catal Today. 2020;355:844-50.

87. Salmerón I, Plakas KV, Sirés I, Oller I, Maldonado MI, Karabelas AJ, *et al.* Optimization of electrocatalytic H2O2 production at pilot plant scale for solar-assisted water treatment. Appl Catal B Environ. 2019;242:327-36.

88. Naji T, Dirany A, Carabin A, Drogui P. Large-scale disinfection of real swimming pool water by electro-oxidation. Environ Chem Lett. 2017;16(2):545-51.

89. Durán FE, de Araújo DM, do Nascimento Brito C, Santos EV, Ganiyu SO, Martínez-Huitle CA. Electrochemical technology for the treatment of real washing machine effluent at pre-pilot plant scale by using active and non-active anodes. J Electroanal Chem. 2018;818:216-22.

90. Souza F, Saéz C, Lanza M, Cañizares P, Rodrigo MA. Towards the scale-up of electrolysis with diamond anodes: effect of stacking on the electrochemical oxidation of 2,4 D. J Chem Technol Biotechnol. 2016;91(3):742-7.

91. Alvarez Pugliese CE, Martínez Hernández L, Imbachi Ordoñez S, Marriaga Cabrales N, Machuca Martínez F. Pilot scale anodic oxidation of pretreated vinasse using boron doped diamond electrodes. CT&F - Ciencia, Tecnología y Futuro. 2016;6(4):67-77.

92. Wu H, Xu F, Liu Z, Zhou C, Lu W, Zuo D. Preparation of large-scale double-side BDD electrodes and their electrochemical performances. Trans Nanjing Univ Aero Astro. 2015;32(6):674-80.

93. Bergmann MEH, Iourtchouk T, Schmidt W, Hartmann J, Fischer M, Nüsske G, *et al.* Laboratory- and technical-scale comparison of chlorate and perchlorate formation during drinking water electrolysis: a field study. J Appl Electrochem. 2015;45(7):765-78.

94. Li H, Yu Q, Yang B, Li Z, Lei L. Electrochemical treatment of artificial humidity condensate by large-scale boron doped diamond electrode. Sep Purif Technol. 2014;138:13-20.

95. Chaplin BP. Critical review of electrochemical advanced oxidation processes for water treatment applications. Environ Sci Process Impacts. 2014;16(6):1182-203.

96. Yang N, Yu S, Macpherson JV, Einaga Y, Zhao H, Zhao G, *et al.* Conductive diamond: synthesis, properties, and electrochemical applications. Chem Soc Rev. 2019;48(1):157-204.

97. Srikanth VVSS, Jiang X. Synthesis of Diamond Films. Synthetic Diamond Films2011. p. 21-55.

98. Mehta Menon P, Edwards A, Feigerle CS, Shaw RW, Coffey DW, Heatherly L, *et al.* Filament metal contamination and Raman spectra of hot filament chemical vapor deposited diamond films. Diamond Relat Mater. 1999;8(1):101-9.

99. Schwander M, Partes K. A review of diamond synthesis by CVD processes. Diamond Relat Mater. 2011;20(9):1287-301.

100. Tang CJ, Fernandes AJS, Costa F, Pinto JL. Effect of microwave power and nitrogen addition on the formation of {100} faceted diamond from microcrystalline to nanocrystalline. Vacuum. 2011;85(12):1130-4.

101. Haenni W, Rychen P, Fryda M, Comninellis C. Chapter V Industrial applications of diamond electrodes. In: Nebel CE, Ristein J, editors. Thin-Film Diamond II. Semiconductors and Semimetals. 77: Elsevier; 2004. p. 149-96.

102. Macpherson JV. A practical guide to using boron doped diamond in electrochemical research. Phys Chem Chem Phys. 2015;17(5):2935-49.

103. Lee KH, Seong WK, Ruoff RS. CVD diamond growth: Replacing the hot metallic filament with a hot graphite plate. Carbon. 2022;187:396-403.

104. Griesser M, Stingeder G, Grasserbauer M, Baumann H, Link F, Wurzinger P, *et al.* Characterization of tantalum impurities in hot-filament diamond layers. Diamond Relat Mater. 1994;3(4-6):638-44.

105. Parikh RP, Adomaitis RA. An overview of gallium nitride growth chemistry and its effect on reactor design: Application to a planetary radial-flow CVD system. J Cryst Growth. 2006;286(2):259-78.

106. Pujol AA, León I, Cárdenas J, Sepúlveda-Guzmán S, Manríquez J, Sirés I, *et al.* Degradation of phenols by heterogeneous electro-Fenton with a Fe3O4-chitosan composite and a boron-doped diamond anode. Electrochim Acta. 2020;337.

107. Chen T-S, Chen P-H, Huang K-L. Electrochemical degradation of N,N-diethyl-m-toluamide on a boron-doped diamond electrode. J Taiwan Inst Chem Eng. 2014;45(5):2615-21.

108. Machini WBS, Enache TA, Jorge SMA, Oliveira-Brett AM. Isotretinoin Oxidation and Electroanalysis in a Pharmaceutical Drug Using a Boron-doped Diamond Electrode. Electroanalysis. 2016;28(11):2709-15.

109. Miao D, Li Z, Chen Y, Liu G, Deng Z, Yu Y, *et al.* Preparation of macro-porous 3D boron-doped diamond electrode with surface micro structure regulation to enhance electrochemical degradation performance. Chem Eng J. 2022;429.

110. Zhu C, Jiang C, Chen S, Mei R, Wang X, Cao J, *et al.* Ultrasound enhanced electrochemical oxidation of Alizarin Red S on boron doped diamond(BDD) anode:Effect of degradation process parameters. Chemosphere. 2018;209:685-95.

111. Li W, Liu G, Miao D, Li Z, Chen Y, Gao X, *et al.* Electrochemical oxidation of Reactive Blue 19 on boron-doped diamond anode with different supporting electrolyte. J Environ Chem Eng. 2020;8(4).
112. Kapałka A, Lanova B, Baltruschat H, Fóti Gr, Comninellis C. A DEMS Study of Methanol and Formic Acid Oxidation on Boron-Doped Diamond Electrode. J Electrochem Soc. 2009;156(11):E149-E53.
113. Lévy-Clément C, Ndao NA, Katty A, Bernard M, Deneuville A, Comninellis C, *et al.* Boron doped diamond electrodes for nitrate elimination in concentrated wastewater. Diamond Relat Mater. 2003;12(3-7):606-12.
114. Migliorini FL, Steter JR, Rocha RS, Lanza MRV, Baldan MR, Ferreira NG. Efficiency study and mechanistic aspects in the Brilliant Green dye degradation using BDD/Ti electrodes. Diamond Relat Mater. 2016;65:5-12.
115. He Y, Wang X, Huang W, Chen R, Lin H, Li H. Application of porous boron-doped diamond electrode towards electrochemical mineralization of triphenylmethane dye. J Electroanal Chem. 2016;775:292-8.
116. Kuchtová G, Chýlková J, Váňa J, Vojs M, Dušek L. Electro-oxidative decolorization and treatment of model wastewater containing Acid Blue 80 on boron doped diamond and platinum anodes. J Electroanal Chem. 2020;863.
117. Mackuľak T, Medvecká E, Vojs Staňová A, Brandeburová P, Grabic R, Golovko O, *et al.* Boron doped diamond electrode – The elimination of psychoactive drugs and resistant bacteria from wastewater. Vacuum. 2020;171.
118. Li X, Li H, Li M, Li C, Sun D, Lei Y, *et al.* Preparation of a porous boron-doped diamond/Ta electrode for the electrocatalytic degradation of organic pollutants. Carbon. 2018;129:543-51.
119. Jiang J, Chang M, Pan P. Simultaneous hydrogen production and electrochemical oxidation of organics using boron-doped diamond electrodes. Environ Sci Technol. 2008;42(8):3059-63.
120. Chang M, Gao C, Jiang J. Electrochemical Oxidation of Organic Compounds Using Boron-Doped Diamond Electrode. J Electrochem Soc. 2009;156(2):E50-E4.
121. Li H, Yu Q, Yang B, Li Z, Lei L. Electro-catalytic oxidation of artificial human urine by using BDD and IrO2 electrodes. J Electroanal Chem. 2015;738:14-9.
122. Triana Y, Tomisaki M, Einaga Y. Oxidation reaction of dissolved hydrogen sulfide using boron doped diamond. J Electroanal Chem. 2020;873:114411.
123. Yamaguchi C, Natsui K, Iizuka S, Tateyama Y, Einaga Y. Electrochemical properties of fluorinated boron-doped diamond electrodes via fluorine-containing plasma treatment. Phys Chem Chem Phys. 2019;21(25):13788-94.
124. Witek MA, Swain GM. Aliphatic polyamine oxidation response variability and stability at boron-doped diamond thin-film electrodes as studied by flow-injection analysis. Anal Chim Acta. 2001;440(2):119-29.

125. Wei J-j, Zhu X-p, Lü F-x, Ni J-r. Comparative study of oxidation ability between boron-doped diamond (BDD) and lead oxide (PbO2) electrodes. Int J Min Met Mater. 2011;18(5):589-93.

126. Ryl J, Burczyk L, Zielinski A, Ficek M, Franczak A, Bogdanowicz R, *et al.* Heterogeneous oxidation of highly boron-doped diamond electrodes and its influence on the surface distribution of electrochemical activity. Electrochim Acta. 2019;297:1018-27.

127. Kondo T, Ito H, Kusakabe K, Ohkawa K, Einaga Y, Fujishima A, *et al.* Plasma etching treatment for surface modification of boron-doped diamond electrodes. Electrochim Acta. 2007;52(11):3841-8.

128. Mitadera M, Spataru N, Fujishima A. Electrochemical oxidation of aniline at boron-doped diamond electrodes. J Appl Electrochem. 2004;34(3):249-54.

129. Murugananthan M, Latha SS, Bhaskar Raju G, Yoshihara S. Role of electrolyte on anodic mineralization of atenolol at boron doped diamond and Pt electrodes. Sep Purif Technol. 2011;79(1):56-62.

130. van der Drift A. Evolutionary selection: a principle governing growth orientation in vapour deposited layers. Philips Research Reports. 1967;22:267–88.

131. Teraji T, Yamamoto T, Watanabe K, Koide Y, Isoya J, Onoda S, *et al.* Homoepitaxial diamond film growth: High purity, high crystalline quality, isotopic enrichment, and single color center formation. Phys Status Solidi A. 2015;212(11):2365-84.

132. Neto MA, Pato G, Bundaleski N, Teodoro OMND, Fernandes AJS, Oliveira FJ, *et al.* Surface modifications on as-grown boron doped CVD diamond films induced by the B2O3–ethanol–Ar system. Diamond Relat Mater. 2016;64:89-96.

133. Sein H, Ahmed W, Jackson M, Polini R. Growth of Polycrystalline Diamond on Titanium Nitride on Silicon Substrates Using Negative Bias Assisted CVD. Jackson MJ, Ahmed W, editors. Materials Park: Asm International; 2006. 1-+ p.

134. Jia F-c, Bai Y-z, Qu F, Sun J, Zhao J-j, Jiang X. The influence of gas pressure and bias current on the crystallinity of highly boron-doped diamond films. New Carbon Mater. 2010;25(5):357-62.

135. Paritosh, Srolovitz DJ, Battaile CC, Li X, Butler JE. Simulation of faceted film growth in two-dimensions: microstructure, morphology and texture. Acta Mater. 1999;47(7):2269-81.

136. Tamor MA, Everson MP. On the role of penetration twins in the morphological development of vapor-grown diamond films. J Mater Res. 2011;9(7):1839-49.

137. Wild C, Herres N, Koidl P. Texture formation in polycrystalline diamond films. J Appl Phys. 1990;68(3):973-8.

138. Wild C, Kohl R, Herres N, Müller-Sebert W, Koidl P. Oriented CVD diamond films: twin formation, structure and morphology. Diamond Relat Mater. 1994;3(4-6):373-81.

139. Einaga Y. Development of Electrochemical Applications of Boron-Doped Diamond Electrodes. B Chem Soc Jpn. 2018;91(12):1752-62.

140. Cifre J, Puigdollers J, Polo MC, Esteve J. Trimethylboron doping of CVD diamond thin films. Diamond Relat Mater. 1994;3(4-6):628-31.
141. Wei C, Chen C-H. The effect of thermal and plastic mismatch on stress distribution in diamond like carbon film under different interlayer/substrate system. Diamond Relat Mater. 2008;17(7-10):1534-40.
142. Vanhove E, de Sanoit J, Arnault JC, Saada S, Mer C, Mailley P, *et al.* Stability of H-terminated BDD electrodes: an insight into the influence of the surface preparation. Phys Status Solidi A. 2007;204(9):2931-9.
143. Baluchová S, Taylor A, Mortet V, Sedláková S, Klimša L, Kopeček J, *et al.* Porous boron doped diamond for dopamine sensing: Effect of boron doping level on morphology and electrochemical performance. Electrochim Acta. 2019;327.
144. Patel AN, Tan SY, Miller TS, Macpherson JV, Unwin PR. Comparison and reappraisal of carbon electrodes for the voltammetric detection of dopamine. Anal Chem. 2013;85(24):11755-64.
145. Read TL, Macpherson JV. Assessment of Boron Doped Diamond Electrode Quality and Application to In Situ Modification of Local pH by Water Electrolysis. Jove-J Vis Exp. 2016(107).
146. Bennett JA, Wang J, Show Y, Swain GM. Effect of sp2-Bonded Nondiamond Carbon Impurity on the Response of Boron-Doped Polycrystalline Diamond Thin-Film Electrodes. J Electrochem Soc. 2004;151(9):E306-E13.
147. Prawer S, Nemanich RJ. Raman spectroscopy of diamond and doped diamond. Philos Trans A Math Phys Eng Sci. 2004;362(1824):2537-65.
148. Jagannadham K, Lance MJ, Butler JE. Laser annealing of neutron irradiated boron-10 isotope doped diamond. J Mater Sci. 2010;46(8):2518-28.
149. Ballutaud D, Jomard F, Kociniewski T, Rzepka E, Girard H, Saada S. Sp3/sp2 character of the carbon and hydrogen configuration in micro- and nanocrystalline diamond. Diamond Relat Mater. 2008;17(4-5):451-6.
150. Dychalska A, Popielarski P, Franków W, Fabisiak K, Paprocki K, Szybowicz M. Study of CVD diamond layers with amorphous carbon admixture by Raman scattering spectroscopy. Mater Sci-Poland. 2015;33(4):799-805.
151. Isshiki H, Yoshida M, Tobita R, Shigeeda T, Kinoshita M, Matsushima K, *et al.* Enhancement of Diamond Nucleation by Atomic Silicon Microaddition. Jpn J Appl Phys. 2012;51(9).
152. Štenclová P, Vyskočil V, Szabó O, Ižák T, Potocký Š, Kromka A. Structured and graphitized boron doped diamond electrodes: Impact on electrochemical detection of Cd2+ and Pb2+ ions. Vacuum. 2019;170.
153. Ferrari AC, Robertson J. Raman spectroscopy of amorphous, nanostructured, diamond-like carbon, and nanodiamond. Philos Trans A Math Phys Eng Sci. 2004;362(1824):2477-512.

154. Kowalska M, Paprocki K, Szybowicz M, Wrzyszczyński A, Łoś S, Fabisiak K. Electrochemical sensitivity of undoped CVD diamond films as function of their crystalline quality. J Electroanal Chem. 2020;859:113811.

155. Gheeraert E, Gonon P, Deneuville A, Abello L, Lucazeau G. Effect of boron incorporation on the “quality” of MPCVD diamond films. Diamond Relat Mater. 1993;2(5-7):742-5.

156. Espinoza LC, Aranda M, Contreras D, Henríquez A, Salazar R. Effect of the sp3/sp2 Ratio in Boron-Doped Diamond Electrodes on the Degradation Pathway of Aniline by Anodic Oxidation. ChemElectroChem. 2019;6(18):4801-10.

157. McNamara KM, Gleason KK, Vestyck DJ, Butler JE. Evaluation of diamond films by nuclear magnetic resonance and Raman spectroscopy. Diamond Relat Mater. 1992;1(12):1145-55.

158. Vorlíček V, Rosa J, Vaněček M, Nesládek M, Stals LM. Quantitative study of Raman scattering and defect optical absorption in CVD diamond films. Diamond Relat Mater. 1997;6(5-7):704-7.

159. Shroder RE, Nemanich RJ, Glass JT. Analysis of the composite structures in diamond thin films by Raman spectroscopy. Phys Rev B. 1990;41(6):3738-45.

160. Gomez-Ruiz B, Diban N, Urtiaga A. Comparison of microcrystalline and ultrananocrystalline boron doped diamond anodes: Influence on perfluorooctanoic acid electrolysis. Sep Purif Technol. 2019;208:169-77.

161. Williams OA. Nanocrystalline diamond. Diamond Relat Mater. 2011;20(5-6):621-40.

162. Pleskov Y. Electrochemistry of Diamond. In: Brillas E, Martínez-Huitle CA, editors. Synthetic Diamond Films2011. p. 77-108.

163. Lagrange JP, Deneuville A, Gheeraert E. Activation energy in low compensated homoepitaxial boron-doped diamond films. Diamond Relat Mater. 1998;7(9):1390-3.

164. Larsson K. Simulation of Diamond Surface Chemistry: Reactivity and Properties. In: Lipatov E, editor. Some Aspects of Diamonds in Scientific Research and High Technology. London: IntechOpen; 2020.

165. Lu Y-G, Turner S, Verbeeck J, Janssens SD, Wagner P, Haenen K, *et al.* Direct visualization of boron dopant distribution and coordination in individual chemical vapor deposition nanocrystalline B-doped diamond grains. Appl Phys Lett. 2012;101(4).

166. Bernard M, Deneuville A, Muret P. Non-destructive determination of the boron concentration of heavily doped metallic diamond thin films from Raman spectroscopy. Diamond Relat Mater. 2004;13(2):282-6.

167. Azevedo AF, Baldan MR, Ferreira NG. Doping level influence on chemical surface of diamond electrodes. J Phys Chem Solids. 2013;74(4):599-604.

168. Salazar-Banda GR, de Carvalho AE, Andrade LS, Rocha-Filho RC, Avaca LA. On the activation and physical degradation of boron-doped diamond surfaces brought on by cathodic pretreatments. J Appl Electrochem. 2010;40(10):1817-27.

169. Liu Z, Li H, Li M, Li C, Qian L, Su L, *et al.* Preparation of polycrystalline BDD/Ta electrodes for electrochemical oxidation of organic matter. Electrochim Acta. 2018;290:109-17.

170. Wang XH, Ma GHM, Zhu W, Glass JT, Bergman L, Turner KF, *et al.* Effects of boron doping on the surface morphology and structural imperfections of diamond films. Diamond Relat Mater. 1992;1(7):828-35.

171. Notsu H, Fukazawa T, Tatsuma T, Tryk DA, Fujishima A. Hydroxyl Groups on Boron-Doped Diamond Electrodes and Their Modification with a Silane Coupling Agent. Electrochem Solid-State Lett. 2001;4(3):H1-H3.

172. Yagi I, Notsu H, Kondo T, Tryk DA, Fujishima A. Electrochemical selectivity for redox systems at oxygen-terminated diamond electrodes. J Electroanal Chem. 1999;473(1-2):173-8.

173. Salazar-Banda GR, Andrade LS, Nascente PAP, Pizani PS, Rocha-Filho RC, Avaca LA. On the changing electrochemical behaviour of boron-doped diamond surfaces with time after cathodic pre-treatments. Electrochim Acta. 2006;51(22):4612-9.

174. Yano T, Popa E, Tryk DA, Hashimoto K, Fujishima A. Electrochemical Behavior of Highly Conductive Boron-Doped Diamond Electrodes for Oxygen Reduction in Acid Solution. J Electrochem Soc. 2019;146(3):1081-7.

175. Yano T, Tryk DA, Hashimoto K, Fujishima A. Electrochemical Behavior of Highly Conductive Boron-Doped Diamond Electrodes for Oxygen Reduction in Alkaline Solution. J Electrochem Soc. 2019;145(6):1870-6.

176. Liu FB, Wang JD, Liu B, Li XM, Chen DR. Effect of electronic structures on electrochemical behaviors of surface-terminated boron-doped diamond film electrodes. Diamond Relat Mater. 2007;16(3):454-60.

177. Hutton LA, Iacobini JG, Bitziou E, Channon RB, Newton ME, Macpherson JV. Examination of the factors affecting the electrochemical performance of oxygen-terminated polycrystalline boron-doped diamond electrodes. Anal Chem. 2013;85(15):7230-40.

178. Bard AJ. Inner-sphere heterogeneous electrode reactions. Electrocatalysis and photocatalysis: the challenge. J Am Chem Soc. 2010;132(22):7559-67.

179. Yuan S, Guo X, Li P, Mao Q, Lu M, Jin Z, *et al.* Insights into the surface oxidation modification mechanism of nano-diamond: An atomistic understanding from ReaxFF simulations. Appl Surf Sci. 2021;540.

180. Chaudhuri S, Hall SJ, Klein BP, Walker M, Logsdail AJ, Macpherson JV, *et al.* Coexistence of carbonyl and ether groups on oxygen-terminated (110)-oriented diamond surfaces. Communications Materials. 2022;3(1).

181. Tryk DA, Tsunozaki K, Rao TN, Fujishima A. Relationships between surface character and electrochemical processes on diamond electrodes: dual roles of surface termination and near-surface hydrogen. Diamond Relat Mater. 2001;10(9-10):1804-9.

182. Lourencao BC, Brocenschi RF, Medeiros RA, Fatibello-Filho O, Rocha-Filho RC. Analytical Applications of Electrochemically Pretreated Boron-Doped Diamond Electrodes. ChemElectroChem. 2020;7(6):1291-311.

183. Yoon J-H, Shim Y-B, Lee B-S, Choi S-Y, Won M-S. Electrochemical Degradation of Phenol and 2-Chlorophenol Using Pt/Ti and Boron-Doped Diamond Electrodes. B Korean Chem Soc. 2012;33(7):2274-8.

184. Kornienko GV, Chaenko NV, Maksimov NG, Kornienko VL, Varnin VP. Electrochemical oxidation of phenol on boron-doped diamond electrode. Russ J Electrochem. 2011;47(2):225-9.

185. Chen P, Mu Y, Chen Y, Tian L, Jiang XH, Zou JP, *et al.* Shifts of surface-bound *OH to homogeneous *OH in BDD electrochemical system via UV irradiation for enhanced degradation of hydrophilic aromatic compounds. Chemosphere. 2022;291(Pt 2):132817.

186. Zhang C, Xian J, Liu M, Fu D. Formation of brominated oligomers during phenol degradation on boron-doped diamond electrode. J Hazard Mater. 2018;344:123-35.

187. McLaughlin MHS, Corcoran E, Pakpour-Tabrizi AC, de Faria DC, Jackman RB. Influence of temperature on the electrochemical window of boron doped diamond: a comparison of commercially available electrodes. Sci Rep. 2020;10(1):15707.

188. Olson EJ, Bühlmann P. Unbiased Assessment of Electrochemical Windows: Minimizing Mass Transfer Effects on the Evaluation of Anodic and Cathodic Limits. J Electrochem Soc. 2012;160(2):A320-A3.

189. Mousavi MPS, Dittmer AJ, Wilson BE, Hu J, Stein A, Bühlmann P. Unbiased Quantification of the Electrochemical Stability Limits of Electrolytes and Ionic Liquids. J Electrochem Soc. 2015;162(12):A2250-A8.

190. Comninellis C, Kapalka A, Malato S, Parsons SA, Poulios I, Mantzavinos D. Advanced oxidation processes for water treatment: advances and trends for R&D. J Chem Technol Biotechnol. 2008;83(6):769-76.

191. Lee C-H, Lee E-S, Lim Y-K, Park K-H, Park H-D, Lim D-S. Enhanced electrochemical oxidation of phenol by boron-doped diamond nanowire electrode. RSC Adv. 2017;7(11):6229-35.

192. Dettlaff A, Sobaszek M, Klimczuk T, Bogdanowicz R. Enhanced electrochemical kinetics of highly-oriented (111)-textured boron-doped diamond electrodes induced by deuterium plasma chemistry. Carbon. 2021;174:594-604.

193. Ueda A, Kato D, Sekioka N, Hirono S, Niwa O. Local imaging of an electrochemical active/inactive region on a conductive carbon surface by using scanning electrochemical microscopy. Anal Sci. 2009;25(5):645-51.

194. Zhang C, Lu X, Lu Y, Ding M, Tang W. Titanium-boron doped diamond composite: A new anode material. Diamond Relat Mater. 2019;98.

195. Lu X-R, Ding M-H, Zhang C, Tang W-Z. Comparative study on stability of boron doped diamond coated titanium and niobium electrodes. Diamond Relat Mater. 2019;93:26-33.

196. Miao D, Liu T, Yu Y, Li S, Liu G, Chen Y, *et al.* Study on degradation performance and stability of high temperature etching boron-doped diamond electrode. Appl Surf Sci. 2020;514.

197. Lu XR, Ding MH, Zhang C, Tang WZ. Comparative study on stability of boron doped diamond coated titanium and niobium electrodes. Diamond Relat Mater. 2019;93:26-33.

198. Lu XR, Ding MH, Zhang C, Tang WZ. Investigation on microstructure evolution and failure mechanism of boron doped diamond coated titanium electrode during accelerated life test. Thin Solid Films. 2018;660:306-13.

199. Chen X, Gao F, Chen G. Comparison of Ti/BDD and Ti/SnO2?Sb2O5 electrodes for pollutant oxidation. J Appl Electrochem. 2005;35(2):185-91.

200. Chen X, Chen G. Proper Hot Filament CVD Conditions for Fabrication of Ti-Boron Doped Diamond Electrodes. J Electrochem Soc. 2004;151(4):B214-B9.

201. He Y, Huang W, Chen R, Zhang W, Lin H. Improved electrochemical performance of boron-doped diamond electrode depending on the structure of titanium substrate. J Electroanal Chem. 2015;758:170-7.

202. Groenen Serrano K, Savall A, Latapie L, Racaud C, Rondet P, Bertrand N. Performance of Ti/Pt and Nb/BDD anodes for dechlorination of nitric acid and regeneration of silver(II) in a tubular reactor for the treatment of solid wastes in nuclear industry. J Appl Electrochem. 2015;45(7):779-86.

203. Brillas E, Sires I, Arias C, Cabot PL, Centellas F, Rodriguez RM, *et al.* Mineralization of paracetamol in aqueous medium by anodic oxidation with a boron-doped diamond electrode. Chemosphere. 2005;58(4):399-406.

204. Enache TA, Chiorcea-Paquim A-M, Fatibello-Filho O, Oliveira-Brett AM. Hydroxyl radicals electrochemically generated in situ on a boron-doped diamond electrode. Electrochem Commun. 2009;11(7):1342-5.

205. Rubí-Juárez H, Cotillas S, Sáez C, Cañizares P, Barrera-Díaz C, Rodrigo MA. Use of conductive diamond photo-electrochemical oxidation for the removal of pesticide glyphosate. Sep Purif Technol. 2016;167:127-35.

206. Panizza M, Cerisola G. Direct and mediated anodic oxidation of organic pollutants. Chem Rev. 2009;109(12):6541-69.

207. Belhadj Tahar N, Savall A. Mechanistic Aspects of Phenol Electrochemical Degradation by Oxidation on a Ta / PbO2 Anode. J Electrochem Soc. 2019;145(10):3427-34.

208. Brillas E, Garrido JA, Rodríguez RM, Arias C, Cabot PL, Centellas F. Wastewaters by electrochemical advanced oxidation processes using a BDD anode and electrogenerated H2O2 with Fe(II) and UVA light as catalysts. Port Electrochim Acta. 2008;26(1):15-46.

209. Moreira FC, Boaventura RAR, Brillas E, Vilar VJP. Electrochemical advanced oxidation processes: A review on their application to synthetic and real wastewaters. Appl Catal B Environ. 2017;202:217-61.

210. Brillas E, Boye B, Sirés I, Garrido JA, Rodríguez RMa, Arias C, *et al.* Electrochemical destruction of chlorophenoxy herbicides by anodic oxidation and electro-Fenton using a boron-doped diamond electrode. Electrochim Acta. 2004;49(25):4487-96.

211. Brillas E. Electro-Fenton, UVA Photoelectro-Fenton and Solar Photoelectro-Fenton Treatments of Organics in Waters Using a Boron-Doped Diamond Anode: A Review. J Mex Chem Soc. 2014;58(3):239-55.

212. Oturan MA, Sirés I, Oturan N, Pérocheau S, Laborde J-L, Trévin S. Sonoelectro-Fenton process: A novel hybrid technique for the destruction of organic pollutants in water. J Electroanal Chem. 2008;624(1-2):329-32.

213. Vidales MJMd, Barba S, Sáez C, Cañizares P, Rodrigo MA. Coupling ultraviolet light and ultrasound irradiation with Conductive-Diamond Electrochemical Oxidation for the removal of progesterone. Electrochim Acta. 2014;140:20-6.

214. Vieira Dos Santos E, Saez C, Canizares P, Martinez-Huitle CA, Rodrigo MA. Treating soil-washing fluids polluted with oxyfluorfen by sono-electrolysis with diamond anodes. Ultrason Sonochem. 2017;34:115-22.

215. Hurwitz G, Hoek EMV, Liu K, Fan L, Roddick FA. Photo-assisted electrochemical treatment of municipal wastewater reverse osmosis concentrate. Chem Eng J. 2014;249:180-8.

216. Cotillas S, de Vidales MJ, Llanos J, Saez C, Canizares P, Rodrigo MA. Electrolytic and electro-irradiated processes with diamond anodes for the oxidation of persistent pollutants and disinfection of urban treated wastewater. J Hazard Mater. 2016;319:93-101.

217. Brillas E, Casado J. Aniline degradation by Electro-Fenton® and peroxi-coagulation processes using a flow reactor for wastewater treatment. Chemosphere. 2002;47(3):241-8.

218. Huang YH, Chen CC, Huang GH, Chou SS. Comparison of a novel electro-Fenton method with Fenton's reagent in treating a highly contaminated wastewater. Water Sci Technol. 2001;43(2):17-24.

219. Clematis D, Panizza M. Electrochemical oxidation of organic pollutants in low conductive solutions. Curr Opin Electrochem. 2021;26.

220. Clematis D, Cerisola G, Panizza M. Electrochemical oxidation of a synthetic dye using a BDD anode with a solid polymer electrolyte. Electrochem Commun. 2017;75:21-4.

221. Murugananthan M, Yoshihara S, Rakuma T, Uehara N, Shirakashi T. Electrochemical degradation of 17β-estradiol (E2) at boron-doped diamond (Si/BDD) thin film electrode. Electrochim Acta. 2007;52(9):3242-9.

222. Rivera FF, León CPd, Walsh FC, Nava JL. The reaction environment in a filter-press laboratory reactor: the FM01-LC flow cell. Electrochim Acta. 2015;161:436-52.

223. de Souza RBA, Ruotolo LAM. Phenol electrooxidation in different supporting electrolytes using boron-doped diamond anodes. Int J Electrochem Sci. 2013;8(1):643-57.

224. Espinoza-Montero PJ, Vasquez-Medrano R, Ibanez JG, Frontana-Uribe BA. Efficient Anodic Degradation of Phenol Paired to Improved Cathodic Production of H2O2at BDD Electrodes. J Electrochem Soc. 2013;160(7):G3171-G7.

225. Daskalaki VM, Fulgione I, Frontistis Z, Rizzo L, Mantzavinos D. Solar light-induced photoelectrocatalytic degradation of bisphenol-A on TiO2/ITO film anode and BDD cathode. Catal Today. 2013;209:74-8.

226. Fabianska A, Bialk-Bielinska A, Stepnowski P, Stolte S, Siedlecka EM. Electrochemical degradation of sulfonamides at BDD electrode: kinetics, reaction pathway and eco-toxicity evaluation. J Hazard Mater. 2014;280:579-87.

227. Zhou M, Liu L, Jiao Y, Wang Q, Tan Q. Treatment of high-salinity reverse osmosis concentrate by electrochemical oxidation on BDD and DSA electrodes. Desalination. 2011;277(1-3):201-6.

228. Zhou M, Särkkä H, Sillanpää M. A comparative experimental study on methyl orange degradation by electrochemical oxidation on BDD and MMO electrodes. Sep Purif Technol. 2011;78(3):290-7.

229. Panizza M, Michaud PA, Cerisola G, Comninellis C. Anodic oxidation of 2-naphthol at boron-doped diamond electrodes. J Electroanal Chem. 2001;507(1-2):206-14.

230. Cano A, Cañizares P, Barrera C, Sáez C, Rodrigo MA. Use of low current densities in electrolyses with conductive-diamond electrochemical — Oxidation to disinfect treated wastewaters for reuse. Electrochem Commun. 2011;13(11):1268-70.

231. Lacasa E, Tsolaki E, Sbokou Z, Rodrigo MA, Mantzavinos D, Diamadopoulos E. Electrochemical disinfection of simulated ballast water on conductive diamond electrodes. Chem Eng J. 2013;223:516-23.

232. Comninellis C, Pulgarin C. Anodic oxidation of phenol for waste water treatment. J Appl Electrochem. 1991;21(8):703-8.

233. Flox C, Garrido JA, Rodríguez RM, Cabot P-L, Centellas F, Arias C, *et al.* Mineralization of herbicide mecoprop by photoelectro-Fenton with UVA and solar light. Catal Today. 2007;129(1-2):29-36.

234. Pacheco MJ, Morão A, Lopes A, Ciríaco L, Gonçalves I. Degradation of phenols using boron-doped diamond electrodes: A method for quantifying the extent of combustion. Electrochim Acta. 2007;53(2):629-36.

235. Rohatgi A. WebPlotDigitizer San Francisco, California, USA, 2019. Available from: https://automeris.io/WebPlotDigitizer.

I.2.10. Supplementary Information

Supplementary Table I.2.1. Details of the Boolean advanced search query: theme, strings, search query, and results, based on the Scopus database.

Theme	Boolean advanced search query	Results
Electrochemical degradation of contaminants with BDD electrodes	*TITLE* (bdd *OR* "boron doped diamond" *OR* "boron-doped diamond") *AND* TITLE (*degradation *OR* treatment *OR* remov* *OR* mineralization *OR* remediation *OR* "electrochemical oxidation" *OR* destruction *OR* *oxidation *OR* incineration *OR* disinfection *OR* wastewater* *OR* combustion *OR* elimination *OR* decomposition)) *AND* (*LIMIT-TO* (*DOCTYPE,* "ar")) *AND* (*LIMIT-TO* (*LANGUAGE*, "English")	Scopus: 875 (04/2022)

Supplementary Table I.2.2. Previously identified commonly used strings for describing the degradation of contaminants with BDD electrodes.

Strings
*degradation (*e.g.* electrodegradation, degradation)
treatment
remov* (*e.g.* removal, removing)
mineralization
remediation
"electrochemical oxidation"
destruction
*oxidation (*e.g.* electrooxidation, electro-oxidation, oxidation)
incineration
disinfection
wastewater* (*e.g.* wastewater, wastewaters)
combustion
elimination
decomposition

Supplementary Table I.2.3. List of commercial BDD suppliers.

Commercial BDD supplier	Country or Province	Website
3betterdiamond[e]	China	https://www.3betterdiamond.com/
Adamant Innotech S.A.[a]	Switzerland	https://adamant-innotech.ch/
Advanced Diamond Technology	USA	http://www.thindiamond.com/
Antec Scientific	The Netherlands	https://antecscientific.com/
BioLogic[e]	France	https://www.biologic.net/
Boromond[e]	China	https://www.boromond.com/
Condias[b]	Germany	https://www.condias.de/
Creating Nano Technologies Inc	Taiwan	http://www.creating-nanotech.com/
CSEM[d]	Switzerland	https://www.csem.ch/
Diaccon	Germany	https://www.diaccon.de/
Diamond Electric[e]	USA	https://diamond-us.com/
Ecotricity[e]	UK	https://www.ecotricity.co.uk/
EUT GmbH	Germany	https://www.eut-eilenburg.de/
Electrolytic Ozone[e]	USA	http://www.eoi-oxygen.com/
Element Six (De Beers Group)	USA	https://www.e6.com/
Eletrocell	Denmark	https://www.electrocell.com/
Eletrolytica	USA	http://www.electrolytica.com/
ESA Biosciences[c,e]	USA	https://www.thermofisher.com/
Evoqua (Magneto Special Anodes B.V.)	The Netherlands	https://www.evoqua.com/
Fraunhofer, CCD - Center for coatings and diamond technologies	USA	https://www.fraunhofer.org/
GL Sciences[e]	Japan	https://www.glsciences.com/
Kraftangalen[e]	Germany	https://www.kraftanlagen.com/
Metakem	Germany	https://metakem.de/
Metrohm DropSens[e]	Spain	https://www.dropsens.com/
Neocoat[a]	Switzerland	https://www.neocoat.ch/
Schunk Carbon Technology[e]	Germany	https://www.schunk-carbontechnology.com/
Shazay[e]	Germany	https://shazay.com/
sp3 Diamond Technologies	USA	https://www.sp3diamondtech.com/
Sumitomo Electric Industries	Japan	https://sumitomoelectric.com/
Umex	Germany	https://www.umex.de/
* Waterdiam France	France	-
WCS Environmental Engineering Ltd[e]	UK	https://wpldiamond.com/
Weiss Technik[e]	Germany	https://www.weiss-technik.com/
Wesco	USA	https://www.wesco.com/
* Windsor Scientific	UK	-
Zhengzhou Abrasives & Grinding Research Institute Co.	China	http://www.zzsm.com/

[a] Spin-off company of CSEM
[b] Spin-off company of Fraunhofer Institute for Thin Films and Surface Technology
[c] Acquisition of Thermo Fischer Scientific
[d] Start-ups or joint ventures based on CSEM technologies: NeoCoat and Adamant Innotech S.A.
[e] Suppliers not identified in the articles from the bibliometric analysis research
*Liquidation

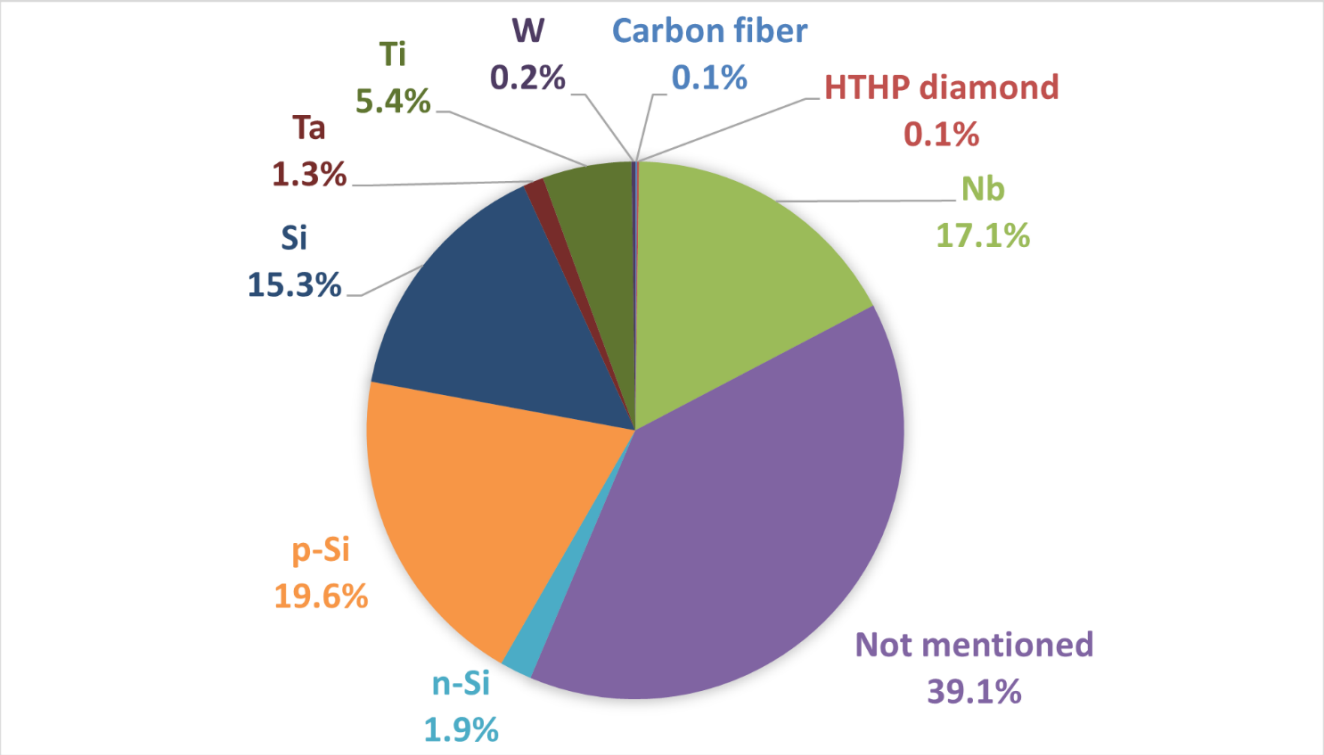

Supplementary Figure I.2.1. Choice of substrate material based on the bibliometric analysis search.

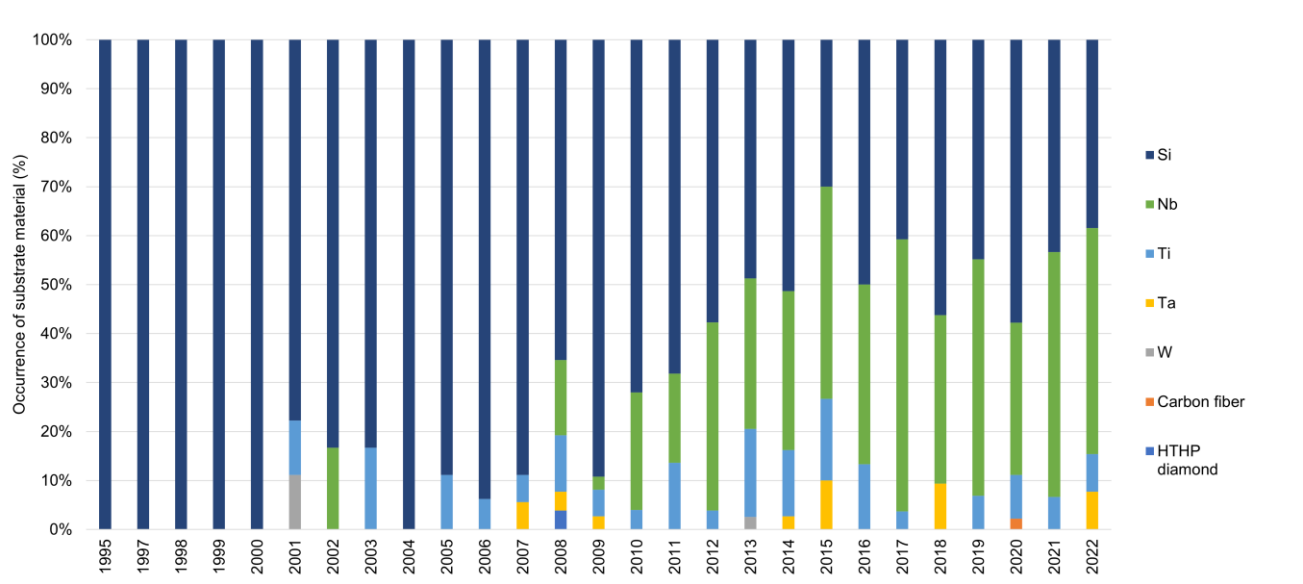

Supplementary Figure I.2.2. Choice of substrate material along the years, based on the bibliometric analysis search.

Supplementary Table I.2.4. Reported studies on phenol degradation using BDD electrodes as anodes in its electrooxidation.

BDD	% removal			Energy Consumption				ACE (%)	Initial concentration		j (mA/cm²)	t (h)	A (cm²)	V (mL)	Initial pH	Supporting Electrolyte	Conductivity (mS/cm)	Flow Rate (mL/s)	T (°C)	Electrochemical Characterization	Ref.
	COD	Phenol	TOC	COD (kWh/kg)	phenol (kWh/kg)	(kWh/m³)	TOC (kWh/kg)		Phenol (mg/L)	COD (mg/L)											
In house HFCVD	100%	-	-	112	-	-	-	-	240	548	20	3.2	24	200	3	0.05 M Na_2SO_4 and 2 M H_2SO_4	-	-	10	RE: SCE ES: 0.05 M Na_2SO_4 EPW: - OEP: ~1.8V	(1)
In house MPCVD	-	-	85%	-	-	-	-	-	941.1	-	70-900	~68.5	2	1000	-	0.1 M H_2SO_4	-	7	-	RE: Pd/H_2 ES: 0.1 M H_2SO_4 EPW: - OEP: 1.5V	(2)
In house HFCVD	95%	100%	-	-	-	8.15	-	21.8%	94.11	224	15	~15	1.5	100	2	0.5 M Na_2SO_4	-	-	RT	RE: SCE ES: 0.5 M H_2SO_4 EPW: 1.5 to 2.5 V OEP: 2.5V	(3)
In house HFCVD	94%	-	80%	-	-	27.5 (for 80% removal)	-	15.6%	94.11	-	30	5	16	500	-	0.5 M Na_2SO_4	-	16.67	-	RE: Ag/AgCl ES: 0.5 M H_2SO_4 EPW: 1.9 V OEP: 1.6 V	(4)
In house HFCVD	-	-	55%	-	-	-	29	* 18% (MCE)	-	-	50	3	4	250	-	0.1 M Na_2SO_4	-	-	RT	RE: Ag/AgCl ES: 0.5 M H_2SO_4 EPW: 3.1 V OEP: 2.2 V	(5)
In house MPCVD	70%	78%	-	-	-	-	-	23.8%	94.11	-	20	5	4	250	12	0.2 M Na_2SO_4	-	-	RT	RE: SCE ES: 0.2 M Na_2SO_4 EPW: 3.1 V OEP: 2.1 V	(6)
In house HFCVD	-	90%	-	-	-	-	-	22.3%	470.55	-	60	2,1	50	500	-	1 M $HClO_4$	-	-	25	RE: SHE ES: 1 M $HClO_4$ EPW: - OEP: 2.3 V	(7)
In house HFCVD	51%	-	-	-	-	-	-	-	3.764.4	9153	100	4	3	40	-	H_2SO_4	-	-	-	RE: SCE ES: - EPW: 3.29 V OEP: 2.42 V	(8)
In house HFCVD	96.6%	-	-	-	-	-	-	78.5%	-	1175	10	-	6.25	30	-	2000 mg/L Na_2SO_4	-	-	30	RE: NHE ES: 0.5 M H_2SO_4 EPW: 3.0 V OEP: 2.4 V	(9)
In house HFCVD	95.7%	-	-	-	-	-	-	-	-	1175	10	-	5	-	4.70–6.73	1500 mg/L Na_2SO_4	-	-	30	RE: NHE ES: 0.5 M H_2SO_4 EPW: - OEP: 2.7 V	(10)
In house HFCVD	97%	-	-	-	-	-	-	-	50	-	50	-	0.15	-	2–3	0.1 M H_2SO_4	-	-	20	RE: Ag/AgCl ES: 0.1 M H_2SO_4 EPW: 2.4 to 3.5 V OEP: 2.0 to 2.2 V	(11)
Adamant Technologies	-	93%	-	-	-	-	-	-	941.1	-	-	4	21	80	-	0.5 M H_2SO_4	-	-	-	-	(12)
Adamant Technologies	-	-	79.8%	-	-	-	-	-	941.1	-	32.5	3	6.16	30	-	0.1 M KNO_3	-	-	-	-	(13)
Adamant Technologies	-	100%	100%	-	-	-	-	-	100	-	2.5	9	40	500	2	0.04 M Na_2SO_4 / 0.05 H2SO4	18.1	12.5	23 ± 2	-	(14)
Adamant Technologies	51%	-	46%	-	-	-	-	76%	300	-	10	10	70	30000	-	0.035 M Na_2SO_4	-	138.89	-	-	(15)

BDD	% removal			Energy Consumption				ACE (%)	Initial concentration		j (mA/cm²)	t (h)	A (cm²)	V (mL)	Initial pH	Supporting Electrolyte	Conductivity (mS/cm)	Flow Rate (mL/s)	T (°C)	Electrochemical Characterization	Ref.
	COD	Phenol	TOC	COD (kWh/kg)	phenol (kWh/kg)	(kWh/m³)	TOC (kWh/kg)		Phenol (mg/L)	COD (mg/L)											
Adamant Technologies	34-42%	-	-	-	-	-	-	-	-	1000	30	~4	2.5	150	-	0.035 M Na_2SO_4 / NaOH	-	-	20	RE: SCE ES: Na_2SO_4 EPW: - OEP: 0.5V	(16)
Condias	77%	-	-	31	-	-	-	-	-	633	8.5	1.33	2904	4501	-	-	3	0.85-9.38	-	-	(17)
Condias	98.9%	100%	100%	57	-	-	-	19.1%	100	-	30	3.5	78.5	2000	4.8	1100 mg/L Na_2SO_4	-	-	23 ± 3	-	(18)
Condias	-	77%	40%	-	-	-	-	-	50	-	9.04	1	77.44	500	-	10 mM $NaNO_2$	-	6.68	-	RE: SCE ES: $NaNO_3$ EPW: - OEP: 1.77 V	(19)
Condias	-	97%	58%	-	-	-	-	-	94.11	-	20	8	4	250	-	0.2 M Na_2SO_4	-	-	25	-	(20)
Condias	-	-	58%	-	-	-	-	-	94.11	-	20	4	4	250	11	0.2 M Na_2SO_4	-	-	25	-	(21)
Condias	-	32%	-	-	-	-	-	-	47.06	-	10	1	2	200	6.50	20 mM Na_2SO_4	-	-	-	RE: Ag/AgCl ES: 20 mM Na_2SO_4 EPW: 2.3 V OEP: 1.93 V	(22)
Condias	91%	100%	99%	-	99	-	-	82%	1000	-	30	4.5	78.5	2000	2	1000 mg/L Na_2SO_4	-	-	-	-	(23)
Condias	-	-	-	-	329.52	-	-	19.89%	65.99	135.99	30	0.5	78.5	2000	4.8	1100 mg/L Na_2SO_4	-	-	RT	-	(24)
Condias	86%	-	-	-	-	-	-	-	-	-	20	5	4	250	-	0.2 M Na_2SO_4	-	-	25	RE: SCE ES: 0.2 M Na_2SO_4 EPW: - OEP: 2.1 V	(25)
Condias	80%	-	-	110	-	-	-	-	-	500	19.5	1.15	24	-	-	0.05 M Na_2SO_4	-	-	-	-	(26)
Condias	100%	-	-	-	-	-	-	19%	100	-	30	2.5	78.5	2000	-	1100 mg/L Na_2SO_4	-	-	-	-	(27)
Condias	98%	-	-	-	-	-	-	87%	200	-	30	8	8	150	-	-	-	8.35	25	-	(28)
CSEM	100%	-	-	-	-	-	-	56%	-	2400	30	-	78	-	2	5000 mg/L Na_2SO_4 / H_2SO_4	-	41.67	25	-	(29)
CSEM	99%	-	-	-	-	80	-	-	1882.2	-	47	5	63	990	-	0.1 M H_2SO_4	-	55.55	-	-	(30)
EUT	96%	-	96%	82	-	-	-	23%	280	666	50	5.8	28	-	-	Na_2SO_4	-	-	27-30	RE: Ag/AgCl ES: 0.3 M Na_2SO_4 EPW: - OEP: 1.0 V	(31)
EUT	91%	-	94%	26.6	-	-	-	-	-	378	30	8	16	2560	-	0.1 M H_2SO_4	-	40	30	-	(32)
Magneto Special Anodes B.V.	-	99.54%	-	-	470	-	-	-	200	590	5	1.25	176	500	1.97	Na_2SO_4	15.63	-	20	-	(33)
Umex	78%	-	78%	475	-	-	-	-	210	500	150	8	28	2500	0.76 – 0.87	0.1 M H_2SO_4	-	-	26-28	RE: Ag/AgCl ES: 0.1 M H_2SO_4 EPW: - OEP: 2.0 V	(34)
-	~100%	-	-	-	-	-	-	-	1985	-	215	3	7	100	13	0.1 M Na_2SO_4	-	-	30	-	(35)
-	99%	-	-	-	-	-	-	-	202-222	-	30	6.2	10.14	250	7	0.1 M Na_2CO_3	-	-	25	-	(36)

BDD	% removal			Energy Consumption				ACE (%)	Initial concentration		j (mA/cm²)	t (h)	A (cm²)	V (mL)	Initial pH	Supporting Electrolyte	Conductivity (mS/cm)	Flow Rate (mL/s)	T (°C)	Electrochemical Characterization	Ref.
	COD	Phenol	TOC	COD (kWh/kg)	phenol (kWh/kg)	(kWh/m³)	TOC (kWh/kg)		Phenol (mg/L)	COD (mg/L)											
-	98%	-	-	-	-	-	-	12.3%	240	548	20	3	24	200	3	0.05 M Na_2SO_4 / 2 M H_2SO_4	-	-	-	RE: SCE ES: 0.05 M Na_2SO_4 EPW: - OEP: ~1.5 V	(37)
-	84%	-	-	-	-	-	-	-	280	666	100	8	70	1500	2.0–3.5	0.1 M Na_2SO_4 / H_2SO_4 / NaOH	-	-	27–30	-	(38)
-	-	100%	20%	-	-	-	-	*45% (MCE)	50	-	40	0.5	100	20000	7	-	2480	1111.11	-	-	(39)
-	-	80.1%	62.5%	-	-	-	-	-	50	-	6.46	2	77.44	500	-	1 mM NaBr	-	6.68	-	RE: SCE ES: 1 mM NaBr EPW: - OEP: 1.9 V	(40)

EC = energy consumption; RT = room temperature; EPW = electrochemical potential window; ES = electrolyte solution; RE =: reference electrode

Supplementary Table I.2.5. Reported studies on landfill leachate degradation using BDD electrodes as anodes in its electrooxidation.

BDD	COD_0 (mg O_2/L)	COD removal (%)	ACE (%)	EC (kWh/kg COD)	j (mA/cm²)	t (h)	Anode area (cm²)	Volume (mL)	Initial pH	Supporting Electrolyte	Conductivity (mS/cm)	Flow Rate (mL/s)	T (°C)	Electrochemical characterization	Ref.
In house HFCVD	3778.56 ± 42.91	87.5%	41.7%	*223.2 kWh/m³	50	6	24	200	5.16 ± 0.12	1 M NaOH	40.16 ± 0.25	1.67	-	ES: 1 M H_2SO_4 RE: Ag/AgCl EPW: 3.0 V OEP: 2.3 V	(41)
In house MPCVD	3608 ± 123	91%	28%	285	100	4	10.5	400	7.8-9.4	-	-	-	25 ± 1	ES: 1 M KCl RE: Ag/AgCl EPW: 3.9 V OEP: 1.4 V	(42)
In house MPCVD	4002.11 ± 13.12	69%	43.9%	*215.4 kWh/m³	50	5.5	30	200	6.01 ± 0.01	-	12.4 ± 0.1	1.53	-	ES: 0.5 M H_2SO_4 RE: Ag/AgCl EPW: 2.2 V OEP: 1.6 V	(43)
Adamant Technologies	1130	100%	-	-	15-90	6-8	70	1000	7.51	-	14.36	183.33	20		(44)
CSEM	780	100%	24.5%	*150 kWh/m³	40	4	50	350	8.20	-	9.77	116.67	25		(45)
Adamant Technologies	3385	51%	-	102-134 (for 30% removal)	90-120	8	70	10000	8.4	NaCl	22.6	166.67	-		(46)
Adamant Technologies	860	100%	-	-	30-120	4-8	10500	230000	-	-	9.4	5000	-		(47)
Condias	5800	88%	-	-	30	6	10	200	8.4 ± 0.4	0.03 M Na_2SO_4	22.1	-	25		(48)
Fraunhofer	1168	93%	-	5.7	37.5	8	8	2000	5	Na_2SO_4		7	-		(49)
NeoCoat	6200 ± 400	40%	-	*64 kWh/m³	30	6	10	200	9.0 ± 0.1	-	22.0 ± 1.2	-	22–25		(50)
De Nora	3308–3540	95.17%	14.4%	160	83	8	6	-	2	NaOH or H_2SO_4	17.3–18.5	2.78	-		(51)
-	2040	49%	-	86.4	100	7	8	1000	8.5	-	10.74	2	-		(52)
-	2011	74%	-	-	50	4	8	1000	3	0.05 M NaCl		5	-		(53)
-	816	87%	193%	45.8	67	8	6	2000	6	H_2SO_4	2.91	5	-		(54)
-	888	92%	21.68%	136.0	36	4	84	950	7.65	-	19.31	-	-		(55)

EC = energy consumption; EPW = electrochemical potential window; ES = electrolyte solution; RE = reference electrode

References

1. Zhao G, Gao J, Shen S, Liu M, Li D, Wu M, *et al.* Ultrasound enhanced electrochemical oxidation of phenol and phthalic acid on boron-doped diamond electrode. J Hazard Mater. 2009;172(2-3):1076-81.

2. Hagans PL, Natishan PM, Stoner BR, O'Grady WE. Electrochemical Oxidation of Phenol Using Boron-Doped Diamond Electrodes. J Electrochem Soc. 2001;148(7):E298-E301.

3. Sun J, Lu H, Lin H, Du L, Huang W, Li H, *et al.* Electrochemical oxidation of aqueous phenol at low concentration using Ti/BDD electrode. Sep Purif Technol. 2012;88:116-20.

4. Lee C-H, Lee E-S, Lim Y-K, Park K-H, Park H-D, Lim D-S. Enhanced electrochemical oxidation of phenol by boron-doped diamond nanowire electrode. RSC Adv. 2017;7(11):6229-35.

5. Li H, Yang W, Ma L, Liu G, Yu Y, Cao J, *et al.* 3D-printed highly ordered Ti networks-based boron-doped diamond: An unprecedented robust electrochemical oxidation anode for decomposition of refractory organics. Chem Eng J. 2021;426.

6. Zhu X, Shi S, Wei J, Lv F, Zhao H, Kong J, *et al.* Electrochemical oxidation characteristics of p-substituted phenols using a boron-doped diamond electrode. Environ Sci Technol. 2007;41(18):6541-6.

7. Iniesta J. Electrochemical oxidation of phenol at boron-doped diamond electrode. Electrochim Acta. 2001;46(23):3573-8.

8. Shi L, Xu F, Gao J, Yuen M, Sun S, Xu J, *et al.* Nanostructured boron-doped diamond electrode for degradation of the simulation wastewater of phenol. Diamond Relat Mater. 2020;109:108098.

9. Chen X, Chen G, Gao F, Yue PL. High-performance Ti/BDD electrodes for pollutant oxidation. Environ Sci Technol. 2003;37(21):5021-6.

10. Chen X, Gao F, Chen G. Comparison of Ti/BDD and Ti/SnO2?Sb2O5 electrodes for pollutant oxidation. J Appl Electrochem. 2005;35(2):185-91.

11. Kornienko GV, Chaenko NV, Maksimov NG, Kornienko VL, Varnin VP. Electrochemical oxidation of phenol on boron-doped diamond electrode. Russ J Electrochem. 2011;47(2):225-9.

12. Pujol AA, León I, Cárdenas J, Sepúlveda-Guzmán S, Manríquez J, Sirés I, *et al.* Degradation of phenols by heterogeneous electro-Fenton with a Fe3O4-chitosan composite and a boron-doped diamond anode. Electrochim Acta. 2020;337.

13. Yoon J-H, Shim Y-B, Lee B-S, Choi S-Y, Won M-S. Electrochemical Degradation of Phenol and 2-Chlorophenol Using Pt/Ti and Boron-Doped Diamond Electrodes. B Korean Chem Soc. 2012;33(7):2274-8.
14. Espinoza-Montero PJ, Vasquez-Medrano R, Ibanez JG, Frontana-Uribe BA. Efficient Anodic Degradation of Phenol Paired to Improved Cathodic Production of H2O2at BDD Electrodes. J Electrochem Soc. 2013;160(7):G3171-G7.
15. Lopes A, Ciríaco L, Pacheco MJ, Sobreira S. Effect of the Hydrodynamic Conditions on the Electrochemical Degradation of Phenol on a BDD Anode. Port Electrochim Acta. 2011;29(5):343-8.
16. Cañizares P, Sáez C, Martínez F, Rodrigo MA. The Role of the Characteristics of p-Si BDD Anodes on the Efficiency of Wastewater Electro-oxidation Processes. Electrochem Solid-State Lett. 2008;11(7):E15-E9.
17. Zhu X, Ni J, Wei J, Xing X, Li H, Jiang Y. Scale-up of BDD anode system for electrochemical oxidation of phenol simulated wastewater in continuous mode. J Hazard Mater. 2010;184(1-3):493-8.
18. Jarrah N, Mu'azu ND. Simultaneous electro-oxidation of phenol, CN−, S2− and NH4+ in synthetic wastewater using boron doped diamond anode. J Environ Chem Eng. 2016;4(3):2656-64.
19. Zhang C, Dong J, Liu M, Zhao W, Fu D. The role of nitrite in electrocatalytic oxidation of phenol: An unexpected nitration process relevant to groundwater remediation with boron-doped diamond electrode. J Hazard Mater. 2019;373:547-57.
20. Jiang H, Dang C, Liu W, Wang T. Radical attack and mineralization mechanisms on electrochemical oxidation of p-substituted phenols at boron-doped diamond anodes. Chemosphere. 2020;248:126033.
21. Jiang Y, Zhu X, Xing X. Electrochemical Oxidation of Phenolic Compounds at Boron-Doped Diamond Anodes: Structure-Reactivity Relationships. J Phys Chem A. 2017;121(22):4326-33.
22. Chen P, Mu Y, Chen Y, Tian L, Jiang XH, Zou JP, *et al.* Shifts of surface-bound *OH to homogeneous *OH in BDD electrochemical system via UV irradiation for enhanced degradation of hydrophilic aromatic compounds. Chemosphere. 2022;291(Pt 2):132817.
23. Dalhat Mu N, H. Al-Mala M. Influence of Some Operating Parameters on Electro-Oxidation of Phenol using Boron Doped Diamond Anode and Graphite Cathode. J Environ Sci Technol. 2012;5(6):460-74.

24. Mu'azu ND, Al-Malack MH, Jarrah N. Electrochemical oxidation of low phenol concentration on boron doped diamond anodes: optimization via response surface methodology. Desalin Water Treat. 2013;52(37-39):7293-305.
25. Zhu X, Ni J, Li H, Jiang Y, Xing X, Borthwick AGL. Effects of ultrasound on electrochemical oxidation mechanisms of p-substituted phenols at BDD and PbO2 anodes. Electrochim Acta. 2010;55(20):5569-75.
26. Wei J, Zhu X, Ni J. Electrochemical oxidation of phenol at boron-doped diamond electrode in pulse current mode. Electrochim Acta. 2011;56(15):5310-5.
27. Muazu ND, Jarrah N, Bukhari A. Kinetic modeling of electrochemical oxidation of phenol on boron-doped diamond anode in the presence of some inorganic species. Desalin Water Treat. 2014;56(11):1-8.
28. Pacheco MJ, Morão A, Lopes A, Ciríaco L, Gonçalves I. Degradation of phenols using boron-doped diamond electrodes: A method for quantifying the extent of combustion. Electrochim Acta. 2007;53(2):629-36.
29. Canizares P, Lobato J, Paz R, Rodrigo MA, Saez C. Electrochemical oxidation of phenolic wastes with boron-doped diamond anodes. Water Res. 2005;39(12):2687-703.
30. Weiss E, Groenen-Serrano K, Savall A. A comparison of electrochemical degradation of phenol on boron doped diamond and lead dioxide anodes. J Appl Electrochem. 2007;38(3):329-37.
31. de Souza RBA, Ruotolo LAM. Phenol electrooxidation in different supporting electrolytes using boron-doped diamond anodes. Int J Electrochem Sci. 2013;8(1):643-57.
32. Farinos RM, Ruotolo LAM. Comparison of the electrooxidation performance of three-dimensional RVC/PbO2 and boron-doped diamond electrodes. Electrochim Acta. 2017;224:32-9.
33. Yavuz Y, Koparal AS, Öğütveren ÜB. Phenol Degradation in a Bipolar Trickle Tower Reactor Using Boron-Doped Diamond Electrode. J Environ Eng. 2008;134(1):24-31.
34. Britto-Costa PH, Ruotolo LAM. Phenol removal from wastewaters by electrochemical oxidation using boron doped diamond (BDD) and Ti/Ti0.7Ru0.3O2 dsa® electrodes. Braz J Chem Eng. 2012;29(4):763-73.
35. Bouaziz I, Hamza M, Sellami A, Abdelhedi R, Savall A, Groenen Serrano K. New hybrid process combining adsorption on sawdust and electroxidation using a BDD anode for the treatment of dilute wastewater. Sep Purif Technol. 2017;175:1-8.
36. Morão A, Lopes A, Pessoa de Amorim MT, Gonçalves IC. Degradation of mixtures of phenols using boron doped diamond electrodes for wastewater treatment. Electrochim Acta. 2004;49(9-10):1587-95.

37. Zhao G, Shen S, Li M, Wu M, Cao T, Li D. The mechanism and kinetics of ultrasound-enhanced electrochemical oxidation of phenol on boron-doped diamond and Pt electrodes. Chemosphere. 2008;73(9):1407-13.
38. Souza RBA, Ruotolo LAM. Electrochemical treatment of oil refinery effluent using boron-doped diamond anodes. J Environ Chem Eng. 2013;1(3):544-51.
39. Tawabini BS, Plakas KV, Fraim M, Safi E, Oyehan T, Karabelas AJ. Assessing the efficiency of a pilot-scale GDE/BDD electrochemical system in removing phenol from high salinity waters. Chemosphere. 2020;239:124714.
40. Zhang C, Xian J, Liu M, Fu D. Formation of brominated oligomers during phenol degradation on boron-doped diamond electrode. J Hazard Mater. 2018;344:123-35.
41. Zhou B, Yu Z, Wei Q, Long H, Xie Y, Wang Y. Electrochemical oxidation of biological pretreated and membrane separated landfill leachate concentrates on boron doped diamond anode. Appl Surf Sci. 2016;377:406-15.
42. Wilk BK, Szopinska M, Luczkiewicz A, Sobaszek M, Siedlecka E, Fudala-Ksiazek S. Kinetics of the Organic Compounds and Ammonium Nitrogen Electrochemical Oxidation in Landfill Leachates at Boron-Doped Diamond Anodes. Materials (Basel). 2021;14(17).
43. Zhao Y. Electrochemical Oxidation Treatment of Municipal Solid Waste Landfill Leachate Using Pt Nanoparticles Modified Boron- Doped Diamond Electrode. Int J Electrochem Sci. 2021;16:1-13.
44. Cabeza A, Urtiaga AM, Ortiz I. Electrochemical Treatment of Landfill Leachates Using a Boron-Doped Diamond Anode. Ind Eng Chem Res. 2007;46(5):1439-46.
45. Panizza M, Martinez-Huitle CA. Role of electrode materials for the anodic oxidation of a real landfill leachate--comparison between Ti-Ru-Sn ternary oxide, PbO(2) and boron-doped diamond anode. Chemosphere. 2013;90(4):1455-60.
46. Anglada A, Urtiaga A, Ortiz I, Mantzavinos D, Diamadopoulos E. Boron-doped diamond anodic treatment of landfill leachate: evaluation of operating variables and formation of oxidation by-products. Water Res. 2011;45(2):828-38.
47. Anglada A, Urtiaga A, Ortiz I. Pilot scale performance of the electro-oxidation of landfill leachate at boron-doped diamond anodes. Environ Sci Technol. 2009;43(6):2035-40.
48. Fernandes A, Pacheco MJ, Ciriaco L, Lopes A. Anodic oxidation of a biologically treated leachate on a boron-doped diamond anode. J Hazard Mater. 2012;199-200:82-7.
49. Bagastyo AY, Novitasari D, Nurhayati E, Direstiyani LC. Impact of sulfate ion addition on electrochemical oxidation of anaerobically treated landfill leachate using boron-doped diamond anode. Res Chem Intermed. 2020;46(11):4869-81.

50. Fernandes A, Santos D, Pacheco MJ, Ciríaco L, Lopes A. Nitrogen and organic load removal from sanitary landfill leachates by anodic oxidation at Ti/Pt/PbO2, Ti/Pt/SnO2-Sb2O4 and Si/BDD. Appl Catal B Environ. 2014;148-149:288-94.
51. Luu TL. Post treatment of ICEAS-biologically landfill leachate using electrochemical oxidation with Ti/BDD and Ti/RuO2 anodes. Environ Technol Inno. 2020;20.
52. Agustina F, Bagastyo AY, Nurhayati E. Electro-oxidation of landfill leachate using boron-doped diamond: role of current density, pH and ions. Water Sci Technol. 2019;79(5):921-8.
53. Nurhayati E, Bagastyo AY, Hartatik DD, Direstiyani LC. The enhancement of biodegradability index of mature landfill leachate by electrochemical oxidation process using boron-doped diamond and dimensionally stable anode. Res Chem Intermed. 2020;46(11):4811-22.
54. Bagastyo AY, Hidayati AS, Herumurti W, Nurhayati E. Application of boron-doped diamond, Ti/IrO2, and Ti/Pt anodes for the electrochemical oxidation of landfill leachate biologically pretreated by moving bed biofilm reactor. Water Sci Technol. 2021;83(6):1357-68.
55. Ukundimana Z, Omwene PI, Gengec E, Can OT, Kobya M. Electrooxidation as post treatment of ultrafiltration effluent in a landfill leachate MBR treatment plant: Effects of BDD, Pt and DSA anode types. Electrochim Acta. 2018;286:252-63.

Chapter II

Development of BDD/Si_3N_4-TiN Electrodes

This chapter focuses on developing a new substrate material for BDD electrodes and optimizing the conditions for BDD film deposition. The aim is to ensure that the BDD/substrate assembly exhibits high durability and robustness in service while also delivering excellent performance and efficiency in pollutant removal. This work has been presented in two papers, corresponding each to one of the two sections below.

Section II.1 presents a paper published in the journal *Ceramics International* (1). This section aims to develop fully dense Si_3N_4-TiN ceramic composites with a favorable combination of low electrical resistivity and strong mechanical properties. The primary objective of this study was to develop an innovative substrate material for BDD electrodes to enhance their durability and robustness. To achieve this, various pressureless sintered compositions of Si_3N_4 powder matrix mixed with TiN powder at different volume fractions were tested. The study employed a range of methods to assess the composition, microstructure, microhardness, fracture toughness, elastic modulus, shear modulus, thermal conductivity, bending strength, and electrical resistivity of the samples.

Section II.2 presents a paper accepted for publication in *Diamond and Related Materials* (2). This section employs the Taguchi method to systematically assess the influence of deposition conditions in an HFCVD reactor on the properties of BDD films intended for water treatment applications. Three controllable factors, namely the methane to hydrogen ratio, argon mass flow, and total gas pressure, were investigated. The primary objective was to optimize the quality of BDD films while minimizing the number of experimental trials.

---

1. Brosler P, Silva RF, Tedim J, Oliveira FJ. Electroconductive silicon nitride-titanium nitride ceramic substrates for CVD diamond electrode deposition. Ceram Int. 2023.

2. Brosler P, Neto, MA, Silva RF, Tedim J, Oliveira FJ. Customized boron-doped diamond electrodes for efficient water treatment via HF-CVD parameter optimization. Diam Relat Mater. 2024

II.1. Electroconductive Silicon Nitride-Titanium Nitride Ceramic Substrates for CVD Diamond Electrode Deposition

Priscilla Brosler[1], Rui F Silva[1], João Tedim[1], Filipe J Oliveira[1]

[1] *CICECO Aveiro Institute of Materials, Department of Materials and Ceramic Engineering, University of Aveiro, 3810-193, Aveiro, Portugal*

The present work was published on: *Ceramics International*

Published on: 30 August 2023

doi: 10.1016/j.ceramint.2023.08.327

Abstract

The present investigation was carried out to develop dense ceramics of silicon nitride-titanium nitride (Si_3N_4-TiN) with low electrical resistivity and excellent mechanical properties. The objective was to employ these ceramics as substrates of conductive diamond electrodes produced by chemical vapor deposition (CVD) for electrochemical applications. TiN powder was added to a Si_3N_4 matrix powder composition at varying volume fractions (21-30%). Disc-shaped samples were fabricated by mixing and pressing the powders, followed by pressureless sintering. The crystalline phase composition and microstructure were analyzed using X-ray diffraction and scanning electron microscopy, while the electrical resistivity was measured with a four-point probe configuration. The composites transitioned from insulating to conductive behavior between 23 and 27%vol TiN. The developed compositions displayed superior hardness, fracture toughness, elastic modulus, and thermal conductivity compared to the Si_3N_4 matrix. Notably, the composition containing 30%vol TiN displayed noteworthy properties, including a hardness value of 16.1 GPa, fracture toughness of 7.0 $MPa \cdot m^{1/2}$, and electrical resistivity of 8.9 x 10^{-1} $\Omega \cdot cm$. Finally, the proof-of-concept experiment demonstrated the potential of Si_3N_4-TiN composites as robust and electroconductive substrates for depositing conductive diamond electrodes. This was achieved by successfully depositing conductive diamond films on Si_3N_4-TiN substrates using the Hot Filament Chemical Vapor Deposition (HFCVD) technique.

II.1.1. Introduction

The remarkable physical and mechanical properties of silicon nitride (Si_3N_4) ceramics, including high hardness, excellent wear resistance, chemical stability, thermal resistance, good strength, fracture toughness, low density, and low coefficient of thermal expansion, make Si_3N_4 a highly attractive material for a wide range of applications (1). This material has been utilized in various applications, including the production of cooking plates (1, 2), cutting tools (3), mechanical seals (4), as well as metallurgical components and metal forming devices (5). Additionally, it has found applications in automotive parts, aircraft engines, and gas turbines (6, 7), electronic components (8), space technology (9), ball bearings (10), and prosthetic devices (11, 12).

Silicon nitride can exist in three distinct crystalline structures: α-Si_3N_4 and β-Si_3N_4, which are formed under normal nitrogen pressure, and the γ modification, produced at high temperatures above 2000 K and pressures exceeding 15 GPa, also referred to as c-modification in analogy to the cubic boron nitride (c-BN) structure (13). The α and β phases are hexagonal and consist of SiN_4 tetrahedra connected at the corners, where each nitrogen atom belongs to three tetrahedra (14). However, the c lattice parameter differs between these phases, with the β phase possessing only one layer of SiN_4 tetrahedra. In contrast, the α phase contains two layers that are shifted with respect to each other, resulting in a doubling of the c-parameter in the α unit cell (15). The α-modification is commonly present in Si_3N_4 powders, while the β-modification is found mainly in Si_3N_4 ceramics (16). The α-Si_3N_4 phase is stable only at temperatures below 1450ºC, and during sintering, it becomes metastable and transforms irreversibly to the β-Si_3N_4 phase through dissolution-reprecipitation mechanisms (17, 18).

The low atomic mobility during the sintering of Si_3N_4 is attributed to its predominantly covalent-bond nature, requiring the addition of sintering aids to promote densification (17). Si_3N_4 densification without additives can only be achieved under high pressures and temperatures (19). Sintering aids facilitate densification by reacting with SiO_2 present on the surface of Si_3N_4 powders to form a liquid phase at temperatures above 1500ºC (1). Previous studies have used a range of oxides, including Y_2O_3, Al_2O_3, SiO_2, MgO, CeO_2, Nd_2O_3, and ZrO_2 as sintering aids for Si_3N_4 ceramics (20-28), but the most efficient and commonly used sintering aids are Y_2O_3 and Al_2O_3 (29, 30).

The liquid phase sintering of Si_3N_4 involves three distinct stages (1). During the first stage, sintering additives react with SiO_2 present on the surface of Si_3N_4 particles, forming a eutectic melt that promotes the rearrangement of α-Si_3N_4 particles by capillary forces. In the second stage, β-Si_3N_4 precipitates due to the dissolution of α-Si_3N_4 followed

by diffusion of Si and N through the liquid phase. Finally, in the third phase, β-Si_3N_4 grains grow and coalesce, reducing or eliminating residual porosity (31, 32). After cooling, the resulting microstructure of Si_3N_4 ceramics comprises elongated β-Si_3N_4 grains with a high aspect ratio, surrounded by grain boundaries consisting of amorphous or partially crystallized secondary phases, such as silicates or silicon oxynitrides, that form from the solidification of the liquid phase (33). However, the presence of solidified liquid phase can negatively impact properties such as wear resistance, thermal resistance, and hardness (1). Thus, the starting powder mixture should contain minimal sintering aids to achieve densification without sacrificing mechanical and thermal properties. In addition, the final properties of Si_3N_4 ceramics are influenced by factors such as the quality of starting powders, type of crucibles, powder beds, and furnace atmospheres used during sintering (1).

In order to improve the mechanical properties, more specifically strength and fracture toughness, of Si_3N_4-based ceramics, researchers have turned to reinforcing these ceramics with particulates (34), platelets (35), and whiskers (36). However, obtaining fully dense final products with whisker and platelet reinforcements is challenging and can lead to technical difficulties and high production costs (37). Consequently, particle reinforcement has gained increased attention, which led to the development of electroconductive Si_3N_4-based ceramics that incorporate electrically conductive phases like carbides (TiC) (38), borides (TiB_2, ZrB_2) (39, 40), and nitrides (TiN) (41-43). The ideal particle reinforcement should have a thermal expansion coefficient and elastic modulus values similar to the matrix and be chemically compatible (44). TiN is an adequate candidate for Si_3N_4 particle reinforcement due to its good thermal and electrical conductivity, thermal stability, low density, high hardness, mechanical strength, wear resistance, lubricating characteristics, high melting temperature, and chemical inertness (45). In addition, mixtures of Si_3N_4 and TiN demonstrate chemical compatibility and stability across a broad range of temperatures and nitrogen pressures (1, 46). Therefore, TiN is favorable for reinforcing Si_3N_4 matrixes to produce electroconductive Si_3N_4-based ceramics.

Various processing routes have been explored to fabricate Si_3N_4-TiN composites over the years. The most used approach involves mixing Si_3N_4 and TiN powders with sintering additives for liquid phase sintering. Pressureless (3, 41, 47), hot pressing (3, 41, 48), gas-pressure (41, 49, 50), and spark plasma (51-53) sintering have been used to sinter Si_3N_4-TiN bulk ceramics, with pressureless and hot pressing being the most frequently employed methods. Pressureless sintering is a cost-effective approach, while hot

pressing typically yields ceramics with superior mechanical properties and requires lower amounts of sintering additives (1). However, it is expensive and limited to simpler geometries (1). *In-situ* reaction bonding, which involves the nitridation of Si and Ti powders with sintering additives, is another alternative route for producing Si_3N_4-TiN composites (54). This process can also be based on the nitridation of powder mixtures of Si_3N_4 and TiO_2 (48). Carbothermal reduction nitridation from rutile and quartz has been identified as a low-cost method for preparing Si_3N_4-TiN composite powders (55). Furthermore, Si_3N_4-TiN coatings can be synthesized by chemical vapor deposition (CVD) using gas mixtures such as NH_3, $SiCl_4$, $TiCl_4$, and H_2 (56).

Manufacturing Si_3N_4-TiN composites presents a significant challenge in achieving an optimal TiN content that balances high electrical conductivity characteristics and mechanical properties (57). This balance is essential for substrate materials used in depositing conductive chemically vapor-deposited diamond films that serve as electrodes in electrochemical applications. Especially for large-scale water treatment, these electrodes would be subjected to harsh chemical and erosive environments (58). Several studies have demonstrated the effectiveness of using diamond-based electrodes for water remediation in laboratory and pilot tests (59-62). However, the scalability and durability of these electrodes for scale-up applications pose significant challenges, primarily due to the absence of a suitable substrate (63). The primary cause of diamond electrode failure is the delamination of film from the substrate, which occurs due to inadequate adhesion (63). In preparing diamond electrodes for such applications, the substrate serves two primary functions: facilitating current flow through the electrode assembly and providing mechanical stability to the diamond film (64). Si_3N_4 is an ideal material for CVD diamond growth due to its high affinity and compatibility with the deposition process and its similar coefficient of thermal expansion to diamond (0.7-2.0 × 10^{-6} 1/C°) (65-68), which promotes strong adhesion (69). Therefore, the Si_3N_4-TiN composites could offer a suitable balance of conductivity, mechanical properties, high affinity for CVD diamond growth, chemical stability, and oxidation resistance, meeting the ideal substrate material criteria for producing diamond electrodes with superior service life.

In this study, we investigate the development of fully dense Si_3N_4-TiN ceramic composites with favorable combinations of low electrical resistivity and excellent mechanical properties. To achieve this objective, we tested various pressureless sintered compositions of a Si_3N_4 powder matrix containing Al_2O_3 and Y_2O_3 as sintering aids, mixed with TiN powder at volumes ranging from 21 to 30%vol TiN. This research

aims to identify a composition with the lowest amount of TiN that provides sufficient conductivity without compromising the composites' mechanical properties while keeping the production cost in check. We characterized the samples using Vickers microhardness, fracture toughness, elastic modulus, shear modulus, bending strength, thermal conductivity, X-ray diffraction, scanning electron microscopy, and electrical resistivity. The developed composites are intended to be used as substrates for conductive diamond chemical vapor deposition.

II.1.2. Materials and Methods

The composition of the Si_3N_4 matrix powder and the corresponding sintering cycles were determined based on the prior research works carried out by our group (3, 70-72). The Si_3N_4 matrix comprises a powder blend consisting of 89.3%wt. Si_3N_4 (Grade M11, H.C. Starck, Germany), 7.0%wt. Y_2O_3 (Grade C, H.C. Starck, Germany), and 3.7%wt. Al_2O_3 (CT 3000 SG, Alcoa, USA). The composites were prepared by substituting the matrix with TiN powder (Grade B, H.C. Starck, Germany) at varying volume fractions of 21, 23, 25, 27, and 30%vol. Details on the powder properties, including particle size, specific surface area, and purity, are presented in Table II.1.1.

Table II.1.1. Properties of the powders used in the study.

Powder	Supplier	Particle Size d_{50} (µm)	Specific Surface Area (m^2/g)	Purity
Si_3N_4	H.C. Starck	0.5 – 0.7	12 – 15	Alpha-phase >90%
Y_2O_3	H.C. Starck	0.6 – 0.9	10 – 16	Y_2O_3/TREO* >99.95%
TiN	H.C. Starck	2.0 – 4.0	-	N_2 min. 20% O max. 1.1%
Al_2O_3	Alcoa	0.7**	7**	>99.85%

**TREO = Total Rare Earth Oxides*
***Average*

The powder mixture, Si_3N_4 balls, and 2-propanol were loaded into agate jars, then inserted into a planetary mill, and set to rotate at 200 rpm for 8 hours. The obtained powder slurry underwent a screening process using a 500-mesh sieve. Subsequently, the slurry was dried in an oven at 100ºC for 24 hours. Disc-shaped samples with diameters of 20 mm and 59 mm were prepared through a two-step pressing process. The powder mixtures were first cold uniaxially pressed at a pressure of 3 tons for 2 minutes. Then, they were cold isostatically pressed at a pressure of 200 MPa for 15 minutes. Pressureless sintering was performed in a graphite furnace, specifically a

closed graphite crucible. The powder bed utilized during the sintering process comprised a mixture of 50% Si_3N_4 matrix with sintering aids of Al_2O_3 and Y_2O_3, along with 50% boron nitride (BN, Grade A01, H.C. Starck, Germany). This composition was employed to prevent direct contact with the graphite crucible walls and to minimize the decomposition of the Si_3N_4 powder.

The Si_3N_4 matrix samples were sintered at 1700ºC for 3 hours in an N_2 atmosphere (0.1 MPa) at a heating rate of 10ºC/min. The Si_3N_4-TiN composites were sintered at 1750ºC, at the same heating rate and atmosphere for 5 hours to guarantee full densification. The N_2 flow served two important purposes: to prevent the thermal decomposition of Si_3N_4 by shifting the equilibrium given by Eq. II.1.1 to the left and to prevent the oxidation of TiN powder to TiO_2, which starts to oxidize at around 800°C in air (45).

$$Si_3N_4 \rightleftarrows 3Si_{(g,l)} + 2N_{2(g)} \qquad \textbf{Eq. II.1.1}$$

Following densification, sample densities were determined using the Archimedes method, involving the immersion of the samples in distilled water. The samples were characterized through Vickers microhardness, which involved indentations applying loads of 2 kgf for 10 seconds. The samples' elastic modulus (E) and shear modulus (G) were determined using the resonant frequency method (MK5i, GrindoSonic, Belgium). The latter was preferred due to its accuracy and non-destructive nature. The elastic modulus of the samples was compared with the calculated maximum (Voight) (73) and minimum (Reuss) (74) theoretical limits. These calculations were performed using a reference value of 390 GPa for the elastic modulus of TiN (75). The fracture toughness (K_{IC}) was evaluated by applying 10 kgf loads for 10 seconds and measuring the length of the cracks using the formula established by Antis *et al.* (76), represented by Eq. II.1.2:

$$K_{IC} = 0.016\left(\frac{E}{H}\right)^{1/2}\left(\frac{P}{c^{3/2}}\right) \qquad \textbf{Eq. II.1.2}$$

Where H is the hardness (GPa), E is the elastic modulus (GPa), P is the indentation load (N), and c is the crack length (m). This method was selected for its simplicity, as it requires only conventional hardness equipment and does not demand complex testing apparatus. Three-point bending tests were performed following the ISO 6872:2015

standard (77). A universal testing machine (Autograph AG-IS, Shimadzu, Japan) was used, with a crosshead feed rate of 1 mm/min and a 5 kN load cell.

X-ray diffraction (XRD, PANalytical, X'Pert, United Kingdom) was employed with Cu Kα radiation in 2theta-theta mode to analyze the crystalline phase composition. The densified ceramics underwent a series of post-processing steps for microstructural analysis. Initially, they were subjected to grinding and polishing. Subsequently, plasma etching (K1050X, Emitech, France) using CF_4 was performed for 120 seconds. The microstructures of the ceramics were then examined using Scanning Electron Microscopy/Energy Dispersive Spectroscopy (SEM/EDS, SU-70 EDS, Hitachi, Japan). The electrical resistivity was measured with a Four Point Probe configuration at room temperature using an in-house electrical property measuring apparatus. A thermal conductivity analyzer (C-Therm, TCi, Canada) was used to evaluate the thermal conductivity of the samples at room temperature.

Finally, as a proof of concept, conductive diamond films were deposited on silicon nitride-titanium nitride (Si_3N_4-TiN) substrates using Hot Filament Chemical Vapor Deposition (HFCVD). The resulting films were characterized using several techniques. Scanning Electron Microscopy/Energy Dispersive Spectroscopy (SEM/EDS, SU-70 EDS, Hitachi, Japan) was employed to analyze the morphology and elemental composition of the films. Micro-Raman Spectroscopy, utilizing a 442 nm laser line (Jobin-Yvon LabRam HR, Horiba, Japan), was used to assess the diamond quality and residual stress of the deposited films. Electrical resistivity measurements were performed using a homemade apparatus to determine the films' resistivity. Additionally, the adhesion of BDD films to Si_3N_4-TiN substrates was evaluated by indentation with a Brale indenter in a universal testing machine (Z020, Zwick/Roell, Germany). The applied loads ranged from 100 to 1200 N. The interfacial crack resistance parameter was estimated by measuring the reciprocal slope of the load-crack radius curve, $d_{Load}/d_{Crack\ Radius}$ (78).

II.1.3. Results and discussion

All samples exhibited a densification percentage greater than 99%, and the average shrinkage rate along the samples' largest dimension was 22.7%, as indicated in Table II.1.2. The determination of the densification percentage was accomplished by applying the rule of mixtures to calculate the theoretical density value of the samples. The theoretical density of the Si_3N_4 matrix was calculated as 3.27 g/cm^3.

Table II.1.2. Densification and shrinkage results of the Si_3N_4 and Si_3N_4-TiN samples.

Sample	TiN (%vol)	Sintering	Shrinkage* (%)	Density (g/cm³)	Densification (%)
SN	0%	1700°C - 3h - 10°C/min N_2 0.1 MPa	25%	3.26	99.62%
SNTN21	21%	1750°C - 5h - 10°C/min N_2 0.1 MPa	22%	3.69	99.04%
SNTN23	23%	1750°C - 5h - 10°C/min N_2 0.1 MPa	22%	3.74	99.55%
SNTN25	25%	1750°C - 5h - 10°C/min N_2 0.1 MPa	22%	3.77	99.60%
SNTN27	27%	1750°C - 5h - 10°C/min N_2 0.1 MPa	22%	3.83	99.75%
SNTN30	30%	1750°C - 5h - 10°C/min N_2 0.1 MPa	23%	3.86	99.59%

**Along the largest dimension*

The mechanical and electrical properties of Si_3N_4 and Si_3N_4-TiN were characterized as a function of the percentage of TiN volume, as presented in Table II.1.3, Figure II.1.1, and Figure II.1.2. A trend of increasing fracture toughness (K_{IC}) with increasing TiN volume fraction was observed, consistent with previous findings in the literature (41, 47, 50, 79). The difference in thermal expansion coefficient between the TiN and the Si_3N_4 generates a compressive force from the surrounding Si_3N_4 grains in the TiN agglomerates present in the composite microstructure after sintering, which may contribute to an increase in fracture toughness (47). In addition, other toughening mechanisms in Si_3N_4-TiN composites could be crack deflection due to the elastic modulus mismatch between the TiN and Si_3N_4 and microcracking toughening related to the TiN particle size (41, 50, 79). Although most of the studied compositions experimentally determined elastic modulus values were slightly outside the calculated theoretical limits, they still followed the general trend of increasing with increasing TiN content.

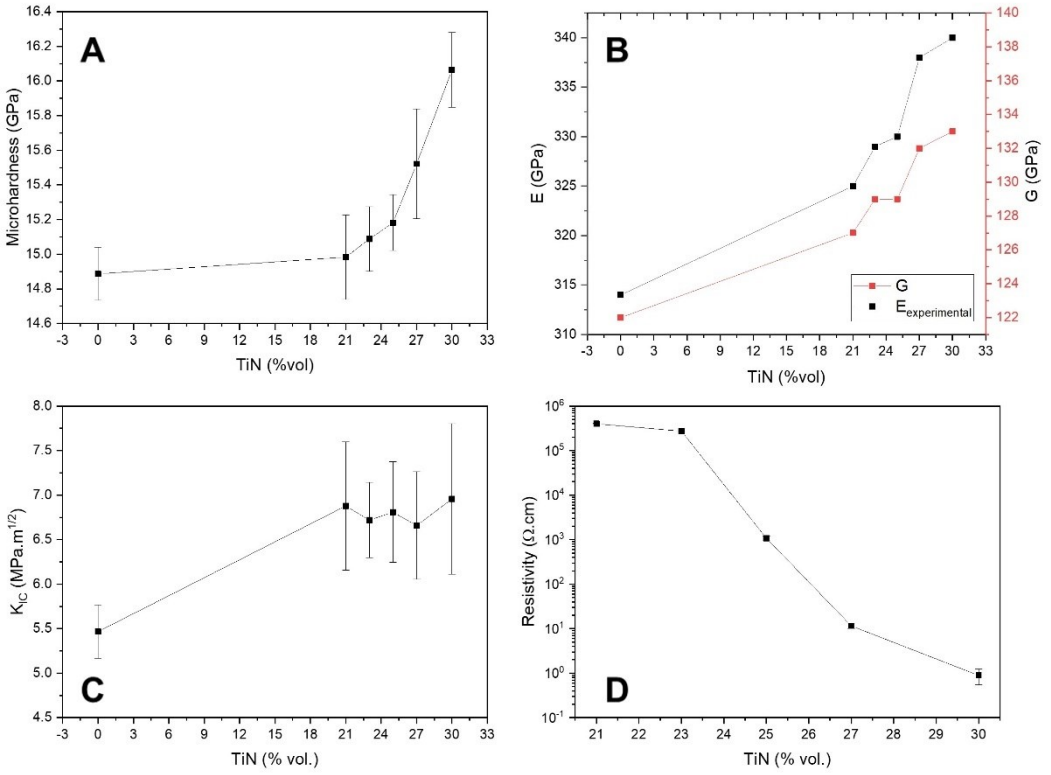

Figure II.1.1. Mechanical and electrical characterization of Si_3N_4-TiN composites as a function of added volume fraction of TiN: (a) Microhardness; (b) Elastic and shear modulus; (c) Fracture toughness; (d) Resistivity.

The TiN starting powder particle size may play an important role in the final mechanical properties of Si_3N_4-TiN composites. Bellosi *et al.* have observed that the Young modulus and the thermal expansion coefficient of the composites increase with the addition of TiN particles regardless of the sintering route and their particle size and distribution (41). However, these factors strongly influenced fracture toughness, hardness, and flexural strength. Bellosi *et al.* found that hardness and fracture toughness were higher in the composites with coarse TiN starting powder particles. However, the flexural strength of these materials was lower than that in composites with smaller TiN particles (41). The results for bending strength (Figure II.1.2) agree with the literature (41, 80, 81). The values are roughly independent of TiN content in the studied range, except for SNTN25, which appears to be an outlier. This may be due to some problem in the manufacturing or sample preparation process. The bending strength seems to decrease slightly with the addition of TiN up to a certain limit and then increase again. This effect was also observed by Belosi *et al.* for Si_3N_4-TiN compositions ranging from 0 to 40%vol TiN

sintered by hot pressing (41). Such variations in the strength are believed to be related to the secondary phase content (41, 82).

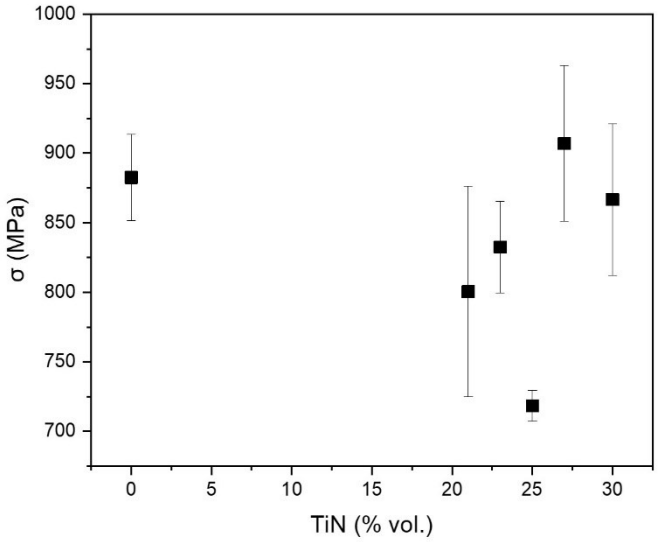

Figure II.1.2. Bending strength of Si_3N_4-TiN composites as a function of added volume fraction of TiN.

The electrical conductivity of Si_3N_4–TiN composites showcases a percolative nature, marked by a substantial increase in conductivity when reaching a particular concentration of TiN, known as the percolation threshold or percolation concentration (57). The percolation threshold was observed to occur between 23 and 27%vol TiN, where the composite transitioned from an insulator to a conductive material. The transition from resistivities of 10^{13} Ω.cm to resistivities down to the order of 10^{-1} Ω.cm was achieved due to the differences in conductivity of Si_3N_4 ($10^{13\text{-}14}$ Ω.cm (45)) and TiN (20 ± 10 x 10^{-6} Ω.cm (45)). The percolation limit is reached when the number of TiN particles added to the Si_3N_4 matrix is enough so the equiaxed TiN grains can form a continuous conductive network. The TiN content, and consequently the degree of connectivity of the TiN grains, is the main factor affecting such network formation. However, the percolation concentration limit shows a significant variation in the literature since it is also influenced by other parameters such as starting powders particle size, shape and distribution, types of additives, sintering time and conditions, resulting microstructure and presence of the secondary intergranular phase formed during liquid phase sintering (52, 83, 84). Smaller TiN starting powder particle size is associated with

lowering the percolation concentration (37). In addition, Guo *et al.* observed that the electrical resistivity of Si_3N_4–TiN samples sintered at 1600ºC by hot pressing and spark plasma sintering differs for four orders of magnitude (52).

Incorporating a conductive phase in Si_3N_4 presents the opportunity to utilize electrical discharge machining (EDM) to produce complex-shaped hard ceramics. Previously, the high resistivity of Si_3N_4 made this manufacturing technique impractical. This advancement becomes particularly valuable considering the challenges, high costs, and limitations of machining hard ceramics using conventional methods, which may render the desired geometries difficult, expensive, or unachievable (45). This advantage is particularly beneficial for electrochemistry applications as it enables the creation of electrodes featuring complex designs to improve performance, for example, by increasing reaction surface areas. In the EDM process, the material is removed by erosion due to the application of short-duration electric discharges between an electrode and the workpiece (85). According to Schubert *et al.*, electrical discharge machining requires a minimum electric conductivity of about 10^{-2} Ω.cm (86). Contrary to Schubert *et al.*'s statement, it has been observed that composites with resistivities as high as 7.5 Ω.cm can be successfully machined using EDM (3).

The SEM micrographs in Figure II.1.3 depict dark grey β-Si_3N_4 grains with a high aspect ratio, surrounded by a white intergranular secondary phase. An increase in TiN content leads to a decrease in β-Si_3N_4 grain size and an increase in the distribution and interparticle contact of TiN grains (in light grey). These changes contribute to forming an electroconductive network with lower resistivities, as demonstrated in Table II.1.3. As reported by Zivkovic *et al.*, larger Si_3N_4 grains and their strong anisotropy inhibit the formation of continuous TiN grain connections, leading to higher resistivity values (57). However, for higher amounts of TiN, the Si_3N_4 grain growth influence appears negligible due to the higher concentration of TiN that forms a better-connected conductive network (57). When comparing the microstructure of composites with varying amounts of TiN, the growth-inhibiting effect of TiN particles becomes more evident. The composite underwent a distinct sintering cycle compared to the matrix, requiring a longer sintering time (from 3 hours to 5 hours) and higher temperature (from 1700ºC to 1750ºC) to guarantee full densification. In typical scenarios, such conditions would promote greater growth of β-Si_3N_4 grains. Surprisingly, the β-Si_3N_4 grain size remains similar between the matrix and the Si_3N_4-TiN composite containing 30%vol. TiN. However, when comparing the composite with 21%vol. TiN to the one with 30%vol. TiN, it is evident that the β-Si_3N_4

grains are larger in the composite with a lower TiN content. These observations highlight the growth-hindering effect exerted by the TiN particles.

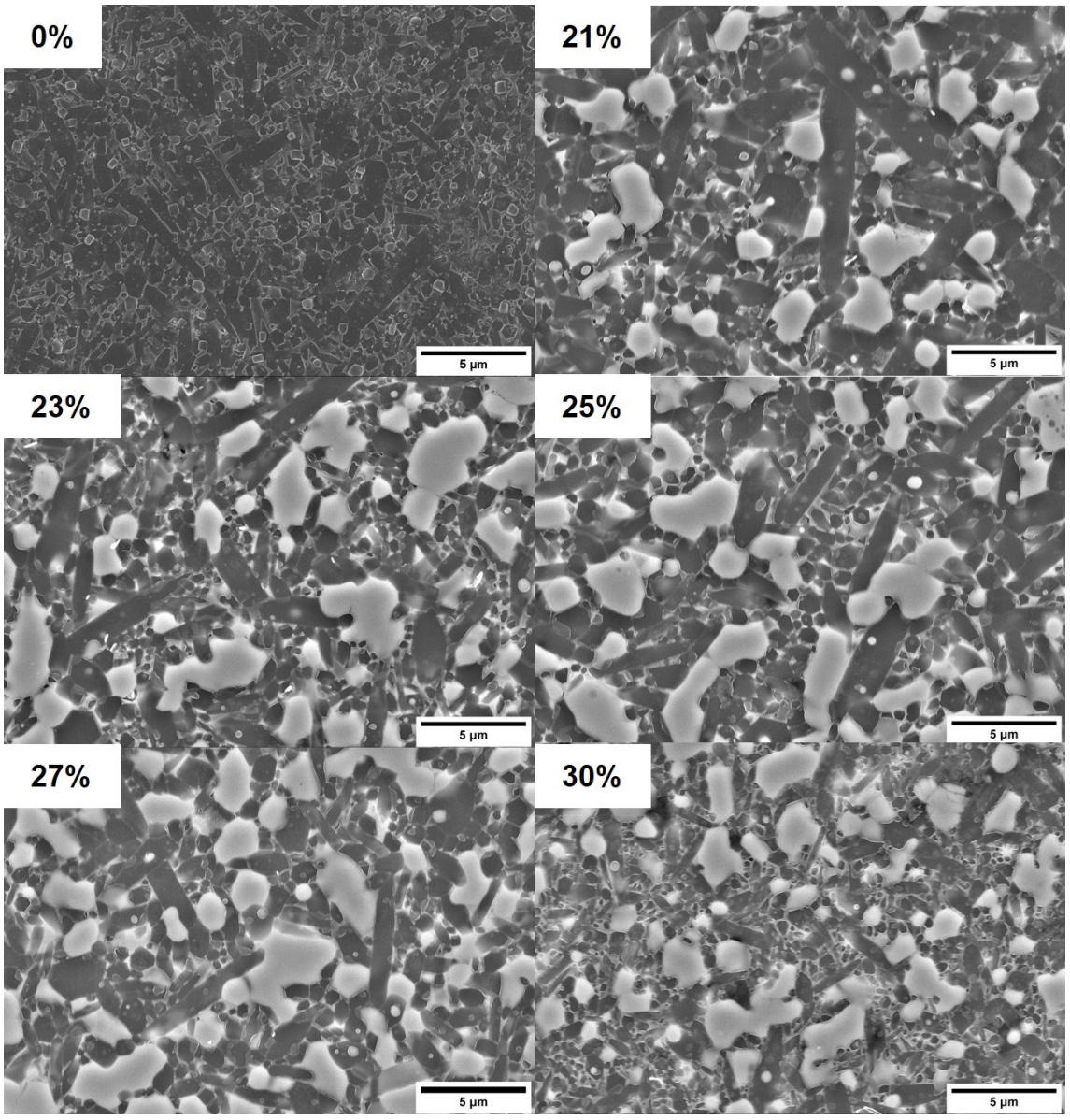

Figure II.1.3. Microstructures of Si_3N_4 and Si_3N_4-TiN with 21, 23, 25, 27, and 30%vol TiN.

Table II.1.3. Properties of the obtained Si_3N_4 and Si_3N_4-TiN ceramics: hardness, fracture toughness (K_{IC}), calculated upper (Voight) and lower (Reuss) limits of the elastic modulus, measured elastic modulus (E), shear modulus (G), bending strength (σ) and resistivity.

TiN (% vol)	Hardness (GPa)	K_{IC} $(MPa.\sqrt{m})$	E [Voight][a] (GPa)	E [Reuss][b] (GPa)	E (GPa)	G (GPa)	σ (MPa)	Resistivity (Ω.cm)
0%	14.89 ± 0.15	5.47 ± 0.30	314	314	314	122	882.61 ± 31.15	1.00×10^{13}
21%	14.98 ± 0.24	6.88 ± 0.72	330	327	325	127	800.58 ± 75.62	4.17×10^{5}
23%	15.09 ± 0.19	6.72 ± 0.42	331	329	335	131	832.5 ± 32.73	3.19×10^{5}
25%	15.18 ± 0.16	6.81 ± 0.57	333	330	330	129	718.49 ± 11.05	9.27×10^{2}
27%	15.52 ± 0.32	6.66 ± 0.60	335	331	340	134	907.01 ± 56.02	1.11×10^{1}
30%	16.06 ± 0.22	6.96 ± 0.84	337	333	340	133	866.84 ± 54.49	8.90×10^{-1}

[a] $E_{Voight} = E_1V_1 + E_2V_2$ *(73)*
[b] $1/E_{Reuss} = V_1/E_1 + V_2/E_2$ *(74)*

The observed increase in hardness values in the composites can be attributed primarily to the higher intrinsic hardness of TiN (18-21 GPa) (45). According to Petzow, the hardness of Si_3N_4 ceramics increases with decreasing grain boundary phase and grain size (1). In this study, TiN replaced the matrix in volume percentages, which led to a lower residual grain boundary phase. The lower residual grain boundary phase may have had a slight effect on the hardness of the composites. However, the primary factor contributing to the increased hardness is likely the higher hardness of TiN itself.

Furthermore, the composites containing higher TiN amounts exhibited smaller Si_3N_4 grain sizes (Figure II.1.3), which may have also contributed to the higher hardness values. However, there are controversies in the literature regarding the increase in hardness with increased TiN amounts, as some studies reported an opposite behavior (3, 41, 48, 49, 87). In contrast, others observed the same increase in hardness with the addition of TiN (37, 50, 51, 88). These differences may arise from several reasons, such as the starting powders' quality, size and shape, sintering method (e.g., pressureless, hot pressing, spark plasma, gas-pressure), sintering cycle, and composition of the sintering additives.

In Figure II.1.4, the phase composition of the samples is presented. The microstructure of the Si_3N_4 matrix primarily consists of β-Si_3N_4, accompanied by a secondary oxynitride

phase (Y_2SiAlO_5N). The oxynitride phase formed due to the liquid phase crystallization during the sintering process. The absence of the α-Si_3N_4 phase suggests that the transformation of α-Si_3N_4 to β-Si_3N_4 was complete and irreversible during liquid phase sintering. The XRD spectra baseline display slight dislocations, indicating that some liquid phase might have remained in the microstructure as a glassy phase after sintering. The Si_3N_4-TiN composites exhibit β-Si_3N_4 and TiN phases and traces of yttrium oxynitrides ($Y_2Ti_2O_{5.5}N$).

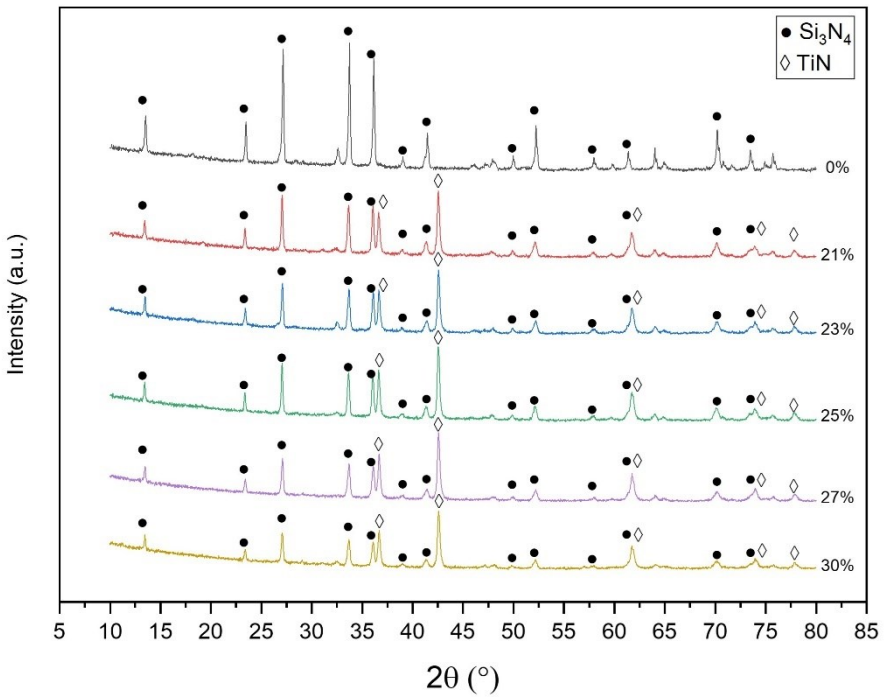

Figure II.1.4. X-ray diffraction of the Si_3N_4 matrix and Si_3N_4-TiN composites.

Figure II.1.5 presents the results of the thermal conductivity measurements conducted on the Si_3N_4-TiN composites. According to the literature, the thermal conductivity of TiN ranges from 28.8-44.0 W/mK (89-91), while the Si_3N_4 matrix exhibited a thermal conductivity value of 18.2 W/mK. The thermal conductivity of the Si_3N_4-TiN composite increased as the TiN content increased, which is expected since TiN has a higher thermal conductivity than the Si_3N_4 matrix. Notably, the composites with the highest TiN content approached the thermal conductivity value of pure TiN. Watari *et al.* reported that the thermal conductivity of Si_3N_4 ceramics at room temperature is not influenced by grain size, but rather by the internal defect structure of the grains, such as point defects and

dislocations (92). Despite the differences, all composite materials exhibited low thermal conductivities, which is favorable for the deposition of CVD diamond. A substrate material with low thermal conductivity will be able to maintain substrate temperature during the CVD process and the cooling step, thereby helping to reduce residual stresses in the diamond film caused by the mismatch in the coefficient of thermal expansion between the substrate and the diamond film.

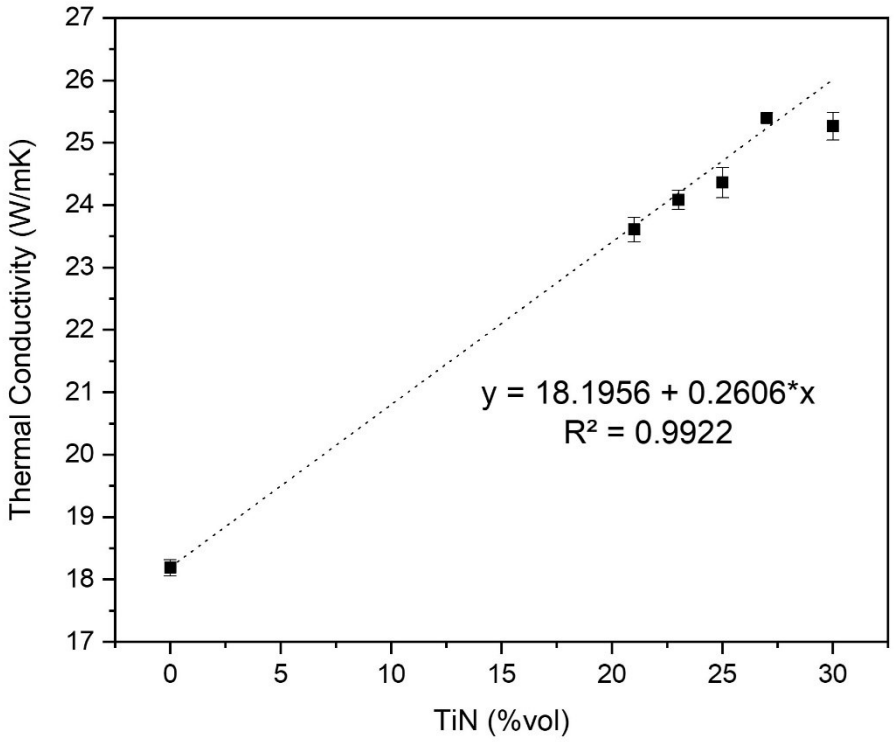

Figure II.1.5. Thermal conductivity at room temperature as a function added %vol TiN.

Table II.1.4 compares the SNTN30 sample outcomes with those reported in the literature for specimens with 30%vol TiN added to the Si_3N_4 matrix. The value of 40%wt was considered equivalent to a 30%vol TiN (~39.6%wt) for articles that expressed the TiN content in weight percentage. All SNTN30 outcomes, including relative density, hardness, fracture toughness, elastic modulus, and resistivity, fall within the range of reported literature results. Significant variations in Si_3N_4-TiN composite properties are evident, depending on sintering methods, temperatures, and the composition of the sintering additives. Hardness and resistivity show the most significant deviations. The

microstructure strongly influences these properties. Variations in fracture toughness are not solely related to the microstructure but can exhibit minor divergences based on the chosen K_{IC} determination method.

Table II.1.4. Comparison of the obtained results of Si_3N_4-TiN with 30%vol TiN with the results from the literature.

Sintering method	Sintering Additives	Relative Density (%)	Hardness (GPa)	K_{IC} $(MPa.\sqrt{m})$	Elastic Modulus (GPa)	Resistivity (Ω.cm)	Ref.
Pressureless 1750ºC	3.7% Al_2O_3 7.0% Y_2O_3	99.6%	16.06 ± 0.22	6.96 ± 0.84	340	8.9 x 10^{-1}	**This work (SNTN30)**
Pressureless 1750ºC	3.7% Al_2O_3 7.0% Y_2O_3	-	~ 15.0	~ 7.6	-	~ 6 x 10^{-1}	(3)
Pressureless 1780°C	10.0% Y_2O_3	~ 99.0%	12.0-13.5	~ 6.7	-	~ 3 x 10^{-1}	(47)
Pressureless 1850°C	3.0% Al_2O_3 8.0% Y_2O_3	97.6%	11.1 ± 0.6	-	-	4.7 x 10^{-2}	(41)
Pressureless 1760°C	10.0% La_2O_3-AlN	96.0%	13.6	8.7	-	7.0 x 10^{-1}	(93)
Gas-pressure 1850°C	3.0% Al_2O_3 8.0% Y_2O_3	100.0%	15.1 ± 0.3	7.3 ± 0.1	342	4.7 x 10^{-3}	(41)
Gas-pressure 1850°C	2.0% Al_2O_3 6.0% Y_2O_3	95.6%	11.35	-	-	1.5 x 10^{1}	(49)
Hot Pressing 1650ºC	3.7% Al_2O_3 7.0% Y_2O_3	-	~ 16.0	~ 7.2	-	~ 4	(3)
Hot pressing 1700ºC	2.5% Al_2O_3 4.5% Y_2O_3	>98.0 %	-	-	-	1.9 x 10^{-1}	(52)
Hot Pressing 1800°C	3.0% Al_2O_3 8.0% Y_2O_3	99.6%	19.2 ± 0.4	9.0 ± 1.0	343	9.4 x 10^{-2}	(41)
Spark plasma 1700ºC	2.5% Al_2O_3 4.5% Y_2O_3	>98.0%	-	-	-	~ 10^{2}	(52)
Spark plasma 1600ºC	No additives	~ 97.0%	11.5 ± 1.9	-	-	~ 10^{-3}	(94)

** Approximate values (~) were estimated from the graphs in the respective articles through the software WebPlotDigitizer (95).*

To prevent delamination during electrode operation, an ideal conductive diamond substrate should possess a resistivity value close to the diamond film. In electrochemical applications, the optimal electrochemical performance is expected from diamond films with metal-like conductivity (96) with resistivities ranging between 10^{-1} and 10^{-3} Ω.cm (97-100). Among the studied compositions, the SNTN30 sample exhibits the closest resistivity value to this range, which was over ten times lower than the second lowest resistivity sample (SNTN27). Furthermore, the SNTN30 composition exhibited the most

favorable mechanical properties. Hence, based on our investigation, replacing the Si_3N_4 matrix with 30%vol TiN is deemed the most suitable choice. To further decrease the composite resistivity to the order of 10^{-3} Ω.cm without hindering mechanical properties, future studies should investigate compositions with volume fractions exceeding 30% or modifications to the production process, such as changes in the pressing method, sintering method, and cycle, starting powder particle size, or sintering additives composition, for example. In addition, cost-effectiveness studies should be conducted to assess the impact of increasing TiN content on the final production cost of Si_3N_4-TiN composites.

To assess the feasibility of depositing high-quality diamond films with low resistivity on the SNTN30 substrates, we conducted a boron-doped diamond (BDD) film deposition using an HFCVD reactor. The following parameters were employed during the experiment: a deposition duration of 5 hours, a pressure of 100 mbar, a total gas flow rate of 220 sccm, CH_4/H_2 ratio of 0.02, Ar/H_2 ratio of 0.10, B_2O_3/CH_4 ratio of 0.625, and substrate temperatures ranging from 800 to 850°C. The filaments' temperature was maintained between 2180 and 2220°C.

After the deposition, the BDD films' morphology, film thickness, and grain size were analyzed using Scanning Electron Microscopy (SEM) and Energy-Dispersive X-ray Spectroscopy (EDS). The results (Figure II.1.6.a and Figure II.1.6.b) revealed that the BDD film had a 4.31 ± 0.16 µm thickness. The mean linear intercept method (ISO Standard No. 4499-2:2020) (101) was employed to determine the grain size, yielding a value of 1.50 ± 0.07 µm. The film exhibited a complete coating on the substrate without any observable cracks or voids.

Furthermore, the diamond quality of the BDD film was evaluated using Raman spectroscopy (Figure II.1.6.c). The analysis demonstrated that the resulting film exhibited favorable diamond quality and low residual stress values (Table II.1.5), indicating its potential for electrochemical applications. Electrical resistivity measurements were conducted to evaluate the conductivity of the deposited diamond films. The results revealed a film resistivity of 4.0 x 10^{-3} Ω.cm, indicating a relatively low resistivity value.

Table II.1.5. Information obtained from the Raman spectra analysis of the BDD films deposited on Si_3N_4-TiN.

Raman Peak	Center (cm^{-1})	FWHM (cm^{-1})	Integral Intensity (a.u.)	Residual Stress (GPa) [a]	I_D/I_G [b]
Diamond	1334.4	10.9	18508	-1.4	0.8
D-band	1350.0	73.7	7596		
G-band	1550.0	126.1	23847		

[a] *$\sigma r = -0.567 \times \Delta\vartheta$, where σr represents the residual stress and $\Delta\vartheta$ indicates the deviation of the diamond peak from the stress-free diamond peak position (1332 cm^{-1}) (102)*

[b] *The phase purity of the diamond film was assessed by calculating the ratio of the integral intensity of the diamond band ($I_{Diamond}$) to the integral intensity of the G band (I_G) (103)*

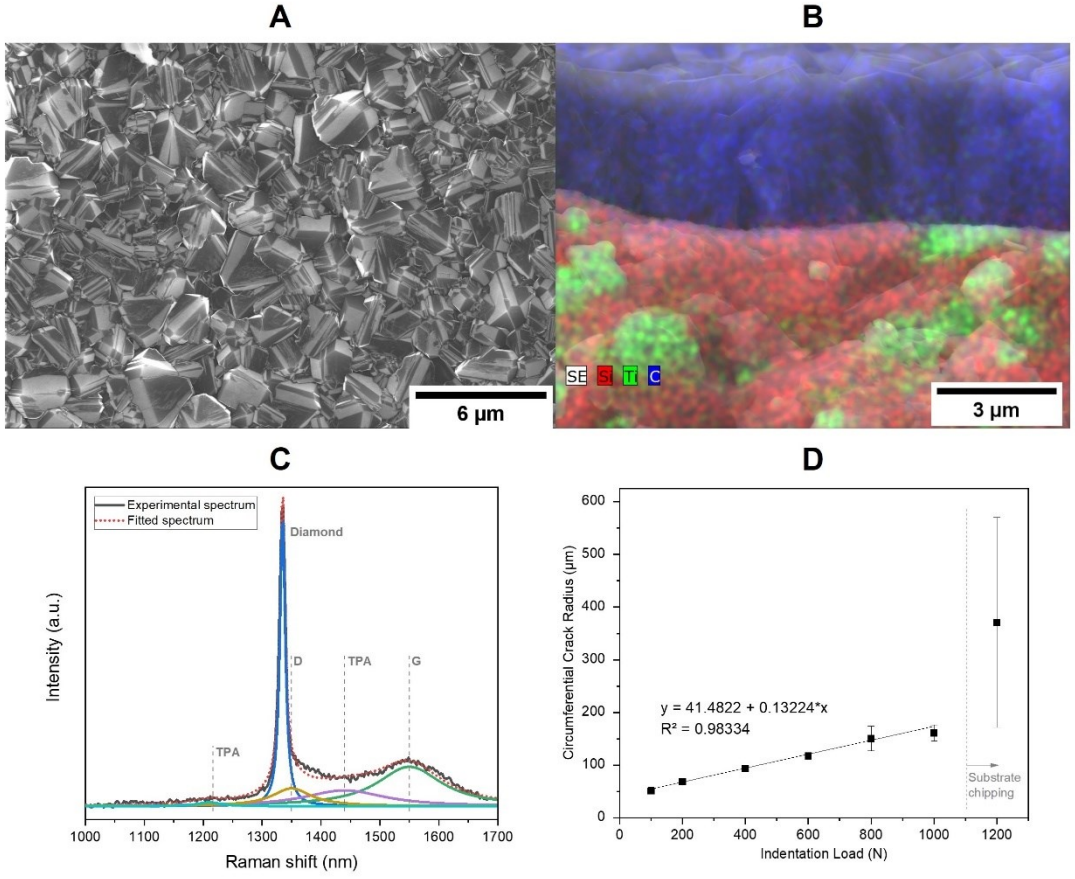

Figure II.1.6. (a) Plan view Scanning Electron Microscopy (SEM) image of a BDD film deposited on SNTN30; (b) Elemental mapping of the cross-section of the BDD film deposited on SNTN30, performed using Scanning Electron Microscopy with Energy-Dispersive X-ray Spectroscopy (SEM-EDS); (c) Raman spectroscopy analysis of the BDD films deposited over SNTN30; (d) Results of the adhesion strength test using a Brale indenter.

The adhesion of BDD films to SNTN30 substrates was evaluated (Figure II.1.6.d). The interfacial crack resistance parameter was measured, and the value was 7.54 ± 0.46 N μm^{-1}. This value is superior to those reported in the literature for diamond films deposited over Si_3N_4-based ceramics (78, 104). In a previous study, our group reported an interfacial crack resistance of 12 N μm^{-1} for CVD diamond deposited over Si_3N_4. However, this value was obtained with a diamond film thickness of 39 μm, approximately eight times thicker than the film studied in this work.

These findings substantiate that conductive diamond films suitable for electrochemical applications can be successfully grown on the Si_3N_4-TiN substrates. It is worth noting that by optimizing the HFCVD deposition conditions specifically for electroconductive Si_3N_4-TiN substrates, further enhancements in various characteristics of the BDD film, such as grain size, thickness, diamond quality, conductivity, and residual stress, can be achieved.

II.1.4. Conclusion

The present study has developed dense Si_3N_4-TiN composites with desirable mechanical and electrical properties for potential application as electroconductive ceramic substrates for CVD deposition of diamond electrodes. The composites were synthesized through pressureless sintering of mixtures of a Si_3N_4 matrix containing Al_2O_3 and Y_2O_3 as sintering aids with TiN powder at varying volume fractions. The resulting composites exhibited superior hardness, fracture toughness, elastic modulus, and thermal conductivity compared to the Si_3N_4 matrix. The electrical resistivity of the composites also decreased with increasing TiN volume fractions. The percolation threshold, where the behavior of the composites shifted from insulating to conductive, occurred when the volume of TiN changed from 23 to 27%. Our findings demonstrate that Si_3N_4-TiN composites containing volume percentages of TiN above 30% are promising substrate candidates for producing CVD diamond electrodes. The proof-of-concept experimental steps performed in this study demonstrated the feasibility of growing conductive diamond films on Si_3N_4-TiN substrates for potential use in electrochemical applications.

II.1.5. References

1. Petzow G, Herrmann M. Silicon Nitride Ceramics. In: Jansen M, editor. High Performance Non-Oxide Ceramics II. Structure and Bonding. Berlin, Heidelberg: Springer Berlin Heidelberg; 2002. p. 47-167.

2. Berroth K. Silicon Nitride Ceramics for Product and Process Innovations. Adv Sci Technol. 2011;65:70-7.

3. Almeida FA, Bóia H, Santos C, Monteiro J, Oliveira FJ, Silva RF. Electroconductive Ceramic Composites for Cutting Tools. Mater Sci Forum. 2006;514-516:638-42.

4. Duan W, Jia D, Cai D, Niu B, Yang Z, Zhou Y. A facile strategy for fabricating self-sealing dense coating grown in-situ on porous silicon nitride ceramics. J Eur Ceram Soc. 2021;41(3):2162-7.

5. Telle R, Muenstermann S, Beyer C. Design, Construction and Performance of Silicon Nitride Tool Parts in Steel Thixoforming. Solid State Phenom. 2006;116-117:690-5.

6. Drawin S, Justin JF. Advanced Lightweight Silicide and Nitride Based Materials for Turbo-Engine Applications. Aerospace Lab. 2011(3):p. 1-13.

7. Wang L, Snidle RW, Gu L. Rolling contact silicon nitride bearing technology: a review of recent research. Wear. 2000;246(1-2):159-73.

8. Robertson J. The Electronic Structure of Silicon Nitride. Recent Dev Condens Matter Phys. 631981. p. 239-45.

9. Torma PT, Sipila HJ, Mattila M, Kostamo P, Kostamo J, Kostamo E, *et al.* Ultra-Thin Silicon Nitride X-Ray Windows. IEEE Trans Nucl Sci. 2013;60(2):1311-4.

10. Yu D, Zhang X, Luo H, Liao D, Wu N. Effect of nozzle inlet parameters on the dry granulation atomization process of Si3N4 ceramic bearing balls. Int J Model, Simul, Sci Comput. 2021;12(06):23.

11. Bucciotti F, Mazzocchi M, Bellosi A. Perspectives of the Si3N4-TiN ceramic composite as a biomaterial and manufacturing of complex-shaped implantable devices by electrical discharge machining (EDM). J Appl Biomater Biomech. 2010;8(1):28-32.

12. Guedes e Silva C. Silicon nitride as biomaterial. New York: Nova Science Publishers, Inc.; 2012 01/01. 149-56 p.

13. Zerr A, Miehe G, Serghiou G, Schwarz M, Kroke E, Riedel R, *et al.* Synthesis of cubic silicon nitride. Nature. 1999;400(6742):340-2.

14. Mo S-D, Ouyang L, Ching WY, Tanaka I, Koyama Y, Riedel R. Interesting Physical Properties of the New Spinel Phase of Si3N4 and C3N4. Phys Rev Lett. 1999;83(24):5046-9.

15. Yashima M, Ando Y, Tabira Y. Crystal structure and electron density of alpha-silicon nitride: experimental and theoretical evidence for the covalent bonding and charge transfer. J Phys Chem B. 2007;111(14):3609-13.

16. Zhu X, Sakka Y. Textured silicon nitride: processing and anisotropic properties. Sci Technol Adv Mater. 2008;9(3):033001.

17. Dressler W, Riedel R. Progress in silicon-based non-oxide structural ceramics. Int J Refract Met Hard Mater. 1997;15(1-3):13-47.

18. Kingery WD, Bowen HK, Uhlmann DR. Introduction to Ceramics. 2 ed. New York: Wiley; 1976.

19. Tanaka I, Pezzotti G, Okamoto T, Miyamoto Y, Koizumi M. Hot Isostatic Press Sintering and Properties of Silicon Nitride without Additives. J Am Ceram Soc. 1989;72(9):1656-60.

20. Ewais EMM, Attia MAA, Abousree-Hegazy A, Bordia RK. Investigation of the effect of ZrO2 and ZrO2/Al2O3 additions on the hot-pressing and properties of equimolecular mixtures of α- and β-Si3N4. Ceram Int. 2010;36(4):1327-38.

21. Rumbao ACSC, Bressiani JC, Bressiani AHA. Influence of Microstructural Characteristics on the Mechanical Properties of Silicon Nitride with Al2O3, Y2O3 and Nd2O3 as Sintering Aids. Mater Sci Forum. 2003;416-418:567-72.

22. Dai Q, He D, Meng F, Liu P, Liu X. Dielectric constant, dielectric loss and thermal conductivity of Si3N4 ceramics by hot pressing with CeO2–MgO as sintering aid. Mater Sci Semicond Process. 2021;121.

23. Haitao Y, Ling G, Runzhang Y, Guotao Y, Peiyun H. Effect of MgO/CeO2 on pressureless sintering of silicon nitride. Mater Chem Phys. 2001;69(1-3):281-3.

24. Zhao Y, Zhang Y, Gong H, Sun H, Li Q. Gas pressure sintering of BN/Si3N4 wave-transparent material with Y2O3–MgO nanopowders addition. Ceram Int. 2014;40(8):13537-41.

25. Trice RW, Halloran JW. Effect of Sintering Aid Composition on the Processing of Si3N4/BN Fibrous Monolithic Ceramics. J Am Ceram Soc. 2004;82(11):2943-7.

26. Jeong K, Tatami J, Iijima M, Takahashi T. Fabrication of Si3N4 ceramics by post-reaction sintering using Si–Y2O3–Al2O3 nanocomposite particles prepared by mechanical treatment. Ceram Int. 2016;42(10):11554-61.

27. Liu X-J, Huang Z-Y, Ge Q-M, Sun X-W, Huang L-P. Microstructure and mechanical properties of silicon nitride ceramics prepared by pressureless sintering with MgO–Al2O3–SiO2 as sintering additive. J Eur Ceram Soc. 2005;25(14):3353-9.

28. Yang WW, Inada M, Tanaka Y, Enomoto N, Hojo J. Effects of Sintering Conditions and Additives on Translucent Silicon Nitride Ceramics. Mater Sci Forum. 2012;724:282-6.

29. Kuzjukevics A, Ishizaki K. Sintering of Silicon Nitride with YAlO3 Additive. J Am Ceram Soc. 1993;76(9):2373-5.

30. Hotta M, Shinoura T, Enomoto N, Hojo J. Spark Plasma Sintering of Nanosized Amorphous Silicon Nitride Powder with a Small Amount of Sintering Additive. J Am Ceram Soc. 2010;93(6):1544-6.

31. Bowen LJ, Weston RJ, Carruthers TG, Brook RJ. Hot-pressing and the α-β phase transformation in silicon nitride. J Mater Sci. 1978;13(2):341-50.

32. Suematsu H, Mitomo M, Mitchell TE, Petrovic JJ, Fukunaga O, Ohashi N. The α-β Transformation in Silicon Nitride Single Crystals. J Am Ceram Soc. 1997;80(3):615-20.

33. Mazzocchi M, Bellosi A. On the possibility of silicon nitride as a ceramic for structural orthopaedic implants. Part I: processing, microstructure, mechanical properties, cytotoxicity. J Mater Sci: Mater Med. 2008;19(8):2881-7.

34. Zuo F, Meng F, Lin D-T, Lv J, Yu J-J, Chen Q, *et al.* Effect of current pattern and conductive phase on sintering behavior of Si3N4-based ceramic composite. Ceram Int. 2018;44(8):9561-7.

35. Kvetková L, Duszová A, Hvizdoš P, Dusza J, Kun P, Balázsi C. Fracture toughness and toughening mechanisms in graphene platelet reinforced Si3N4 composites. Scr Mater. 2012;66(10):793-6.

36. Chang-an W, Yong H, Hongxiang Z. The effect of whisker orientation in SiC whisker-reinforced Si3N4 ceramic matrix composites. J Eur Ceram Soc. 1999;19(10):1903-9.

37. Gogotsi YG. Particulate silicon nitride-based composites. J Mater Sci. 2004;29(10):2541-56.

38. Peni F, Crampon J, Duclos R. The effect of TiN and TiC dispersoids on the high-temperature deformation mechanisms of Si3N4. Ceram Int. 1992;18(6):413-25.

39. Mc Murtry CH, Boecher WDG, Seshardri SG, Zanghi JS, Garnier JE. Microstructure and material properties of SiC-TiB2 particulate composites. Am Ceram Soc Bull. 1987;66(2).

40. Jimbou R, Suzuki Y, Takahashi K. Effect of Dispersion of Zrb2 on Resistivity of Sic-Zrb2 Electroconductive Ceramic Composites. J Ceram Soc Jpn. 1990;98(2):225-30.
41. Bellosi A, Guicciardi S, Tampieri A. Development and characterization of electroconductive Si3N4-TiN composites. J Eur Ceram Soc. 1992;9(2):83-93.
42. Bellosi A, Tampieri A, Liu Y-Z. Oxidation behaviour of electroconductive Si3N4□TiN composites. Mater Sci Eng, A. 1990;127(1):115-22.
43. Gogotsi YG, Porz F. The oxidation of particulate-reinforced Si3N4-TiN composites. Corros Sci. 1992;33(4):627-40.
44. Donald IW, McMillan PW. Ceramic-matrix composites. J Mater Sci. 1976;11(5):949-72.
45. Pierson HO. Covalent Nitrides. In: Pierson HO, editor. Handbook of Refractory Carbides and Nitrides. Westwood, NJ: William Andrew Publishing; 1996. p. 223-47.
46. Vepek S. Nanostructured Superhard Materials. In: Riedel R, editor. Handbook of Ceramic Hard Materials2000. p. 104-39.
47. Bošković S, Sigulinski F, Živković L. Liquid-Phase Sintering and Properties of Si3N4–TiN Composites. J Mater Synth Process. 1999;7(2):119-26.
48. Gao L, Li J, Kusunose T, Niihara K. Preparation and properties of TiN–Si3N4 composites. J Eur Ceram Soc. 2004;24(2):381-6.
49. Lee B-T, Yoon Y-J, Lee K-H. Microstructural characterization of electroconductive Si3N4–TiN composites. Mater Lett. 2001;47(1-2):71-6.
50. Herrmann M, Balzer B, Schubert C, Hermel W. Densification, microstructure and properties of Si3N4□Ti(C,N) composites. J Eur Ceram Soc. 1993;12(4):287-96.
51. Kawano S, Takahashi J, Shimada S. Highly electroconductive TiN/Si3N4 composite ceramics fabricated by spark plasma sintering of Si3N4 particles with a nano-sized TiN coating. J Mater Chem. 2002;12(2):361-5.
52. Guo Z, Blugan G, Kirchner R, Reece M, Graule T, Kuebler J. Microstructure and electrical properties of Si3N4–TiN composites sintered by hot pressing and spark plasma sintering. Ceram Int. 2007;33(7):1223-9.
53. Ahmad N, Sueyoshi H. Properties of Si3N4–TiN composites fabricated by spark plasma sintering by using a mixture of Si3N4 and Ti powders. Ceram Int. 2010;36(2):491-6.
54. Lee BT, Kim HD. In situ synthesis of TiN-reinforced Si3N4 matrix composites using Si and sponge Ti powders. J Mater Sci. 1999;34(24):6169-76.
55. Chen K, Huang Z, Fang M, Liu Y-G. Synthesis of TiN-Si3N4 composites from rutile and quartz by carbothermal reduction nitridation. Sci Sintering. 2012;44(1):57-64.

56. Hirai T, Hayashi S. Preparation and some properties of chemically vapour-deposited Si3N4-TiN composite. J Mater Sci. 1982;17(5):1320-8.

57. Zivkovic L, Nikolic Z, Boskovic S, Miljkovic M. Microstructural characterization and computer simulation of conductivity in Si3N4–TiN composites. J Alloys Compd. 2004;373(1-2):231-6.

58. Yang W, Tan J, Chen Y, Li Z, Liu F, Long H, *et al.* Relationship between substrate type and BDD electrode structure, performance and antibiotic tetracycline mineralization. J Alloys Compd. 2022;890.

59. Alvarez Pugliese CE, Martínez Hernández L, Imbachi Ordoñez S, Marriaga Cabrales N, Machuca Martínez F. Pilot scale anodic oxidation of pretreated vinasse using boron doped diamond electrodes. CT&F - Ciencia, Tecnología y Futuro. 2016;6(4):67-77.

60. Anglada A, Urtiaga A, Ortiz I. Pilot scale performance of the electro-oxidation of landfill leachate at boron-doped diamond anodes. Environ Sci Technol. 2009;43(6):2035-40.

61. Anglada A, Urtiaga AM, Ortiz I. Laboratory and pilot plant scale study on the electrochemical oxidation of landfill leachate. J Hazard Mater. 2010;181(1-3):729-35.

62. dos Santos EV, Sena SF, da Silva DR, Ferro S, De Battisti A, Martinez-Huitle CA. Scale-up of electrochemical oxidation system for treatment of produced water generated by Brazilian petrochemical industry. Environ Sci Pollut Res Int. 2014;21(14):8466-75.

63. Chaplin BP. Critical review of electrochemical advanced oxidation processes for water treatment applications. Environ Sci Process Impacts. 2014;16(6):1182-203.

64. Chen G. Electrochemical technologies in wastewater treatment. Sep Purif Technol. 2004;38(1):11-41.

65. Moelle C, Klose S, Szücs F, Fecht HJ, Johnston C, Chalker PR, *et al.* Measurement and calculation of the thermal expansion coefficient of diamond. Diamond Relat Mater. 1997;6(5-7):839-42.

66. Luong JH, Male KB, Glennon JD. Boron-doped diamond electrode: synthesis, characterization, functionalization and analytical applications. Analyst. 2009;134(10):1965-79.

67. Gracio JJ, Fan QH, Madaleno JC. Diamond growth by chemical vapour deposition. J Phys D: Appl Phys. 2010;43(37).

68. Almeida FA, Amaral M, Oliveira FJ, Fernandes AJS, Silva RF. Nano to micrometric HFCVD diamond adhesion strength to Si3N4. Vacuum. 2007;81(11-12):1443-7.

69. Almeida FA, Oliveira FJ, Silva RF, Baptista DL, Peripolli SB, Achete CA. High resolution study of the strong diamond/silicon nitride interface. Appl Phys Lett. 2011;98(17).

70. Carrapichano JM, Taillaire A, Oliveira FJ, Silva RF. Complete Densification of Si3N4 – SiC Ceramic Matrix Composites (CMC's) by a Pressureless Sintering Route. Mater Sci Forum. 2004;455-456:225-9.

71. Belmonte M, Fernandes AJS, Costa FM, Oliveira FJ, Silva RF. Adhesion behaviour assessment on diamond coated silicon nitride by acoustic emission. Diamond Relat Mater. 2003;12(3-7):733-7.

72. Tallaire A, Silva VA, Fernandes AJS, Costa FM, Silva RF. Effect of intergranular phase of Si3N4 substrates on MPCVD diamond deposition. Surf Coat Technol. 2002;151-152:521-5.

73. Voigt W. Ueber die Beziehung zwischen den beiden Elasticitätsconstanten isotroper Körper. Annalen der Physik. 1889;274(12):573-87.

74. Reuss A. Berechnung der Fließgrenze von Mischkristallen auf Grund der Plastizitätsbedingung für Einkristalle. ZAMM - Zeitschrift für Angewandte Mathematik und Mechanik. 1929;9(1):49-58.

75. Baba S, Goto T, Cho S, Sekino T. Microstructure and mechanical properties of TiN dispersed Si3N4 ceramics via in-situ nitridation of coarse metallic Ti. Epitoanyag J Silic Compos Mater. 2018;70(6):195-203.

76. Anstis GR, Chantikul P, Lawn BR, Marshall DB. A Critical Evaluation of Indentation Techniques for Measuring Fracture Toughness: I, Direct Crack Measurements. J Am Ceram Soc. 1981;64(9):533-8.

77. Standardization IOf. ISO 6872:2015 Dentistry — Ceramic materials. 2015.

78. Almeida FA, Belmonte M, Fernandes AJS, Oliveira FJ, Silva RF. MPCVD diamond coating of Si3N4–TiN electroconductive composite substrates. Diamond Relat Mater. 2007;16(4-7):978-82.

79. Huang J-L, Lee M-T, Lu H-H, Lii D-F. Microstructure, fracture behavior and mechanical properties of TiN/Si3N4 composites. Mater Chem Phys. 1996;45(3):203-9.

80. Blugan G, Hadad M, Janczak-Rusch J, Kuebler J, Graule T. Fractography, Mechanical Properties, and Microstructure of Commercial Silicon Nitride-Titanium Nitride Composites. J Am Ceram Soc. 2005;88(4):926-33.

81. Lee M, Xiao YN, Wittmer DE, Graber TJ, Mini SM. Residual stresses in particle-reinforced ceramic composites using synchrotron radiation. J Mater Sci. 2002;37(20):4437-43.

82. Hasselman DPH, Fulrath RM. Proposed Fracture Theory of a Dispersion-Strengthened Glass Matrix. J Am Ceram Soc. 1966;49(2):68-72.
83. Lux F. Models proposed to explain the electrical conductivity of mixtures made of conductive and insulating materials. J Mater Sci. 1993;28(2):285-301.
84. Živković L, Nikolić ZS, Bošković S. Electrical Properties and Percolation Concentration in Si3N4-TiN Based Composites. Key Eng Mater. 2001;206-213:1489-92.
85. Murai M, Kawahara A, Sakurai A, Nakashima Y, inventors; FANUC Corp, assignee. Electric discharge apparatus. United States2002.
86. Schubert A, Zeidler H, Kühn R, Hackert-Oschätzchen M. Microelectrical Discharge Machining: A Suitable Process for Machining Ceramics. J Ceram. 2015;2015:9.
87. Ferreira TS, Carvalho FMS, Guedes-Silva CC. Densification and microstructure of Si3N4-TiN ceramic composites. Cerâmica. 2019;65(suppl 1):87-91.
88. Vincenzini P. Ceramics today-tomorrow's ceramics: Proceedings of the 7th International Meeting on Modern Ceramics Technologies. In: Vincenzini P, editor. Materials Science Monographs: Elsevier; 1991.
89. Tamura M, Iida T, Setoura K. Plasmonic nanoscale temperature shaping on a single titanium nitride nanostructure. Nanoscale. 2022;14(35):12589-94.
90. Ishii S, Higashino M, Goya S, Shkondin E, Tanaka K, Nagao T, *et al.* Extreme thermal anisotropy in high-aspect-ratio titanium nitride nanostructures for efficient photothermal heating. J Nanophotonics. 2021;10(5):1487-94.
91. Parali L, Kurbanov MA, Bayramov AA, Tatardar FN, Sultanakhmedova RI, Xanlar HG. Effects of Electric Discharge Plasma Treatment on the Thermal Conductivity of Polymer–Metal Nitride/Carbide Composites. J Electron Mater. 2015;44(11):4322-33.
92. Watari K, Hirao K, Toriyama M, Ishizaki K. Effect of Grain Size on the Thermal Conductivity of Si3N4. J Am Ceram Soc. 2004;82(3):777-9.
93. Jiang Y, Wu LE, Huang ZK. Electric Conductive Si3N4/TiN Composite Ceramic Manufactured by Liquid-Qhase Sintering. Key Eng Mater. 2012;512-515:832-6.
94. Kawano S, Takahashi J, Shimada S. Fabrication of TiN/Si3N4Ceramics by Spark Plasma Sintering of Si3N4Particles Coated with Nanosized TiN Prepared by Controlled Hydrolysis of Ti(O-i-C3H7)4. J Am Ceram Soc. 2003;86(4):701-5.
95. Rohatgi A. WebPlotDigitizer San Francisco, California, USA, 2019. Available omeris.io/WebPlotDigitizer.

96. Yang N, Yu S, Macpherson JV, Einaga Y, Zhao H, Zhao G, *et al.* Conductive diamond: synthesis, properties, and electrochemical applications. Chem Soc Rev. 2019;48(1):157-204.

97. Hutton LA, Iacobini JG, Bitziou E, Channon RB, Newton ME, Macpherson JV. Examination of the factors affecting the electrochemical performance of oxygen-terminated polycrystalline boron-doped diamond electrodes. Anal Chem. 2013;85(15):7230-40.

98. Mei R, Zhu C, Wei Q, Ma L, Li W, Zhou B, *et al.* The Dependence of Oxidation Parameters and Dyes' Molecular Structures on Microstructure of Boron-Doped Diamond in Electrochemical Oxidation Process of Dye Wastewater. J Electrochem Soc. 2018;165(7):H324-H32.

99. Liu Z, Li H, Li M, Li C, Qian L, Su L, *et al.* Preparation of polycrystalline BDD/Ta electrodes for electrochemical oxidation of organic matter. Electrochim Acta. 2018;290:109-17.

100. Ivandini TA, Watanabe T, Matsui T, Ootani Y, Iizuka S, Toyoshima R, *et al.* Influence of Surface Orientation on Electrochemical Properties of Boron-Doped Diamond. J Phys Chem C. 2019;123(9):5336-44.

101. Standardization IOf. ISO 4499-2:2020 - Hardmetals. Metallographic determination of microstructure — Part 2: Measurement of WC grain size2020.

102. Ralchenko VG, Smolin AA, Pereverzev VG, Obraztsova ED, Korotoushenko KG, Konov VI, *et al.* Diamond deposition on steel with CVD tungsten intermediate layer. Diamond Relat Mater. 1995;4(5-6):754-8.

103. Prawer S, Nemanich RJ. Raman spectroscopy of diamond and doped diamond. Philos Trans A Math Phys Eng Sci. 2004;362(1824):2537-65.

104. Mallika K, Komanduri R. Low pressure microwave plasma assisted chemical vapor deposition (MPCVD) of diamond coatings on silicon nitride cutting tools. Thin Solid Films. 2001;396(1-2):146-66.

II.2. Customized Boron-Doped Diamond Electrodes for Efficient Water Treatment via HFCVD Parameter Optimization

Priscilla Brosler[1], Miguel Ângelo Neto[1], Rui F Silva[1], João Tedim[1], Filipe J Oliveira[1]

[1] CICECO Aveiro Institute of Materials, Department of Materials and Ceramic Engineering, University of Aveiro, 3810-193, Aveiro, Portugal

The present work was published on: *Diamond and Related Materials*

doi: 10.1016/j.diamond.2023.110595

Abstract

Among the Design of Experiments (DoE) approaches available, the Taguchi method offers a methodical and effective way to optimize designs with fewer experimental trials. The effects of deposition conditions on the final properties of boron-doped diamond (BDD) films for water treatment applications deposited in a Hot Filament Chemical Vapor Deposition (HFCVD) reactor were evaluated by applying a Taguchi Matrix. Methane to hydrogen (CH_4/H_2) ratio, argon mass flow, and total gas pressure were the controllable factors, each in three different levels. Diamond quality was affected by a combination of the three considered factors. A 0.02 CH_4/H_2 ratio was found as the optimal value to yield films with reduced non-diamond carbon inclusions in our CVD system. Resistivity, residual stress, double-layer capacitance, and surface roughness were mainly affected by total pressure and argon content. The methane content and the total pressure significantly influenced growth rate and grain size. The latter was primarily responsible for changes in the electrochemical potential window and the electron transfer process of the BDD films. Within the studied range of deposition conditions, the optimal deposition parameters to obtain BDD films for water treatment applications were: 0.02 CH_4/H_2 ratio, 25 mbar total gas pressure, and 30 sccm argon mass flow.

II.2.1. Introduction

Among the seventeen Sustainable Development Goals (SDG) established by the United Nations Member States in 2015, two of them are directly related to water: ensure availability and sustainable management of water and sanitation for all (SDG 6), and conserve and sustainably use the oceans, seas, and marine resources for sustainable development (SDG 14) (1). The presence of recalcitrant organic pollutants in waters, primarily due to improper treatment of industrial, domestic, and agricultural effluents, offers a significant threat to human health and the ecosystem (2). Therefore, properly removing these persistent pollutants from water is vital for sustainable development. However, most conventional methods used for treating these contaminants in water are not effective and reliable (3). Therefore, developing treatment technologies is essential for achieving water quality within the accepted standards. Electrochemical advanced oxidation processes (EAOPs) are a promising alternative to conventional water treatment methods (4). EAOPs can eliminate recalcitrant pollutants and pathogens from contaminated waters, in an environmentally friendly way, with high efficiency and low cost (5). Many electrode materials have been tested for EAOPs, such as graphite, platinum, iridium oxides, tin oxides, lead oxides, sub-stoichiometric titanium oxide, and boron-doped diamond (BDD) (6-8). Among them, BDD anodes show the highest removal rate and current efficiency in removing organic pollutants, outperforming other materials (9). BDD's superior performance is due to its outstanding properties, which include high chemical stability, the widest known potential window, inert surface with low adsorption properties, excellent efficiency in the production of hydroxyl radicals, low double-layer capacitance, and reduced background current (10). This particular set of properties turns the BDD capable of generating reactive oxidizing species, such as hydroxyl radicals, peroxosulfate, peroxocarbonate, peroxophosphate, hydrogen peroxide, ozone, and chlorine, which are responsible for degrading organic pollutants or even promoting water disinfection (11).

However, the outstanding electrochemical behavior of BDD electrodes can vary drastically depending on their physicochemical properties (9), which can be controlled and optimized by a proper adjustment of the experimental conditions applied during the synthesis of BDD by Chemical Vapor Deposition (CVD) techniques (12). The CVD process involves numerous experimental parameters, such as gas composition, gas flow rates, chamber pressure, substrate temperature, and reactor design, that directly affect the kinetics and local chemistry inside the deposition chamber and influence the nucleation and growth of diamond films (13). By tweaking these settings, one can control

the BDD film's final microstructure, growth rate, carbon sp^2 content, and boron doping level. Such properties are key factors that determine the BDD's electrocatalytic behavior (9).

Using traditional approaches to optimize CVD deposition conditions by changing each parameter at a time is time-consuming and costly since it requires many experiments (14). Among the Design of Experiments (DoE) techniques available, the Taguchi method provides an efficient and systematic approach to optimize designs with minimum experimental trials, reducing costs and time (15). In addition, it allows the analysis of several different variables simultaneously (16). In ideal circumstances, the variables employed within the Taguchi matrix should exhibit independence from one another. However, it is well understood that the parameters utilized in CVD processes often demonstrate interdependencies. Nonetheless, the Taguchi matrix will function as a guiding compass to discern the impact of these variables with a reduced number of experimental trials, a crucial advantage given the high cost associated with CVD processes. The Taguchi method has been applied in the optimization of CVD depositions of several carbon-based materials, such as diamond (12, 14), carbon nanotubes (17, 18 , 19-22), and graphene (23-25). Although the Taguchi method has already been applied to optimize diamond depositions, there are no reports in the literature on this approach to optimize boron-doped films.

For organics degradation, it is generally required that BDD electrodes have a low carbon sp^2 content and a sufficiently high level of boron doping to achieve metal-like conductivity (26). High sp^3/sp^2 ratios are associated with more efficient pollutant degradation processes since carbon sp^3 enhances the generation of radicals on the electrode surface, favoring direct mineralization over indirect oxidation (27). The latter can lead to the formation of undesired or even harmful secondary species (27). Therefore, finding an optimum boron doping level is mandatory for achieving the best performance of a BDD electrode. Although metal-like conductivity is required, high boron concentrations increase the sp^2 impurity level (28). They may also reduce the oxidation potential of BDD electrodes (29). The ideal doping level for better charge transfer and electroanalytical performance seems to be immediately above the metal-like conductivity threshold (30). Furthermore, a larger film thickness is associated with a grain size increase and improved diamond quality (31). Thus, in this work, we applied the Taguchi method to determine the optimal operating conditions of our in-house developed Hot Filament CVD reactor for producing BDD electrodes with metal-like conductivity, low carbon sp^2 content, and high growth rate for water treatment through EAOPs.

II.2.2. Materials and methods

The BDD films were deposited over silicon substrates (undoped Si <100>, Siegert Wafer, Ø 50.8 ± 0.3 mm, Prime Grade, >10,000 ohm.cm). Before HFCVD deposition, the substrates were submitted to ultrasonic seeding in an ethanol solution with abrasive diamond powder (0.5-1.0 µm and 10-20 µm, Diamecânica, Portugal) to improve the diamond nucleation density and guarantee uniform film deposition. Eight parallel tungsten wires (Ø = 0.3 mm, 8 cm length) were used as filaments. They were placed at a constant distance of approximately 7 mm from the substrates. The substrates were placed over a non-conductive Si_3N_4 sample holder, with the absence of any applied bias voltage. Prior to the film deposition, the tungsten filaments were subjected to carburization through exposure to a 0.05 CH_4/H_2 mixture for a duration of 45 minutes, with the filaments maintained at temperatures between 2100-2300°C. During deposition, the filaments' temperature was kept at 2100-2300ºC and measured with a two-color pyrometer. The excitation power of the filaments per unit coating area fell within the range of 21-30 W/cm². The substrate's temperature was kept in the 750-800ºC range. All depositions were performed for 5 hours, followed by a 90-minute cooling step under an H_2 atmosphere. The boron source was a solution of boron oxide (B_2O_3) diluted in ethanol (10,000 ppm), which was placed inside a canister with pressurized argon gas at 2 bar. The amount of dopant feed into the deposition chamber was set using a mass flow controller in conjunction with a CEM (Controlled Evaporator Mixer) device, which heated and mixed the boron solution with the process gases at 70ºC. To analyze the influence of three different factors with three levels each, an L9 orthogonal array Taguchi Matrix was selected and built to optimize the deposition parameters of the HFCVD reactor with a minimum number of experimental trials. The controlled parameters were gas composition (CH_4/H_2), total pressure, and argon mass flow, as shown in Table II.2.1. The limits chosen for each parameter and the boron source flow (2.5 µL/min) were specified according to a previous study (Section 2 - Supplementary Information) and within the operating limits of our in-house developed reactor.

Table II.2.1. Taguchi matrix of the HFCVD parameters.

Dep.	CH_4/H_2	Total Pressure (mbar)	Ar (sccm)	B_2O_3/CH_4	Total Mass Flow (sccm)
L1	0.010	75	15	1.250	217
L2	0.010	125	0	1.250	202
L3	0.010	25	30	1.250	232
L4	0.020	125	15	0.625	219
L5	0.020	25	0	0.625	204
L6	0.020	75	30	0.625	234
L7	0.005	25	15	2.500	216
L8	0.005	75	0	2.500	201
L9	0.005	125	30	2.500	231

The BDD films were characterized by Scanning Electron Microscopy/Energy Dispersive X-ray Spectroscopy (SEM/EDS, Hitachi, SU-70) and Micro-Raman Spectroscopy (acquired with a 532 nm laser line, 532 ER, Wasatch Photonics, USA). The growth rate and the average grain size were estimated by image analysis of the SEM micrographs. An adaptation of the linear intercept method as outlined in ISO 4499-2:2020 (32) was employed to estimate the grain size of diamond films. From the Micro-Raman spectra, quality factor, residual stress, and boron concentration were estimated. Peak fitting was performed using the PeakFit software (Systat Software Inc., version 4.11). All spectra were normalized to unity, and the main peaks were fitted using a pseudo-Voigt function. The quality factor was determined from the ratio $I_{diamond}/I_G$, where $I_{diamond}$ is the integrated area of the diamond peak (at ~1332 cm^{-1}), and I_G is the integrated area of the G-band (at ~1550 cm^{-1}) (33). The residual stress (σ_r) was determined by measuring the diamond peak shift $(\Delta\vartheta)$ from the natural stress-free diamond peak (1332 cm^{-1}), according to Eq. II.2.1 (34).

$$\sigma_r = -0.567 \times \Delta\vartheta \qquad \textbf{Eq. II.2.1}$$

The boron concentration [B] was estimated using a non-destructive and contactless method that estimates boron doping from the Raman spectrum (Eq. II.2.2) for concentrations within the 2 x 10^{20} to 10^{22} cm^{-3} range (35).

$$[B]\ (cm^{-3}) = 8.44\ \times 10^{30} \times \exp\left(-0.048\ \times\ \omega_{500}\right) \qquad \textbf{Eq. II.2.2}$$

Where ω_{500} is the wavenumber (cm^{-1}) of the Lorentzian component of the peak located at about 500 cm^{-1} in the Raman spectrum. According to Bernard *et al.*, although the Si substrate exhibits a narrow peak at 520 cm^{-1}, it decreases with increased boron doping levels (35). Once the BDD film achieves metallic conductivity, it becomes opaque at the applied excitation wavelength, the Si peak completely disappears, and a new peak at approximately 500 cm^{-1} arises (35). The 500 cm^{-1} peak in the Raman spectrum of boron-doped diamond has been attributed to different sources. Some studies proposed that it is due to local vibrational modes of pairs of boron atoms (36-38). Vlasov *et al.*, on the other hand, argued that it is a vibrational mode of diamond that is only observed in heavily boron-doped samples due to the breaking of the translation symmetry of the crystal lattice (39). This is supported by the fact that the 500 cm^{-1} peak is also observed in $^{11}B^{12}C$ and amorphous carbon (39). A peak often accompanies the 500 cm^{-1} peak at approximately 1220-1230 cm^{-1}, which is also considered a vibrational mode of diamond (39).

The electrical resistivity of the thin films was accessed using a homemade apparatus with two independent copper wires attached to the BDD film with silver glue. The electrochemical properties of the BDD electrodes were investigated with a potentiostat (PGSTAT302N, Metrohm Autolab, Switzerland) controlled by computer software (Nova 2.1.5, Metrohm Autolab). A Pt plate was used as the counter electrode, and a Saturated Calomel Electrode (SCE) as the reference electrode. Cyclic voltammetry (CV) was performed in a three-electrode electrochemical cell, in 0.1 M H_2SO_4 electrolyte solution, at a scan rate of 100 mV/s to determine the electrochemical potential window (EPW) of the BDD films. Electrochemical Impedance Spectroscopy (EIS) was performed in 0.1 M KNO_3 electrolyte at open circuit potential (OCP), from 10^5 Hz to 10^{-2} Hz, with 7 points per decade. Quantitative data were estimated using an equivalent electric circuit in the Zview software (Scribner Associates, USA). The film's surface roughness was assessed by Vertical Scanning Interferometry (VSI) in confocal mode (25 mm, 10x objective), using a 3D optical profiler (S Neox, SensoFar, Spain). In order to determine the optimal conditions for depositing BDD films with high diamond quality (Q), high growth rate (G), large average grain size (AGS), low resistivity (ρ), and low residual stress (σ_r), a Figure-of-Merit (FOM) was designed to evaluate the intrinsic properties of the films according to Eq. II.2.3. For calculating the FOM, each property considered was normalized to unity. Throughout this study, the evaluation of each sample's EPW, double-layer capacitance,

and electron transfer process was carried out and duly considered. However, it is noteworthy that these properties were not included in the FOM, as they are the outcome of the properties specifically chosen for the FOM equation.

$$FOM = \left| \frac{Q \times G \times AGS}{\rho \times \sigma_r} \right| \qquad \textbf{Eq. II.2.3}$$

II.2.3. Results and discussion

II.2.3.1. Taguchi method optimization

The main results from the nine depositions are summarized in Table II.2.2. Among the Taguchi matrix parameters, the BDD film with the highest FOM value was obtained with the deposition conditions used for sample L5: 0.02 CH_4/H_2 ratio, 25 mbar chamber pressure, and no introduction of argon in the gas mixture.

Table II.2.2. Characteristics of the BDD films.

Dep.	CH_4/H_2	Ar (sccm)	P (mbar)	APF (kW)	G (µm/h)	Q ($I_{dia.}/I_G$)	ρ (Ω.cm)	[B] (cm^{-3})	AGS (µm)	σ_r (GPa)	EPW [a] (V vs. SCE)	C (µF/cm²)	Sa (nm)	FOM
L1	0.01	15	75	1.35	0.53	0.38	1.17	*< 2 x 10^{20}	0.71 ± 0.13	-2.0	3.04	1.39	16.9	0.03
L2	0.01	0	125	1.64	0.65	0.42	2.23	*< 2 x 10^{20}	0.73 ± 0.10	-1.7	2.93	1.17	19.4	0.27
L3	0.01	30	25	1.55	0.39	1.47	2.61 x 10^{-3}	3.2 x 10^{21}	0.50 ± 0.03	-18.1	2.59	89.48	6.7	31.36
L4	0.02	15	125	1.68	0.98	0.79	3.92 x 10^{-2}	*< 2 x 10^{20}	1.35 ± 0.04	-2.1	2.91	3.61	40.2	65.62
L5	0.02	0	25	1.49	0.87	1.14	3.87 x 10^{-3}	5.4 x 10^{20}	1.03 ± 0.25	-3.4	2.67	1.23	72.4	401.28
L6	0.02	30	75	1.66	1.24	2.72	1.22 x 10^{-1}	2.4 x 10^{20}	1.98 ± 0.51	-2.2	2.78	1.42	133.8	128.60
L7	0.005	15	25	1.36	0.19	0.17	1.02 x 10^{-2}	*< 2 x 10^{20}	0.74 ± 0.14	-3.9	2.70	6.15	99.2	3.11
L8	0.005	0	75	1.20	0.30	1.59	2.15 x 10^{-1}	*< 2 x 10^{20}	0.79 ± 0.11	-2.4	2.57	1.23	20.0	3.77
L9	0.005	30	125	1.43	0.48	0.93	5.48 x 10^{-2}	2.5 x 10^{20}	0.71 ± 0.05	-3.0	2.73	1.62	49.9	9.96

P: Pressure; PF: Average Power of the Filaments; G: Growth Rate; Q: Diamond Quality Factor; ρ: Resistivity; σ_r: Residual Stress; AGS: Average Grain Size; EPW: Electrochemical Potential Window; C: Capacitance; Sa: Arithmetical Mean Height; FOM: Figure-of-merit.

[a] EPW in 0.1 M H_2SO_4.

** The Raman spectrum does not show the peak at ~500 cm^{-1}, only the Si substrate peak at 520 cm^{-1}.*

In order to define the ideal HFCVD operating conditions, a detailed Taguchi analysis graph (Figure II.2.1) was constructed to elucidate each parameter's influence in the BDD films' final characteristics.

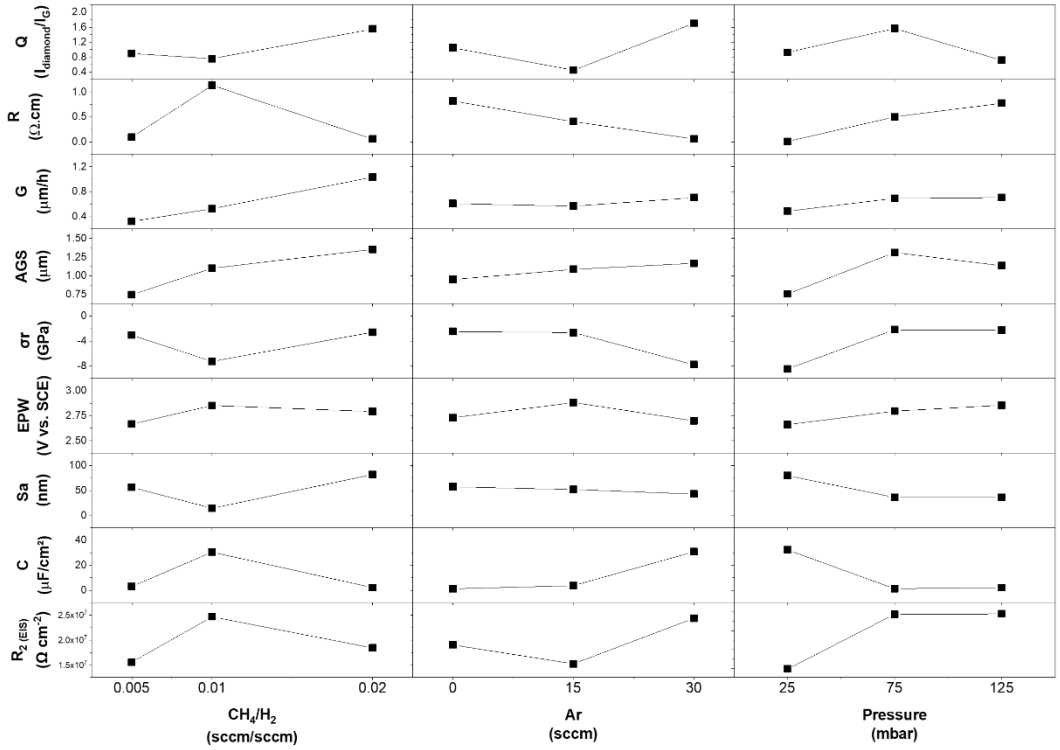

Figure II.2.1. Detailed analysis of the Taguchi experiment.

The plan view micrographs of the BDD films obtained by SEM are shown in Figure II.2.2. The columns from left to right increase in argon content, and the rows from top to bottom increase in CH_4/H_2 ratio. All nine conditions could coat the Si substrates with microcrystalline diamond films in a complete and even manner, without defects caused by uncoated regions, even for low CH_4/H_2 ratios such as 0.005. For CH_4/H_2 ratios in the 0.005-0.02 range, larger grain sizes were achieved by increasing the CH_4/H_2 ratio, the total pressure, and the argon content. However, in our previous study (Section 2 - Supplementary Information), in which the CH_4/H_2 ratios were in the 0.02-0.06 range, increasing the CH_4/H_2 ratio had the opposite effect. Thus, for our in-house HFCVD system, a 0.02 CH_4/H_2 ratio is ideal for obtaining BDD films with large grain sizes.

In addition, from a visual analysis of Figure II.2.2, it can be suggested that films grown with a 0.02 CH_4/H_2 ratio have a more uniform grain size distribution and show diamond grains with mixed crystallographic orientations, with a notable preference towards (111) and (110) as the primary orientations. In contrast, films grown with lower CH_4/H_2 ratios

(0.005 and 0.01) seem to have less uniform grain size distribution. Furthermore, high surface roughness is desirable for BDD electrodes for water treatment applications. Rougher surfaces improve the contact between organic compounds and the BDD film and promote more sites for the reactions, leading to the additional production of hydroxyl radicals and, consequently, the oxidation of organic compounds (29). Surface roughness was mainly affected by the CH_4/H_2 ratio and the total pressure. Although the Taguchi analysis did not reveal a significant influence of Argon content on surface roughness, it is anticipated that elevated Argon concentrations will facilitate nanodiamond growth, subsequently resulting in smoother surfaces. A reduction in overall pressure was observed to correspond with increased surface roughness. Decreased pressures and a lower CH_4/H_2 ratios reduce the production of sp^2 carbon structures. This phenomenon is attributed to the reduced residence time of species within the CVD reactor chamber and a decreased number of collisions among them. Sample L6 presented the highest surface roughness value, which agrees with the less uniform grain size distribution measured through its SEM micrograph.

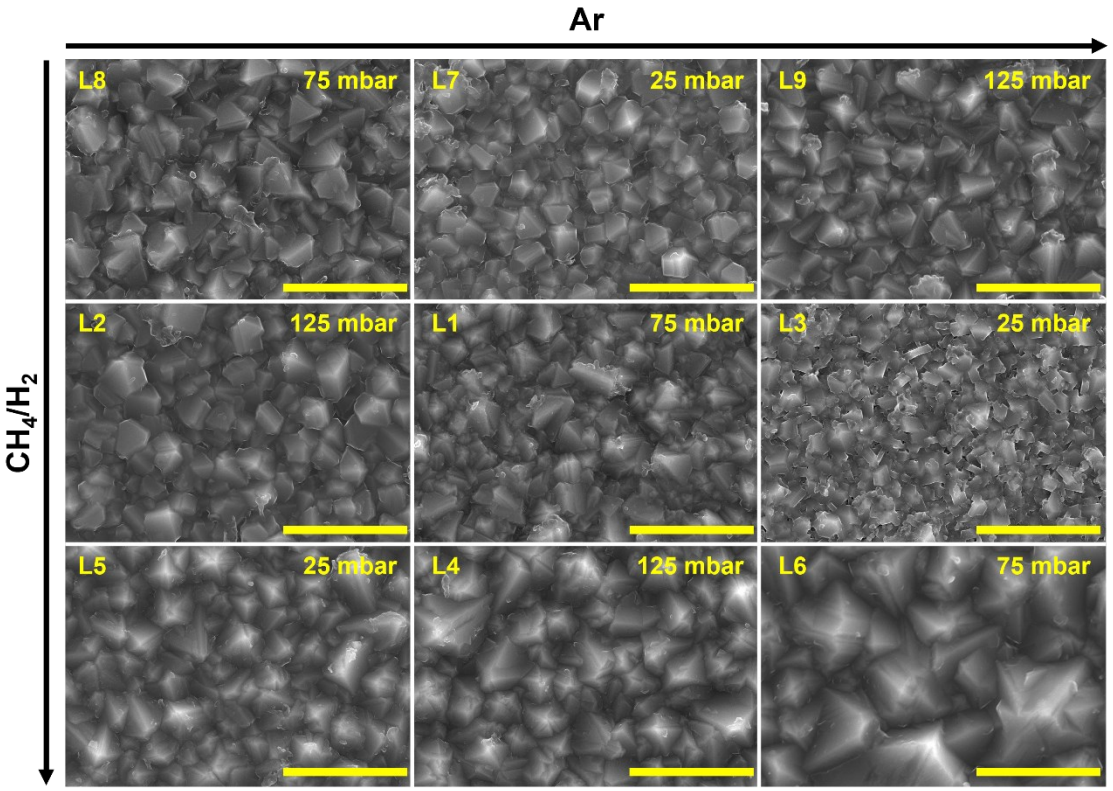

Figure II.2.2. SEM micrographs in the plan view of BDD films obtained under the Taguchi matrix conditions (Scale: 5 µm).

A high-quality BDD film with minimum or no non-diamond carbon inclusions is essential for water treatment applications (40). The presence of sp^2 increases the adsorption of organics in the film's surface, promoting electrode fouling and reducing the service life of BDD electrodes (9). Diamond films with sp^2 inclusions show vibrations in the Raman spectrum at 1350 cm^{-1} (D band) and at 1550 cm^{-1} (G band), which correspond to the presence of all sp^2 structures and the C=C sp^2 bond stretching mode, respectively (41). The Raman spectra of the samples are shown in Figure II.2.3. BDD films with minimal presence of sp^2-carbon were obtained with a 0.02 ratio, 30 sccm argon mass flow, and 75 mbar pressure. Again, when combining data from our previous study (Section 2 – Supplementary Information), where the adopted CH_4/H_2 ratios were in the 0.02-0.06 range, one can conclude that a 0.02 CH_4/H_2 ratio is ideal for obtaining BDD films with the least amount of non-diamond carbon in our HFCVD system. Comparing the plan view micrographs (Figure II.2.2) with the Raman results makes it possible to observe an increase in diamond quality with grain size. Films with larger grain sizes possess smaller grain boundary densities, thus less non-diamond carbon content (42). The Raman spectra also show that the trans-polyacetylene (TPA) peaks, located at 1150 and 1470 cm^{-1} (43), are more pronounced for films with lower resistivities. Furthermore, the peak at approximately 1220 cm^{-1}, associated with disordered diamond, is also more intense in samples with lower resistivities, most probably due to distortions caused by high Boron incorporation in the diamond lattice (35). These observations agree with the [B] estimated from the Lorentzian component of the peak located at about 500 cm^{-1} in the Raman spectrum (Supplementary Figure II.2.1).

Although the Taguchi matrix did not directly consider the B_2O_3/CH_4 ratio, its influence is indirectly implicated through the CH_4/H_2 ratio employed in each experiment, given that the flow of B_2O_3 was identical across all experiments. Additionally, although sample L3 exhibited the lowest resistivity among all samples, the findings suggest that, on average, the lowest resistivities were achieved for the experimental group that implemented a B_2O_3/CH_4 ratio of 0.625 (samples L4, L5, and L6). The combination of superior diamond quality, growth rate, and grain size with the low resistivity achieved in this experimental set (0.02 CH_4/H_2 ratio, thus 0.625 B_2O_3/CH_4 ratio) produced the three highest FOM values.

It is also important to note that the resistivity of BDD films is not directly proportional to the estimated boron concentration (44). For example, samples L3 and L5 have similar resistivity values, but their boron concentrations differ by almost an order of magnitude. This suggests that other factors, such as the location of boron atoms, heterogeneities in

the film, and film thickness, may have also affected the resistivity of the BDD films. Boron atoms are not electrically active when incorporated within the grain boundaries (45). This means that the resistivity of a BDD film may be lower than expected if the boron atoms are concentrated in the grain boundaries. Heterogeneities in the film, such as non-diamond carbon, lattice hydrogen, and dangling bonds, can also cause local variations in the film's resistivity (46). In addition, the resistivity of BDD films has been shown to decrease with increasing film thickness due to the reduction of defects in the films. This is because thicker films have a larger grain size and a lower grain boundary density, which reduces the number of electrically inactive boron atoms and other defects (47).

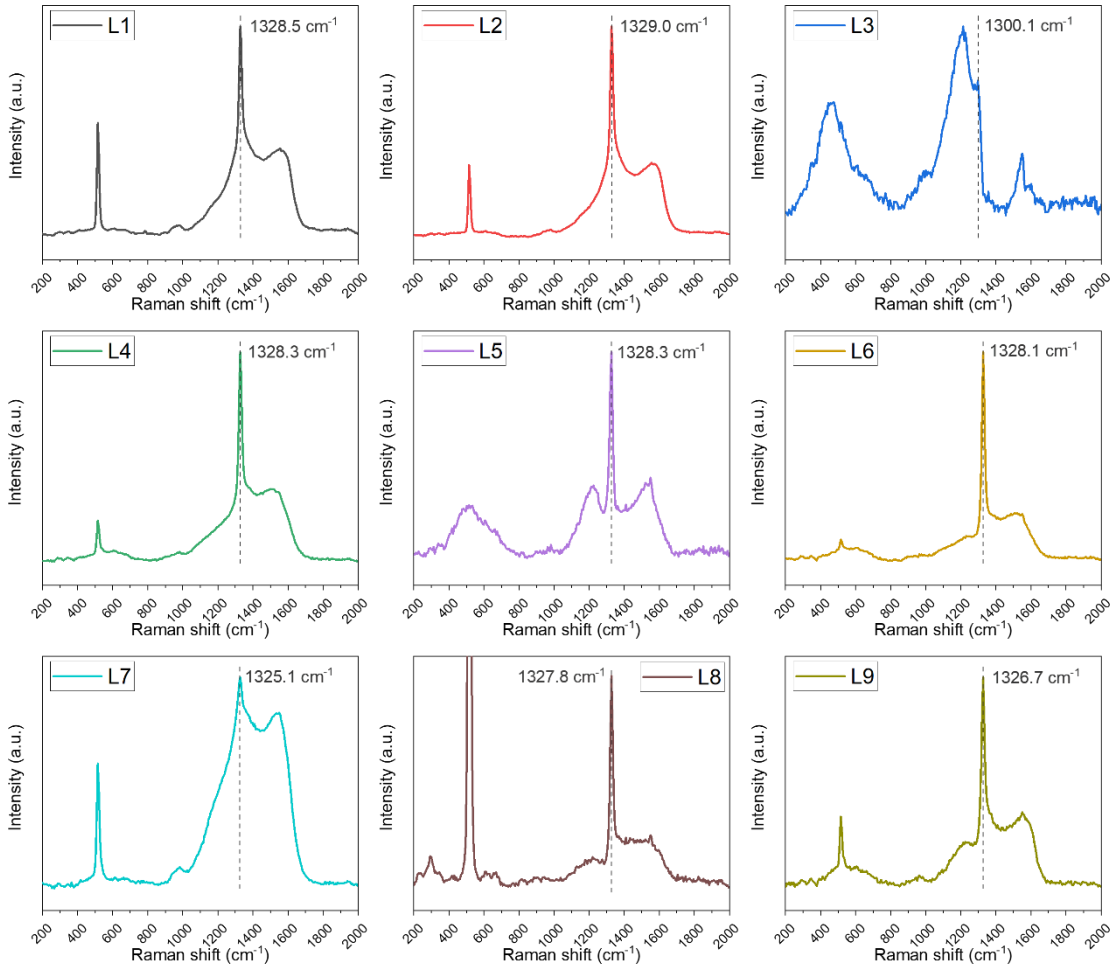

Figure II.2.3. Raman spectra of the BDD films obtained under the Taguchi matrix conditions, with a 532 nm laser line.

Ideally, a BDD film should present no or very low residual stress to avoid premature electrode failure due to delamination from the substrate. All depositions resulted in films

with compressive intrinsic residual stress. A faster cooling rate would imply higher residual stresses due to the differences between the coefficient of thermal expansion of the substrate material and the diamond film. Since the substrate material (Si) and the cooling rate were the same for all depositions, the sample's intrinsic residual stresses mainly relate to non-diamond carbon present at the grain boundaries and structural defects, such as dislocations, microtwins, and impurities (48). In general, lowering the argon mass flow and increasing the chamber pressure simultaneously has shown a positive effect, reducing the residual stress. In addition, on average, 0.02 CH_4/H_2 ratios showed the lowest residual stress values, which agrees with less carbon sp^2 impurities generated with such gas composition.

The cross-section SEM micrographs of BDD films are shown in Figure II.2.4. As in the plan view micrographs, the columns from left to right increase in argon concentration, and the rows from top to bottom increase in CH_4 content. Increasing the CH_4/H_2 ratio has shown a high impact on the growth rate of the BDD films, yielding films with larger thicknesses. Increased pressures have also shown a significant effect on growth rates. The argon mass flow effect on film thickness was less pronounced. However, the average growth rate was higher for films deposited with 30 sccm of argon.

It is worth noting that we used in this study an HFCVD system with a boron doping source provided by B_2O_3 and ethanol. Adding these compounds to the CH_4/H_2 gas mixture during CVD diamond growth creates unique conditions for partial diamond surface oxidation (49). This is because the oxygen-rich compounds, such as B_2O_2, CO, and CO_2, formed during the gas mixture's interaction with the tungsten filaments can react with the diamond surface to form oxygen-bonded carbon species (49). The presence of oxygen bonded to carbon has been found to have a number of effects on the properties of BDD films, such as increasing the hydrophilicity of the films, altering the electrical properties, and reducing the concentration of sp^2 carbon in the films (49). However, the presence of oxygen can also have negative effects, such as reducing the growth rate of the films and increasing the defect density (49). The specific effects of oxygen species on the properties of BDD films will depend on the type of gas mixture used, the pressure, and the temperature (49).

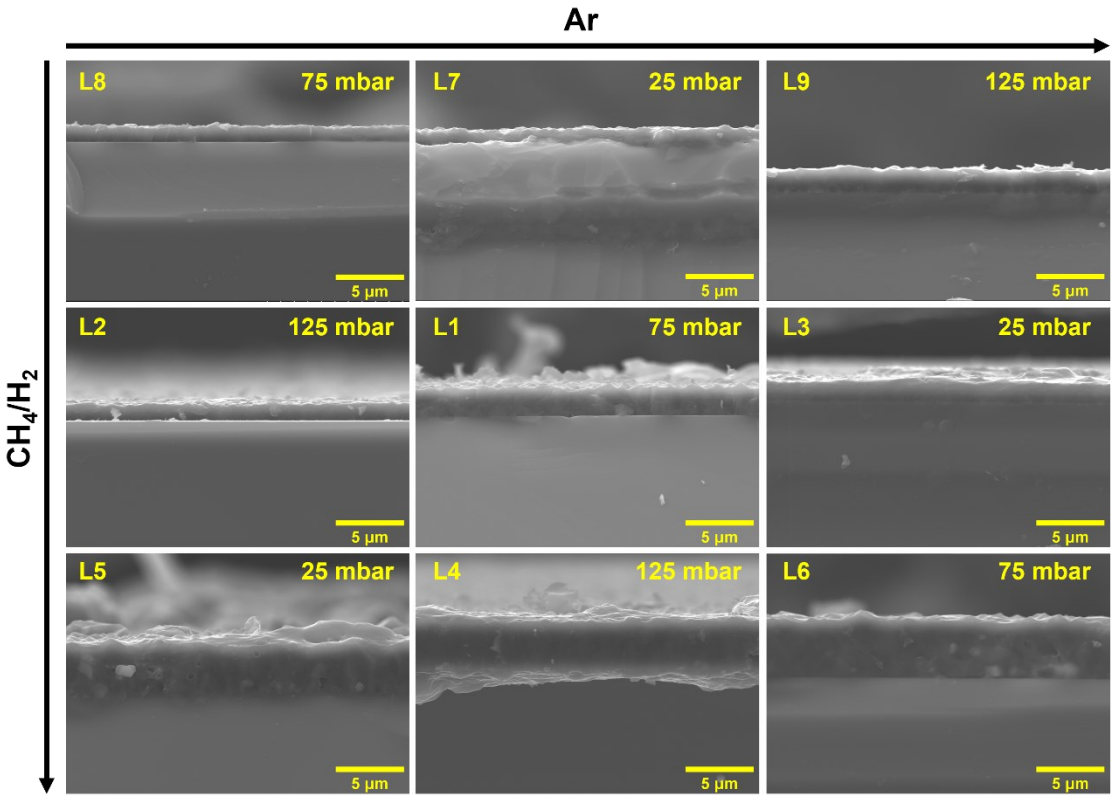

Figure II.2.4. SEM micrographs in cross-section of the BDD films obtained under the Taguchi matrix conditions.

The cyclic voltammograms (CVs) of the samples and their corresponding Raman spectrum are shown in Figure II.2.5. Samples L3, L4, L5, L6, and L9 showed acceptable voltammetry responses with low background current, no presence of oxidation/reduction peaks, and a wide electrochemical potential window. Samples L1, L7, and L8 showed a mixed behavior between BDD and glassy carbon (26), with the presence of oxidation/reduction peaks most probably related to the higher presence of sp^2 impurities in the diamond film that act as catalytic sites for oxygen reduction (28). When comparing the CVs with the Raman spectra, samples L1, L7, and L8 show more prominent G-band peaks in their Raman spectrum associated with sp^2-carbon (50). In Supplementary Figure II.2.6, the cyclic voltammogram of a microcrystalline BDD film is compared with a nanocrystalline one. The nanocrystalline electrode showed a peak at approximately -0.4 V vs. SCE (as seen also in sample L2) related to sp^2 inclusions and an EPW shift towards more negative potentials. Consequently, a microcrystalline structure, thus a larger grain size, was favored over a nanocrystalline diamond film in selecting optimal BDD deposition conditions for water treatment applications.

BDD films for the electrooxidation of pollutants must have a "metal-like" conductivity to be effective and energy efficient (30). The lowest resistivities were obtained by increasing the argon mass flow and decreasing the chamber pressure. As the boron doping level increases, the BDD's resistivity decreases, resulting in a higher background current and a narrower potential window (51). The EPW width decrease is related to boron-rich sites being directly involved during the required adsorption steps for gas evolution reactions (30). Sample L3 shows the narrowest EPW and lowest resistivity among all depositions, confirming its superior boron concentration (~ 3 x 10^{21} cm^{-3}) compared to the others.

The Raman spectrum of sample L3 is the most representative of a highly doped diamond film. It exhibits a more intense peak at 1220 cm^{-1}, asymmetry of the diamond peak, and a significant shift of the diamond peak from 1332 cm^{-1} towards smaller wavelengths. Such a significant shift is associated with the so-called Fano effect in heavily doped diamond films caused by quantum interference between electronic transitions and the diamond zone-center optical phonon (52). This effect is responsible for the high residual stress value obtained for sample L3 from Eq. II.2.1, which could be inaccurate.

For electrochemical applications, especially sensors, a large EPW is ideal (53). Although high boron doping levels are desired, once they are responsible for narrowing the EPW, a compromise must be made to achieve the perfect balance between resistivity and EPW to fit the requirements of each specific BDD application. In this study, the difference between the widest and narrower EPW is 0.45 V vs. SCE, which may be sufficiently important and limiting depending on the type of application. According to the Taguchi analysis, larger EPWs were obtained by increasing the pressure. Moreover, Figure II.2.1 indicates that a combination of 0.01 CH_4/H_2 ratio, 15 sccm argon mass flow, and 125 mbar pressure is ideal for obtaining the widest EPW within the studied deposition parameter ranges.

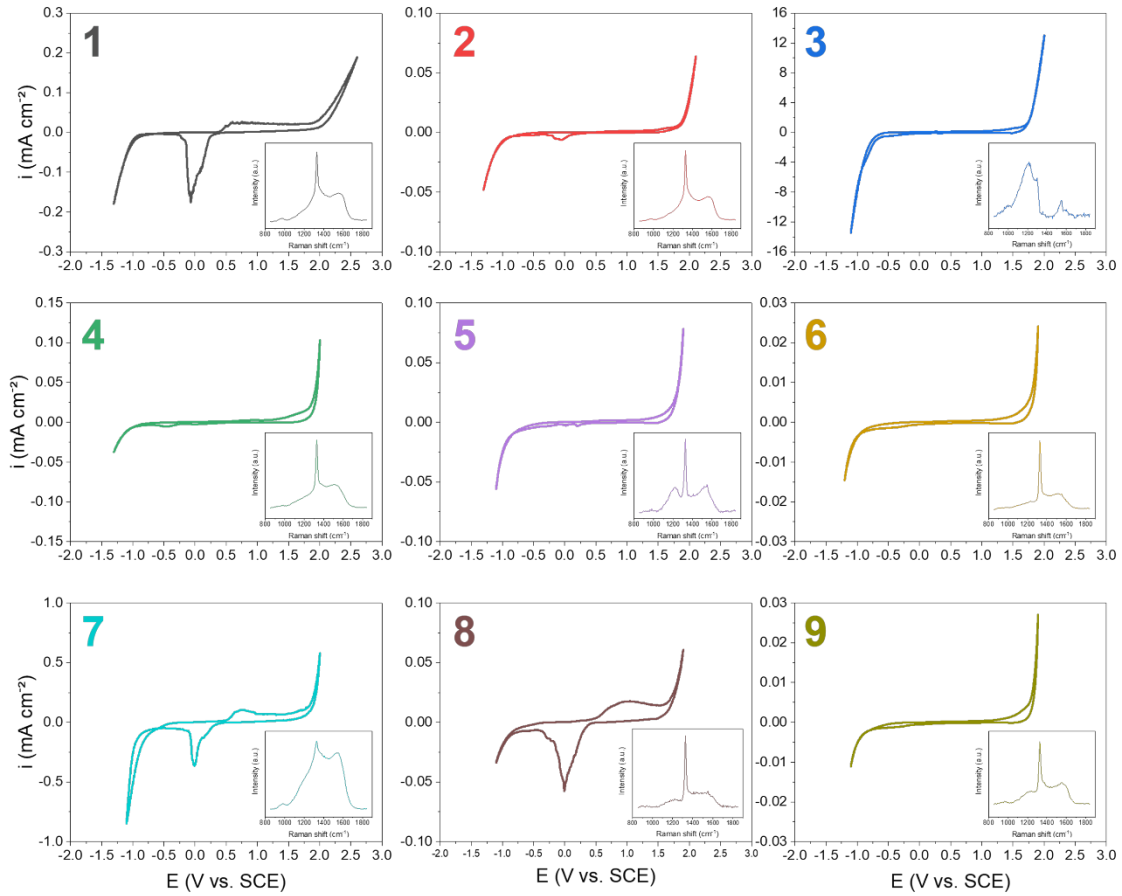

Figure II.2.5. Cyclic voltammograms of the BDD films obtained under the Taguchi matrix conditions, recorded in a 0.1 M H_2SO_4 electrolyte at 100 mV/s scan rate.

The Nyquist plots obtained from the EIS analysis are given in Figure II.2.6, showing semicircles representing charge transfer-limited processes. Moreover, the plots indicate that the capacitance of all samples depends on frequency. Thus, the equivalent electric circuit of the electrodes includes a frequency-dependent constant phase element (CPE), reflecting the reactivity distribution brought on by the surface electrochemical heterogeneity, which may result from the samples' high surface roughness (54) or uneven distribution of boron atoms in the diamond coating (55). The double-layer capacitance of the BDD films was calculated by Eq. II.2.4 according to the circuit model containing a CPE in parallel with a resistor (depressed semicircle model), assuming the CPE impedance (Z_{CPE}) established by Eq. II.2.5 (56).

$$C = \frac{(Q_0 \times R)^{1/n}}{R} \qquad \textbf{Eq. II.2.4}$$

$$Z_{CPE} = \frac{1}{Q_0 \times (j \times \omega_f)^n} \qquad \textbf{Eq. II.2.5}$$

Where C is the double-layer capacitance, Q_0 and n are the characteristic parameters of the CPE, R is the solution resistance, Z_{CPE} is the CPE impedance, j is the imaginary number, and ω_f is the angular frequency. When n = 0, C is indeterminable, and the CPE behaves as a pure resistor. When n = 1, the CPE behaves as a pure capacitor, and C = Q_0. The ZView software was used to estimate the average values from the EIS spectra (Table II.2.3) through the equivalent electric circuit.

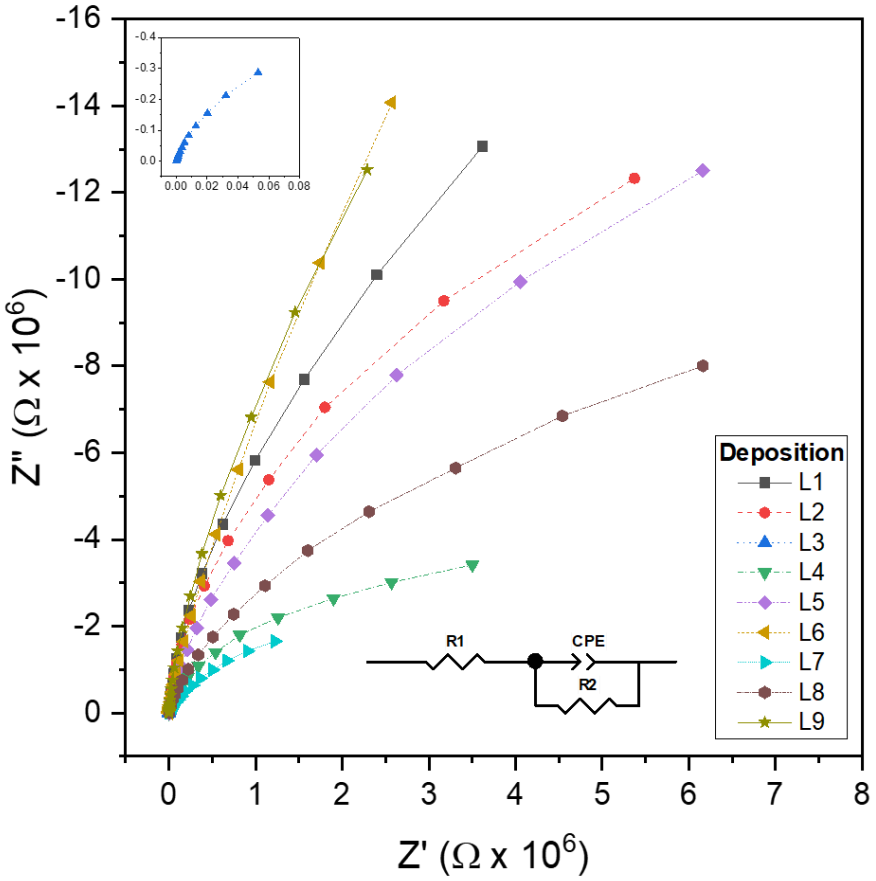

Figure II.2.6. Nyquist plots obtained by EIS of the BDD films obtained through the Taguchi matrix conditions: (a) All samples; (b) Samples L4, L5, L7, and L8; (c) Sample L3.

Table II.2.3. Average values estimated from the EIS spectra through the equivalent electric circuit using the ZView software.

Dep.	Q_0 (Ω^{-1} cm^{-2} s^n)	n	R_2 (Ω cm^{-2})	C (μF/cm²)	χ2
L1	1.23 x 10^{-6}	0.969	3.64 x 10^7	1.4	0.00150
L2	1.06 x 10^{-6}	0.973	2.97 x 10^7	1.2	0.00122
L3	6.59 x 10^{-5}	0.953	7.93 x 10^6	89.5	0.00094
L4	2.45 x 10^{-6}	0.881	7.25 x 10^6	3.6	0.00084
L5	1.04 x 10^{-6}	0.947	1.93 x 10^7	1.2	0.00023
L6	1.26 x 10^{-6}	0.968	2.87 x 10^7	1.4	0.00026
L7	4.60 x 10^{-6}	0.885	2.04 x 10^6	6.2	0.00112
L8	1.07 x 10^{-6}	0.940	8.07 x 10^6	1.2	0.00180
L9	1.47 x 10^{-6}	0.976	3.65 x 10^7	1.6	0.00046

The electron transfer resistance (R_2) reflects the electrode performance since it expresses the electrode's ability for charge transfer across the liquid-solid interface (57). Samples L3, L4, L7, and L8 showed R_2 values reduced in one order of magnitude compared to the other samples. Lower charge transfer resistances represent improved charge transfer processes (57). The direct oxidation process of organic contaminants can be facilitated by the improved charge transfer at the liquid-solid interface (58). The Taguchi analysis as a function of R_2 indicates that low gas pressures are beneficial towards a lower R_2.

All depositions resulted in films with low double-layer capacitance. A low double-layer capacitance is desirable for water treatment applications. However, sample L3 showed a higher capacitance value by almost two orders of magnitude compared to the average of the remaining samples. The overall Taguchi experiment analysis points out that lower argon levels and higher pressures reduce the BDD films' capacitance.

The slopes in the detailed Taguchi analysis (Figure II.2.1) suggest that BDD films could be further improved outside the limits chosen in the design of the Taguchi matrix. By comparing this study with the previous Taguchi method optimization (Section 2 - Supplementary Information), the questions formed upon the presence of these slopes can be partially answered. From both studies, it can be concluded that a 0.02 CH_4/H_2 ratio is ideal for this specific HFCVD reactor. Regarding the optimal balance between diamond quality and resistivity, a 25 mbar chamber pressure shows superior results compared to higher pressure values. However, such low-pressure yields films with lower

growth rates. Larger film thicknesses can be achieved by simply increasing the deposition time since it is directly influenced by the deposition duration (59). However, increasing the deposition time implies a higher production cost, so finding an optimal balance between the desired thickness and the operating costs is necessary. Both studies suggest that using pressures lower than 25 mbar could be beneficial. According to Lee *et al.*, the mean free path of active species is increased at low pressures, promoting fewer species collisions during their transport to the substrate and subsequently increasing the concentration of nucleating species (60). However, 25 mbar is already at the limit where our equipment can maintain the pressure constant throughout the deposition. Additionally, an attempt to improve FOM results would be to increase further the argon content in the gas mixture (> 30 sccm) and check if higher mass flows yield better results or if the FOM value decreases again. When we analyze the influence of each parameter on the properties of the films independently, especially in the case of argon, the highest diamond quality and growth rate and the lowest resistivity were obtained using 30 sccm of argon instead of not adding it to the gas mixture. Among the properties analyzed to produce BDD electrodes for pollutant degradation, the order of priority we adopted to select the optimal deposition conditions was from highest to lowest: low resistivity > high diamond quality > high growth rate > low absolute residual stress > large grain size > high surface roughness > wide EPW > low double layer capacitance > improved electron transfer process (low R_2). Therefore, the detailed analysis of the Taguchi experiments indicates that the optimal parameters would be: 0.02 CH_4/H_2 ratio, 25 mbar total pressure, and 30 sccm argon mass flow.

II.2.3.2. Validation of the optimized HFCVD deposition conditions

A new deposition was carried out to validate the Taguchi-optimized experimental conditions. The results of the optimized sample (OPT) are shown in Figure II.2.7 and Table II.2.4. The FOM value obtained for the optimized deposition parameters was 6% superior to deposition L5, which presented the highest FOM value among the Taguchi experiment depositions. Significant differences were observed regarding growth rate, residual stress, and surface roughness. The optimized film presented a superior growth rate and lower residual stress. Furthermore, the optimized condition yielded films with a more uniform grain size distribution. Both samples were nearly similar in diamond quality and EPW width. However, the OPT's conductivity and surface roughness were inferior. Sample L5 presented a slightly lower resistivity value than OPT, and a rougher surface, which is beneficial for pollutant degradation. Although conditions were optimized to high

diamond quality, the Raman spectrum still shows significant non-diamond carbon inclusions. Tweaking the temperature of the filaments or the substrates and controlling the substrate temperature using a substrate heater instead of relying only upon substrate heating by the filaments could be possible solutions to increase the quality of the films. For future practical application purposes, the estimated price for electrical energy per square meter of the optimized diamond electrode would be 222.85 €/m^2, considering an energy rate of 0.1566 €/kWh. Moreover, it is essential to emphasize that these conditions are only optimal for the specific HFCVD reactor used in this study. Reactors with different dimensions, configurations, and characteristics may generate films with different properties than expected, mainly due to changes in temperature gradients and kinetics inside the reactor's chamber. Therefore, it is ideally necessary to determine the optimal deposition conditions for each reactor. Nevertheless, this study offers essential directions to understand the effect of gas composition and total gas pressure on the main characteristics of BDD films to be applied as electrodes for pollutant electrooxidation.

In industrial applications, BDD electrodes are expected to deliver lifetimes beyond 1000 hours. To assess the chemical and electrochemical stability of the optimized BDD film, a series of 150 cyclic voltammetry cycles in a 0.1 M H_2SO_4 electrolyte solution were conducted, as well as chronopotentiometry experiments in the same electrolyte, lasting 5 hours with an applied current density of 30 mA/cm². Following these stability assessments, SEM/EDS analysis was performed to investigate any structural or compositional changes that may have occurred due to extensive electrochemical cycling and exposure to acidic conditions.

Table II.2.4. Characteristics of the optimized BDD films compared with sample L5 (highest FOM in the Taguchi experiment).

Dep.	CH_4/H_2	Ar (sccm)	P (mbar)	G (µm/h)	Q ($I_{diamond}/I_G$)	ρ (Ω.cm)	[B] (cm^{-3})	AGS (µm)	σ_r (GPa)	EPW [a] (V vs. SCE)	C (µF/cm²)	Sa (nm)	FOM
L5	0.02	0	25	0.87	1.14	3.87×10^{-3}	5.4×10^{20}	0.73 ± 0.53	-3.4	2.67	1.23	133.8	401.28
OPT	0.02	30	25	1.45	1.19	8.56×10^{-3}	4.4×10^{20}	0.86 ± 0.04	-2.1	2.75	0.58	52.7	426.68

** Opt.: Optimized; P: Pressure; G: Growth Rate; Q: Diamond Quality Factor; R: Resistivity; σ_r: Residual Stress; AGS: Average Grain Size; EPW: Electrochemical Potential Window; C: Capacitance; Sa: Arithmetical Mean Height; FOM: Figure-of-merit.*

[a] EPW in 0.1 M H_2SO_4.

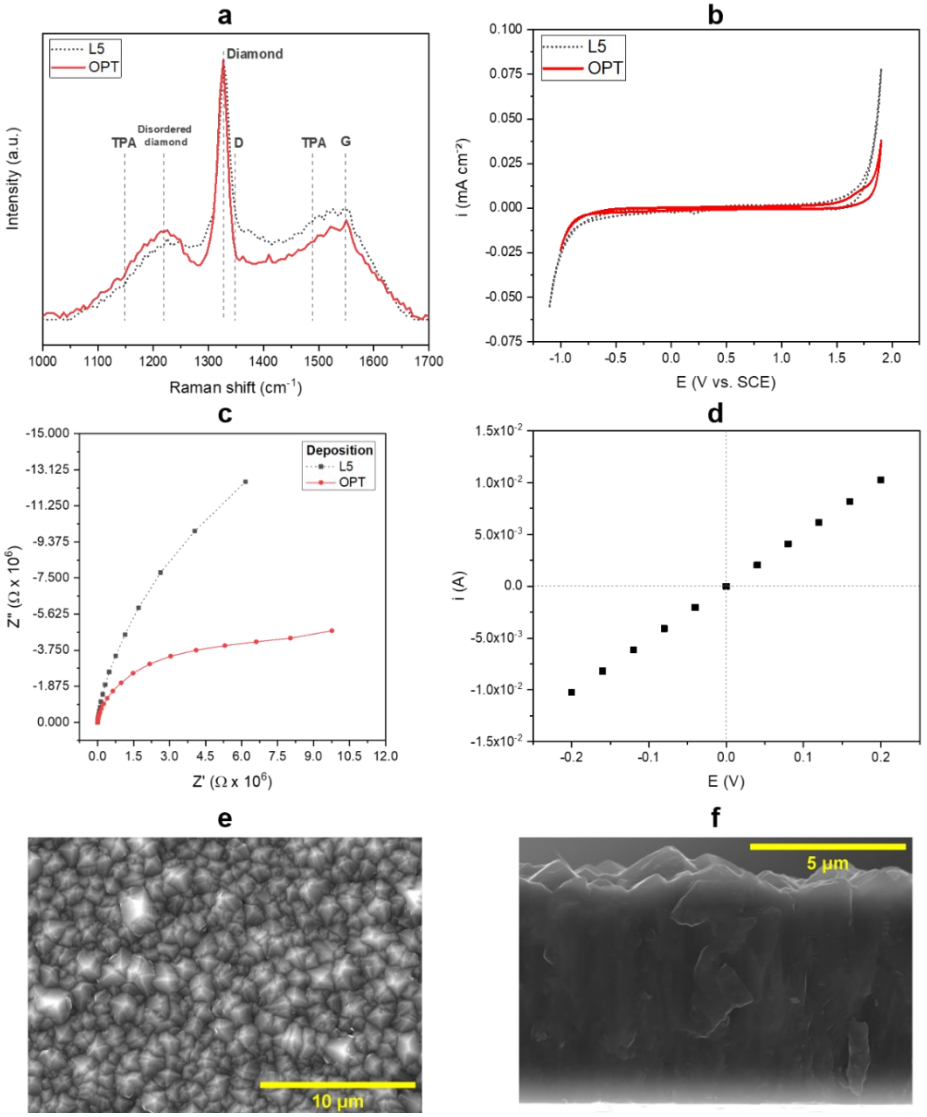

Figure II.2.7. Characterization of the BDD film obtained under the optimized deposition conditions: (a) Raman spectrum obtained with a 532 nm laser line compared with deposition L5; (b) Cyclic voltammogram recorded in 0.1 M H_2SO_4 electrolyte at a 100 mV/s scan rate, compared with deposition L5; (c) Nyquist plots of the EIS spectrum compared with deposition L5; (d) Characteristic current-voltage curve; SEM micrographs in plan view and (f) cross-section.

The cyclic voltammogram in Figure II.2.8.a illustrates a minor expansion of the potential window after the first cycle, with an approximate increase of +0.1V/SCE in the oxygen evolution overpotential. Notably, from the second cycle through all 150 cycles, no substantial alteration in the electrode response during cyclic voltammetry was observed, suggesting high electrochemical stability. SEM/EDS results (Figure II.2.8.b and II.2.8.c) after the chemical and electrochemical stability assessments confirm the film's integrity, with no signs of delamination or areas susceptible to solution permeation. It is worth

noting that EDS analysis detected only carbon and oxygen, without any indication of silicon from the substrate, providing further support for the absence of delamination. The SEM micrograph revealed residual surface contamination after the stability tests, likely originating from organic materials. These results indicate that the optimized deposition conditions in this study are suitable for electrochemical water treatment applications. Additionally, the film's exceptional stability underscores its potential for long-term performance in practical electrochemical systems.

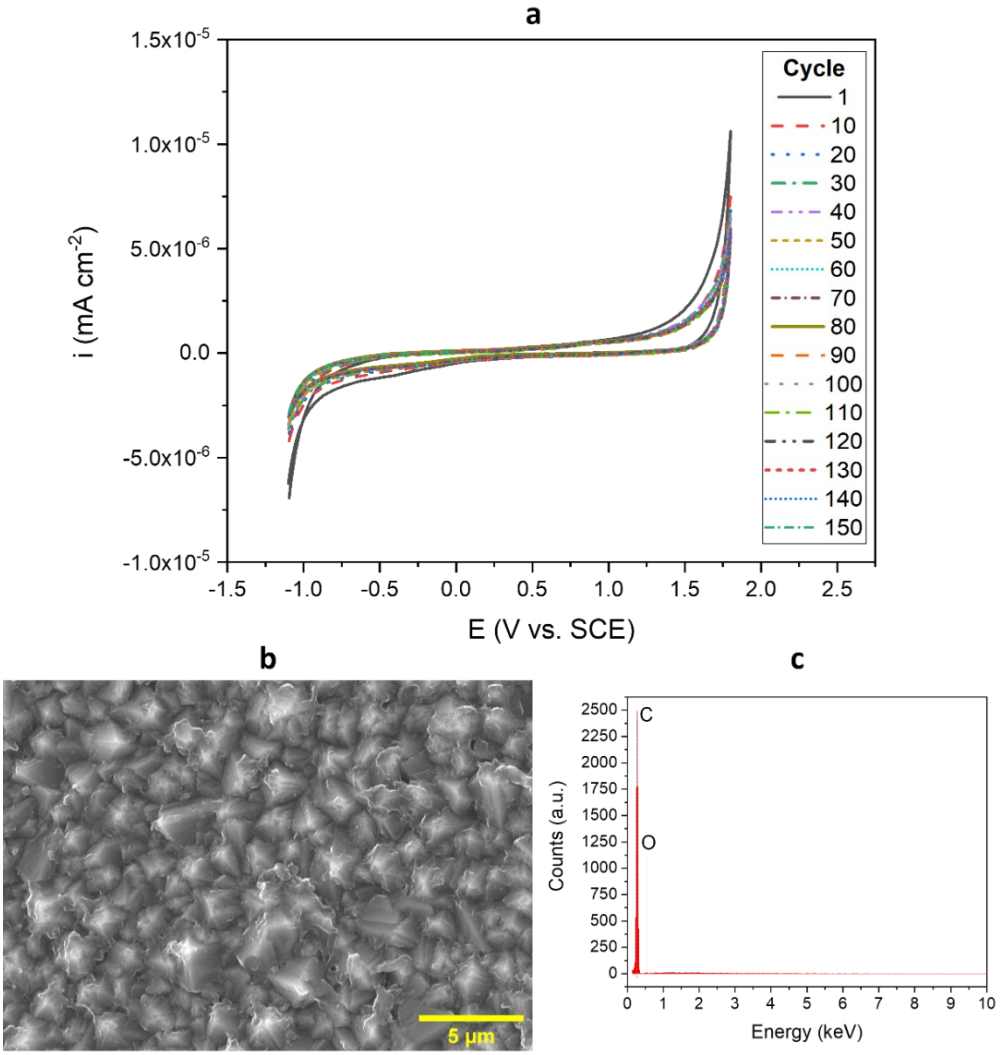

Figure II.2.8. (a) Cyclic voltammogram of the optimized BDD film recorded for 150 cycles in a 0.1 M H_2SO_4 electrolyte at 100 mV/s scan rate; SEM micrographs (b) and EDS analysis (c) of the optimized BDD film after chemical and electrochemical stability assessments.

II.2.4. Conclusions

The Taguchi technique was proven as a great tool to systematically determine optimal BDD deposition conditions in CVD reactors with fewer experimental trials. A Figure-of-Merit (FOM) equation was proposed for optimizing BDD films for water treatment applications. The analysis of the combined effects of gas composition and total gas pressure on the properties and electrochemical activity of BDD films deposited by HFCVD based on the Taguchi approach led to the following conclusions:

- Diamond quality was influenced by a combination of the three studied factors. The ideal CH_4/H_2 ratio and argon flow to obtain BDD films with the least amount of non-diamond carbon inclusions in the specific HFCVD system used in this study were 0.02 and 30 mbar, respectively. Depositions with CH_4/H_2 ratios above and below this optimum value tend to yield films with reduced diamond quality. A chamber pressure of 25 mbar produced BDD films with the optimal balance of diamond quality and resistivity.
- Reduced film resistivities were obtained by increasing the argon concentration and decreasing the total gas pressure;
- Increased grain sizes and growth rates were acquired by increasing the CH_4/H_2 ratio and the total gas pressure. A more negligible impact on these two properties was also observed with changes in argon mass flow. A 0.02 CH_4/H_2 ratio was found ideal for obtaining BDD films with larger grain sizes;
- Lower residual stresses were obtained in reduced argon flows and increased pressures;
- Wider electrochemical potential windows were observed in films grown under higher pressures;
- Lower double-layer capacitance values were observed in films grown in atmospheres with decreased argon concentration and higher pressure;
- Reduced total pressures seem to improve the electron transfer process of BDD films.

The Taguchi experiment detailed analysis indicated that the optimum deposition conditions within the considered ranges for producing BDD electrodes for water treatment applications would be a 0.02 CH_4/H_2 ratio, 25 mbar total pressure, and 30 sccm Argon mass flow, considering the following characteristics from highest to lowest priority: low resistivity > high diamond quality > high growth rate > low absolute residual stress > large grain size > high surface roughness > wide EPW > low double layer capacitance > improved electron transfer process. Such conclusions were validated, and the optimized

deposition conditions FOM value was superior to the highest value obtained within the depositions applied in the Taguchi matrix.

II.2.5. References

1. United Nations. The 17 goals - Sustainable Development Goals; [reviewed 2023 July 5; cited date 2023 July 5]. Available from: https://sdgsunorg/goals.

2. Chowdhary P, Bharagava RN, Mishra S, Khan N. Role of Industries in Water Scarcity and Its Adverse Effects on Environment and Human Health. Environmental Concerns and Sustainable Development: Springer, Singapore; 2020.

3. Karpińska J, Kotowska U. Removal of Organic Pollution in the Water Environment. Water-Sui. 2019;11(10).

4. Santos MC, Antonin VS, Souza FM, Aveiro LR, Pinheiro VS, Gentil TC, *et al.* Decontamination of wastewater containing contaminants of emerging concern by electrooxidation and Fenton-based processes - A review on the relevance of materials and methods. Chemosphere. 2022;307(Pt 3):135763.

5. Qiao J, Xiong Y. Electrochemical oxidation technology: A review of its application in high-efficiency treatment of wastewater containing persistent organic pollutants. J Water Process Eng. 2021;44.

6. Voglar D, Lestan D. Electrochemical treatment of spent solution after EDTA-based soil washing. Water Res. 2012;46(6):1999-2008.

7. Cavalcanti EB, Garcia-Segura S, Centellas F, Brillas E. Electrochemical incineration of omeprazole in neutral aqueous medium using a platinum or boron-doped diamond anode: Degradation kinetics and oxidation products. Water Res. 2013;47(5):1803-15.

8. Moreira FC, Boaventura RAR, Brillas E, Vilar VJP. Electrochemical advanced oxidation processes: A review on their application to synthetic and real wastewaters. Appl Catal B Environ. 2017;202:217-61.

9. Nidheesh PV, Divyapriya G, Oturan N, Trellu C, Oturan MA. Environmental Applications of Boron-Doped Diamond Electrodes: 1. Applications in Water and Wastewater Treatment. ChemElectroChem. 2019;6(8):2124-42.

10. Brosler P, Girão AV, Silva RF, Tedim J, Oliveira FJ. In-house vs. commercial boron-doped diamond electrodes for electrochemical degradation of water pollutants: A critical review. Front Mater. 2023;10.

11. Brosler P, Girão AV, Silva RF, Tedim J, Oliveira FJ. Electrochemical Advanced Oxidation Processes Using Diamond Technology: A Critical Review. Environments. 2023;10(2).

12. Salgueiredo E, Amaral M, Neto MA, Fernandes AJS, Oliveira FJ, Silva RF. HFCVD diamond deposition parameters optimized by a Taguchi Matrix. Vacuum. 2011;85(6):701-4.

13. Parikh RP, Adomaitis RA. An overview of gallium nitride growth chemistry and its effect on reactor design: Application to a planetary radial-flow CVD system. J Cryst Growth. 2006;286(2):259-78.

14. Ali N, Neto VF, Mei S, Cabral G, Kousar Y, Titus E, *et al.* Optimisation of the new time-modulated CVD process using the Taguchi method. Thin Solid Films. 2004;469-470(SPEC. ISS.):154-60.

15. Ghasemi E, Aaghaie A, Cudney EA. Mahalanobis Taguchi system: a review. International Journal of Quality & Reliability Management. 2015;32(3):291-307.

16. Karna SK, Sahai R. An Overview on Taguchi Method. International Journal of Mathematical, Engineering and Management Sciences. 2022(1):1-7.

17. Kaushal A, Alexander R, Rao PT, Prakash J, Dasgupta K. Artificial neural network, Pareto optimization, and Taguchi analysis for the synthesis of single-walled carbon nanotubes. Carbon Trends. 2021;2.

18. Qistina O, Salmiaton A, Choong TSY, Taufiq-Yap YH, Izhar S. Optimization of carbon nanotube-coated monolith by direct liquid injection chemical vapor deposition based on taguchi method. Catalysts. 2020;10(1).

19. Santangelo S, Lanza M, Piperopoulos E, Milone C. Optimized CVD production of CNT-based nanohybrids by taguchi robust design. Journal of Nanoscience and Nanotechnology. 2012;12(3):2424-36.

20. Sufian S, Yusup S, Ahmadun FR. Optimization for development of carbon nanotubes using Taguchi method at constant temperature. J Nano Res-Sw. 2010;11:95-100.

21. Ting JH, Chang CC, Chen SL, Lu DS, Kung CY, Huang FY. Optimization of field emission properties of carbon nanotubes by Taguchi method. Thin Solid Films. 2006;496(2):299-305.

22. Sharon M, Apte PR, Purandare SC, Zacharia R. Application of the taguchi analytical method for optimization of effective parameters of the chemical vapor deposition process controlling the production of nanotubes/nanobeads. Journal of Nanoscience and Nanotechnology. 2005;5(2):288-95.

23. Şimşek B. TOPSIS based Taguchi design optimization for CVD growth of graphene using different carbon sources: Graphene thickness, defectiveness and homogeneity. Chinese Journal of Chemical Engineering. 2019;27(3):685-94.

24. Mehedi HA, Baudrillart B, Alloyeau D, Mouhoub O, Ricolleau C, Pham VD, *et al.* Synthesis of graphene by cobalt-catalyzed decomposition of methane in plasma-enhanced CVD: Optimization of experimental parameters with Taguchi method. J Appl Phys. 2016;120(6).

25. Choi D, Pyo Y, Jung SB, Kim Y, Yoon EH, Lee CS. Application of the Taguchi method to optimize graphene coatings on copper nanoparticles formed using a solid carbon source. Materials Transactions. 2016;57(7):1177-82.

26. Watanabe T, Honda Y, Kanda K, Einaga Y. Tailored design of boron-doped diamond electrodes for various electrochemical applications with boron-doping level and sp2

-bonded carbon impurities. Phys Status Solidi A. 2014;211(12):2709-17.

27. Marcionilio SMLdO, Araújo DM, Nascimento TdV, Martínez-Huitle CA, Linares JJ. Evaluation of the toxicity reduction of an ionic liquid solution electrochemically treated using BDD films with different sp3/sp2 ratios. Electrochem Commun. 2020;118.

28. Garcia-Segura S, Vieira dos Santos E, Martínez-Huitle CA. Role of sp3/sp2 ratio on the electrocatalytic properties of boron-doped diamond electrodes: A mini review. Electrochem Commun. 2015;59:52-5.

29. Karim AV, Nidheesh PV, Oturan MA. Boron-doped diamond electrodes for the mineralization of organic pollutants in the real wastewater. Curr Opin Electrochem. 2021;30.

30. Muzyka K, Sun J, Fereja TH, Lan Y, Zhang W, Xu G. Boron-doped diamond: current progress and challenges in view of electroanalytical applications. Anal Methods. 2019;11(4):397-414.

31. Qi Y, Long H, Ma L, Wei Q, Li S, Yu Z, *et al.* Enhanced selectivity of boron doped diamond electrodes for the detection of dopamine and ascorbic acid by increasing the film thickness. Appl Surf Sci. 2016;390:882-9.

32. Standardization IOf. ISO 4499-2:2020 - Hardmetals. Metallographic determination of microstructure — Part 2: Measurement of WC grain size2020.

33. Prawer S, Nemanich RJ. Raman spectroscopy of diamond and doped diamond. Philos Trans A Math Phys Eng Sci. 2004;362(1824):2537-65.

34. Ralchenko VG, Smolin AA, Pereverzev VG, Obraztsova ED, Korotoushenko KG, Konov VI, *et al.* Diamond deposition on steel with CVD tungsten intermediate layer. Diamond Relat Mater. 1995;4(5-6):754-8.

35. Bernard M, Deneuville A, Muret P. Non-destructive determination of the boron concentration of heavily doped metallic diamond thin films from Raman spectroscopy. Diamond Relat Mater. 2004;13(2):282-6.

36. Bernard M, Baron C, Deneuville A. About the origin of the low wave number structures of the Raman spectra of heavily boron doped diamond films. Diamond Relat Mater. 2004;13(4-8):896-9.

37. Bourgeois E, Bustarret E, Achatz P, Omnes F, Blase X. Impurity dimers in superconducting B-doped diamond: Experiment and first-principles calculations. Physical Review B. 2006;74(9).

38. Umezawa H, Takenouchi T, Takano Y, Kobayashi K, Nagao M, Sakaguchi I, *et al.* Advantage on Superconductivity of Heavily Boron-Doped (111) Diamond Films. arXiv. 2005.

39. Vlasov II, Gavrilov IP, Artemenko SN, Basov AA. On the origin of the Raman scattering in heavily boron-doped diamond. arXiv. 2008.

40. Medeiros de Araújo D, Cañizares P, Martínez-Huitle CA, Rodrigo MA. Electrochemical conversion/combustion of a model organic pollutant on BDD anode: Role of sp 3 /sp 2 ratio. Electrochem Commun. 2014;47:37-40.

41. Ferrari AC, Robertson J. Raman spectroscopy of amorphous, nanostructured, diamond-like carbon, and nanodiamond. Philos Trans A Math Phys Eng Sci. 2004;362(1824):2477-512.

42. Azevedo AF, Baldan MR, Ferreira NG. Doping level influence on chemical surface of diamond electrodes. J Phys Chem Solids. 2013;74(4):599-604.

43. Ferrari AC, Robertson J. Origin of the1150−cm−1Raman mode in nanocrystalline diamond. Physical Review B. 2001;63(12).

44. Yang N, Yu S, Macpherson JV, Einaga Y, Zhao H, Zhao G, *et al.* Conductive diamond: synthesis, properties, and electrochemical applications. Chem Soc Rev. 2019;48(1):157-204.

45. Lu Y-G, Turner S, Verbeeck J, Janssens SD, Wagner P, Haenen K, *et al.* Direct visualization of boron dopant distribution and coordination in individual chemical vapor deposition nanocrystalline B-doped diamond grains. Appl Phys Lett. 2012;101(4).

46. Einaga Y, Foord JS, Swain GM. Diamond electrodes: Diversity and maturity. Mrs Bull. 2014;39(6):525-32.

47. Li H, Zhang T, Li L, Lü X, Li B, Jin Z, *et al.* Investigation on crystalline structure, boron distribution, and residual stresses in freestanding boron-doped CVD diamond films. J Cryst Growth. 2010;312(12-13):1986-91.

48. Ferreira NG, Abramof E, Leite NF, Corat EJ, Trava-Airoldi VJ. Analysis of residual stress in diamond films by x-ray diffraction and micro-Raman spectroscopy. J Appl Phys. 2002;91(4):2466-72.

49. Neto MA, Pato G, Bundaleski N, Teodoro OMND, Fernandes AJS, Oliveira FJ, *et al.* Surface modifications on as-grown boron doped CVD diamond films induced by the B2O3–ethanol–Ar system. Diamond Relat Mater. 2016;64:89-96.

50. Dychalska A, Popielarski P, Franków W, Fabisiak K, Paprocki K, Szybowicz M. Study of CVD diamond layers with amorphous carbon admixture by Raman scattering spectroscopy. Mater Sci-Poland. 2015;33(4):799-805.

51. Ivandini TA, Einaga Y. Polycrystalline boron-doped diamond electrodes for electrocatalytic and electrosynthetic applications. Chem Commun. 2017;53(8):1338-47.

52. Pruvost F, Deneuville A. Analysis of the Fano in diamond. Diamond Relat Mater. 2001;10(3-7):531-5.

53. Sarakhman O, Svorc L. A Review on Recent Advances in the Applications of Boron-Doped Diamond Electrochemical Sensors in Food Analysis. Crit Rev Anal Chem. 2022;52(4):791-813.

54. Hirschorn B, Orazem ME, Tribollet B, Vivier V, Frateur I, Musiani M. Determination of effective capacitance and film thickness from constant-phase-element parameters. Electrochim Acta. 2010;55(21):6218-27.

55. Bogdanowicz R, Ryl J. Structural and electrochemical heterogeneities of boron-doped diamond surfaces. Curr Opin Electrochem. 2022;31.

56. Chang B-Y. Conversion of a Constant Phase Element to an Equivalent Capacitor. Journal of Electrochemical Science and Technology. 2020;11(3):318-21.

57. Mei R, Wei Q, Zhu C, Ye W, Zhou B, Ma L, *et al.* 3D macroporous boron-doped diamond electrode with interconnected liquid flow channels: A high-efficiency electrochemical degradation of RB-19 dye wastewater under low current. Appl Catal B Environ. 2019;245:420-7.

58. Yang W, Deng Z, Wang Y, Ma L, Zhou K, Liu L, *et al.* Porous boron-doped diamond for efficient electrocatalytic elimination of azo dye Orange G. Sep Purif Technol. 2022;293.

59. van der Drift A. Evolutionary selection: a principle governing growth orientation in vapour deposited layers. Philips Research Reports. 1967;22:267–88.

60. Lee ST, Lam YW, Lin Z, Chen Y, Chen Q. Pressure effect on diamond nucleation in a hot-filament CVD system. Physical Review B. 1997;55(23):15937-41.

II.2.6. Supplementary Information

II.2.6.1. Taguchi experiment supplementary information

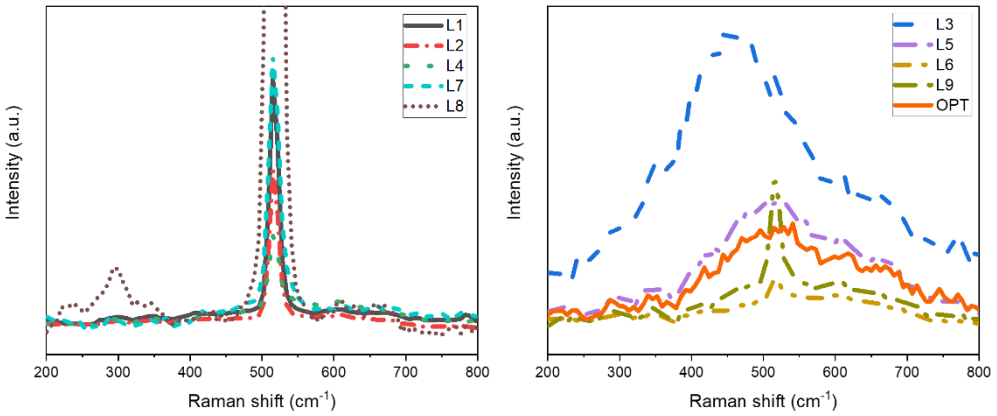

Supplementary Figure II.2.1. Details on the peaks at approximately 500 cm^{-1} in the Raman spectra (532 nm laser line) of the BDD films obtained under the Taguchi matrix conditions (Table II.2.1): (a) Samples with boron doping levels below 2 x 10^{20}, showing an intense Si substrate peak at ~520 cm^{-1}; (b) Samples that show the peat at ~500 cm^{-1}, related to boron doping levels above 2 x 10^{20} (metallic conduction) that promotes partial or complete disappearance of the Si substrate peak.

II.2.6.2. Previously studied Taguchi matrix

An L9 orthogonal array Taguchi Matrix was built to optimize the deposition parameters of an HFCVD. The controlled parameters were gas composition (CH_4/H_2), total pressure, argon mass flow and boron mass flow. Three levels were selected for each of these parameters. The films were deposited over Si substrates (Siegert Wafer, Ø 50.8 ± 0.3 mm, Prime Grade), with the previous seeding by scratching the surface with abrasive diamond powder (0.5-1.0 μm) on a polishing cloth.

Supplementary Table II.2.1. Previously studied Taguchi matrix of the HFCVD parameters and characteristics of the BDD films.

# dep.	CH_4/H_2	Total Pressure (mbar)	Ar (sccm)	B (µL/min)	Growth rate (µm/h)	Quality factor ($I_{diamond}/I_G$)	Resistivity (Ω.cm)	Average grain size (µm)	Residual Stress (GPa)
1	0.02	50	10	1.25	0.42	1.90	7.15×10^{-3}	1.20	-1.2
2	0.04	50	15	2.5	0.63	0.46	8.82×10^{-3}	0.69	-1.3
3	0.06	50	20	3.75	0.33	0.19	4.63×10^{-1}	0.02	-1.7
4	0.02	75	15	3.75	0.71	0.58	5.38×10^{-3}	1.01	-4.0
5	0.04	75	20	1.25	0.93	0.23	1.47×10^{-2}	0.53	-3.1
6	0.06	75	10	2.5	0.82	0.17	5.38×10^{-2}	0.03	-2.3
7	0.02	100	20	2.5	1.05	0.75	4.89×10^{-3}	1.32	-5.5
8	0.04	100	10	3.75	1.09	0.36	1.30×10^{-2}	0.84	-3.4
9	0.06	100	15	1.25	0.81	0.03	5.21×10^{-2}	0.31	-2.8

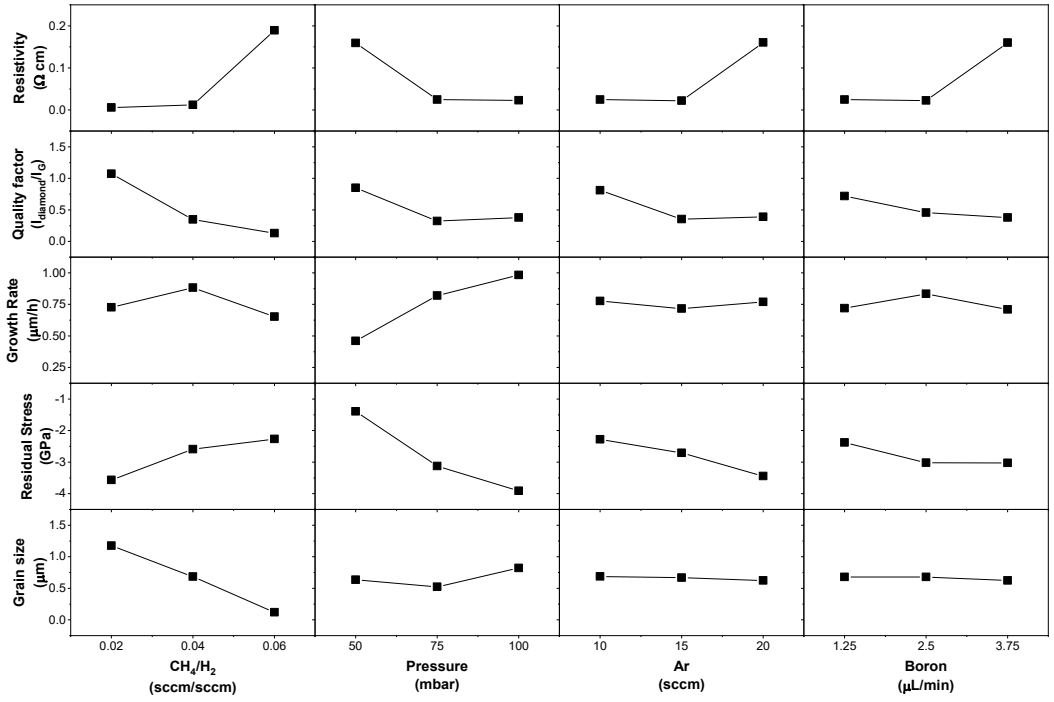

Supplementary Figure II.2.2. Analysis of the previously performed Taguchi experiment.

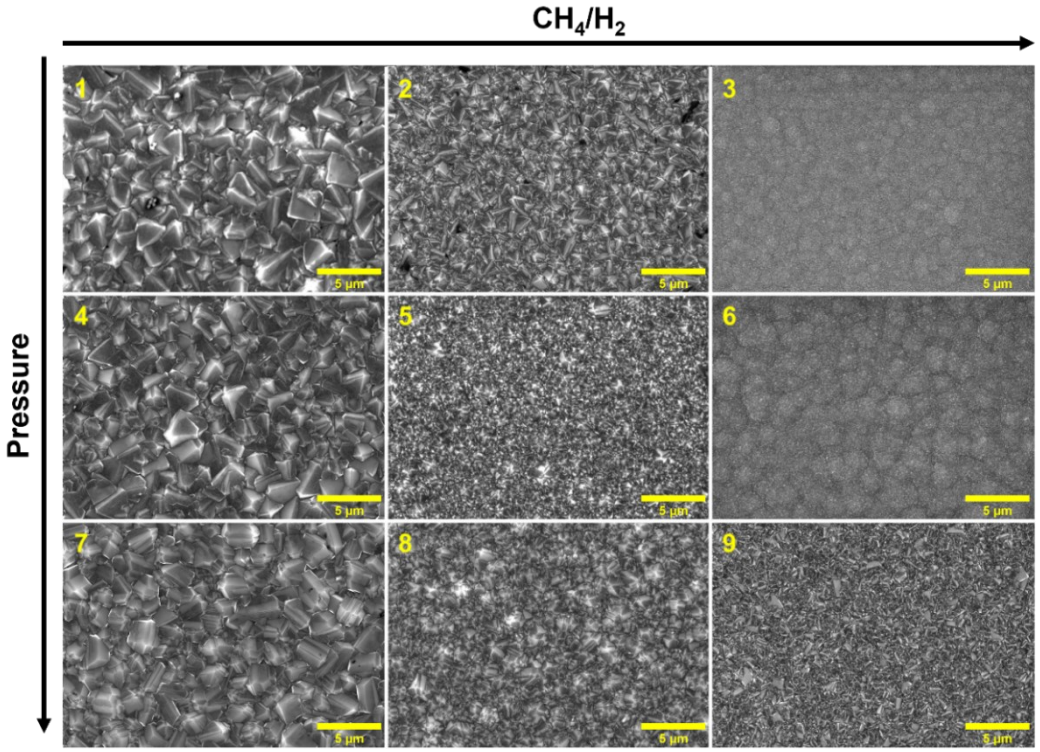

Supplementary Figure II.2.3. SEM micrographs in the plan view of BDD films obtained under the previously studied Taguchi matrix conditions.

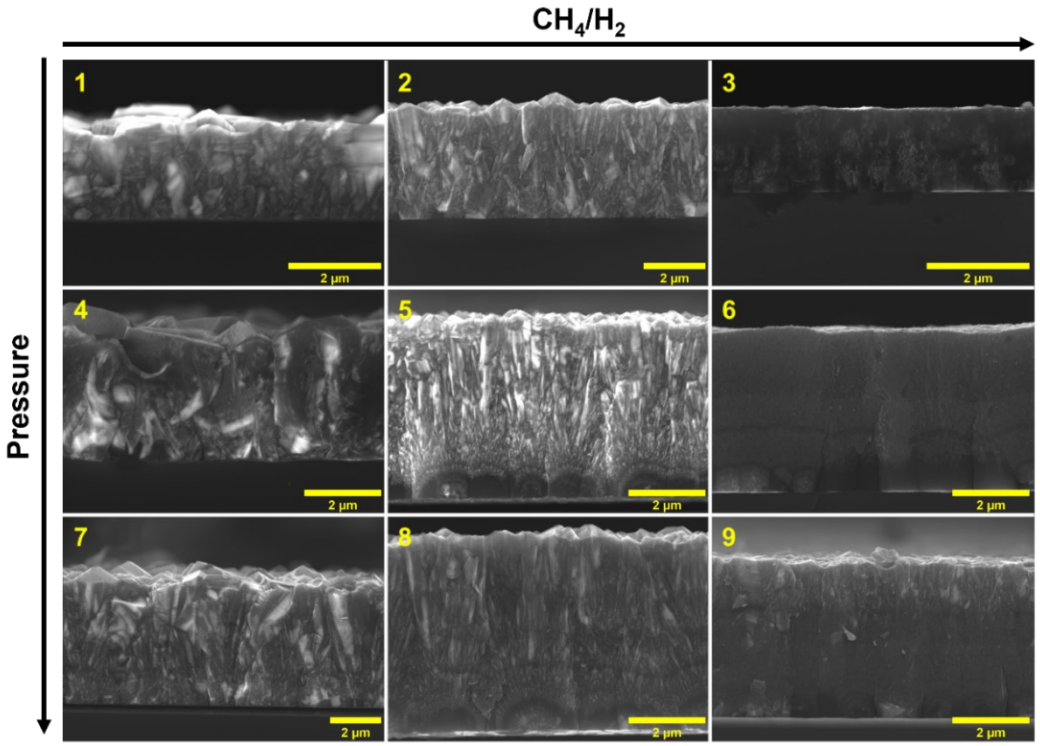

Supplementary Figure II.2.4. SEM micrographs in cross-section of BDD films obtained under the previously studied Taguchi matrix conditions.

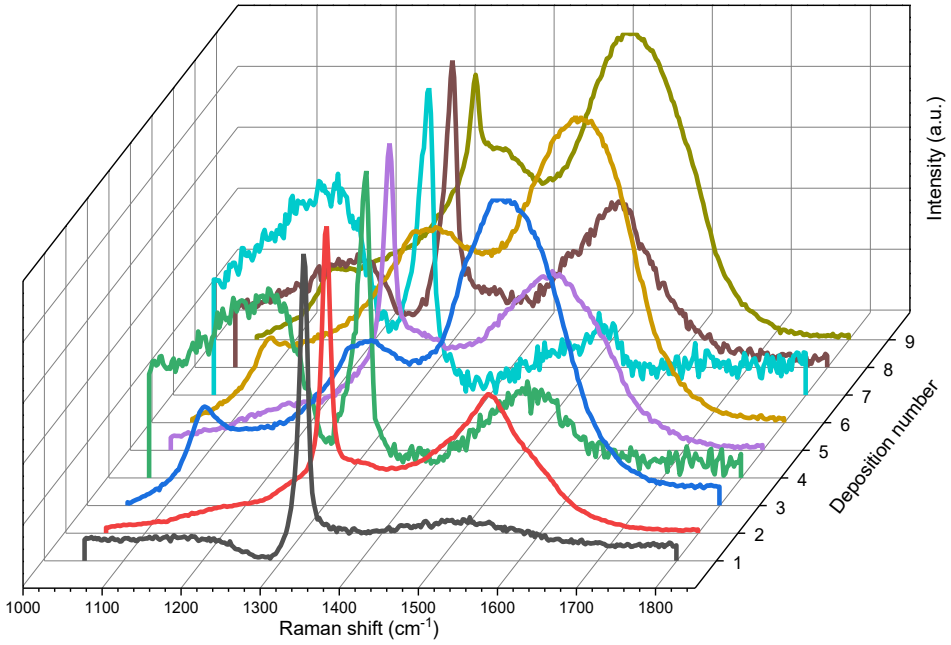

Supplementary Figure II.2.5. Raman spectra of BDD films obtained under the previously studied Taguchi matrix conditions, recorded with a 442 nm laser line.

After a thorough analysis of the Taguchi experiment and the resulting characteristics of the BDD films (diamond quality, resistivity, growth rate, residual stress, and grain size), the optimized deposition conditions for microcrystalline and nanocrystalline boron-doped diamond films were selected within the adopted limits of each HFCVD deposition parameter, as shown in Supplementary Table II.2.2.

Supplementary Table II.2.2. Optimized HFCVD deposition conditions defined based on the previously performed Taguchi experiment depending on microstructure.

	CH_4/H_2 (%)	**Total Pressure (mbar)**	**Ar (sccm)**	**B (µL/min)**
Microcrystalline	0.02	100	20	2.50
Nanocrystalline	0.06	25	10	2.50

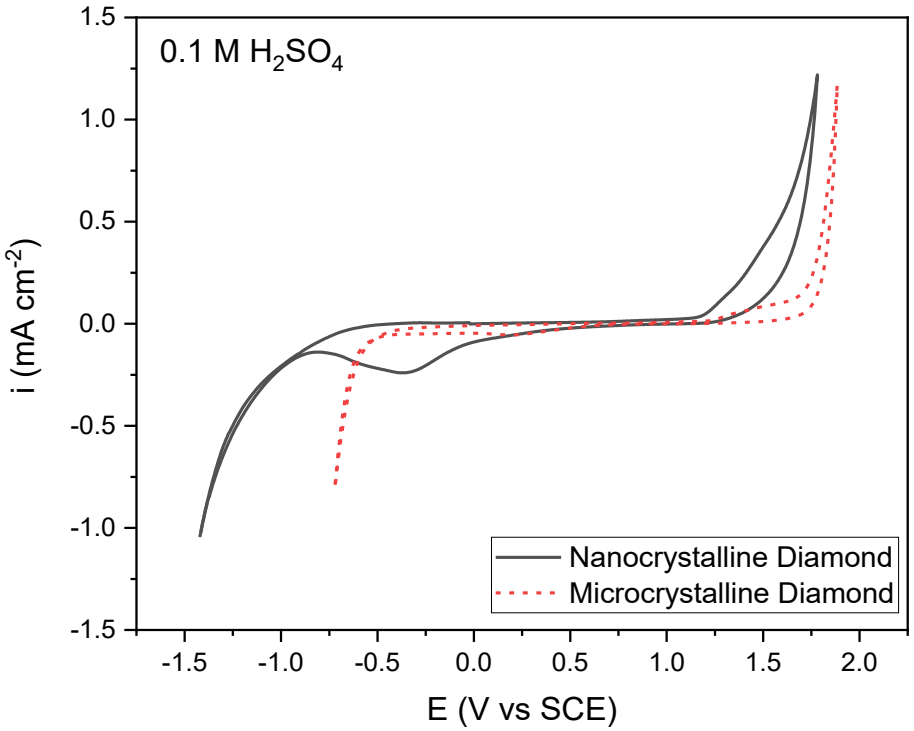

Supplementary Figure II.2.6. Cyclic voltammogram of microcrystalline and nanocrystalline BDD films deposited under optimized conditions (previous Taguchi experiment), recorded in 0.1 M H_2SO_4 electrolyte at a 100 mV/s scan rate.

Chapter III

Performance Evaluation of BDD/Si_3N_4-TiN Electrodes in Water Treatment

This chapter is dedicated to demonstrating the concept of BDD electrodes deposited on electroconductive Si_3N_4-TiN substrates. This was achieved through the characterization of the assembly and its practical application in the removal of phenol, one of the most common persistent organic pollutants found in industrial and municipal sewage, primarily originating from the chemical, petroleum, dye, agricultural, and pharmaceutical industries. This work was consolidated in two papers, the first submitted for publication and the second on the process of first submission.

The work presented in **Section III.1** was submitted to *Next Sustainability* and aims to establish a sustainable and durable solution for large-scale water treatment using Electrochemical Advanced Oxidation Processes, by validating the concept of BDD/Si_3N_4-TiN electrodes. In this study, BDD films were deposited via Hot Filament Chemical Vapor Deposition onto electroconductive Si_3N_4-TiN substrates. The resulting BDD/Si_3N_4-TiN electrodes underwent analysis, including examination of their microstructure, diamond quality, conductivity, adhesion strength, service life, and electrochemical properties. To evaluate the electrodes in practical applications, phenol was chosen as a model pollutant to assess the electrode's effectiveness in oxidizing pollutants.

Section III.2 describes radiofrequency plasma treatments with different gases to functionalize BDD/Si_3N_4-TiN surfaces. The primary aim of this study was to determine whether modifying the surface chemistry of BDD electrodes through chemical functionalization could enhance their electrochemical performance in water treatment applications. The evaluation of the modified BDD/Si_3N_4-TiN surfaces involved several methods, including Raman spectroscopy, sessile drop contact angle measurements, resistivity measurements, cyclic voltammetry, electrochemical impedance spectroscopy, and Mott-Schottky analysis. A comparative analysis was conducted between the plasma-treated BDD electrodes and as-grown BDD films in the context of electrochemical phenol oxidation.

III.1. Long-lasting BDD/Si_3N_4-TiN Electrodes for Sustainable Water Remediation

Priscilla Brosler[1], Isabel Sousa[1], Helena G. A. Nadais[2], Rui F. Silva[1], João Tedim[1], Filipe J. Oliveira[1]

[1] CICECO - Aveiro Institute of Materials & Department of Materials and Ceramic Engineering, University of Aveiro, 3810-193 Aveiro, Portugal
[2] CESAM - Centre for Environmental and Marine Studies & Department of Environment and Planning, University of Aveiro, 3810-193 Aveiro, Portugal

The present work was submitted to *Next Sustainability*

Abstract

Boron-doped diamond (BDD) thin films have the potential to revolutionize water remediation through electrochemical oxidation, converting persistent pollutants into CO_2 and water. However, a significant challenge in implementing BDDs on a large scale is the choice of substrate material. Electrode failure typically occurs due to BDD delamination from the substrate. We propose using a ceramic composite of silicon nitride (Si_3N_4) and titanium nitride (TiN) as a substrate to address this issue. This electroconductive composite combines Si_3N_4's high wear resistance, chemical stability, and high affinity for diamond film growth with the TiN's metal-like conductivity. In this work, BDD films were grown by Hot Filament Chemical Vapor Deposition (HFCVD) over Si_3N_4-TiN substrates containing 30%vol. TiN. The resulting BDD/Si_3N_4-TiN electrodes were analyzed concerning their microstructure, diamond quality, conductivity, adhesion strength, service life, and electrochemical properties. Phenol was used as a model to test the electrode's ability to oxidize pollutants. We found that the BDD/Si_3N_4-TiN electrode could eliminate phenol entirely and up to 98.8% of the model solution's Chemical Oxygen Demand (COD) after 5 hours of direct anodic oxidation, with an Average Current Efficiency (ACE) of 14% and an energy consumption of 138 kWh kg_{COD}^{-1}. Furthermore, the BDD/Si_3N_4-TiN electrode could withstand more than 2016 h of accelerated life test without film delamination. Overall, the results demonstrate that BDD/Si_3N_4-TiN electrodes are a potential long-lasting solution for large-scale water treatment by electrochemical advanced oxidation processes (EAOPs) in a sustainable manner, especially if combined with renewable energy sources.

III.1.1. Introduction

Boron-doped diamond (BDD) electrodes have been extensively studied for the treatment of many sources of contaminated water, such as the treatment of organic pollutants (1), dyes (2), pharmaceuticals (3), synthetic wastewater (4), industrial wastewater (5-7), swimming pool water (8), landfill leachate (9, 10), among others. BDD is considered one of the most promising electrode materials (11). It has multiple electrochemical applications due to its remarkable properties, which include high chemical and electrochemical stability (even in very aggressive media), an inert surface with low adsorption properties, and a strong tendency to resist deactivation, the widest known potential window in aqueous and nonaqueous electrolytes, a high overpotential for water decomposition (+2.3 V vs. SHE), excellent efficiency in the production of hydroxyl radicals, and a very low double-layer capacitance and background current (12, 13). When applied in electrochemical advanced oxidation processes (EAOPs), BDD electrodes can generate highly reactive oxidizing agents, such as hydroxyl radicals, which have the ability to degrade specific pollutants completely and non-selectively into CO_2 and H_2O, with high current efficiencies (14-16). From an environmental point of view, EAOPs are fascinating methods since they require no or low amounts of chemical reagents and catalysts during water treatment processes (16).

Although laboratory and pilot tests on wastewaters have been successful (7, 9, 17, 18), the size and service life of BDD-based electrodes remain a challenge for their application on a large scale, mainly due to the lack of an appropriate substrate. The main factor that causes electrode failure is the BDD film delamination, caused by poor film adhesion to the substrate (19). The primary function of the substrate used in preparing BDD electrodes for electrochemical applications is to allow the flow of current to run through the electrode assembly and provide support for the BDD film so the electrode has enough mechanical stability (20). The ideal substrate material for the production of BDD electrodes should be resistant to the harsh Chemical Vapor Deposition (CVD) growth conditions, have a high affinity for diamond growth, possess high mechanical strength, sufficient electrical conductivity, and electrochemical inertness, or at least the ability to quickly form a protective passivation layer on its surface (21). Electrodes for large-scale water treatment applications are subjected to a particularly chemically aggressive environment with high erosive potential, so wear resistance is also desirable for the substrate material (22). BDD films were already deposited over Si, Ti, Nb, Ta, W, among others. (23)

However, these materials are still not ideal due to either low adhesion strength, low conductivity, low mechanical strength, or high cost (21, 24).

Silicon nitride (Si_3N_4) is a refractory ceramic material compatible with the CVD deposition conditions. It has a high affinity for CVD diamond growth since its coefficient of thermal expansion (CTE) is similar to that of diamond (25), promoting good diamond adhesion strength (26). In addition, Si_3N_4 has high resistance to erosive and abrasive wear, chemical stability in strong acids and bases, and a set of excellent mechanical properties, such as high hardness, fracture toughness, and high elasticity modulus (27). Due to their numerous interesting properties and applications, Si_3N_4-based ceramics have already been applied in cutting tools (28), biomedical prosthetic devices (29, 30), ball bearings (31), seals (32), metallurgy components and metal forming devices (33), automotive parts, aircraft engines and gas turbines (34, 35), space technology (36), electronic components (37), and cooking plates (27, 38). Reinforcing the Si_3N_4 with TiN particles increase fracture toughness, wear resistance, and flexural strength, and reduces the intrinsic electrical resistivity of the ceramic (39-41). All the ideal BDD substrate material requirements could be fulfilled by applying Si_3N_4-TiN composites by gathering their low conductivity, mechanical properties, chemical stability, oxidation resistance, wear resistance, affinity for CVD diamond growth, and ability to obtain complex shapes through EDM. Thus, we took this technology and tested our previously developed electroconductive Si_3N_4-TiN composite containing 30%vol. of TiN as a novel substrate material to produce long-service life BDD electrodes suitable for water treatment on an industrial scale (41).

The literature on diamond coatings over Si_3N_4-TiN is limited (42), with no reported studies on BDD coatings. Previous research on Si_3N_4-based materials as substrates for CVD diamond deposition has primarily been focused on applications such as cutting tools (43-45), dental prostheses (46), dental drill bits (47), articular prostheses (47-49), heat flux sensors (50), self-mated rings (51), and mechanical seals (52). The utilization of BDD/Si_3N_4-TiN electrodes in EAOPs represents an innovative and unexplored field with potential for future applications in BDD water treatment.

The growth of BDD films on Si_3N_4-TiN substrates with 30%vol. TiN by Hot Filament Chemical Vapor Deposition (HF-CVD) is investigated in this work. We present a comprehensive analysis of the resulting BDD/Si_3N_4-TiN electrodes, including their microstructure, diamond quality, conductivity, adhesion strength, service life, and

electrochemical properties. Phenol is utilized as a model compound to assess the electrode's effectiveness in oxidizing pollutants.

III.1.2. Experimental Section

III.1.2.1. Fabrication and characterization of Si_3N_4-TiN ceramics

The Si_3N_4 matrix powder composition and the sintering cycles were defined accordingly to previous works of our group (28, 53-55), aiming for fully dense materials with good mechanical properties. The composition of the Si_3N_4 matrix was a powder mixture of 89.3%wt. Si_3N_4 (H.C. Starck – Grade M11, Germany), 3.7%wt. de Al_2O_3 (Alcoa - CT 3000 SG, USA), and 7.0%wt. Y_2O_3 (H.C. Starck – Grade C, Germany). To obtain the Si_3N_4-TiN composite, we substituted the matrix with 30%vol. of TiN powder (H.C. Starck – Grade B, Germany). The substrate composition development was previously detailed in a prior publication (41)(Section II.1). The powders were mixed in agate jars with Si_3N_4 balls in a planetary mill for 8 hours at 200 rpm in an isopropanol medium. After milling, the powder slurry was screened through a 500-mesh and oven-dried at 100 °C for 24 hours. Discs (Ø 20 mm and Ø 59 mm) were prepared by cold uniaxial pressing (3 ton, 2 min) followed by cold isostatic pressing (200 MPa, 15 min). These were then pressureless sintered in a graphite furnace (Thermal Technology Inc, USA), in a closed graphite crucible with a powder bed composed of a mixture containing 50% of the Si_3N_4 matrix composition and 50% boron nitride (H.C. Starck – Grade A01, Germany) to avoid direct contact with the surrounding graphite walls and reduce the decomposition of the Si_3N_4 powder. The Si_3N_4-TiN composite was sintered at 1750 °C for 5 hours in an N_2 atmosphere (0.1 MPa) at a 10 °C min^{-1} heating rate. The Si_3N_4 matrix was also prepared and sintered at 1700 °C for 3 hours in an N_2 atmosphere (0.1 MPa) at a 10 °C min^{-1} heating rate for comparison with the Si_3N_4-TiN composite. After densification, the density of the samples was determined using the Archimedes method by immersion in distilled water. The Ø 59 mm discs were cut into bars (34 mm x 4.5 mm x 3 mm) to fabricate BDD/Si_3N_4-TiN anodes for organics oxidation.

The ceramics were characterized by Vickers microhardness indentation with applied loads of 2 kgf for 10 seconds. Indentation fracture toughness (K_{IC}) was measured from indentation marks with applied loads of 10 kgf for 10 seconds by measuring the lengths of the cracks and applying the method developed by Antis *et al.* (56). The electrical resistivity was measured using the Four Point Probe configuration at room

temperature. The resonant frequency method was used to obtain the elastic modulus (E) and the shear modulus (G). For comparison, the samples' maximum (Voigt) (57) and minimum (Reuss) (58) elastic modulus theoretical limit were calculated considering a reference value of 390 GPa (59) for the TiN elastic modulus. The crystalline phase composition was analyzed by X-ray diffraction (Cu K-α radiation, PANalytical, X'Pert, United Kingdom) through database search using the ICDD's PDF-4 database (60). The densified ceramics were ground, polished, and then plasma etched (K1050X, Emitech, France) with CF_4 for 120 seconds for microstructure observation through Scanning Electron Microscopy/Energy Dispersive Spectroscopy (SEM/EDS, SU-70 EDS, Hitachi, Japan).

III.1.2.2. BDD/Si_3N_4-TiN electrode deposition

The films were deposited over densified Si_3N_4-TiN on a lab-made Hot Filament Chemical Vapor Deposition (HF-CVD) reactor with a chamber volume of 5.4 L. Prior to the HF-CVD deposition, the ceramic substrates were ground with a diamond grinding wheel, flat lapped with an abrasive diamond suspension (15-WP, Kemet, United Kingdom), and plasma etched (K1050X, Emitech, France) with CF_4 for 120 seconds to improve the diamond film adhesion to the substrate according to previous works from our group (61). Next, the substrates were subjected to seeding by scratching the surface with a solution of abrasive diamond powder (0.5-1.0 μm and 10-20 μm, Diamecânica, Portugal) in ethanol, on an ultrasound bath for 45 minutes to improve the diamond nucleation density and to guarantee a homogeneous seeding over the ceramic disk surface. Eight parallel tungsten wires (Ø = 0.3 mm, 8 cm length, 99.95% purity, GoodFellow, United Kingdom) were used as filaments. They were kept at a constant distance of approximately 7 mm from the substrates and a 7 mm-distance between filaments. The temperature of the filaments was kept at 2180-2220 °C during HF-CVD deposition, measured with a two-color pyrometer (RAYMR1SCSF, Raytek, USA). The substrates' temperature was measured with a type K thermocouple, placed in the center of the HF-CVD sample holder, and kept in the 800-850 °C range. The HFCVD reactor's deposition parameters were previously optimized using an L9 orthogonal array Taguchi Matrix (Section II.2), where the controlled parameters were gas composition (CH_4/H_2), total pressure, and argon mass flow. The optimized conditions are shown in Table III.1.1.

Table III.1.1. BDD optimized deposition parameters.

t (h)	P (mbar)	T.G.F. (sccm)	CH_4/H_2	Ar/H_2	B_2O_3/CH_4	S.T. (°C)	F.T. (°C)
5	25	230	0.02	0.15	0.625	800-850	2180-2220

t: Deposition Time; P: Pressure; T.G.F.: Total Gas Flow; S.T.: Substrate Temperature; F.T.: Filament's Temperature.

A boron oxide (B_2O_3) solution dissolved in ethanol (10,000 ppm) was used as the boron source. The solution was introduced into the reactor chamber by evaporating it from a canister through a continuous flow of argon gas at a pressure of 2 bar. Figure III.1.1 provides a schematic depiction of the BDD/Si_3N_4-TiN electrode preparation process.

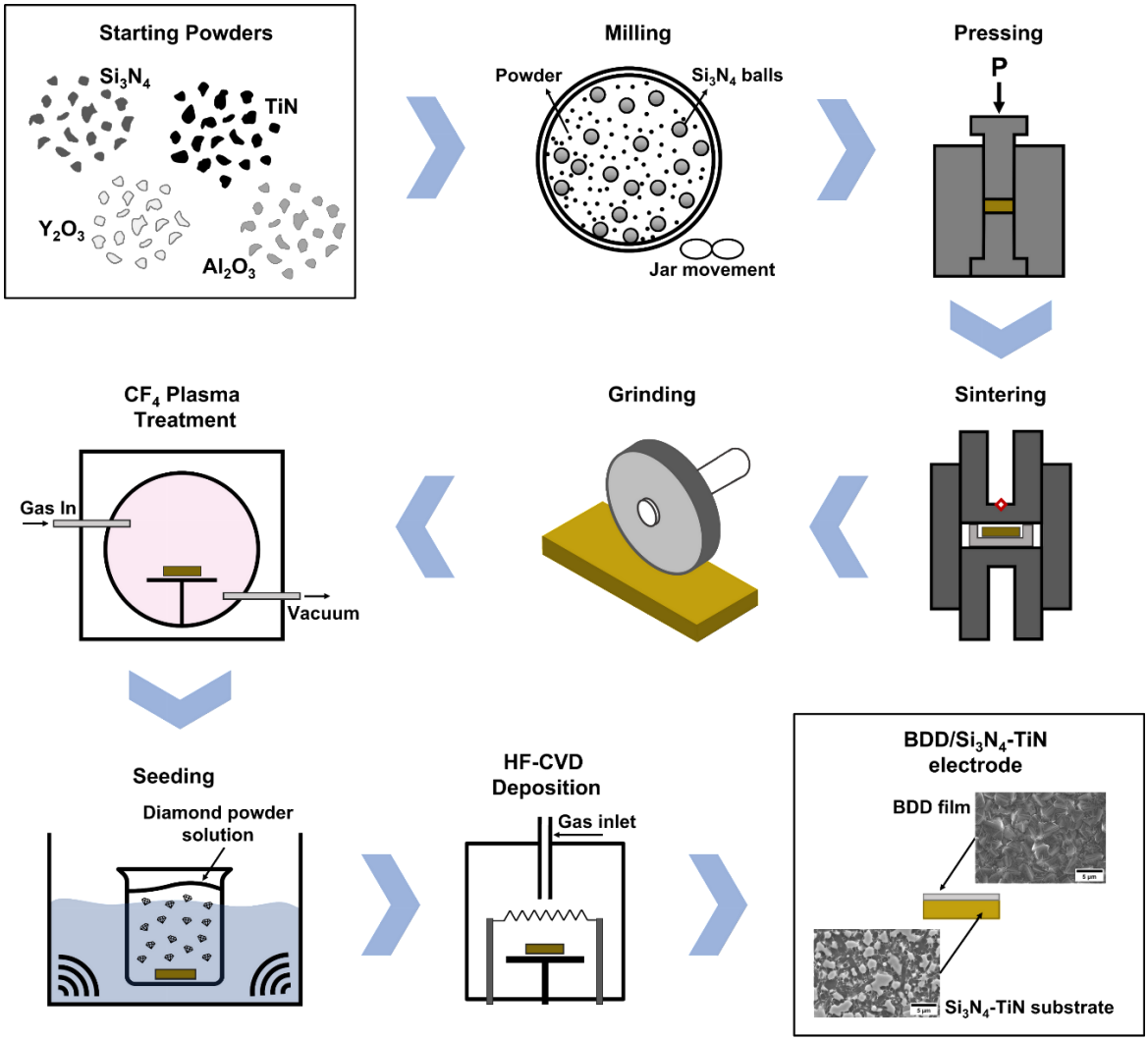

Figure III.1.1. Schematic representation of the BDD/Si_3N_4-TiN electrode preparation.

III.1.2.3. BDD/Si_3N_4-TiN electrode characterization

The microstructure analysis of the BDD film was conducted using Scanning Electron Microscopy/Energy Dispersive Spectroscopy (SEM/EDS, SU-70 EDS, Hitachi, Japan). Additionally, Micro-Raman Spectroscopy was performed using a 442 nm laser line (Jobin-Yvon LabRam HR, Horiba, Japan) to assess the quality of the diamond and measure residual stress. The electrical resistivity of the diamond film was studied using a homemade apparatus with two independent copper wires attached with silver glue to the diamond films. Sessile drop contact angle measurements were conducted utilizing a goniometer (Attention Theta, Biolin Scientific, Sweden). The contact angles (θ) between the BDD/Si_3N_4-TiN surface and 3 µL droplets of deionized water were measured at four distinct points. The OneAttension software (Version 4.1.3, Biolin Scientific, Sweden) was employed to accurately measure contact angles. The crystalline phase composition of the BDD deposited over Si_3N_4-TiN was analyzed by grazing angle X-ray diffraction (Cu K-α radiation, PANalytical, X'Pert, United Kingdom). The adhesion of the BDD films to the Si_3N_4-TiN substrate was evaluated by indentation with a Brale indenter placed in a universal testing machine (Z020, Zwick/Roell, Germany) with applied loads ranging from 100 to 1200 N (41)(Section II.1). The service life of the BDD/Si_3N_4-TiN electrodes was evaluated by applying them as both anode and cathode (without interchanging positions) in an accelerated life test consisting of water electrolysis in 3 M H_2SO_4 (95-97% purity, Merck, Germany) medium with an applied current density of 1 A cm^{-2}. Additionally, to evaluate the substrates' chemical resistance, the weight loss, and the microstructures of Si_3N_4 and Si_3N_4-TiN ceramics were analyzed by SEM (SU-70 EDS, Hitachi, Japan) after being submerged in 3 M H_2SO_4 (95-97% purity, Merck, Germany) for 60 days.

The electrochemical properties of the BDD electrode were investigated with a potentiostat (PGSTAT302N, Metrohm Autolab, Switzerland) controlled by computer software (Metrohm Autolab Nova 2.1.5), based in one-time measurements. Cyclic voltammetry measurements were conducted using a custom-designed three-electrode electrochemical cell built in Teflon, specifically designed for disc-shaped BDD electrodes. A platinum plate electrode was employed as the counter electrode, while a reference electrode consisting of a saturated calomel electrode (SCE) was utilized. The geometric surface area of the BDD working electrode was 0.785 cm^2.

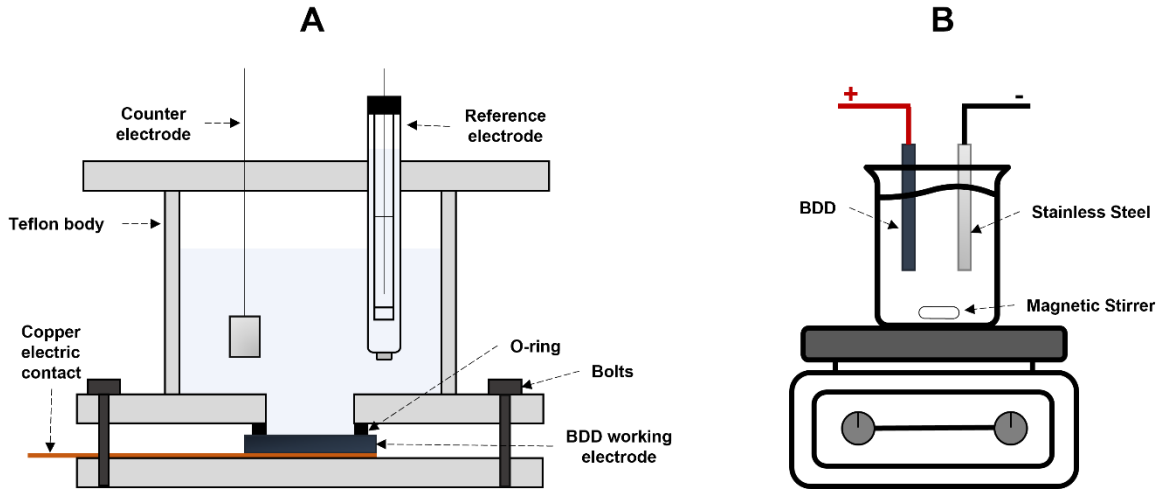

Figure III.1.2. Schematic of the electrochemical cell used for (a) electrochemical characterization and (b) for electrochemical oxidation (monopolar configuration).

The BDD electrode was pressed between an O-ring and a Teflon disc screwed to the bottom of the single-compartment Teflon cell (Figure III.1.2.a). All electrochemical characterization experiments were carried out in a solution volume of 20 mL at room temperature. The kinetics of the $Fe(CN)_3^{-3}/Fe(CN)_4^{-4}$ and $Ru(NH_3)_6^{3+}/Ru(NH_3)_6^{2+}$ redox systems were studied in solutions of 1 mM of potassium hexacyanoferrate(III) (> 98% purity, Honeywell Fluka, USA) in 0.1 M KCl (> 99.5% purity, Sigma-Aldrich, USA), and 1 mM of hexaammineruthenium(III) chloride (98% purity, Sigma-Aldrich, USA) in 0.1 M KCl, respectively, with scan rates ranging from 10-300 mV s^{-1}. The potential window of the electrode was evaluated through cyclic voltammograms recorded in 1 M $HClO_4$ (70% purity, Honeywell Fluka, USA) electrolyte at a 100 mV s^{-1} scan rate and compared with other common electrode materials (Pt, Glassy Carbon, and Au) under the same conditions.

III.1.2.4. Anodic oxidation of phenol with BDD/Si_3N_4-TiN electrodes

Phenol was chosen as a model pollutant for comparison with the literature due to the high number of publications concerning its degradation using BDD electrodes. Phenol degradation was performed by anodic oxidation using a bar-shaped BDD/Si_3N_4-TiN anode and a stainless steel (AISI 316) cathode (Figure III.1.2.b) with a fixed interelectrode distance of 10 mm. The geometric area of the BDD/Si_3N_4-TiN anode exposed to the solution was 0.8 cm^2. Electrooxidation tests were carried out in batch mode, at room temperature, with 20 mL solutions of 1 mM phenol (94.11 mg L^{-1}, ≥99% purity, Sigma-Aldrich, USA) in 0.1 M Na_2SO_4 (≥99.0% purity, Sigma-

Aldrich, USA) electrolyte. The evolution of phenol degradation at the BDD/Si_3N_4-TiN anode was evaluated by applying a current density of 30 mA cm^{-2} for 300 minutes. Additional tests were conducted applying different current densities (60, 90, 120 mA cm^{-2}) for 180 minutes to verify their influence on removal rates and energy consumption. The treated solutions were analyzed by UV-Vis Spectroscopy (Flex, Sarspec, Portugal) to estimate phenol concentration. Chemical Oxygen Demand (COD) measurements were performed by adding aliquots of 2.5 mL of each solution into vials containing potassium dichromate and a mixture of H_2SO_4 (95-97% purity, Merck, Germany) and Ag_2SO_4 (≥99.5% purity, Sigma-Aldrich, USA). All samples were tested in triplicates. The vials were heated to 150°C for 2 hours. After cooling, the digested vials were analyzed using a photometer (AL250 COD VARIO, Aqualytic, Germany) to determine the corresponding COD value. The total energy consumption was estimated as a function of COD (Eq. III.1.1), the volume of treated solution (Eq. III.1.2), and phenol concentration (Eq. III.1.3):

$$\mathrm{EC_{COD}\ (Wh\ kg_{COD}{}^{-1})} = \frac{\mathrm{EjAt}}{\mathrm{V\ \Delta COD}} \qquad \textbf{Eq. III.1.1}$$

$$\mathrm{EC_{Volume}\ (Wh\ L^{-1})} = \frac{\mathrm{EjAt}}{\mathrm{V}} \qquad \textbf{Eq. III.1.2}$$

$$\mathrm{EC_{phenol}\ (Wh\ kg_{phenol}{}^{-1})} = \frac{\mathrm{EjAt}}{\mathrm{V\ \Delta C_{phenol}}} \qquad \textbf{Eq. III.1.3}$$

Where E is the applied potential (V); j is the applied current density (A m^{-2}); A is the electrode geometric area (m^2); t is the electrolysis time (h); V is the electrolyte volume (L); ∆COD is the total amount of COD removed ($kgO_2\ L^{-1}$); ΔC_{phenol} is the total concentration of phenol removed from the solution ($kg_{phenol}\ L^{-1}$). The Average Current Efficiency (ACE) and Instantaneous Current Efficiency (ICE), expressed in Eq. III.1.4 and III.1.5 (62), respectively, were estimated as a function of COD values:

$$\mathrm{ACE} = \frac{\mathrm{F\ V\ (COD_0 - COD_t)}}{\mathrm{8\ I\ \Delta t}} \qquad \textbf{Eq. III.1.4}$$

$$\mathrm{ICE} = \frac{\mathrm{F\ V\ (COD_t - COD_{t+\Delta t})}}{\mathrm{8\ I\ \Delta t}} \qquad \textbf{Eq. III.1.5}$$

Where F is the Faraday constant (96485 C mol^{-1}); V is the electrolyte volume (L); t is the electrolysis time (s); COD_0 is the initial COD concentration (gO_2 L^{-1}); COD_t and $COD_{t+\Delta t}$ are the COD concentrations at times t and t+Δt (s), respectively; 8 is the equivalent mass of oxygen (gO_2 eq^{-1}); and I is the applied current (A).

III.1.3. Results and Discussion

III.1.3.1. Si_3N_4-TiN ceramics

The composite samples were successfully densified (> 99%), and the average shrinkage rate along the largest dimension of the samples was 23%, as shown in Table III.1.2. For determining the densification percentage, the theoretical density value of the samples was calculated according to the rule of mixtures. A 3.27 g cm^{-3} theoretical value was calculated for the Si_3N_4 matrix and 3.88 g cm^{-3} for the Si_3N_4-TiN(30%) ceramic.

Table III.1.2. Characterization results of the obtained Si_3N_4 and Si_3N_4-TiN ceramics. Adapted from ref. (41).

TiN (% vol.)	**0%**	**30%**
Sintering	1700°C - 3h	1750°C - 5h
	10°C min^{-1}	10°C min^{-1}
	N_2 0.1 MPa	N_2 0.1 MPa
Shrinkage [a] (%)	25%	23%
Density (g cm^{-3})	3.26	3.86
Densification (%)	99.62%	99.59%
Hardness (GPa)	14.89 ± 0.15	16.06 ± 0.22
K_{IC} $(MPa.\sqrt{m})$	5.47 ± 0.30	6.96 ± 0.84
$E_{theoretical\ (Voigt)}$ [b] (GPa)	314	337
$E_{theoretical\ (Reuss)}$ [c] (GPa)	314	333
$E_{experimental}$ (GPa)	314	340
$G_{experimental}$ (GPa)	122	134
Resistivity (Ω cm)	1.00 x 10^{13}	8.9 x 10^{-1}
Thermal Conductivity (W mK^{-1})	18.19 ± 0.12	25.40 ± 0.08
Bending Strength (MPa)	882.61 ± 31.15	866.84 ± 54.49

[a] Along the largest dimension; [b] $E_{Voigt} = E_1V_1 + E_2V_2$ (57); [c] $1/E_{Reuss} = V_1/E_1 + V_2/E_2$ (58)

The addition of TiN to the matrix further enhances the hardness of the composite due to the higher intrinsic hardness of TiN (18-21 GPa) (63) and the reduction of the residual sintering liquid phase in the microstructure. Furthermore, incorporating TiN significantly increases fracture toughness (K_{IC}) (39, 40, 64, 65).

Toughening mechanisms are related to the CTE mismatch, elastic modulus mismatch, and microcracking toughening associated with the TiN particle size (39). The elastic modulus of the composite is found to be within theoretical limits and increases with the addition of TiN to the matrix. Additionally, the 30%vol. TiN composition lies after the percolation threshold, where the electrical resistivity of the composite drastically decreases, promoting the transition from an insulator to a conductor. The phase composition of the samples is presented in Figure III.1.3.a, including the presence of β-Si_3N_4 (ICDD's PDF 04-005-4900), TiN (ICDD's PDF 04-002-2466), and traces of yttrium oxynitride secondary ($Y_2Ti_2O_{5.5}N$, ICDD's PDF 04-005-5509) formed due to crystallization of the liquid phase during cooling in the sintering process. It is worth noting that the samples present no α-Si_3N_4 phase, indicating a complete and irreversible transformation from α-Si_3N_4 to β-Si_3N_4 during the sintering process. The slight dislocation observed in the XRD baselines suggests that part of the liquid phase may not have crystallized entirely after sintering, remaining as a glassy phase in the microstructure.

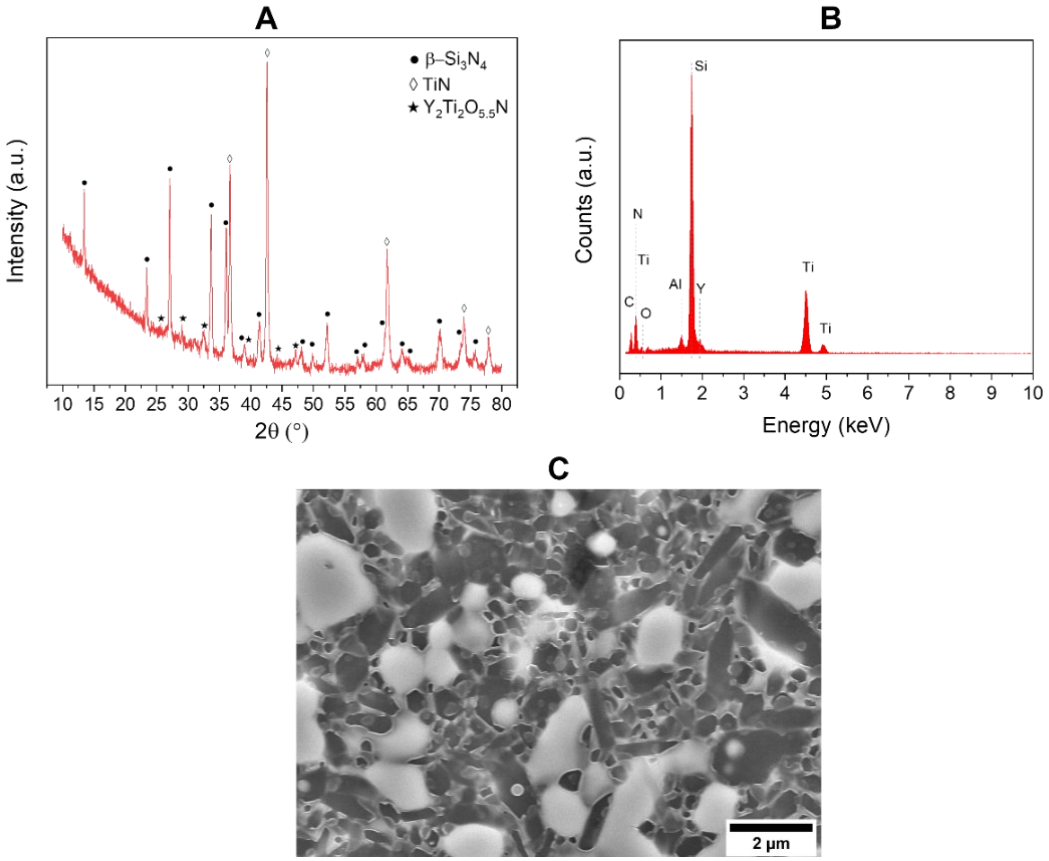

Figure III.1.3. (a) X-ray diffraction and (b) EDS analysis of the Si3N4-TiN (30%vol.) composite; (c) SEM microstructure of Si_3N_4-TiN with 30%vol. of TiN (with CF4 plasma treatment). Adapted from ref. (41).

SEM micrographs (Figure III.1.3.b and Figure III.1.3.c) reveal the presence of β-Si_3N_4 grains (appearing in dark grey) with a high aspect ratio, surrounded by the intergranular secondary phase (appearing in white). With the addition of TiN, a decrease in the size of β-Si_3N_4 grains is observed. The distribution and interparticle contact of the TiN grains (appearing in light grey) contributes to forming an electroconductive network with lower resistivities. Despite using higher temperatures and a longer sintering cycle for the Si_3N_4-TiN composite, there was no excessive increase in the size of β-Si_3N_4 grains. This lack of significant growth can be attributed to the growth-hindering effect of the TiN particles present in the composite. All findings regarding the development and characterization of Si_3N_4-TiN ceramic substrates have been previously presented in a prior study (41). Further insights into the interpretation of current results and the composition of substrate phases can be found in the aforementioned research.

III.1.3.2. BDD/Si_3N_4-TiN characterization

The quality of the BDD films was evaluated using SEM and Micro-Raman spectroscopy. The BDD films were found to cover the substrate uniformly (Figure III.1.4.a) without any voids or cracks on the surface, which are defects commonly caused by an inadequate seeding process. The average diamond grain size was measured to be 1.45 ± 0.37 µm by the mean linear intercept method, according to the ISO Standard No. 4499-2:2020 (66). The average film thickness was 4.95 ± 0.36 µm (Figure III.1.4.b), indicating average diamond growth rates of 0.99 µm h^{-1}.

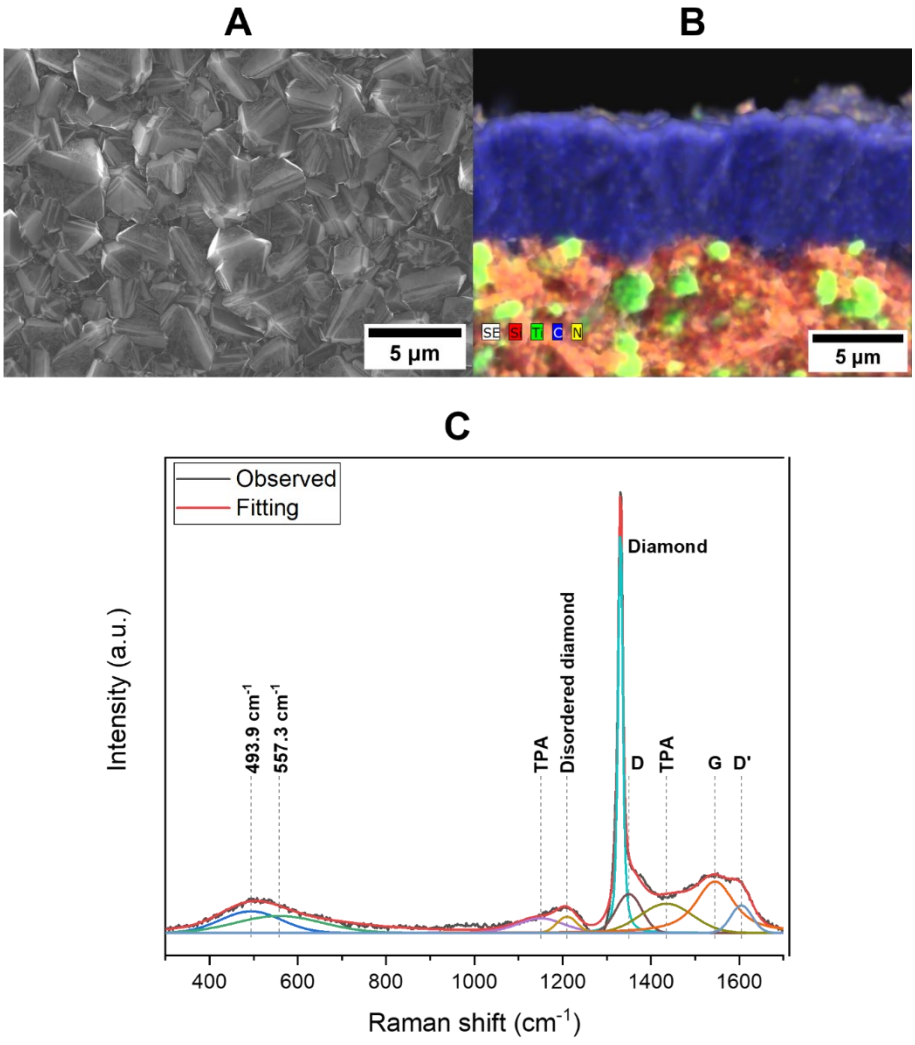

Figure III.1.4. (a) SEM micrograph in the plan view of a BDD film deposited over Si_3N_4-TiN; (b) SEM-EDS elemental mapping of the cross-section of the BDD/Si_3N_4-TiN electrode; (c) Raman spectroscopy spectrum of the BDD films deposited over Si_3N_4-TiN.

The Raman spectra (Figure III.1.4.c) was analyzed to evaluate the quality of the diamond by deconvoluting it into peaks associated with the diamond and non-diamond components of the film. The non-diamond carbon peaks observed in the Raman spectra are primarily related to sp^2 carbon in the grain boundaries. The natural diamond band is typically found at 1332 cm^{-1} (67). The peaks observed at 1150 and 1440 cm^{-1} are attributed to trans-polyacetylene (TPA) present in the grain boundaries of the BDD film (68, 69). The 1220 cm^{-1} peak is linked to disordered diamond, primarily caused by boron incorporation in the diamond lattice (70-72). The D-band at ~1350 cm^{-1} and D'-band at ~1620 cm^{-1} are assigned to defect-induced Raman features related to carbon sp^2 structures, and the G band at ~1550 cm^{-1} is associated with the C=C sp^2 bond stretching mode (67, 69, 73). The phase purity of the BDD film was measured by dividing the integral intensity of the diamond band ($I_{Diamond}$) by the integral intensity of the G band (I_G) (74). Results are presented in Table III.1.3. The average diamond phase purity figure-of-merit was 1.1, indicating good diamond quality.

Table III.1.3. Data extracted from the Raman spectra of the BDD films deposited over Si_3N_4-TiN.

Raman Peak	Center (cm^{-1})	FWHM (cm^{-1})	Integral Intensity (a.u.)	Residual Stress (GPa)	$I_{Diamond}/I_G$
Diamond	1330.9	12.3	17.2	-0.6	1.1
D-band	1350.0	69.5	5.8		
G-band	1527.8	104.9	16.2		

The deviation of the diamond band from 1332 cm^{-1} in the Raman spectrum is a function of the intrinsic residual stresses present in the BDD film (75), which primarily arise during the cooling step after BDD deposition inside the CVD chamber due to the mismatch in the thermal expansion coefficient of the substrate and the BDD film. Non-diamond carbon impurities may also induce residual stress at grain boundaries and structural defects (76). The residual stress (σ_r) was determined by measuring the diamond peak shift ($\Delta\vartheta$) from the natural stress-free diamond peak (1332 cm^{-1}) in the Raman spectrum, following Eq. III.1.6 (75).

$$\sigma_r = -0.567 \times \Delta\vartheta \qquad \textbf{Eq. III.1.6}$$

The Raman spectrum reveals that the BDD film deposited on the Si_3N_4-TiN substrate is under compressive residual stress, with an average value of -0.6 GPa. Such a low value supports our proposition that the Si_3N_4-TiN composite is a promising substrate for BDD electrodes. The low residual stress obtained using Si_3N_4-TiN substrates is likely attributed to the close CTE of Si_3N_4 to that of diamond (25).

Boron doping levels in the BDD/Si_3N_4-TiN composite were quantified using the Raman Spectrum analysis, employing the methodology outlined by Bertrand *et al.* (70), which uses the Lorentzian component of the peak located at approximately 500 cm^{-1} (493.9 cm^{-1}, Figure III.1.4.c) to estimate boron concentration. The obtained results revealed a boron doping concentration of approximately 4.27 x 10^{20}, a value that indicates metal-like conductivity (77). This finding underscores the successful incorporation of boron into the BDD film, which is crucial for water treatment applications.

The estimated water contact angle value measured on the surface of BDD/Si_3N_4-TiN was found to be 86.5 ± 1.6 ° (Figure III.1.5.a). The measured water contact angle, falls within the range of 80 to 100°, aligning with the typical range reported in the literature for as-grown hydrogen-terminated BDD surfaces (78). This result underscores the hydrophobic nature of the as-grown BDD/Si_3N_4-TiN surface.

The grazing angle XRD spectrum depicted in Figure III.1.5.b showcases the crystallographic characteristics of the BDD layer deposited over the Si_3N_4-TiN composite. Notably, the XRD analysis unveiled mixed crystallographic orientations, with the (111) orientation being the most predominant one.

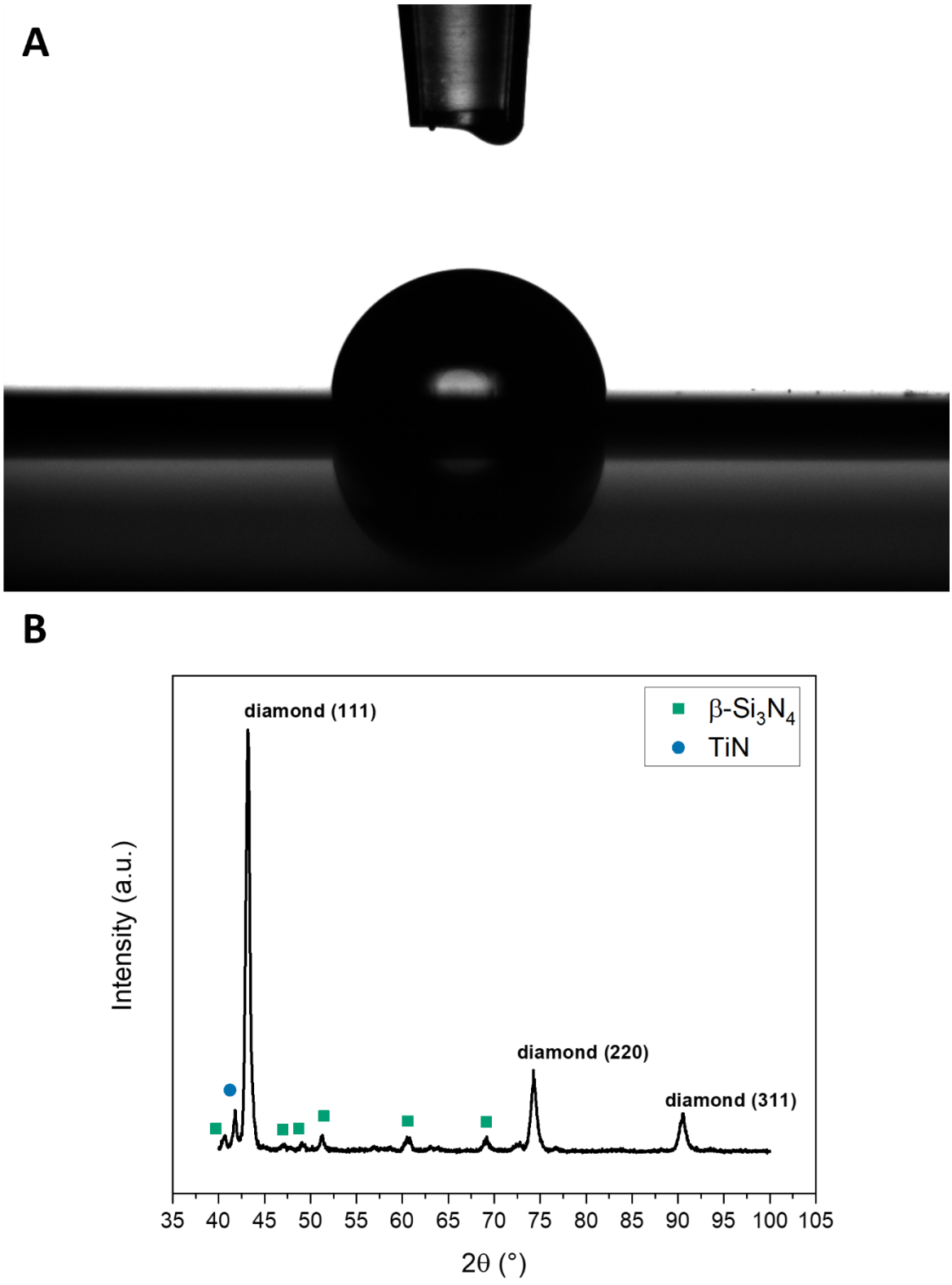

Figure III.1.5. (a) Contact angle measurements of distilled water over the BDD/Si_3N_4-TiN surface; (b) Grazing angle X-ray diffraction of the BDD film deposited over Si_3N_4-TiN (Diamond: ICDD's PDF 04-013-9778).

III.1.3.3. The service life of BDD/Si_3N_4-TiN electrodes

The BDD film adhesion to the Si_3N_4-TiN substrate can be estimated by measuring the interfacial crack resistance parameter from the reciprocal slope $d_{Load}/d_{Crack\ Radius}$ (Figure III.1.6.b) (42). We estimated a crack resistance value of 7.54 ± 0.46 N μm^{-1}. Indentation loads were applied in the range of 100 to 1200 N (41)(Section II.1). Delamination of the film started to be observed from an applied load of 1000 N and substrate chipping with an applied load of 1200 N (Figure III.1.6.a). This result is superior to the ones obtained for CVD diamond deposited over Si_3N_4-TiN with similar amounts of TiN, as reported in previous works from our group (42). The interfacial crack resistance is also higher than the reported in the literature (5 N μm^{-1}) for diamond films deposited over Si_3N_4 (79). However, the value is lower than obtained in a previous work published by our group on the adhesion of CVD diamond deposited over Si_3N_4, whose value was 12 N μm^{-1} (25). Nonetheless, this high value was obtained with a diamond film thickness of 39 μm, approximately eight times thicker than the film studied in this work. If accounting for this difference, the adhesion result obtained in this work is almost five times higher than the best result given in the literature for diamond adhesion to Si_3N_4-based substrates. Such an excellent result may be the key to solving one of the main problems in selecting a suitable substrate to produce BDD electrodes: film adhesion strength.

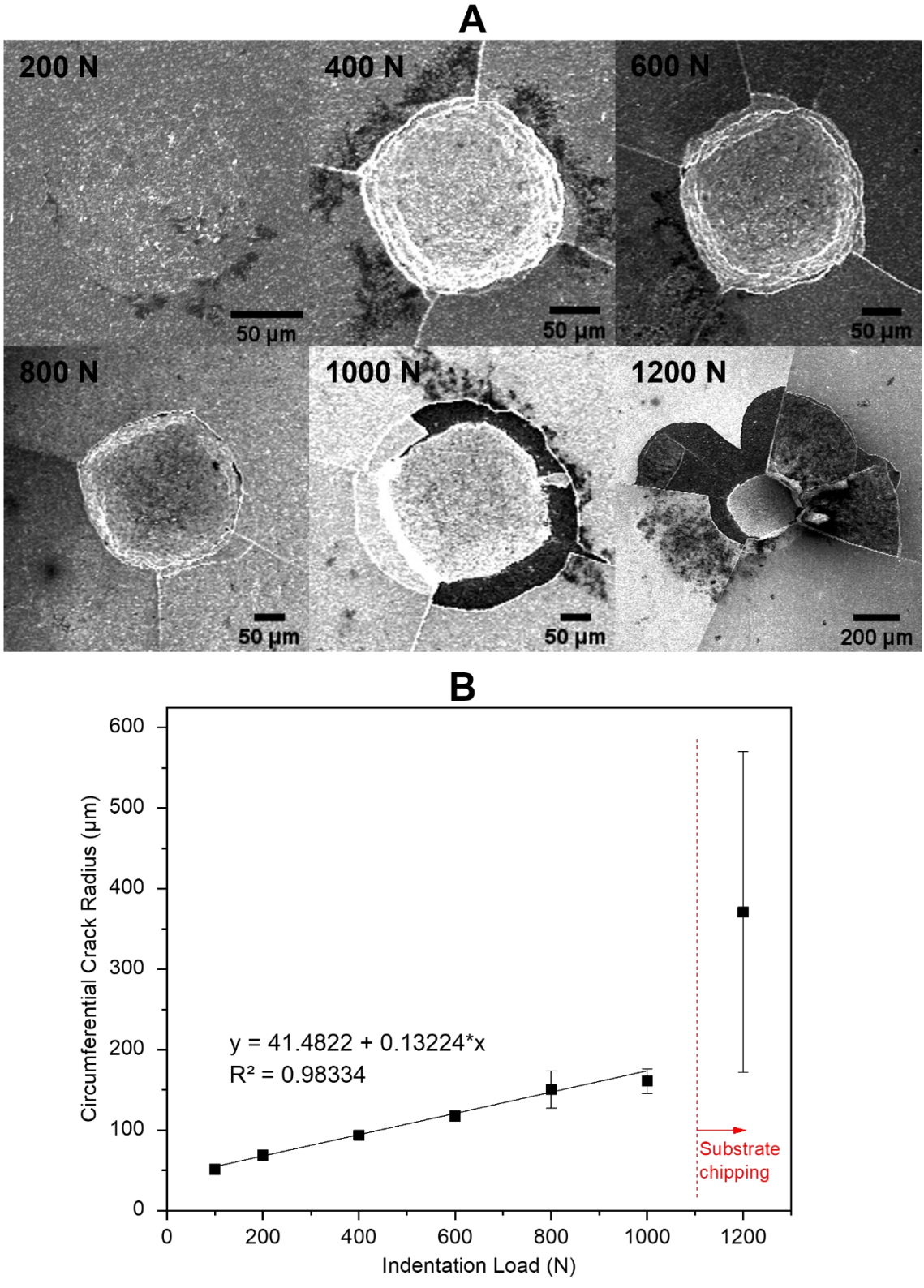

Figure III.1.6. (a) SEM micrographs of the Brale indenter imprints at 200, 400, 600, 800, 1000, and 1200 N indentation loads; (b) Circumferential crack radius versus indentation load (Adapted from ref. (41)).

An accelerated life test of BDD/Si_3N_4-TiN electrodes was conducted in 3 M H_2SO_4 for 2016 hours. The test revealed that the electrodes exhibited no film delamination (Figure III.1.7.a). The latter would be indicated by an abrupt increase in cell potential (80). The average cell potential during the test was 7.8 ± 0.3 V, with a slow increase from 7.4 V to 8.6 V observed throughout the test. This variation could be attributed to the gradual oxidation of the predominantly hydrogen-terminated as-grown BDD surface. Hydrogen-terminated BDD surfaces undergo a phenomenon known as surface transfer doping, which increases their surface conductivity (81). However, over time, particularly in the context of electrolysis in H_2SO_4 under high current density, these surfaces undergo oxidation processes, becoming predominantly oxygen-terminated, resulting in a substantial reduction in surface conductivity (81,82). The SEM micrograph of the BDD/Si_3N_4-TiN electrode surface (Figure III.1.7.b) following the accelerated life test confirms the absence of BDD film delamination, with the film remaining intact and free from voids or points of solution permeability. Additionally, EDS analysis of the surface (Figure III.1.7.c) reveals the presence of only carbon and oxygen, indicative of the exclusive presence of the BDD film with potential superficial residual contamination post-use. The BDD electrodes fabricated with Si_3N_4-TiN substrates demonstrated comparable or superior results to those tested under the same conditions and fabricated with other substrate materials such as Nb, Si, Ta, Ti, and WC-Co (Table III.1.4). These results further confirm that growing BDD on Si_3N_4-TiN substrates is a viable approach for producing BDD electrodes with long service life. This combination may facilitate the scaling-up of electrochemical oxidation processes using BDD anodes and enhance their technology readiness level.

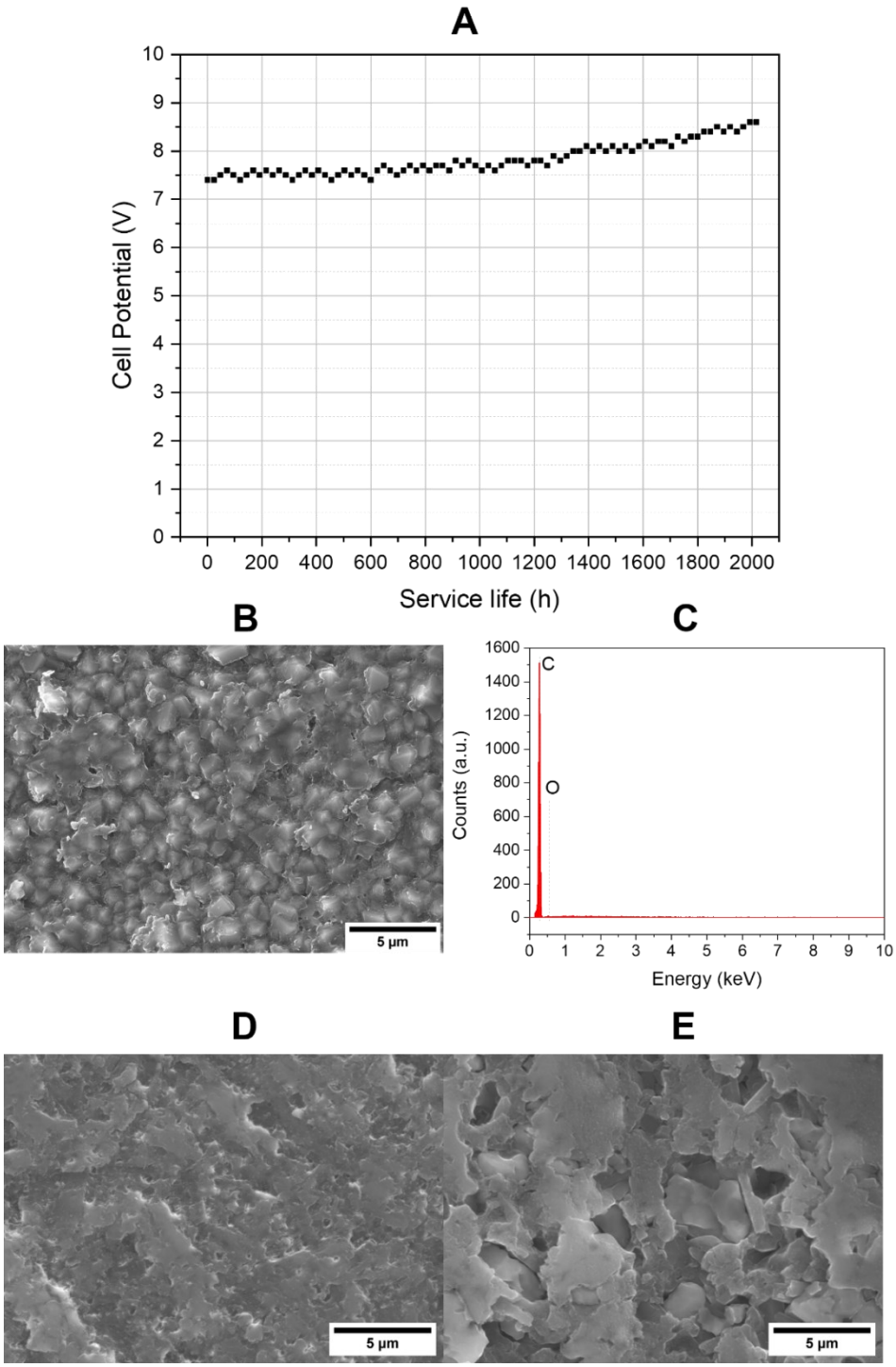

Figure III.1.7. (a) Accelerated life test of BDD/Si_3N_4-TiN electrodes. Solution: 3 M H_2SO_4. Current density: 1 A cm^{-2}; SEM micrograph (b) and EDS (c) of the BDD/Si_3N_4-TiN electrode surface after the accelerated life test; (c) SEM micrographs of (d) Si_3N_4 and (b) Si_3N_4-TiN ceramics after submersion in 3 M H_2SO_4 for 60 days at room temperature.

Further information to support the service life analysis of BDD/Si_3N_4-TiN electrodes was extracted by immersing uncoated Si_3N_4 and Si_3N_4-TiN ceramic disks in 3 M

H_2SO_4 solutions for 60 days (1440 hours) at room temperature. The samples were weighed and examined using SEM to evaluate their chemical resistance. The results showed that the Si_3N_4 ceramic (Figure III.1.7.d) exhibited fewer signs of chemical etching compared to the Si_3N_4-TiN ceramic (Figure III.1.7.e), which displayed pits resulting from the etching of TiN grains (appearing in light grey). As reported by Monteverde *et al.*, the corrosion of Si_3N_4 by H_2SO_4 primarily involves the consumption of grain boundary phases (83). The weight loss for Si_3N_4 was 7.2%, while the weight loss for Si_3N_4-TiN was 10.1%. These findings suggest that even if the BDD film delaminates from the substrate during water treatment processes, the BDD/Si_3N_4-TiN electrode may still function for additional hours, even in aggressive environments.

Table III.1.4. Accelerated life test of BDD/Si_3N_4-TiN electrodes compared with the literature.

Substrate material	Electrolyte	Current density ($A\ cm^{-2}$)	Service life (h)	Ref.
Si_3N_4-TiN	3 M H_2SO_4	1.0	> 2016	This work
Nb	0.5 M H_2SO_4	10.0	850	(84)
	1 M H_2SO_4	1.0	484	(81)
	1 M H_2SO_4	1.3	88-130	(85)
	3 M H_2SO_4	1.0	> 1600	(22)
	6 M HNO_3	0.5	1620-1810	(86)
Si	1 M H_2SO_4	1.0	262	(87)
	3 M H_2SO_4	1.0	> 1600	(22)
Ta	3 M H_2SO_4	1.0	> 1600	(22)
Ti	1 M H_2SO_4	0.5	~500	(88)
	1 M H_2SO_4	1.0	127	(81, 89)
	3 M H_2SO_4	0.5	89	(90)
	3 M H_2SO_4	1.0	1530	(22)
	3 M H_2SO_4	1.0	264	(91)
	3 M H_2SO_4	1.0	95	(92)
Porous Ti	3 M H_2SO_4	0.5	111	(90)
WC-Co	3 M H_2SO_4	1.0	1440	(93)
-	1 M H_2SO_4	0.5	295	(88)

III.1.3.4. Electrochemical reactivity of BDD/Si_3N_4-TiN electrodes

The electrochemical response of BDD is strongly affected by factors such as boron doping level, surface termination, grain size, crystallographic orientation, resistivity, and the presence of impurity phases (94). The reactivity of BDD electrodes was studied using both electroactive species characterized with charged inner-sphere electron transfer (1 mM $K_3[Fe(CN)_6]$ in 0.1 M KCl) and outer-sphere electron transfer (1 mM $[Ru(NH_3)_6]Cl_3$ in 0.1 M KCl) (Figure III.1.8). Results show that the peak-to-peak separation between oxidation and reduction potentials increased with increasing scan rate (10 mV s^{-1} to 300 mV s^{-1}), from 73 mV to 122 mV for the inner-sphere redox couple, and from 70 mV to 116 mV for the outer-sphere redox couple. An ohmic potential drop may account for the observed increase in peak-to-peak separation with increasing scan rates (95). The peak-to-peak separation measurements indicate a quasi-reversible electron transfer for both redox couples, with some symmetry observed between oxidation and reduction peaks. While reversibility could be improved by reducing residual sp^2 carbon and surface imperfections on the BDD film, the BDD/Si_3N_4-TiN electrode seems suitable for electrochemical oxidation processes. According to the Randles-Sevcik equation, the peak current is proportional to the square root of the scan rate for diffusion-limited electrochemical reactions (96). The linearity between the anodic current peak and the square root of the scan rate observed in both redox systems reactions at the BDD/Si_3N_4-TiN electrode (Figure III.1.8.c and Figure III.1.8.d) indicates they are controlled by diffusion. As the scan rate increases, the concentration gradient near the electrode surface increases due to the reduced time available for the diffusion of species, resulting in higher peak currents. Furthermore, these linear relationships also reinforce the evidence for the quasi-reversibility of both redox processes ($Fe(CN)_6^{3-/4-}$ and $Ru(NH_3)_6^{2+/3+}$).

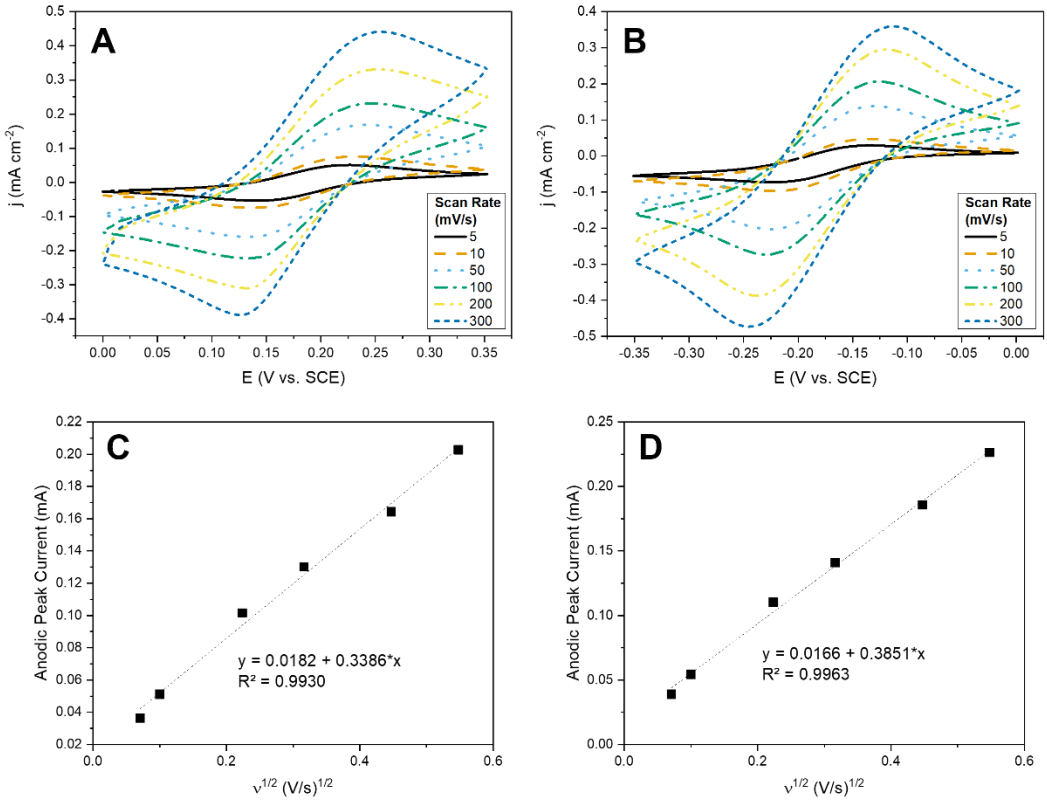

Figure III.1.8. Cyclic voltammograms of the BDD/Si_3N_4-TiN electrode in 0.1 M KCl solutions containing (a) 1 mM $K_3[Fe(CN)_6]$ and (b) 1 mM $[Ru(NH_3)_6]Cl_3$, with scan rates ranging from 10 to 300 mV s^{-1}. Plots of the anodic peak current versus the square root of the scan rate for (c) $Fe(CN)_6^{3-/4-}$ and (d) $Ru(NH_3)_6^{2+/3+}$ redox couples. Temperature: room temperature.

To evaluate the performance of the BDD/Si_3N_4-TiN electrode, cyclic voltammetry was conducted in 1M $HClO_4$ electrolyte. The latter aimed to determine the magnitude of the background current and the electrochemical potential window, which serves as an indicator of the electrode's operating limit. Results revealed low background current values and a wide working potential window of 3.5 V vs. SCE for the BDD/Si_3N_4-TiN electrode (Figure III.1.9). This wide electrochemical potential window of water stability further indicates a high-quality diamond with low defects, grain boundary density, and non-diamond carbon, as previously observed through Raman spectroscopy. Additionally, the BDD/Si_3N_4-TiN electrode presents the widest potential window and the lowest background current among commonly applied electrode materials, such as Pt, Reticulated Glassy Carbon, and Au.

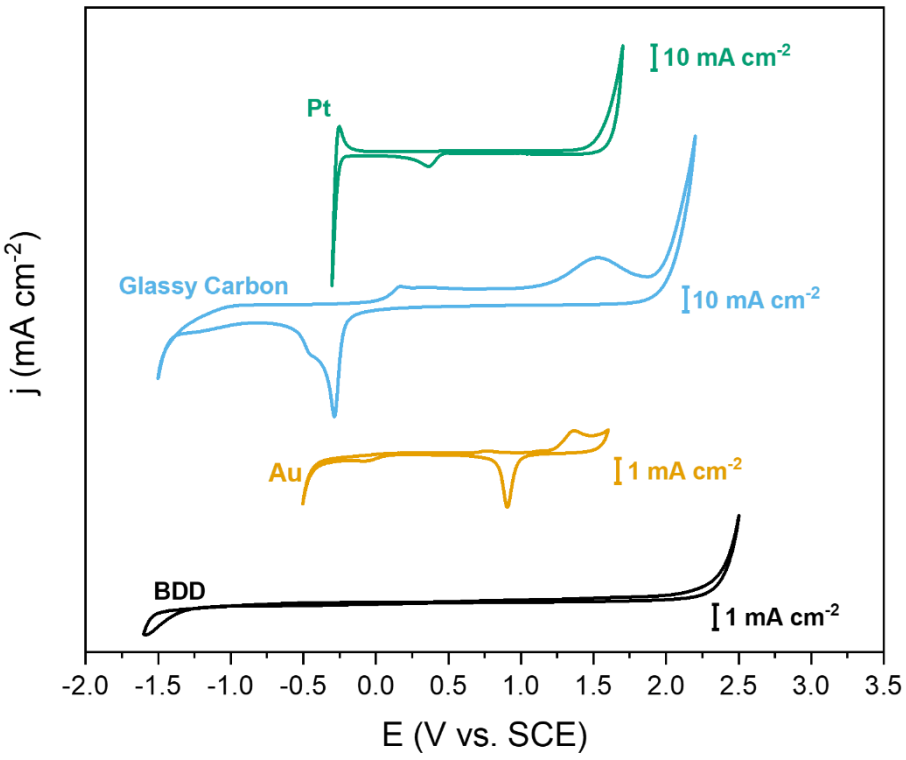

Figure III.1.9. Cyclic voltammetry of BDD/Si_3N_4-TiN electrodes immersed in 1 M $HClO_4$ compared with Pt, Glassy Carbon, and Au electrodes. Temperature: room temperature.

III.1.3.5. Phenol electrooxidation with BDD/Si_3N_4-TiN electrodes

The BDD/Si_3N_4-TiN electrode was able to eliminate phenol completely and remove up to 98.8% of the COD in the tested solution after 5 hours of electrooxidation at an applied current density of 30 mA cm^{-2} (Figure III.1.10.a). The normalized remaining phenol and COD concentrations were fitted to a first-order kinetic model, as described in Eq. III.1.7 (95), to determine the kinetic constants.

$$C/C_0 = e^{-k_{app}t} \qquad \textbf{Eq. III.1.7}$$

Where C is the respective concentration (mg L^{-1}) at time t (h); C_0 is the initial concentration; and k_{app} is the apparent rate constant. The later was used to estimate the half-life ($t_{1/2}$), according to Eq. III.1.8.

$$t_{1/2} = \frac{\ln 2}{k_{app}} \qquad \textbf{Eq. III.1.8}$$

The first-order rate constant was determined to be 0.697 h^{-1} (R^2 = 0.9872) and 0.676 h^{-1} (R^2 = 0.9715) for phenol and COD removal, respectively. The corresponding half-life ($t_{1/2}$), which reflects the time required for the initial concentration to decrease by 50%, was calculated to be 0.995 h and 1.025 h for phenol and COD, respectively.

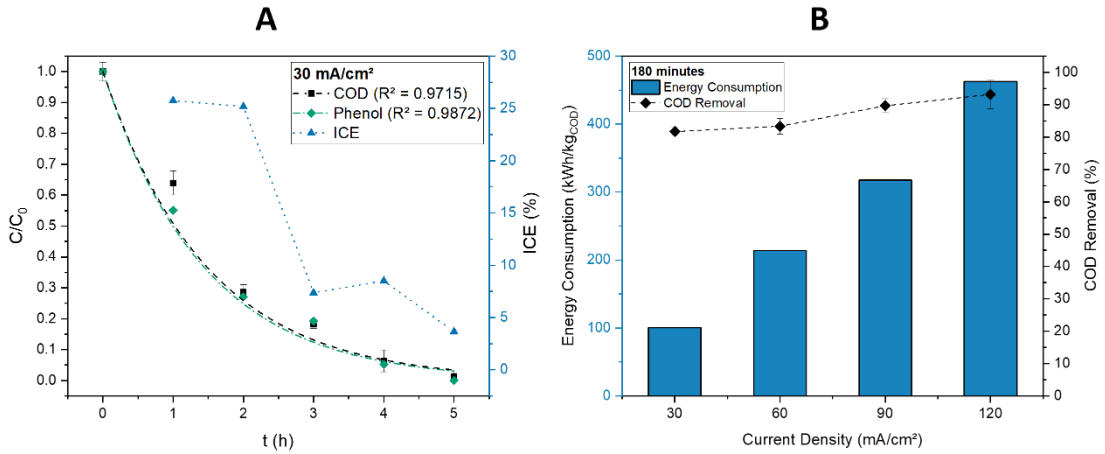

Figure III.1.10. (a) BDD/Si_3N_4-TiN electrode performance in the anodic oxidation of phenol with an applied current density of 30 mA cm^{-2} for 300 minutes; (b) Energy consumption and COD removal depending on the applied current density (30, 60, 90 or 120 mA cm^{-2}) using a BDD/Si_3N_4-TiN anode for phenol electrooxidation. Cell configuration: Batch mode. Cathode: Stainless steel 316. Initial concentration: 1 mM phenol (94.11 mg L^{-1}). Electrolyte: 0.1 M Na_2SO_4. Anode geometric area: 0.8 cm^2. Volume of solution: 20 mL. Temperature: room temperature.

Anodic oxidation of phenol was carried out for 180 minutes at varying current densities (30, 60, 90, and 120 mA cm^{-2}) (Figure III.1.10.b) to evaluate the effect of applied current density on electrode performance. Results indicated that increasing the current density led to faster phenol degradation rates due to the increased production of reactive oxygen species at the electrode surface (97). However, it also resulted in higher specific energy consumption, highlighting the need for a balance between degradation rate and energy efficiency. As illustrated in Figure III.1.10.b, within the studied range of applied current density (30-120 mA cm^{-2}) and a volume-to-area (V/A) ratio of 25 (cm^3/cm^2), an applied current density of 30 mA cm^{-2} represents the optimal compromise between degradation rate and energy consumption.

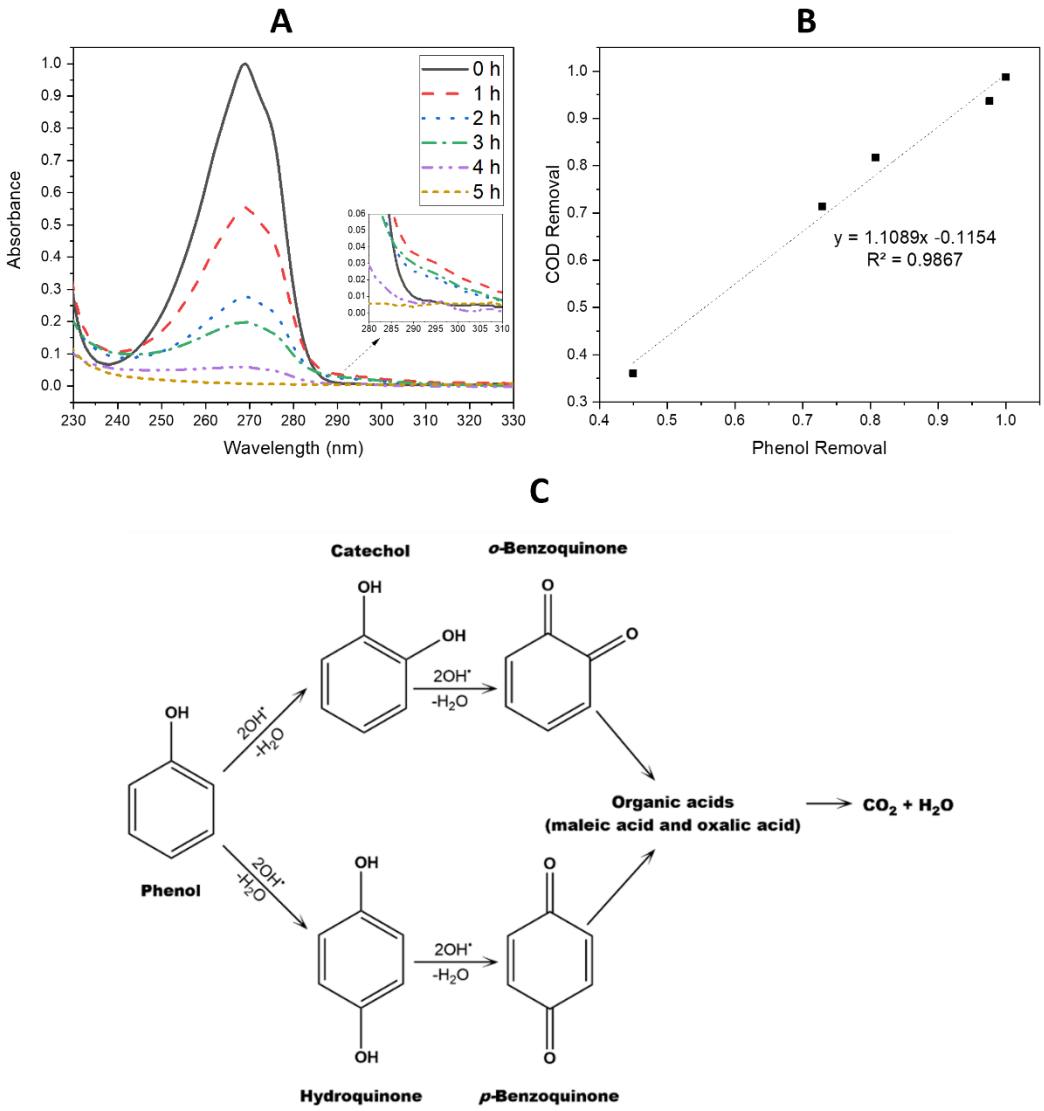

Figure III.1.11. (a) UV-Vis spectra of solutions containing 1 mM phenol in 0.1 M Na_2SO_4 treated by anodic oxidation with a BDD/Si_3N_4-TiN anode; (b) Relationship between phenol removal estimated by UV-Vis Spectroscopy and COD removal; (c) Proposed phenol indirect oxidation to aromatic compounds at the BDD anode (adapted from (99)). Cell configuration: Batch mode. Cathode: Stainless steel 316. Initial concentration: 1 mM phenol (94.11 mg L^{-1}). Electrolyte: 0.1 M Na_2SO_4. Applied current density: 30 mA cm^{-2}. Anode geometric area: 0.8 cm^2. Volume of solution: 20 mL. Temperature: room temperature.

During the electrooxidation process, the cell potential was maintained above the water decomposition overpotential (E > 2.05 V vs. SCE) at all applied current densities. Such high anodic potentials prevent electrode deactivation, and phenol oxidation primarily occurs through the generation of hydroxyl radicals via water discharge (100). As shown in Figure III.1.11.a, the UV-Vis spectra of samples treated

at a current density of 30 mA cm^{-2} for various electrolysis times indicate a decrease in absorbance of the main peak λ_{max}(Phenol) 269 nm. Additionally, as the phenol peak decreases, small peaks at longer wavelengths (280-300 nm) in the UV-vis spectra were observed, which are likely indicative of the presence of oxidation byproducts of phenol, which may be attributed to hydroquinone (101). Figure III.1.10.a illustrates that the complete elimination of phenol occurred slightly faster than that of COD, which also suggests the potential conversion of phenol to other intermediate aromatic compounds. These observations support the presence of indirect electrooxidation, as depicted in Figure III.1.11.c (99, 102).

The similarity in the apparent first-order rate constant for phenol and COD removal, the linear relationship between phenol and COD removal rates (as shown in Figure III.1.11.b), as well as the UV-vis spectra (Figure III.1.11.a) suggest that the phenol concentration exhibits a monotonically decreasing trend, reaching a negligible level at the 300th minute. The intermediate species exhibit a slight increase up to 180 minutes and then decrease to a negligible level by the 300th minute. These findings suggest that the phenol oxidation to CO_2 and H_2O (Eq. III.1.9) may be complete within 180 minutes (100). Alternatively, if any intermediate species form near the electrode, they will likely undergo rapid mineralization into CO_2 and H_2O after 180 minutes of treatment.

$$C_6H_5OH \xrightarrow{28OH^{\bullet}} 6CO_2 + 17H_2O \qquad \textbf{Eq. III.1.9}$$

III.1.3.6. BDD/Si_3N_4-TiN electrodes compared with the literature

To understand the advances of the BDD/Si_3N_4-TiN electrode system in comparison to the reported literature, a performance comparison was conducted considering similar experimental conditions. A detailed table summarizing the results of this comparison can be found in Supplementary Information Table III.1.1. Regarding energy consumption, the BDD/Si_3N_4-TiN electrode exhibited lower energy consumption values than the average results reported in the literature. One strategy to make the process more sustainable by improving its energy efficiency in the electrochemical water treatment using BDD anodes is by applying renewable energy sources, such as wind, tidal, or solar power. This approach can potentially lead to the development of self-sufficient and sustainable water treatment processes. It is important to note that the interpretation of results can be misleading when

experimental parameters, such as initial pollutant concentration, applied current density, type, and concentration of electrolyte, V/A ratio, and cell/reactor configuration, are not considered (23).

The type and concentration of electrolyte affect the solution's conductivity, which directly impacts the duration of electrooxidation required to achieve complete degradation of a given pollutant and the applied potential. These factors, in turn, significantly impact the final energy consumption. Therefore, meaningful comparisons can only be made between experiments conducted with the same solution conductivity. Additionally, the V/A ratio can significantly impact the performance of a single BDD electrode, as reactions involving the direct electrooxidation of organics at BDD electrodes occur at the electrode surface (103). Mass transport can be improved by reducing cell volume (104), which makes it easier for organic species to reach the electrode's surface. In a configuration where the V/A ratio is as low as possible, degradation rates could be faster, making the process more effective and energy efficient. With such a configuration, water treatment with BDD electrodes could be performed in a constant flow-through process that requires only a short time to achieve complete degradation of organics. Furthermore, a smaller electrode area is beneficial in terms of cost, production of BDD electrodes, and current distribution. The conductivity of BDD is not uniformly distributed across its surface (105). Thus, a larger electrode area may lead to poor current density distribution, resulting in lower degradation efficiency and the potential formation of undesired byproducts (105). Additionally, the configuration of the electrochemical cell, along with the reactor shape and geometric parameters, affect flow dispersion and mass transport, influencing the potential and current distribution in the BDD anodes (105, 106). This directly impacts the current efficiency and energy consumption of the degradation process (107, 108).

As seen in Supplementary Information Table III.1.1, only a few studies correspond to the same V/A ratio and applied current densities used in this work (109-113). In some cases (110, 112), the electrolyte concentration was significantly higher (> 7 M) than the one applied in this study (0.1 M), which aimed to simulate conditions closer to real-world applications (sea water). Regardless of electrolyte concentration and cell configuration, the BDD/Si_3N_4-TiN electrode demonstrated removal rates and ACE values comparable to those obtained by other BDD electrodes studied under similar experimental conditions (V/A ratio, applied current density, and electrolysis time) in the literature.

III.1.4. Conclusions

In conclusion, our study has demonstrated that using an electroconductive ceramic composite of silicon nitride (Si_3N_4) and titanium nitride (TiN) as a substrate for BDD electrodes can effectively address the issue of electrode failure due to BDD delamination. The BDD/Si_3N_4-TiN electrode could withstand more than 2016 hours of accelerated life test without film delamination and exhibited an interfacial crack resistance value of 7.54 N μm^{-1}. Furthermore, the BDD/Si_3N_4-TiN electrode could eliminate phenol entirely and up to 98.8% of the model solution's Chemical Oxygen Demand (COD) after 5 hours of direct anodic oxidation, with an Average Current Efficiency (ACE) of 14% and an energy consumption of 138 kWh kg_{COD}^{-1}. The BDD/Si_3N_4-TiN electrode exhibited lower energy consumption values compared to the average results reported in the literature. Renewable energy sources such as wind, tidal, or solar power can be considered to improve energy efficiency and open the possibility of self-sufficient and sustainable water treatment processes. Furthermore, it was found that the BDD/Si_3N_4-TiN electrode can achieve comparable degradation rates and ACE values to other BDD electrodes studied under similar experimental conditions. There is still much ground to cover to understand the potential of BDD/Si_3N_4-TiN electrodes fully. Further research is needed to investigate the optimum treatment conditions (e.g., current density, electrolyte type and concentration, volume-to-area ratio, cell design, pH, electrode geometry), test them with different organic molecules and real wastewater systems, compare their performance in different EAOPs, and perform a cost-effectiveness analysis for future large-scale applications. These steps will help to optimize the performance of the electrochemical oxidation process, understand its limitations and advantages, and ultimately pave the way for its integration into sustainable water treatment systems. Overall, our results suggest that BDD/Si_3N_4-TiN electrodes are a potential long-lasting solution for large-scale water treatment and may facilitate the scaling-up of electrochemical advanced oxidation processes (EAOPs) using diamond technology.

III.1.5. References

1. Scialdone O, Randazzo S, Galia A, Silvestri G. Electrochemical oxidation of organics in water: role of operative parameters in the absence and in the presence of NaCl. Water Res. 2009;43(8):2260-72.
2. Saez C, Panizza M, Rodrigo MA, Cerisola G. Electrochemical incineration of dyes using a boron-doped diamond anode. J Chem Technol Biotechnol. 2007;82(6):575-81.
3. Zhao X, Qu J, Liu H, Qiang Z, Liu R, Hu C. Photoelectrochemical degradation of anti-inflammatory pharmaceuticals at Bi2MoO6–boron-doped diamond hybrid electrode under visible light irradiation. Appl Catal B Environ. 2009;91(1-2):539-45.
4. Mascia M, Vacca A, Polcaro AM, Palmas S, Ruiz JR, Da Pozzo A. Electrochemical treatment of phenolic waters in presence of chloride with boron-doped diamond (BDD) anodes: experimental study and mathematical model. J Hazard Mater. 2010;174(1-3):314-22.
5. Yavuz Y, Koparal AS, Öğütveren ÜB. Treatment of petroleum refinery wastewater by electrochemical methods. Desalination. 2010;258(1-3):201-5.
6. Urtiaga A, Gómez P, Arruti A, Ortiz I. Electrochemical removal of tetrahydrofuran from industrial wastewaters: anode selection and process scale-up. J Chem Technol Biotechnol. 2014;89(8):1243-50.
7. dos Santos EV, Sena SF, da Silva DR, Ferro S, De Battisti A, Martinez-Huitle CA. Scale-up of electrochemical oxidation system for treatment of produced water generated by Brazilian petrochemical industry. Environ Sci Pollut Res Int. 2014;21(14):8466-75.
8. Matthée T, Fryda M, Schäfer L, Tröster I. Electrochemical advanced oxidation process using DiaChem®electrodes. Water Sci Technol. 2004;49(4):207-12.
9. Anglada A, Urtiaga AM, Ortiz I. Laboratory and pilot plant scale study on the electrochemical oxidation of landfill leachate. J Hazard Mater. 2010;181(1-3):729-35.
10. Dominguez-Ramos A, Aldaco R, Irabien A. Electrochemical Oxidation of Lignosulfonate: Total Organic Carbon Oxidation Kinetics. Ind Eng Chem Res. 2008;47(24):9848-53.
11. Brosler P, Girão AV, Silva RF, Tedim J, Oliveira FJ. Electrochemical Advanced Oxidation Processes Using Diamond Technology: A Critical Review. Environments. 2023;10(2).
12. Sarakhman O, Svorc L. A Review on Recent Advances in the Applications of Boron-Doped Diamond Electrochemical Sensors in Food Analysis. Crit Rev Anal Chem. 2022;52(4):791-813.

13. Cobb SJ, Ayres ZJ, Macpherson JV. Boron Doped Diamond: A Designer Electrode Material for the Twenty-First Century. Annu Rev Anal Chem (Palo Alto Calif). 2018;11(1):463-84.
14. Martínez-Huitle CA, Rodrigo MA, Sirés I, Scialdone O. A critical review on latest innovations and future challenges of electrochemical technology for the abatement of organics in water. Appl Catal B Environ. 2023;328.
15. Karim AV, Nidheesh PV, Oturan MA. Boron-doped diamond electrodes for the mineralization of organic pollutants in the real wastewater. Curr Opin Electrochem. 2021;30.
16. McBeath ST, Wilkinson DP, Graham NJD. Application of boron-doped diamond electrodes for the anodic oxidation of pesticide micropollutants in a water treatment process: A critical review. Environ Sci Water Res Technol. 2019;5(12):2090-107.
17. Alvarez Pugliese CE, Martínez Hernández L, Imbachi Ordoñez S, Marriaga Cabrales N, Machuca Martínez F. Pilot scale anodic oxidation of pretreated vinasse using boron doped diamond electrodes. CT&F - Ciencia, Tecnología y Futuro. 2016;6(4):67-77.
18. Anglada A, Urtiaga A, Ortiz I. Pilot scale performance of the electro-oxidation of landfill leachate at boron-doped diamond anodes. Environ Sci Technol. 2009;43(6):2035-40.
19. Chaplin BP. Critical review of electrochemical advanced oxidation processes for water treatment applications. Environ Sci Process Impacts. 2014;16(6):1182-203.
20. Chen G. Electrochemical technologies in wastewater treatment. Sep Purif Technol. 2004;38(1):11-41.
21. He Y, Lin H, Guo Z, Zhang W, Li H, Huang W. Recent developments and advances in boron-doped diamond electrodes for electrochemical oxidation of organic pollutants. Sep Purif Technol. 2019;212:802-21.
22. Yang W, Tan J, Chen Y, Li Z, Liu F, Long H, et al. Relationship between substrate type and BDD electrode structure, performance and antibiotic tetracycline mineralization. J Alloys Compd. 2022;890.
23. Brosler P, Girão AV, Silva RF, Tedim J, Oliveira FJ. In-house vs. commercial boron-doped diamond electrodes for electrochemical degradation of water pollutants: A critical review. Front Mater. 2023;10.
24. Nidheesh PV, Divyapriya G, Oturan N, Trellu C, Oturan MA. Environmental Applications of Boron-Doped Diamond Electrodes: 1. Applications in Water and Wastewater Treatment. ChemElectroChem. 2019;6(8):2124-42.
25. Almeida FA, Amaral M, Oliveira FJ, Fernandes AJS, Silva RF. Nano to micrometric HFCVD diamond adhesion strength to Si3N4. Vacuum. 2007;81(11-12):1443-7.

26. Almeida FA, Oliveira FJ, Silva RF, Baptista DL, Peripolli SB, Achete CA. High resolution study of the strong diamond/silicon nitride interface. Appl Phys Lett. 2011;98(17).
27. Petzow G, Herrmann M. Silicon Nitride Ceramics. In: Jansen M, editor. High Performance Non-Oxide Ceramics II. Structure and Bonding. Berlin, Heidelberg: Springer Berlin Heidelberg; 2002. p. 47-167.
28. Almeida FA, Bóia H, Santos C, Monteiro J, Oliveira FJ, Silva RF. Electroconductive Ceramic Composites for Cutting Tools. Mater Sci Forum. 2006;514-516:638-42.
29. Bucciotti F, Mazzocchi M, Bellosi A. Perspectives of the Si3N4-TiN ceramic composite as a biomaterial and manufacturing of complex-shaped implantable devices by electrical discharge machining (EDM). J Appl Biomater Biomech. 2010;8(1):28-32.
30. Guedes e Silva C. Silicon nitride as biomaterial. New York: Nova Science Publishers, Inc.; 2012 01/01. 149-56 p.
31. Yu D, Zhang X, Luo H, Liao D, Wu N. Effect of nozzle inlet parameters on the dry granulation atomization process of Si3N4 ceramic bearing balls. Int J Model, Simul, Sci Comput. 2021;12(06):23.
32. Duan W, Jia D, Cai D, Niu B, Yang Z, Zhou Y. A facile strategy for fabricating self-sealing dense coating grown in-situ on porous silicon nitride ceramics. J Eur Ceram Soc. 2021;41(3):2162-7.
33. Telle R, Muenstermann S, Beyer C. Design, Construction and Performance of Silicon Nitride Tool Parts in Steel Thixoforming. Solid State Phenom. 2006;116-117:690-5.
34. Drawin S, Justin JF. Advanced Lightweight Silicide and Nitride Based Materials for Turbo-Engine Applications. Aerospace Lab. 2011(3):p. 1-13.
35. Wang L, Snidle RW, Gu L. Rolling contact silicon nitride bearing technology: a review of recent research. Wear. 2000;246(1-2):159-73.
36. Torma PT, Sipila HJ, Mattila M, Kostamo P, Kostamo J, Kostamo E, et al. Ultra-Thin Silicon Nitride X-Ray Windows. IEEE Trans Nucl Sci. 2013;60(2):1311-4.
37. Robertson J. The Electronic Structure of Silicon Nitride. Recent Dev Condens Matter Phys. 631981. p. 239-45.
38. Berroth K. Silicon Nitride Ceramics for Product and Process Innovations. Adv Sci Technol. 2011;65:70-7.
39. Bellosi A, Guicciardi S, Tampieri A. Development and characterization of electroconductive Si3N4-TiN composites. J Eur Ceram Soc. 1992;9(2):83-93.
40. Herrmann M, Balzer B, Schubert C, Hermel W. Densification, microstructure and properties of Si3N4□Ti(C,N) composites. J Eur Ceram Soc. 1993;12(4):287-96.

41. Brosler P, Silva RF, Tedim J, Oliveira FJ. Electroconductive silicon nitride-titanium nitride ceramic substrates for CVD diamond electrode deposition. Ceram Int. 2023.

42. Almeida FA, Belmonte M, Fernandes AJS, Oliveira FJ, Silva RF. MPCVD diamond coating of Si3N4–TiN electroconductive composite substrates. Diamond Relat Mater. 2007;16(4-7):978-82.

43. Endler I, Leonhardt A, Scheibe HJ, Born R. Interlayers for diamond deposition on tool materials. Diamond Relat Mater. 1996;5(3-5):299-303.

44. Almeida FA, Amaral M, Oliveira FJ, Silva RF. Machining behaviour of silicon nitride tools coated with micro-, submicro- and nanometric HFCVD diamond crystallite sizes. Diamond Relat Mater. 2006;15(11-12):2029-34.

45. Martinho RP, Silva FJG, Baptista APM. Wear behaviour of uncoated and diamond coated Si3N4 tools under severe turning conditions. Wear. 2007;263(7-12):1417-22.

46. Fernandes AJS, Salgueiredo E, Oliveira FJ, Silva R, Costa FM. Directly MPCVD diamond-coated Si3N4 disks for dental applications. Diamond Relat Mater. 2005;14(3-7):626-30.

47. Salgueiredo E, Vila M, Silva MA, Lopes MA, Santos JD, Costa FM, et al. Biocompatibility evaluation of DLC-coated Si3N4 substrates for biomedical applications. Diamond Relat Mater. 2008;17(4-5):878-81.

48. Maru MM, Amaral M, Rodrigues SP, Santos R, Gouvea CP, Archanjo BS, et al. The High performance of nanocrystalline CVD diamond coated hip joints in wear simulator test. J Mech Behav Biomed Mater. 2015;49:175-85.

49. Amaral M, Rodrigues SP, Oliveira FJ, Silva RF. Chapter 14: Nanocrystalline Diamond Coatings on Silicon Nitride Bioceramic Bearings. Mater Total Jt Arthroplasty. 2015:413-30.

50. Follador RC, Minucci MAS, Toro PGP, Trava-Airoldi VJ, Ferreira NG. Preliminary study of CVD diamond film to improve the performance of heat flux sensors for hypersonic experiments. Diamond Relat Mater. 2005;14(3-7):637-40.

51. Salgueiredo E, Abreu CS, Amaral M, Oliveira FJ, Gomes JR, Silva RF. Self-mated tribological systems based on multilayer micro/nanocrystalline CVD diamond coatings. Wear. 2013;303(1-2):225-34.

52. Vila M, Carrapichano JM, Gomes JR, Camargo SS, Achete CA, Silva RF. Ultra-high performance of DLC-coated Si3N4 rings for mechanical seals. Wear. 2008;265(5-6):940-4.

53. Carrapichano JM, Taillaire A, Oliveira FJ, Silva RF. Complete Densification of Si3N4 – SiC Ceramic Matrix Composites (CMC's) by a Pressureless Sintering Route. Mater Sci Forum. 2004;455-456:225-9.

54. Belmonte M, Fernandes AJS, Costa FM, Oliveira FJ, Silva RF. Adhesion behaviour assessment on diamond coated silicon nitride by acoustic emission. Diamond Relat Mater. 2003;12(3-7):733-7.

55. Tallaire A, Silva VA, Fernandes AJS, Costa FM, Silva RF. Effect of intergranular phase of Si3N4 substrates on MPCVD diamond deposition. Surf Coat Technol. 2002;151-152:521-5.

56. Anstis GR, Chantikul P, Lawn BR, Marshall DB. A Critical Evaluation of Indentation Techniques for Measuring Fracture Toughness: I, Direct Crack Measurements. J Am Ceram Soc. 1981;64(9):533-8.

57. Voigt W. Ueber die Beziehung zwischen den beiden Elasticitätsconstanten isotroper Körper. Annalen der Physik. 1889;274(12):573-87.

58. Reuss A. Berechnung der Fließgrenze von Mischkristallen auf Grund der Plastizitätsbedingung für Einkristalle. ZAMM - Zeitschrift für Angewandte Mathematik und Mechanik. 1929;9(1):49-58.

59. Baba S, Goto T, Cho S, Sekino T. Microstructure and mechanical properties of TiN dispersed Si3N4 ceramics via in-situ nitridation of coarse metallic Ti. Epitoanyag J Silic Compos Mater. 2018;70(6):195-203.

60. Gates-Rector S, Blanton T. The Powder Diffraction File: a quality materials characterization database. Powder Diffraction. 2019;34(4):352-60.

61. Amaral M, Almeida F, Fernandes AJS, Costa FM, Oliveira FJ, Silva RF. The role of surface activation prior to seeding on CVD diamond adhesion. Surf Coat Technol. 2010;204(21-22):3585-91.

62. Comninellis C, Pulgarin C. Anodic oxidation of phenol for waste water treatment. J Appl Electrochem. 1991;21(8):703-8.

63. Pierson HO. Covalent Nitrides. In: Pierson HO, editor. Handbook of Refractory Carbides and Nitrides. Westwood, NJ: William Andrew Publishing; 1996. p. 223-47.

64. Bošković S, Sigulinski F, Živković L. Liquid-Phase Sintering and Properties of Si3N4–TiN Composites. J Mater Synth Process. 1999;7(2):119-26.

65. Huang J-L, Lee M-T, Lu H-H, Lii D-F. Microstructure, fracture behavior and mechanical properties of TiN/Si3N4 composites. Mater Chem Phys. 1996;45(3):203-9.

66. Standardization IOf. ISO 4499-2:2020 - Hardmetals. Metallographic determination of microstructure — Part 2: Measurement of WC grain size2020.

67. Ballutaud D, Jomard F, Kociniewski T, Rzepka E, Girard H, Saada S. Sp3/sp2 character of the carbon and hydrogen configuration in micro- and nanocrystalline diamond. Diamond Relat Mater. 2008;17(4-5):451-6.

68. Ferrari AC, Robertson J. Origin of the1150−cm−1Raman mode in nanocrystalline diamond. Physical Review B. 2001;63(12).

69. Ferrari AC, Robertson J. Raman spectroscopy of amorphous, nanostructured, diamond-like carbon, and nanodiamond. Philos Trans A Math Phys Eng Sci. 2004;362(1824):2477-512.

70. Bernard M, Deneuville A, Muret P. Non-destructive determination of the boron concentration of heavily doped metallic diamond thin films from Raman spectroscopy. Diamond Relat Mater. 2004;13(2):282-6.

71. Ghodbane S, Deneuville A. Specific features of 325 nm Raman excitation of heavily boron doped polycrystalline diamond films. Diamond Relat Mater. 2006;15(4-8):589-92.

72. Zhang RJ, Lee ST, Lam YW. Characterization of heavily boron-doped diamond films. Diamond Relat Mater. 1996;5(11):1288-94.

73. Pimenta MA, Dresselhaus G, Dresselhaus MS, Cancado LG, Jorio A, Saito R. Studying disorder in graphite-based systems by Raman spectroscopy. Phys Chem Chem Phys. 2007;9(11):1276-91.

74. Prawer S, Nemanich RJ. Raman spectroscopy of diamond and doped diamond. Philos Trans A Math Phys Eng Sci. 2004;362(1824):2537-65.

75. Ralchenko VG, Smolin AA, Pereverzev VG, Obraztsova ED, Korotoushenko KG, Konov VI, et al. Diamond deposition on steel with CVD tungsten intermediate layer. Diamond Relat Mater. 1995;4(5-6):754-8.

76. Ferreira NG, Abramof E, Leite NF, Corat EJ, Trava-Airoldi VJ. Analysis of residual stress in diamond films by x-ray diffraction and micro-Raman spectroscopy. J Appl Phys. 2002;91(4):2466-72.

77. Lagrange JP, Deneuville A, Gheeraert E. Activation energy in low compensated homoepitaxial boron-doped diamond films. Diamond Relat Mater. 1998;7(9):1390-3.

78. Bogdanowicz R, Sawczak M, Niedzialkowski P, Zieba P, Finke B, Ryl J, et al. Novel Functionalization of Boron-Doped Diamond by Microwave Pulsed-Plasma Polymerized Allylamine Film. J Phys Chem C. 2014;118(15):8014-25.

79. Mallika K, Komanduri R. Low pressure microwave plasma assisted chemical vapor deposition (MPCVD) of diamond coatings on silicon nitride cutting tools. Thin Solid Films. 2001;396(1-2):146-66.

80. Lu X-R, Ding M-H, Zhang C, Tang W-Z. Comparative study on stability of boron doped diamond coated titanium and niobium electrodes. Diamond Relat Mater. 2019;93:26-33.

81. Ristein J. Surface transfer doping of diamond. J Phys D: Appl Phys. 2006;39(4):R71-R81.

82. Neto MA, Pato G, Bundaleski N, Teodoro OMND, Fernandes AJS, Oliveira FJ, et al. Surface modifications on as-grown boron doped CVD diamond films induced by the B2O3–ethanol–Ar system. Diamond Relat Mater. 2016;64:89-96.

83. Monteverde F, Mingazzini C, Giorgi M, Bellosi A. Corrosion of silicon nitride in sulphuric acid aqueous solution. Corros Sci. 2001;43(10):1851-63.

84. Fryda M, Herrmann D, Schafer L, Klages CP, Perret A, Haenni W, et al. Properties of diamond electrodes for wastewater treatment. New Diamond Front Carbon Technol. 1999;9(3):229-40.

85. Choi Y-S, Lee Y-K, Kim J-Y, Kim K-M, Lee Y-K. Influence of Manufacturing Conditions for the Life Time of the Boron-Doped Diamond Electrode in Wastewater Treatment. Korean J Mater Res. 2017;27(3):137-43.

86. Groenen Serrano K, Savall A, Latapie L, Racaud C, Rondet P, Bertrand N. Performance of Ti/Pt and Nb/BDD anodes for dechlorination of nitric acid and regeneration of silver(II) in a tubular reactor for the treatment of solid wastes in nuclear industry. J Appl Electrochem. 2015;45(7):779-86.

87. Miao D, Liu T, Yu Y, Li S, Liu G, Chen Y, et al. Study on degradation performance and stability of high temperature etching boron-doped diamond electrode. Appl Surf Sci. 2020;514.

88. Zhang C, Lu X, Lu Y, Ding M, Tang W. Titanium-boron doped diamond composite: A new anode material. Diamond Relat Mater. 2019;98.

89. Lu X-R, Ding M-H, Zhang C, Tang W-Z. Investigation on microstructure evolution and failure mechanism of boron doped diamond coated titanium electrode during accelerated life test. Thin Solid Films. 2018;660:306-13.

90. He Y, Huang W, Chen R, Zhang W, Lin H. Improved electrochemical performance of boron-doped diamond electrode depending on the structure of titanium substrate. J Electroanal Chem. 2015;758:170-7.

91. Chen X, Gao F, Chen G. Comparison of Ti/BDD and Ti/SnO2?Sb2O5 electrodes for pollutant oxidation. J Appl Electrochem. 2005;35(2):185-91.

92. Chen X, Chen G. Proper Hot Filament CVD Conditions for Fabrication of Ti-Boron Doped Diamond Electrodes. J Electrochem Soc. 2004;151(4):B214-B9.

93. Zhang T, Xue Z, Xie Y, Huang G, Peng G. Fabrication of a boron-doped nanocrystalline diamond grown on an WC-Co electrode for degradation of phenol. RSC Adv. 2022;12(41):26580-7.

94. Dettlaff A, Sobaszek M, Klimczuk T, Bogdanowicz R. Enhanced electrochemical kinetics of highly-oriented (111)-textured boron-doped diamond electrodes induced by deuterium plasma chemistry. Carbon. 2021;174:594-604.
95. Batchelor-McAuley C, Ngamchuea K, Compton RG. Simulated low-support voltammetry: Deviations from Ohm's Law. J Electroanal Chem. 2018;830-831:88-94.
96. Bard AJ, Faulkner LR. Electrochemical Methods: Fundamentals and Applications. 2 ed: John Wiley & Sons; 2001.
97. Nadais H, Li X, Alves N, Couras C, Andersen HR, Angelidaki I, et al. Bio-electro-Fenton process for the degradation of Non-Steroidal Anti-Inflammatory Drugs in wastewater. Chem Eng J. 2018;338:401-10.
98. El-Ghenymy A, Centellas F, Garrido JA, Rodríguez RM, Sirés I, Cabot PL, et al. Decolorization and mineralization of Orange G azo dye solutions by anodic oxidation with a boron-doped diamond anode in divided and undivided tank reactors. Electrochim Acta. 2014;130:568-76.
99. Yi Z, Jia-qing X, Ci L, Jun LI, Hong-li S. Mechanism of Oxidation of Aqueous Phenol by H2O2 Catalysed by a Macrocyclic Iron(II) Complex. Prog React Kinet Mech. 2008;33(3):241-52.
100. Iniesta J. Electrochemical oxidation of phenol at boron-doped diamond electrode. Electrochim Acta. 2001;46(23):3573-8.
101. Murillo-Acevedo YS, Giraldo L, Poon PS, Matos J, Moreno-Pirajan JC. The Cramer's rule for the parametrization of phenol and its hydroxylated byproducts: UV spectroscopy vs. high performance liquid chromatography. Environ Sci Pollut Res Int. 2021;28(6):6746-57.
102. Meng X-G, Zhu J, Yan J, Xie J-Q, Kou X-M, Kuang X-F, et al. Studies on the oxidation of phenols catalyzed by a copper(II)-Schiff base complex in aqueous solution under mild conditions. J Chem Technol Biotechnol. 2006;81(1):2-7.
103. Martínez-Huitle CA, Panizza M. Electrochemical oxidation of organic pollutants for wastewater treatment. Curr Opin Electrochem. 2018;11:62-71.
104. Lacasa E, Tsolaki E, Sbokou Z, Rodrigo MA, Mantzavinos D, Diamadopoulos E. Electrochemical disinfection of simulated ballast water on conductive diamond electrodes. Chem Eng J. 2013;223:516-23.
105. Cano A, Barrera C, Cotillas S, Llanos J, Cañizares P, Rodrigo MA. Use of DiaCell modules for the electro-disinfection of secondary-treated wastewater with diamond anodes. Chem Eng J. 2016;306:433-40.
106. Xu SG. Modeling and Experimental Study of Electrochemical Oxidation of Organics on Boron-Doped Diamond Anode. CNL Nucl Rev. 2016:1-15.

107. Cornejo OM, Murrieta MF, Castañeda LF, Nava JL. Characterization of the reaction environment in flow reactors fitted with BDD electrodes for use in electrochemical advanced oxidation processes: A critical review. Electrochim Acta. 2020;331:135373.
108. Rivera FF, León CPd, Walsh FC, Nava JL. The reaction environment in a filter-press laboratory reactor: the FM01-LC flow cell. Electrochim Acta. 2015;161:436-52.
109. Lee C-H, Lee E-S, Lim Y-K, Park K-H, Park H-D, Lim D-S. Enhanced electrochemical oxidation of phenol by boron-doped diamond nanowire electrode. RSC Adv. 2017;7(11):6229-35.
110. Dalhat Mu N, H. Al-Mala M. Influence of Some Operating Parameters on Electro-Oxidation of Phenol using Boron Doped Diamond Anode and Graphite Cathode. J Environ Sci Technol. 2012;5(6):460-74.
111. Muazu ND, Jarrah N, Bukhari A. Kinetic modeling of electrochemical oxidation of phenol on boron-doped diamond anode in the presence of some inorganic species. Desalin Water Treat. 2014;56(11):1-8.
112. Jarrah N, Mu'azu ND. Simultaneous electro-oxidation of phenol, CN−, S2− and NH4+ in synthetic wastewater using boron doped diamond anode. J Environ Chem Eng. 2016;4(3):2656-64.
113. Morão A, Lopes A, Pessoa de Amorim MT, Gonçalves IC. Degradation of mixtures of phenols using boron doped diamond electrodes for wastewater treatment. Electrochim Acta. 2004;49(9-10):1587-95.

.

III.1.6. Supplementary Information

To enhance the comprehension of the advancements accomplished by the BDD/Si_3N_4-TiN electrode system, we present a comprehensive performance comparison in Supplementary Table III.1.1. This table offers an extensive overview of the experimental results obtained specifically for phenol degradation using BDD electrodes. It serves as a valuable resource for evaluating the progress made by the BDD/Si_3N_4-TiN electrode system in comparison to the existing literature.

Supplementary Table III.1.1. Phenol degradation performance of BDD/Si_3N_4-TiN electrodes compared to other BDD electrodes across the literature.

Substrate	j	t	V/A ratio	COD_0	$[Ph]_0$	COD Removal	Phenol Removal	EC			ICE_t	ACE_t	SE	Ref.
	mA/cm²	min	cm³/cm²	mgO_2/L	mg/L	%	%	kWh/kg_{COD}	kWh/m^3	kWh/kg_{Ph}	%	%		
Si_3N_4-TiN	30	*300*	25.0	250	94.1	*98.8%*	99.8%	138.3	3.4	*369.8*	3.6%	13.8%	0.1 M Na_2SO_4	This work
Si_3N_4-TiN	30	*180*	25.0	250	94.1	*81.7%*	80.7%	100.2	2.1	*274.8*	7.2%	19.1%	0.1 M Na_2SO_4	
Si_3N_4-TiN	60	*180*	25.0	250	94.1	*83.3%*	91.1%	213.9	4.5	*529.8*	-	9.7%	0.1 M Na_2SO_4	
Si_3N_4-TiN	90	*180*	25.0	250	94.1	*89.7%*	97.9%	317.3	7.1	*787.1*	-	7.0%	0.1 M Na_2SO_4	
Si_3N_4-TiN	120	*180*	25.0	250	94.1	*93.2%*	100.0%	462.7	10.8	*1167.8*	-	5.4%	0.1 M Na_2SO_4	
WC-Co	100	-	-	5795	2352.8	*98.5%*	-	-	-	-	42.1%	-	0.5 M H_2SO_4	(1)
Si	20	*660*	8.3	548	-	*99.7%*	-	435.0	-	-	7.0%	-	0.05 M Na_2SO_4	(2)

Substrate	j	t	V/A ratio	COD_0	$[Ph]_0$	COD Removal	Phenol Removal	EC			ICE_t	ACE_t	SE	Ref.
	mA/cm²	min	cm³/cm²	mgO_2/L	mg/L	%	%	kWh/kg_{COD}	kWh/m^3	kWh/kg_{Ph}	%	%		
Si	30	*300*	31.3	200	94.1	*94.4%*	-	-	27.5**	-	3.0%	15.6%	0.5 M Na_2SO_4	(3)
Si	50	-	-	-	50.0	*94.0%*	-	-	-	-	-	-	0.1 M H_2SO_4	(4)
Si	100	-	-	-	50.0	*95.0%*	-	-	-	-	-	-	0.1 M H_2SO_4	
Si	150	-	-	-	50.0	*93.0%*	-	-	-	-	-	-	0.1 M H_2SO_4	
Si	30	*240*	60.0	1000	941.1	*42.0%*	-	-	-	-	-	-	0.035 M Na_2SO_4	(5)
Si	30	*360*	6.4	2400	-	*100.0%*	-	-	-	-	-	28.5%	0.035 M Na_2SO_4	(6)
Si	47	-	15.7	-	1882.2	*99.0%*	-	-	80.0	-	-	-	0.1 M H_2SO_4	(7)
Si	100	-	15.7	-	1882.2	*96.4%*	-	-	-	-	-	-	0.1 M H_2SO_4	
Si	142	-	15.7	-	1882.2	*98.4%*	-	-	-	-	-	-	0.1 M H_2SO_4	
Si	60	*3600*	10.0	-	470.6	-	88.3%	-	-	*112.0*	-	-	1 M $HClO_4$	(8)
Ti	15	*900*	66.7	224	94.1	*95.0%*	-	-	8.2	-	6.0%	-	0.5 M Na_2SO_4	(9)
Ti	100	*240*	13.3	9153	3.8	*50.9%*	-	-	-	-	-	52.1%	H_2SO_4	(10)
Ti	100	*240*	13.3	9153	3.8	*63.3%*	-	-	-	-	-	64.7%	H_2SO_4	

Substrate	j	t	V/A ratio	COD_0	$[Ph]_0$	COD Removal	Phenol Removal	EC			ICE_t	ACE_t	SE	Ref.
	mA/cm²	min	cm³/cm²	mgO_2/L	mg/L	%	%	kWh/kg_{COD}	kWh/m^3	kWh/kg_{Ph}	%	%		
Ti	10	*140*	4.8	1175	-	*96.7%*	-	-	-	-	-	78.5%	0.01 M Na_2SO_4	(11)
Ti	10	-	-	1175	500.0	*96.6%*	-	-	-	-	-	-	0.01 M Na_2SO_4	(12)
Ti	20	*300*	62.5	-	94.1	*70.0%*	-	-	-	-	-	23.8%	0.2 M Na_2SO_4	(13)
Nb	27	*68*	1.6	300	-	*85.4%*	-	587.4	-	-	-	-	Na_2SO_4	(14)
Nb	9	*80*	1.5	633	-	*77.0%*	-	31.0	-	-	-	-	Na_2SO_4	
Nb	30	*270*	25.5	-	100.0	*99.3%*	-	-	-	-	-	10.5%	0.01 M Na_2SO_4	(15)
Nb	45	*270*	25.5	-	100.0	*71.9%*	-	-	-	-	-	1.6%	0.01 M Na_2SO_4	
Nb	60	*270*	25.5	-	100.0	*79.6%*	-	-	-	-	-	-	0.01 M Na_2SO_4	
Nb	20	*69*	1.6	500	-	*80.0%*	-	110.0	-	-	-	-	0.05 M Na_2SO_4	(16)
Nb	30	*150*	25.5	-	100.0	*100.0%*	-	-	-	-	20.0%	-	0.01 M Na_2SO_4	(17)
Nb	50	*350*	-	666	280.0	*96.0%*	-	81.3	-	-	-	22.7%	Na_2SO_4	(18)
Nb	30	*480*	160.0	378	-	*91.0%*	-	26.6	-	-	-	61.0%	0.1 M Na_2SO_4	(19)
Nb	50	*480*	89.3	500	210.0	*77.3%*	-	122.0	-	-	-	-	0.1 M H_2SO_4	(20)

Substrate	j	t	V/A ratio	COD_0	$[Ph]_0$	COD Removal	Phenol Removal	EC			ICE_t	ACE_t	SE	Ref.
	mA/cm²	min	cm³/cm²	mgO_2/L	mg/L	%	%	kWh/kg_{COD}	kWh/m^3	kWh/kg_{Ph}	%	%		
Nb	50	*350*	21.4	666	280.0	*97.0%*	-	-	-	-	-	-	0.1 M Na_2SO_4	(21)
Nb	20	*1200*	63.0	-	94.1	-	97.0%	-	-	-	-	-	0.2 M Na_2SO_4	(22)
Nb	4	*234*	6.0	-	50.0	-	65.4%	-	-	-	-	-	1 mM $NaNO_2$	(23)
Nb	7	*390*	6.0	-	50.0	-	99.0%	-	-	-	-	-	10 mM NaBr	(24)
Nb	30	*1800*	25.0	-	100.0	-	100.0%	-	-	*443.0*	-	-	7.75 M Na_2SO_4	(25)
Nb	30	*1800*	25.0	-	100.0	-	97.6%	-	-	*487.0*	-	-	7.05 M Na_2SO_4	(15)
Nb	60	*3600*	25.0	-	100.0	-	100.0%	-	-	*691.0*	-	-	7.05 M Na_2SO_4	
-	30	*120*	11.4	-	300.0	*94.0%*	-	-	-	-	-	-	0.035 M Na_2SO_4	(26)
-	10	*600*	428.6	-	300.0	*51.0%*	-	-	-	-	-	-	0.04 M Na_2SO_4	
-	30	*210*	12.7	-	100.0	*98.9%*	-	57.0	-	-	-	19.1%	0.01 M Na_2SO_4	(25)
-	20	*300*	62.5	-	94.1	*86.0%*	-	-	-	-	-	-	0.2 M Na_2SO_4	(27)
-	10	*480*	21.4	-	200.0	*92.0%*	-	-	-	-	-	-	-	(28)

-	30	*480*	18.8	-	200.0	*98.0%*	-	-	-	-	-	-	-	
Substrate	**j**	**t**	**V/A ratio**	**COD_0**	**$[Ph]_0$**	**COD Removal**	**Phenol Removal**	**EC**			**ICE_t**	**ACE_t**	**SE**	**Ref.**
	mA/cm²	**min**	**cm³/cm²**	**mgO_2/L**	**mg/L**	**%**	**%**	**kWh/kg$_{COD}$**	**kWh/m³**	**kWh/kg$_{Ph}$**	**%**	**%**		
-	215	*240*	14.3	-	1985.0	*100.0%*	-	-	-	-	-	-	0.1 M Na_2SO_4	(29)
-	30	*375*	24.7	-	222.0	*78.5%*	-	-	-	-	-	-	0.1 M Na_2CO_3	(30)
-	20	*300*	8.3	540	240.0	*68.5%*	-	-	-	-	-	12.3%	0.05 M Na_2SO_4	(31)
-	10	*600*	100.0	-	47.1	-	31.5%	-	-	-	-	-	0.2 M Na_2SO_4	(32)

** t: Electrolysis time; j: Applied current density; V/A ratio – Volume-to-Area ratio; COD_0 Initial Chemical Oxygen Demand; $[Ph]_0$ - Initial Phenol concentration; EC - Energy Consumption; ICE_t - Intantenous Current Efficiency at t; ACE_t - Average Current Efficiency at t; SE – Supporting electrolyte.*

*** For 80% mineralization.*

References

1. Zhang T, Xue Z, Xie Y, Huang G, Peng G. Fabrication of a boron-doped nanocrystalline diamond grown on an WC-Co electrode for degradation of phenol. RSC Adv. 2022;12(41):26580-7.
2. Zhao G, Gao J, Shen S, Liu M, Li D, Wu M, *et al.* Ultrasound enhanced electrochemical oxidation of phenol and phthalic acid on boron-doped diamond electrode. J Hazard Mater. 2009;172(2-3):1076-81.
3. Lee C-H, Lee E-S, Lim Y-K, Park K-H, Park H-D, Lim D-S. Enhanced electrochemical oxidation of phenol by boron-doped diamond nanowire electrode. RSC Adv. 2017;7(11):6229-35.
4. Kornienko GV, Chaenko NV, Maksimov NG, Kornienko VL, Varnin VP. Electrochemical oxidation of phenol on boron-doped diamond electrode. Russ J Electrochem. 2011;47(2):225-9.
5. Cañizares P, Sáez C, Martínez F, Rodrigo MA. The Role of the Characteristics of p-Si BDD Anodes on the Efficiency of Wastewater Electro-oxidation Processes. Electrochem Solid-State Lett. 2008;11(7):E15-E9.
6. Canizares P, Lobato J, Paz R, Rodrigo MA, Saez C. Electrochemical oxidation of phenolic wastes with boron-doped diamond anodes. Water Res. 2005;39(12):2687-703.
7. Weiss E, Groenen-Serrano K, Savall A. A comparison of electrochemical degradation of phenol on boron doped diamond and lead dioxide anodes. J Appl Electrochem. 2007;38(3):329-37.
8. Iniesta J. Electrochemical oxidation of phenol at boron-doped diamond electrode. Electrochim Acta. 2001;46(23):3573-8.
9. Sun J, Lu H, Lin H, Du L, Huang W, Li H, *et al.* Electrochemical oxidation of aqueous phenol at low concentration using Ti/BDD electrode. Sep Purif Technol. 2012;88:116-20.
10. Shi L, Xu F, Gao J, Yuen M, Sun S, Xu J, *et al.* Nanostructured boron-doped diamond electrode for degradation of the simulation wastewater of phenol. Diamond Relat Mater. 2020;109:108098.
11. Chen X, Chen G, Gao F, Yue PL. High-performance Ti/BDD electrodes for pollutant oxidation. Environ Sci Technol. 2003;37(21):5021-6.
12. Chen X, Gao F, Chen G. Comparison of Ti/BDD and Ti/SnO2?Sb2O5 electrodes for pollutant oxidation. J Appl Electrochem. 2005;35(2):185-91.
13. Zhu X, Shi S, Wei J, Lv F, Zhao H, Kong J, *et al.* Electrochemical oxidation characteristics of p-substituted phenols using a boron-doped diamond electrode. Environ Sci Technol. 2007;41(18):6541-6.

14. Zhu X, Ni J, Wei J, Xing X, Li H, Jiang Y. Scale-up of BDD anode system for electrochemical oxidation of phenol simulated wastewater in continuous mode. J Hazard Mater. 2010;184(1-3):493-8.
15. Dalhat Mu N, H. Al-Mala M. Influence of Some Operating Parameters on Electro-Oxidation of Phenol using Boron Doped Diamond Anode and Graphite Cathode. J Environ Sci Technol. 2012;5(6):460-74.
16. Wei J, Zhu X, Ni J. Electrochemical oxidation of phenol at boron-doped diamond electrode in pulse current mode. Electrochim Acta. 2011;56(15):5310-5.
17. Muazu ND, Jarrah N, Bukhari A. Kinetic modeling of electrochemical oxidation of phenol on boron-doped diamond anode in the presence of some inorganic species. Desalin Water Treat. 2014;56(11):1-8.
18. de Souza RBA, Ruotolo LAM. Phenol electrooxidation in different supporting electrolytes using boron-doped diamond anodes. Int J Electrochem Sci. 2013;8(1):643-57.
19. Farinos RM, Ruotolo LAM. Comparison of the electrooxidation performance of three-dimensional RVC/PbO2 and boron-doped diamond electrodes. Electrochim Acta. 2017;224:32-9.
20. Britto-Costa PH, Ruotolo LAM. Phenol removal from wastewaters by electrochemical oxidation using boron doped diamond (BDD) and Ti/Ti0.7Ru0.3O2 dsa® electrodes. Braz J Chem Eng. 2012;29(4):763-73.
21. Souza RBA, Ruotolo LAM. Electrochemical treatment of oil refinery effluent using boron-doped diamond anodes. J Environ Chem Eng. 2013;1(3):544-51.
22. Jiang H, Dang C, Liu W, Wang T. Radical attack and mineralization mechanisms on electrochemical oxidation of p-substituted phenols at boron-doped diamond anodes. Chemosphere. 2020;248:126033.
23. Zhang C, Xian J, Liu M, Fu D. Formation of brominated oligomers during phenol degradation on boron-doped diamond electrode. J Hazard Mater. 2018;344:123-35.
24. Zhang C, Dong J, Liu M, Zhao W, Fu D. The role of nitrite in electrocatalytic oxidation of phenol: An unexpected nitration process relevant to groundwater remediation with boron-doped diamond electrode. J Hazard Mater. 2019;373:547-57.
25. Jarrah N, Mu'azu ND. Simultaneous electro-oxidation of phenol, CN−, S2− and NH4+ in synthetic wastewater using boron doped diamond anode. J Environ Chem Eng. 2016;4(3):2656-64.
26. Lopes A, Ciríaco L, Pacheco MJ, Sobreira S. Effect of the Hydrodynamic Conditions on the Electrochemical Degradation of Phenol on a BDD Anode. Port Electrochim Acta. 2011;29(5):343-8.

27. Zhu X, Ni J, Li H, Jiang Y, Xing X, Borthwick AGL. Effects of ultrasound on electrochemical oxidation mechanisms of p-substituted phenols at BDD and PbO2 anodes. Electrochim Acta. 2010;55(20):5569-75.

28. Pacheco MJ, Morão A, Lopes A, Ciríaco L, Gonçalves I. Degradation of phenols using boron-doped diamond electrodes: A method for quantifying the extent of combustion. Electrochim Acta. 2007;53(2):629-36.

29. Bouaziz I, Hamza M, Sellami A, Abdelhedi R, Savall A, Groenen Serrano K. New hybrid process combining adsorption on sawdust and electroxidation using a BDD anode for the treatment of dilute wastewater. Sep Purif Technol. 2017;175:1-8.

30. Morão A, Lopes A, Pessoa de Amorim MT, Gonçalves IC. Degradation of mixtures of phenols using boron doped diamond electrodes for wastewater treatment. Electrochim Acta. 2004;49(9-10):1587-95.

31. Zhao G, Shen S, Li M, Wu M, Cao T, Li D. The mechanism and kinetics of ultrasound-enhanced electrochemical oxidation of phenol on boron-doped diamond and Pt electrodes. Chemosphere. 2008;73(9):1407-13.

32. Chen P, Mu Y, Chen Y, Tian L, Jiang XH, Zou JP, *et al.* Shifts of surface-bound *OH to homogeneous *OH in BDD electrochemical system via UV irradiation for enhanced degradation of hydrophilic aromatic compounds. Chemosphere. 2022;291(Pt 2):132817.

III.2. Surface Characterization and Electrooxidation Efficiency of Boron-Doped Diamond Electrodes Modified by Plasma Treatment: Implications for Water Treatment

Priscilla Brosler[1], Cristina Neves[1], Rui F. Silva[1], João Tedim[1], Filipe J. Oliveira[1]

[1] CICECO - Aveiro Institute of Materials & Department of Materials and Ceramic Engineering, University of Aveiro, 3810-193 Aveiro, Portugal

The present work is in the form of a manuscript (to be published)

Abstract

Boron-doped diamond (BDD) electrode surface modification holds promise for improving their electrochemical performance in water treatment applications. In this study, we employed radiofrequency (RF) plasma treatments with different gases (O_2, Ar, and CF_4) to functionalize BDD surfaces. We characterized the modified BDD surfaces using Raman spectroscopy, sessile drop contact angle measurements, cyclic voltammetry (CV), electrochemical impedance spectroscopy (EIS), and Mott-Schottky analysis. Our investigation included a comparative analysis between the plasma-treated BDD electrodes and as-grown BDD films in the context of electrochemical phenol oxidation, serving as a model pollutant. Our results revealed significant alterations induced by RF plasma treatments, covering changes in the electrochemical potential window, kinetics towards the $Fe(CN)_6^{3-/4-}$ and $Ru(NH_3)_6^{2+/3+}$ redox couples, surface wettability, and flat-band potential. The diamond quality and capacitance of the films remained largely unaffected. After plasma treatment, the samples exhibited enhanced hydrophilicity, particularly following O_2 and Ar treatments, as compared to their as-grown counterparts. When subjected to specific electrolytes, plasma-treated surfaces also demonstrated a substantially expanded electrochemical potential window. Notably, the generation of byproducts during the phenol electrooxidation tests was significantly reduced in both the as-grown and the Ar-treated BDD electrode. However, the standout revelation from our experiments was that the superior performance of untreated as-grown BDD film in electrochemical phenol oxidation. This suggests that, for water treatment applications, plasma treatments might not yield substantial improvements in the electrochemical activity of BDD electrodes. Nonetheless,

these plasma treatments hold promise for diverse applications of BDD electrodes, including sensing. In conclusion, our study reveals the potential of RF plasma treatments to modify the surface characteristics of BDD films. However, their suitability for water remediation appears limited. These results have important implications for developing more effective strategies for functionalizing BDD electrodes for several applications.

III.2.1. Introduction

Electrochemical oxidation is a promising technique for removing organic pollutants from water due to its high efficiency and low environmental impact (1). Boron-doped diamond (BDD) electrodes for water treatment have gained significant attention in recent years due to their exceptional properties, such as high chemical stability, low background current, and high oxygen evolution overpotential (2). These electrodes are grown by Chemical Vapor Deposition (CVD) processes in H_2-rich atmospheres, resulting in H-terminated surfaces that slowly react with oxygen (3). However, the performance of BDD electrodes can be further improved by modifying their surface chemistry through chemical functionalization (4).

Chemical functionalization comprises the chemical introduction of functional groups onto the surface of BDD electrodes. These functional groups can change the surface properties, such as wettability, conductivity, and electrochemical properties (5). This approach can potentially increase electrode performance in water treatment through Electrochemical Advanced Oxidation Processes (EAOPs). Chemical functionalization can be performed by several methods, such as plasma treatments (3, 6-9), wet chemical methods (10-13), deposition of thin films (14-17), ion implantation and electrodeposition (18-26), and photochemical modification (27).

One straightforward solution for functionalizing BDD surfaces is through plasma treatment. It involves the generation of a plasma, which is a state of matter that occurs when a gas is partially ionized, resulting in a mixture of neutral and charged particles (28). The latter strikes the surface and knocks off surface atoms, promoting surface modification (28). Depending on the gases employed, the resultant surface can be functionalized with various chemical groups (29). Several types of gas such as H_2 (30-32), O_2 (8, 30, 31, 33, 34), Ar (5, 31), CF_4 (5, 7), CF_4-He (6), C_3F_8 (35), Cl_2 (5), CH_4 (5), NH_3 (36), and NH_3/N_2 (37) have already been employed in BDD plasma treatment. Hydrogen-, oxygen-, fluorine-, and amine-terminated diamond surfaces were successfully obtained in various studies (5-8, 30-37).

One of the primary benefits of plasma treatment for chemical functionalization is that it is a versatile, simple, and cost-effective method that can be easily scaled up for industrial applications (5). They allow highly reproducible results once conditions such as treatment time, plasma power, pressure, and gas flow can by precisely controlled (5). Furthermore, reports demonstrate that diamond surface modification can be reached after only one minute of plasma treatment (34).

This study aims to characterize plasma-modified BDD electrodes deposited by HFCVD and evaluate their performance for the electrochemical oxidation of persistent organics

pollutants in water. Radiofrequency (RF) plasma treatment is used to modify the BDD surfaces. We investigate the effect of different plasma treatment gas types (O_2, Ar, and CF_4) on the electrochemical activity of the BDD electrodes employing various techniques such as Raman Spectroscopy, Sessile Drop Contact Angle, Cyclic Voltammetry (CV), Electrochemical Impedance Spectroscopy (EIS), and Mott-Schottky plots. We also explore the potential applications of these functionalized BDD surfaces in water treatment through electrochemical oxidation, choosing phenol as a model pollutant. The results obtained in this study will provide insights into the design of diamond electrodes with enhanced electrochemical activity and efficiency for removing organic pollutants from water.

III.2.2. Materials and Methods

III.2.2.1. BDD Electrode Preparation

A Si_3N_4-TiN electroconductive ceramic substrate was chosen as the substrate material (Section II.1) (38). The substrate was previously flat-lapped using an abrasive diamond suspension (15 µm, 15-WP, Kemet, UK) to achieve a smooth surface. To enhance the adhesion of the BDD film, the substrate was plasma etched with CF_4 for 120 seconds. The substrate was then seeded in an ultrasonic bath for 45 minutes, using a solution of abrasive diamond powder (0.5-1.0 µm and 10-20 µm, Diamecânica, Portugal) in ethanol. Following seeding, the substrate was thoroughly ultrasonically cleaned in isopropanol for 15 minutes to remove residual particles and contaminants.

The BDD deposition was conducted using a laboratory-made HFCVD system using eight parallel tungsten filaments (Ø 0.3 mm, 99.95% purity, GoodFellow, UK). The temperature of the filaments was closely monitored using a two-color pyrometer (RAYMR1SCSF, Raytek, USA) to maintain it within a range of 2180 to 2220ºC throughout the deposition process. Boron doping was achieved by introducing a boron oxide solution (10000 ppm) diluted in ethanol into the system. This boron source was dragged into the reactor from a canister through an Ar flow, maintained at a constant pressure of 2 bar. A B_2O_3/CH_4 ratio of 0.625 was chosen for the films. After deposition, the HFCVD reactor was kept in a hydrogen-rich atmosphere for 45 minutes and then cooled slowly to ensure H-terminated BDD surfaces. The detailed deposition conditions are outlined in Table III.2.1.

Table III.2.1. Specific Parameters Employed in BDD HFCVD Deposition

Duration (h)	Pressure (mbar)	Total Gas Flow (sccm)	CH_4/H_2 ratio	Ar/H_2 ratio	B_2O_3/CH_4	Substrate Temperature (°C)	Filament's temperature (°C)
5	25	230	0.02	0.15	0.625	800-850	2180-2220

III.2.2.2. Surface Modification and Characterization

Three different BDD electrodes were selected. Each one underwent a different surface modification though RF plasma etchings (K1050X, Emitech, France) containing Ar, O_2, or CF_4 for 10 minutes. An "as-grown" BDD electrode was kept referencing a predominantly H-terminated surface.

Electrical resistivity measurements were performed using a homemade apparatus with two independent copper wires attached with silver glue to the diamond films. Raman Spectroscopy (acquired with a 532 nm laser line, 532 ER, Wasatch Photonics, USA) was carried out for diamond quality assessment. The concentration of boron [B] was determined using a non-invasive and contactless technique that assesses boron doping through the Raman spectrum (Eq. III.2.1) within the range of 2 x 10^{20} to 10^{22} cm^{-3} (39). In this equation, ω_{500} represents the wavenumber (cm^{-1}) of the Lorentzian component of the peak situated around 500 cm^{-1} in the Raman spectrum (39).

$$[B]\ (cm^{-3}) = 8.44\ \times 10^{30} \times \exp\left(-0.048\ \times\ \omega_{500}\right) \qquad \textbf{Eq. III.2.1}$$

Sessile drop contact angle measurements were carried out using a goniometer (Attention Theta, Biolin Scientific, Sweden) by measuring in 4 different points the contact angle (θ) between each treated BDD surface and droplets of 3 µL of deionized water, 1 µL of di-iodomethane, 1 µL of formamide, and 1 µL of ethylene glycol at room temperature and atmospheric pressure. The software OneAttension (Version 4.1.3, Biolin Scientific, Sweeden) was used to measure the contact angles.

III.2.2.3. Electrochemical Characterization

Cyclic Voltammetry (CV) and Electrochemical Impedance Spectroscopy (EIS) measurements were performed using a potentiostat (PGSTAT302N, Metrohm Autolab, Switzerland) controlled by computer software (Nova 2.1.5, Metrohm Autolab, Switzerland) in a three-electrode configuration with a platinum foil as the counter electrode and a SCE reference electrode, in a single-compartment Teflon cell. The geometric surface area of the

BDD working electrode was 0.785 cm^2. All experiments were carried out in a solution volume of 25 mL at room temperature.

The kinetics of the $Fe(CN)_3^{-3/-4}$ and $Ru(NH_3)_6^{3+/2+}$ redox systems were studied in solutions of 1 mM of potassium hexacyanoferrate(III) (>98% purity, Honeywell Fluka, USA) in 0.1 M KCl (>99.5% purity, Sigma-Aldrich, USA), and 1 mM of hexaammineruthenium(III) chloride (98% purity, Sigma-Aldrich, USA) in 0.1 M KCl, respectively, at scan rates ranging from 5 to 300 mV/s.

The potential window of the electrodes was evaluated through voltammograms recorded in a 1 M $HClO_4$ (70% purity, Honeywell Fluka, USA), 0.1 M KNO_3, (98% purity, Sigma-Aldrich, USA) and 0.1 M H_2SO_4 (95-97% purity, Merck, Germany) electrolytes at a 100 mV/s scan rate. EIS measurements were performed in 0.1 M KCl electrolyte. The frequency range for the EIS measurements was from 10^5 Hz to 10^{-2} Hz, with 7 points per decade. The EIS data were fitted to an equivalent circuit model using the Zview software (Version 3.5g, Scribner Associates, USA). The charge transfer resistance (R_{ct}) and the double layer capacitance (C_{dl}) were extracted from the EIS data and analyzed. Mott-Schottky plots were constructed from multiple EIS measurements of the BDD electrodes submerged in 0.1 M KCl electrolyte at potentials ranging from -0.3 V to 0.6 V vs. SCE, from 10^5 Hz to 0.1 Hz. The Mott-Schottky plots were generated by plotting $1/C^2$ as a function of bias voltage for each BDD electrode. The acceptor concentration and the flat-band potential were determined from the slope and the intercept of the linear region of the Mott-Schottky plot.

III.2.2.4. Electrooxidation Tests

Anodic oxidation of phenol was carried out for each treated surface to understand the effect of the RF plasma surface treatments on the organics electrooxidation ability of BDD electrodes. The electrode configuration remained consistent with that employed for electrochemical characterization techniques. Volumes of 20 mL containing solutions of 1 mM phenol (94.11 mg L^{-1}, ≥99% purity, Sigma-Aldrich, USA) in 0.1 M Na_2SO_4 (≥99.0% purity, Sigma-Aldrich, USA) were electrooxidized with an applied current density of 30 mA/cm², at room temperature. Aliquots were collected every 60 minutes and analyzed by UV-Vis spectroscopy (Flex, Sarspec, Portugal) to determine the remaining phenol concentration in the solution. Volumes of 2.5 mL of the treated solutions were mixed with potassium dichromate (≥99.0% purity, Sigma-Aldrich, USA) and a mixture of H_2SO_4 (95-97% purity, Merck, Germany) and Ag_2SO_4 (≥99.5% purity, Sigma-Aldrich, USA) in vials to measure the Chemical Oxygen Demand (COD). These vials were heated to 150°C for 2 hours and then analyzed using a photometer (AL250 COD VARIO, Aqualytic, Germany).

III.2.3. Results and Discussion

III.2.3.1. Diamond Quality

The quality assessment of the BDD films was carried out using Micro-Raman spectroscopy. The Raman spectra (Figure III.2.1) were subjected to deconvolution to discern peaks corresponding to the film's diamond and non-diamond components.

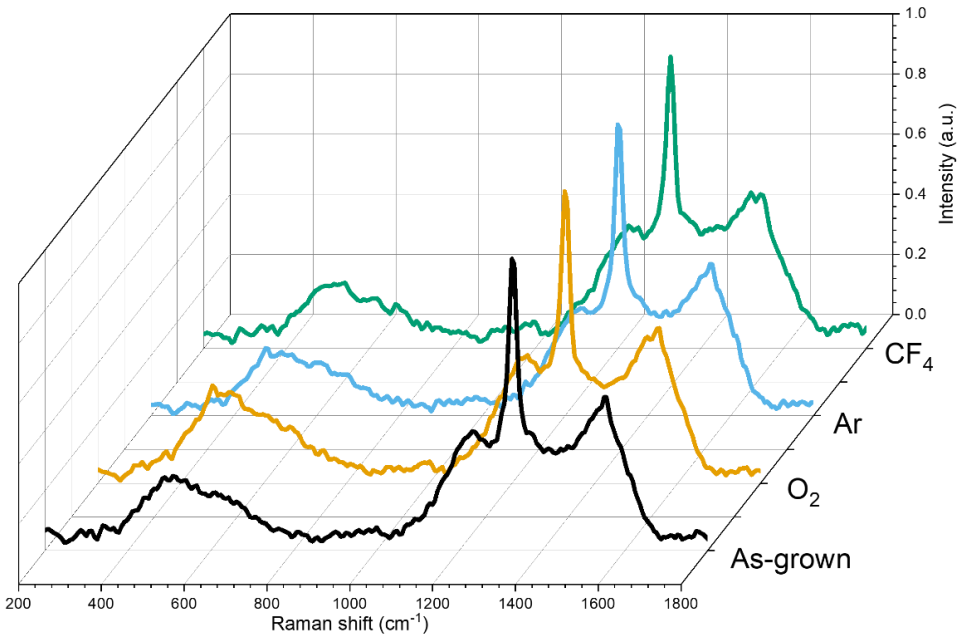

Figure III.2.1. Raman Spectroscopy Analysis of plasma-modified BDD surfaces.

The characteristic natural diamond band is commonly observed around 1332 cm^{-1} (40). The shift of the diamond band from 1332 cm^{-1} is directly related to the inherent residual stresses in the BDD film (41). The G band at approximately 1550 cm^{-1} and the D-band at approximately 1350 cm^{-1} are assigned to defect-induced Raman features associated with carbon sp^2 structures. The peak at 1220 cm^{-1} is linked to disordered diamond, primarily due to boron incorporation in the diamond lattice (42). Peaks at 1150 and 1440 cm^{-1} are attributed to trans-polyacetylene (TPA) located at the grain boundaries of the BDD film (43). The presence of non-diamond carbon peaks in the Raman spectra primarily points towards sp^2 carbon at grain boundaries. All spectra display the characteristic asymmetry of the diamond peak related to the Fano resonance in BDD films, indicating the presence of

metallic doping (44). The purity of the BDD films was quantified by dividing the integral intensity of the diamond band (I_{diam}) by the integral intensity of the G band (I_G) (45). The results are presented in Table III.2.2.

Table III.2.2. Data extracted from the Raman Spectra plasma-modified BDD surfaces.

	Diamond Band Center (DBC)	**Residual Stress* (GPa)**	**I_{diam}/I_G**	**R^2**
As-grown	1332.26	-0.15	0.95	0.9933
O_2	1332.12	-0.07	0.95	0.9947
Ar	1332.71	-0.40	0.92	0.9910
CF_4	1332.04	-0.02	0.94	0.9895

* $\sigma_r = -0.567 \times (DBC - 1332)$ *(41)*

It is important to note that no significant visible distinctions are apparent between the samples. Following the deconvolution of the peaks, a slight reduction in the I_{diam}/I_G ratio was observed in the sample treated with Ar, indicating lower diamond quality attributable to heightened intensities of sp^2-related peaks. Foord and Goeting's findings point that Ar^+ ion bombardment has been shown to potentially lead to surface amorphization by forming an insulating diamond-like carbon layer, thereby affecting the electrochemical properties of BDD electrodes (46). However, evidence from the Raman spectra in this study is insufficient to point out surface amorphization once the sp^2-related peaks retained similar intensities in all samples. Furthermore, all samples exhibit low compressive residual stress with negligible deviations between them. The slight disparities noted in the data resulting from the peak deconvolution of the Raman spectra are likely a consequence of subtle fluctuations in film quality across various regions, dependent upon the sample's positioning during the Raman spectroscopy analysis. Hence, it can be stated that the 10-minute plasma treatments did not lead to significant alterations in the diamond film's quality. It is plausible that such effects might manifest with prolonged treatments, as reported in existing literature (5, 47).

III.2.3.2. Resistivity

The resistivity values of the plasma-treated samples are provided in Table III.2.3. It can be observed that there was significant passivation, exceeding an order of magnitude, following the plasma treatments. Among all the treatments, the sample treated with Ar exhibited the most substantial passivation. Variations in the resistivity of the plasma-treated samples

compared to the as-grown condition could be strongly linked to changes in surface bond polarity. The as-grown samples deposited through HFCVD in our reactor are predominantly terminated with hydrogen owing to controlled cooling under a hydrogen atmosphere (48). Hydrogen termination involves surface bond polarity, giving rise to electrostatic interactions that impact the energy levels of valence and conduction bands (49). For diamond surfaces terminated in hydrogen, both bands exhibit increased levels, and the conduction band is positioned above the vacuum level, resulting in a negative electron affinity (49, 50). This phenomenon gains significance when the diamond electrode is immersed in an aqueous solution, enabling electron transfer between the valence band and $H_3O_{(aq)}^+$ (49, 50). This leads to a positively charged accumulation layer on the surface—a process known as surface transfer doping—which notably enhances surface conductivity (49-51).

In contrast, oxygen-terminated surfaces exhibit an opposing bond polarity that diminishes valence and conduction band levels, yielding a positive electron affinity (49). In the case of argon treatment, the relatively larger size of Ar molecules may remove surface species from the as-grown samples. This suggests that the primary impact of Ar treatment could be surface cleansing rather than substantial modification. This effect could be linked to the elimination of the positively charged accumulation layer formed through surface transfer doping on the as-grown samples, potentially contributing to the decline in the performance of these modified electrodes. In the case of CF_4 treatment, as observed by Ristein *et al.*, the introduction of fluorine atoms onto the diamond surface results in an increase in conductivity (49). Fluorinated derivatives of C_{60}, like $C_{60}F_{18}$ and $C_{60}F_{48}$, are particularly effective in improving surface conductivity (49). However, it is important to note that an increase in conductivity was not observed in our samples treated with CF_4.

Table III.2.3. Plasma-modified BDD surface resistivity values.

	Resistivity (Ω cm)
As-grown	0.014 ± 0.010
O_2	0.187 ± 0.022
Ar	0.678 ± 0.201
CF_4	0.210 ± 0.053

III.2.3.3. Contact Angle and Surface Tension

Measuring the wettability of BDD electrodes holds great significance in the domain of electrochemical water treatment. The wettability of the electrode surface plays a vital role in determining the effectiveness of the electrochemical oxidation process. A more hydrophilic surface can promote the detachment of gas bubbles from the electrode surface, improving the area of contact between the electrode and water, thereby increasing the process's efficiency (52). When interfacial interactions are key, the ability of a solid surface to interact with a liquid is a crucial factor. It directly influences whether and to what extent these interactions can occur. If a solid/liquid interface does not allow for good wetting or does not wet at all, it results in poor interaction and efficiency.

In contrast, better wetting leads to more effective interfacial interactions. Consequently, managing the wettability of BDD surfaces is essential for improving their interaction with water, thus optimizing their performance as electrodes. Furthermore, this control ensures a consistent distribution of current density (53), underscoring its importance in electrochemical water treatment processes.

The Zisman plot (54), an established graphical approach, was employed to determine the surface tension of the plasma-treated BDD surfaces by determining the critical surface tension. The critical surface tension indicates the liquid's surface tension required for completely wetting a given solid surface. The Zisman plot is constructed by plotting the Young's contact angle as a function of the surface tension of liquids interacting with the solid surface. To estimate the surface tension of the plasma-treated BDD films using the Zisman plot, a range of liquids with distinct surface tensions were deposited on their surface, and the contact angle was measured (Figure III.2.2). The cosine of the contact angle was then calculated and plotted against the surface tension of the liquids (Figure III.2.3). The critical surface tension was determined by plotting a line indicating a contact angle of 0° ($\cos \theta = 1$) on the Zisman plot and identifying the point at which this line intersects with the Zisman plot. Typically, the critical surface tension closely approximates the surface tension of the solid surface, making it a valuable parameter for characterizing the wettability of the surface of BDD electrodes.

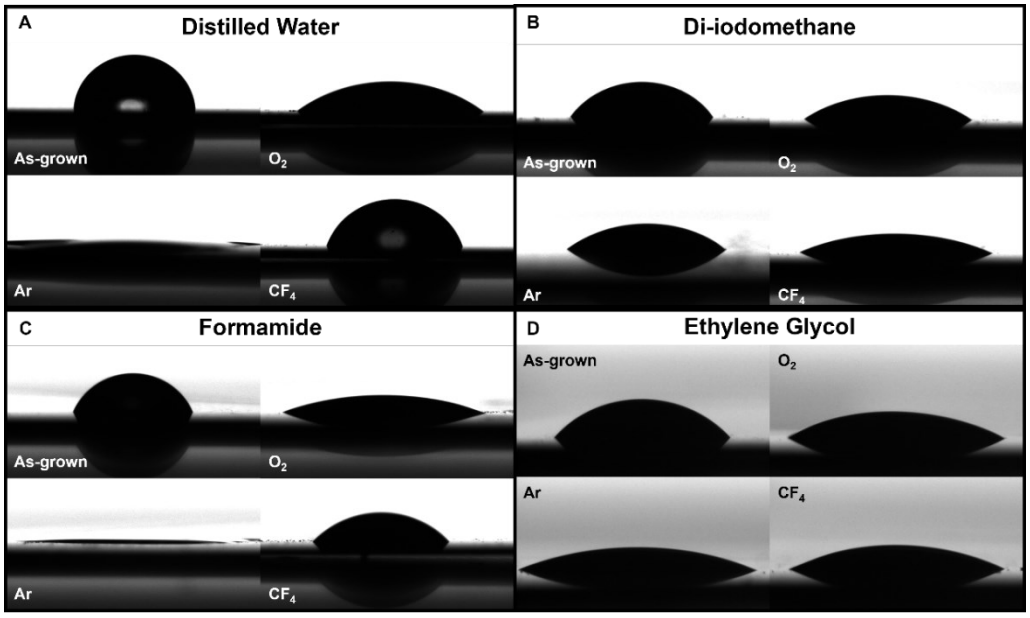

Figure III.2.2. Contact angle measurements of (a) distilled water, (b) di-iodomethane, (c) formamide, and (d) ethylene glycol droplets over plasma-modified BDD surfaces.

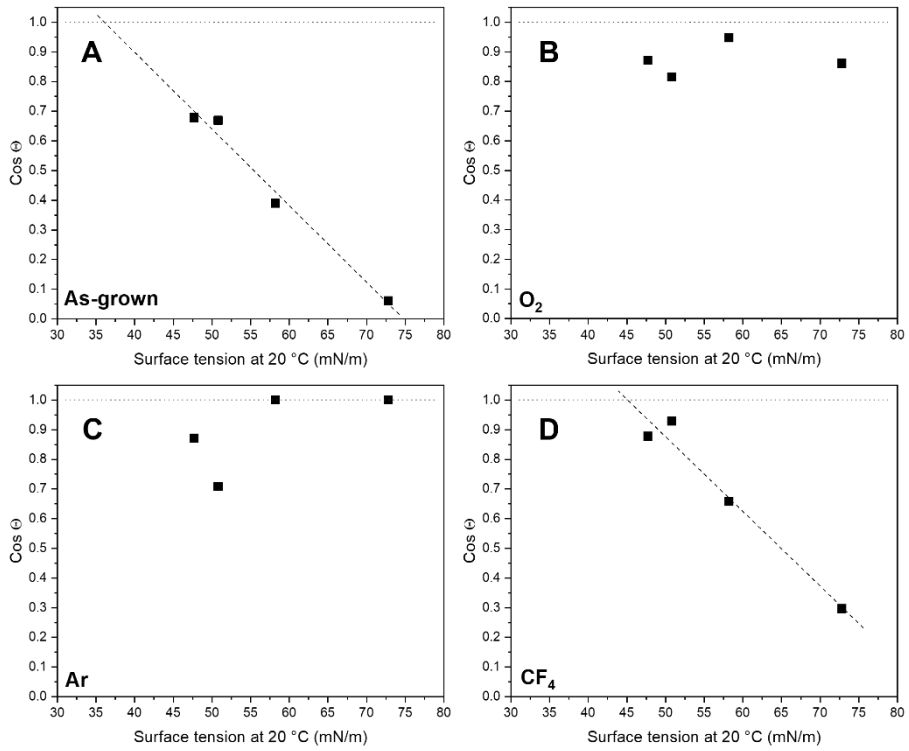

Figure III.2.3. Zisman plot for estimating the surface tension of plasma-modified BDD surfaces: (a) as-grown; (b) O_2-treated; (c) Ar-treated; (d) CF_4-treated.

Table III.2.4. Contact angle measurements and critical surface tension of plasma-modified BDD surfaces.

Liquid	Surface tension at 20°C (mN/m)	Contact Angle (°)			
		As-grown	O_2	Ar	CF_4
Ethylene Glycol	47.7	47.26 ± 5.04	29.38 ± 3.34	29.32 ± 8.69	28.66 ± 7.68
Di-iodomethane	50.8	47.98 ± 6.04	35.35 ± 1.03	44.85 ± 3.72	21.66 ± 2.71
Formamide	58.2	67.05 ± 3.46	18.6 ± 1.19	0	48.84 ± 2.68
Distilled Water	72.8	86.5 ± 1.6	30.53 ± 2.89	0	72.74 ± 2.13
Critical Surface Tension (mN/m)		36.08	-	-	45.12

As-grown hydrogen-terminated BDD surfaces are typically associated with water contact angles ranging from 80 to 100°, falling within the hydrophobic range (55). Our results are in line with this range for as-grown BDD surfaces. All plasma treatments resulted in more hydrophilic surfaces. However, this effect was less pronounced in samples treated with CF_4. Notably, the surface treated with Ar became entirely hydrophilic, to the extent that measuring the water contact angle was not even possible.

The critical surface tension quantifies the force required to maintain a liquid's cohesion and serves as an approximation for the surface tension of a given surface. Materials with high surface energy tend to exhibit greater wetting behavior, whereas those with lower surface energy tend to be less wettable. The variability in contact angle results obtained for surfaces treated with O_2 and Ar prevented the estimation of their critical surface tension. Our results indicate that CF_4-treated surfaces tend to be more wettable than the as-grown surfaces when exposed to various liquids. As previously mentioned, surfaces with greater wetting behavior could potentially enhance the electrooxidation performance of BDD electrodes.

III.2.3.4. Electrochemical Potential Window

The electrochemical potential window of BDD electrodes is defined by various characteristics of the diamond film, including diamond quality, dopant concentration, surface imperfections, and the nature of the electrolyte solution used (56-58). Figure III.2.4 illustrates cyclic voltammograms recorded in 1 M $HClO_4$, 0.1 M KNO_3, and 0.1 M H_2SO_4 electrolytes at the plasma-treated Si_3N_4-TiN/BDD electrode. The electrochemical potential window was assessed using the linear fit method (59), and the resulting values are presented in Table III.2.5.

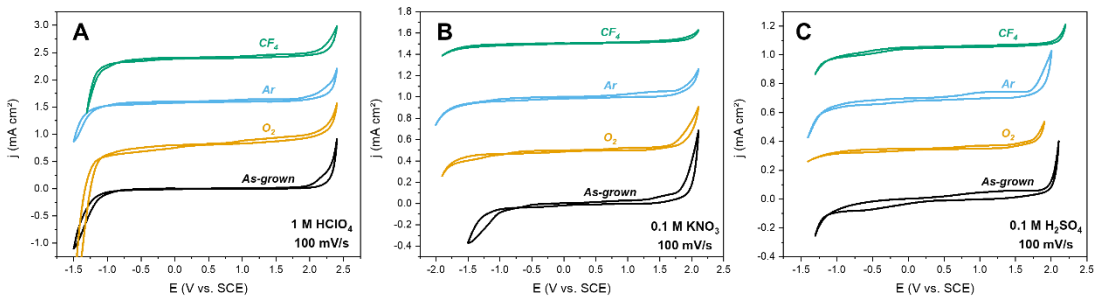

Figure III.2.4. Cyclic Voltammograms of Plasma-Surface Modified BDD Electrodes in Various Electrolytes: (a) 1 M $HClO_4$, (b) 0.1 M KNO_3, and (c) 0.1 M H_2SO_4 solutions.

Table III.2.5. Electrochemical potential window of plasma-modified BDD surfaces across different electrolytes

	Electrochemical Potential Window (V vs. SCE)		
	1 M $HClO_4$	**0.1 M KNO_3**	**0.1 M H_2SO_4**
As-grown	3.3	3.0	3.1
O_2	3.4	3.4	2.8
Ar	3.4	3.6	2.9
CF_4	3.3	3.5	3.2

The wide potential windows observed in the cyclic voltammograms indicate the preservation of inertness against surface adsorption of ions like H^+ and OH^- after treatment. The low background current on the treated surfaces indicates that the 10-minute plasma etching treatments did not lead to substantial surface roughening.

An enlargement of the potential window has been consistently observed in all plasma-treated samples immersed in 1 M $HClO_4$ and 0.1 M KNO_3 electrolytes, indicating less absorption of H^+ and OH^- ions. In all cases, the potential windows were mostly extended towards more cathodic potentials.

In the case of 0.1 M H_2SO_4 electrolyte, only the CF_4-treated sample exhibited a slight increase in the potential window compared to the as-grown counterpart. Such an effect was notably evident in prior investigations involving CF_4 plasma treatment of BDD surfaces, extending the potential window to around 5 V in aqueous conditions (6). This represented an increase of about 1.5 V compared to untreated BDD electrodes (6). Sine *et al.* proposed that fluorine surface groups present in diamond films weaken the adsorption of water molecules and atomic hydrogen while inhibiting the hydrogen evolution reaction, thereby

causing the widening of the potential window (6). Thus, the lack of a comparably wide potential window in our study could be attributed to the possibility that the fluorine coverage on our treated surfaces was insufficient to effectively inhibit the adsorption of water molecules and atomic hydrogen to a significant extent, such as 1.5 V.

The notably expanded potential window observed in the plasma-treated surfaces, particularly when exposed to 1 M $HClO_4$ and 0.1 M KNO_3 electrolytes, indicates a promising avenue for utilizing plasma-treated BDD cathodes in reactions demanding extremely negative potentials. This is also desirable for sensing applications. However, optimizing plasma treatments is essential to fully exploit the potential for inhibiting the hydrogen evolution reaction to a maximum extent.

III.2.3.5. Kinetics Towards Redox Couples

The $Fe(CN)_6^{3-/4-}$ constitutes an inner-sphere redox couple, thereby considered surface sensitive (60). Consequently, the electron transfer rates of the $Fe(CN)_6^{3-/4-}$ redox couple rely on the surface termination of BDD electrodes. In Figure III.2.5, cyclic voltammograms depict the behavior of plasma-modified BDD surfaces immersed in a 0.1 M KCl electrolyte containing the $Fe(CN)_6^{3-/4-}$ redox couple. The anodic and cathodic peak potentials shifted symmetrically in the positive and negative directions from their starting values only in the as-grown samples. Significant changes in the separation of the anodic (E_{pa}) and cathodic (E_{pc}) peaks (Figure III.2.7) after plasma treatment can be observed in the modified BDD surfaces towards the $Fe(CN)_6^{3-/4-}$ redox couple. All surface modifications led to slower electron transfer kinetics, requiring higher potentials to induce electron transfer.

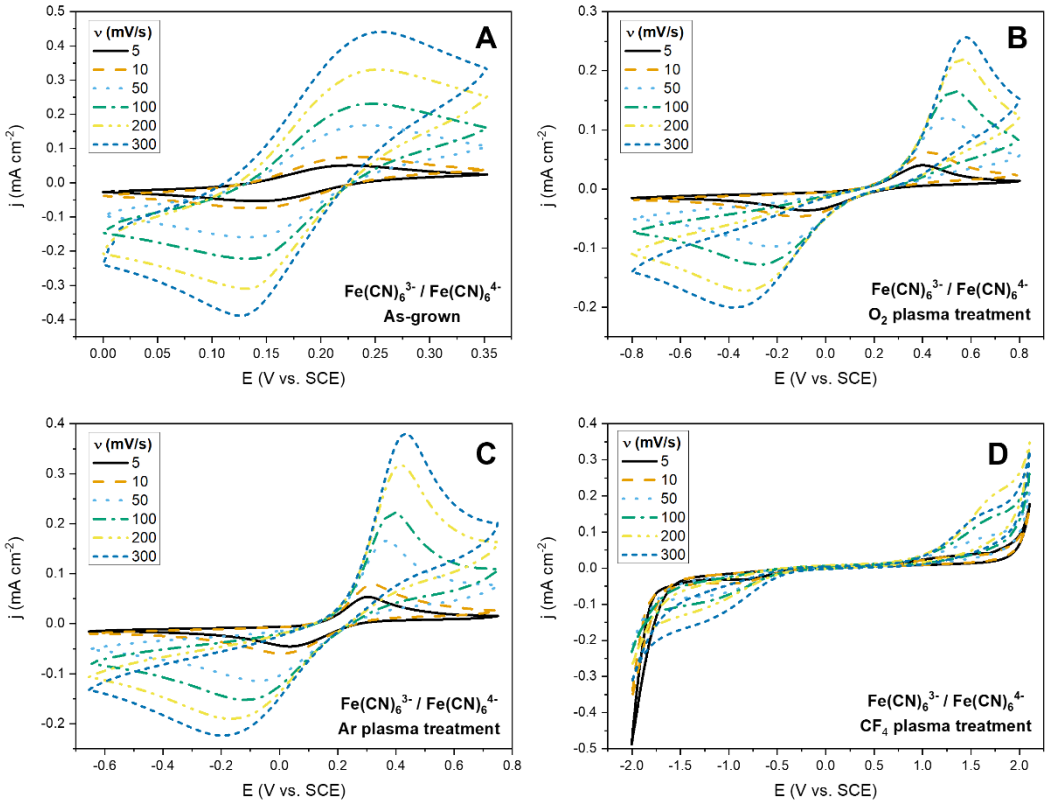

Figure III.2.5. Cyclic voltammograms of plasma-modified BDD surfaces in 0.1 M KCl electrolyte with the $Fe(CN)_6^{3-/4-}$ redox couple: (a) as-grown; (b) O_2-treated; (c) Ar-treated; (d) CF_4-treated.

In contrast to the $Fe(CN)_6^{3-/4-}$ redox couple, the $Ru(NH_3)_6^{2+/3+}$ redox couple is classified as an outer-sphere redox couple, indicating a lack of direct interaction with the surface that leads to surface insensitivity (60). The literature indicates that BDD electrodes exhibit reversibility in the case of the $Ru(NH_3)_6^{2+/3+}$ redox couple only when the primary electrical transport mechanism within the film is metallic conduction (61). In Figure III.2.6, cyclic voltammograms illustrate the behavior of plasma-modified BDD surfaces immersed in a 0.1 M KCl electrolyte containing the $Ru(NH_3)_6^{2+/3+}$ redox couple. In contrast to the scenario observed with $Fe(CN)_6^{3-/4}$, the redox kinetics of $Ru(NH_3)_6^{2+/3+}$ were less affected by the surface modifications of BDD electrodes. Symmetry between the anodic and cathodic peaks is evident in all samples. However, it is also noticeable that the peak separation has nearly doubled in all plasma-treated samples compared to the as-grown ones (Figure III.2.7).

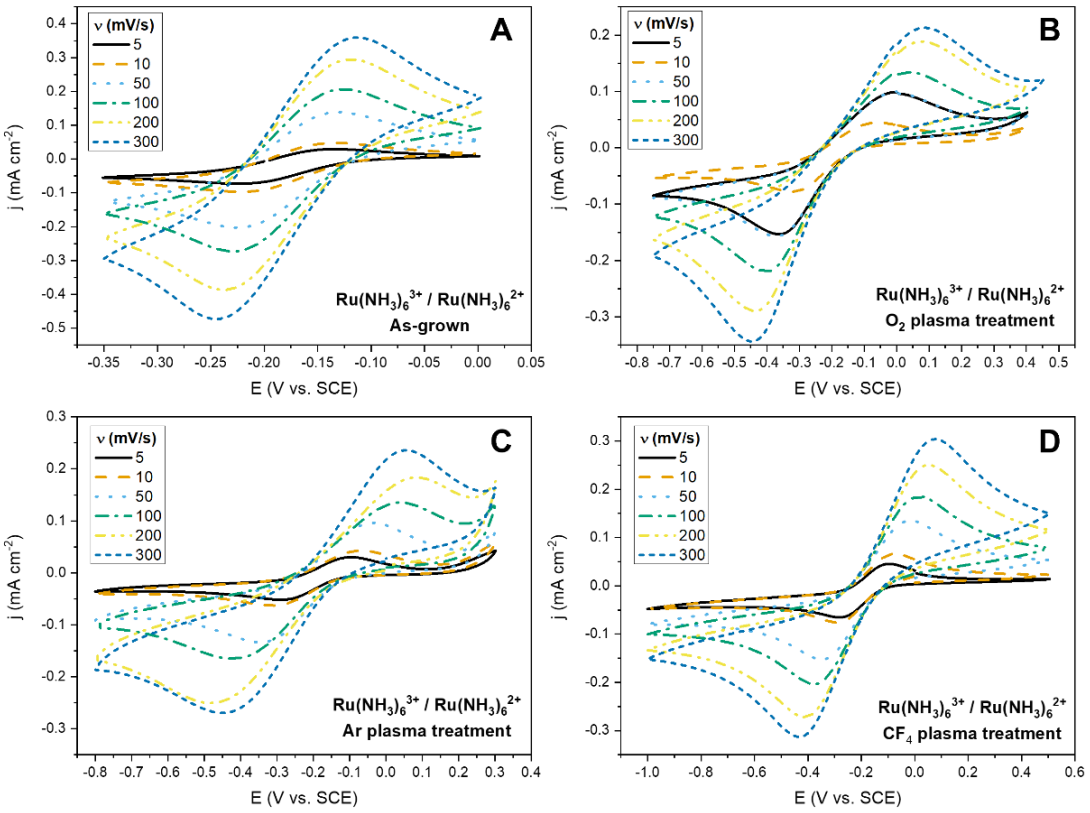

Figure III.2.6. Cyclic voltammograms of plasma-modified BDD surfaces in 0.1 M KCl electrolyte with the $Ru(NH_3)_6^{2+/3+}$ redox couple: (a) as-grown; (b) O_2-treated; (c) Ar-treated; (d) CF_4-treated.

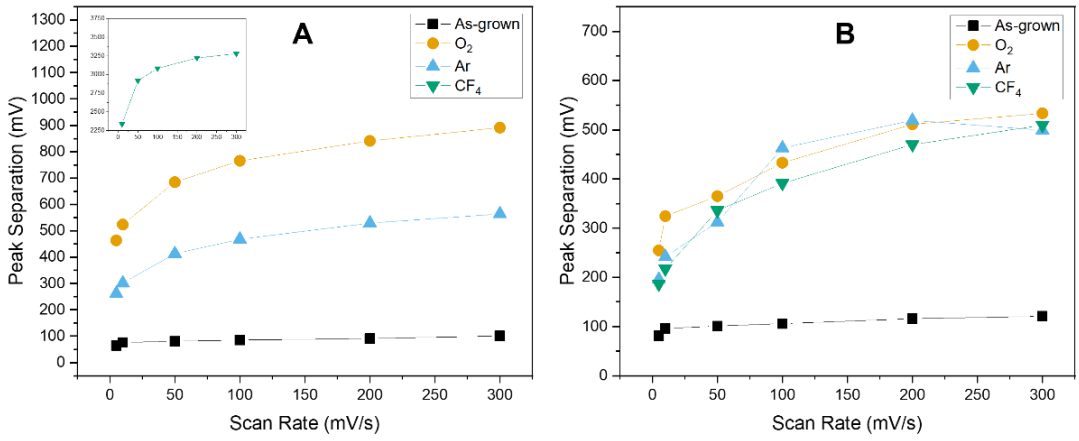

Figure III.2.7. Peak separation of plasma-modified BDD surfaces in 0.1 M KCl electrolyte with (a) $Fe(CN)_6^{3-/4-}$ and (b) $Ru(NH_3)_6^{2+/3+}$ redox couples.

As per the Randles-Sevcik equation (Eq. III.2.2), in diffusion-limited electrochemical reactions, the peak current is directly proportional to the square root of the scan rate.

$$i_p = 0.4463nC_0AF\left(\frac{nF\nu D}{RT}\right)^{\frac{1}{2}} \qquad \textbf{Eq. III.2.2}$$

Where D is the diffusion coefficient (cm^2/s), I_p is the peak current (A), R is the gas constant (8.314 J/mol K), T is the temperature (K), n is the number of electrons transferred in the reaction, C_0 is initial concentration (mol/cm^3), A is the surface area (cm^2), F is the Faraday constant (96485 C/mol), ν is the scan rate (V/s).

Regarding peak current (I_p) versus the square root of the scan rate, all four surfaces provided a good linear fit (Figure III.2.8) in both redox couples. Thus, electron transfer is most likely occurring in a homogenous, diffusion-controlled manner, with no analyte absorption in the electrode surface prior to electron transfer.

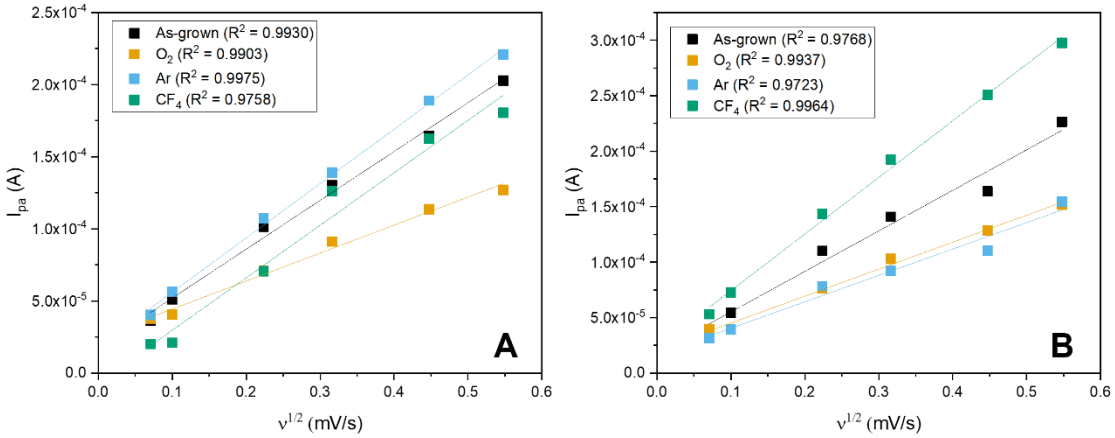

Figure III.2.8. Peak current (Ip) vs. square root of scan rate for plasma-modified BDD surfaces in 0.1 M KCl electrolyte with (a) $Fe(CN)_6^{3-/4-}$ and (b) $Ru(NH_3)_6^{2+/3+}$ redox couples.

The heterogeneous standard rate constant (k_0) of electron transfer was calculated from the method proposed by Lavagnini *et al.* (62), which combines the Nicholson method (Eq. III.2.3) (63) and the Klingler and Kochi method (Eq. III.2.4) (64). Such method allows the determination of k_0 in a vast range of peak separations (ΔE). Thus, it is suitable for all systems, from reversible to totally irreversible. The calculations incorporated diffusion coefficients for $Fe(CN)_6^{3-/4-}$ and $Ru(NH_3)_6^{2+/3+}$ based on literature values, which were 7.20 and 7.86 × 10^6 cm^2/s, respectively (65).

$$\Psi = k_0 \sqrt{\frac{\pi DnFv}{RT}} \quad \textbf{Eq. III.2.3}$$

$$k^0 = 2.18 \sqrt{\frac{\alpha DnFv}{RT}} \, exp\left[\frac{-\alpha^2 nF\Delta E}{RT}\right] \quad \textbf{Eq. III.2.4}$$

Where Ψ is the kinetic parameter, D is the diffusion coefficient (cm^2/s), n is the number of electrons transferred in the reaction, F is the Faraday constant (96485 C/mol), ν is the scan rate (V/s), R is the gas constant (8.314 J/mol K), T is the temperature (K), α is the transfer coefficient for the electrode process, and ΔE is the peak separation (V).

The heterogeneous standard rate constant (k_0) was obtained from the slope of the plot of the kinetic parameter estimated by the equation proposed by Lavagnini *et al.* (Eq. III.2.5) (62) versus $[\pi DnFv/(RT)]^{1/2}$.

$$\Psi = \frac{-0.6288 + 0.0021n\Delta E}{1 - 0.017n\Delta E} \quad \textbf{Eq. III.2.5}$$

In Table III.2.6, we provide the electrochemical parameters for the $Fe(CN)_6^{3-/4-}$ and $Ru(NH_3)_6^{2+/3+}$ reaction at the surfaces of plasma-modified BDD electrodes, utilizing a scan rate of 5 mV/s, offering a comprehensive overview of the redox processes on these modified surfaces.

Table III.2.6. Electrochemical Parameters of the reaction of $Fe(CN)_6^{3-/4-}$ and $Ru(NH_3)_6^{2+/3+}$ on the surface of plasma-modified BDD surfaces (scan rate: 5 mV/s)

Redox Couple	Treatment	E_{pa} (mV)	E_{pc} (mV)	E_0[a] (mV)	ΔE (mV)	I_{pa} (A)	I_{pc} (A)	I_{pa}/I_{pc}	k_0 (cm/s)
$Fe(CN)_6^{3-/4-}$	As-grown	217	151	184	65	3.63×10^{-5}	-3.72×10^{-5}	0.98	7.670×10^{-3}
	O_2	398	-65	166	463	3.79×10^{-5}	-4.24×10^{-5}	0.89	9.03×10^{-5}
	Ar	302	40	171	262	4.04×10^{-5}	-3.48×10^{-5}	1.16	2.10×10^{-4}
	CF_4	1536	-836	350	2372	2.36×10^{-6}	-2.06×10^{-5}	0.90	1.20×10^{-5}
$Ru(NH_3)_6^{2+/3+}$	As-grown	227	146	186	81	3.89×10^{-5}	-3.77×10^{-5}	1.03	1.91×10^{-3}
	O_2	-76	-307	-191	232	7.44×10^{-5}	-9.57×10^{-5}	0.52	2.04×10^{-4}
	Ar	-96	-292	-194	196	3.15×10^{-5}	-3.20×10^{-5}	0.98	3.78×10^{-4}
	CF_4	-94	-281	-187	186	5.30×10^{-5}	-6.45×10^{-5}	0.82	4.25×10^{-4}

[a] $E_0 = (E_{pa} + E_{pc})/2$

The as-grown BDD surface presented a quasi-reversible behavior for the $Fe(CN)_6^{3-/4-}$ redox couple with a 65 mV peak separation at 5 mV/s. However, plasma treatment for 10 minutes with O_2 and CF_4 led to a strong irreversibility of the electrochemical process towards $Fe(CN)_6^{3-/4-}$, especially in the case of CF_4, that showed a peak separation of 2372 mV at 5 mV/s. Although modification with Ar also led to slower electron transfer, the Ar-modified BDD surface presented a heterogeneous standard rate constant (k_0) laying within the quasi-reversible range ($0.020 > k_s > 5.0 \times 10^{-5}$ cm/s) (66). The literature suggests that, in the case of both oxidized and fluorinated surfaces, electrostatic repulsion can arise between their surface dipoles characterized by high electronegativity and the charges present on the redox ion (5). This repulsion phenomenon may contribute to a reduction in electron transfer kinetics.

In the case of the $Ru(NH_3)_6^{2+/3+}$ redox couple, despite all plasma-treated samples displaying k_0 values indicative of quasi-reversible behavior, the electron transfer kinetics slowed down by more than one order of magnitude compared to the untreated electrode.

Consequently, for both redox systems, it was observed that the electron-transfer rate was diminished on the plasma-treated BDD surfaces compared to as-grown surfaces. This effect

can be attributed to the reduced surface conductivity of the plasma-treated samples. As mentioned previously, surface termination can potentially modify the electric structure of the diamond surface/electrolyte interface through an electrochemical transfer doping mechanism, which significantly impacts electrode kinetics. Additionally, the decline in electron transfer rates for redox reactions resulting from plasma treatment may also be attributed to the inhibition of redox species adsorption onto the electrode surface (67).

III.2.3.6. Electrochemical Impedance Spectroscopy

The Nyquist plots (Figure III.2.9), generated through EIS measurements in a 0.1 M KCl solution, were simulated using an equivalent circuit model. The ZView software was employed to simulate the equivalent electrical circuit to estimate data from the EIS spectra (Table III.2.7). The Nyquist plots exhibit semicircles representing processes limited by electron transfer. Furthermore, the plots reveal that the capacitance of all samples varies with frequency. An impedance phase angle of 45° points to the presence of Warburg impedance (W), accounting for diffusion-controlled charge transfer processes at the electrode/electrolyte interface.

Consequently, the electrode's equivalent circuit incorporates a Warburg diffusion element and a frequency-dependent constant phase element (CPE). This CPE reflects the distribution of reactivity due to surface electrochemical heterogeneity. Such heterogeneity might originate from the different surface terminations, the surface roughness of the samples, or uneven dispersion of boron atoms within the diamond film (68, 69). By utilizing the circuit model with mixed kinetic and charge-transfer control comprising a CPE in parallel with a resistor and a Warburg element, the double-layer capacitance (C_{dl}) of the BDD films was estimated.

A low double-layer capacitance is desirable for sensing and water treatment applications because it reduces background current and improves signal-to-noise ratio (70). Notably, all samples demonstrated films with notably low C_{dl} values. Although minor variations in C_{dl} were observed among different surface treatments, these differences are probably not significant enough to notably affect the electrode performance in electrooxidation.

Among the extracted information from the EIS spectra, the charge transfer resistance (R_{ct}) reflects the electrode capability to transfer electrons at the liquid-solid interface (71). Diminished charge transfer resistances indicate improved electron transfer processes, facilitating the direct oxidation of organic pollutants (71, 72). A reduction in R_{ct} was observed for the samples treated with Ar and CF_4 compared to the as-grown reference. However, an increase in R_{ct} was noted for the samples treated with O_2.

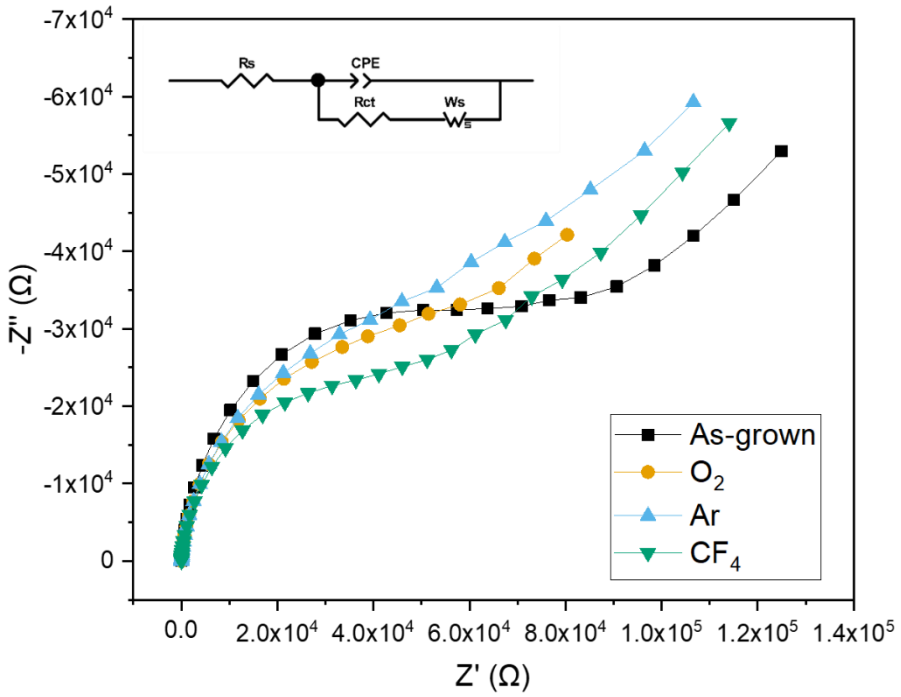

Figure III.2.9. Nyquist plots obtained by EIS of plasma-modified BDD surfaces immersed in 0.1 M KCl.

Table III.2.7. Data extracted from the EIS spectra utilizing the ZView software and equivalent electrical circuit.

	OCP (V vs. SCE)	R_s (Ω/cm²)	Q_0 (1/Ω cm² s^{-n})	n	R_{ct} (Ω/cm²)	W (1/Ω cm²)	C_{dl} (μF/cm²)	χ2
As-grown	0.19	15.57	5.94 x 10^{-6}	0.95	2.60 x 10^4	2.53 x 10^5	3.74	0.000350
O_2	0.17	10.36	1.56 x 10^{-5}	0.91	3.18 x 10^4	1.95 x 10^5	6.83	0.002058
Ar	0.18	17.58	1.01 x 10^{-5}	0.94	1.77 x 10^4	1.06 x 10^6	5.58	0.000105
CF_4	0.16	8.72	2.60 x 10^{-6}	0.96	1.58 x 10^4	3.42 x 10^5	1.64	0.000129

III.2.3.7. Mott-Schottky Plots

The measurement of the Mott–Schottky plot enables the estimation of flat-band potential (E_{FB}) and dopant density (N_A). The Mott-Schottky plot consists of plotting $1/C^2$ as a function

of bias voltage. The dopant density can be determined from the Mott-Schottky plot's slope via Eq. III.2.6 (73, 74).

$$N_A = -\frac{2}{qA^2\varepsilon_0\varepsilon_r}\left[\frac{d(C^{-2})}{dV}\right]^{-1} \qquad \textbf{Eq. III.2.6}$$

Where C is the capacitance, V is the applied bias voltage, q is the elementary charge, A is the apparent geometric area of the electrode, ε_0 is the permittivity of vacuum, ε_r is the relative permittivity, and N_A is the doping density at the edge of the depletion region. To estimate doping density, BDD's permittivity was assumed as $\varepsilon = 5.51$ according to reports in the literature for polycrystalline BDD films (75). The built-in potential, or flat-band potential, can be estimated from the intercept to the x-axis of the Mott-Schottky plot (73, 74). Results are shown in Figure III.2.10 and Table III.2.8.

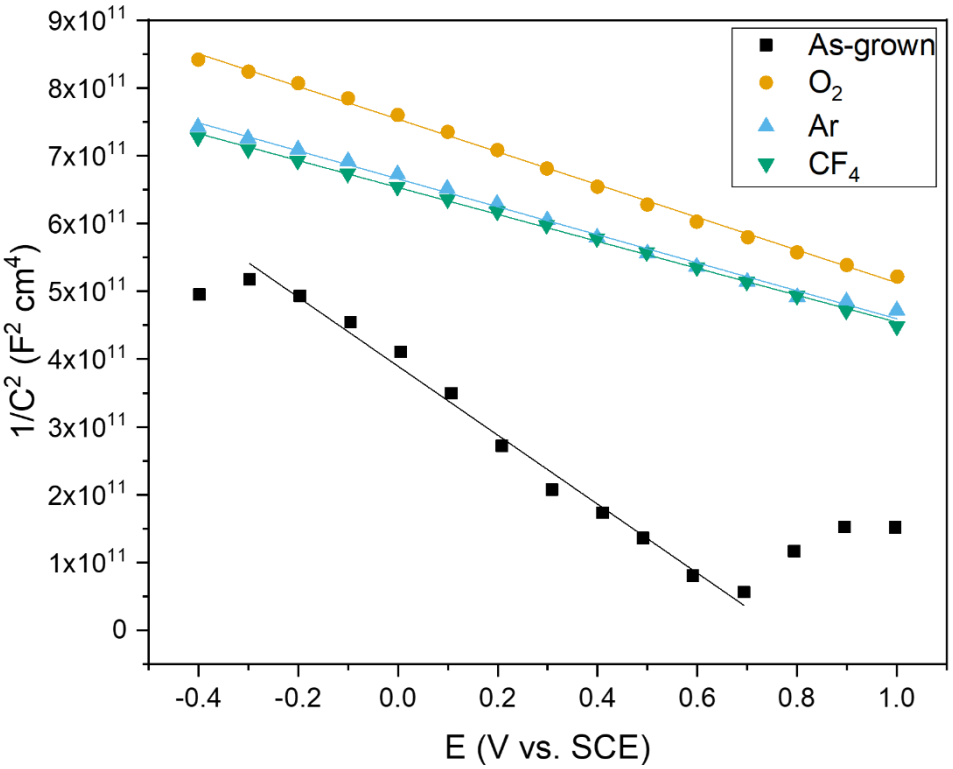

Figure III.2.10. Room temperature Mott-Schottky plots (C^{-2} versus the potential) of plasma-modified BDD surfaces immersed in 0.1 M KCl.

Table III.2.8. Estimated values of flat band potential and acceptor concentration extracted from Mott-Schottky plots and boron concentration from Raman spectroscopy.

	As-grown	O_2	Ar	CF_4
E_{FB} (V vs. SCE)	0.75	3.00	3.09	3.40
N_A (cm^{-3})	1.88×10^{21}	4.30×10^{21}	5.00×10^{21}	5.22×10^{21}
$[B]_{Raman}$ (cm^{-3})	1.10×10^{21}	1.55×10^{21}	3.12×10^{21}	2.18×10^{21}

Measuring the E_{FB} is one of the fundamental properties of any semiconductor–electrolyte system due to its direct relation to the availability of charge carriers for electrochemical processes (61, 76). The E_{FB} represents the applied potential at which band bending and charge depletion are absent at the interface between a semiconductor and an electrolyte (77). This happens when the Fermi level of the semiconductor is at the same level as the redox Fermi level of the electrolyte. For potentials other than the E_{FB}, an electric field forms at the semiconductor interface, which will either push the electrogenerated electrons into the bulk (in a state of depletion) or towards the surface (in a state of accumulation) (76). For a p-type semiconductor such as BDD, depletion regions arise when applied potentials are more negative than the E_{FB}, leading to increased charge transfer, especially in the case of low-doped BDD (78, 79). On the other hand, accumulation regions occur when applied potentials become less negative than the E_{FB}, inducing a decrease in the charge transfer (78, 79). These regions can potentially influence the chemical reactivity of the surface, the formation of chemical bonds, and the adsorption of molecules on the surface.

Regarding surface modification, the E_{FB}'s position is closely linked to the surface chemistry of the BDD electrode (80). Variations in the E_{FB} can indicate alterations in the electrode's surface termination, such as the introduction of oxygenated groups (80). Understanding the relationship between the E_{FB} and the surface chemistry can help optimize these electrodes' performance.

The E_{FB} values for hydrogenated diamond electrodes have been extensively covered in the literature. The reported values range from 0 V/SCE to +1.9 V/SCE (73, 80-85) and are influenced by various factors such as film deposition methods, sample preparation processes, the presence of sp^2 carbon and surface pre-treatments (73, 80, 81, 85).

In this study, our oxygen-modified BDD surface exhibited a much more positive E_{FB} value (+3.0 V/SCE) than the hydrogenated as-grown surface (+0.75 V/SCE). Such shift in the E_{FB} upon oxidation of diamond surfaces has been observed in several studies (57, 86-88), with

the degree of shift depending on the chemical type of oxygenated terminations (80). The noticeable shift in the E_{FB}'s position implies a correlation between reduced charge transfer and the displacement of band edges. Studies suggest a tight relation exists between the E_{FB} position of BDD electrodes and the proportions of specific C–O groups, like hydroxyl or ether groups (80, 89). These functional groups are associated with an increase in the potential drop in the Helmholtz layer and a reduction of the surface and subsurface hydrogen (90). A notable negative shift in the E_{FB} was observed in BDD electrodes after cathodic reduction that contributed to the increase of hydrogen terminations (80). Such shift to lower potentials might be related to forming C–H functional groups on the surface of diamond films (91).

We noticed a similar positive shift in the E_{FB} for the BDD films treated with Ar and CF_4 gases. The CF_4 results align with what Yamaguchi *et al.* found (36). They observed that BDD films plasma treated with C_3F_8 gas have a larger band bending at the electrode/electrolyte interface, restraining the interfacial electron transfer between BDD and the target redox species (36). This could be why the cyclic voltammograms of CF_4-treated samples show strong irreversibility towards the $Fe(CN)_6^{3-/4-}$ redox couple. Moreover, there was an observed electrostatic repulsion between BDD and analytes in the case of C_3F_8-treated BDD films (36). This observation holds significant potential for electrochemical applications, as it could help prevent the adsorption of some compounds on the BDD surface that cause electrode fouling.

To the best of our knowledge, there are no records on the E_{FB} measurements of diamond surfaces modified with Ar plasma treatment. The substantial positive shift of the E_{FB} observed in BDD films treated with O_2, Ar, and CF_4 indicates considerable surface state modifications. These results emphasize the significance of surface termination in the electrochemical behavior of diamond electrodes.

When considering the acceptor concentration determined using Mott-Schottky plots, it is important to acknowledge the influence of the chosen electrolyte. This choice can lead to significant variations in the estimated acceptor concentration, even up to an order of magnitude. For instance, in a study by Alehashem *et al.*, the same electrode showed an acceptor concentration of 1.4×10^{19} when tested in a 0.1 M KBr solution, while it yielded a value of 1.3×10^{20} in a 0.1 M H_2SO_4 solution. Our estimated acceptor concentration values align with the literature (80, 85) and the boron concentrations estimated from the Raman spectrum's peak at approximately 500 cm^{-1}. Furthermore, both methods suggest that the film doping is above the semiconductor-to-metallic conduction transition in CVD-diamond films, with acceptor concentrations surpassing 3×10^{20} cm^{-3} (79).

While the estimation of the E_{FB} using the Mott-Schottky technique is widely accepted, it is crucial to remember that the results obtained might not accurately represent the actual E_{FB} value. This is particularly evident in cases of highly doped BDD, where the estimated values do not solely represent the space charge layer (85). According to Živcová *et al.* (85), Mott-Schottky plots applied to highly-doped BDD face challenges in representing pure space-charge capacitance because the potential drop occurs primarily on the solution part of the interface, leading to impedance data that do not solely characterize the diamond's semiconductor properties. These observations could be relevant given that our films exhibit acceptor concentrations surpassing the transition to metallic conductivity.

III.2.3.8. Electrooxidation Tests

To assess the efficiency of the plasma-modified BDD electrodes in the degradation of water pollutants, anodic oxidation tests were conducted using 1 mM phenol solutions in 0.1 M Na_2SO_4. UV-vis spectroscopy and COD analyses were conducted to quantify the outcomes achieved in the phenol degradation processes using each electrode type. The UV-vis spectra depicted in Figure III.2.11 display a noticeable phenol peak positioned around 269 nm, which exhibits a gradual reduction in intensity throughout the electrooxidation treatment duration. Throughout the treatment, minor peaks emerge in the UV-Vis spectra (indicated by dark grey arrows), near the wavelength range of the primary 269 nm peak. These observations strongly imply the presence of oxidation byproducts of phenol, such as hydroquinone (92). However, it is noteworthy that this phenomenon of byproduct emergence is notably reduced in both the as-grown BDD electrode and the Ar-treated sample. This attenuated effect indicates a potential variation in the oxidation pathway or a differential rate of byproduct formation for these specific samples, suggesting possible distinct interactions between the modified-surfaces and phenol during the oxidation process.

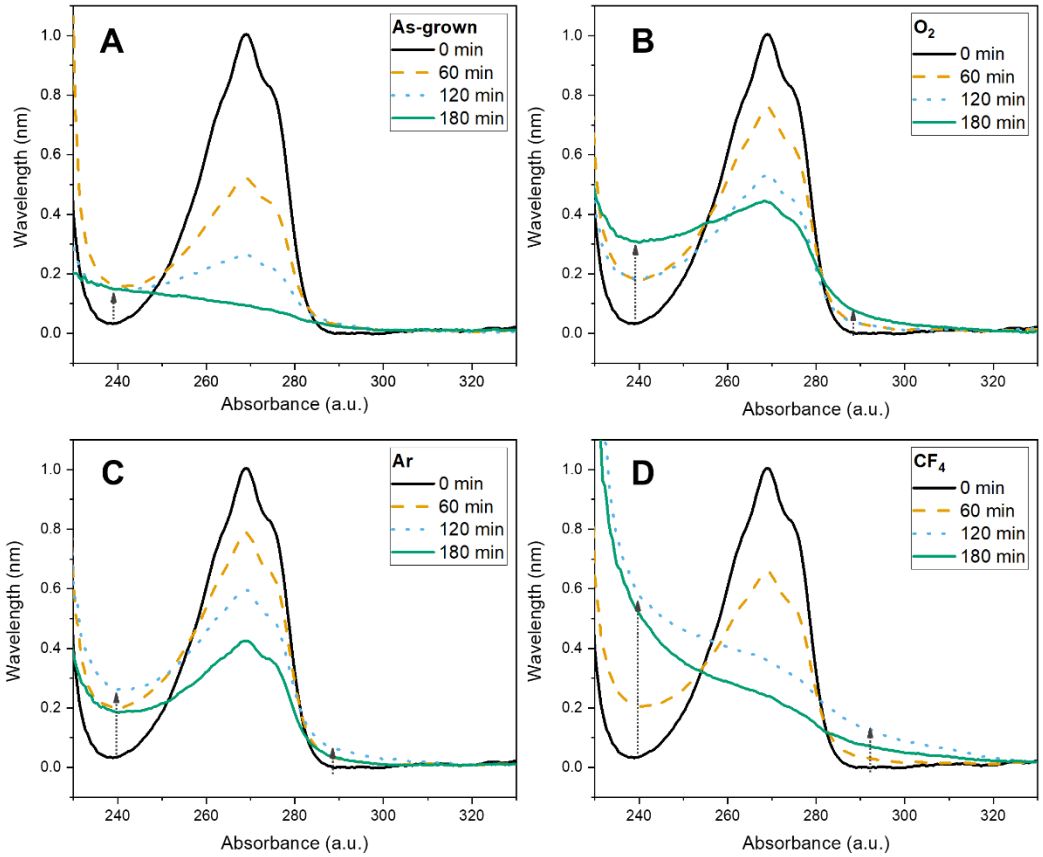

Figure III.2.11. UV-Vis spectra of 1 mM phenol solutions in 0.1 M Na_2SO_4 treated by anodic oxidation using plasma-modified BDD electrodes: (a) as-grown; (b) O_2-treated; (c) Ar-treated; (d) CF_4-treated.

The phenol degradation results were fitted to a first-order kinetic model, described in Eq. III.2.7 (93).

$$C/C_0 = e^{-k_{app}t} \qquad \textbf{Eq. III.2.7}$$

Where C represents the concentration (mg/L) at a given time t (h), while C_0 stands for the initial concentration. Eq. III.2.7 in question is employed to calculate the apparent rate constant (k_{app}). Based on the determined values of k_{app}, the corresponding half-life ($t_{1/2}$) can be deduced. This parameter indicates the duration required for the initial concentration to reduce by 50%, following Eq: 8.

$$t_{1/2} = \frac{ln\,2}{k_{app}} \qquad \textbf{Eq. III.2.8}$$

The average current efficiency (ACE), as shown in Eq. III.2.9, was determined concerning the COD values.

$$\mathrm{ACE} = \frac{\mathrm{F\,V\,(COD_0 - COD_t)}}{8\,\mathrm{I}\,\Delta\mathrm{t}} \qquad \textbf{Eq. III.2.9}$$

Where F represents the Faraday constant (96485 C/mol); V stands for the electrolyte volume (L); t signifies the duration of electrolysis (s); COD_0 represents the initial COD concentration (gO_2/L); COD_t and $COD_{t+\Delta t}$ indicate the COD concentrations at times t and t+Δt (s), respectively; 8 denotes the equivalent mass of oxygen (gO_2/eq); and I represents the applied current (A).

Figure III.2.12 provides the degradation process of a solution containing 1 mM phenol in 0.1 M Na_2SO_4 in terms of phenol and COD removal, treated through anodic oxidation using the surface-modified BDD electrodes.

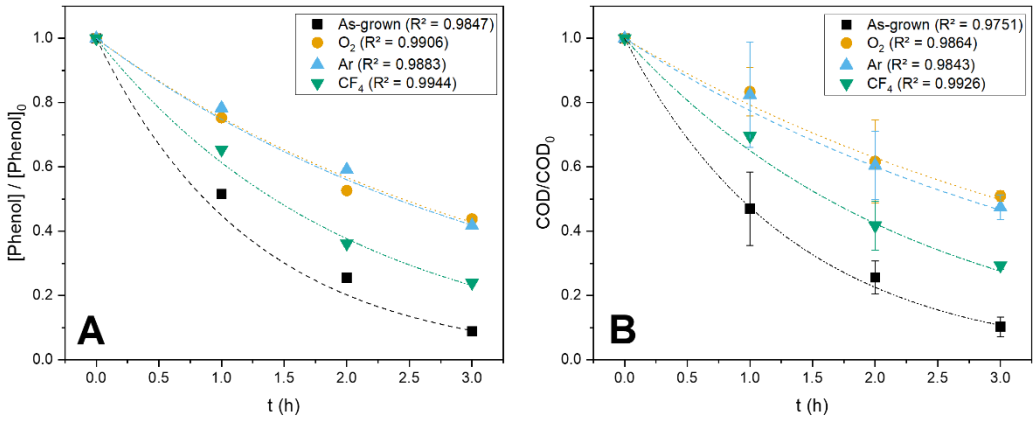

Figure III.2.12. (a) Decay of phenol concentration and (b) COD reduction in 1 mM phenol solutions in 0.1 M Na_2SO_4 treated by anodic oxidation with 30 mA/cm^2 for 3 hours using plasma-modified BDD electrodes

Table III.2.9 presents the degradation performance of plasma-modified BDD electrodes in relation to the phenol and COD removal after 3 hours, energy consumption, apparent rate constant (k_{app}), half-life ($t_{1/2}$), and average current efficiency (ACE).

Table III.2.9. Degradation Performance Metrics of Plasma-Modified BDD Electrodes.

	As-grown	**O_2**	**Ar**	**CF_4**
Phenol removal after 3 h	91.1%	56.2%	58.2%	76.1%
Energy Consumption (kWh/kg_{phenol})	242.0	466.8	424.6	359.8
k_{app}	0.7997	0.2834	0.2897	0.4881
$t_{1/2}$ (min)	52	147	144	85
COD removal after 3 h	89.8%	49.0%	52.6%	70.7%
Energy Consumption (kWh/kg_{COD})	95.3	207.7	182.4	150.2
ACE (%)	20.4%	11.1%	11.9%	16.1%
$k_{app\ (COD)}$	0.7447	0.2321	0.2547	0.4268
$t_{1/2\ (COD)}$ (min)	56	179	163	97

Considering the obtained results, it is evident that as-grown BDD electrodes exhibit superior performance in phenol oxidation compared to surfaces treated with O_2, Ar, and CF_4 plasmas. The as-grown films exhibited superior outcomes in terms of phenol reduction, COD reduction, energy consumption, and ACE. Notably, predominantly hydrogen-terminated as-grown surfaces appear to present superior performance than the plasma surface-modified ones due to the preservation of a high surface conductivity. The CF_4 plasma treatment was more effective in terms phenol and COD removal when compared to O_2 and Ar plasma treatments. Such an enhanced performance compared to O_2 and Ar plasma-modified electrodes might be linked to reduced fouling effects caused by electrostatic repulsion between BDD and analytes in fluorinated BDD surfaces (35, 49).

Despite the near zero contact angle results observed on surfaces treated with O_2 and Ar, suggesting an enhancement in the efficiency of the water treatment process due to increased hydrophilicity, the electrooxidation tests did not align with this expectation. Regarding the kinetics of the reactions involving the redox couples, the electrooxidation results are consistent with the higher electron transfer rates observed in the as-grown films. The CF_4 plasma-treated sample's lower double-layer capacitance may have contributed to its superior performance compared to the O_2- and Ar-treated samples. The resistivity results of the films also correspond to the electrooxidation efficiency results, as the plasma-treated films exhibited a substantial passivation of surface conductivity.

While our results strongly advocate for the effectiveness of as-grown BDD electrodes, it is crucial to acknowledge the temporal evolution of hydrogen-terminated surfaces. Over time, these surfaces undergo oxidation processes, potentially transitioning towards behaviors intermediate between hydrogen-terminated and oxygen-terminated surfaces (48, 94, 95).
It is worth noting that conventional practices in BDD electrode cleaning involve anodic polarization in sulfuric acid, a method known to induce surface oxidation (96). Therefore, cathodic polarization (95) or hydrogen plasma treatment for surface rejuvenation might be more appropriate to ensure sustained and optimal electrode performance. However, it is important to exercise caution, as hydrogen plasma treatment, while offering potential benefits such as removing non-diamond phases selectively (97) and reducing lattice distortion and defect density (98), has also been associated with boron acceptors passivation (99, 100) and could potentially incur additional costs in terms of equipment, feed gas, and energy consumption. Therefore, for practical applications, the preferred strategy would be to employ cathodic polarization for surface rejuvenation.

III.2.4. Conclusions

In conclusion, our study delved into the electrooxidation efficiency of plasma-modified boron-doped diamond electrodes for persistent organic pollutants degradation using various source gases. We meticulously characterized the surfaces through various techniques, including Raman spectroscopy, the sessile drop method, cyclic voltammetry, electrochemical impedance spectroscopy, and Mott-Schottky plots, shedding light on their electrochemical behavior. The results revealed that as-grown BDD electrodes outperformed their plasma-treated counterparts primarily due to their superior surface conductivity. As-grown BDD electrodes exhibited remarkable phenol and COD removal efficiency, indicating their effectiveness in water pollutant degradation. Furthermore, both as-grown and Ar-treated BDD electrodes exhibited reduced byproduct generation during phenol electrooxidation. These findings underscore the crucial role of surface termination in electrode efficiency. Among the plasma treatments, CF_4 treatment showed promise, potentially due to reduced fouling effects. While our study has provided valuable insights into BDD electrode behavior in water pollutant degradation, there is room for further exploration. Future studies should delve into more effective treatment conditions by varying parameters such as treatment time and plasma power. Notably, our investigation has highlighted that brief plasma etching treatment can effectively create diverse functionalized BDD surfaces depending on the plasma source. The plasma-treated surfaces displayed enhanced hydrophilicity and a notably expanded potential window in the presence of specific electrolytes, rendering them a promising option for scenarios demanding highly negative potentials, including sensor applications and green hydrogen production. Our study provides valuable insights into BDD electrode behavior in water pollutant degradation and emphasizes the need to consider electrode surface characteristics in optimizing electrooxidation processes. We also recommend exploring methods such as cathodic polarization or hydrogen plasma treatment to ensure sustained and optimal electrode performance. These findings pave the way for future research endeavors in this critical field of environmental remediation.

III.2.5. References

1. Najafinejad MS, Chianese S, Fenti A, Iovino P, Musmarra D. Application of Electrochemical Oxidation for Water and Wastewater Treatment: An Overview. Molecules. 2023;28(10).

2. Brosler P, Girão AV, Silva RF, Tedim J, Oliveira FJ. Electrochemical Advanced Oxidation Processes Using Diamond Technology: A Critical Review. Environments. 2023;10(2).

3. Notsu H, Yagi I, Tatsuma T, Tryk DA, Fujishima A. Surface carbonyl groups on oxidized diamond electrodes. J Electroanal Chem. 2000;492(1):31-7.

4. Luong JH, Male KB, Glennon JD. Boron-doped diamond electrode: synthesis, characterization, functionalization and analytical applications. Analyst. 2009;134(10):1965-79.

5. Kondo T, Ito H, Kusakabe K, Ohkawa K, Einaga Y, Fujishima A, et al. Plasma etching treatment for surface modification of boron-doped diamond electrodes. Electrochim Acta. 2007;52(11):3841-8.

6. Siné G, Ouattara L, Panizza M, Comninellis C. Electrochemical behavior of fluorinated boron-doped diamond. Electrochem Solid-State Lett. 2003;6(9):D9-D11.

7. Ferro S, De Battisti A. Physicochemical properties of fluorinated diamond electrodes. J Phys Chem B. 2003;107(31):7567-73.

8. Notsu H, Fukazawa T, Tatsuma T, Tryk DA, Fujishima A. Hydroxyl groups on boron-doped diamond electrodes and their modification with a silane coupling agent. Electrochem Solid-State Lett. 2001;4(3):H1-H3.

9. Masuda H, Watanabe M, Yasni K, Tryk D, Rao T, Fiijishima A. Fabrication of a nanoslructured diamond honeycomb film. Adv Mater. 2000;12(6):444-7.

10. Kondo T, Honda K, Tryk DA, Fujishima A. Covalent modification of single-crystal diamond electrode surfaces. J Electrochem Soc. 2005;152(1):E18-E23.

11. Matrab T, Chehimi MM, Boudou JP, Benedic F, Wang J, Naguib NN, et al. Surface functionalization of ultrananocrystalline diamond using atom transfer radical polymerization (ATRP) initiated by electro-grafted aryldiazonium salts. Diamond Relat Mater. 2006;15(4-8):639-44.

12. Sarapuu A, Helstein K, Schififrin DJ, Tammeveski K. Kinetics of oxygen reduction on quinone-modified HOPG and BDD electrodes in alkaline solution. Electrochem Solid-State Lett. 2005;8(2):E30-E3.

13. Shin D, Tokuda N, Rezek B, Nebel CE. Periodically arranged benzene-linker molecules on boron-doped single-crystalline diamond films for DNA sensing. Electrochem Commun. 2006;8(5):844-50.
14. Chatterjee A, Foord J. Electrochemical deposition of nanocrystalline zinc oxide at conductive diamond electrodes. Diamond Relat Mater. 2006;15(4-8):664-7.
15. Hyde M, Saterlay AJ, Wilkins SJ, Foord JS, Compton RG, Marken F. Deposition and characterisation of a porous Sn(IV) semiconductor nanofilm on boron-doped diamond. J Solid State Electrochem. 2002;6(3):183-7.
16. Manivannan A, Spataru N, Arihara K, Fujishima A. Electrochemical deposition of titanium oxide on boron-doped diamond electrodes. Electrochem Solid-State Lett. 2005;8(10):C138-C40.
17. Spataru N, Terashima C, Tokuhiro K, Sutanto I, Tryk DA, Park SM, et al. Electrochemical behavior of cobalt oxide films deposited at conductive diamond electrodes. J Electrochem Soc. 2003;150(7):E337-E41.
18. Bennett JA, Show Y, Wang S, Swain GM. Pulsed galvanostatic deposition of Pt particles on microcrystalline and nanocrystalline diamond thin-film electrodes I. Characterization of as-deposited metal/diamond surfaces. J Electrochem Soc. 2005;152(5):E184-E92.
19. Duo I, Michaud PA, Haenni W, Perret A, Comninellis C. Activation of boron-doped diamond with IrO 2 clusters. Electrochem Solid-State Lett. 2000;3(7):325-6.
20. Ivandini TA, Sato R, Makide Y, Fujishima A, Einaga Y. Electroanalytical application of modified diamond electrodes. Diamond Relat Mater. 2004;13(11-12):2003-8.
21. Ivandini TA, Sato R, Makide Y, Fujishima A, Einaga Y. Pt-implanted boron-doped diamond electrodes and the application for electrochemical detection of hydrogen peroxide. Diamond Relat Mater. 2005;14(11-12):2133-8.
22. Ivandini TA, Sato R, Makide Y, Fujishima A, Einaga Y. Electrochemical detection of arsenic(III) using indium-implanted boron-doped diamond electrodes. Anal Chem. 2006;78(18):6291-8.
23. McKenzie KJ, Marken F. Electrochemical characterization of hydrous ruthenium oxide nanoparticle decorated boron-doped diamond electrodes. Electrochem Solid-State Lett. 2002;5(9):E47-E50.
24. Siné G, Duo I, El Roustom B, Fóti G, Comninellis C. Deposition of clusters and nanoparticles onto boron-doped diamond electrodes for electrocatalysis. J Appl Electrochem. 2006;36(8):847-62.

25. Siné G, Fóti G, Comninellis C. Boron-doped diamond (BDD)-supported Pt/Sn nanoparticles synthesized in microemulsion systems as electrocatalysts of ethanol oxidation. J Electroanal Chem. 2006;595(2):115-24.
26. Welch CM, Simm AO, Compton RG. Oxidation of electrodeposited copper on boron doped diamond in acidic solution: Manipulating the size of copper nanoparticles using voltammetry. Electroanalysis. 2006;18(10):965-70.
27. Yang W, Auciello O, Butler JE, Cai W, Carlisle JA, Gerbi JE, et al. DNA-modified nanocrystalline diamond thin-films as stable, biologically active substrates. Nat Mater. 2002;1(4):253-7.
28. Sturrock P. Plasma physics: An introduction to the theory of astrophysical, Geophysical, and laboratory plasmas. Cambridge: Cambridge University Press; 2003.
29. Szunerits S, Boukherroub R. Different strategies for functionalization of diamond surfaces. J Solid State Electrochem. 2007;12(10):1205-18.
30. Couto AB, Santos LCD, Matsushima JT, Baldan MR, Ferreira NG. Hydrogen and oxygen plasma enhancement in the Cu electrodeposition and consolidation processes on BDD electrode applied to nitrate reduction. Appl Surf Sci. 2011;257(23):10141-6.
31. Bhardwaj K, Parvis F, Wang Y, Blanchard GJ, Swain GM. Effect of Surface Oxygen on the Wettability and Electrochemical Properties of Boron-Doped Nanocrystalline Diamond Electrodes in Room-Temperature Ionic Liquids. Langmuir. 2020;36(21):5717-29.
32. Liu F, Wang J, Liu B, Li X, Chen D, editors. Effect of surface termination on electronic structure of nano-crystalline diamond film. 1st IEEE International Conference on Nano Micro Engineered and Molecular Systems, 1st IEEE-NEMS; 2006; Zhuhai.
33. Jaggernauth A, Silva RM, Neto MA, Oliveira FJ, Bdikin IK, Alegre MP, et al. Interfacial integrity enhancement of atomic layer deposited alumina on boron doped diamond by surface plasma functionalization. Surf Coat Tech. 2020;397.
34. Yagi I, Notsu H, Kondo T, Tryk DA, Fujishima A. Electrochemical selectivity for redox systems at oxygen-terminated diamond electrodes. J Electroanal Chem. 1999;473(1-2):173-8.
35. Yamaguchi C, Natsui K, Iizuka S, Tateyama Y, Einaga Y. Electrochemical properties of fluorinated boron-doped diamond electrodes via fluorine-containing plasma treatment. Phys Chem Chem Phys. 2019;21(25):13788-94.
36. Coffinier Y, Szunerits S, Jama C, Desmet R, Melnyk O, Marcus B, et al. Peptide immobilization on amine-terminated boron-doped diamond surfaces. Langmuir. 2007;23(8):4494-7.

37. Simon N, Decorse-Pascanut C, Gonçalves AM, Ballutaud D, Charrier G, Etcheberry A. Nitrogenation of boron doped diamond: Comparison of an electrochemical treatment in liquid ammonia and a NH3/N2 plasma. Diamond Relat Mater. 2009;18(5-8):890-4.
38. Brosler P, Silva RF, Tedim J, Oliveira FJ. Electroconductive silicon nitride-titanium nitride ceramic substrates for CVD diamond electrode deposition. Ceram Int. 2023.
39. Bernard M, Deneuville A, Muret P. Non-destructive determination of the boron concentration of heavily doped metallic diamond thin films from Raman spectroscopy. Diamond Relat Mater. 2004;13(2):282-6.
40. Ferrari AC, Robertson J. Raman spectroscopy of amorphous, nanostructured, diamond-like carbon, and nanodiamond. Philos Trans A Math Phys Eng Sci. 2004;362(1824):2477-512.
41. Ralchenko VG, Smolin AA, Pereverzev VG, Obraztsova ED, Korotoushenko KG, Konov VI, et al. Diamond deposition on steel with CVD tungsten intermediate layer. Diamond Relat Mater. 1995;4(5-6):754-8.
42. Bernard M, Baron C, Deneuville A. About the origin of the low wave number structures of the Raman spectra of heavily boron doped diamond films. Diamond Relat Mater. 2004;13(4-8):896-9.
43. Ferrari AC, Robertson J. Origin of the1150−cm−1Raman mode in nanocrystalline diamond. Physical Review B. 2001;63(12).
44. Ager JW, Walukiewicz W, McCluskey M, Plano MA, Landstrass MI. Fano interference of the Raman phonon in heavily boron-doped diamond films grown by chemical vapor deposition. Appl Phys Lett. 1995;66(5):616-8.
45. Prawer S, Nemanich RJ. Raman spectroscopy of diamond and doped diamond. Philos Trans A Math Phys Eng Sci. 2004;362(1824):2537-65.
46. Foord JS, Goeting CH. Diamond electrodes modified by argon ion bombardment. Phys Status Solidi A. 2004;201(11):2439-43.
47. Kondo T, Ito H, Kusakabe K, Ohkawa K, Honda K, Einaga Y, et al. Characterization and electrochemical properties of CF4 plasma-treated boron-doped diamond surfaces. Diamond Relat Mater. 2008;17(1):48-54.
48. Neto MA, Pato G, Bundaleski N, Teodoro OMND, Fernandes AJS, Oliveira FJ, et al. Surface modifications on as-grown boron doped CVD diamond films induced by the B2O3–ethanol–Ar system. Diamond Relat Mater. 2016;64:89-96.
49. Ristein J. Surface transfer doping of diamond. J Phys D: Appl Phys. 2006;39(4):R71-R81.

50. Maier F, Riedel M, Mantel B, Ristein J, Ley L. Origin of surface conductivity in diamond. Phys Rev Lett. 2000;85(16):3472-5.
51. Ristein J. Physics. Surface transfer doping of semiconductors. Science. 2006;313(5790):1057-8.
52. Zhao L, Li Y, Yu M, Peng Y, Ran F. Electrolyte-Wettability Issues and Challenges of Electrode Materials in Electrochemical Energy Storage, Energy Conversion, and Beyond. Adv Sci (Weinh). 2023;10(17):e2300283.
53. Jeon DH. Wettability in electrodes and its impact on the performance of lithium-ion batteries. Energy Storage Materials. 2019;18:139-47.
54. Zisman WA. Relation of the Equilibrium Contact Angle to Liquid and Solid Constitution. In: Fowkes FM, editor. Contact Angle, Wettability, and Adhesion. 43. USA: AMERICAN CHEMICAL SOCIETY; 1964.
55. Bogdanowicz R, Sawczak M, Niedzialkowski P, Zieba P, Finke B, Ryl J, et al. Novel Functionalization of Boron-Doped Diamond by Microwave Pulsed-Plasma Polymerized Allylamine Film. J Phys Chem C. 2014;118(15):8014-25.
56. Medeiros de Araújo D, Cañizares P, Martínez-Huitle CA, Rodrigo MA. Electrochemical conversion/combustion of a model organic pollutant on BDD anode: Role of sp 3 /sp 2 ratio. Electrochem Commun. 2014;47:37-40.
57. Tryk DA, Tsunozaki K, Rao TN, Fujishima A. Relationships between surface character and electrochemical processes on diamond electrodes: dual roles of surface termination and near-surface hydrogen. Diamond Relat Mater. 2001;10(9-10):1804-9.
58. Salazar-Banda GR, de Carvalho AE, Andrade LS, Rocha RC, Avaca LA. On the activation and physical degradation of boron-doped diamond surfaces brought on by cathodic pretreatments. J Appl Electrochem. 2010;40(10):1817-27.
59. McLaughlin MHS, Corcoran E, Pakpour-Tabrizi AC, de Faria DC, Jackman RB. Influence of temperature on the electrochemical window of boron doped diamond: a comparison of commercially available electrodes. Sci Rep. 2020;10(1):15707.
60. Bard AJ. Inner-sphere heterogeneous electrode reactions. Electrocatalysis and photocatalysis: the challenge. J Am Chem Soc. 2010;132(22):7559-67.
61. Macpherson JV. A practical guide to using boron doped diamond in electrochemical research. Phys Chem Chem Phys. 2015;17(5):2935-49.
62. Lavagnini I, Antiochia R, Magno F. An Extended Method for the Practical Evaluation of the Standard Rate Constant from Cyclic Voltammetric Data. Electroanalysis. 2004;16(6):505-6.

63. Nicholson RS. Theory and Application of Cyclic Voltammetry for Measurement of Electrode Reaction Kinetics. Anal Chem. 1965;37(11):1351-5.

64. Klingler RJ, Kochi JK. Electron-transfer kinetics from cyclic voltammetry. Quantitative description of electrochemical reversibility. The Journal of Physical Chemistry. 2002;85(12):1731-41.

65. Moldenhauer J, Meier M, Paul DW. Rapid and Direct Determination of Diffusion Coefficients Using Microelectrode Arrays. J Electrochem Soc. 2016;163(8):H672-H8.

66. Barbooti MM. Environmental Applications of Instrumental Chemical Analysis. 1st ed. Barbooti MM, editor. New York, USA: Apple Academic Press; 2015.

67. Luo D, Ma D, Liu S, Nakata K, Fujishima A, Wu L. Electrochemical reduction of CO2 on fluorine-modified boron-doped diamond electrode. Diamond Relat Mater. 2022;121.

68. Hirschorn B, Orazem ME, Tribollet B, Vivier V, Frateur I, Musiani M. Determination of effective capacitance and film thickness from constant-phase-element parameters. Electrochim Acta. 2010;55(21):6218-27.

69. Bogdanowicz R, Ryl J. Structural and electrochemical heterogeneities of boron-doped diamond surfaces. Curr Opin Electrochem. 2022;31.

70. Fan B, Zhu Y, Rechenberg R, Rusinek CA, Becker MF, Li W. Large-scale, all polycrystalline diamond structures transferred onto flexible Parylene-C films for neurotransmitter sensing. Lab Chip. 2017;17(18):3159-67.

71. Mei R, Wei Q, Zhu C, Ye W, Zhou B, Ma L, et al. 3D macroporous boron-doped diamond electrode with interconnected liquid flow channels: A high-efficiency electrochemical degradation of RB-19 dye wastewater under low current. Appl Catal B Environ. 2019;245:420-7.

72. Yang W, Deng Z, Wang Y, Ma L, Zhou K, Liu L, et al. Porous boron-doped diamond for efficient electrocatalytic elimination of azo dye Orange G. Sep Purif Technol. 2022;293.

73. Pleskov YV. Russ J Electrochem. 2002;38(12):1275-91.

74. Grundmann M. The Physics of Semiconductors. Switzerland: Springer; 2016.

75. Ding M, Liu Y, Lu X, Li Y, Tang W. Boron doped diamond films: A microwave attenuation material with high thermal conductivity. Appl Phys Lett. 2019;114(16).

76. Hankin A, Alexander JC, Kelsall GH. Constraints to the flat band potential of hematite photo-electrodes. Phys Chem Chem Phys. 2014;16(30):16176-86.

77. Gelderman K, Lee L, Donne SW. Flat-Band Potential of a Semiconductor: Using the Mott–Schottky Equation. Journal of Chemical Education. 2007;84(4).

78. Bot AW. Electrochemistry of Semiconductors. Current Separations. 1998;17(3).

79. Lagrange JP, Deneuville A, Gheeraert E. Activation energy in low compensated homoepitaxial boron-doped diamond films. Diamond Relat Mater. 1998;7(9):1390-3.

80. Girard HA, Simon N, Ballutaud D, Etcheberry A. Correlation between flat-band potential position and oxygenated termination nature on boron-doped diamond electrodes. C R Chim. 2008;11(9):1010-5.

81. Boonma L, Yano T, Tryk DA, Hashimoto K, Fujishima A. Observation of Photocurrent from Band-to-Band Excitation of Semiconducting p-Type Diamond Thin Film Electrodes. J Electrochem Soc. 1997;144(6):L142-L5.

82. Pleskov YV, Evstefeeva YE, Varnin VP, Teremetskaya IG. Synthetic Semiconductor Diamond Electrodes: Electrochemical Characteristics of Homoepitaxial Boron-doped Films Grown at the (111), (110), and (100) Faces of Diamond Crystals. Russ J Electrochem. 2004;40(9):886-92.

83. Alehashem S, Chambers F, Strojek JW, Swain GM, Ramesham R. Cyclic Voltammetric Studies of Charge Transfer Reactions at Highly Boron-Doped Polycrystalline Diamond Thin-Film Electrodes. Anal Chem. 1995;67(17):2812-21.

84. Sakharova AY, Pleskov YV, Diquarto F, Piazza S, Sunseri C, Teremetskaya IG, et al. Synthetic diamond electrodes - photoelectrochemical investigation of undoped and boron-doped polycrystalline thin-films. J Electrochem Soc. 1995;142(8):2704-9.

85. Živcová ZV, Petrák V, Frank O, Kavan L. Electrochemical impedance spectroscopy of polycrystalline boron doped diamond layers with hydrogen and oxygen terminated surface. Diamond Relat Mater. 2015;55:70-6.

86. Actis P, Denoyelle A, Boukherroub R, Szunerits S. Influence of the surface termination on the electrochemical properties of boron-doped diamond (BDD) interfaces. Electrochem Commun. 2008;10(3):402-6.

87. Kondo T, Honda K, Tryk DA, Fujishima A. AC impedance studies of anodically treated polycrystalline and homoepitaxial boron-doped diamond electrodes. Electrochim Acta. 2003;48(19):2739-48.

88. Rao TN, Tryk DA, Hashimoto K, Fujishima A. Band-Edge Movements of Semiconducting Diamond in Aqueous Electrolyte Induced by Anodic Surface Treatment. J Electrochem Soc. 1999;146(2):680-4.

89. Simon N, Girard H, Ballutaud D, Ghodbane S, Deneuville A, Herlem M, et al. Effect of H and O termination on the charge transfer of moderately boron doped diamond electrodes. Diamond Relat Mater. 2005;14(3-7):1179-82.

90. Baldan MR, Azevedo AF, Couto AB, Ferreira NG. Cathodic and anodic pre-treated boron doped diamond with different sp2 content: Morphological, structural, and impedance spectroscopy characterizations. J Phys Chem Solids. 2013;74(12):1830-5.
91. Azevedo AF, Souza FA, Hammer P, Baldan MR, Ferreira NG. The influence of hydrogen plasma pre-treatment on the structure of BDND electrode surface applied for phenol detection. J Nanopart Res. 2011;13(11):6133-9.
92. Murillo-Acevedo YS, Giraldo L, Poon PS, Matos J, Moreno-Pirajan JC. The Cramer's rule for the parametrization of phenol and its hydroxylated byproducts: UV spectroscopy vs. high performance liquid chromatography. Environ Sci Pollut Res Int. 2021;28(6):6746-57.
93. Nadais H, Li X, Alves N, Couras C, Andersen HR, Angelidaki I, et al. Bio-electro-Fenton process for the degradation of Non-Steroidal Anti-Inflammatory Drugs in wastewater. Chem Eng J. 2018;338:401-10.
94. Vanhove E, de Sanoit J, Arnault JC, Saada S, Mer C, Mailley P, et al. Stability of H-terminated BDD electrodes: an insight into the influence of the surface preparation. Phys Status Solidi A. 2007;204(9):2931-9.
95. Salazar-Banda GR, Andrade LS, Nascente PAP, Pizani PS, Rocha-Filho RC, Avaca LA. On the changing electrochemical behaviour of boron-doped diamond surfaces with time after cathodic pre-treatments. Electrochim Acta. 2006;51(22):4612-9.
96. Hutton LA, Iacobini JG, Bitziou E, Channon RB, Newton ME, Macpherson JV. Examination of the factors affecting the electrochemical performance of oxygen-terminated polycrystalline boron-doped diamond electrodes. Anal Chem. 2013;85(15):7230-40.
97. Ivanov OA, Muchnikov AB, Chernov VV, Bogdanov SA, Vikharev AL, Butler JE. Experimental study of hydrogen plasma etching of (100) single crystal diamond in a MPACVD reactor. Mater Lett. 2015;151:115-8.
98. Li K, Kang X, Gou L. Mechanical behavior of BDD films after different heat treatments. Surf Coat Technol. 2021;427.
99. Chevallier J, Theys B, Lusson A, Grattepain C, Deneuville A, Gheeraert E. Hydrogen-boron interactions inp-type diamond. Physical Review B. 1998;58(12):7966-9.
100. Barjon J, Habka N, Chevallier J, Jomard F, Chikoidze E, Mer-Calfati C, et al. Hydrogen-induced passivation of boron acceptors in monocrystalline and polycrystalline diamond. Phys Chem Chem Phys. 2011;13(24):11511-6.

Chapter IV

Improving the Electrooxidation Efficiency of BDD/Si_3N_4-TiN Electrodes

This chapter is dedicated to the development of a strategy to enhance the efficiency of electrochemical oxidation processes using BDD electrodes, with a particular focus on reducing the time and energy consumption involved in these processes.

An innovative approach for energy-efficient electrochemical water treatment, with a specific focus on degrading phenol is here introduced. The method involves electrooxidation with the concomitant fouling followed by a rapid reactivation process applied to a BDD/Si_3N_4-TiN electrode using a square wave pattern in a cyclic way. The main goal was to accelerate the conversion of phenol into compounds that are more readily degradable through this fouling-reactivation cycle, while minimizing both the time and energy requirements associated with electrochemical oxidation processes. This approach was driven by the urgent demand for more cost effective and environmentally friendly water treatment methods.

IV.1. Saving Energy in Electrochemical Water Treatment Using BDD Electrodes Through Forced Fouling-Reactivation Cycles: Optimizing Frequency and Duty Cycle

Priscilla Brosler[1], Rui F. Silva[1], João Tedim[1], Filipe J. Oliveira[1]

[1] CICECO - Aveiro Institute of Materials & Department of Materials and Ceramic Engineering, University of Aveiro, 3810-193 Aveiro, Portugal

The present work was submitted to *Separation and Purification Technology*

Abstract

This study presents an innovative approach for energy-efficient electrochemical water treatment, specifically targeting phenol degradation. The proposed method is based on cyclic steps of electrooxidation that results in fouling and a rapid reactivation in a sequence applied to a boron-doped diamond (BDD) electrode employing a square wave pattern. The primary objective was to accelerate the transformation of phenol into more easily degradable compounds by leveraging this fouling-reactivation cycle. A three-level full factorial experimental design was employed to fine-tune the frequency and duty cycle of the square wave pattern, determining the most energy-efficient fouling and reactivation steps. The results demonstrated that the newly proposed approach outperformed conventional continuous anodic oxidation processes regarding energy efficiency. The energy consumption was reduced by more than four times while achieving superior levels of phenol elimination. This research underscores the potential of the fouling-reactivation strategy to significantly enhance the energy efficiency of water treatment processes, making strides toward sustainable and environmentally friendly solutions.

IV.1.1. Introduction

Phenolic compounds are significant industrial chemicals found as pollutants in various environmental contexts such as water systems, the atmosphere, and food products (1). These compounds, originating from wastewaters and industrial emissions, adversely affect human health and the environment (2-4). Electrochemical Advanced Oxidation Processes (EAOPs) have emerged as a promising approach for removing persistent pollutants like phenolic compounds from water (5). Among these processes, boron-doped diamond (BDD) electrodes have gained attention due to their exceptional properties that make them well-suited for this purpose, such as wide potential window, low background current, high physical and chemical stability, inert surface with low adsorption properties, high electrocatalytic activity, and high self-cleaning capability (6).

However, a key concern for the widespread application of EAOPs is the associated energy consumption and the occurrence of electrode fouling (7). Electrode fouling, also known as electrode passivation, occurs due to the accumulation of a non-conductive impermeable layer on the electrode surface (8). This phenomenon obstructs electron transfer and leads to a reduction in current, thus limiting the effectiveness of electrochemical water treatment methods (9). The fouling layer blocks direct analyte-electrode interaction and can obstruct active reaction sites on the electrode surface, further reducing the accessibility of target molecules (9, 10).

As outlined by Whang *et al.*, the occurrence of electrode fouling due to phenol is fundamentally a multi-step procedure encompassing the deprotonation, oxidation, and polymerization of phenol. In aqueous solutions, particularly those with pH values near or higher than the pK_a of phenol (9.98, 25 °C) (11), when a potential below the region of water stability (E < 2.3 V/SHE) is applied, phenol experiences deprotonation and oxidation, forming phenoxy radicals through a rapid one-electron-transfer process (12, 13). These radicals can subsequently combine with each other or with phenol molecules, leading to polymerization (13). The resultant polymeric layer gradually builds up on the electrode surface.

At high applied potentials (E > 2.3 V/SHE), electrode fouling is avoided by a facilitated reaction pathway leading to the mineralization of phenol, driven by accelerated reaction rates in the generation of phenoxide radicals and the subsequent formation of phenoxonium ions (14). In fact, a widely adopted technique for BDD electrode reactivation involves anodic polarization at elevated potentials, a process that yields hydroxyl radicals capable of oxidative elimination of the fouling deposit (15, 16).

Studies have been conducted to analyze the composition of the fouling layer generated by phenol. These investigations have pointed to quinone groups attributed to polyphenol, which emerges from either the direct or indirect oxidation of phenol involving intermediates (8). Furthermore, oxidative intermediate products of phenol, including pyrocatechol and hydroquinone, have also been identified (8).

While the precise details of the fouling mechanism may exhibit variations, several models have been proposed to elucidate this phenomenon. Among these models are the area blocking or active site poisoning model (10), the film diffusion model (17), and a semiempirical model based on electron tunneling and the Tafel equation (10).

During chronoamperometry experiments using BDD electrodes in aqueous solutions containing phenol, we observed cyclic variations in the current density response over time, particularly at elevated potentials such as 4 V/SCE. As we increased the applied potential, these cycles exhibited a progressively higher frequency. Following these observations, we chose to explore these cycles in an effort to achieve a more efficient oxidation of phenol. We embarked on an investigation to examine the hypothesis of enhancing energy efficiency by implementing a cyclic sequence involving rapid fouling and subsequent reactivation of BDD electrodes using a two-step square wave pattern. The underlying premise of this approach is based on the notion that the accumulation of phenolic compounds on the BDD electrode surface via electropolymerization at low applied potentials could be immediately succeeded by applying a suitably elevated potential. This elevated potential is intended to detach the polymeric layer while simultaneously initiating its partial or complete oxidation. The resulting oxidized polymeric layer is hypothesized to either return to the solution as more readily degradable products or to be destroyed by the electrogenerated hydroxyl radicals on the BDD surface (8, 16). By iteratively executing this process across a series of cycles, the anticipated outcome would be an accelerated mineralization of phenol, accompanied by a notable reduction in energy consumption compared to the typical anodic oxidation process. A schematic illustrating the anticipated mechanisms during fouling and reactivation stages in phenol oxidation in aqueous solution is depicted in Figure IV.1.

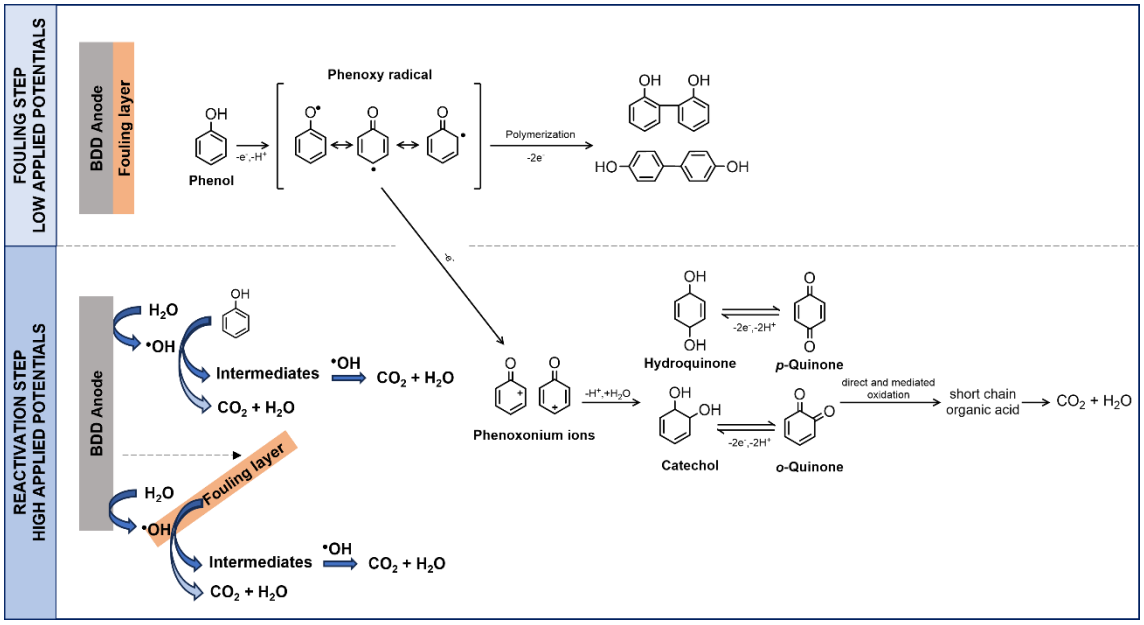

Figure IV.1. Schematic representation of potential reaction mechanisms of phenol in aqueous medium during fouling and reactivation stages. Adapted from ref. (8, 14-16).

Utilizing the fouling phenomenon in combination with BDD's self-cleaning properties presents an opportunity to enhance the efficiency of water treatment processes. In this study, our objective is to investigate the interplay between fouling and BDD electrodes, leading to the development of an innovative approach for optimizing electrochemical water treatment efficiency. By examining the fouling process, determining the optimal fouling potential, and fine-tuning reactivation conditions, our goal is to minimize the energy consumption of the process. Through the strategic utilization of fouling effects and the inherent self-cleaning attributes of BDD electrodes, we aspire to contribute to the advancement of more effective and energy-efficient techniques for removing phenolic compounds from water systems. We expect that this study will pave the way for applying this strategy not only to phenolic compounds but also to other persistent organic pollutants present in water bodies.

IV.1.2. Materials and Methods

An innovative two-step square wave pattern approach was adopted, comprising a fouling phase and a subsequent self-cleaning, or reactivation, phase, employing a BDD electrode. The BDD electrodes employed in this investigation were deposited over electroconductive Si_3N_4-TiN substrates using an HFCVD reactor. Detailed information about the fabrication of these BDD electrodes can be found in Section III.1.

Cyclic Voltammetry (CV) was conducted to comprehend the BDD electrode's fouling process. The CV experiments were conducted within a potential range of -1.3 to 2.3 V/SCE, employing a scan rate of 100 mV/s. For the determination of the optimal timing and potential parameters for the fouling and subsequent reactivation phases, linear sweep voltammetry (LSV) and Chronoamperometry was employed. The LSV and Chronoamperometry experiments were performed under the same conditions as the CV experiments. All experiments were conducted in triplicate to ensure the reliability and consistency of the results. Further insight into the reactivation process of the BDD electrode was obtained through Chronoamperometry experiments.

All CV, LSV, and chronoamperometry experiments were conducted using a Gamry Reference 600 potentiostat within a three-electrode setup. This setup included a platinum counter electrode, a saturated calomel electrode (SCE) as a reference electrode, and a disc-shaped BDD/Si_3N_4-TiN working electrode with an area of 0.785 cm^2 exposed to the solution. The electrolyte solution used was 0.1 M Na_2SO_4 (≥99.0% purity, Sigma-Aldrich, USA), containing a phenol concentration of 1 mM (94.11 mg L-1, ≥99% purity, Sigma-Aldrich, USA).

Cyclic and continuous chronoamperometry was used for phenol degradation employing the square wave pattern, with optimized frequency and duty cycle, utilizing the same Gamry Reference 600 potentiostat. Bar-shaped BDD/Si_3N_4-TiN electrodes with a total submerged area of 0.8 cm^2 served as both working and reference electrodes. These electrodes were kept at a fixed distance of 5 mm from each other. A SCE reference electrode was employed. The solution composition, using a volume of 25 mL for each trial, was the same as the preceding experiments (0.1 M Na_2SO_4, phenol concentration of 1 mM).

Quantification of phenol concentration in the post-degradation solutions was performed using UV-Vis spectroscopy (FAbS, Sarspec, Portugal). Measurements were taken within the wavelength range of 200 to 500 nm, where the absorbance at 269 nm was directly proportional to the phenol concentration within the solution.

A three-level full factorial experimental design was employed to optimize the phenol degradation process using the square wave pattern. This involved studying the impact of fouling time at a fixed potential and reactivation time at a fixed potential over a series of cycles equivalent to 1 hour of treatment. After each experiment, the response variable evaluated was the phenol concentration and energy consumption. A phenol degradation assay was performed for comparative analysis through anodic oxidation at a constant applied potential of 8 V/SCE for 1 hour.

IV.1.3. Results and Discussion

To comprehend the process of electrode fouling in the BDD electrode, CV experiments were conducted using the same aqueous solution that will be employed in the water treatment assays, contaminated with phenol (1 mM phenol in 0.1 M Na_2SO_4). Figure IV.2 depicts ten consecutive cycles of the electrode immersed in the solution. The observed fouling phase is characterized by a substantial reduction in the current associated with an anodic oxidation peak located around 1.55 V/SCE. Notably, the current demonstrates a considerable decrease from the second cycle onward. From the fourth to the tenth cycle, there is a marked absence of substantial current changes indicative of electrode deactivation and the establishment of a fouling layer. In Figure IV.3, a schematic diagram depicts the stepwise process employed to determine the square wave potential signal.

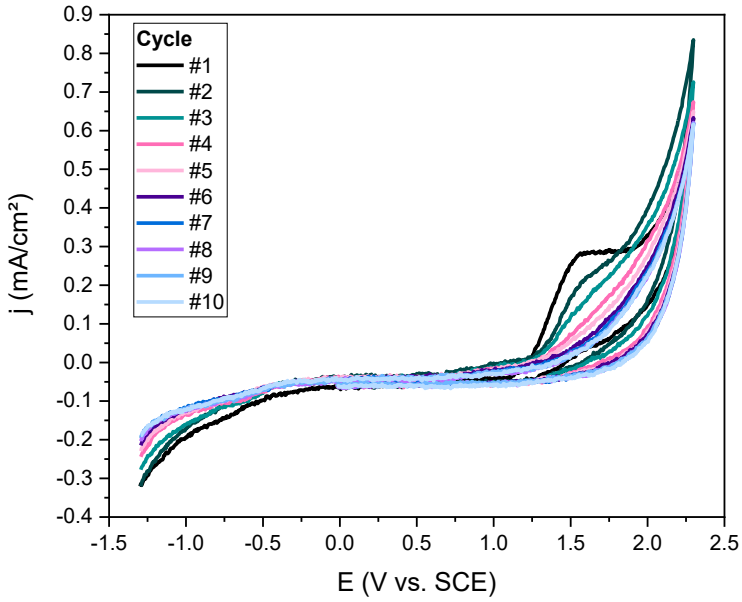

Figure IV.2. Cyclic voltammograms of the BDD electrode after 10 cycles in a 0.1 M Na_2SO_4 solution containing 1 mM phenol (Scan Rate: 100 mV/s).

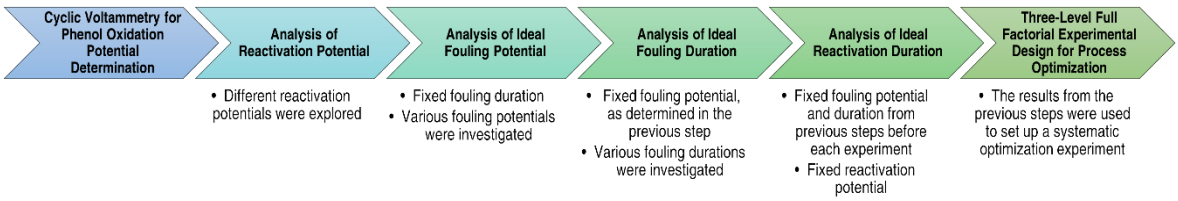

Figure IV.3. Schematic representation of the stepwise process for determining the square wave potential signal.

To elucidate the electrode reactivation process and aid in determining the reactivation time, chronoamperometric assays were conducted at various potentials (from 2.5 to 10V/SCE) for 5 minutes. Figure IV.4 depicts the initial 40 seconds of these assays at applied potentials of 2.5, 4.0, and 8.0 V/SCE. Upon careful examination of the current-time profiles, we noticed cyclic changes in current for potentials above 4 V/SCE, with the frequency of these cycles rising in parallel with the increasing potential. The 8 V/SCE potential was chosen to achieve rapid BDD reactivation, well above the region associated with water stability. This facilitates the generation of abundant electrogenerated hydroxyl radicals and oxygen bubbles capable of detaching the fouling layer from the BDD surface (16, 18). Additionally, the selection of an 8 V/SCE potential took into account the equipment's limitations under maximum operating conditions, as we experienced potentiostat overload in some longer experiments when applying higher potentials. After analyzing the selected reactivation potential, it was determined that this cyclic pattern possessed a duration of approximately 10 seconds, which could be the ideal reactivation duration.

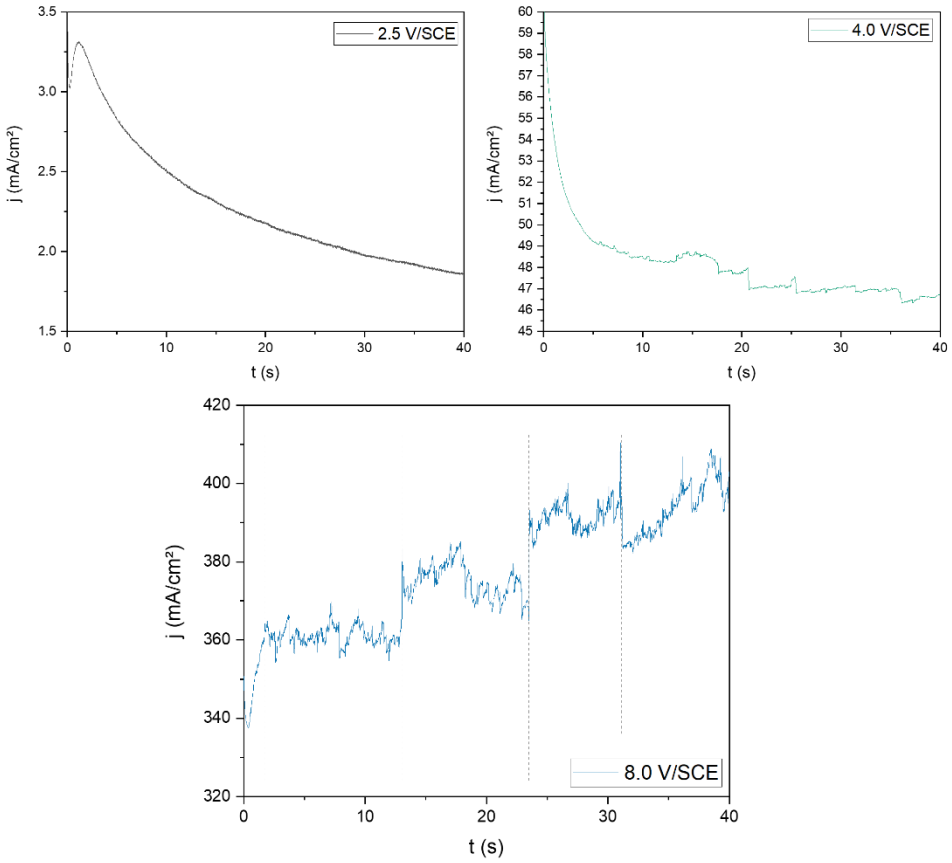

Figure IV.4. Chronoamperometric responses of the BDD electrode at 2.5, 4.0 and 8.0 V/SCE applied potentials.

Observing the cyclic voltammograms (Figure IV.2) prompted several investigations employing LSV to determine the most suitable fouling potential for rapid electrode deactivation. Chronoamperometry was conducted to induce fouling of the electrodes at each analyzed potential for a duration of 12 s. This duration was determined based on preliminary studies of the fouling process, in which we verified that this time was sufficient to observe changes in the LSV response for analyzing the fouling process. Potentials ranging from 0 to 10 V/SCE were tested, emphasizing potentials proximate to the peak at approximately 1.55 V/SCE, as identified in the voltammograms. Subsequently, LSV analyses were conducted to assess the reduction in current corresponding to this peak. Three trials were conducted for each potential, and between each analysis, electrode reactivations were carried out by applying 10 V/SCE for 60 seconds in a 0.1 M Na_2SO_4 electrolyte solution without phenol using Chronoamperometry. The averaged results of the triplicate responses for each fouling potential are presented in Figure IV.5. Upon careful analysis, it was observed that the lowest currents were attained when potentials ranging from 1.7 to 1.8 V/SCE were applied. Considering the primary objective of minimizing energy consumption within the electrochemical water treatment process, the potential of 1.7 V/SCE was chosen for the fouling plateau in the square wave pattern.

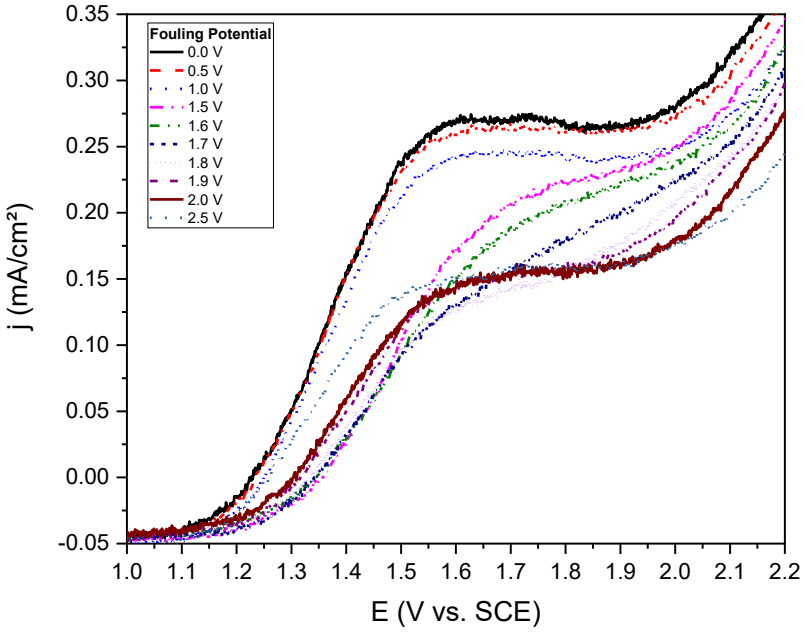

Figure IV.5. Linear sweep voltammogram of the BDD electrode to determine the optimal potential for the fouling phase (Scan Rate: 100 mV/s).

Subsequently, to conclude the determination of parameters corresponding to the fouling plateau in the square wave pattern, further experiments were conducted using LSV to determine the optimal duration of the fouling step. Similarly to the procedure for determining the fouling potential, triplicate trials were performed for each forced fouling duration. Forced fouling was executed through chronoamperometry by applying the previously established 1.7 V/SCE potential for varying durations. The electrode reactivation procedure between each analysis remained consistent (applying 10 V for 60 seconds in 0.1 M Na_2SO_4 without phenol). The outcomes are depicted in Figure IV.6. Upon analyzing the lowest currents corresponding to the 1.55 V/SCE peak, it was observed that the ideal fouling duration fell between 10 and 12 seconds, effectively maximizing electrode deactivation. Additionally, a minor increase in current was noted beyond 13 seconds, suggesting a concurrent reactivation of the electrode surface.

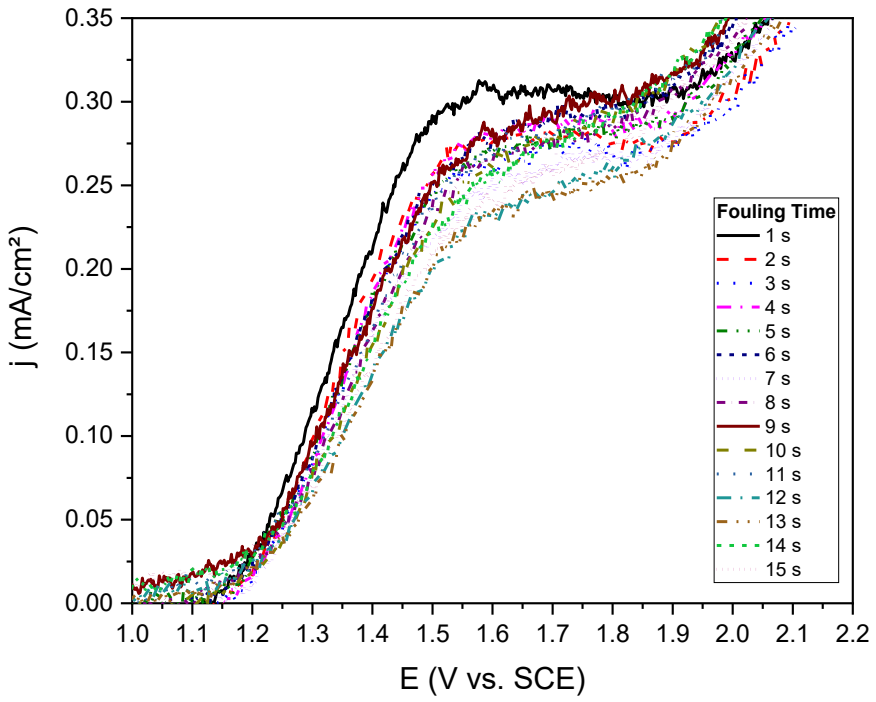

Figure IV.6. Linear sweep voltammogram of the BDD electrode to determine the appropriate fouling duration (Scan Rate: 100 mV/s).

A strategy analogous to the fouling process was employed to determine the parameters of the BDD reactivation plateau. LSV was once again utilized to determine the optimal

reactivation duration. The trials were conducted in triplicate. Each measurement comprised four sequential steps: firstly, chronoamperometry was employed to induce forced fouling by applying 1.7 V/SCE for 12 seconds, followed by reactivation using the analyzed reactivation duration. Subsequently, LSV was conducted to determine the current at 1.55 V/SCE. Finally, another reactivation step was executed by applying 10 V/SCE for 60 seconds in an electrolyte solution of 0.1 M Na_2SO_4 without phenol to ensure a clean surface for the subsequent trial. The LSV results for the electrode reactivation times are presented in Figure IV.7. The time yielding the highest current was 4 seconds, while the lowest was 20 seconds. The gradual decrease in current observed up to 20 seconds, followed by a subsequent increase from 25 seconds onwards, suggests the concurrent nature of fouling and reactivation processes again, even under significantly elevated applied potentials such as 8 V/SCE. This observation emphasizes that the complex interplay between these two processes may persist despite the energetic conditions set by the high applied potential.

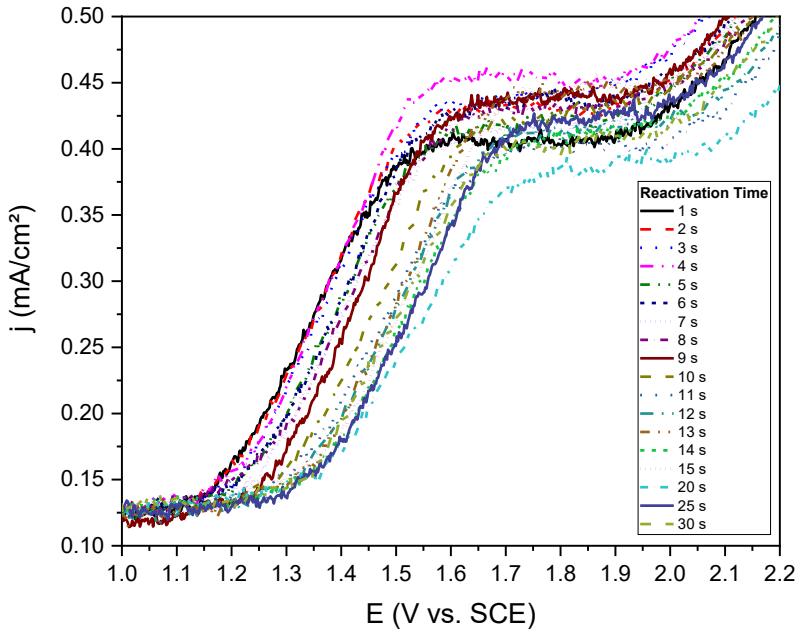

Figure IV.7. Linear sweep voltammogram of the BDD electrode to determine the optimal reactivation duration (Scan Rate: 100 mV/s).

To clarify any doubts regarding the optimal times for each step in defining the square wave pattern, a three-level (3^2) full factorial experimental design was constructed. This design encompassed the fouling and reactivation times as analyzed factors, each with three levels. This approach was also adopted to verify the energy efficiency associated with each factor.

For instance, it aimed to determine whether achieving maximum fouling and reactivation at each step yielded the most energy-efficient outcome or if a balance involving partial processes (e.g., shorter times at each step) resulted in lower energy consumption. Thus, the three-level full factorial design presented in Table IV.1 was formulated, considering fouling times of 2, 6, and 12 seconds and reactivation times of 2, 6, and 10 seconds. This systematic experimental approach aimed to provide insights into the optimal times for the fouling and reactivation steps to achieve both efficient phenol degradation and energy usage in the electrochemical water treatment process.

Table IV.1. Three-level full factorial experimental design detailing the combinations of fouling and reactivation durations based on linear sweep voltammetry and Chronoamperometry analyses.

Experiment	Fouling [1.7 V/SCE] (s)	Reactivation [8 V/SCE] (s)
L1	2	2
L2	2	6
L3	2	10
L4	6	2
L5	6	6
L6	6	10
L7	12	2
L8	12	6
L9	12	10

Electrooxidation assays were conducted based on the experimental configurations designed in the factorial matrix. After each process, the solutions underwent UV-vis spectroscopic analysis to assess the remaining quantity of phenol in the solution. The spectroscopic results are depicted in Figure IV.8. The distinctive peaks at 269 nm highlight the variations in phenol concentration achieved through different experimental conditions. Configurations 3, 5, and 9 notably exhibited the most pronounced reduction in the peak corresponding to phenol after 1 hour of treatment. These outcomes underscore the effectiveness of these settings in facilitating significant phenol degradation.

For comparison, a conventional anodic oxidation assay was conducted by applying 8 V/SCE for 1 hour. To discern the configuration yielding superior energy efficiency, the consumption for each assay was calculated by applying Eq. IV.1:

$$EC_{phenol}\,[Wh\ kg_{phenol}{}^{-1}] = \frac{EjAt}{V\,\Delta C_{phenol}} \qquad \textbf{Eq. IV.1}$$

Where E represents the applied potential (V), while j stands for the applied current density (A m^{-2}). A denotes the electrode's geometric area (m^2), and t signifies the duration of electrolysis (h). V indicates the electrolyte volume (L), and ΔC_{phenol} represents the total decrease in phenol concentration within the solution ($kg_{phenol}\ L^{-1}$).

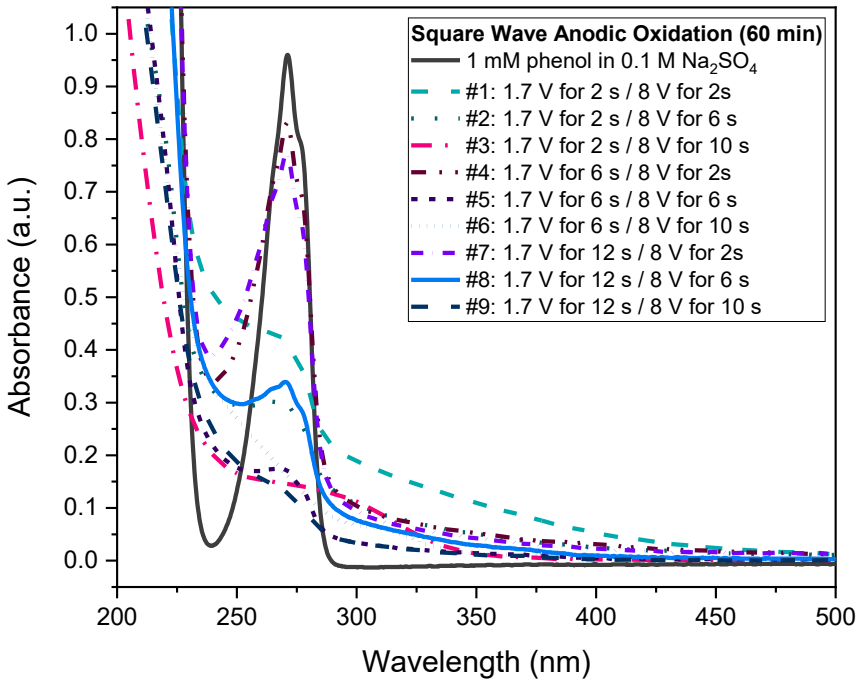

Figure IV.8. UV-Vis spectroscopy results depict phenol concentration after 60 minutes of each square wave pattern experiment.

The amount of phenol removed from the solution and the energy consumption for each assay are presented in Table IV.2. The condition exhibiting the lowest energy consumption in combination with the highest phenol removal was the L9 configuration, characterized by a fouling step at 1.7 V/SCE applied for 12 seconds, and a reactivation step involving 8 V/SCE applied for 10 seconds. In comparison to the continuous application of 8 V/SCE for 1 hour, the L9 condition demonstrated superior phenol removal from the solution with an average energy consumption that was 4.2 times lower.

We conducted a multivariable optimization of the experimental outcomes derived from the three-level full factorial design using the Minitab® software (19), and the findings are showcased in Figure IV.9. Our primary objective was to maximize phenol removal while minimizing energy consumption. The optimization process identified an optimal fouling duration of 12 seconds and a subsequent reactivation period of 10 seconds, resulting in predicted simulation values of 81.99% for phenol removal and 51.02 kWh/kg_{Phenol} for energy consumption. These predicted values closely align with the optimized parameters obtained directly from experimental observations. The predicted simulation values exhibited a minimal deviation from the experimental results, with errors of 7% for phenol removal and 2% for energy consumption. The multivariate analysis also reveals that the poorest outcomes are achieved when fouling and reactivation times are set to 2 seconds.

Table IV.2. Comparative results of phenol degradation experiments, indicating both phenol removal efficiency and energy consumption for each approach.

Experiment	Fouling [1.7 V/SCE] (s)	Reactivation [8 V/SCE] (s)	Phenol Removed (%)	Energy Consumption (kWh/kg_{Phenol})
L1	2	2	60.24%	73.93
L2	2	6	72.70%	144.49
L3	2	10	88.19%	145.81
L4	6	2	19.04%	76.27
L5	6	6	85.55%	54.81
L6	6	10	85.15%	79.28
L7	12	2	25.02%	24.12
L8	12	6	68.85%	30.10
L9 (Avg.)*	12	10	88.21%	50.01
Continuous Anodic Oxidation	-	3600	83.23%	209.49

** The L9 experiment was performed in triplicate to ensure the results' robustness and reliability.*

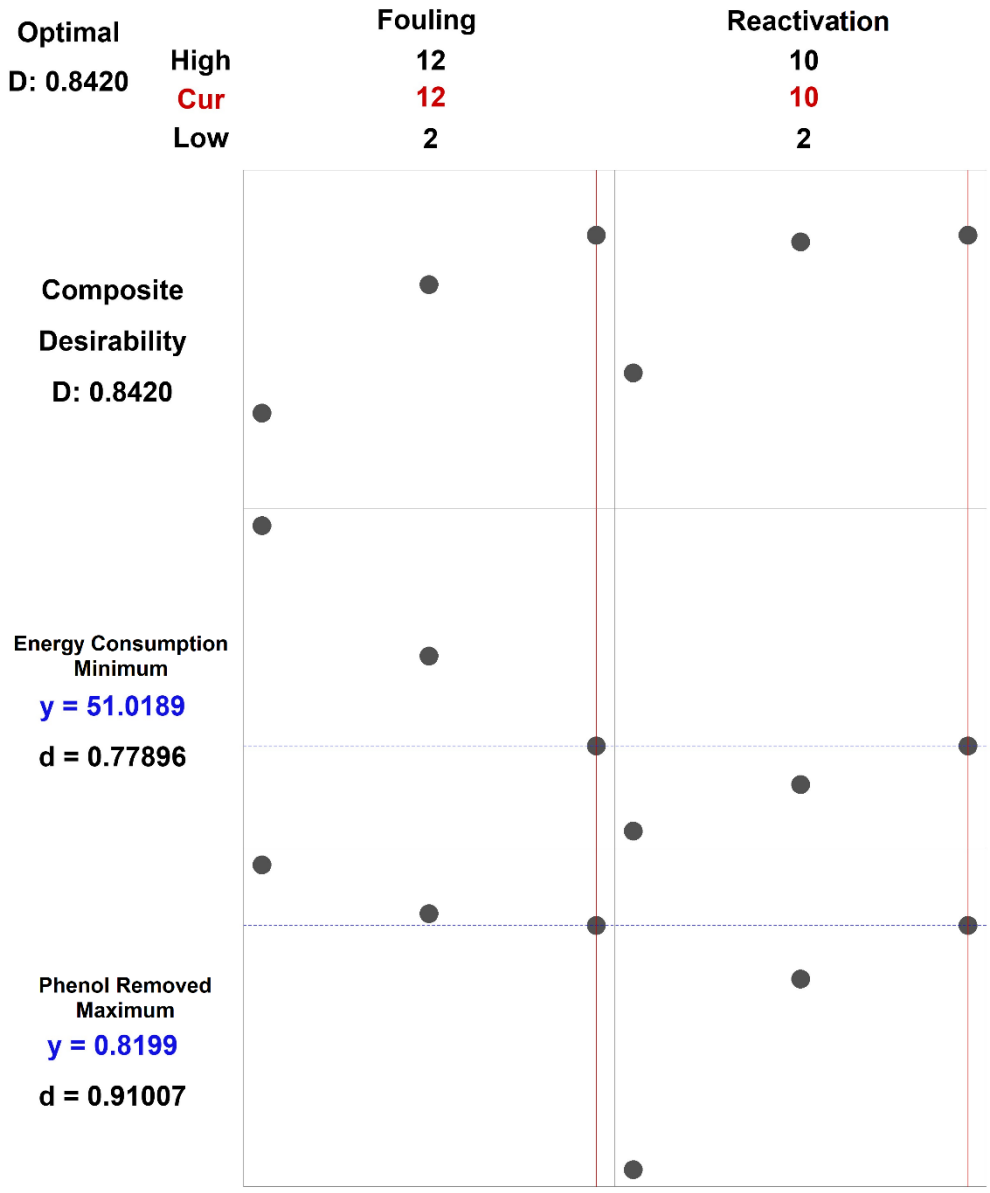

Figure IV.9. Predicted Outcomes from Multivariate Optimization of the Three-Level Full Factorial Experimental Design.

Figure IV.10 provides a comparison of the phenol degradation progression every 15 minutes during the L9 assay in comparison to the continuous process. These results underscore the substantial efficiency of the L9 configuration, which not only enhances phenol removal but also significantly reduces energy consumption compared to the continuous process. While continuous anodic oxidation required 209.49 kWh/kg_{Phenol} for an

83.23% phenol removal rate, the L9 configuration achieved an 88.21% removal with an energy consumption of only 50.01 kWh/kg_{Phenol}.

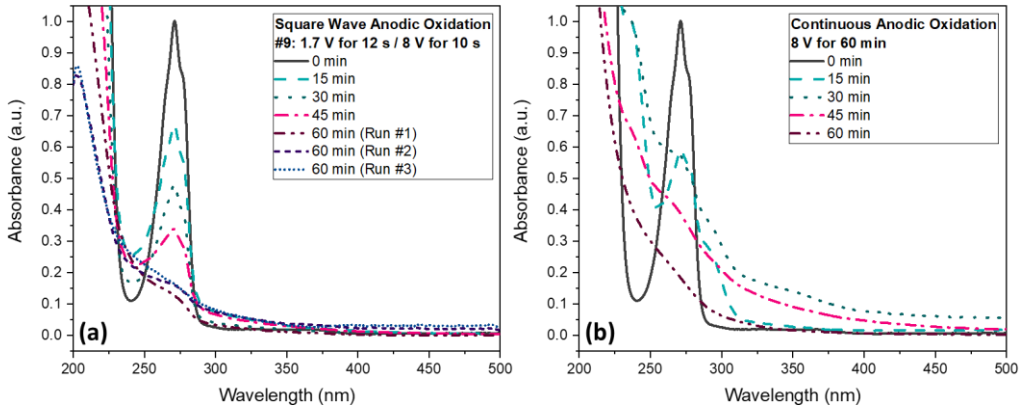

Figure IV.10. UV-Vis spectroscopy comparison illustrating the phenol degradation progression over a 1-hour duration in two distinct assays. (a) Phenol degradation using the optimized conditions of the novel square wave anodic oxidation approach (fouling: 1.7V, 12s; reactivation: 8V, 10s). (b) Phenol degradation through conventional continuous anodic oxidation at 8V.

The UV-Vis spectroscopy curves of the L9 process exhibit a monotonic reduction in the 269 nm peak up to 45 minutes. On the other hand, the curves of the continuous process display substantial baseline variation, indicating the possible presence of undesired phenol byproducts in the solution. The lower presence of intermediate compounds in the square wave anodic oxidation approach may indicate that the phenol oxidation mechanism in the two studied processes is distinct. This reinforces the significance of employing the square wave anodic oxidation process. The consistent decline of the peak in the L9 process highlights its efficacy in achieving phenol degradation with a less pronounced generation of undesirable byproducts. A final representation of the optimized square wave pattern, designed to substantially reduce energy consumption in the electrochemical oxidation of phenol using BDD electrodes, is presented in Figure IV.11. This illustration encapsulates the culmination of the study's efforts in achieving an effective and energy-efficient electrochemical water treatment approach for phenol degradation.

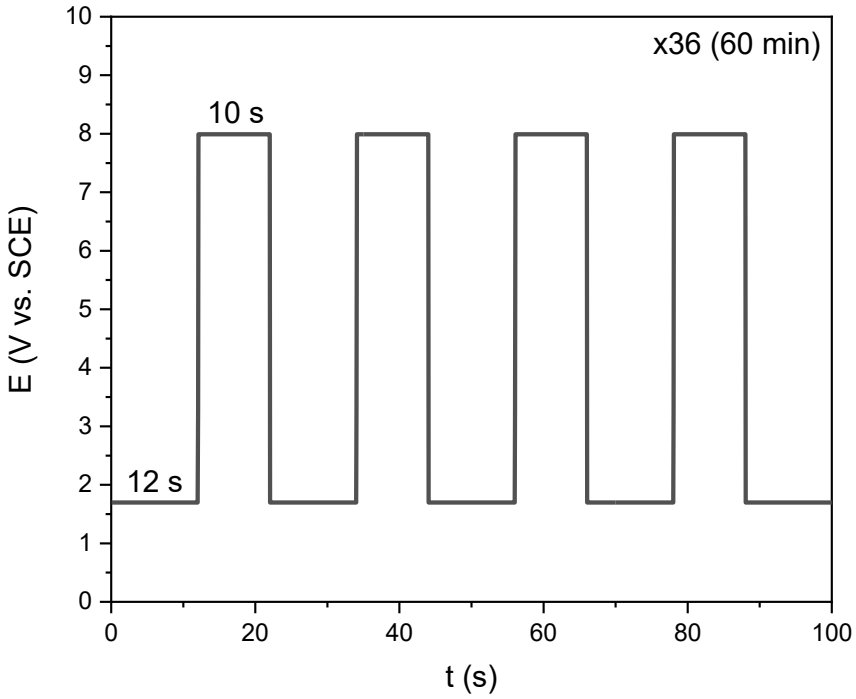

Figure IV.11. Optimized square wave cycle illustrating the innovative approach aimed at enhancing the energy-efficient phenol degradation process.

The results of this study support the proposed hypothesis aimed at enhancing energy efficiency through the cyclic application of rapid fouling and subsequent reactivation of BDD electrodes using a two-step square wave pattern. The experimental evidence presented here suggests that the accumulation of phenolic compounds on the BDD electrode surface, coupled with the application of elevated potentials for detachment and oxidation of the formed polymeric layer, indeed leads to accelerated mineralization of phenol and a substantial reduction in energy consumption. However, further investigations are warranted to gain a deeper understanding of the underlying mechanisms that make this approach more efficient than the continuous process. Future studies should delve into the intricacies of the electrochemical and chemical interactions taking place during the cyclic fouling and reactivation steps and explore how these interactions contribute to the observed outcomes. Such efforts would refine our understanding of the phenomenon and potentially unlock opportunities to optimize and extend the applicability of this novel approach to other persistent pollutants in water treatment processes. Optimal frequencies and duty cycles of the square wave pattern derive from a delicate balance between electrochemical processes and temporal dynamics at the surface. The right fouling potential efficiently deactivates the

electrode, while a carefully chosen fouling time avoids saturation of the fouling layer, which would lead to lower process efficiency. Optimal reactivation times maximize target compound degradation while managing energy consumption. By refining the techniques and principles established in this study, there is a promising avenue to address diverse water contaminants more rapidly and efficiently, aligning with the broader goal of achieving more sustainable and effective environmental remediation strategies.

V.1.4. Conclusion

This study introduces an innovative approach to enhance the energy efficiency of electrochemical water treatment processes, with a specific focus on phenolic compound degradation. The strategy involves cyclic fouling and reactivation sequences applied to boron-doped diamond electrodes using a two-step square wave pattern. The goal was to accelerate the conversion of phenol into more easily degradable forms by leveraging fouling and subsequent reactivation, resulting in rapid phenol elimination from the solution.

By exploiting on the interplay between fouling and reactivation, the proposed approach demonstrated significant potential to enhance energy efficiency while achieving superior phenol removal levels, offering a promising avenue for sustainable solutions. The novel square wave anodic oxidation technique demonstrated exceptional phenol removal efficiency, requiring only 50.01 kWh/kg_{Phenol} for an 88.21% removal rate. In contrast, continuous anodic oxidation consumed 209.49 kWh/kg_{Phenol} to achieve an 83.23% removal rate. Consequently, the novel square wave anodic oxidation technique consumes more than four times less energy compared to conventional anodic oxidation.

Optimized frequency and duty cycles derived from a comprehensive three-level full factorial experimental design and multivariate optimization yielded predicted values closely aligning with experimental outcomes. While this study has made significant strides in establishing the efficacy of the proposed approach, further research is required to delve deeper into the underlying mechanisms that contribute to its enhanced performance. Investigating the electrochemical and chemical interactions occurring during the fouling and reactivation steps will provide valuable insights into the precise processes driving the observed outcomes. These insights will not only advance our understanding of the phenomenon but also pave the way for this approach's optimization and potential extension to address a wider range of persistent pollutants in water treatment. Future research is also required to explore the scalability of this approach under industrial and environmental contexts.

In conclusion, this study underscores the novel approach's effectiveness in achieving phenol degradation while addressing energy efficiency concerns, contributing to sustainable water treatment methods.

.

V.1.5. References

1. William WA, Messai AM, Penny PG. Phenolic Compounds in Water: Sources, Reactivity, Toxicity and Treatment Methods. In: Marcos S-H, Mariana P-T, Maria del Rosario G-M, editors. Phenolic Compounds. Rijeka: IntechOpen; 2017. p. Ch. 17.

2. Rahman MM, Rahaman MS, Islam MR, Rahman F, Mithi FM, Alqahtani T, *et al.* Role of Phenolic Compounds in Human Disease: Current Knowledge and Future Prospects. Molecules. 2021;27(1).

3. Panigrahy N, Priyadarshini A, Sahoo MM, Verma AK, Daverey A, Sahoo NK. A comprehensive review on eco-toxicity and biodegradation of phenolics: Recent progress and future outlook. Environ Technol Inno. 2022;27.

4. Bruce RM, Santodonato J, Neal MW. Summary review of the health effects associated with phenol. Toxicol Ind Health. 1987;3(4):535-68.

5. Brosler P, Girão AV, Silva RF, Tedim J, Oliveira FJ. Electrochemical Advanced Oxidation Processes Using Diamond Technology: A Critical Review. Environments. 2023;10(2).

6. Brosler P, Girão AV, Silva RF, Tedim J, Oliveira FJ. In-house vs. commercial boron-doped diamond electrodes for electrochemical degradation of water pollutants: A critical review. Front Mater. 2023;10.

7. Moradi M, Vasseghian Y, Khataee A, Kobya M, Arabzade H, Dragoi E-N. Service life and stability of electrodes applied in electrochemical advanced oxidation processes: A comprehensive review. J Ind Eng Chem. 2020;87:18-39.

8. Liu X, You S, Ma F, Zhou H. Characterization of electrode fouling during electrochemical oxidation of phenolic pollutant. Frontiers of Environmental Science & Engineering. 2020;15(4).

9. Gattrell M, Kirk DW. The electrochemical oxidation of aqueous phenol at a glassy carbon electrode. The Canadian Journal of Chemical Engineering. 1990;68(6):997-1003.

10. Gattrell M, Kirk DW. A Study of Electrode Passivation during Aqueous Phenol Electrolysis. J Electrochem Soc. 1993;140(4):903-11.

11. Liptak MD, Gross KC, Seybold PG, Feldgus S, Shields GC. Absolute pK(a) determinations for substituted phenols. J Am Chem Soc. 2002;124(22):6421-7.

12. Iniesta J. Electrochemical oxidation of phenol at boron-doped diamond electrode. Electrochim Acta. 2001;46(23):3573-8.

13. Wang Y, Compton RG. An Approach to the Electroanalysis of Electrode Passivating Analytes: The Determination of Phenol. ChemElectroChem. 2020;7(16):3508-16.

14. Zhi J-F, Wang H-B, Nakashima T, Rao TN, Fujishima A. Electrochemical Incineration of Organic Pollutants on Boron-Doped Diamond Electrode. Evidence for Direct Electrochemical Oxidation Pathway. J Phys Chem B. 2003;107(48):13389-95.
15. Rao TN, Loo BH, Sarada BV, Terashima C, Fujishima A. Electrochemical detection of carbamate pesticides at conductive diamond electrodes. Anal Chem. 2002;74(7):1578-83.
16. Panizza M. Electrochemical Detection of 2-Naphthol on Boron-Doped Diamond Influence of Anodic Treatment. Electrochem Solid-State Lett. 1999;3(9).
17. Babai M, Gottesfeld S. Ellipsometric study of the polymeric surface films formed on platinum electrodes by the electrooxidation of phenolic compounds. Surf Sci. 1980;96(1-3):461-75.
18. Kiran R, Scorsone E, de Sanoit J, Arnault J-C, Mailley P, Bergonzo P. Boron Doped Diamond Electrodes for Direct Measurement in Biological Fluids: An In Situ Regeneration Approach. J Electrochem Soc. 2012;160(1):H67-H73.
19. Minitab®. Minitab® Statistical Software. 20.3 ed2021.

Chapter V

Conclusions and Future Perspectives

Concluding this thesis, this chapter offers a summary of its key findings and explores their significance, impact, and potential for future research.

Section V.1 presents the main outcomes of this thesis.

Section V.2 discusses the opportunities for future research.

Section V.3 details how this thesis' results were shared with the scientific community.

V.1. Conclusions

The key findings of this research are outlined in the following points, acknowledging that there are existing limitations to address and various aspects to explore in future investigations.

- Anodic electrooxidation (AO) with boron-doped diamond (BDD) technology offers promise as an eco-friendly electrochemical advanced oxidation process (EAOP) for water treatment. The primary advantage of AO is its sole reliance on electrical current input. When synergistically paired with BDD technology, EAOPs demonstrate remarkable efficiency in the degradation and mineralization of pollutants. Moreover, the incorporation of Fenton-based processes and add-ons such as persulfate radicals, electrogenerated ozone, and photocatalysis can enhance the AO process using BDD technology. However, the integration of these techniques may introduce heightened complexity and costs, particularly when implemented on a larger scale.
- Comparing BDD electrodes produced by different sources for water treatment poses challenges due to variations in their physicochemical characteristics, deposition conditions, and experimental methods used for their characterization and performance evaluation. The lack of essential information makes it impossible to perform accurate comparisons. To address this issue, a figure-of-merit equation proposed in Section I.2 normalizes BDD degradation results, enabling meaningful comparisons across various experimental conditions.
- There is a pressing need for a standardized procedure, achieved through collaboration between the scientific community and manufacturers, to comprehensively evaluate and compare BDD electrode performance. Establishing a consensus on best practices would not only accelerate development but also facilitate the transition of laboratory-made BDD electrodes to commercial production.
- Data analysis suggests that commercial BDD electrodes tend to consume less energy and exhibit better current efficiency for phenol degradation and landfill leachate treatment. However, the variability in reported operating conditions limits the conclusiveness of these indications. The analysis also hints at the potential for laboratory-made electrodes to match or even surpass the performance of their commercial counterparts with further optimization.

- The Taguchi method was an effective tool for optimizing BDD film deposition conditions in a laboratory-made HFCVD reactor, reducing the number of required experimental trials and enhancing efficiency. Detailed analysis explored the impact of gas composition and total gas pressure on various BDD film properties and electrochemical activity. Ideal conditions were identified for diamond quality, film resistivity, grain size, residual stress, electrochemical potential window, double-layer capacitance, and electron transfer efficiency. These findings provided a practical guide for maximizing BDD electrode performance.
- Si_3N_4-TiN composites demonstrate superior mechanical and electrical properties compared to the dielectric Si_3N_4 matrix without TiN.
- Si_3N_4-TiN composites, when used as substrates for diamond electrode deposition, offer enhanced compatibility for CVD diamond growth, mechanical strength, and chemical resistance, compared to conventional substrate materials like Si, Ti, Nb, and Ta.
- The successful growth of conductive diamond films on electroconductive Si_3N_4-TiN substrates containing 30%vol. TiN shows promise for practical diamond electrode production.
- Using an electroconductive ceramic composite of Si_3N_4-TiN as a substrate for BDD electrodes effectively prevents electrode failure due to BDD delamination. The BDD/Si_3N_4-TiN electrode demonstrated exceptional durability, withstanding over 2016 hours of an accelerated life test in aggressive conditions without film delamination. The extended lifespan of these electrodes represents a promising path towards large-scale sustainable water treatment. While BDD electrodes come with a high initial cost, their extended lifespan justifies the initial investment.
- The BDD/Si_3N_4-TiN electrode showed lower energy consumption compared to average reported results, while maintaining comparable degradation rates and current efficiency values to other BDD electrodes in similar experimental conditions.
- The investigation into plasma-modified BDD electrodes for water pollutant degradation highlights the superior performance of as-grown BDD electrodes compared to their plasma-treated counterparts, primarily attributed to their enhanced surface conductivity associated with hydrogen termination. As-grown BDD electrodes demonstrate remarkable efficiency in phenol and COD removal, underscoring their effectiveness in pollutant degradation. This study underscores the critical role of surface termination in electrode efficiency, with CF_4 treatment showing promise, potentially due to reduced fouling effects. These findings offer

valuable insights into BDD electrode behavior in degrading organic pollutants and emphasize the importance of considering electrode surface characteristics when optimizing electrooxidation processes.

- The innovative approach involving cyclic fouling and reactivation sequences applied to BDD electrodes aimed to enhance energy efficiency while achieving superior removal of pollutants, specifically targeting phenolic compounds. The square wave anodic oxidation technique exhibited remarkable efficiency, requiring only 50.01 kWh/kg_{Phenol} to achieve an impressive 88.21% phenol removal rate in one hour of electrooxidation—more than four times less than the 209.49 kWh/kg_{Phenol} consumed by continuous anodic oxidation to attain an 83.23% phenol removal rate. In addition to the reduced energy consumption, this novel method offers a substantial reduction in the time required for pollutant degradation when we compare the results obtained in Section III.1, where 274.8 kWh/kg_{Phenol} of energy consumption was required to eliminate 80.7% of phenol in 3 hours, and Section III.2, which the as-grown BDD demonstrated 242.0 kWh/kg_{Phenol} of energy consumption to eliminate 91.1% of phenol within the same 3-hour timeframe. Systematic exploration of fouling and reactivation mechanisms of BDD electrodes showcases the substantial potential of this approach for enhancing energy efficiency and achieving superior pollutant removal from wastewater. Such achievements reduce the limitations of EAOPs using BDD technology for water treatment in terms of associated costs due to high energy consumption, bringing practical application of the technology closer to large-scale implementation.

V.2. Recommendations for future work

Several avenues for future research and exploration emerge from the findings and limitations identified throughout this thesis. Recommendations for future research are outlined in the following points.

- The exploration of anodic oxidation add-ons to BDD technology, such as persulfate radicals, electrogenerated ozone, photocatalysis, and Fenton-based processes has revealed their potential to improve electrooxidation processes. Future studies can delve deeper into optimizing these add-ons, exploring their effectiveness with different types of wastewaters, and assessing their long-term cost-effectiveness.
- The proposal of a figure-of-merit equation for normalizing BDD degradation results is a significant step towards comparing the electrooxidation performance of different electrodes. Further research should focus on developing a standardized procedure for evaluating and comparing BDD electrodes, considering various contaminants and types of wastewaters, experimental conditions, and electrode characteristics.
- The synthesis of Si_3N_4-TiN composites as electroconductive ceramic substrates for HFCVD deposition of diamond electrodes shows promise. Future work should explore their performance with different diamond film deposition techniques and assess their scalability for practical applications.
- The use of the Taguchi method to optimize BDD film deposition conditions has offered valuable insights. Future research should consider exploring variations in reactor designs and configurations.
- BDD/Si_3N_4-TiN electrodes have demonstrated their potential for sustainable water treatment. Although these findings are promising, comprehensive research is needed to optimize treatment conditions, assess their performance across diverse pollutants and real wastewater scenarios. Furthermore, future research should conduct standardized comparisons with BDD electrodes deposited over other substrate materials, as well as comprehensive sustainability analyses, considering factors such as economic feasibility, environmental impact, and energy efficiency when scaling up these electrodes for large-scale water treatment.
- Although as-grown BDD electrodes showed superior performance compared to their plasma-treated counterparts, further research is necessary to explore optimal plasma treatment conditions, including varying parameters such as treatment time and plasma power.

- The innovative approach introduced involving cyclic fouling and reactivation sequences for BDD electrodes shows potential in enhancing energy efficiency in phenolic compound degradation. Further studies should investigate the underlying mechanisms driving this approach, extend its applicability to a wider range of persistent pollutants, and assess its scalability for industrial and environmental contexts.
- Considering the potential for improving energy efficiency in water treatment, future work should explore the integration of renewable energy sources such as wind, tidal, or solar power to power electrochemical processes. This could lead to self-sufficient and sustainable water treatment systems.

V.3. Thesis outputs and dissemination

V.3.1. Publications included as thesis sections

- P. Brosler, M.A. Neto, R.F. Silva, J. Tedim, F.J. Oliveira, “Customized boron-doped diamond electrodes for efficient water treatment via HF-CVD parameter optimization”, Diamond and Related Materials, 2024.
- P. Brosler, R. F. Silva, J. Tedim, and F. J. Oliveira, “Electroconductive silicon nitride-titanium nitride ceramic substrates for CVD diamond electrode deposition”, Ceramics International, 2023, doi: 10.1016/j.ceramint.2023.08.327.
- P. Brosler, A. V. Girão, R. F. Silva, J. Tedim, and F. J. Oliveira, "In-house vs. commercial boron-doped diamond electrodes for electrochemical degradation of water pollutants: A critical review" Frontiers in Materials, vol. 10, 2023, doi: 10.3389/fmats.2023.1020649.
- P. Brosler, A. V. Girão, R. F. Silva, J. Tedim, and F. J. Oliveira, "Electrochemical Advanced Oxidation Processes Using Diamond Technology: A Critical Review," Environments, vol. 10, no. 2, 2023, doi: 10.3390/environments10020015.

V.3.2. Oral presentations

- Brosler, P., Silva, R. F., Tedim J., Oliveira, F. J. (2023, July). Surface Modification of Boron-Doped Diamond Electrodes for Water Treatment using Plasma Etching: Experimental Evaluation of the Impacts on Electrochemical Activity. Research Summit 2023.
- Brosler, P., Girão, A. V., Silva, R. F., Tedim J., Oliveira, F. J. (2022, October). In-house vs. commercial boron-doped diamond electrodes for electrochemical degradation of water pollutants. Jornadas CICECO 2022.
- Brosler, P., Sousa, I., Silva, R. F., Tedim J., Oliveira, F. J. (2022, July). Si_3N_4-TiN as a substrate for BDD electrodes: from cutting tools and biomedical applications to water treatment. Research Summit 2022.
- Brosler, P., Tedim, J., Oliveira, F. J. (2021, Junho). Electroactive diamond surfaces for the removal of pollutants from wastewaters of the Petrochemical industry. Research Summit 2021.

V.3.3. Poster presentations

- Brosler, P., Sousa, I., H. Nadais, Silva, R. F., Tedim J., Oliveira, F. J. (2023, July). Electroconductive silicon nitride ceramic: a novel substrate material for BDD electrodes for water remediation. Jornadas CICECO 2023.
- Brosler, P., Sousa, I., Silva, H. Nadais, R. F., Tedim J., Oliveira, F. J. (2023, July). Electroconductive silicon nitride ceramic: a novel substrate material for BDD electrodes for water remediation. Ciência 2023.
- Brosler, P., Sousa, I., H. Nadais, Silva, R. F., Tedim J., Oliveira, F. J. (2023, April). Electroconductive silicon nitride ceramic: a novel substrate material for BDD electrodes for water remediation. Materiais 2023 – XXI Congresso da Sociedade Portuguesa de Materiais and XII International Symposium on Materials.
- Brosler, P., Sousa, I., Silva, R. F., Tedim J., Oliveira, F. J. (2022, July). Si_3N_4-TiN as a substrate for BDD electrodes: from cutting tools and biomedical applications to water treatment. Junior EUROMAT 2022.
- Brosler, P., Mennucci, M. M., Silva, R. F., Tedim J., Oliveira, F. J. (2021, October). Characterization of BDD electrodes deposited over Si_3N_4-based substrates for refinery wastewater treatment. Jornadas CICECO 2021.
- Brosler, P., Mennucci, M. M., Neto, M., Silva, R. F., Tedim J., Oliveira, F. J. (2020, November). The impact of substrate surface finish on the performance of BDD electrodes deposited over Si_3N_4-TiN substrates for water treatment applications. Jornadas CICECO 2020.
- Brosler, P., Sharma, D. K., Neto, M., Silva, R. F., Tedim J., Oliveira, F. J. (2019, June). Optimization of HFCVD boron-doped diamond deposition parameters using the Taguchi method. Jornadas CICECO 2019.